

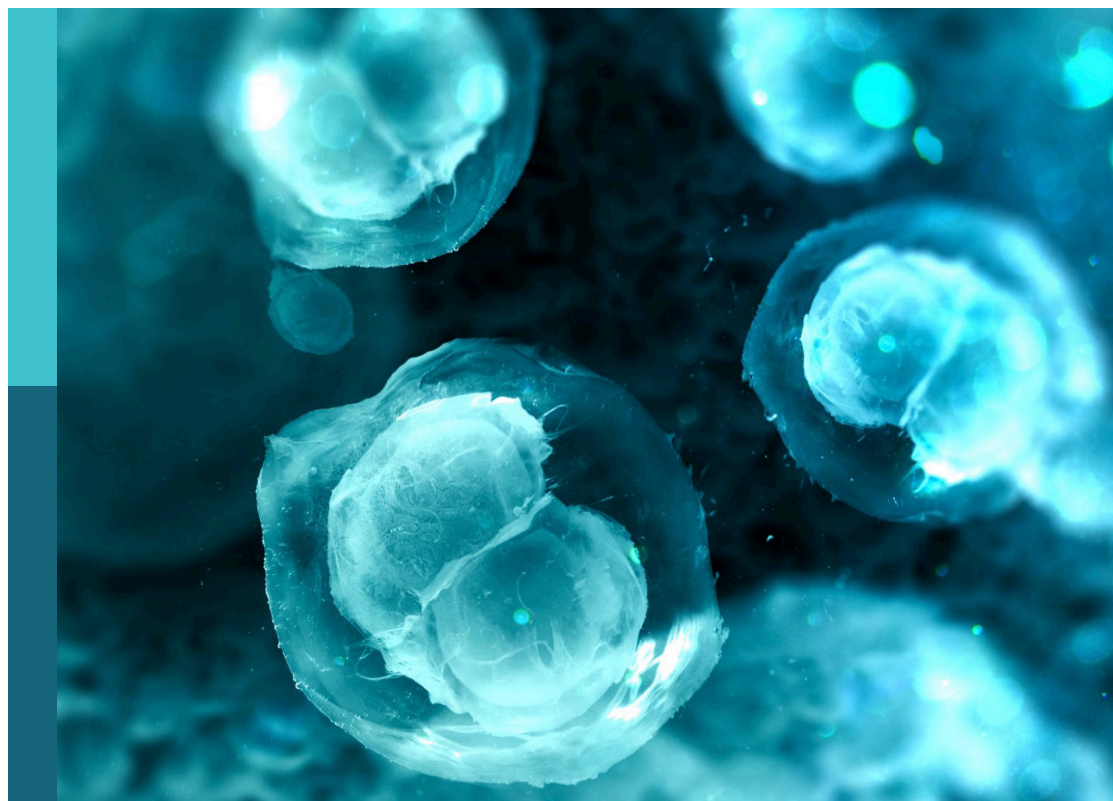
Early animal development: From fertilization to gastrulation

Edited by

Silvia L. López, Maria Cecilia Cirio and Silvia Garagna

Published in

Frontiers in Cell and Developmental Biology



FRONTIERS EBOOK COPYRIGHT STATEMENT

The copyright in the text of individual articles in this ebook is the property of their respective authors or their respective institutions or funders. The copyright in graphics and images within each article may be subject to copyright of other parties. In both cases this is subject to a license granted to Frontiers.

The compilation of articles constituting this ebook is the property of Frontiers.

Each article within this ebook, and the ebook itself, are published under the most recent version of the Creative Commons CC-BY licence. The version current at the date of publication of this ebook is CC-BY 4.0. If the CC-BY licence is updated, the licence granted by Frontiers is automatically updated to the new version.

When exercising any right under the CC-BY licence, Frontiers must be attributed as the original publisher of the article or ebook, as applicable.

Authors have the responsibility of ensuring that any graphics or other materials which are the property of others may be included in the CC-BY licence, but this should be checked before relying on the CC-BY licence to reproduce those materials. Any copyright notices relating to those materials must be complied with.

Copyright and source acknowledgement notices may not be removed and must be displayed in any copy, derivative work or partial copy which includes the elements in question.

All copyright, and all rights therein, are protected by national and international copyright laws. The above represents a summary only. For further information please read Frontiers' Conditions for Website Use and Copyright Statement, and the applicable CC-BY licence.

ISSN 1664-8714
ISBN 978-2-83251-640-9
DOI 10.3389/978-2-83251-640-9

About Frontiers

Frontiers is more than just an open access publisher of scholarly articles: it is a pioneering approach to the world of academia, radically improving the way scholarly research is managed. The grand vision of Frontiers is a world where all people have an equal opportunity to seek, share and generate knowledge. Frontiers provides immediate and permanent online open access to all its publications, but this alone is not enough to realize our grand goals.

Frontiers journal series

The Frontiers journal series is a multi-tier and interdisciplinary set of open-access, online journals, promising a paradigm shift from the current review, selection and dissemination processes in academic publishing. All Frontiers journals are driven by researchers for researchers; therefore, they constitute a service to the scholarly community. At the same time, the *Frontiers journal series* operates on a revolutionary invention, the tiered publishing system, initially addressing specific communities of scholars, and gradually climbing up to broader public understanding, thus serving the interests of the lay society, too.

Dedication to quality

Each Frontiers article is a landmark of the highest quality, thanks to genuinely collaborative interactions between authors and review editors, who include some of the world's best academicians. Research must be certified by peers before entering a stream of knowledge that may eventually reach the public - and shape society; therefore, Frontiers only applies the most rigorous and unbiased reviews. Frontiers revolutionizes research publishing by freely delivering the most outstanding research, evaluated with no bias from both the academic and social point of view. By applying the most advanced information technologies, Frontiers is catapulting scholarly publishing into a new generation.

What are Frontiers Research Topics?

Frontiers Research Topics are very popular trademarks of the *Frontiers journals series*: they are collections of at least ten articles, all centered on a particular subject. With their unique mix of varied contributions from Original Research to Review Articles, Frontiers Research Topics unify the most influential researchers, the latest key findings and historical advances in a hot research area.

Find out more on how to host your own Frontiers Research Topic or contribute to one as an author by contacting the Frontiers editorial office: frontiersin.org/about/contact

Early animal development: From fertilization to gastrulation

Topic editors

Silvia L. López — CONICET Instituto de Biología Celular y Neurociencias (IBCN), Argentina

Maria Cecilia Cirio — Institute of Physiology, Molecular Biology and Neurosciences, National Council for Scientific and Technical Research, Argentina

Silvia Garagna — University of Pavia, Italy

Citation

López, S. L., Cirio, M. C., Garagna, S., eds. (2023). *Early animal development: From fertilization to gastrulation*. Lausanne: Frontiers Media SA.
doi: 10.3389/978-2-83251-640-9

Table of contents

- 05 **Editorial: Early animal development: From fertilization to gastrulation**
Silvia L. López, M. Cecilia Cirio and Silvia Garagna
- 07 **Reduced Retinoic Acid Signaling During Gastrulation Induces Developmental Microcephaly**
Michal Gur, Liat Bendelac-Kapon, Yehuda Shabtai, Graciela Pillemer and Abraham Fainsod
- 27 **Retinoic Acid is Required for Normal Morphogenetic Movements During Gastrulation**
Michal Gur, Tamir Edri, Sally A. Moody and Abraham Fainsod
- 44 **Maternal Factors and Nodal Autoregulation Orchestrate *Nodal* Gene Expression for Embryonic Mesendoderm Induction in the Zebrafish**
Cencan Xing, Weimin Shen, Bo Gong, Yaqi Li, Lu Yan and Anming Meng
- 57 **MiR-202-3p determines embryo viability during mid-blastula transition**
Ruiqin Hu, Yanna Xu, Bingshe Han, Yi Chen, Wenhao Li, Guijun Guan, Peng Hu, Yan Zhou, Qianghua Xu and Liangbiao Chen
- 76 **Eomes function is conserved between zebrafish and mouse and controls left-right organiser progenitor gene expression via interlocking feedforward loops**
Conor D. Talbot, Mark D. Walsh, Stephen J. Cutty, Randa Elsayed, Eirini Vlachaki, Ashley E. E. Bruce, Fiona C. Wardle and Andrew C. Nelson
- 94 **Bicaudal-C Post-transcriptional regulator of cell fates and functions**
Megan E. Dowdle, Charlotte R. Kanzler, Cole R. K. Harder, Samuel Moffet, Maya N. Walker and Michael D. Sheets
- 105 **Comparison of RNA localization during oogenesis within *Acipenser ruthenus* and *Xenopus laevis***
Viktoria Iegorova, Ravindra Naraine, Martin Psenicka, Monika Zelazowska and Radek Sindelka
- 121 **Initial characterization of gap phase introduction in every cell cycle of *C. elegans* embryogenesis**
Ming-Kin Wong, Vincy Wing Sze Ho, Xiaotai Huang, Lu-Yan Chan, Dongying Xie, Runsheng Li, Xiaoliang Ren, Guoye Guan, Yiming Ma, Boyi Hu, Hong Yan and Zhongying Zhao

- 138 **Developmental atlas of the indirect-developing sea urchin *Paracentrotus lividus*: From fertilization to juvenile stages**
Laurent Formery, Axel Wakefield, Maeva Gesson, Ludovic Toisoul, Guy Lhomond, Laurent Gilletta, Régis Lasbleiz, Michael Schubert and Jenifer C. Croce
- 178 **Mechano-biochemical marine stimulation of inversion, gastrulation, and endomesoderm specification in multicellular Eukaryota**
Ngoc Minh Nguyen, Tatiana Merle, Florence Broders-Bondon, Anne-Christine Brunet, Aude Battistella, Emelie Britt Linnea Land, Florian Sarron, Aditya Jha, Jean-Luc Gennisson, Eric Röttinger, María Elena Fernández-Sánchez and Emmanuel Farge



OPEN ACCESS

EDITED AND REVIEWED BY

Moises Mallo,
Gulbenkian Institute of Science (IGC),
Portugal

*CORRESPONDENCE

Silvia L. López,
✉ slopez@fmed.uba.ar

SPECIALTY SECTION

This article was submitted to
Morphogenesis and Patterning,
a section of the journal
Frontiers in Cell and Developmental
Biology

RECEIVED 17 January 2023

ACCEPTED 20 January 2023

PUBLISHED 26 January 2023

CITATION

López SL, Cirio MC and Garagna S (2023),
Editorial: Early animal development: From
fertilization to gastrulation.
Front. Cell Dev. Biol. 11:1146778.
doi: 10.3389/fcell.2023.1146778

COPYRIGHT

© 2023 López, Cirio and Garagna. This is
an open-access article distributed under
the terms of the [Creative Commons
Attribution License \(CC BY\)](https://creativecommons.org/licenses/by/4.0/). The use,
distribution or reproduction in other
forums is permitted, provided the original
author(s) and the copyright owner(s) are
credited and that the original publication in
this journal is cited, in accordance with
accepted academic practice. No use,
distribution or reproduction is permitted
which does not comply with these terms.

Editorial: Early animal development: From fertilization to gastrulation

Silvia L. López^{1,2*}, M. Cecilia Cirio³ and Silvia Garagna⁴

¹Universidad de Buenos Aires, Facultad de Medicina, Departamento de Biología Celular e Histología/1° U.A. Departamento de Histología, Embriología, Biología Celular y Genética, Buenos Aires, Argentina,

²CONICET–Universidad de Buenos Aires, Instituto de Biología Celular y Neurociencia “Prof. E. De Robertis” (IBCN), Laboratorio de Embriología Molecular “Prof. Dr. Andrés E. Carrasco”, Buenos Aires, Argentina,

³Instituto de Fisiología, Biología Molecular y Neurociencias, CONICET, Facultad de Ciencias Exactas y Naturales, Universidad de Buenos Aires, Buenos Aires, Argentina, ⁴Dipartimento di Biologia e Biotecnologie “Lazzaro Spallanzani”, Università degli Studi di Pavia, Pavia, Italy

KEYWORDS

oocytes, embryogenesis, nodal signaling, T-box transcription factors, retinoic acid, MicroRNAs, β -catenin, bicaudal-C

Editorial on the Research Topic

Early animal development: From fertilization to gastrulation

One of the most fascinating quests in Biology is deciphering how the totipotent zygote gives rise to an animal with complex organs and systems. Several orchestrated processes must be accomplished before organogenesis. Embryos undergo a critical phase termed Maternal-to-Zygotic Transition (MZT) during which developmental control passes from mother to zygote, when a subset of maternal mRNAs and proteins is eliminated, and zygotic transcription begins. Besides, as cell number increases, cell potency decreases allowing the specification of germ layers (ectoderm, mesoderm, and endoderm), from which all tissues and organs derive. The anterior-posterior and dorsal-ventral axes are defined, setting the body plan's coordinates. Germ layers and body axes assume their definitive spatial arrangement through gastrulation, a crucial process that drives endomesoderm internalization.

This Research Topic aimed to reflect on the recent advances in understanding the early events of embryonic development and provide new perspectives on the subject. Nine original articles and one review explore diverse aspects such as maternal cues, cell cycle regulation, morphogenetic movements, and the role of signaling pathways, transcription factors, microRNAs, and RNA binding proteins during MZT, germ layers and body axes development. The articles represent work on invertebrate and vertebrate organisms, extending to Choanoflagellates, considered the closest living relative to Metazoans.

Taking advantage of the oocyte's animal pigmentation in the amphibian *Xenopus laevis* and the fish *Acipenser ruthenus*, [Iégorova et al.](#) present a thorough transcriptomic analysis through oocyte growth along their Animal-Vegetal axis. They identified groups of regionally distributed transcripts and proposed that degradation and *de novo* synthesis create gradient distributions for some of them. This will be a reference work for research in maternal contributions to animal development.

Nodal signaling and the T-box transcription factor Eomesodermin (Eomes) are essential for endomesoderm development in vertebrates. Two works deal with their role in zebrafish, where zygotic expression of two nodal-related genes, *ndr1* and *ndr2*, which begins dorsally and then extends to the whole blastoderm margin, is necessary for endomesoderm induction. Maternal *eomesa* transcripts are enriched vegetally, whereas the maternal transmembrane protein

Huluwa (Hwa), necessary to activate the dorsalizing β -Catenin pathway, accumulates in dorsal blastomeres. Xing et al. demonstrate that zygotic *ndr1* expression depends on maternal Hwa/ β -Catenin promoting *ndr1* expression on the dorsal margin; Eomesa, in the ventrolateral margin; and Nodal autoregulation being responsible for the ventral expansion of *ndr1* expression. In contrast, zygotic *ndr2* expression mainly depends on maternal Eomesa.

While *eomes* deficiency causes early lethality in mice, *eomesa* deficiency is not completely lethal in zebrafish. Talbot et al. demonstrate that the T-box transcription factor Tbx16, which is absent from Eutherians, partially compensates for *eomesa* deficiency during zebrafish endoderm formation. Moreover, *eomesa* participates in the development of the zebrafish left-right organizer (LRO), first repressing the key LRO regulator *vgll4l* and then indirectly activating it through the endoderm/LRO master transcription factor Sox32.

Two articles contributed by the same group address the role of retinoic acid (RA) during *Xenopus* embryogenesis from blastula stage and in head development. In one of them, Gur et al. show that inhibition of RA signaling at blastula stage delays gastrulation progression and migration of early involuting cells, reduces axis elongation, and alters the extracellular matrix over which cells migrate following involution, suggesting a link between RA signaling and the Wnt/PCP pathway in regulating tissue separation during gastrulation. Their observations indicate that functional RA signaling is required before gastrulation for regulating morphogenetic processes critical for normal development. In their other work, Gur et al. demonstrate that a strict balance of RA levels during embryogenesis is required for normal head development, with RA emitted by the gastrula organizer being required to prevent microcephaly. They show that the Aldehyde dehydrogenase 1 family member A3 (*Aldh1a3*), expressed by the anterior endomesodermal cells derived from the early gastrula organizer, is the main enzyme responsible for RA biosynthesis required for head development.

MicroRNAs regulate MZT by enhancing zygotic transcription and maternal mRNA degradation. Hu et al. show that *miR-202-3p* is critical during zebrafish MZT for embryonic viability and development. They demonstrate that in *miR-202* null embryos, abnormal development progression and apoptosis result from dysregulation of a group of three *miR-202-3p* direct target genes: *nfk1aa*, *perp*, and *mgll*. Their evidence points to an important role of *miR-202-3p* in the regulation of zygotic genome activation.

In the early embryos of most metazoan species, the cell cycle consists of the succession of the M and S phases without any gap. The precise timing of appearance of both G1 and G2 is scarcely known. Wong et al. developed multiple fluorescence ubiquitin cell cycle indicator reporters for the study of each cell during embryogenesis of the nematode *C. elegans*. They demonstrate that most embryonic cells skip G1 and G2 phases or have a very brief G1, with the exception of “V5QL” and “V5QR,” whose cell cycle comprises all phases.

In their review, Dowdle et al. focused on RNA binding protein Bicucidal-C (*Bicc1*) functions in vertebrate embryos. The *Xenopus* protein presents a vegetal-to-animal gradient where, by forming a translational repression gradient of target mRNAs, modulates the synthesis of proteins whose activities contribute to anterior-posterior polarity. A role of *Bicc1* RNA regulation in controlling left-right patterning has been demonstrated in mouse, *Xenopus*, and zebrafish. The mechanisms of mRNA binding and regulation of the *Bicc1* protein are described.

Echinoderms are a historically rich source for discovering mechanisms of animal embryogenesis, including the detailed study

of gene regulatory networks during germ layer development. Formery et al. present a comprehensive developmental atlas for the sea urchin *Paracentrotus lividus*, covering previously neglected aspects of development as well as an updated staging scheme from fertilization to post-metamorphic juvenile stages, providing an important reference tool for the scientific community.

The emergence of the primitive gut is one of the decisive events leading to the origin of Metazoans, but the existence of a common evolutionary developmental mechanism for this organ remains uncertain. Nguyen et al. employed hydrodynamic mechanical strains, reminiscent of the soft marine flow context where pre-metazoan colonies evolved, to study tissue invagination in the diploblastic metazoan *Nematostella vectensis* (cnidaria) and the multicellular choanoflagellate *Choanoeca flexa*. They show that hydrodynamic stimulation activates tissue invagination via Myosin-II-dependent mechanotransduction. Like in bilaterian animals, invagination in *N. vectensis* depends on endomesoderm specification via biomechanical-based β -Catenin phosphorylation. They propose that in early Metazoans, primitive gut formation, tissue invagination/gastrulation, and endomesoderm specification may have been initiated by a mechanotransduction mechanism.

We hope that the aspects covered here will reflect on the recent advances in understanding the early events of embryonic development and provide new resources for contemplating this long-standing question of how multicellular organisms evolved and are built.

Author contributions

SL was the Guest Editor of this Research Topic, inviting Co-Editor MC to define the aims, scope, and subjects to be treated. SG joined as Co-Editor and worked together with SL and MC to invite contributors and act as handling editors of manuscripts on the Research Topic. SL wrote the first draft of the Editorial. MC and SG edited the first draft and provided intellectual input.

Funding

Research in SL laboratory is supported by Agencia Nacional de Promoción Científica y Tecnológica, Argentina (PICT 2019-01439). Research in SL and MC laboratories is supported by Consejo Nacional de Investigaciones Científicas y Técnicas, Argentina (PIP 2021-1818).

Conflict of interest

The authors declare that the research was conducted in the absence of any commercial or financial relationships that could be construed as a potential conflict of interest.

Publisher's note

All claims expressed in this article are solely those of the authors and do not necessarily represent those of their affiliated organizations, or those of the publisher, the editors and the reviewers. Any product that may be evaluated in this article, or claim that may be made by its manufacturer, is not guaranteed or endorsed by the publisher.



Reduced Retinoic Acid Signaling During Gastrulation Induces Developmental Microcephaly

Michal Gur[†], Liat Bendelac-Kapon[†], Yehuda Shabtai, Graciela Pillemer and Abraham Fainsod^{*}

Department of Developmental Biology and Cancer Research, Institute for Medical Research Israel-Canada, Faculty of Medicine, The Hebrew University of Jerusalem, Jerusalem, Israel

OPEN ACCESS

Edited by:

Silvia L. López,
CONICET Instituto de Biología Celular
y Neurociencias (IBCN), Argentina

Reviewed by:

James Alan Marrs,
Indiana University—Purdue University
Indianapolis, United States
Jean-Pierre Saint-Jeannet,
New York University, United States

*Correspondence:

Abraham Fainsod
abraham.fainsod@mail.huji.ac.il

[†]These authors share first authorship

Specialty section:

This article was submitted to
Morphogenesis and Patterning,
a section of the journal
Frontiers in Cell and Developmental
Biology

Received: 28 December 2021

Accepted: 24 February 2022

Published: 14 March 2022

Citation:

Gur M, Bendelac-Kapon L, Shabtai Y,
Pillemer G and Fainsod A (2022)
Reduced Retinoic Acid Signaling
During Gastrulation Induces
Developmental Microcephaly.
Front. Cell Dev. Biol. 10:844619.
doi: 10.3389/fcell.2022.844619

Retinoic acid (RA) is a central signaling molecule regulating multiple developmental decisions during embryogenesis. Excess RA induces head malformations, primarily by expansion of posterior brain structures at the expense of anterior head regions, i.e., hindbrain expansion. Despite this extensively studied RA teratogenic effect, a number of syndromes exhibiting microcephaly, such as DiGeorge, Vitamin A Deficiency, Fetal Alcohol Syndrome, and others, have been attributed to reduced RA signaling. This causative link suggests a requirement for RA signaling during normal head development in all these syndromes. To characterize this novel RA function, we studied the involvement of RA in the early events leading to head formation in *Xenopus* embryos. This effect was mapped to the earliest RA biosynthesis in the embryo within the gastrula Spemann-Mangold organizer. Head malformations were observed when reduced RA signaling was induced in the endogenous Spemann-Mangold organizer and in the ectopic organizer of twinned embryos. Two embryonic retinaldehyde dehydrogenases, ALDH1A2 (RALDH2) and ALDH1A3 (RALDH3) are initially expressed in the organizer and subsequently mark the trunk and the migrating leading edge mesendoderm, respectively. Gene-specific knockdowns and CRISPR/Cas9 targeting show that RALDH3 is a key enzyme involved in RA production required for head formation. These observations indicate that in addition to the teratogenic effect of excess RA on head development, RA signaling also has a positive and required regulatory role in the early formation of the head during gastrula stages. These results identify a novel RA activity that concurs with its proposed reduction in syndromes exhibiting microcephaly.

Keywords: retinoic acid biosynthesis, embryo development, *Xenopus* embryo, CRISPR/Cas9, gene knockdown, Fetal Alcohol Syndrome, prechordal mesoderm, retinaldehyde dehydrogenase

Abbreviations: ALDH, aldehyde dehydrogenase; EAE, embryonic alcohol exposure; FASD, Fetal Alcohol Spectrum Disorder; FAS, Fetal Alcohol Syndrome; LEM, leading edge mesendoderm; PCM, prechordal mesoderm; RA, retinoic acid; RAL, retinaldehyde; ROL, retinol; SDR, short-chain dehydrogenase/reductase.

INTRODUCTION

Microcephaly is a condition in which the brain fails to achieve its normal size (Abuelo, 2007; Toi et al., 2009; Mochida, 2009; Dymment et al., 2013; Faheem et al., 2015; Duerinckx and Abramowicz, 2018). Besides the wide variation in head size in the human population (Natale and Rajagopalan, 2014), individuals with head circumferences (occipitofrontal) smaller by 3 standard deviations from the population mean (age, sex, and ethnicity matched), exhibit what is known as clinical microcephaly (Martini et al., 2018). These individuals encompass up to 0.1% of the human population and most of them suffer from significant intellectual disabilities (Abuelo, 2007). Microcephaly can be subdivided into primary, if developed during embryogenesis and present at birth, or secondary, if developed after birth, but this classification is not universally accepted. To date, Online Mendelian Inheritance in Man (OMIM.org) lists close to a thousand genes, diseases, or syndromes associated with microcephaly in addition to numerous environmental factors that can induce this condition. To elucidate the etiology of primary or developmental microcephaly we need to achieve a better understanding of the signals and processes that regulate the induction, patterning, and differentiation of the rostral neuroectoderm and subsequently the forebrain in the embryo (Abuelo, 2007; Mochida, 2009; Toi et al., 2009; Dymment et al., 2013; Faheem et al., 2015; Duerinckx and Abramowicz, 2018) which in turn will affect the size of the head (Koyabu et al., 2014; Ranke et al., 2015; Martini et al., 2018). In *Xenopus* embryos, the group of cells responsible for anterior neuroectoderm induction and patterning, the head organizer, forms as part of the Spemann-Mangold organizer (Spemann and Mangold, 1924; Inui et al., 2012; Kiecker and Lumsden, 2012; Yanagi et al., 2015). Very early during embryogenesis, the leading edge mesendoderm (LEM)/prechordal mesoderm (PCM) cells migrate to the rostral region beneath the prospective cranial neuroectoderm, and at this position, they will perform their inductive and patterning functions (Kaneda and Motoki, 2012; Huang and Winklbauer, 2018).

In humans, *in utero* exposure to alcohol (ethanol, EtOH) is the environmental disturbance that induces Fetal Alcohol Spectrum Disorder (FASD). Individuals suffering from the severe form of FASD, Fetal Alcohol Syndrome (FAS), suffer from a multitude of developmental malformations including microcephaly (Roussotte et al., 2012; Gautam et al., 2015; Popova et al., 2016; Del Campo and Jones, 2017; Jarmasz et al., 2017; Treit et al., 2017; Petrelli et al., 2019). In FAS, cognitive disabilities, behavioral and social problems, reduced executive functioning, and social withdrawal accompany the microcephaly (Niccols, 2007; Spohr and Steinhausen, 2008; Guerri et al., 2009; Gautam et al., 2014; Popova et al., 2016). In recent years, we established and characterized a *Xenopus*-based experimental model that recapitulates many of the developmental malformations characteristic of FAS following alcohol exposure, including microcephaly (Yelin et al., 2005; Yelin et al., 2007; Kot-Leibovich and Fainsod, 2009; Fainsod and Kot-Leibovich, 2018; Shabtai et al., 2018). We have shown that many of the developmental malformations arising from embryonic alcohol

exposure (EAE) are the result of reduced retinoic acid (RA) signaling (Yelin et al., 2005; Kot-Leibovich and Fainsod, 2009; Shabtai et al., 2018; Shabtai and Fainsod, 2018; Fainsod et al., 2020). During early embryogenesis, alcohol clearance and Vitamin A (retinol, ROL) metabolism are performed in part by the same enzymes or enzyme families (Crabb et al., 2004; Shabtai and Fainsod, 2018). Biosynthesis of RA from Vitamin A (retinol, ROL) proceeds through two consecutive oxidation steps, the first performed mainly by short-chain dehydrogenase/reductases (SDR) oxidizing ROL to retinaldehyde (RAL), and the subsequent oxidation step from RAL to RA performed by aldehyde dehydrogenases (ALDH) also known as retinaldehyde dehydrogenases (Kedishvili, 2013; Cunningham and Duester, 2015; Shabtai and Fainsod, 2018). EtOH detoxification in the embryo makes use of some of the same enzymes, sometimes redirecting them from their involvement in RA biosynthesis and other metabolic processes (Duester, 1991; Pullarkat, 1991; Kot-Leibovich and Fainsod, 2009; Shabtai et al., 2018; Shabtai and Fainsod, 2018; Fainsod et al., 2020). As it has extensively been shown, RA is crucial for normal embryonic development and tissue homeostasis (Ross et al., 2000; See et al., 2008; Clagett-Dame and Knutson, 2011; Kin Ting Kam et al., 2012; Rhinn and Dollé, 2012; Cunningham and Duester, 2015; Draut et al., 2019; Nolte et al., 2019), and abnormally high or low levels are extremely teratogenic giving rise to a complex and severe set of developmental malformations (Collins and Mao, 1999; Mark et al., 2006; Ghyselinck and Duester, 2019).

It is widely accepted that increased RA levels adversely affect the formation of the head and in particular, inhibit forebrain development by promoting hindbrain expansion resulting in a microcephalic phenotype (Durstion et al., 1989; Sive et al., 1989; Koide et al., 2001; Halilagic et al., 2003; Crandall et al., 2011). On the other hand, reduced RA signaling levels have been linked to an increasing number of developmental syndromes that exhibit microcephaly including FAS, DiGeorge, Smith-Magenis, Matthew-Wood, and Vitamin A Deficiency (VAD) Syndromes, and others (Twal et al., 1995; Collins and Mao, 1999; Maden, 2000; Clagett-Dame and DeLuca, 2002; Vermot et al., 2003; Yelin et al., 2005; Kot-Leibovich and Fainsod, 2009; Chassaing et al., 2009; Elsea and Williams, 2011; Shabtai et al., 2018; Fainsod et al., 2020; Fainsod et al., 2022). This link between microcephaly and reduced RA levels suggests that RA signaling is required during early head induction and forebrain establishment. In agreement, *retinaldehyde dehydrogenase 2* (*Raldh2*; *Aldh1a2*) mutants die very early during development exhibiting malformations of the anterior head region (Niederreither et al., 1999; Begemann et al., 2001; Perz-Edwards et al., 2001; Halilagic et al., 2007) and dorsal knock-down of the RA nuclear receptor, *RARα2* results in head truncation and malformations (Shiotsugu et al., 2004).

To further characterize the role of RA signaling during gastrulation and in particular, in the process of head formation, we experimentally manipulated its levels. We show that localized reduction of RA levels within the embryonic organizer results in a high incidence of embryos with abnormally small heads. RA biosynthesis inhibition or signaling knockdown in induced secondary axes also reduces

TABLE 1 | Primers for PCR expression analysis, genomic amplification and expression knockdown.

Gene	Forward primer	Reverse primer
<i>RT-qPCR</i>		
<i>admp.S</i>	GCCTTCGAGCAAGCTTACTT	CCTTGTGGCAACTGTATCTTATTTT
<i>cer1.S</i>	CTGGTGCCAAGATGTTCTGGAA	CGGCAAGCAATGGGAACAAGTA
<i>chrd.1.L/S</i>	ACTGCCAGGACTGGATGGT	GGCAGGATTTAGAGTTGCTTC
<i>cyp26a1.S</i>	CGATTCCTCAAGGTTTGGCTTCA	ATTTAGCGGGTAGGTTGTCCACA
<i>dhrs3.L</i>	CAGGCGCAAGAAATCCTAAG	CAAAGGCCACGTTACAGGAT
<i>dlk1.S</i>	TGCCTACCCGCTCTACAGTT	AACCAGAGAGTTGCCGTTTC
<i>frzb1.L</i>	CCAATGCTTACTGTGCTTCGT	AGTGCTGTGGTGAGATGGT
<i>gapdh.S</i>	GCTCCTCTCGCAAAGGTCAT	GGGCCATCCACTGCTTCTG
<i>gsc.L/S</i>	TTCACCGATGAACAACTGGA	TTCCACTTTTGGGCATTTTC
<i>hoxa1.L</i>	CCGCTCACTATATCCACCATT	TGGCAGGAGAACGACAAAC
<i>hoxb1.L</i>	TTGCCCCAGTGCCAATGAC	TCCCCCTCCAACAACAAACC
<i>hoxb4.S</i>	CCAAGGATCTGTGCGTCAA	GCAGGATGGAGGCGAACT
<i>myod1.S</i>	CCCTGTTTCAATACCTCAGACAT	CGTGCTCATCCTCGTTATGG
<i>otx2.L</i>	AAGCCGCAATATAGAAAGGAACA	GGGATTCCCTTGTGCGCAATTAATA
<i>aldh1a1.L</i>	GAACTTTCCGTTTGTGAT	GATAGCAGTCAGTGGAGTTTG
<i>aldh1a2.L</i>	ATGTTTGCCTGGAAGA	GAGAGCAGTGAGCGGA
<i>aldh1a3.L</i>	TAAAGCCCTGTCTGTTTCT	CATACTCTCCAAGTTCCTT
<i>rdh10.L/S</i>	CCCAGAGTAACGAGGAGACG	ATTGCAGCACGGCAGAACT
<i>szl.L/S</i>	AACAAGGTCTGCTCCTTCCA	CTGTGGGTCTGGTCCG
<i>ventx1.2.S</i>	AGGCAGGAGTTCACAGGAAA	TGCCTGTTCCAGTTTGCTT
<i>Genomic nested PCR</i>		
Outer genomic PCR		
<i>aldh1a2.L</i>	CTGGGATCTGCTCATTAGTGT	ACGTTGATTGATCCGTGGTG
<i>aldh1a2.S</i>	CAACAAGTTCAATTTTCTGCTGAA	ATAGGCAGGTCTCTTGGGGA
<i>aldh1a3.L</i>	TCAAAGGAGAAAAGGCTCAGGT	TAGAAATTCACCAGCAGGAAAGC
<i>aldh1a3.S</i>	ACCCCATAAAATGTGTGCTACTCT	TTCTAACAGACTGGGTTGGGATG
Inner genomic PCR		
<i>aldh1a2.L</i>	GTGTACCCTTTGTATGTTGGCAT	GCCATTGTGCTACGGTTTTG
<i>aldh1a2.S</i>	GTCACACACCTTTTCAGTTTTTGG	AGGTCTCTTGGGGAACCTGTG
<i>aldh1a3.L</i>	TTACCAAGTGCAGGGCAACAG	TCTAACAGACTGGGTTGGGAT
<i>aldh1a3.S</i>	AGAACAATTGTGGGGCAGCA	TGCTGCATCTAGCTATAGAAACCC
<i>Antisense morpholino oligonucleotides</i>		
ALDH1A2.L/S	CTATTTTACTGGAAGTCATGTCTGG	—
ALDH1A3.L/S	TAGTGGTTGTCATGTTGATAGAGGC	—
Control MO	CCTCTTACCTCAGTTACAATTTATA	—
<i>CRISPR (crRNA)</i>		
<i>aldh1a2.L/S</i>	GAATGGATGCCTCAGAAAGG	—
<i>aldh1a3.L/S</i>	CAGCAGTCTCCCTCGGCCAT	—

the efficiency of head formation in the twinned embryos. These observations support the suggestion that RA signaling is required for normal head development. In *Xenopus* embryos, the *aldh1a2* gene is initially expressed within the organizer domain but soon thereafter its expression becomes lateralized and is absent from the dorsal midline (Chen et al., 2001). This pattern of expression prompted us to search for additional RA biosynthetic enzymes that could produce the RA required for head induction. *Aldh1a3* (*raldh3*) transcripts were detected in the early organizer (Lupo et al., 2005), and subsequently in the rostrally migrating LEM/PCM cells. We show that *aldh1a3* knockdown with antisense morpholino oligonucleotides or by gene targeting with CRISPR/Cas9 efficiently hampers the formation of head structures,

resulting in microcephaly in both the endogenous and induced secondary axes. These results indicate that RA signaling is required in the LEM/PCM cells for normal head formation. Further, we show that ALDH1A3 is the main enzyme involved in producing the RA needed for this process.

MATERIALS AND METHODS

Embryo Culture and Treatments

Xenopus laevis embryos were obtained by *in vitro* fertilization, incubated in 0.1% Modified Barth's Solution and Hepes (MBSH) and staged according to Nieuwkoop and Faber (1967). All

experiments were performed after obtaining ethics approval and under the supervision of the Institutional Animal Care and Use Committee (IACUC) of the Hebrew University (Ethics approval no. MD-17-15281-3). Treatments with 4-Diethylaminobenzaldehyde (DEAB, Sigma) or 3,7-Dimethyl-2,6-octadialenal (citrinal, Aldrich), were performed in 0.1% MBSH from the mid-blastula transition (MBT, stage 8) until the desired stage for analysis.

Embryos were injected at the 1-4 cell stage with *in vitro* transcribed capped RNA, expression plasmids, antisense morpholino oligonucleotides, or CRISPR/Cas9 single guide RNAs (sgRNAs). Capped RNAs were prepared using the appropriate RNA polymerase. Cap analog [m7G(5')ppp(5')G; New England Biolabs, United States] was added to the reaction mixture using a cap:GTP ratio of 5:1. Expression plasmids were linearized and transcribed as previously described: *wnt8a* (Christian and Moon, 1993), *tALK3* (Graff et al., 1994), *cyp26a1* (Holleman et al., 1998), *bmp4* (Fainsod et al., 1994), *dkk1* (Glinka et al., 1998). Antisense morpholino oligonucleotides (Table 1) were obtained from Gene Tools LLC (United States).

Generation of CRISPR Embryos

For gene-specific single guide RNA design (sgRNA), genomic DNA sequences were selected from Xenbase.org (Nenni et al., 2019) for the L and S homoeologs when present and used CRISPRdirect (Naito et al., 2015) and CRISPRscan (Moreno-Mateos et al., 2015) for target site search. Computational estimation of the sgRNA efficiency was determined using the inDelphi software (Shen et al., 2018; Naert et al., 2020). sgRNA target sequences used are listed in Table 1. For the generation of F0 CRISPR embryos, we injected one-cell stage embryos with Cas9 ribonucleoprotein (RNP) complexes employing the two-RNA component (crRNA:tracrRNA) approach (Hoshijima et al., 2019). Briefly, chemically synthesized and modified for stability (Alt-R) RNAs (crRNA and tracrRNA; IDT, United States) (Table 1) were annealed to generate the double guide complexes (crRNA:tracrRNA), and were incubated (10 min at 37°C) with *S. pyogenes* Cas9 protein (IDT, United States) to generate RNP complexes. Eight nanoliters of the RNP complex solution were injected into the cytoplasm of one-cell stage embryos.

To determine the efficiency of indel induction, genomic DNA was extracted from 5 individual embryos at mid-gastrula (st. 11) or later, employing the GenElute Mammalian Genomic DNA Miniprep Kit (SIGMA). The genomic region containing the CRISPR/Cas9 targeted region was PCR amplified using a nested PCR approach (Table 1) and the size-selected and cleaned product was sequenced. Genome editing efficiency was analyzed by decomposition analysis (Brinkman et al., 2014) using the Synthego ICE algorithm (Hsiau et al., 2018).

Whole-Mount *in Situ* Hybridization

Whole-mount *in situ* hybridization and double *in situ* hybridization were performed as previously described (Epstein et al., 1997). Probes were prepared by *in vitro* transcription using Digoxigenin or Fluorescein labeling mix (Roche). Double staining was performed by either 5-Bromo-6-chloro-3-indolyl phosphate

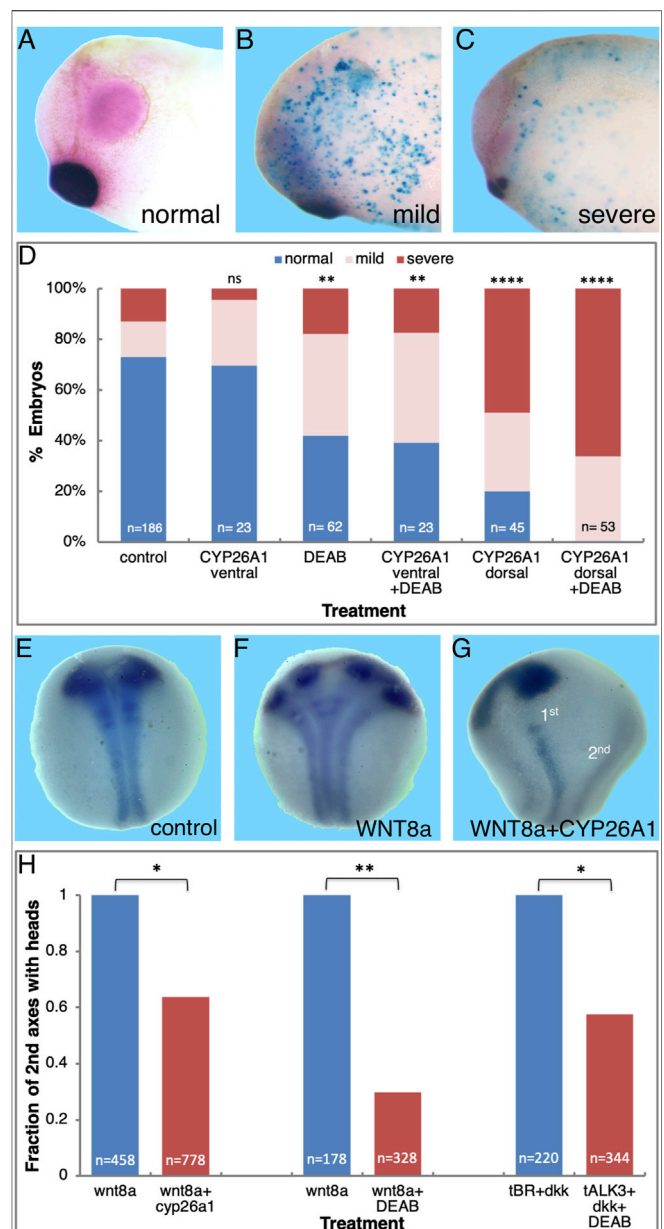


FIGURE 1 | Retinoic acid is required for normal head development. Embryos were injected with RNA encoding CYP26A1 and treated with DEAB to reduce the endogenous levels of RA. (A) Control embryo (st. 30) processed for *in situ* hybridization with *pax6* (eyes, pink) and *muc2* (cement gland, purple) specific probes. (B) Embryo injected dorsally with *cyp26a1* RNA exhibiting mild microcephaly. Turquoise staining is the *LacZ* lineage tracer. (C) Severe microcephaly in an embryo injected with *cyp26a1* mRNA in the dorsal region. (D) Frequency of microcephaly induction by combined RA knockdown in embryos injected dorsally or ventrally with *cyp26a1* RNA and treated with DEAB. (E) Control st. 14/15 embryo processed for *in situ* hybridization with *pax6* (eyes) and *ncam* (neural plate). (F) Embryo ventrally injected with *wnt8a* RNA to induce a secondary axis analyzed for eye and neural plate formation. (G) Loss of anterior head structures (eyes, *pax6*) in the induced secondary axis by co-injection of *cyp26a1* RNA with the *wnt8a* mRNA. The primary and secondary axes are labeled (1st, 2nd). (H) Inhibition of anterior head formation in twinned embryos induced by ventral *wnt8a* injection or parallel inhibition of BMP (*tALK3*) and Wnt (*DKK1*) signaling and reduction of RA levels (DEAB treatment or CYP26A1 overexpression). The overall number of embryos injected or manipulated is shown (n =). *, $p < 0.05$; **, $p < 0.01$; ****, 0.0001; ns, not significant.

p-Toluidine salt (Magenta phosphate, Sigma) or BM purple (Roche) for the first probe and 5-Bromo-4-chloro-3-indolyl phosphate p-Toluidine salt (BCIP, Roche) for the second probe. Probes were transcribed as previously described: *pax6* (Li et al., 1997), *ncam1* (Krieg et al., 1989), *muc2* (XCG-1) (Sive et al., 1989), *chrd.1* (*chordin*) (Sasai et al., 1994), *gsc* (*goosecoid*) (Cho et al., 1991), *cyp26a1* (Holleman et al., 1998), *aldh1a2* (*raldh2*) (Chen et al., 2001), *aldh1a3* (*raldh3*) (Lupo et al., 2005), *otx2* (Smith et al., 1993).

Quantitative Reverse Transcription Real-Time PCR (qPCR)

Total RNA from embryos was extracted with the Aurum™ Total RNA Mini Kit (Bio-Rad) and cDNA was synthesized using the iScript cDNA Synthesis Kit (Bio-Rad). The real-time PCR reactions were performed using the CFX384 Real-Time System (Bio-Rad) and iTaq Universal SYBR Green Supermix (Bio-Rad). Each experiment was repeated at least three independent times and each time the samples were run in triplicate. GAPDH was used as the housekeeping reference gene. The primers used are listed in Table 1.

β-Galactosidase Activity Assays

Chemiluminescent quantification of the reporter pRAREhspLacZ plasmid (Rossant et al., 1991) activity was performed using β-gal Juice Plus (PJK, Germany) as previously described (Yelin et al., 2005). Chemiluminescence activity was measured on a TD-20/20 Luminometer (Turner Designs). *LacZ* RNA was prepared from a clone containing a nuclear localization signal (pSP6nuc β-gal) in pGEM-3Z (Promega). The staining of embryos for β-galactosidase activity was performed with 5-bromo-4-chloro-3-indolyl-β-D-galactopyranoside (Xgal).

Statistical Analysis

All statistical comparisons were carried out using the Prism software package (Graph Pad Software Inc., San Diego, CA). Results are given as the mean ± standard error of the mean (SEM). Tests used were the 2-tailed t-test for two-sample comparisons, Dunnett's (ANOVA) multiple comparisons test, or Fisher test. Differences between means were considered significant at a significance level of $p < 0.05$.

RESULTS

Retinoic Acid Signaling Reduction Induces Microcephaly

To support the requirement for RA signaling in the formation of the head, we reduced the endogenous RA levels by localized dorsal or ventral injection of mRNA encoding CYP26A1. The CYP26A1 enzyme is a RA hydroxylase rendering it biologically inactive, thus reducing the activity of this signaling pathway (Catharine Ross and Zolfaghari, 2011). RNA encoding β-galactosidase (*LacZ*) was co-injected as a lineage tracer to monitor and verify the injection site. To study the effect on anterior head structure formation and to determine whether the embryos exhibit normal, mild, or severe

microcephaly, we analyzed the development of the eyes (*pax6*) and cement gland (*muc2*) by *in situ* hybridization (Figures 1A–C). Dorsal CYP26A1 overexpression induced microcephaly with high efficiency (80%), with the majority of the embryos exhibiting severe microcephaly (61.1%; Figures 1B–D). Ventral *cyp26a1* RNA injections resulted in a distribution of head phenotypes similar to control embryos (13.9% very mild microcephaly; Figure 1D). To support the requirement for normal RA signaling levels in head development, we also performed systemic RA biosynthesis inhibition with 4-diethylaminobenzaldehyde (DEAB; 150 μM) (Russo et al., 1988; Morgan et al., 2015; Shabtai et al., 2016). The DEAB treatment induced mild microcephaly in 40.3% of the embryos (Figure 1D). Combined ventral *cyp26a1* mRNA injection with DEAB treatment had no significant additive effect compared to the DEAB treatment alone, increasing only slightly the proportion of mild microcephalic embryos to 43.5%. In contrast, the addition of DEAB to dorsally *cyp26a1* RNA injected embryos increased the incidence of microcephaly to 100% of the embryos (Figure 1D), showing that most of the RA signaling activity required for normal head development is localized dorsally.

Based on the organizer-restricted expression of *aldh1a2* and the activation of RA signaling in the gastrula organizer (Chen et al., 2001; Yelin et al., 2005), we expect activation of RA signaling in supernumerary organizers induced on the ventral side of the embryo. For this reason, we induced secondary axes by either ventral activation of Wnt/β-catenin signaling (*wnt8a* RNA injection) (Sokol et al., 1991), or inhibition of BMP signaling by *smad6* (Marom et al., 2005) or a dominant negative BMP receptor (*tALK3*) (Graff et al., 1994) mRNA injection. Activation of RA signaling in the secondary organizer was monitored using the RA reporter pRAREhspLacZ (RAREZ) plasmid (Rossant et al., 1991; Yelin et al., 2005) which was co-injected with the axis-inducing RNA. Expression from this reporter plasmid relies on an RA responsive element (RARE), which in turn depends on the availability of the RA ligand, the retinoic acid nuclear receptors, and their cofactors, i.e., an active RA signaling pathway. During gastrula (st. 10.25) and early neurula (st. 14/15) expression of the RAREZ reporter plasmid was detected irrespective of the mode of secondary axis induction employed (Supplementary Figure S1). During early gastrula, the induced secondary organizers exhibited RAREZ activity in about 76% of the embryos (Supplementary Figure S1C). This observation shows that although secondary dorsal lips, organizers, are induced, not all of them manage to activate the RAREZ reporter. It is important to note that activity of this reporter plasmid is totally dependent on the local biosynthesis of RA and expression of the RAR and RXR nuclear receptors. These results show that the induced secondary organizer also exhibits active RA signaling, although a more effective and efficient induction might be needed to activate a detectable RA signal trace.

As induced secondary organizers exhibit active RA signaling, we studied the requirement for this signal in the head organizer activity by studying the effect of reduced RA signaling on head development in secondary axis head induction. Ventral *wnt8a* mRNA injection was selected for axis induction as a large percentage of the secondary axes form anterior head structures (Sokol et al., 1991). Co-injection of *cyp26a1* mRNA together with

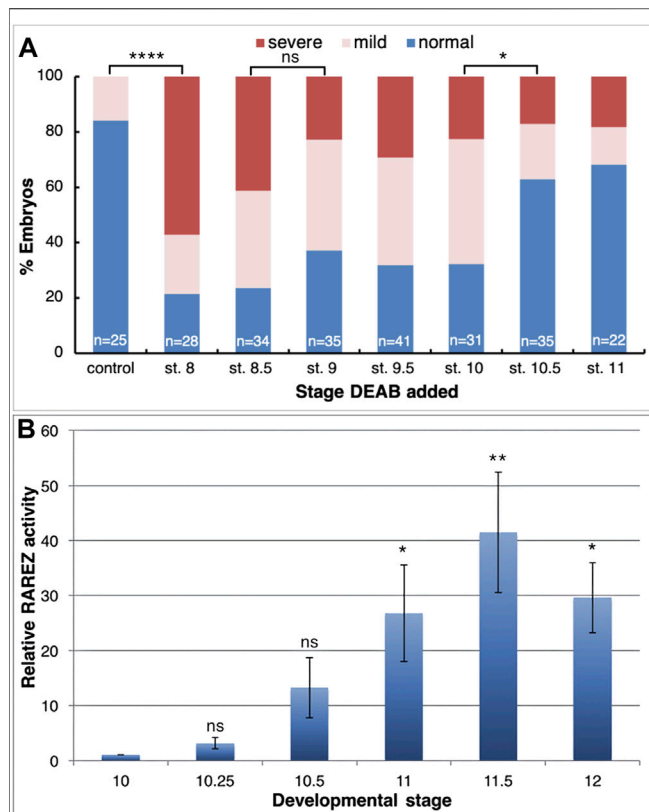


FIGURE 2 | RA function is required during the early gastrula stages for normal anterior head development. **(A)** Embryos were treated with DEAB starting at different developmental stages and analyzed for the effect on head development during tailbud stages (st. 32). **(B)** Untreated embryos were injected with the RA reporter plasmid, RAREZ. At different gastrula stages, groups of embryos (5) were collected and processed for chemiluminescent analysis of the β -galactosidase activity. Samples were normalized to the st. 10 sample. *, $p < 0.05$; **, $p < 0.01$; ****, $p < 0.0001$; ns, not significant.

the *wnt8a* RNA was used to reduce, in a localized manner, the RA level in the induced secondary axes. Embryos were processed for *in situ* hybridization with *ncam1* as a marker of the neural plate to score the secondary trunk, while anterior head formation was determined using *pax6* as an eye marker (Figures 1E–G). The efficiency of secondary axis induction was not significantly affected by the reduction in RA signaling compared to control embryos (61.3%, $n = 856$ and 55.5%, $n = 1,450$, respectively; Figure 1H). Analysis of the presence of anterior head structures morphologically and by marker gene expression showed that in the control group, 43.8% of the secondary axes had anterior head structures (Figures 1F,H). In contrast, RA knock-down reduced the proportion of secondary axes containing anterior head structures to only 27.9% of all the injected embryos, representing a reduction of 36.3% in full secondary axes (Figures 1G,H). These results show that RA is also required for the head organizer activity in induced secondary axes, similar to the endogenous organizer.

Additional support for the requirement for RA during head formation was obtained using additional means of secondary axis

induction and RA signaling inhibition. Embryos were injected ventrally with *wnt8a* mRNA and subsequently treated with the RALDH inhibitor, DEAB. The DEAB treatment reduced the efficiency of head formation in the secondary axes by 59.6% ($n = 328$; Figure 1H), further supporting that RA is required for head formation. In addition, we induced head-containing secondary axes by simultaneous inhibition of BMP and Wnt signaling by co-injection of RNA encoding the dominant-negative BMP receptor, tALK3, and the Wnt antagonist, DKK1 (Glinka et al., 1998). Similar to the previous combined treatments, DEAB-mediated inhibition of RA biosynthesis resulted in a 41.1% decrease in head formation in the induced secondary axes ($n = 344$; Figure 1H). We conclude that RA signaling is required for efficient anterior head structure development both in the endogenous and induced organizers.

Retinoic Acid is Required for Normal Head Formation During Early Gastrula

To map the developmental window when RA signaling is required for normal head development, we inhibited RA biosynthesis by initiating the DEAB treatment at different developmental stages and analysis of the resulting head malformations at st. 32 (Figures 1A–C). Inhibition of RA synthesis from mid to late blastula stages (st. 8–9) resulted in 62–78% of the embryos developing microcephaly (Figure 2A). In the st. 8 sample, most embryos (57%) developed severe head malformations and 21% of them had mild head defects (Figure 2A). DEAB treatment from early gastrula (st. 10) resulted in a similar frequency of affected embryos (Figure 2A). Inhibition of RA biosynthesis from mid gastrula (st. 10.5) onwards showed a significant decrease in the induction of microcephaly, identifying a shift in the requirement for RA in the head organizer; only 37% of the embryos exhibit some form of microcephaly, 20% mild and 17% severe (Figure 2A). These results show a requirement for RA signaling during late blastula-early gastrula for normal head development.

RA and its biosynthetic intermediates have been detected in the gastrula organizer in vertebrate embryos (Chen et al., 1992; Hogan et al., 1992; Creech Kraft et al., 1994; Chen et al., 1994; Kraft et al., 1994; Niederreither et al., 1997; Chen et al., 2001; Yelin et al., 2005), suggesting an active role for this signaling pathway in this central embryonic regulatory structure. It is generally accepted that the appearance of the retinaldehyde dehydrogenase activity with the onset of *aldh1a2* (*raldh2*) expression marks the completion of the biosynthetic pathway and the onset of RA signaling (Ang and Duester, 1999; Niederreither et al., 1999; Chen et al., 2001; Shabtai et al., 2018). To obtain a better picture of the onset of RA signaling in the embryo, we took advantage of the RA reporter plasmid, RAREZ (Rossant et al., 1991), and determined the kinetics of increase in β -galactosidase activity by chemiluminescence for maximal sensitivity. Embryos injected radially with the RAREZ plasmid (Yelin et al., 2005) were analyzed at different developmental stages from the midblastula transition (MBT; st. 8.5) to late gastrula (st. 12) (Figure 2B). This analysis shows that the RA reporter plasmid becomes active at the onset of gastrulation (st. 10–10.25) and its activity increases towards mid/late gastrula

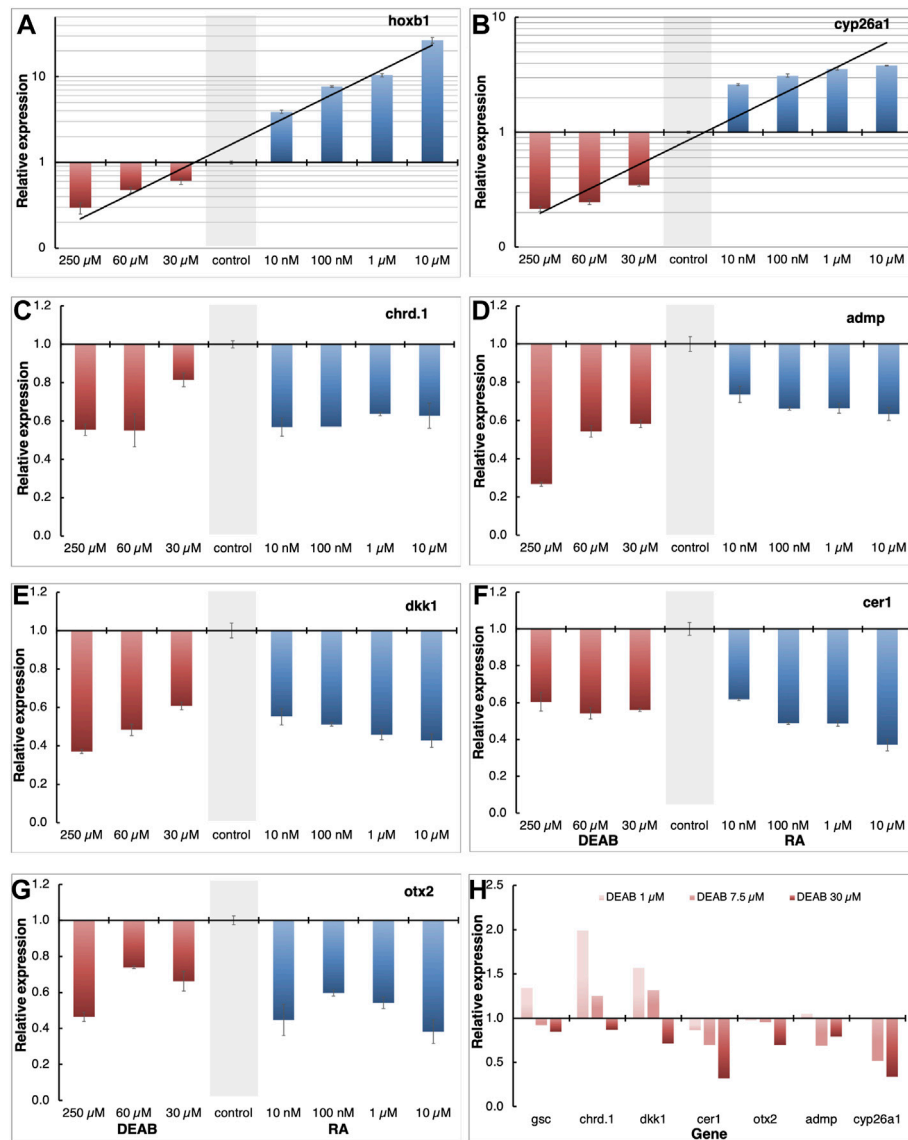


FIGURE 3 | Positive and negative regulation of organizer genes by RA. (A–G) Embryos were treated with increasing concentrations of atRA (10 nM–10 μM) or DEAB (30–250 μM) from late blastula to early gastrula. Expression changes of *hoxb1* (A), *cyp26a1* (B), *chrd.1* (C), *admp* (D), *dkk1* (E), *cer1* (F), and *otx2* (G) were studied by qPCR. Samples were normalized to control expression levels (gray bar). (H) Fine titration of RA biosynthesis inhibition using DEAB (1–30 μM). Expression changes were determined for *gsc*, *cyp26a1*, *chrd.1*, *admp*, *dkk1*, *cer1*, and *otx2* by qPCR.

stages (st. 11.5–12). This temporal pattern of RAREZ activity places the onset of RA signaling around the beginning of gastrulation and, from then on, it increases towards late gastrula overlapping with the expression of *aldh1a2* (Chen et al., 2001; Shabtai et al., 2018) and the proposed activity of the head organizer and the transition to trunk organizer (Niehrs, 2004).

Retinoic Acid is Required for Normal Gene Expression in the Head Organizer

Using transgenic embryos, we previously showed that the RA pathway is active during early/mid gastrula mainly in the organizer and subsequently along the dorsal midline (Yelin

et al., 2005). The early requirement for RA signaling for normal head development led us to study the role of RA within the organizer at a stage when both RA producing enzymes, ALDH1A2 and ALDH1A3 are expressed in this embryonic region. We manipulated the endogenous level of RA in the embryo and determined the effect of such manipulations on organizer-specific gene expression and, in particular, genes important for the head organizer activity. To decrease or increase the RA signaling levels, embryos were treated with increasing concentrations of DEAB (30–250 μM), or all-trans retinoic acid (atRA; 10 nM–10 μM) respectively, and incubated to early gastrula stages (st. 10.25) for expression analysis. To support the generation of different RA signaling

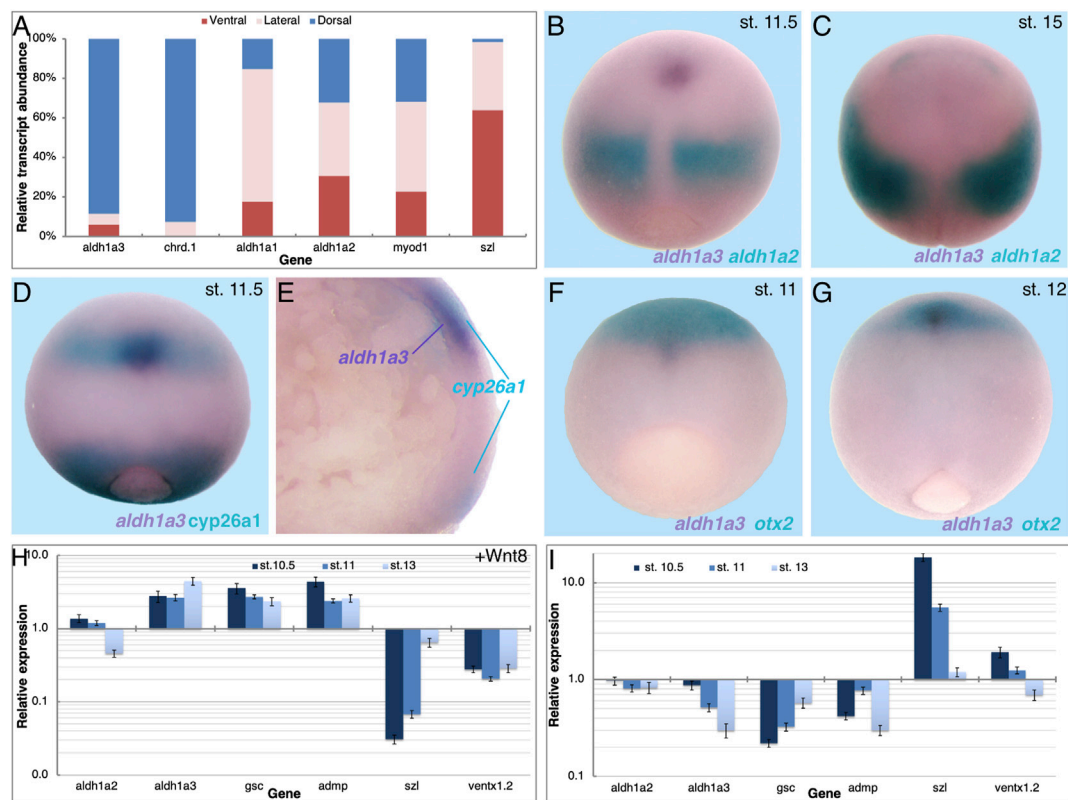


FIGURE 4 | Expression of *aldh1a3* in the migrating LEM/PCM cells. **(A)** Mid-gastrula embryos (st. 11) were dissected into dorsal, lateral, and ventral regions, and RNA was extracted from each region. The relative abundance of *aldh1a1*, *aldh1a2*, and *aldh1a3* was studied by qPCR. The accuracy of the dissections was determined by qPCR of *chrd.1*, *myod1*, and *szl* as dorsal, lateral, and ventral markers, respectively. In comparison to the *szl* transcript distribution, all other genes had a significantly different distribution, $p < 0.0001$ using the Fisher exact probability test. Spatial expression pattern comparison between *aldh1a3* and *aldh1a2* **(B,C)**, *aldh1a3* and *cyp26a1* **(D,E)**, and *aldh1a3* and *otx2* **(F,G)**. **(B–D,F,G)** dorsal view, anterior to the top. **(H,I)** Embryos were injected with mRNA encoding WNT8a **(H)** or BMP4 **(I)** and samples were collected during early and mid-gastrula, and early neurula stages (st. 10.5, 11, and 13). qPCR analysis was performed for *aldh1a2* and *aldh1a3*, the dorsal markers *gsc* and *admp*, and the ventral genes *szl* and *ventx1.2*. Relative expression was normalized to levels in control embryos. Groups of injected embryos were incubated to tailbud stages to determine their dorsoanterior index (DAI) (Kao and Elinson, 1988). *wnt8a*, DAI = 5.67; *bmp4*, DAI = 3.64.

levels we monitored the expression of the RA-regulated genes, *hoxb1* and *cyp26a1* by qPCR. This analysis revealed that our manipulations efficiently created an RA activity gradient ranging from a strong knockdown to gain-of-function (**Figures 3A,B**). Under these conditions, we studied the effect of RA manipulation on the expression of the organizer-specific genes; *cer1*, *admp*, *dkk1*, *chrd.1*, and *otx2*. The decrease in RA levels resulted in the downregulation of all the genes studied (**Figures 3C–G**). The downregulation ranged from about 40 to 60% from normal expression levels, suggesting that RA is a required signal for the normal expression of these organizer genes. Surprisingly, increasing the RA levels also reduced the expression of all genes studied by about 40–60% (**Figures 3C–G**). These results suggest that the embryo has close to optimal amounts of RA in the early gastrula organizer and any deviation results in reduced expression of the organizer genes studied.

To obtain support of whether the organizer normally contains almost optimal levels of RA to control the expression level of genes like *gsc*, *cer1*, *admp*, *dkk1*, *chrd.1*, and *otx2*, we performed a fine titration of the inhibition of RA biosynthesis using DEAB

(**Figure 3H**). For *gsc*, *chrd.1*, and *dkk1*, the lowest amount of DEAB used (1 μ M) resulted in upregulation of their expression, whereas higher concentrations had either no effect or had an opposite effect and downregulated their expression (**Figure 3H**). For *cer1*, *otx2*, *admp*, and *cyp26a1*, low DEAB concentrations had no effect, but higher concentrations induced lower expression levels (**Figure 3H**). These results show that RA has a complex gene regulatory role within the organizer, both positively and negatively controlling the levels of gene expression in a concentration and threshold-dependent manner to fine-tune the expression of the organizer genes.

Expression of *aldh1a2*, and *aldh1a3* During Gastrula Stages

The results show that RA signaling is required during late blastula or early gastrula for normal organizer-specific gene expression and this early function contributes to the activity of the head organizer. We previously described the temporal pattern of expression of the three retinaldehyde dehydrogenase-encoding

genes, *aldh1a1*, *aldh1a2*, and *aldh1a3* (*raldh1*, *raldh2*, and *raldh3*, respectively) in early *Xenopus* embryos and their relative transcript abundance (Shabtai et al., 2018; Parihar et al., 2021). The results showed that all three genes exhibit similar temporal expression patterns and are upregulated above background levels with the onset of gastrulation, but *aldh1a2* is the most abundant transcript. Since transcripts of *aldh1a2* and *aldh1a3* have been detected in the embryonic organizer (Chen et al., 2001; Lupo et al., 2005) we compared their spatial expression patterns by qPCR and double whole-mount *in situ* hybridization (dWISH) later during gastrulation. The relative localization of the *aldh1a1*, *aldh1a2*, and *aldh1a3* transcripts was determined by dissecting dorsal, lateral, and ventral marginal zones (DMZ, LMZ, and VMZ, respectively) from embryos during mid-gastrula (st. 11). The RNA from these regions was analyzed by qPCR to determine the relative transcript distribution (Figure 4A). Although expressed at very low levels (Shabtai et al., 2018), most of the *aldh1a1* transcripts are localized in the LMZ explants (Figure 4A). With this type of analysis, *aldh1a2* expression appears ubiquitous with similar abundance in all three regions in agreement with its wide expression domain during mid/late gastrula stages as observed by WISH (Figures 4B,C, turquoise). Expression of *aldh1a3* is mostly localized to the DMZ with almost no transcripts in other embryonic regions (Figure 4A). This *aldh1a3* transcript distribution is in agreement with the expression being restricted to the organizer and to cells along the dorsal midline, suggesting that this gene might be involved in the head-promoting role of RA. The accuracy of the embryonic dissections was corroborated by analyzing the expression of *chrd.1* as a dorsal marker, *myod1* as a lateral marker, and *szl* as a ventral marker (Figure 4A).

To better understand the pattern of *aldh1a3* expression, we studied its spatial expression in parallel to *aldh1a2*, *cyp26a1*, and *otx2*. Comparative analysis of the *aldh1a2* and *aldh1a3* expression patterns clearly shows that by mid/late gastrula (st. 11.5) both genes are expressed in non-overlapping domains (Figure 4B). While the *aldh1a2* expression remains posterior, close to the blastopore, *aldh1a3* expression is restricted to a small cluster of cells, probably representing the migrating LEM/PCM (Figure 4B). By early neurula stages (st. 15) *aldh1a3* expression becomes undetectable and only the expression of *aldh1a2* in the prospective trunk is observed (Figure 4C). The rostral localization of *aldh1a3* expression during late gastrula prompted us to look at its position relative to other genes expressed in the same region. First, we analyzed the spatial localization relative to *cyp26a1*, another member of the RA metabolic network known to be expressed in the neuroectoderm of the prospective forebrain region (Holleman et al., 1998; de Roos et al., 1999). The dWISH results show that the *aldh1a3* expressing cells (purple) appear to overlap with the cranial domain of *cyp26a1* expression (turquoise; Figure 4D). To better understand this apparent overlap between the *aldh1a3* and *cyp26a1* expression domains in the rostral region, embryos were bisected sagittally for analysis. While the *cyp26a1* expression localizes to more superficial cells in the rostral as well as the blastopore expression domain, the *aldh1a3* expressing cells localize just below the rostral *cyp26a1* positive cells

(Figure 4E). Although we cannot rule out a slight overlap in the future head domain, *cyp26a1* is expressed in the ectodermal cells whereas *aldh1a3* is expressed in the migrating mesendodermal cells. To better understand the relative position of the *aldh1a3*-positive cells within the rostral domain we compared it to the *otx2* expression domain, another early anterior head marker (Blitz and Cho, 1995; Pannese et al., 1995). Analysis of the overlap shows a small group of *aldh1a3* positive cells (purple) migrating rostrally towards the prospective midbrain/forebrain domain marked by *otx2* expression during mid gastrula (st. 11) (turquoise; Figure 4F). During late gastrula (st. 12), the small cluster of *aldh1a3* positive cells can be detected beneath a larger *otx2* expressing domain (Figure 4G). Also, in this case, the *aldh1a3* expressing cells localize ventrally to the *otx2* expression domain. These results support the conclusion that *aldh1a3* is expressed in the anterior mesendodermal, LEM/PCM cells.

The enzymatic function of *aldh1a3* as a producer of RA places a dynamic, second RA signaling center in the dorsal region of the gastrula embryo. The expression pattern of *aldh1a3* during gastrula and early neurula is characteristic of organizer genes that continue to have dorsal midline expression. To further study the dorsal identity of *aldh1a3*-expressing cells, embryos were dorsalized by promoting Wnt/ β -catenin signaling, or ventralized by increasing the BMP signal. Embryos were injected with *wnt8a* or *bmp4* mRNA to induce dorsalization and ventralization, respectively, and samples were collected during early/mid gastrula (st. 10.5), mid gastrula (st. 11), and early neurula (st. 13) to account for the dynamic nature of the expression patterns. To verify the efficacy of the RNA injections, we studied the responses of *gsc* and *admp* as dorsal genes and *szl* and *ventx1.2* as ventral genes by qPCR. In agreement with their dorsal expression, *gsc* and *admp* were upregulated by *wnt8a* RNA injection dorsalization and downregulated by *bmp4* ventralization (Figures 4H,I). *szl* and *ventx1.2*, on the other hand, exhibited the expected opposite responses as ventral targets of BMP4 signaling, downregulation by *wnt8a*, and upregulation by *bmp4* overexpression (Figures 4H,I). At all stages studied, *aldh1a3* was upregulated by *wnt8a* overexpression and downregulated by *bmp4*, similar to *gsc* and *admp* (Figures 4H,I). These results show that *aldh1a3* responds like a typical organizer and dorsal midline gene to the manipulation of dorsal-ventral patterning. In contrast, from stage 10.5, the *aldh1a2* domain of expression expands laterally and its transcripts are eliminated from the organizer or midline region (Figures 4A–C) (Chen et al., 2001). In agreement, activation of the early Wnt/ β -catenin pathway has a very slight upregulatory effect, and during later stages, it weakly represses *aldh1a2* expression. The changes induced by Wnt/ β -catenin activation emphasize the dynamic changes in *aldh1a2* expression with the progression of gastrulation (Figure 4H) (Chen et al., 2001). Manipulation of the BMP signal had no effect on the *aldh1a2* expression (Figure 4I).

ALDH1A3 Produces Retinoic Acid Required for Head Formation

Characterization of the *aldh1a3* and *aldh1a2* expression patterns showed that while *aldh1a2* expression begins in the organizer and then expands and shifts laterally, *aldh1a3* expression begins in the

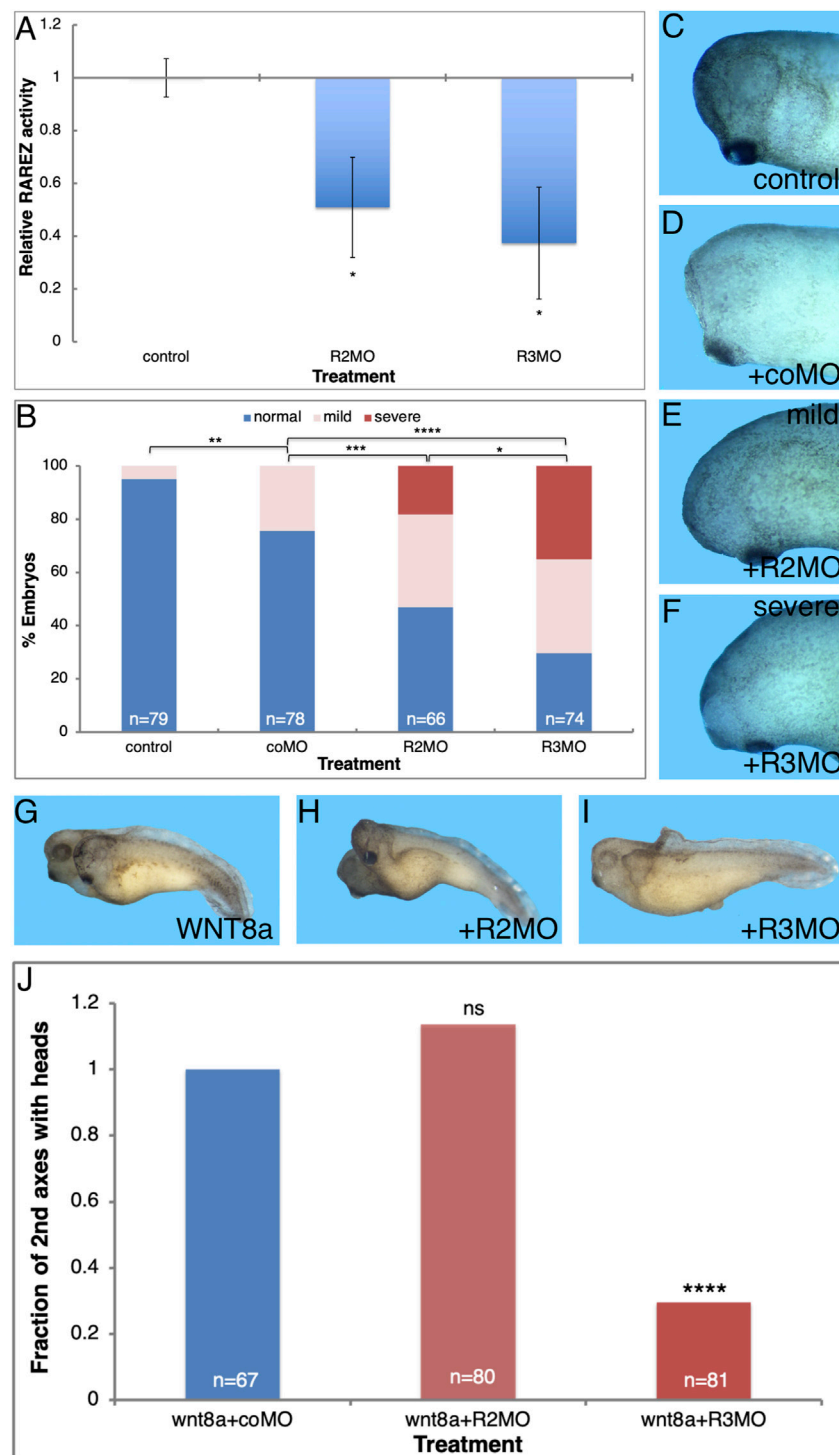


FIGURE 5 | ALDH1A3 is necessary for normal head development. Embryos were injected with the R2MO or R3MO to reduce the activity of ALDH1A2 or ALDH1A3, respectively. **(A)** Analysis of the effect on the RA signaling level by co-injection of the RA reporter plasmid and chemiluminescent analysis of the β -galactosidase activity. **(B–F)** Embryos injected dorsally with the R2MO, R3MO, or coMO to induce ALDH1A2 or ALDH1A3 knockdown in the Spemann-Mangold organizer. Embryos were sensitized for changes in RA levels by co-injection of low, non-teratogenic, amounts of *cyp26a1* RNA. The extent of microcephaly induction was quantitated **(B)**. Examples of head development for control uninjected **(C)**, coMO **(D)**, R2MO **(E)**, and R3MO **(F)** injected embryos are shown. **(G–J)** Analysis of head malformations in secondary axes induced by ventral injection of *wnt8a* RNA together with ALDH1A2 or ALDH1A3 knockdown. **(G)** Control embryo. **(H)** ALDH1A2 knockdown. **(I)** ALDH1A3 knockdown. **(J)** Quantitation of the effect of ALDH1A2 or ALDH1A3 knockdown on head development in the induced secondary axes. The overall number of embryos injected or manipulated is shown (*n* =). *, *p* < 0.05 **, *p* < 0.01; ***, *p* < 0.001 ****, *p* < 0.0001; ns, not significant.

organizer and until late gastrula remains restricted to the dorsal midline, rostrally migrating LEM/PCM cells (Figures 4B,C). From the shared expression patterns in the gastrula organizer and the timing of the RA signal we were unable to identify whether one of these enzymes has a more prominent role in normal head development. To functionally determine which RA-producing enzyme contributes to head formation, we designed antisense morpholino oligonucleotides (MO) targeting either *aldh1a3* or *aldh1a2* (R3MO or R2MO, respectively). To determine the efficiency and specificity of R2MO and R3MO we constructed GFP variants containing the *aldh1a3* and *aldh1a2* MO target sequences (R3GFP or R2GFP, respectively). RNAs encoding the GFP variants were co-injected with the R3MO, R2MO, or control MO (coMO) into *Xenopus* embryos (Supplementary Figure S2). Only when R2GFP was co-injected with the R2MO or R3GFP was co-injected with the R3MO, was the GFP fluorescence strongly reduced (Supplementary Figures S2D,I). Co-injection with the control MO had no effect on the fluorescence intensity of the GFP variants (Supplementary Figures S2B,C,G,H). These results demonstrate that R2MO and R3MO are efficient tools for the knock-down of their respective proteins.

Knockdown of the ALDH1A3 or ALDH1A2 enzymes is expected to reduce their activity and ultimately result in a reduction in RA signaling. For this reason, additional validation of the efficacy of the MOs directed against *aldh1a2* and *aldh1a3* (R2MO and R3MO) tested their effect on RA signaling levels. The effect of ALDH1A3 and ALDH1A2 knockdown on RA signaling was studied by co-injection with the RA reporter plasmid, RAREZ. Embryos injected with RAREZ and either R3MO or R2MO were collected at early/mid gastrula (st. 10.5) and the level of β -galactosidase activity was determined using its chemiluminescent substrate (Figure 5A). This analysis showed that knockdown of either enzyme, ALDH1A3 or ALDH1A2, efficiently reduces the level of RA signaling by about 50–60% of control levels (Figure 5A). Thus, R3MO and R2MO efficiently hamper the production of RA, and both enzymes contribute to RA in the early gastrula embryo.

Our results of systemic RA reduction by CYP26A1 overexpression or the use of RA biosynthesis inhibition (DEAB) show that this signal is required for normal head development and its reduction results in microcephaly. Taking advantage of R2MO and R3MO we determined the relative contribution of ALDH1A3 and ALDH1A2 to normal head development. We reduced the expression of ALDH1A3 or ALDH1A2 by MO-mediated knockdown in the endogenous organizer by injecting embryos dorsally with R2MO, R3MO, or coMO, and the extent of induced microcephaly was quantitated (Figures 5B–F). The R2MO and R3MO efficiently induce knockdown of the endogenous activity, but we have shown that different embryo clutches respond differently to RA inhibition probably establishing a compensatory robustness response (Blum et al., 2015; Shukrun et al., 2019; Parihar et al., 2021). For these reasons, the experiment was performed in embryos sensitized for changes in RA levels by co-injection of low, non-teratogenic, amounts of *cyp26a1* RNA which weakly reduces the levels of RA (Figure 5D) to improve the

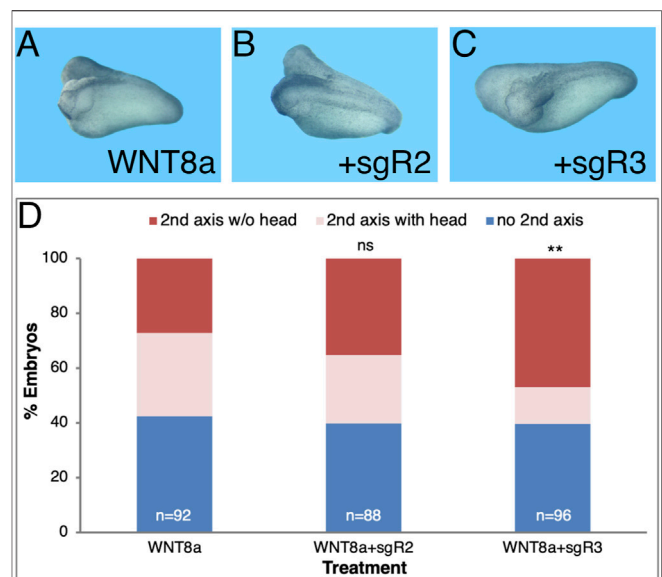


FIGURE 6 | *aldh1a3* CRISPR/Cas9-mediated knockdown on head formation in the induced secondary axes. The overall number of embryos injected or manipulated is shown (n =). Percent embryos *wnt8a* mRNA injected, embryos with secondary axes without heads and with heads. **, $p < 0.01$; ns, not significant.

effect of the MOs injected. The results show that under these conditions, ALDH1A3 knockdown induces severe microcephaly in a large proportion of embryos (35.1%; Figures 5B,F). By comparison, ALDH1A2 knockdown induces severe microcephaly in only 18.2% of the embryos (Figures 5B,E). The coMO had a weak effect on head morphology, inducing mild microcephaly in 24.6% of the embryos compared to 34.8 and 35.1% for R2MO and R3MO, respectively (Figures 5B,D). These results support the role of ALDH1A3 as providing the main retinaldehyde dehydrogenase activity producing the RA that is required for head formation, whereas ALDH1A2 appears to play a less prominent role in head development.

To corroborate the requirement for the function ALDH1A3 in normal head formation, we studied head-containing secondary axes induced by ventral injection of *wnt8a* mRNA. The role of ALDH1A3 or ALDH1A2 in head formation was studied by injection of the R2MO or R3MO together with the induction of the secondary axis (Figures 5G,H). ALDH1A3 knockdown dramatically reduced the efficiency of head formation in the induced secondary axes by 70% (Figures 5I,J); in contrast, ALDH1A2 knockdown did not affect the efficiency of head formation as compared to control *wnt8a* RNA injected embryos (Figures 5F,J). Neither morpholino significantly affects the efficiency of secondary axis induction (Figure 5J). These results show that ALDH1A3 has a strong effect on head

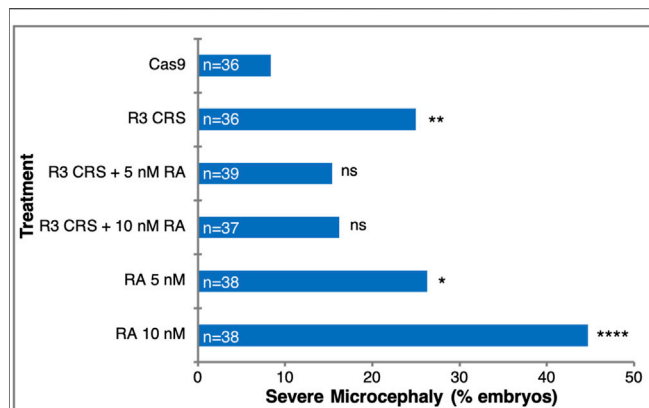


FIGURE 7 | RA rescues the microcephaly induced by loss of ALDH1A3 activity. Microcephaly was induced in *Xenopus* embryos by targeting the *aldh1a3* gene with CRISPR/Cas9+sgR3. As controls, embryos were injected with Cas9 only. For rescue of the microcephalic phenotype, embryos were treated with 5 nM or 10 nM RA. The rescue efficiency was calculated by Chi-square, comparing each treatment to the Cas9 control microcephaly level. *, $p < 0.05$; **, $p < 0.01$; ****, $p < 0.0001$; ns, not significant.

development and appears to be a central RA producing enzyme required for this process.

To validate the MO results on head formation, we designed single guide RNAs (sg) to induce indels in either the *aldh1a2* or *aldh1a3* genes (sgR2 and sgR3, respectively) using the CRISPR/Cas9 approach (Tandon et al., 2017; Naert et al., 2020). The sgR2 and sgR3 RNAs were designed to target both homologs of either *aldh1a2* or *aldh1a3*, respectively (Table 1; Supplementary Figures S3A,B). One-cell embryos were injected with RNP complexes of either sgR2 or sgR3 RNA together with Cas9 protein to generate CRISPR embryos that were allowed to develop to early tailbud stages (st.32) for genomic DNA extraction. Sequencing of the genomic region targeted by the sgRNAs revealed clear disruption of the normal sequence (Supplementary Figures S3C–E). Decomposition analysis of the genomic sequences estimated a frameshift efficiency higher than 78% (Supplementary Figure S3C). The efficiency of the sgR2 and sgR3 allow us to perform gene editing experiments and analyze the injected founder (F0) individuals, CRISPR embryos.

Taking advantage of the generation of CRISPR embryos, we performed the head formation inhibition assay in secondary axes by injecting CRISPR/Cas9 with either sgR2 or sgR3 (Figure 6). Embryos were injected ventrally with a combination of *wnt8a* RNA for secondary axis induction together with the sgRNA/Cas9 RNP complex. The sgRNA/Cas9 complex had no effect on the secondary axis induction efficiency which was around 60% of the injected embryos in control *wnt8a* only and sgR2 or sgR3 CRISPR embryos (Figures 6A,C). Indel induction in the *aldh1a3* CRISPR embryos significantly increased the loss of secondary head formation efficiency (55.5% loss; Figures 6C,D). Knockdown of the ALDH1A2 activity had a slight (17.9%) and not significant effect on head formation in the secondary axes (Figures 6B,D). These results confirm that loss-of-function the ALDH1A3 activity by CRISPR/Cas9 gene targeting is critical for normal head development.

The knockdown experiments suggest a novel function for RA signaling during gastrulation by providing a required signal for normal head development. To further support this RA requirement in head formation we performed rescue experiments. Microcephaly was induced by generating *aldh1a3* CRISPR embryos and the head malformations were rescued by the addition of low amounts of RA (5 nM or 10 nM) (Figure 7). Whereas, among Cas9 injected control embryos only 8.4% developed severe microcephaly, targeting the *aldh1a3* gene with sgR3 resulted in a significant three-fold increase (25%) of embryos with severe microcephaly (Figure 7). The addition of low amounts of RA to the *aldh1a3* CRISPR embryos reduced the extent of severe microcephaly by about a third (to 15.4–16.2%). It is important to note that low amounts of RA alone induced severe microcephaly (26.3% for 5 nM and 44.7% for 10 nM) through inhibition of forebrain fates. These results show that RA supplementation of *aldh1a3* CRISPR embryos partially rescues the microcephaly induced by the loss of the RA producing enzyme.

Retinoic Acid Regulatory Functions During Early Head Formation

RA is well known to regulate the genes that affect its level. To better characterize the molecular, gene-regulatory role of RA signaling in the head organizer, we studied the effect of RA addition on the expression of *aldh1a2* and *aldh1a3* and a number of head organizer genes. The initial activation of *aldh1a2* expression is probably RA-independent but soon thereafter the RA self-regulation might contribute to the expression of RA network genes including *aldh1a2* and *aldh1a3*. To determine the responsiveness to increased levels of RA of gastrula expressed RA metabolic genes, we treated embryos with 100 nM RA from late blastula to early/mid (st. 10.25) and late gastrula stages (st. 12). Analysis of *hoxb1* expression revealed the expected RA-dependent upregulation at both gastrula stages supporting the efficiency of this treatment (Figure 8A). Similarly, the expression of genes important for attenuating RA signaling, *dhfr3*, and *cyp26a1*, was upregulated relative to controls in agreement with their enzymatic role (Figure 8A). In contrast, genes encoding RA biosynthetic enzymes, *aldh1a2*, *aldh1a3*, and *rdh10* exhibit weak, not significant responses to the RA increase during early gastrula stages (Figure 8A); *aldh1a2* and *rdh10* exhibit slight downregulation, whereas *aldh1a3* exhibits weak upregulation (Figure 8A). During late gastrula, however, all three RA biosynthetic genes exhibit a more robust and significant, RA-mediated downregulation (Figure 8A). These results indicate the very early establishment of RA self-regulatory network gene responses. While increased RA levels upregulate genes encoding enzymes that suppress the levels of RA from early gastrula, genes involved in the production of RA are downregulated only by late gastrula (Figure 8A).

To understand the contribution of the RA signaling centers during gastrulation to head development, we took advantage of the sgR2 and sgR3 gene-specific CRISPR embryos and analyzed the effect on organizer genes previously shown to be involved in head development, i.e., head organizer genes. CRISPR embryos were collected

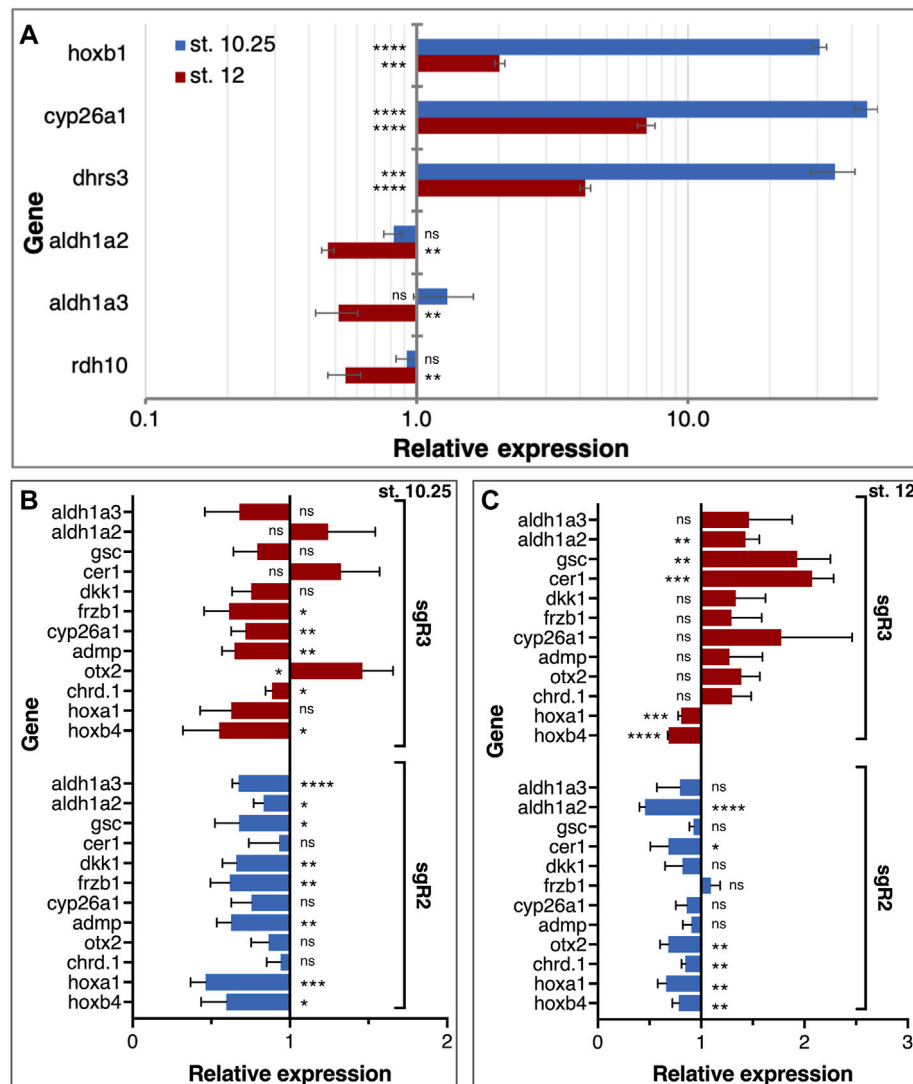


FIGURE 8 | RA autoregulation and control of LEM/PCM gene expression. **(A)** Embryos were treated with RA (100 nM) during late blastula stages and RNA samples were collected during early (st. 10.25) and late (st. 12) gastrula stages. The effect of the manipulation on RA network gene expression (*dhars3*, *cyp26a1*, *aldh1a2*, *aldh1a3*, and *rdh10*) was determined by qPCR. The expression of *hoxb1* was studied to monitor the changes in RA level. Samples were normalized to control expression level at each stage. **(B,C)** The expression of organizer genes linked to head formation (*gsc*, *cer1*, *dkk1*, *frzb1*, *admp*, *otx2*, and *chrd.1*) was analyzed in *aldh1a2* and *aldh1a3* CRISPRants. The RA-regulated genes, *cyp26a1*, *hoxa1*, *hoxb4*, *aldh1a2*, and *aldh1a3*, were studied in parallel. The gene expression analysis was performed at st. 10.25 **(B)** and st. 12 **(C)**. Relative expression was normalized to control expression levels at each stage. *, $p < 0.05$; **, $p < 0.01$; ***, $p < 0.001$; ****, $p < 0.0001$; ns, not significant.

at early gastrula (st. 10.25) when the domains of *aldh1a2* and *aldh1a3* overlap, and during late gastrula when their domains are separate (Figure 4B). qPCR analysis of *gsc*, *cer1*, *dkk1*, *frzb1*, *admp*, *otx2*, and *chrd.1* was performed, in addition to a number of known RA-regulated genes: *cyp26a1*, *hoxa1*, *hoxb4*, *aldh1a2*, and *aldh1a3* (Figures 8B,C). During early gastrula, most genes studied exhibited some degree of downregulation in both *aldh1a2* and *aldh1a3* CRISPRants (Figure 8B). This observation is in agreement with the required role of RA in the normal gene expression in the organizer and surrounding regions supporting the results of systemic RA manipulations (Figure 3). Interestingly, knockdown of either gene had similar effects

suggesting that both enzymes contribute to the production of RA in the organizer. By late gastrula, however, the effect of the *aldh1a2* and *aldh1a3* CRISPRants differs. While the gene expression changes to *aldh1a2* knockdown are very slight, in *aldh1a3* CRISPRants most genes tested exhibited weak upregulation (Figure 8C). These results suggest that ALDH1A2 has a very limited effect on the expression of organizer genes that continue to be expressed in the LEM/PCM cells. In agreement with a role in head formation, ALDH1A3 knockdown affects most genes tested suggesting that in the LEM/PCM cells, RA modulates their expression.

DISCUSSION

Retinoic Acid is Required for Head Formation

Induction of the anterior neuroectoderm including formation of the head is the focus of extensive study in developmental biology. In addition to the interest in the basic understanding of these processes, multiple human conditions arise from defects in these events including microcephaly and its accompanying cognitive disabilities. Numerous mutations or exposure to environmental factors can induce microcephaly in humans (Abuelo, 2007; Mochida, 2009; Dymment et al., 2013; Faheem et al., 2015; Duerinckx and Abramowicz, 2018). Alcohol (ethanol) exposure during pregnancy also induces microcephaly as part of the developmental malformations characteristic of FAS (Gautam et al., 2015; Popova et al., 2016; Del Campo and Jones, 2017; Jarmasz et al., 2017; Petrelli et al., 2019). Over the last years, evidence has accumulated showing that FAS induction by ethanol is mediated in part by a reduction in RA signaling (Kot-Leibovich and Fainsod, 2009; Muralidharan et al., 2015; Shabtai et al., 2018; Shukrun et al., 2019). This reduction in RA signaling and the resulting microcephaly in FAS suggested that RA signaling has a novel, and as yet unexplored function required for the normal formation of the head. In the present study we employed multiple assays to demonstrate the involvement of RA signaling in early head development. Irrespective of the assay used, RA knockdown resulted in a microcephalic phenotype similar to alcohol exposure (Nakatsuji, 1983; Shabtai et al., 2018; Shukrun et al., 2019).

It is commonly accepted that RA has an inhibitory function on the development of the rostral neuroectodermal domain by promoting hindbrain expansion and malformations (Durstion et al., 1989; Sive et al., 1990; Koide et al., 2001; Ribes et al., 2007). The *Hox* genes are some of the earliest targets of RA signaling in the hindbrain and are thought to mediate this effect because many of the observed head malformations can be reproduced by their overexpression (Conlon and Rossant, 1992; Alexandre et al., 1996; Whiting, 1997; Zaffran et al., 2018). The prospective forebrain region is believed to be devoid of RA signaling during early embryogenesis based primarily on the expression of CYP26A1 in this head domain (Hollemann et al., 1998; Ribes et al., 2007; Tanibe et al., 2008; Nolte et al., 2019). Surprisingly, our analysis based on RA signaling knockdown using biosynthesis inhibitors or CYP26A1 overexpression resulted in the induction of microcephaly by reduced RA. This developmental malformation was obtained by targeting the embryonic organizer irrespective of whether the endogenous organizer was targeted or whether an ectopic, secondary organizer was experimentally induced and targeted. These results demonstrate that RA is required for normal head formation. Reduced RA signaling has previously been linked to forebrain malformations in mutants encoding components of the RA metabolic and signaling network like *aldh1a2*, *aldh1a3*, *rdh10*, and several *rar* genes (Lohnes et al., 1994; Mendelsohn et al., 1994; Dupé et al., 2003; Mic et al., 2004; Ribes et al., 2006; Molotkova et al.,

2007; Sandell et al., 2007; Mark et al., 2009; Rhinn et al., 2011). Also, knockdown of RA network components like *sdr16c5* (*rdhe2*) or *rdh10* resulted in microcephalic phenotypes (Strate et al., 2009; Belyaeva et al., 2012). Vitamin A deficient quail embryos and *Xenopus* embryos treated with RA biosynthesis inhibitors also exhibit microcephaly (Halilagic et al., 2003; Halilagic et al., 2007; Kot-Leibovich and Fainsod, 2009; Shabtai et al., 2018). These studies probably describe several RA functions taking place at different developmental stages in different regions of the embryo (Petrelli et al., 2019), while the present study focuses on one of the earliest functions of RA signaling in the embryo.

The Head-Promoting Activity of Retinoic Acid Localizes to the Organizer

Multiple studies have shown that RA is already present in the vertebrate embryonic organizer during early gastrula stages (Hogan et al., 1992; Creech Kraft et al., 1994; Kraft et al., 1994; Ulven et al., 2000). Functional RA signaling has been localized mainly to the embryonic organizer at similar stages (Rossant et al., 1991; Deltour et al., 1996; Yelin et al., 2005; Samarut et al., 2015). Our results using a reporter plasmid show that RA signaling becomes activated at the onset of gastrulation and continues to increase towards neurula stages. Activation of the RA pathway follows the temporal expression and transcript accumulation of *aldh1a2*, the retinaldehyde dehydrogenase activity required at those stages to complete the biosynthesis of RA (Ang and Duester, 1997; Niederreither et al., 1999; Grandel et al., 2002). Analysis of the temporal sensitivity window by RA biosynthesis inhibition at different developmental stages identified late blastula and the beginning of gastrulation as the window during which this signal is required for normal head development. These observations thus defined that the RA signal required for head formation initiates at around the onset of gastrulation and is localized to the gastrula organizer. In agreement, previous studies have shown that in *Xenopus* embryos, the LEM interacts with the prospective cranial neuroectoderm already during early gastrula stages (Koide et al., 2002).

Although RA accumulation and signaling in the organizer has been known for many years, the gene-regulatory function of this early RA signal has remained elusive. Taking advantage of the inhibition of RA biosynthesis or all-*trans* RA treatments we manipulated embryos creating samples that contain a gradient of RA concentrations above and below the normal endogenous amount. In these samples we studied the expression of organizer genes known to contribute to the formation of the head. The results showed that the unmanipulated embryo contains an almost optimal amount of RA and that experimentally induced small concentration changes in either direction results in reduced organizer-specific gene expression. Therefore, RA is normally required for the expression of all the organizer genes tested, but it also prevents the overexpression of these genes.

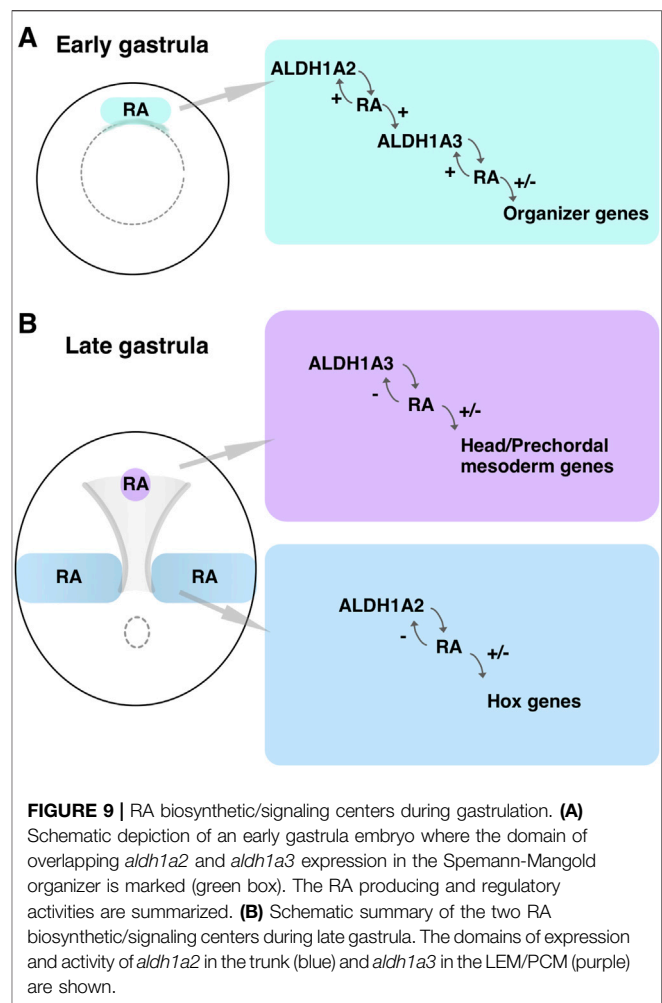
The observation that RA signaling in the early organizer is required for head formation raised a number of possibilities regarding the identity of the cells affected and the genetic

network involved. The genes we analyzed in the RA manipulated embryos have all been shown to play an early role in the formation of the head (Matsuo et al., 1995; Dosch and Niehrs, 2000; Kuroda et al., 2004; Ishibashi et al., 2008; Tanaka et al., 2017). Together all this data would point to the subpopulation commonly termed the “head organizer” in *Xenopus* (Niehrs et al., 2001; Koide et al., 2002). The head, trunk and tail organizers are functional definitions of either subpopulations originating from the organizer or the inductive potential of the organizer at different times during embryogenesis (Kaneda and Motoki, 2012; Huang and Winklbauer, 2018). At the cellular level, one of the earliest cell populations invaginating and migrating rostrally in *Xenopus* embryos is the LEM that migrates cranially, and localizes below the prospective rostral neuroectoderm, a tissue they play a role in inducing.

RALDH3 Produces the Retinoic Acid Needed for Head Formation

The results using inhibitors of RA biosynthesis (DEAB and citral) or degradation of the RA itself (CYP26A1) support a requirement for this signal during formation of the anterior head domain. To conclusively determine the involvement of RA in the early steps of head formation we set out to identify the source of this signal, i.e., the retinaldehyde dehydrogenase producing the RA for this activity. Two *aldh1a* genes are known to be expressed in the Spemann-Mangold organizer. *Aldh1a2* is the first retinaldehyde dehydrogenase expressed at the onset of gastrulation (Chen et al., 2001; Shabtai et al., 2018; Parihar et al., 2021). The appearance of this enzyme completes the biosynthesis of RA, making this pathway active apparently for the first time. This gene is initially expressed in the organizer, but by mid-gastrula the dorsal midline becomes devoid of transcripts and *aldh1a2* is expressed in more lateral regions (Chen et al., 2001). Our results show that *aldh1a3* is transcribed in a similar temporal pattern albeit at lower levels than *aldh1a2* (Shabtai et al., 2018), but with a different spatial pattern. *Aldh1a3* is co-expressed with *gsc* and *aldh1a2* in the early organizer and subsequently, remains co-expressed with *gsc* in the LEM/PCM as these cells migrate rostrally. The cells expressing *aldh1a3* within the prospective head domain appear to coincide axially with the *cyp26a1* and *otx2* expression domains but they are actually located beneath them. This pattern is in agreement with the PCM cells being a source of RA at these stages when the rostral neuroectoderm undergoes induction to form the anterior brain regions.

To characterize the function of ALDH1A3 we took advantage of a knockdown approach. We could show that reducing ALDH1A3 activity induces microcephaly and prevents head formation in a secondary axis induction assay. These results show that from its earliest expression, ALDH1A3 is present in the cells normally involved in the formation of the head. Thus, RA is required for the normal induction and formation of the head and a retinaldehyde dehydrogenase is expressed in the right cells at the right developmental stages. The source of RA for the head-forming activity is provided by the *aldh1a3*-expressing cells that induce the head. ALDH1A2 knockdown induced a weaker microcephaly suggesting that the ALDH1A3 activity might



play a more central role in the induction and formation of the head and *aldh1a2* performs a very early function that can be partially compensated by *aldh1a3*.

Positive and Negative Regulation of Rostral Head Domains by Retinoic Acid

It is widely accepted that RA is a negative regulator of anterior brain regions based on extensive experimental evidence describing the transformation of anterior neural tissues to more posterior identities following RA treatment or mutation of genes involved in the attenuation of the RA signal (Durst et al., 1989; Sive et al., 1990; Hollemann et al., 1998; Koide et al., 2001; Ribes et al., 2007; Tanibe et al., 2008; Nolte et al., 2019). During early stages of brain development, the neuroectodermal region rostral to the midbrain-hindbrain boundary expresses CYP26A1 performing a protective role by hydroxylation and subsequent degradation of RA secreted from adjacent tissues (Koide et al., 2001; Weston et al., 2003; Tanibe et al., 2012; Zhong et al., 2019). Our results show that very early in gastrulation, RA signaling is also required for the development of a normal head. Soon after the onset of gastrulation, both *aldh1a2* and *aldh1a3* are

expressed in the Spemann-Mangold organizer in *Xenopus* (Figure 9A). Similar expression patterns at comparative developmental stages have been described in other vertebrate embryos (Begemann et al., 2001; Blentic et al., 2003; Liang et al., 2008). Analysis of gene expression changes following RA manipulation and gene-specific knockdowns placed the RA produced by these enzymes as an important signal regulating multiple organizer genes (Figure 9A). Our results show that this early RA activity is required for normal head formation and possibly additional organizer functions. By early/mid gastrula the expression domains of *aldh1a2* and *aldh1a3* separate, establishing two RA biosynthetic/signaling centers (Figure 9B). The *aldh1a2* expression remains posterior, close to the blastopore, while the *aldh1a3*-expressing cells migrate cranially. The early cranially migrating cells, the LEM/PCM, will interact with the overlying ectoderm to induce the rostral neuroectoderm (Kaneda and Motoki, 2012; Huang and Winklbauer, 2018), and this interaction might take place very soon after the onset of migration (Koide et al., 2002; Lloret-Vilaspa et al., 2010; Yanagi et al., 2015). These same cells express *aldh1a3*, whose knockdown results in microcephaly and abnormal expression of head organizer genes, further supporting an early role for RA signaling and ALDH1A3 in the formation of the head (Figure 9B).

A possible explanation for the apparent discrepancy between positive and negative regulation of head formation by RA could be a combination of timing and location. During early gastrula, we have previously described a delay in the invagination and migration of the LEM/PCM cells under reduced RA signaling conditions (Yelin et al., 2007; Yelin et al., 2005). In support of a role in the regulation of morphogenetic movements, vitamin A deficiency alters the extracellular matrix and the cellular activities dependent on it (Barber et al., 2014). On the other hand, the function of the RARs as protective during head formation was mainly studied during late gastrula/early neurula stages. The mid gastrula expression of the *rar* genes, *cyp26a1*, and the co-repressor genes in the ectoderm, localizes mainly to the prospective rostral neuroectoderm suggests an early protective function from neighboring RA source(s) (Holleman et al., 1998; Koide et al., 2001). Analysis of the *raldh3* and *cyp26a1* transcripts in the prospective head region showed adjacent expression domains, which might be relevant to later functions of RA signaling in neuroectodermal differentiation. Then, reduced RA signaling could induce microcephaly by affecting the morphogenetic movements of the *aldh1a3*-expressing LEM/PCM cells out of the Spemann-Mangold organizer, or by directly affecting the inductive signals from these cells.

REFERENCES

- Abuelo, D. (2007). Microcephaly Syndromes. *Semin. Pediatr. Neurol.* 14, 118–127. doi:10.1016/j.spen.2007.07.003
- Alexandre, D., Clarke, J. D., Oxtoby, E., Yan, Y. L., Jowett, T., and Holder, N. (1996). Ectopic Expression of Hoxa-1 in the Zebrafish Alters the Fate of the Mandibular Arch Neural Crest and Phenocopies a Retinoic Acid-Induced Phenotype. *Development* 122, 735–746. doi:10.1242/dev.122.3.735
- Ang, H. L., and Duester, G. (1997). Initiation of Retinoid Signaling in Primitive Streak Mouse Embryos: Spatiotemporal Expression Patterns

DATA AVAILABILITY STATEMENT

The original contributions presented in the study are included in the article/Supplementary Material, further inquiries can be directed to the corresponding author.

ETHICS STATEMENT

The animal study was reviewed and approved by the Institutional Animal Care and Use Committee (IACUC) of the Hebrew University (Ethics approval no. MD-17-15281-3).

AUTHOR CONTRIBUTIONS

AF, MG, and LB-K. conceived and designed the experiments and analysis methodology. AF supervised the study and received funding. MG, LB-K, YS, and GP performed embryo experiments, designed sgRNAs and morpholino oligonucleotides, performed real-time PCR expression analysis and developed the figures. MG, LB-K, and AF interpreted the results and drafted the manuscript.

FUNDING

This work was funded in part by grants from the United States-Israel Binational Science Foundation (2017199), The Israel Science Foundation (668/17), the Manitoba Liquor and Lotteries (RG-003-21), and the Wolfson Family Chair in Genetics to AF.

ACKNOWLEDGMENTS

We wish to thank Martin Blum and Tim Ott for introducing us to the CRISPR/Cas9 approach in *Xenopus* embryos. We thank Sally Moody for critically reading the manuscript.

SUPPLEMENTARY MATERIAL

The Supplementary Material for this article can be found online at: <https://www.frontiersin.org/articles/10.3389/fcell.2022.844619/full#supplementary-material>

of Receptors and Metabolic Enzymes for Ligand Synthesis. *Dev. Dyn.* 208, 536–543. doi:10.1002/(SICI)1097-0177(199704)208:4<536::AID-AJA9>3.0.CO;2-J

Ang, H. L., and Duester, G. (1999). Stimulation of Premature Retinoic Acid Synthesis in *Xenopus* Embryos Following Premature Expression of Aldehyde Dehydrogenase ALDH1. *Eur. J. Biochem.* 260, 227–234. doi:10.1046/j.1432-1327.1999.00139.x

Barber, T., Esteban-Pretel, G., Marin, M., and Timoneda, J. (2014). Vitamin A Deficiency and Alterations in the Extracellular Matrix. *Nutrients* 6, 4984–5017. doi:10.3390/nu6114984

Begemann, G., Schilling, T. F., Rauch, G.-J., Geisler, R., and Ingham, P. W. (2001). The Zebrafish Neckless Mutation Reveals a Requirement for *raldh2* in

- Mesodermal Signals that Pattern the Hindbrain. *Development* 128, 3081–3094. doi:10.1242/dev.128.16.3081
- Belyaeva, O. V., Lee, S.-A., Adams, M. K., Chang, C., and Kedishvili, N. Y. (2012). Short Chain Dehydrogenase/reductase Rdhe2 is a Novel Retinol Dehydrogenase Essential for Frog Embryonic Development. *J. Biol. Chem.* 287, 9061–9071. doi:10.1074/jbc.M111.336727
- Blentic, A., Gale, E., and Maden, M. (2003). Retinoic Acid Signalling Centres in the Avian Embryo Identified by Sites of Expression of Synthesising and Catabolising Enzymes. *Dev. Dyn.* 227, 114–127. doi:10.1002/dvdy.10292
- Blitz, I. L., and Cho, K. W. (1995). Anterior neur ectoderm is progressively induced during gastrulation: the role of the *Xenopus* homeobox gene orthodenticle. *Development* 121, 993–1004. doi:10.1242/dev.121.4.993
- Blum, M., De Robertis, E. M., Wallingford, J. B., and Niehrs, C. (2015). Morpholinos: Antisense and Sensibility. *Develop. Cel* 35, 145–149. doi:10.1016/j.devcel.2015.09.017
- Brinkman, E. K., Chen, T., Amendola, M., and van Steensel, B. (2014). Easy Quantitative Assessment of Genome Editing by Sequence Trace Decomposition. *Nucleic Acids Res.* 42, e168. doi:10.1093/nar/gku936
- Catharine Ross, A., and Zolfaghari, R. (2011). Cytochrome P450s in the Regulation of Cellular Retinoic Acid Metabolism. *Annu. Rev. Nutr.* 31, 65–87. doi:10.1146/annurev-nutr-072610-145127
- Chassaing, N., Golzio, C., Odent, S., Lequeux, L., Vigouroux, A., Martinovic-Bouriel, J., et al. (2009). Phenotypic Spectrum of STRA6 Mutations: from Matthew-Wood Syndrome to Non-lethal Anophthalmia. *Hum. Mutat.* 30, E673–E681. doi:10.1002/humu.21023
- Chen, Y., Huang, L., Russo, A. F., and Solursh, M. (1992). Retinoic Acid is Enriched in Hensen's Node and is Developmentally Regulated in the Early Chicken Embryo. *Proc. Natl. Acad. Sci.* 89, 10056–10059. doi:10.1073/pnas.89.21.10056
- Chen, Y., Huang, L., and Solursh, M. (1994). A Concentration Gradient of Retinoids in the Early *Xenopus laevis* Embryo. *Develop. Biol.* 161, 70–76. doi:10.1006/dbio.1994.1008
- Chen, Y., Pollet, N., Niehrs, C., and Pieler, T. (2001). Increased XRALDH2 Activity has a Posteriorizing Effect on the central Nervous System of *Xenopus* Embryos. *Mech. Develop.* 101, 91–103. doi:10.1016/S0925-4773(00)00558-X
- Cho, K. W. Y., Blumberg, B., Steinbeisser, H., and De Robertis, E. M. (1991). Molecular Nature of Spemann's Organizer: the Role of the *Xenopus* Homeobox Gene Goosecoid. *Cell* 67, 1111–1120. doi:10.1016/0092-8674(91)90288-a
- Christian, J. L., and Moon, R. T. (1993). Interactions between Xwnt-8 and Spemann Organizer Signaling Pathways Generate Dorsal-Ventral Pattern in the Embryonic Mesoderm of *Xenopus*. *Genes Dev.* 7, 13–28. doi:10.1101/gad.7.1.13
- Clagett-Dame, M., and DeLuca, H. F. (2002). The Role of Vitamin A in Mammalian Reproduction and Embryonic Development. *Annu. Rev. Nutr.* 22, 347–381. doi:10.1146/annurev.nutr.22.010402.102745E
- Clagett-Dame, M., and Knutson, D. (2011). Vitamin A in Reproduction and Development. *Nutrients* 3, 385–428. doi:10.3390/nu3040385
- Collins, M. D., and Mao, G. E. (1999). Teratology of Retinoids. *Annu. Rev. Pharmacol. Toxicol.* 39, 399–430. doi:10.1146/annurev.pharmtox.39.1.399
- Conlon, R. A., and Rossant, J. (1992). Exogenous Retinoic Acid Rapidly Induces Anterior Ectopic Expression of Murine Hox-2 Genes *In Vivo*. *Development* 116, 357–368. doi:10.1242/dev.116.2.357
- Crabb, D. W., Matsumoto, M., Chang, D., and You, M. (2004). Overview of the Role of Alcohol Dehydrogenase and Aldehyde Dehydrogenase and Their Variants in the Genesis of Alcohol-Related Pathology. *Proc. Nutr. Soc.* 63, 49–63. doi:10.1079/PNS2003327
- Crandall, J. E., Goodman, T., McCarthy, D. M., Duester, G., Bhide, P. G., Dräger, U. C., et al. (2011). Retinoic Acid Influences Neuronal Migration from the Ganglionic eminence to the Cerebral Cortex. *J. Neurochem.* 119, 723–735. doi:10.1111/j.1471-4159.2011.07471.x
- Creech Kraft, J., Schuh, T., Juchau, M. R., and Kimelman, D. (1994). Temporal Distribution, Localization and Metabolism of All-Trans-Retinol, Didehydroretinol and All-Trans-Retinal during *Xenopus* Development. *Biochem. J.* 301 (Pt 1), 111–119. doi:10.1042/bj3010111
- Cunningham, T. J., and Duester, G. (2015). Mechanisms of Retinoic Acid Signalling and its Roles in Organ and Limb Development. *Nat. Rev. Mol. Cel Biol.* 16, 110–123. doi:10.1038/nrm3932
- de Roos, K., Sonneveld, E., Compaan, B., ten Berge, D., Durston, A. J., and van der Saag, P. T. (1999). Expression of Retinoic Acid 4-hydroxylase (CYP26) during Mouse and *Xenopus laevis* Embryogenesis. *Mech. Develop.* 82, 205–211. doi:10.1016/S0925-4773(99)00016-7
- Del Campo, M., and Jones, K. L. (2017). A Review of the Physical Features of the Fetal Alcohol Spectrum Disorders. *Eur. J. Med. Genet.* 60, 55–64. doi:10.1016/j.ejmg.2016.10.004
- Deltour, L., Ang, H. L., and Duester, G. (1996). Ethanol Inhibition of Retinoic Acid Synthesis as a Potential Mechanism for Fetal Alcohol Syndrome. *FASEB J.* 10, 1050–1057. doi:10.1096/fasebj.10.9.8801166
- Dosch, R., and Niehrs, C. (2000). Requirement for Anti-dorsalizing Morphogenetic Protein in Organizer Patterning. *Mech. Develop.* 90, 195–203. doi:10.1016/S0925-4773(99)00245-2
- Draut, H., Liebenstein, T., and Begemann, G. (2019). New Insights into the Control of Cell Fate Choices and Differentiation by Retinoic Acid in Cranial, Axial and Caudal Structures. *Biomolecules* 9, 860. doi:10.3390/biom9120860
- Duerinckx, S., and Abramowicz, M. (2018). The Genetics of Congenitally Small Brains. *Semin. Cel Develop. Biol.* 76, 76–85. doi:10.1016/j.semcdb.2017.09.015
- Duester, G. (1991). A Hypothetical Mechanism for Fetal Alcohol Syndrome Involving Ethanol Inhibition of Retinoic Acid Synthesis at the Alcohol Dehydrogenase Step. *Alcohol. Clin. Exp. Res.* 15, 568–572. doi:10.1111/j.1530-0277.1991.tb00562.x
- Dupé, V., Matt, N., Garnier, J.-M., Chambon, P., Mark, M., and Ghyselinck, N. B. (2003). A Newborn Lethal Defect Due to Inactivation of Retinaldehyde Dehydrogenase Type 3 is Prevented by Maternal Retinoic Acid Treatment. *Proc. Natl. Acad. Sci.* 100, 14036–14041. doi:10.1073/pnas.2336223100
- Durston, A. J., Timmermans, J. P. M., Hage, W. J., Hendriks, H. F. J., de Vries, N. J., Heideveld, M., et al. (1989). Retinoic Acid Causes an Anteroposterior Transformation in the Developing central Nervous System. *Nature* 340, 140–144. doi:10.1038/340140a0
- Dyment, D. A., Sawyer, S. L., Warman-Chardon, J., and Boycott, K. M. (2013). Recent Advances in the Genetic Etiology of Brain Malformations. *Curr. Neurol. Neurosci. Rep.* 13, 364. doi:10.1007/s11910-013-0364-1
- Elsea, S. H., and Williams, S. R. (2011). Smith-Magenis Syndrome: Haploinsufficiency of RAI1 Results in Altered Gene Regulation in Neurological and Metabolic Pathways. *Expert Rev. Mol. Med.* 13, e14. doi:10.1017/S1462399411001827
- Epstein, M., Pillemer, G., Yelin, R., Yisraeli, J. K., and Fainsod, A. (1997). Patterning of the Embryo along the Anterior-Posterior axis: the Role of the Caudal Genes. *Development* 124, 3805–3814. doi:10.1242/dev.124.19.3805
- Faheem, M., Naseer, M. I., Rasool, M., Chaudhary, A. G., Kumosani, T. A., Ilyas, A. M., et al. (2015). Molecular Genetics of Human Primary Microcephaly: an Overview. *BMC Med. Genomics* 8 (Suppl. 1), S4. doi:10.1186/1755-8794-8-S1-S4
- Fainsod, A., and Kot-Leibovich, H. (2018). *Xenopus* Embryos to Study Fetal Alcohol Syndrome, a Model for Environmental Teratogenesis. *Biochem. Cel Biol.* 96, 77–87. doi:10.1139/bcb-2017-0219
- Fainsod, A., Steinbeisser, H., and De Robertis, E. M. (1994). On the Function of BMP-4 in Patterning the Marginal Zone of the *Xenopus* Embryo. *EMBO J.* 13, 5015–5025. doi:10.1002/j.1460-2075.1994.tb06830.x
- Fainsod, A., Bendelac-Kapon, L., and Shabtai, Y. (2020). Fetal Alcohol Spectrum Disorder: Embryogenesis under Reduced Retinoic Acid Signaling Conditions. *Subcell Biochem.* 95, 197–225. doi:10.1007/978-3-030-42282-0_8
- Fainsod, A., Abbou, T., Bendelac-Kapon, L., Edri, T., and Pillemer, G. (2022). “Fetal Alcohol Spectrum Disorder as a Retinoic Acid Deficiency Syndrome,” in *Fetal Alcohol Spectrum Disorder. Advances in Research and Practice*. Editors A. E. Chudley and G. G. Hicks (New York, NY: Springer Nature).
- Gautam, P., Nuñez, S. C., Narr, K. L., Kan, E. C., and Sowell, E. R. (2014). Effects of Prenatal Alcohol Exposure on the Development of white Matter Volume and Change in Executive Function. *NeuroImage Clin.* 5, 19–27. doi:10.1016/j.nicl.2014.05.010
- Gautam, P., Lebel, C., Narr, K. L., Mattson, S. N., May, P. A., Adnams, C. M., et al. (2015). Volume Changes and Brain-Behavior Relationships in white Matter and Subcortical gray Matter in Children with Prenatal Alcohol Exposure. *Hum. Brain Mapp.* 36, 2318–2329. doi:10.1002/hbm.22772
- Ghyselinck, N. B., and Duester, G. (2019). Retinoic Acid Signaling Pathways. *Development* 146, dev167502. doi:10.1242/dev.167502
- Glinka, A., Wu, W., Delius, H., Monaghan, A. P., Blumenstock, C., and Niehrs, C. (1998). Dickkopf-1 is a Member of a New Family of Secreted Proteins and Functions in Head Induction. *Nature* 391, 357–362. doi:10.1038/34848

- Graff, J. M., Thies, R. S., Song, J. J., Celeste, A. J., and Melton, D. A. (1994). Studies with a *Xenopus* BMP Receptor Suggest that Ventral Mesoderm-Inducing Signals Override Dorsal Signals *In Vivo*. *Cell* 79, 169–179. doi:10.1016/0092-8674(94)90409-x
- Grandel, H., Lun, K., Rauch, G.-J., Rhinn, M., Piotrowski, T., Houart, C., et al. (2002). Retinoic Acid Signalling in the Zebrafish Embryo is Necessary during Pre-segmentation Stages to Pattern the Anterior-Posterior axis of the CNS and to Induce a Pectoral Fin Bud. *Development* 129, 2851–2865. doi:10.1242/dev.129.12.2851
- Guerri, C., Bazinet, A., and Riley, E. P. (2009). Foetal Alcohol Spectrum Disorders and Alterations in Brain and Behaviour. *Alcohol Alcohol* 44, 108–114. doi:10.1093/alcalc/agn105
- Halilagic, A., Zile, M. H., and Studer, M. (2003). A Novel Role for Retinoids in Patterning the Avian Forebrain during Presomite Stages. *Development* 130, 2039–2050. doi:10.1242/dev.00423
- Halilagic, A., Ribes, V., Ghyselinck, N. B., Zile, M. H., Dollé, P., and Studer, M. (2007). Retinoids Control Anterior and Dorsal Properties in the Developing Forebrain. *Development* 134, 362–375. doi:10.1016/j.ydbio.2006.11.021
- Hogan, B. L. M., Thaller, C., and Eichele, G. (1992). Evidence that Hensen's Node is a Site of Retinoic Acid Synthesis. *Nature* 359, 237–241. doi:10.1038/359237a0
- Hollemann, T., Chen, Y., Grunz, H., and Pieler, T. (1998). Regionalized Metabolic Activity Establishes Boundaries of Retinoic Acid Signalling. *EMBO J.* 17, 7361–7372. doi:10.1093/emboj/17.24.7361
- Hoshijima, K., Juryne, M. J., Klatt Shaw, D., Jacobi, A. M., Behlke, M. A., and Grunwald, D. J. (2019). Highly Efficient CRISPR-Cas9-Based Methods for Generating Deletion Mutations and F0 Embryos that Lack Gene Function in Zebrafish. *Development* 151, 645–657. doi:10.1016/j.devcel.2019.10.004
- Hsiao, T., Conant, D., Rossi, N., Maures, T., Waite, K., Yang, J., et al. (2018). Inference of CRISPR Edits from Sanger Trace Data. *BioRxiv*. doi:10.1101/251082
- Huang, Y., and Winklbauer, R. (2018). Cell Migration in the *Xenopus* Gastrula. *WIREs Dev. Biol.* 7, e325. doi:10.1002/wdev.325
- Inui, M., Montagner, M., Ben-Zvi, D., Martello, G., Soligo, S., Manfrin, A., et al. (2012). Self-regulation of the Head-Inducing Properties of the Spemann Organizer. *Proc. Natl. Acad. Sci. USA* 109, 15354–15359. doi:10.1073/pnas.1203000109
- Ishibashi, H., Matsumura, N., Hanafusa, H., Matsumoto, K., Robertis, E. M. D., and Kuroda, H. (2008). Expression of Siamois and Twin in the Blastula Chordin/Noggin Signaling center is Required for Brain Formation in *Xenopus laevis* Embryos. *Mech. Development* 125, 58–66. doi:10.1016/j.mod.2007.10.005
- Jarmasz, J. S., Basalah, D. A., Chudley, A. E., and Del Bigio, M. R. (2017). Human Brain Abnormalities Associated with Prenatal Alcohol Exposure and Fetal Alcohol Spectrum Disorder. *J. Neuropathol. Exp. Neurol.* 76, 813–833. doi:10.1093/jnen/nlx064
- Kaneda, T., and Motoki, J.-y. D. (2012). Gastrulation and Pre-gastrulation Morphogenesis, Inductions, and Gene Expression: Similarities and Dissimilarities between Urodelean and Anuran Embryos. *Development* 139, 1–18. doi:10.1016/j.ydbio.2012.05.019
- Kao, K. R., and Elinson, R. P. (1988). The Entire Mesodermal Mantle Behaves as Spemann's Organizer in Dorsoanterior Enhanced *Xenopus laevis* Embryos. *Development* 102, 64–77. doi:10.1016/0012-1606(88)90189-3
- Kedishvili, N. Y. (2013). Enzymology of Retinoic Acid Biosynthesis and Degradation. *J. Lipid Res.* 54, 1744–1760. doi:10.1194/jlr.R037028
- Kiecker, C., and Lumsden, A. (2012). The Role of Organizers in Patterning the Nervous System. *Annu. Rev. Neurosci.* 35, 347–367. doi:10.1146/annurev-neuro-062111-150543
- Kin Ting Kam, R., Deng, Y., Chen, Y., and Zhao, H. (2012). Retinoic Acid Synthesis and Functions in Early Embryonic Development. *Cell Biosci.* 2, 11. doi:10.1186/2045-3701-2-11
- Koide, T., Downes, M., Chandraratna, R. A. S., Blumberg, B., and Umesono, K. (2001). Active Repression of RAR Signaling is Required for Head Formation. *Genes Dev.* 15, 2111–2121. doi:10.1101/gad.908801
- Koide, T., Umesono, K., and Hashimoto, C. (2002). When Does the Anterior Endomesoderm Meet the Anterior-Most Neuroectoderm during *Xenopus* Gastrulation? *Int. J. Dev. Biol.* 46, 777–783.
- Kot-Leibovich, H., and Fainsod, A. (2009). Ethanol Induces Embryonic Malformations by Competing for Retinaldehyde Dehydrogenase Activity during Vertebrate Gastrulation. *Dis. Model. Mech.* 2, 295–305. doi:10.1242/dmm.001420
- Koyabu, D., Werneburg, I., Morimoto, N., Zollikofer, C. P. E., Forasiepi, A. M., Endo, H., et al. (2014). Mammalian Skull Heterochrony Reveals Modular Evolution and a Link between Cranial Development and Brain Size. *Nat. Commun.* 5, 3625. doi:10.1038/ncomms4625
- Kraft, J. C., Schuh, T., Juchau, M., and Kimelman, D. (1994). The Retinoid X Receptor Ligand, 9-Cis-Retinoic Acid, is a Potential Regulator of Early *Xenopus* Development. *Proc. Natl. Acad. Sci.* 91, 3067–3071. doi:10.1073/pnas.91.8.3067
- Krieg, P. A., Sakaguchi, D. S., and Kintner, C. R. (1989). Primary Structure and Developmental Expression of a Large Cytoplasmic Domain Form of *Xenopus* Laevis Neural Cell Adhesion Molecule (NCAM). *Nucl. Acids Res.* 17, 10321–10335. doi:10.1093/nar/17.24.10321
- Kuroda, H., Wessely, O., and Robertis, E. M. D. (2004). Neural Induction in *Xenopus*: Requirement for Ectodermal and Endomesodermal Signals via Chordin, Noggin, β -Catenin, and Cerberus. *Plos Biol.* 2, E92. doi:10.1371/journal.pbio.0020092
- Li, H., Tierney, C., Wen, L., Wu, J. Y., and Rao, Y. (1997). A Single Morphogenetic Field Gives Rise to Two Retina Primordia under the Influence of the Prechordal Plate. *Development* 124, 603–615. doi:10.1242/dev.124.3.603
- Liang, D., Zhang, M., Bao, J., Zhang, L., Xu, X., Gao, X., et al. (2008). Expressions of Raldh3 and Raldh4 during Zebrafish Early Development. *Gene Expr. Patterns* 8, 248–253. doi:10.1016/j.gep.2007.12.007
- Lloret-Vilaspasa, F., Jansen, H. J., Deroos, K., Chandraratna, R. A. S., Zile, M. H., Stern, C. D., et al. (2010). Retinoid Signalling is Required for Information Transfer from Mesoderm to Neuroectoderm during Gastrulation. *Int. J. Dev. Biol.* 54, 599–608. doi:10.1387/ijdb.082705f1
- Lohnes, D., Mark, M., Mendelsohn, C., Dollé, P., Dierich, A., Gorczy, P., et al. (1994). Function of the Retinoic Acid Receptors (RARs) during Development (I). Craniofacial and Skeletal Abnormalities in RAR Double Mutants. *Development* 120, 2723–2748. doi:10.1242/dev.120.10.2723
- Lupo, G., Liu, Y., Qiu, R., Chandraratna, R. A. S., Barsacchi, G., He, R.-Q., et al. (2005). Dorsoroventral Patterning of the *Xenopus* Eye: a Collaboration of Retinoid, Hedgehog and FGF Receptor Signaling. *Development* 132, 1737–1748. doi:10.1242/dev.01726
- Maden, M. (2000). The Role of Retinoic Acid in Embryonic and post-embryonic Development. *Proc. Nutr. Soc.* 59, 65–73. doi:10.1017/s0029665100000082
- Mark, M., Ghyselinck, N. B., and Chambon, P. (2006). Function of Retinoid Nuclear Receptors: Lessons from Genetic and Pharmacological Dissections of the Retinoic Acid Signaling Pathway during Mouse Embryogenesis. *Annu. Rev. Pharmacol. Toxicol.* 46, 451–480. doi:10.1146/annurev.pharmtox.46.120604.141156
- Mark, M., Ghyselinck, N. B., and Chambon, P. (2009). Function of Retinoic Acid Receptors during Embryonic Development. *Nucl. Recept. Signal.* 7, nrs.07002. doi:10.1621/nrs.07002
- Marom, K., Levy, V., Pillemer, G., and Fainsod, A. (2005). Temporal Analysis of the Early BMP Functions Identifies Distinct Anti-organizer and Mesoderm Patterning Phases. *Development* 132, 442–454. doi:10.1016/j.ydbio.2005.03.024
- Martini, M., Klausning, A., Lüchters, G., Heim, N., and Messing-Jünger, M. (2018). Head Circumference - a Useful Single Parameter for Skull Volume Development in Cranial Growth Analysis? *Head Face Med.* 14, 3. doi:10.1186/s13005-017-0159-8
- Matsuo, I., Kuratani, S., Kimura, C., Takeda, N., and Aizawa, S. (1995). Mouse Otx2 Functions in the Formation and Patterning of Rostral Head. *Genes Dev.* 9, 2646–2658. doi:10.1101/gad.9.21.2646
- Mendelsohn, C., Lohnes, D., Décimo, D., Lufkin, T., LeMeur, M., Chambon, P., et al. (1994). Function of the Retinoic Acid Receptors (RARs) during Development (II). Multiple Abnormalities at Various Stages of Organogenesis in RAR Double Mutants. *Development* 120, 2749–2771. doi:10.1242/dev.120.10.2749
- Mic, F. A., Molotkov, A., Molotkova, N., and Duester, G. (2004). Raldh2 Expression in Optic Vesicle Generates a Retinoic Acid Signal Needed for Invagination of Retina during Optic Cup Formation. *Dev. Dyn.* 231, 270–277. doi:10.1002/dvdy.20128
- Mochida, G. H. (2009). Genetics and Biology of Microcephaly and Lissencephaly. *Semin. Pediatr. Neurol.* 16, 120–126. doi:10.1016/j.spen.2009.07.001
- Molotkova, N., Molotkov, A., and Duester, G. (2007). Role of Retinoic Acid during Forebrain Development Begins Late when Raldh3 Generates Retinoic Acid in

- the Ventral Subventricular Zone. *Develop. Biol.* 303, 601–610. doi:10.1016/j.ydbio.2006.11.035
- Moreno-Mateos, M. A., Vejnar, C. E., Beaudoin, J.-D., Fernandez, J. P., Mis, E. K., Khokha, M. K., et al. (2015). CRISPRscan: Designing Highly Efficient sgRNAs for CRISPR-Cas9 Targeting *In Vivo*. *Nat. Methods* 12, 982–988. doi:10.1038/nmeth.3543
- Morgan, C. A., Parajuli, B., Buchman, C. D., Dria, K., and Hurley, T. D. (2015). N,N-diethylaminobenzaldehyde (DEAB) as a Substrate and Mechanism-Based Inhibitor for Human ALDH Isoenzymes. *Chem. Biol. Interact.* 234, 18–28. doi:10.1016/j.cbi.2014.12.008
- Muralidharan, P., Sarmah, S., and Marrs, J. A. (2015). Zebrafish Retinal Defects Induced by Ethanol Exposure are Rescued by Retinoic Acid and Folic Acid Supplement. *Alcohol* 49, 149–163. doi:10.1016/j.alcohol.2014.11.001
- Naert, T., Tulkens, D., Edwards, N. A., Carron, M., Shaidani, N.-I., Wlzl, M., et al. (2020). Maximizing CRISPR/Cas9 Phenotype Penetrance Applying Predictive Modeling of Editing Outcomes in *Xenopus* and Zebrafish Embryos. *Sci. Rep.* 10, 14662. doi:10.1038/s41598-020-71412-0
- Naito, Y., Hino, K., Bono, H., and Ui-Tei, K. (2015). CRISPRdirect: Software for Designing CRISPR/Cas Guide RNA with Reduced Off-Target Sites. *Bioinformatics* 31, 1120–1123. doi:10.1093/bioinformatics/btu743
- Nakatsuji, N. (1983). Craniofacial Malformation in *Xenopus laevis* Tadpoles Caused by the Exposure of Early Embryos to Ethanol. *Teratology* 28, 299–305. doi:10.1002/tera.1420280220
- Natale, V., and Rajagopalan, A. (2014). Worldwide Variation in Human Growth and the World Health Organization Growth Standards: a Systematic Review. *BMJ Open* 4, e003735. doi:10.1136/bmjopen-2013-003735
- Nenni, M. J., Fisher, M. E., James-Zorn, C., Pells, T. J., Ponferrada, V., Chu, S., et al. (2019). Xenbase: Facilitating the Use of *Xenopus* to Model Human Disease. *Front. Physiol.* 10, 154. doi:10.3389/fphys.2019.00154
- Niccols, A. (2007). Fetal Alcohol Syndrome and the Developing Socio-Emotional Brain. *Brain Cogn.* 65, 135–142. doi:10.1016/j.bandc.2007.02.009
- Niederreither, K., McCaffery, P., Dräger, U. C., Chambon, P., and Dollé, P. (1997). Restricted Expression and Retinoic Acid-Induced Downregulation of the Retinaldehyde Dehydrogenase Type 2 (RALDH-2) Gene during Mouse Development. *Mech. Develop.* 62, 67–78. doi:10.1016/S0925-4773(96)00653-3
- Niederreither, K., Subbarayan, V., Dollé, P., and Chambon, P. (1999). Embryonic Retinoic Acid Synthesis is Essential for Early Mouse post-implantation Development. *Nat. Genet.* 21, 444–448. doi:10.1038/7788
- Niehrs, C., Kazanskaya, O., Wu, W., and Glinka, A. (2001). Dickkopf1 and the Spemann-Mangold Head Organizer. *Int. J. Dev. Biol.* 45, 237–240.
- Niehrs, C. (2004). Regionally Specific Induction by the Spemann-Mangold Organizer. *Nat. Rev. Genet.* 5, 425–434. doi:10.1038/nrg1347
- Nieuwkoop, P. D., and Faber, J. (1967). *Normal Table of Xenopus laevis (Daudin): A Systematical and Chronological Survey of the Development from the Fertilized Egg till the End of Metamorphosis*. Amsterdam: North-Holland Publishing Company.
- Nolte, C., De Kumar, B., and Krumlauf, R. (2019). Hox Genes: Downstream “Effectors” of Retinoic Acid Signaling in Vertebrate Embryogenesis. *Genesis* 57, e23306. doi:10.1002/dvg.23306
- Pannese, M., Polo, C., Andreazzoli, M., Vignali, R., Kablar, B., and Barsacchi, G. (1995). The *Xenopus* homologue of Otx2 is a maternal homeobox gene that demarcates and specifies anterior body regions. *Development* 121, 707–720. doi:10.1242/dev.121.3.707
- Parihar, M., Bendelac-Kapon, L., Gur, M., Abbou, T., Belorkar, A., Achanta, S., et al. (2021). Retinoic Acid Fluctuation Activates an Uneven, Direction-dependent Network-wide Robustness Response in Early Embryogenesis. *Front. Cell Dev. Biol.* 9, 747969. doi:10.3389/fcell.2021.747969
- Perz-Edwards, A., Hardison, N. L., and Linney, E. (2001). Retinoic Acid-Mediated Gene Expression in Transgenic Reporter Zebrafish. *Develop. Biol.* 229, 89–101. doi:10.1006/dbio.2000.9979
- Petrelli, B., Bendelac, L., Hicks, G. G., and Fainsod, A. (2019). Insights into Retinoic Acid Deficiency and the Induction of Craniofacial Malformations and Microcephaly in Fetal Alcohol Spectrum Disorder. *Genesis* 57, e23278. doi:10.1002/dvg.23278
- Popova, S., Lange, S., Shield, K., Mihic, A., Chudley, A. E., Mukherjee, R. A. S., et al. (2016). Comorbidity of Fetal Alcohol Spectrum Disorder: a Systematic Review and Meta-Analysis. *The Lancet* 387, 978–987. doi:10.1016/S0140-6736(15)01345-8
- Pullarkat, R. K. (1991). Hypothesis: Prenatal Ethanol-Induced Birth Defects and Retinoic Acid. *Alcohol. Clin. Exp. Res.* 15, 565–567. doi:10.1111/j.1530-0277.1991.tb00561.x
- Ranke, M. B., Krägeloh-Mann, I., and Vollmer, B. (2015). Growth, Head Growth, and Neurocognitive Outcome in Children Born Very Preterm: Methodological Aspects and Selected Results. *Dev. Med. Child. Neurol.* 57, 23–28. doi:10.1111/dmcn.12582
- Rhinn, M., and Dollé, P. (2012). Retinoic Acid Signalling during Development. *Development* 139, 843–858. doi:10.1242/dev.065938
- Rhinn, M., Schuhbaur, B., Niederreither, K., and Dollé, P. (2011). Involvement of Retinol Dehydrogenase 10 in Embryonic Patterning and rescue of its Loss of Function by Maternal Retinaldehyde Treatment. *Proc. Natl. Acad. Sci.* 108, 16687–16692. doi:10.1073/pnas.1103877108
- Ribes, V., Wang, Z., Dolle, P., and Niederreither, K. (2006). Retinaldehyde Dehydrogenase 2 (RALDH2)-Mediated Retinoic Acid Synthesis Regulates Early Mouse Embryonic Forebrain Development by Controlling FGF and Sonic Hedgehog Signaling. *Development* 133, 351–361. doi:10.1242/dev.02204
- Ribes, V., Fraulob, V., Petkovich, M., and Dollé, P. (2007). The Oxidizing Enzyme CYP26a1 Tightly Regulates the Availability of Retinoic Acid in the Gastrulating Mouse Embryo to Ensure Proper Head Development and Vasculogenesis. *Dev. Dyn.* 236, 644–653. doi:10.1002/dvdy.21057
- Ross, S. A., McCaffery, P. J., Drager, U. C., and De Luca, L. M. (2000). Retinoids in Embryonal Development. *Physiol. Rev.* 80, 1021–1054. doi:10.1152/physrev.2000.80.3.1021
- Rossant, J., Zirngibl, R., Cado, D., Shago, M., and Giguère, V. (1991). Expression of a Retinoic Acid Response Element-hsplaZ Transgene Defines Specific Domains of Transcriptional Activity during Mouse Embryogenesis. *Genes Dev.* 5, 1333–1344. doi:10.1101/gad.5.8.1333
- Roussotte, F. F., Sulik, K. K., Mattson, S. N., Riley, E. P., Jones, K. L., Adnams, C. M., et al. (2012). Regional Brain Volume Reductions Relate to Facial Dysmorphology and Neurocognitive Function in Fetal Alcohol Spectrum Disorders. *Hum. Brain Mapp.* 33, 920–937. doi:10.1002/hbm.21260
- Russo, J. E., Hauquitz, D., and Hilton, J. (1988). Inhibition of Mouse Cytosolic Aldehyde Dehydrogenase by 4-(diethylamino) benzaldehyde. *Biochem. Pharmacol.* 37, 1639–1642. doi:10.1016/0006-2952(88)90030-5
- Samarut, E., Fraher, D., Laudet, V., and Gibert, Y. (2015). ZebRA: An Overview of Retinoic Acid Signaling during Zebrafish Development. *Biochim. Biophys. Acta Gene Regul. Mech.* 1849, 73–83. doi:10.1016/j.bbagr.2014.05.030
- Sandell, L. L., Sanderson, B. W., Moiseyev, G., Johnson, T., Mushegian, A., Young, K., et al. (2007). RDH10 is Essential for Synthesis of Embryonic Retinoic Acid and is Required for Limb, Craniofacial, and Organ Development. *Genes Dev.* 21, 1113–1124. doi:10.1101/gad.1533407
- Sasai, Y., Lu, B., Steinbeisser, H., Geissert, D., Gont, L. K., and De Robertis, E. M. (1994). *Xenopus* Chordin: a Novel Dorsalizing Factor Activated by Organizer-specific Homeobox Genes. *Cell* 79, 779–790. doi:10.1016/0092-8674(94)90068-x
- See, A. W.-M., Kaiser, M. E., White, J. C., and Clagett-Dame, M. (2008). A Nutritional Model of Late Embryonic Vitamin A Deficiency Produces Defects in Organogenesis at a High Penetrance and Reveals New Roles for the Vitamin in Skeletal Development. *Develop. Biol.* 316, 171–190. doi:10.1016/j.ydbio.2007.10.018
- Shabtai, Y., and Fainsod, A. (2018). Competition between Ethanol Clearance and Retinoic Acid Biosynthesis in the Induction of Fetal Alcohol Syndrome. *Biochem. Cell Biol.* 96, 148–160. doi:10.1139/bcb-2017-0132
- Shabtai, Y., Jubran, H., Nassar, T., Hirschberg, J., and Fainsod, A. (2016). Kinetic Characterization and Regulation of the Human Retinaldehyde Dehydrogenase 2 Enzyme during Production of Retinoic Acid. *Biochem. J.* 473, 1423–1431. doi:10.1042/BCJ20160101
- Shabtai, Y., Bendelac, L., Jubran, H., Hirschberg, J., and Fainsod, A. (2018). Acetaldehyde Inhibits Retinoic Acid Biosynthesis to Mediate Alcohol Teratogenicity. *Sci. Rep.* 8, 347. doi:10.1038/s41598-017-18719-7
- Shen, M. W., Arbab, M., Hsu, J. Y., Worstell, D., Culbertson, S. J., Krabbe, O., et al. (2018). Predictable and Precise Template-free CRISPR Editing of Pathogenic Variants. *Nature* 563, 646–651. doi:10.1038/s41586-018-0686-x
- Shiotsugu, J., Katsuyama, Y., Arima, K., Baxter, A., Koide, T., Song, J., et al. (2004). Multiple Points of Interaction between Retinoic Acid and FGF Signaling during Embryonic Axis Formation. *Development* 131, 2653–2667. doi:10.1242/dev.01129

- Shukrun, N., Shabtai, Y., Pillemer, G., and Fainsod, A. (2019). Retinoic Acid Signaling Reduction Recapitulates the Effects of Alcohol on Embryo Size. *Genesis* 57, e23284. doi:10.1002/dvg.23284
- Sive, H. L., Hattori, K., and Weintraub, H. (1989). Progressive Determination during Formation of the Anteroposterior axis in *Xenopus laevis*. *Cell* 58, 171–180. doi:10.1016/0092-8674(89)90413-3
- Sive, H. L., Draper, B. W., Harland, R. M., and Weintraub, H. (1990). Identification of a Retinoic Acid-Sensitive Period during Primary axis Formation in *Xenopus laevis*. *Genes Dev.* 4, 932–942. doi:10.1101/gad.4.6.932
- Smith, W. C., Knecht, A. K., Wu, M., and Harland, R. M. (1993). Secreted Noggin Protein Mimics the Spemann Organizer in Dorsalizing *Xenopus* Mesoderm. *Nature* 361, 547–549. doi:10.1038/361547a0
- Sokol, S., Christian, J. L., Moon, R. T., and Melton, D. A. (1991). Injected Wnt RNA Induces a Complete Body axis in *Xenopus* Embryos. *Cell* 67, 741–752. doi:10.1016/0092-8674(91)90069-b
- Spemann, H., and Mangold, H. (1924). über Induktion von Embryonalanlagen durch Implantation artfremder Organisatoren. *Archiv F Mikr Anat. U Entwicklungsmechanik* 100, 599–638. doi:10.1007/bf02108133
- Spohr, H.-L., and Steinhausen, H.-C. (2008). Fetal Alcohol Spectrum Disorders and their Persisting Sequelae in Adult Life. *Dtsch Arztebl Int.* 105, 693–698. doi:10.3238/arztebl.2008.0693
- Strate, I., Min, T. H., Iliev, D., and Pera, E. M. (2009). Retinol Dehydrogenase 10 is a Feedback Regulator of Retinoic Acid Signalling during axis Formation and Patterning of the central Nervous System. *Development* 136, 461–472. doi:10.1242/dev.024901
- Tanaka, S., Hosokawa, H., Weinberg, E. S., and Maegawa, S. (2017). Chordin and Dickkopf-1b are Essential for the Formation of Head Structures through Activation of the FGF Signaling Pathway in Zebrafish. *Develop. Biol.* 424, 189–197. doi:10.1016/j.ydbio.2017.02.018
- Tandon, P., Conlon, F., Furlow, J. D., and Horb, M. E. (2017). Expanding the Genetic Toolkit in *Xenopus*: Approaches and Opportunities for Human Disease Modeling. *Develop. Biol.* 426, 325–335. doi:10.1016/j.ydbio.2016.04.009
- Tanibe, M., Michiue, T., Yukita, A., Danno, H., Ikuzawa, M., Ishiura, S., et al. (2008). Retinoic Acid Metabolizing Factor xCyp26c is Specifically Expressed in Neuroectoderm and Regulates Anterior Neural Patterning in *Xenopus laevis*. *Int. J. Dev. Biol.* 52, 893–901. doi:10.1387/ijdb.082683mt
- Tanibe, M., Ishiura, S.-I., Asashima, M., and Michiue, T. (2012). xCOUP-TF-B Regulates xCyp26 Transcription and Modulates Retinoic Acid Signaling for Anterior Neural Patterning in *Xenopus*. *Int. J. Dev. Biol.* 56, 239–244. doi:10.1387/ijdb.113482mt
- Toi, A., Chitayat, D., and Blaser, S. (2009). Abnormalities of the Foetal Cerebral Cortex. *Prenat. Diagn.* 29, 355–371. doi:10.1002/pd.2211
- Treit, S., Chen, Z., Zhou, D., Baugh, L., Rasmussen, C., Andrew, G., et al. (2017). Sexual Dimorphism of Volume Reduction but Not Cognitive Deficit in Fetal Alcohol Spectrum Disorders: A Combined Diffusion Tensor Imaging, Cortical Thickness and Brain Volume Study. *NeuroImage Clin.* 15, 284–297. doi:10.1016/j.nicl.2017.05.006
- Twal, W., Roze, L., and Zile, M. H. (1995). Anti-retinoic Acid Monoclonal Antibody Localizes All-Trans-Retinoic Acid in Target Cells and Blocks normal Development in Early Quail Embryo. *Develop. Biol.* 168, 225–234. doi:10.1006/dbio.1995.1075
- Ulven, S. M., Gundersen, T. E., Weedon, M. S., Landaas, V. Ø., Sakhi, A. K., Fromm, S. H., et al. (2000). Identification of Endogenous Retinoids, Enzymes, Binding Proteins, and Receptors during Early Postimplantation Development in Mouse: Important Role of Retinal Dehydrogenase Type 2 in Synthesis of All-Trans-Retinoic Acid. *Develop. Biol.* 220, 379–391. doi:10.1006/dbio.2000.9634
- Vermot, J., Niederreither, K., Garnier, J.-M., Chambon, P., and Dollé, P. (2003). Decreased Embryonic Retinoic Acid Synthesis Results in a DiGeorge Syndrome Phenotype in Newborn Mice. *Proc. Natl. Acad. Sci.* 100, 1763–1768. doi:10.1073/pnas.0437920100
- Weston, A. D., Blumberg, B., and Underhill, T. M. (2003). Active Repression by Unliganded Retinoid Receptors in Development. *J. Cel Biol.* 161, 223–228. doi:10.1083/jcb.200211117
- Whiting, J. (1997). Craniofacial Abnormalities Induced by the Ectopic Expression of Homeobox Genes. *Mutat. Res. Fund. Mol. Mech. Mutagen.* 396, 97–112. doi:10.1016/s0027-5107(97)00177-2
- Yanagi, T., Ito, K., Nishihara, A., Minamino, R., Mori, S., Sumida, M., et al. (2015). The S Pemann Organizer Meets the Anterior-most Neuroectoderm at the Equator of Early Gastrulae in Amphibian Species. *Develop. Growth Differ.* 57, 218–231. doi:10.1111/dgd.12200
- Yelin, R., Ben-Haroush Schyr, R., Kot, H., Zins, S., Frumkin, A., Pillemer, G., et al. (2005). Ethanol Exposure Affects Gene Expression in the Embryonic Organizer and Reduces Retinoic Acid Levels. *Develop. Biol.* 279, 193–204. doi:10.1016/j.ydbio.2004.12.014
- Yelin, R., Kot, H., Yelin, D., and Fainsod, A. (2007). Early Molecular Effects of Ethanol during Vertebrate Embryogenesis. *Differentiation* 75, 393–403. doi:10.1111/j.1432-0436.2006.00147.x
- Zaffran, S., Odelin, G., Stefanovic, S., Lescroart, F., and Etchevers, H. C. (2018). Ectopic Expression of Hoxb1 Induces Cardiac and Craniofacial Malformations. *Genesis* 56, e23221. doi:10.1002/dvg.23221
- Zhong, G., Hogarth, C., Snyder, J. M., Palau, L., Topping, T., Huang, W., et al. (2019). The Retinoic Acid Hydroxylase Cyp26a1 Has Minor Effects on Postnatal Vitamin A Homeostasis, but is Required for Exogenous atRA Clearance. *J. Biol. Chem.* 294, 11166–11179. doi:10.1074/jbc.RA119.009023

Conflict of Interest: The authors declare that the research was conducted in the absence of any commercial or financial relationships that could be construed as a potential conflict of interest.

Publisher's Note: All claims expressed in this article are solely those of the authors and do not necessarily represent those of their affiliated organizations, or those of the publisher, the editors and the reviewers. Any product that may be evaluated in this article, or claim that may be made by its manufacturer, is not guaranteed or endorsed by the publisher.

Copyright © 2022 Gur, Bendelac-Kapon, Shabtai, Pillemer and Fainsod. This is an open-access article distributed under the terms of the Creative Commons Attribution License (CC BY). The use, distribution or reproduction in other forums is permitted, provided the original author(s) and the copyright owner(s) are credited and that the original publication in this journal is cited, in accordance with accepted academic practice. No use, distribution or reproduction is permitted which does not comply with these terms.



Retinoic Acid is Required for Normal Morphogenetic Movements During Gastrulation

Michal Gur^{1†}, Tamir Edri^{1†}, Sally A. Moody^{2*} and Abraham Fainsod^{1*}

¹Department of Developmental Biology and Cancer Research, Institute for Medical Research Israel-Canada, Faculty of Medicine, The Hebrew University of Jerusalem, Jerusalem, Israel, ²Department of Anatomy and Cell Biology, School of Medicine and Health Sciences, George Washington University, Washington, DC, United States

OPEN ACCESS

Edited by:

Maria Cecilia Cirio,
CONICET Institute of Physiology,
Molecular Biology and Neurosciences
(IFIBYNE), Argentina

Reviewed by:

Chenbei Chang,
University of Alabama at Birmingham,
United States
Francois Fagotto,
Université de Montpellier, France
Dale Frank,
Technion Israel Institute of
Technology, Israel

*Correspondence:

Sally A. Moody
samood@gwu.edu
Abraham Fainsod
abraham.fainsod@mail.huji.ac.il

[†]These authors have contributed
equally to this work

Specialty section:

This article was submitted to
Morphogenesis and Patterning,
a section of the journal
Frontiers in Cell and Developmental
Biology

Received: 18 January 2022

Accepted: 21 March 2022

Published: 21 April 2022

Citation:

Gur M, Edri T, Moody SA and
Fainsod A (2022) Retinoic Acid is
Required for Normal Morphogenetic
Movements During Gastrulation.
Front. Cell Dev. Biol. 10:857230.
doi: 10.3389/fcell.2022.857230

Retinoic acid (RA) is a central regulatory signal that controls numerous developmental processes in vertebrate embryos. Although activation of *Hox* expression is considered one of the earliest functions of RA signaling in the embryo, there is evidence that embryos are poised to initiate RA signaling just before gastrulation begins, and manipulations of the RA pathway have been reported to show gastrulation defects. However, which aspects of gastrulation are affected have not been explored in detail. We previously showed that partial inhibition of RA biosynthesis causes a delay in the rostral migration of some of the earliest involuting cells, the leading edge mesendoderm (LEM) and the prechordal mesoderm (PCM). Here we identify several detrimental gastrulation defects resulting from inhibiting RA biosynthesis by three different treatments. RA reduction causes a delay in the progression through gastrulation as well as the rostral migration of the *goosecoid*-positive PCM cells. RA inhibition also hampered the elongation of explanted dorsal marginal zones, the compaction of the blastocoel, and the length of Brachet's cleft, all of which indicate an effect on LEM/PCM migration. The cellular mechanisms underlying this deficit were shown to include a reduced deposition of fibronectin along Brachet's cleft, the substrate for their migration, as well as impaired separation of the blastocoel roof and involuting mesoderm, which is important for the formation of Brachet's cleft and successful LEM/PCM migration. We further show reduced non-canonical Wnt signaling activity and altered expression of genes in the Ephrin and PDGF signaling pathways, both of which are required for the rostral migration of the LEM/PCM, following RA reduction. Together, these experiments demonstrate that RA signaling performs a very early function critical for the progression of gastrulation morphogenetic movements.

Keywords: retinoic acid signaling, embryo development, gastrulation delay, *Xenopus* embryo, morphogenetic movements, Brachet's cleft, tissue separation

Abbreviations: RA, retinoic acid; LEM, leading edge mesendoderm; PCM, prechordal mesoderm; ALDH, aldehyde dehydrogenase; BCR, blastocoel roof; MZ, marginal zone; DMZ, dorsal marginal zone; DM, dorsal mesoderm; MBSH, Modified Barth's Solution Hepes DEAB, 4-Diethylaminobenzaldehyde; 3,7-Dimethyl-2,6-octadienal, citral; ethanol, EtOH; MBT, mid-blastula transition; veh, vehicle; qPCR, quantitative reverse transcription real-time PCR; FN, fibronectin.

INTRODUCTION

Retinoic acid (RA) is a central regulatory signal controlling numerous developmental processes in vertebrate embryos, and it is a major contributor to tissue homeostasis in adults (Metzler and Sandell, 2016; le Maire and Bourguet, 2014; Nolte et al., 2019; Draut et al., 2019; Summerbell and Maden, 1990). RA is produced *in vivo* by two sequential oxidation reactions from vitamin A (retinol), first to retinaldehyde and subsequently to the acid form (Kedishvili, 2016; Shabtai and Fainsod, 2018; Blanter, 2019; Ghyselinck and Duester, 2019). Based on retinoid content analysis and mutant or RA-manipulated embryos, it was suggested that late blastula vertebrate embryos are poised to initiate RA signaling but it still requires the expression of a retinaldehyde dehydrogenase activity to finalize the biosynthesis of RA (Chen et al., 1994; Creech Kraft et al., 1994; Kraft et al., 1994; Niederreither et al., 1999; Begemann et al., 2001; Lloret-Vilaspa et al., 2010; Zile, 2010). Premature RA signaling can be experimentally elicited by precocious expression of a retinaldehyde dehydrogenase (Ang and Duester, 1999). Retinoids including RA, have been detected in the gastrula organizer, called the Spemann-Mangold organizer in *Xenopus*, a central embryonic regulatory structure (Chen et al., 1992, 1994, 2001; Hogan et al., 1992; Creech Kraft et al., 1994; Kraft et al., 1994; Niederreither et al., 1997; Yelin et al., 2005). The early expression pattern of *aldehyde dehydrogenase 1a2* (*aldh1a2*; *raldh2*) is consistent with the suggestion that the retinaldehyde dehydrogenase encoded by this gene is central for RA biosynthesis in the embryo from gastrula stages (Niederreither et al., 1997; Begemann et al., 2001; Chen et al., 2001; Blentic et al., 2003; Halilagic et al., 2003; Liang et al., 2008; Shabtai et al., 2018), and in agreement, mutant *aldh1a2* embryos exhibit developmental defects soon after gastrulation and subsequently die (Niederreither et al., 1999; Begemann et al., 2001). Early expression of *aldh1a2* in the gastrula organizer has been identified in several vertebrate embryos (Chen et al., 2001; Blentic et al., 2003; Halilagic et al., 2003).

The onset of gastrulation involves a series of morphogenetic processes involving cell shape changes, cell rearrangements, and internalization of the mesoderm and endoderm that involves vegetal rotation, mesenchymal-like, and ameboid migration (Kaneda and Motoki, 2012; Huang and Winklbauer, 2018; Winklbauer, 2020). These extensive cell movements result in the reorganization of the embryo into the three primary germ layers (Fagotto, 2020; Keller and Sutherland, 2020). Close to the onset of gastrulation, the *Xenopus* embryo has a multilayered epithelium on the animal side that partially envelopes the blastocoel to form the blastocoel roof (BCR). On the vegetal side, the blastocoel is surrounded by the marginal zone (MZ) and the endoderm (Kaneda and Motoki, 2012; Huang and Winklbauer, 2018; Winklbauer, 2020). Involution of the MZ forms the mesodermal and endodermal germ layers during gastrulation and involves an inward folding of the MZ around the BCR to form the blastopore, starting from the dorsal side. This involution event creates an apposition of the mesendodermal layer and the BCR separated by a small gap, Brachet's cleft (Keller et al., 2003; Gorny and Steinbeisser, 2012). Formation of Brachet's

cleft separating the internalized mesendoderm and the enveloping ectoderm involves multiple signals including the Wnt receptor Frizzled 7 (Winklbauer et al., 2001; Köster et al., 2010; Kraft et al., 2012; Brinkmann et al., 2016; Lee et al., 2016). The involuted mesendodermal cells migrate towards the animal pole using the BCR as the substrate (Keller et al., 2003). As the involution extends all around the blastopore, migration of the internalized mesendoderm towards the prospective rostral region results in compaction of the blastocoel (Keller et al., 2003).

Classically, activation of *Hox* expression is considered one of the earliest functions of RA signaling in the embryo (Lloret-Vilaspa et al., 2010; Neijts and Deschamps, 2017; Nolte et al., 2019). However, a number of studies have reported very early functions of RA, close to the onset of gastrulation (Yelin et al., 2005; Janesick et al., 2018; Shukrun et al., 2019). We previously described that as a result of partial inhibition of RA biosynthesis, we observed a delay in the rostral migration of some of the earliest involuting cells, the leading edge mesendoderm (LEM) and the prechordal mesoderm (PCM) (Yelin et al., 2007). Here we identified several detrimental gastrulation defects resulting from inhibiting RA biosynthesis. Inhibition of RA signaling induces a delay in the progression through gastrulation and a delay in the rostral migration of the *gooseoid*-positive PCM cells after their involution. Supporting this conclusion, we observe that RA inhibition hampers the elongation of explanted dorsal MZs (DMZs). Analysis of several gastrulation processes important for rostral migration of the LEM/PCM cells revealed that reduced RA signaling reduces the deposition of fibronectin along Brachet's cleft. The tissue separation behavior important for Brachet's cleft formation is also reduced when RA biosynthesis is inhibited. Abnormal morphogenetic movements were observed in manipulated embryos affecting the position of the neural plate, the compaction of the blastocoel, and the length of Brachet's cleft. These results show that in *Xenopus* embryos, RA signaling performs a very early function important for the early progression of gastrulation morphogenetic movements.

MATERIALS AND METHODS

Embryo Culture and Treatments

Xenopus laevis frogs were purchased from Xenopus 1 or Nasco (Dexter, MI or Fort Atkinson, WI, United States). Experiments were performed after approval and under the supervision of the Institutional Animal Care and Use Committee (IACUC) of the Hebrew University (Ethics approval no. MD-17-15281-3) and the George Washington University (Ethics approval no. A233). Embryos were obtained by *in vitro* fertilization, incubated in 0.1% Modified Barth's Solution and Hepes (MBSH), and staged according to (Nieuwkoop and Faber, 1967). Treatments with 4-Diethylaminobenzaldehyde (DEAB, Sigma, dissolved in DMSO) or 3,7-Dimethyl-2,6-octadienal (cital, Aldrich, diluted in EtOH), were performed in 0.1% MBSH from the midblastula transition (MBT, stage 8.5) until the desired stage for analysis.

Whenever necessary, embryos were injected at the one to four cell stage with *in vitro* transcribed capped mRNA or the ATF2 reporter plasmid. Capped mRNAs were prepared using the

TABLE 1 | Primers for qPCR analysis.

Gene	Forward Primer	Reverse Primer
<i>efnb1.L</i>	TCACATGGAAGCTGCGAGAA	AGTATTTCATAAGGCTGGGAAGAG
<i>efnb2.S</i>	GATCCGAGGTGGCCTTATTT	CAACAACAGCACAACAAGAGTG
<i>efnb3.S</i>	OCTCTACCAATCTCCCATGTTT	GCAGACCCATCCCAATACTC
<i>epha4.L/S</i>	GTGGTGCTGATGGAGAGTG	TCTGTTGAGAGGGCTTTGTAG
<i>ephb4.L/S</i>	CTGGCTCCTCCTCCTGTGT	CCCCTGTCCGTCCACTTT
<i>pdch8.L/S</i>	AATCTGGTCGCCTCACTCTT	ATGACTCGCACGATGACTTT
<i>pdgfra.L/S</i>	GTCAAGTGCCAGCCATCAA	GATGTTTCCTCTAACCACACAA
<i>pdgfra.L</i>	GCTGCTGTCTTGGTCTCTCT	TTACTCGCCATCTTATTTTCATACC

appropriate RNA polymerase. Cap analog (m7G (5')ppp (5')G; New England Biolabs, USA) was added to the reaction mixture using a cap:GTP ratio of 5:1. Expression plasmids were linearized and transcribed as previously described: *cyp26a1* (Holleman et al., 1998); dominant-negative *frizzled7* (*dnfzd7*) (Winklbauer et al., 2001); β -galactosidase (Yan et al., 2009).

Quantitative Reverse Transcription Real-Time PCR (qPCR)

Total RNA from embryos was extracted with the Aurum Total RNA Mini Kit (Bio-Rad), and cDNA was synthesized using iScript cDNA Synthesis Kit (Bio-Rad). The real-time PCR reactions were performed using the CFX384 Real-Time System (Bio-Rad) and iTaq universal SYBR Green Supermix (Bio-Rad). Each experiment was repeated at least three independent times and each time the samples were run in triplicate. GAPDH was used as the housekeeping reference gene. The primers used for qPCR analysis are listed in Table 1.

Whole-Mount *in situ* Hybridization

Whole-mount *in situ* hybridization and double *in situ* hybridization were performed as previously described (Epstein et al., 1997). Embryos treated with DEAB (300 μ M) or citral (70 μ M) as well as untreated siblings, were fixed at stage 15 in 4% paraformaldehyde in MEM buffer (0.1 M MOPS, 0.5 M NaCl, 1 mM EGTA, 2 mM $MgSO_4$), and processed for whole-mount *in situ* hybridization. Probes were prepared by *in vitro* transcription using Digoxigenin or Fluorescein labeling mix (Roche). Probes were transcribed as previously described: *gsc* (*goosecoid*) (Cho et al., 1991), *sox3* (Penzel et al., 1997).

Fibronectin (FN) Immunodetection

Embryos treated with DEAB (300 μ M), citral (70 μ M) or diluent alone, or embryos microinjected at cleavage stages with *cyp26a1* mRNA, as well as untreated, control siblings, were fixed when controls reached stage 10.5 in 4% paraformaldehyde in MEM buffer, washed and bisected along the midsagittal plane. Embryos were processed for immunohistochemical detection of fibronectin according to Davidson et al. (2004) using a mouse anti-fibronectin monoclonal antibody (1 μ g/ml; Developmental Hybridoma Bank #4H2) and goat anti-mouse HRP-conjugated IgG (1:250, Cell Signaling #7076). After the diaminobenzidine chromogen reaction, post-fixed bisected embryos were

photographed using the cellSens program on an Olympus SZX16 stereomicroscope.

Measurements of Gastrula Morphology

Embryos were treated with citral (70 μ M) or diluent alone, as above. The treated embryos and their untreated, control siblings were fixed when controls reached stage 10.5 as above. Embryos were bisected along the midsagittal plane and the width of the floor of the blastocoele, the length of Brachet's cleft, and the length of the archenteron were measured using the cellSens program on an Olympus SZX16 stereomicroscope.

Lineage Tracing of Blastomere Clones

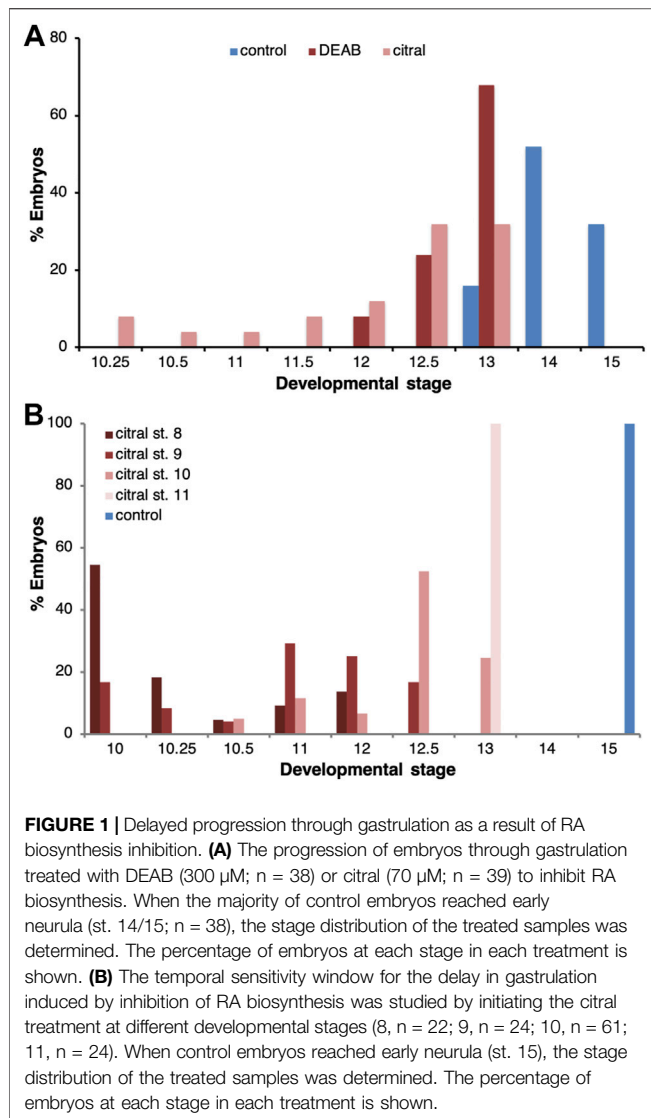
Embryos were chosen at the 2-cell stage if the first cleavage furrow bisected the grey crescent in order to accurately identify the dorsal-ventral axis (Klein, 1987; Moody, 2018). When selected embryos reached the 32-cell stage, a single blastomere of known fate (Dale and Slack, 1987; Moody, 1987) was microinjected with 100 pg of nuclear-localizing β -galactosidase mRNA. Embryos were then treated with citral (70 μ M) or diluent alone from blastula stages, and harvested when untreated, control siblings reached appropriate stages. They were fixed as above, processed for the histochemical detection of β -Galactosidase activity, as previously described (Yan et al., 2009), and the position of the labeled descendant cells mapped as previously described (Dale and Slack, 1987; Moody, 1987; Bauer et al., 1994).

Tissue Separation Behavior Assay

Embryos were treated with DEAB (300 μ M), citral (70 μ M) or diluent alone, or microinjected at cleavage stages with *cyp26a1* mRNA. When their untreated, control siblings reached stage 10+, the blastocoele roof (BCR) and the anterior, involuting dorsal mesoderm (DM) were dissected and combined to form aggregates according to the method of Wacker et al. (2000). Aggregates were made with treated or untreated BCRs combined with treated or untreated DM pieces. BCRs were cultured on 2% agarose with the inner surface facing up, and two to three DM pieces were placed on this surface. After 40 min of culture, each DM was scored for whether it remained separated as a compact mass in the inner surface of the BCR, or had integrated into the BCR.

β -Galactosidase Activity Assays

Chemiluminescent quantification of the reporter pRAREhsplacZ plasmid (Rossant et al., 1991) activity was



performed using β -gal Juice Plus (PJK, Germany) as previously described (Yelin et al., 2005). Chemiluminescence activity was measured on a TD-20/20 Luminometer (Turner Designs). *LacZ* RNA was prepared from a clone containing a nuclear localization signal (pSP6nuc β -gal) in pGEM-3Z (Promega). The staining of embryos for β -galactosidase activity was performed with 5-bromo-4-chloro-3-indolyl- β -D-galactopyranoside (Xgal).

Statistical Analysis

All statistical comparisons were carried out using the Prism software package (Graph Pad Software Inc. San Diego, CA). Results are given as the mean \pm standard error of the mean (SEM). Tests used were the 2-tailed *t*-test for two-sample comparisons, Dunnett's (ANOVA) multiple comparisons test, or Fisher test. Differences between means were considered significant at a significance level of $p < 0.05$.

RESULTS

Inhibition of RA Biosynthesis Delays the Progression Through Gastrulation

To characterize the effect of reduced RA signaling on gastrulation, we performed a series of experiments employing two different inhibitors of RA biosynthesis, 4-diethylaminobenzaldehyde (DEAB) and 3,7-dimethyl-2,6-octadienal (citral) (Shabtai et al., 2018). Both inhibitors were used at relatively high, but sub-lethal concentrations (DEAB, 300 μ M; citral, 70 μ M), as previously determined (Shukrun et al., 2019). Groups of embryos were treated with one of the RA biosynthesis inhibitors from the midblastula transition (st. 8.5) (Nieuwkoop and Faber, 1967) and allowed to develop until the majority of the embryos in the control group reached early neurula stages (st. 14) (Figure 1A), at which time both control and treated embryos were fixed and staged. Both RA biosynthesis inhibitors induced a delay in the progression through gastrulation; when sibling control embryos reached stages 13–15, 86.8% of the DEAB-treated group and 76.9% of the citral-treated group were at stages 12–13 (Figure 1A). None of the treated embryos advanced beyond st. 13. These results support previous observations that RA signaling is required for the normal progression through gastrulation (Durstion et al., 1989; Sive et al., 1990).

To determine whether there is a critical window for the requirement of RA signaling, RA biosynthesis inhibition (citral) was initiated at different developmental stages and the treatment continued until the control group reached early neurula (st. 15). Analysis of the stage distribution in the experimental groups again showed that RA biosynthesis inhibition delayed gastrulation irrespective of the stage at which the inhibition was initiated (Figure 1B). While most control embryos reached stage 15, when embryos were treated with citral starting at stage 9 they only reached stage 11–12.5 and when the treatment was initiated at stage 11, they only reached stage 13 (Figure 1B). Thus, the earlier the citral treatment was initiated, the more severe the delay in gastrulation. These observations indicate that RA is required for the progression through gastrulation at all stages studied but late blastula/early gastrula appears more sensitive to its inhibition.

RA Signaling Affects the Migration of the Early Involuting Cells

A major parameter during *Xenopus* gastrulation that contributes to assigning an embryo to a particular stage is the size of the blastopore, which is a reflection of the extent of involution (Nieuwkoop and Faber, 1967; Keller and Shook, 2008; Keller and Sutherland, 2020). Therefore, we next assessed the effects of RA biosynthesis inhibition on cell involution. Since involution initiates at the dorsal blastopore lip, i.e., the organizer, and is followed by the rostral the migration of the earliest invaginating cells, the LEM/PCM, embryos treated with DEAB or citral were allowed to develop to a late gastrula stage (st. 12) and probed for *gsc* expression by *in situ* hybridization (Cho et al., 1991) to

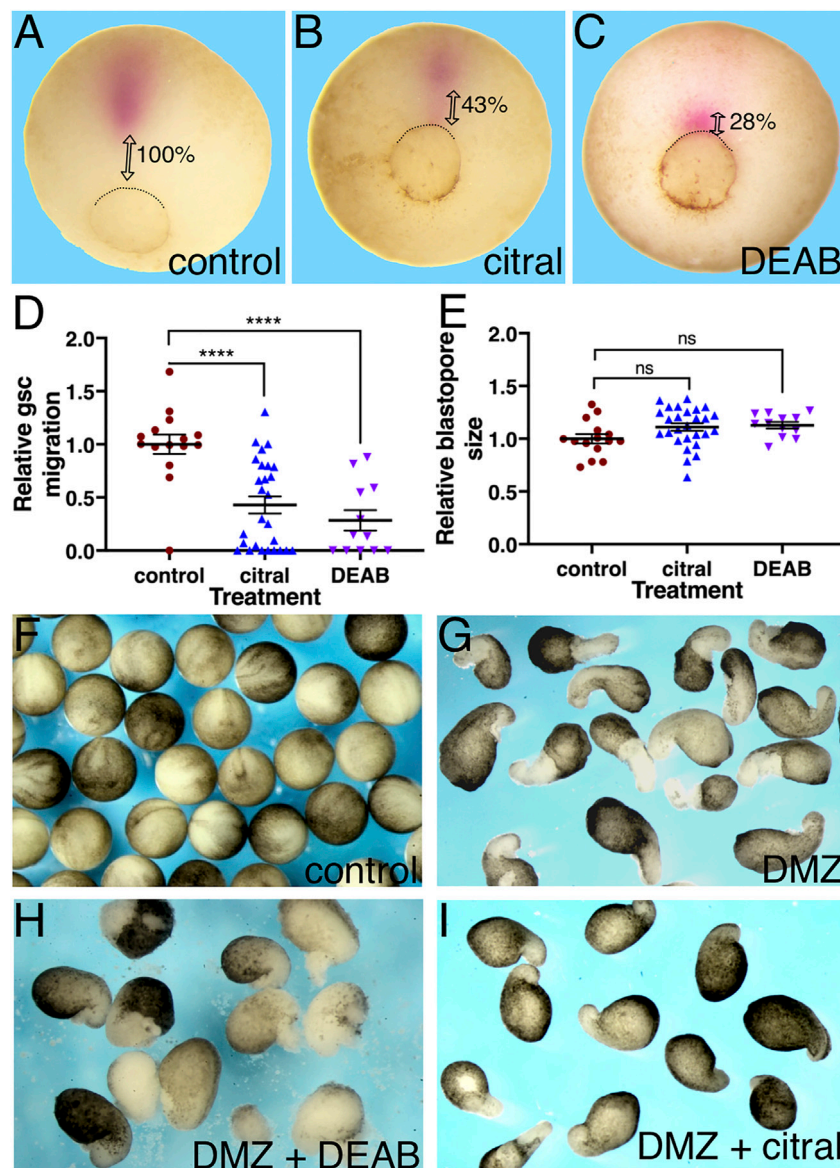


FIGURE 2 | RA inhibition delays the rostral migration of the PCM. **(A–E)** Embryos were treated with citral or DEAB to inhibit the biosynthesis of RA. The extent of migration of the PCM during involution was determined by measuring their distance from the dorsal lip of the blastopore. The PCM cells were identified by *gsc* *in situ* hybridization. **(A)** Control embryo ($n = 15$). **(B)** Citral ($70 \mu\text{M}$) treated embryo ($n = 27$). **(C)** DEAB ($300 \mu\text{M}$) treated embryo ($n = 12$). **(D)** Relative PCM migration distribution. The migration distance was normalized to the embryo diameter. **(E)** Relative blastopore size distribution indicates embryos were at the same developmental stage. For each embryo, we measured its diameter and the diameter of the blastopore and calculated the ratio between them. **(F–H)** The inhibitory effect of reduced RA signaling was studied in explanted DMZs. RA biosynthesis was inhibited in explanted DMZs by incubation in citral or DEAB until control embryos reached st. 18 **(F)**. **(G)** Control DMZ explants all had elongated columns of unpigmented mesoderm ($n = 34$) whereas in DEAB-treated DMZ explants ($n = 16$) **(H)** and citral-treated DMZ explants ($n = 27$) **(I)** these were missing or stunted. ****, $p < 0.0001$; ns, not significant.

identify the PCM cells (Huang and Winklbauer, 2018). Inhibition of RA biosynthesis by either DEAB or citral resulted in a delay in the rostral migration of the *gsc*-positive cells compared to the control samples (Figures 2A–C). To quantitate the extent of delayed migration, the distance the *gsc*-expressing PCM cells migrated from the blastopore was measured. Migration of the PCM is a very dynamic process dependent on the progression of gastrulation. To minimize the effect of slight size differences

between the embryos (Leibovich et al., 2020), the migration distance was normalized to the embryo diameter and presented as a relative migration from the value in control embryos (Figure 2D). The results showed that citral treatment inhibited PCM migration by 57.1% and DEAB inhibited it by 71.7%. This significant migration delay was observed despite the fact that all embryos were allowed to develop to the same developmental stage. During gastrula stages, the size of the

blastopore decreases constantly, which normally is linked to the extent of PCM migration (Kaneda and Motoki, 2012; Keller and Shook, 2008). To ensure that our visual staging selected embryos within a limited range of blastopore sizes, for each embryo we measured its diameter and the diameter of the blastopore and calculated the ratio between them (**Figure 2E**). The use of this ratio has been shown to normalize staging of embryos of different sizes during gastrulation stages (Leibovich et al., 2020). This comparison of the relative blastopore sizes supported the conclusion that the treated and control embryos were at statistically similar developmental stages, and that the reduction of PCM migration was a direct result of reduced RA signaling rather than overall developmental delay.

To corroborate the RA requirement for the rostral morphogenetic movements of the PCM, we explanted dorsal marginal zones (DMZs) from control and treated embryos. DMZ explants undergo elongation that recapitulates in part the morphogenetic movements of the dorsally involuting cells (Shih and Keller, 1992). The DMZs were incubated until the control sibling embryos reached stage 18 (**Figure 2F**). In support of the previous conclusion of a delay in the PCM rostral migration (**Figure 2D**), the DMZ explants treated with either DEAB (**Figure 2H**) or citral (**Figure 2I**), exhibited a partial inhibition in their elongation, whereas DMZs explanted from control embryos exhibited the expected elongation resulting from morphogenetic movements of dorsal regions in the *Xenopus* embryo (**Figure 2G**). These results further support that RA signaling is required for the normal morphogenetic movement of dorsal cells during gastrulation.

We previously showed that the effects on the rostral migration of the PCM by RA signaling reduction with ethanol are transient and these cells reach their normal cranial position by early neurula stages (Yelin et al., 2007). In accord with this finding, analysis of the *gsc* and *chrd.1* expression patterns during early neurula stages (st. 13), revealed that in embryos treated with either DEAB or citral, the PCM cells expressing these markers reached their normal cranial position (**Supplementary Figure S1**). Interestingly, the notochord, another *chrd.1*-expressing tissue, appears shortened in the embryos with reduced RA levels (**Supplementary Figure S1E,F**). These observations show that the effect of reduced RA levels on the rostral migration of the PCM cells is transient, while there might be an additional effect on the convergent extension of the notochord (Wilson et al., 1989; Keller and Jansa, 1992; Yelin et al., 2007).

RA Signaling is Required for Fibronectin Deposition During Gastrulation

Previous studies showed that mesoderm involution requires the extracellular deposition of fibronectin (FN) along Brachet's cleft (Winklbauer and Schürfeld, 1999; Gorny and Steinbeisser, 2012). To assess whether the disrupted involution and rostral migration of the PCM cells after inhibition of RA biosynthesis might involve loss of FN deposition, we analyzed early/mid gastrula (st. 10.5) embryos by immunostaining with anti-FN antibodies (Davidson et al., 2004). RA levels were reduced by either citral or DEAB treatment, or by injection of RNA encoding CYP26A1, an

enzyme belonging to the cytochrome P450 family that renders RA biologically inactive and targets it for degradation (Ribes et al., 2007; Thatcher and Isoherranen, 2009). We found that reducing RA levels by these three different methods reduced FN deposition along Brachet's cleft during gastrulation. In control embryos, a thin line of FN deposition along Brachet's cleft is notable in stage 10.5 gastrula embryos (**Figure 3A, A'**; $n = 47$). The same FN staining was observed in vehicle-treated siblings (EtOH: **Figure 3B, B'**, $n = 20$; DMSO: **Figure 3F, n = 24**). However, embryos treated with either citral ($n = 15$) or DEAB ($n = 52$) to block RA signaling (**Figure 3C, C', E**), or embryos overexpressing the RA hydroxylating enzyme CYP26A1 (**Figure 3D, D'**, $n = 18$) showed severely reduced to not detectable FN-immunostaining in Brachet's cleft. In samples showing reduced FN staining, the cytoplasmic FN in both the ectodermal BCR and the MZ mesoderm was reduced, indicating that the defect was not specific to one germ layer (e.g., **Figure 3 C, C'**). These assays indicate that a major target of disrupted RA signaling during gastrulation is the deposition of a suitable extracellular FN matrix upon which the LEM/PCM cells can migrate along the BCR in a rostral direction.

Reduced RA Biosynthesis Results in Abnormal Gastrula Morphogenetic Movements

Incubation of embryos treated with DEAB or citral to early neurula stages (st. 15) uncovered another morphogenetic defect from the efficient inhibition of RA signaling. When observing living control embryos, their natural buoyancy in the aqueous medium causes the dorsal side containing the neural plate to face up in the culture dish (**Figure 4A**). In contrast, living DEAB- or citral-treated embryos in the culture dish appeared to lack a neural plate (**Figures 4C,E**). However, manually turning the living DEAB- or citral-treated embryos revealed the presence of an apparent neural plate on the side of the embryo facing the dish, which normally would be the ventral side. Processing these embryos for *in situ* hybridization with the neural plate marker, *sox3* (Penzel et al., 1997), confirmed the presence of neural plate tissue (cf. **Figure 4B to Figures 4D,F**). These observations suggested that reduction of RA signaling caused the neural plate to form on the ventral side of the embryo.

We tested the possibility of respecification of cell fates by lineage tracing the blastomere progenitors of the neural plate (**Figure 5**). *Xenopus* blastomeres with different fates can be visually distinguished by the location of the first cleavage furrow and darker pigmentation of the ventral-animal quadrant (Klein, 1987; Moody, 2018). Therefore, we lineage labeled a single dorsal-animal blastomere of the 32-cell embryo (D112) (Jacobson and Hirose, 1981; Moody, 1987), also known as B1 (Nakamura et al., 1978; Dale and Slack, 1987) (**Figure 5G**) that is the major progenitor of the neural plate (Dale and Slack, 1987; Moody, 1987) to mark its progeny at later stages. In sibling controls, the D112 clone was located in the neural plate extending along the dorsal midline from the posterior blastopore to a broadened fan in the anterior neural plate (**Figure 5A**), in accord with published fate maps

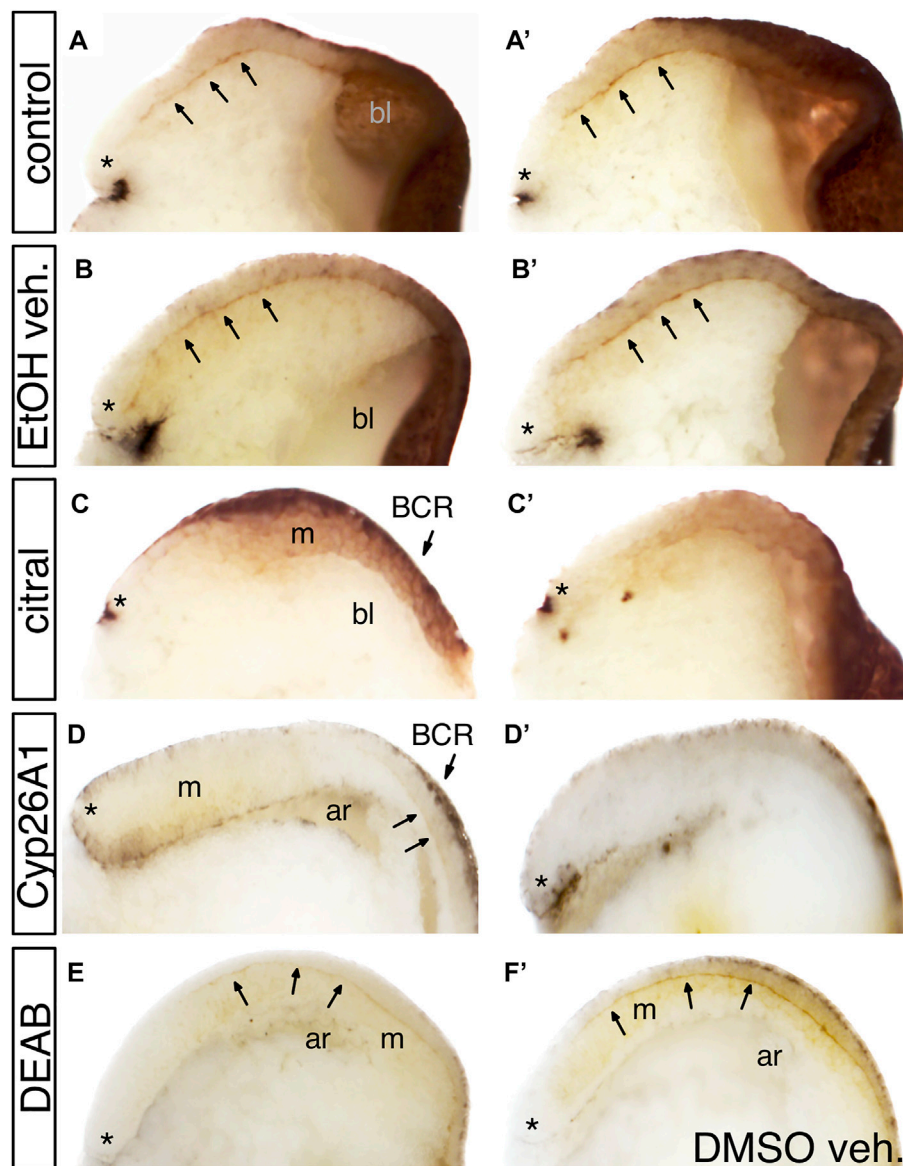


FIGURE 3 | The effect of reduced RA signaling on fibronectin (FN) deposition. Embryos were treated with DEAB or citral or injected with RNA encoding CYP26A1 to reduce RA levels. **(A,A')** Two examples of untreated sibling control embryos. Arrows point to fibronectin deposited along Brachet's cleft. * indicates the dorsal lip of the blastopore; bl, blastocoel. **(B,B')** Two examples of embryos treated with EtOH vehicle only. FN deposition was equivalent to untreated controls. **(C,C')** Two examples of embryos treated with citral. FN is detected in the ectoderm of the blastocoel roof (BCR) and mesoderm (m), but is not deposited along Brachet's cleft. **(D,D')** Two examples of embryos injected with *cyp26a1* mRNA. FN is not detected in the BCR, the mesoderm (m), or Brachet's cleft (arrows). ar, archenteron. **(E)** Embryo treated with DEAB showed reduced FN staining along Brachet's cleft compared to a sibling embryo treated only with DMSO vehicle **(F)**.

(Moody, 1987; Dale and Slack, 1987). The D112 clone in every citral-treated neurula embryo was distributed in an identical pattern (**Figure 5B**), indicating that reduced RA signaling does not cause a reversal in cell fate maps. This is supported by the observation that in the gastrula (st. 10.5), the labeled clone of cells derived from a dorsal-vegetal blastomere (D212, aka C1; **Figure 5G**) that is a major contributor to the involuting organizer mesoderm (Bauer et al., 1994), is located in the dorsal lip in citral-treated embryos (**Figure 5C**). Thus, blastomeres that normally contribute to dorsal ectoderm

(D112) and dorsal mesoderm (D212) continue to do so in embryos in which RA signaling was reduced; the cell fate map is not altered.

However, the distribution of ventral ectodermal clones was altered by reduced RA signaling. Labeling a single ventral-animal blastomere of the 32-cell embryo (V111, aka A4; **Figure 5G**) produces a coherent clone stretching across the ventrolateral epidermis of the neurula (**Figure 5D**), as previously described (Dale and Slack, 1987; Moody, 1987). Although the V111 clone in citral-treated neurulae also was located in the ventral epidermis, it

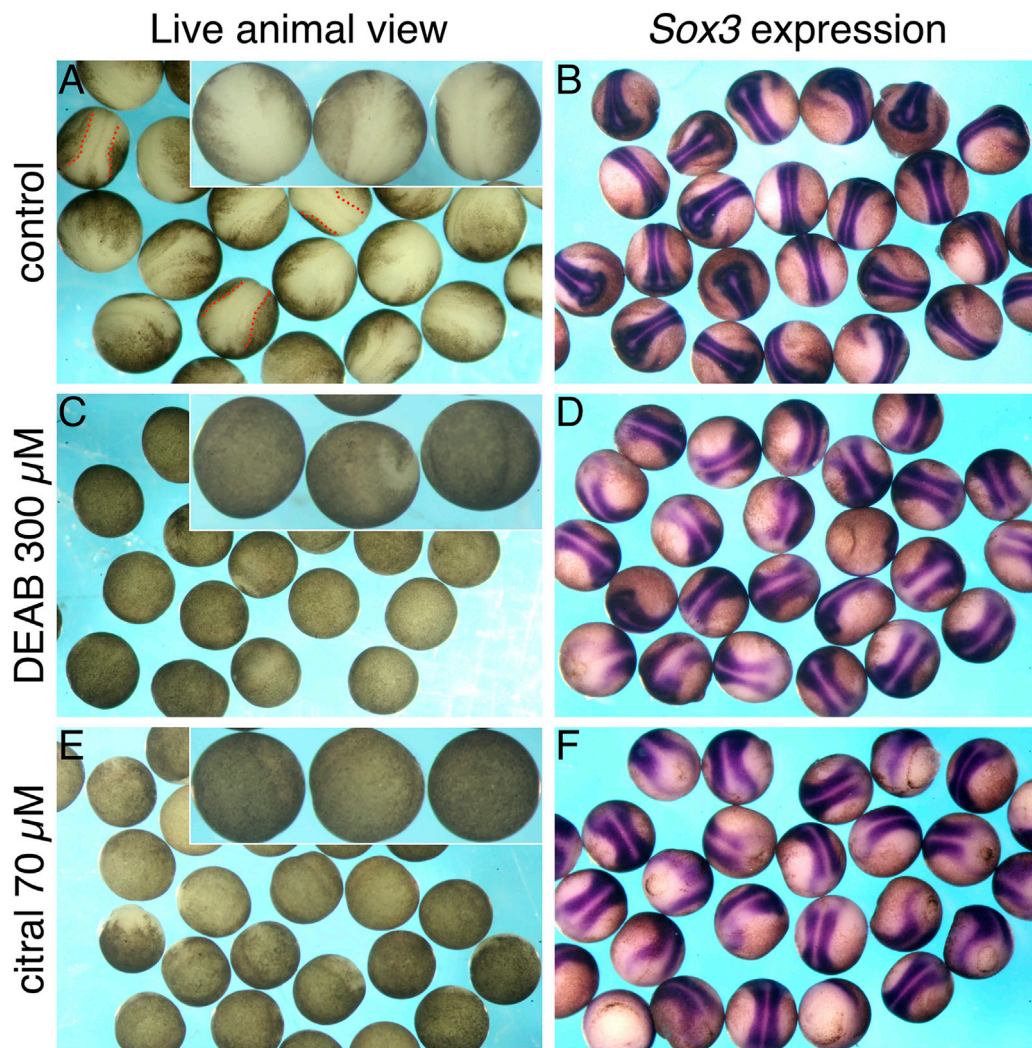


FIGURE 4 | Reduced RA signaling affects the apparent location of the neural plate. Embryos were treated with DEAB or citral to inhibit the biosynthesis of RA. At st. 15, embryos were analyzed for the formation of the neural plate while alive by visual examination (**A,C,E**), or after *in situ* hybridization with the neural plate marker, *sox3* (**B,D,F**). (**A,B**) Control embryos (n = 25). (**C,D**) Embryos treated with DEAB (300 μ M; n = 23). (**E,F**) Treatment of embryos with citral (70 μ M; n = 26).

was more midline and the cells were more dispersed (**Figure 5E**). Since the V111 clone is confined to the animal cap ectoderm at gastrula stages (10.5), as expected for prospective epidermal cells (**Figures 5F,H**), these results confirm that the dorsal-ventral fate map is not reversed, but that there is an interruption or delay in morphogenetic movements. Performing the lineage analysis of the V111 (A4) blastomere at tailbud stages (st. 30) confirmed this. While most of the control embryos exhibited descendants flanking the neural tube in the dorsolateral epidermis (**Figures 5I,J**), in the citral-treated embryos this clone was significantly more frequently located in a more ventral position (**Figures 5I,K**). Perhaps this accounts for the neural plates of the RA-reduced embryos often appearing broader than those of controls (**Figures 4B,D,F**). Thus, lineage analyses at gastrula, neurula, and tailbud stages demonstrate that reduced RA signaling does not reverse the dorsal-ventral fate map of the embryo, but instead

alters some morphogenetic movements that cause living embryos to orient “upside-down” in the culture dish (**Figure 4**).

RA Regulates the Internal Reorganization of the Gastrula Embryo

A notable phenotype of the living neural plate stage embryos in which RA signaling was reduced was the presence of a large, fluid-filled cavity oriented in the “up” position facing away from the culture dish (**Figures 4C,E**)—a position normally occupied by the neural plate (**Figure 4A**). In control embryos, the blastocoel forms during cleavage stages separating the animal cells from vegetal cells by blastula stages. During gastrulation, the blastocoel is pushed ventrally by the involuting dorsal mesoderm, shrinks in size, and eventually disappears by the end of gastrulation (around st. 13). We hypothesized that the unusual cavity in the RA-

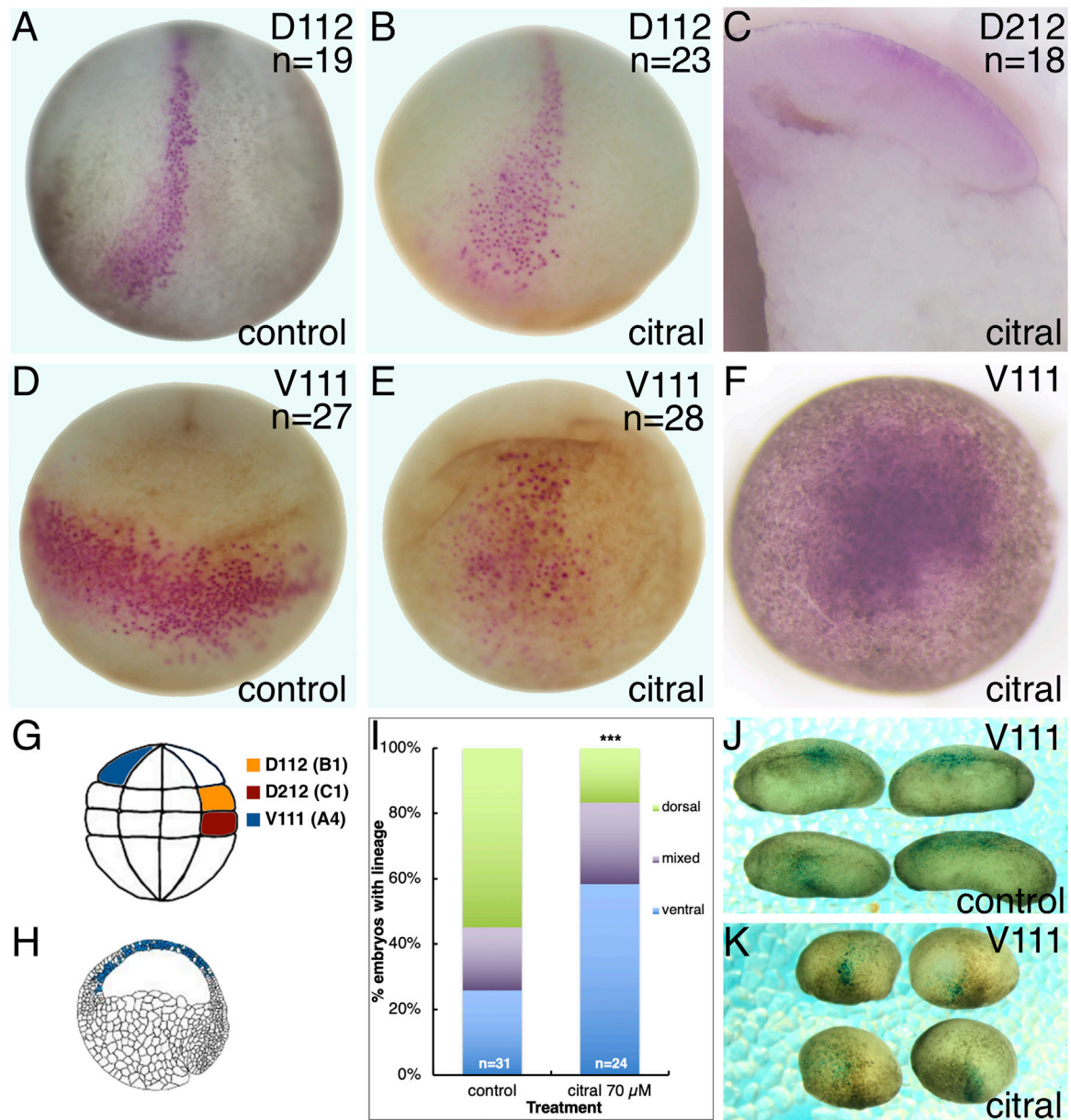


FIGURE 5 | Reduced RA signaling does not alter the dorsal-ventral axis. Single 32-cell blastomeres were injected with lineage tracer mRNA and labeled clones mapped at different developmental stages. **(A,B)** At stage 15, the D112/B1 clone (pink cells) occupies the medial and anterior neural plate in both untreated control **(A)** and citral treated **(B)** embryos. Dorso-anterior views. **(C)** The D212/C1 blastomere that normally contributes to the involuting dorsal mesoderm at gastrulation (st 10.5; Bauer et al., 1984) also does so in citral-treated embryos. Mid-sagittal section with anterior to the left and dorsal to the top. **(D)** At stage 17, the V111/A4 clone in untreated control embryos forms a coherent ventrolateral clone. Ventral view with anterior to the top. **(E)** In citral-treated sibling embryos, the stage 17 V111/A4 clone remains medial, i.e., has not expanded laterally, and the cells are more dispersed. Ventral view with anterior to the top. **(F)** At gastrula stages (st 10.5), the V111/A4 clone in citral-treated embryos occupies the blastocoel roof, similar to control embryos (cf. H). **(G)** Location of the 32-cell blastomeres that were lineage traced. Dorsal to the right, animal to the top. **(H)** Location of the V111/A4 clone (blue cells) at early gastrulation, modified from Bauer et al. (1984). Animal to the top and dorsal to the right. **(I)** Percentage of embryos in which the V111/A4 clone was located predominantly in the dorsal, ventral, or both (mixed) epidermis at tailbud stages. **(J)** Examples of control embryos showing V111/A4 descendants (blue cells) mostly in the dorsolateral epidermis. Dorsal to the top, anterior to the left. **(K)** Examples of citral treated embryos showing V111/A4 descendants (blue cells) mostly in the ventral and ventrolateral epidermis. Dorsal to the top, anterior to the left.

disrupted embryo, which causes the ventral side of the embryo to be buoyant so that their ventral side faces “up” (**Figures 4C,E**), is a persistent blastocoel that is not eliminated due to the abnormal timing and extent of LEM/PCM involution (**Figures 1, 2**).

Therefore, we examined the internal morphology of gastrulating citral-treated embryos. In control embryos that reached mid-gastrula (st. 11), the LEM/PCM have moved along the BCR, compressing the blastocoel into an ovoid

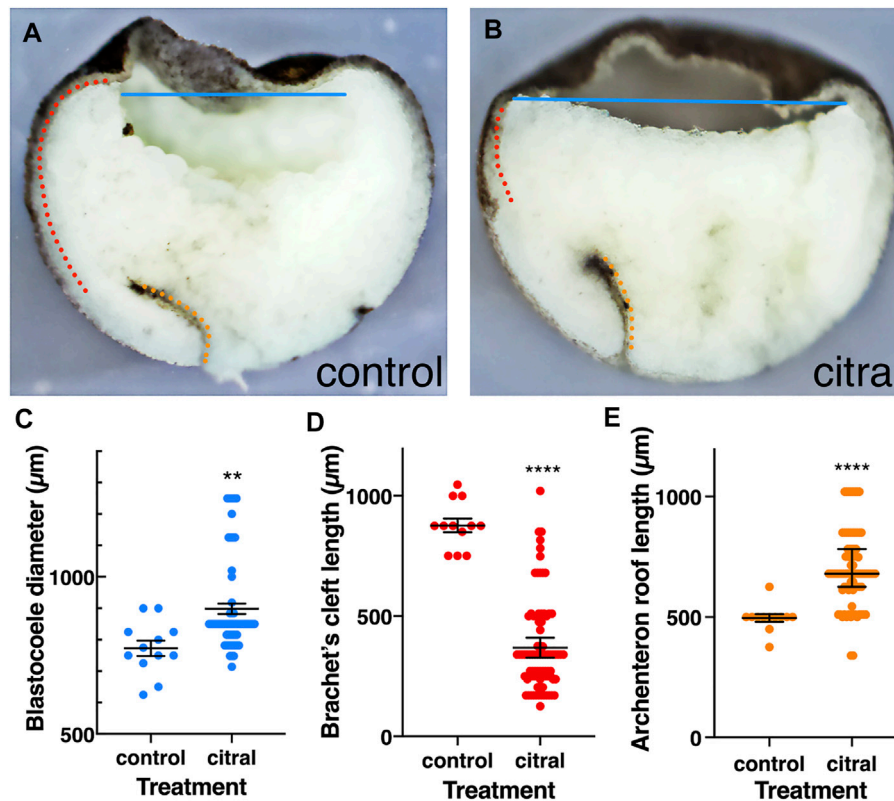


FIGURE 6 | Internal reorganization of the embryo as a result of reduced RA signaling. Control ($n = 12$) and citral-treated ($n = 84$) embryos were incubated to mid-gastrula (st. 11) and bisected sagittally. **(A,B)** Control and citral-treated bisected embryos. Blastocoel diameter, blue line; Brachet's cleft; dotted red line; Archenteron roof, dotted orange line. **(C)** Distribution of the blastocoel diameter in control and citral-treated embryos. **(D)** Measurement of Brachet's cleft length in citral-treated and control embryos. **(E)** Length of the archenteron roof in citral-treated and control embryos. Citral-treated embryos were compared to the control values. **, $p < 0.01$; ****, $p < 0.0001$.

shape (Figure 6A). In contrast, although the dorsal lip of the blastopore forms in citral-treated siblings that were time-matched to controls, the blastocoel remains wide with a flat floor that extends across the entire animal hemisphere (Figure 6B). Indeed, measuring the blastocoel diameter in time-matched untreated embryos and their citral-treated siblings confirmed that the blastocoel is significantly larger in citral-treated embryos (Figure 6C). Another morphological change indicating a disruption of mesoderm involution is the significantly shorter length of Brachet's cleft. This cleft, located between the involuting dorsal mesoderm and BCR is created by the BCR pushing down on the mesoderm and the vegetal endoderm rotating to push the leading edge of the mesoderm toward the animal pole (Winklbauer and Schürfeld, 1999; Yanagi et al., 2015). Brachet's cleft is significantly shorter in citral-treated embryos compared to untreated time-matched siblings (Figures 6B,D). This is not due to a failure of the archenteron to form (Figure 6B). In fact, the length of the archenteron was significantly longer in citral-treated embryos (Figure 6E), which likely is due to the ability of the vegetal cells to internalize and blastopore closure to take place in the absence of mesoderm involution, as shown in embryos after the removal of the blastocoel roof (Keller and Jansa (1992). Together, these morphological measurements indicate that

one consequence of reducing RA signaling by citral treatment is the disruption of the progression of LEM/PCM involution during gastrulation.

RA is Required for Efficient Tissue Separation and Wnt/PCP Signaling

Previous studies showed that the movement of the LEM/PCM upon the blastocoel roof requires a repulsive interaction between these two populations across Brachet's cleft, termed tissue separation (Wacker et al., 2000; Winklbauer et al., 2001). To determine whether the migratory deficiency in RA-disrupted embryos originates from either the cells in the dorsal mesoderm (DM) or the blastocoel roof (BCR), we performed a separation behavior explant assay, designed to test the regulation of tissue separation across Brachet's cleft (Winklbauer et al., 2001). We tested whether the RA-disrupting treatments specifically affected either the DM or BCR by hampering the separation behavior required for invagination and rostral migration (Gorny and Steinbeisser, 2012). Explants composed of DM and BCR from RA-reduced treated and control samples in multiple combinations were analyzed. As previously shown (Winklbauer et al., 2001; Gorny and Steinbeisser, 2012), when untreated DM (DMwt) were explanted onto vehicle-treated BCR

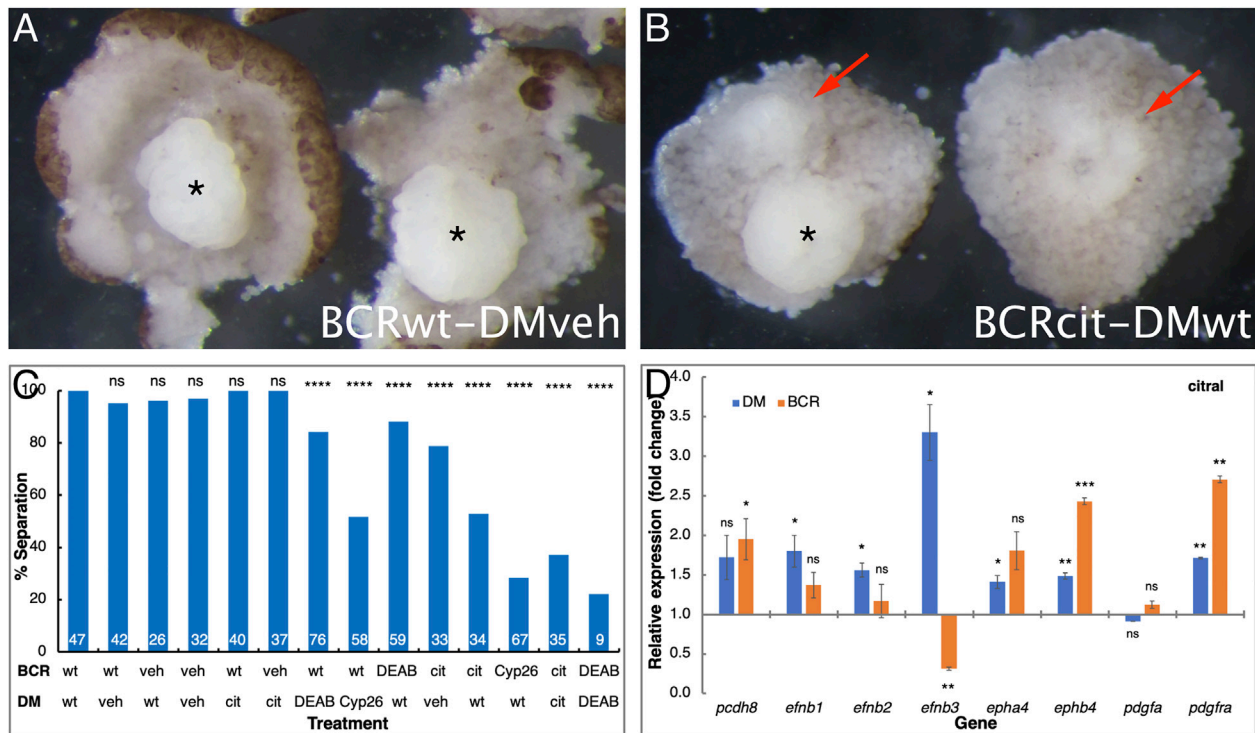


FIGURE 7 | RA regulates the tissue separation behavior across Brachet's cleft. Embryos were manipulated to reduce RA signaling levels by treatment with DEAB, citral, or injected with mRNA encoding CYP26A1. For controls, embryos were treated with the diluent alone (veh) for the DEAB or citral dilutions or left untreated (wt). The explanted BCR or DM regions were analyzed separately or conjugated for the separation behavior assay. **(A)** Control examples of separation behavior assay conjugates between control (wt) BCR and vehicle (veh) treated DM (asterisk). **(B)** Loss of separation behavior (arrows) when control DM was placed onto BCR treated with citral. * indicates a DM that did remain separated. **(C)** The extent of separation behavior (%) in all the assays performed in all combinations. # separation/# total: 47/47 DMwt/BCRwt; 40/42 DMveh/BCRwt; 25/26 DMwt/BCRveh; 31/32 DMveh/BCRveh; 40/40 DMcit/BCRwt; 37/37 DMcit/BCRveh; 64/76 DMDEAB/BCRwt; 30/58 DM Cyp26/BCRwt; 52/59 DMwt/BCRDEAB; 26/33 DMveh/BCRcit; 18/34 DMwt/BCRcit; 19/67 DMwt/BCRCyp26; 13/35 DMcit/BCRcit; 2/9 DMDEAB/BCRDEAB. **(D)** qPCR analysis of *pcdh8*, *efnb1*, *efnb2*, *efnb3*, *epha4*, *ephb4*, *pdgfa*, and *pdgfra* gene expression changes in the DM and BCR following citral treatment. **, $p < 0.01$; ***, $p < 0.001$; ****, $p < 0.0001$; ns, not significant.

(BCRveh), or when the reverse combination was performed, the explants remained separated in nearly every case (Figures 7A,C). The regulatory role of RA signaling in tissue separation across Brachet's cleft then was analyzed in explants treated with either DEAB, citral, or overexpressing CYP26A1. RA signaling reduction in the BCR consistently and robustly hindered the separation behavior resulting in the sinking of the DM into the BCR (Figures 7B,C). Interestingly, RA signaling reduction in the dorsal mesoderm also hindered the separation behavior, although it had a weaker effect (Figure 7C). RA manipulation of both explants prior to performing the separation assay resulted in an additive effect supporting the role of RA in both the DM and the BCR for the separation behavior (Figure 7C). The separation behavior is clearly affected by RA signaling acting on both the DM and the BCR. This is consistent with reduced FN expression in both the ectoderm and mesoderm (Figure 3C, C').

Previous studies identified a number of molecules that are responsible for the formation of Brachet's cleft, tissue separation, and LEM involution (reviewed in Gorny and Steinbeisser, 2012). To identify whether any of the genes encoding these proteins are perturbed by disrupting RA signaling during gastrula, we dissected the DM and BCR from citral and vehicle-treated

embryos and their untreated siblings. RNA from DM, BCR, and whole embryos was analyzed by qPCR (Figure 7D). Analysis of *pcdh8*, *efnb1*, *efnb2*, *efnb3*, *epha4*, *ephb4*, *pdgfa*, and *pdgfra* revealed that RA signaling fulfills a complex regulatory role in the interaction between the DM and the BCR. In the DM, the citral treatment resulted in significant up-regulation of the *efnb1*, *efnb2*, *epha4*, *ephb4*, and *pdgfra* genes suggesting that RA negatively regulates their expression (Figure 7D). The citral treatment also significantly up-regulated the expression of *ephb4* and *pdgfra* in the BCR, again supporting a fine-tuning role of RA along Brachet's cleft. Only the expression of *efnb3* was significantly down-regulated by citral in the BCR, suggesting that normal RA signaling is required for the expression of this gene in the non-involuting ectoderm. The reduction in *efnb3* expression is also in agreement with the observation that any RA reduction in the BCR hampers the tissue separation behavior across Brachet's cleft (Figures 7A–C). These results also demonstrate that reduced RA signaling affects both the DM and BCR.

Previously, Frizzled7-dependent non-canonical Wnt signaling was shown to be important for the tissue separation behavior (Winklbauer et al., 2001; Medina et al., 2004; Luu et al., 2015).

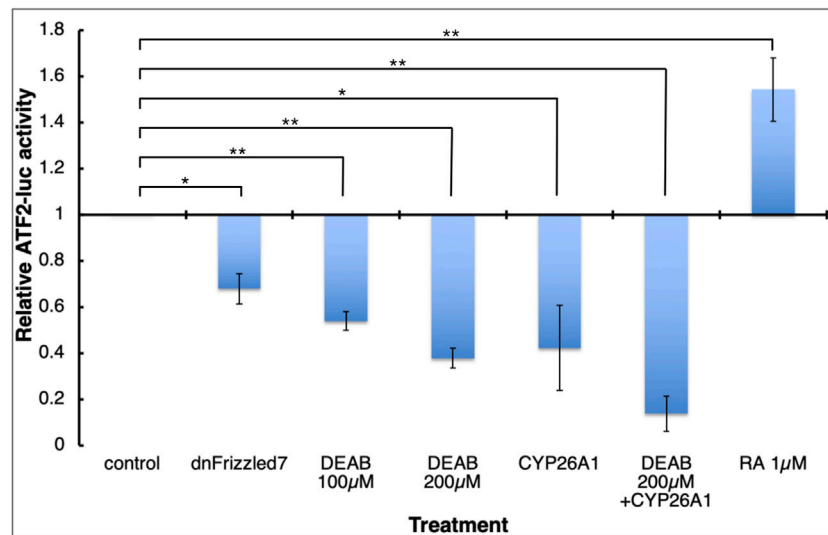


FIGURE 8 | RA signaling is necessary for normal Wnt/PCP activity. Embryos were injected with the ATF2-based non-canonical Wnt signaling reporter plasmid and subjected to DEAB or RA treatments, or co-injected with mRNA encoding dominant-negative Frizzled 7 or CYP26A1. During late gastrula (st. 12) embryos were collected and analyzed and the effect on the reporter activity (luciferase) was determined. *, $p < 0.05$; **, $p < 0.01$.

Although Wnt/PCP signaling can proceed through several downstream signaling pathways (Sokol, 2015; Ng et al., 2019), the ATF2-based non-canonical Wnt signaling reporter plasmid (Ohkawara and Niehrs, 2011) allows us study the effect of RA signaling manipulation on the non-canonical Wnt activity. Embryos were injected along the marginal zone with the ATF2 reporter plasmid and either co-injected with mRNA encoding CYP26A1 or treated with DEAB. During late gastrula (st. 12) embryos were collected, and the level of luciferase activity was determined. The activity of the ATF2 reporter plasmid exhibited a concentration-dependent reduction in response to increasing DEAB concentrations (Figure 8). A similar reduction was observed in embryos overexpressing CYP26A1 and this effect was enhanced by adding DEAB to these embryos. In agreement with a promoting effect of RA signaling on non-canonical Wnt signaling, treatment with RA increased the transcriptional activity of the reporter plasmid (Figure 8). As a control for the involvement of non-canonical Wnt signaling in the activity of the ATF2 reporter, RNA encoding a dominant-negative form of the Frizzled 7 receptor was also co-injected resulting in a significant reduction as expected. These results support a requirement for RA signaling for the non-canonical signaling activity during gastrulation.

DISCUSSION

Reduced RA Delays Gastrulation and Morphogenetic Movements

RA signaling is well established to play pivotal roles in embryonic axis formation and patterning. Supplying excess RA to the culture medium affects progression through *Xenopus* gastrulation, including a delay in the closure of the blastopore (Durst et al., 1989; Sive et al., 1990). Excess RA signaling caused by DHRS3 knockdown, a

retinaldehyde reductase whose normal activity reduces the production of RA, affects the migration of the *gsc*- and *lhx1*-positive cells during gastrulation (Kam et al., 2013). Other studies have relied on pharmacological inhibitors of RA biosynthesis to reduce endogenous RA levels and shown similar effects, as discussed below. The similar effects of increased and decreased RA signaling on the progression of gastrulation suggests a complex regulatory role of RA during early embryogenesis (Gur et al., 2022).

The two most commonly used pharmacological inhibitors of RA biosynthesis are DEAB and citral. Our studies using DEAB or citral concentrations above the inhibition constants (K_i) for the human ALDH1A2 enzyme (Shabtai et al., 2016) revealed an as yet uncharacterized effect of reduced RA signaling: a significant delay in the progression through gastrulation. Similar results were observed when embryos were treated with ethanol, another RA biosynthesis inhibitor (Shabtai et al., 2018; Yelin et al., 2007, 2005). Two retinaldehyde dehydrogenases that produce RA, ALDH1A2, and ALDH1A3, are expressed during early gastrulation (Chen et al., 2001; Blentic et al., 2003; Halilagic et al., 2003; Lupo et al., 2005; Shabtai et al., 2018; Gur et al., 2022). Mutation of each of these genes in vertebrate embryos results in post-gastrula delays and loss of viability (Niederreither et al., 1999; Begemann et al., 2001; Sandell et al., 2007). Therefore, we propose that the pharmacological inhibitors of RA biosynthesis used in these and the present study (DEAB, citral, ethanol) likely target more than one ALDH enzyme during early embryogenesis (Morgan et al., 2015; Cho et al., 2021). The specificity of the RA reduction by these reagents is supported by the similar results obtained by overexpressing Cyp26a1, an RA catabolic enzyme (Yelin et al., 2005; this work).

Reduced RA signaling might delay gastrulation movements by a number of mechanisms. Although germ layer induction or patterning could be affected, we observed the appropriate dorsal

midline expression of *gsc*-, and *chrd.1*-positive cells. In other studies, reduced RA signaling by ethanol treatment or Cyp26a1 overexpression also showed dorsal midline expression of *gsc*-, *chrd.1*-, *otx2*-, and *not*-positive cells (Yelin et al., 2007, 2005). Thus, prechordal mesoderm appears to be induced and appropriately patterned. However, subtle effects on expression levels on these genes and other components of the mesoderm network should be further studied.

One consistent effect of these various methods of reducing RA, however, was a delay in the movement of *gsc*-positive PCM cells from the organizer to their ultimate cranial position, which in normal embryos results in the formation of the notochord (De Robertis et al., 1994; Huang and Winklbauer, 2018). This movement involves convergence-extension movements, which can be assessed by the extent that DMZ explants elongate (Keller and Shook, 2008; Keller and Sutherland, 2020; Winklbauer, 2020). This report and previous studies (Yelin et al., 2005) clearly demonstrate that the elongation of DMZ explants subjected to reduced RA signaling is severely impaired, indicating a reduced capacity of these cells to perform convergence-extension. Interestingly, we previously showed that the *gsc*-positive PCM cells in ethanol treated embryos eventually reach their cranial position (Yelin et al., 2007, 2005), but the delay likely affected inductive interactions with the neural ectoderm that should have taken place earlier (Gur et al., 2022). Together, these reports indicate that in addition to its early role in the organizer RA also has an early effect on the morphogenetic movements of the involuting mesoderm. It will be important to determine whether altered RA signaling affects all subdivisions of mesoderm or specifically LEM, PCM or mesendodermal cells.

Reduced RA Leads to an Internal Reorganization of the *Xenopus* Embryo

The delayed rostral migration of the cells expressing organizer-specific genes at the onset of gastrulation is probably one of the earliest effects of reduced RA signaling, one consequence of which might be altered patterning of the body axis due to delayed or defective inductive signaling, as previously suggested (Gur et al., 2022). This possibility seemed likely because reduced RA signaling gave rise to embryos whose neural plates appeared to be mislocalized to the ventral side. We performed a series of lineage tracing experiments to determine whether this phenotype resulted from altered cell fates leading to reversed dorsal-ventral axes or abnormal cell movements. For the lineages studied that are destined to give rise to dorsal ectoderm or dorsal mesoderm, the clones exhibited the expected distribution at neurula stages, even under reduced RA signaling conditions. However, the V111 (A4) blastomere, which is fated to give rise to the ventral-lateral epidermis, exhibited an abnormal distribution in embryos subjected to reduced RA signaling. These results ruled out changes in cell fates but supported effects on morphogenetic movements, leading us to postulate that reducing RA signaling at blastula stages would result in an altered internal organization of the embryo.

Consistent with this idea, we noted that reduced RA signaling neurulae appeared to contain a persistent blastocoel that forced the apparent repositioning of the neural plate. Analysis of the

blastocoel during gastrula stages in fact demonstrated it to be significantly broader than in controls, indicating a defect in the internalization and subsequent anterior migration of the MZ that is instrumental for blastocoel compaction. We further observed that Brachet's cleft, an indicator of the initiation of mesoderm migration onto the blastocoel roof, was significantly shorter in reduced RA signaling embryos. LEM/PCM involution and migration requires the deposition of a FN substrate along Brachet's cleft (Keller and Jansa 1992; Winklbauer and Schürfeld, 1999; Gorny and Steinbeisser, 2012; Huang and Winklbauer 2018; Forecki et al., 2018). We found that reducing RA signaling by three different approaches resulted in a significant reduction in FN deposition, indicating an effect on LEM/PCM migration. Both phenotypes, the shortened Brachet's cleft and the inefficient deposition of FN, are linked to defective involution of the mesendoderm (Keller and Jansa, 1992; Shook and Keller, 2008; Gorny and Steinbeisser, 2012; Barua et al., 2021). Interestingly, even in the absence of dorsal mesoderm migration, notochord formation anomalies develop, and involution and closure of the blastopore, continues resulting in internalization of the vegetal cells (Keller and Jansa, 1992). In future experiments, it will be important to determine the precise cellular effects of reduced RA signaling on both the migrating mesoderm and the ectodermal substrate utilizing the many sophisticated explant approaches that have been developed in *Xenopus*.

Inhibition of RA Signaling Affects the Tissue Separation Behavior

The delay in the involution of cells expressing organizer-specific genes (Yelin et al., 2005, 2007; this work), the shortening of Brachet's cleft and the reduced deposition of FN in the cleft prompted us to study the tissue separation behavior of the involuting marginal zone cells (Gorny and Steinbeisser, 2012; Winklbauer, 2020). Inhibition of RA signaling in either the BCR or the DM cells reduced the extent of tissue separation. The slightly higher sensitivity in the BCR may account for the reduced FN deposition along the cleft, which should be assessed in future experiments. We suggest that defective tissue separation likely is the cause of the shortened Brachet's cleft due to partial fusion of the mesoderm and ectoderm. However, differences in the relative positions of PCM, chordal mesoderm and mesendoderm in RA inhibitor-treated and control gastrulae might contribute to the observed tissue separation defects. Performing these experiments with precisely fate-mapped pre-involution mesoderm pieces would discriminate between these possibilities.

Nonetheless, the tissue separation defect was shown to most likely involve the non-canonical Wnt signaling pathway as the activity of a non-canonical Wnt signaling reporter plasmid (Ohkawara and Niehrs, 2011) was reduced by inhibiting RA biosynthesis in a concentration-dependent manner. The effect of reduced RA signaling on the non-canonical Wnt pathway phenocopied the known effect of dominant negative Frizzled 7 overexpression on this pathway and on the tissue separation behavior (Winklbauer et al., 2001). Tissue separation also has been shown to also involve multiple ephrins and their Eph receptors in addition to PDGF and paraxial protocadherin

(Gorny and Steinbeisser, 2012; Fagotto, 2020). Manipulation of RA levels in the BCR cells, in particular, resulted in the reduction in the expression of *efnb3*. This response suggests that RA signaling is important for the expression of *efnb3* in the ectoderm where it is normally enriched (Fagotto et al., 2014). Many of the other genes tested exhibited some degree of up-regulation following RA knockdown. These observations support the hypothesis that RA signaling plays a regulatory role in the tissue separation behavior during gastrulation.

A number of reports showed a regulatory link between RA signaling and Wnt/PCP, an important pathway regulating multiple morphogenetic movements (Wallingford, 2012; Sokol, 2015; Brinkmann et al., 2016). For example, RA regulates components of the Wnt pathway (Zhao and Duester, 2009; Carron and Shi, 2016) and RA target genes interact with components of this pathway (Harada et al., 2007; Zhang et al., 2013). Ethanol similarly interacts with the Wnt/PCP pathway (Sarmah et al., 2020; Sidik et al., 2021). These observations suggest that the RA effects on gastrulation and the rostral movement of the LEM/PCM involve an interaction with the Wnt/PCP pathway to regulate morphogenetic movements.

CONCLUSION

Herein we report that reducing endogenous levels of RA at blastula stages results in multiple defects in the ability of the mesoderm to involute that leads to later morphological defects including a persistent blastocoel, delayed cranial elongation of the notochord and broader neural plate. Together, these observations indicate that one of the earliest roles of RA signaling in the embryo is the regulation of several morphogenetic processes that are critically important for the normal progression of gastrulation. We speculate that an underlying result of delaying the involution and rostral movement of LEM/PCM cells is that some of the ectodermal cells are likely to have lost their competence to respond to mesoderm derived signals. Support for this abnormal inductive timing was observed in embryos manipulated for reduced RA signaling that developed microcephaly (Gur et al., 2022). The remarkable versatility of *Xenopus* explants, including precise dissection of the different mesodermal precursor populations, tissue separation and migration assays, will be instrumental to further characterize the signaling pathways, cell adhesion molecules and substrates that are altered by reduced RA signaling.

REFERENCES

- Ang, H. L., and Duester, G. (1999). Stimulation of Premature Retinoic Acid Synthesis in *Xenopus* Embryos Following Premature Expression of Aldehyde Dehydrogenase ALDH1. *Eur. J. Biochem.* 260, 227–234. doi:10.1046/j.1432-1327.1999.00139.x
- Barua, D., Nagel, M., and Winklbauer, R. (2021). Cell-cell Contact Landscapes in *Xenopus* Gastrula Tissues. *Proc. Natl. Acad. Sci. U.S.A.* 118. doi:10.1073/pnas.2107953118
- Bauer, D. V., Huang, S., and Moody, S. A. (1994). The Cleavage Stage Origin of Spemann's Organizer: Analysis of the Movements of Blastomere Clones before

DATA AVAILABILITY STATEMENT

The original contributions presented in the study are included in the article and **Supplementary Material**, further inquiries can be directed to the corresponding authors.

ETHICS STATEMENT

The animal studies were reviewed and approved by Institutional Animal Care and Use Committee (IACUC) of the Hebrew University (Ethics approval no. MD-17-15281-3) and the George Washington University (Ethics approval no. A233).

AUTHOR CONTRIBUTIONS

AF and SM conceived and supervised the study and designed the experiments and analysis methodology. MG, TE, SM, and AF performed embryo experiments, and real-time PCR assessment and developed figures. MG, TE, SM, and AF interpreted the results and drafted the manuscript.

FUNDING

This work was funded in part by grants from the United States-Israel Binational Science Foundation (2017199) to SM and AF, and The Israel Science Foundation (668/17), the Manitoba Liquor and Lotteries (RG-003-21), and the Wolfson Family Chair in Genetics to AF.

ACKNOWLEDGMENTS

We wish to thank Martin Blum and Herbert Steinbeisser for discussions on embryonic morphogenetic movements. We thank Graciela Pillemer for reading the manuscript.

SUPPLEMENTARY MATERIAL

The Supplementary Material for this article can be found online at: <https://www.frontiersin.org/articles/10.3389/fcell.2022.857230/full#supplementary-material>

and during Gastrulation in *Xenopus*. *Development* 120, 1179–1189. doi:10.1242/dev.120.5.1179

Begemann, G., Schilling, T. F., Rauch, G.-J., Geisler, R., and Ingham, P. W. (2001). The Zebrafish *neckless* mutation Reveals a Requirement for *Alx2* in Mesodermal Signals that Pattern the Hindbrain. *Development* 128, 3081–3094. doi:10.1242/dev.128.16.3081

Blaner, W. S. (2019). Vitamin A Signaling and Homeostasis in Obesity, Diabetes, and Metabolic Disorders. *Pharmacol. Ther.* 197, 153–178. doi:10.1016/j.pharmthera.2019.01.006

Blentic, A., Gale, E., and Maden, M. (2003). Retinoic Acid Signalling Centres in the Avian Embryo Identified by Sites of Expression of Synthesising and Catabolising Enzymes. *Dev. Dyn.* 227, 114–127. doi:10.1002/dvdy.10292

- Brinkmann, E.-M., Mattes, B., Kumar, R., Hagemann, A. I. H., Gradl, D., Scholpp, S., et al. (2016). Secreted Frizzled-Related Protein 2 (sFRP2) Redirects Non-canonical Wnt Signaling from Fz7 to Ror2 during Vertebrate Gastrulation. *J. Biol. Chem.* 291, 13730–13742. doi:10.1074/jbc.M116.733766
- Carron, C., and Shi, D. L. (2016). Specification of Anteroposterior axis by Combinatorial Signaling during *Xenopus* Development. *Wires Dev. Biol.* 5, 150–168. doi:10.1002/wdev.217
- Chen, Y., Huang, L., Russo, A. F., and Solursh, M. (1992). Retinoic Acid Is Enriched in Hensen's Node and Is Developmentally Regulated in the Early Chicken Embryo. *Proc. Natl. Acad. Sci. U.S.A.* 89, 10056–10059. doi:10.1073/pnas.89.21.10056
- Chen, Y., Huang, L., and Solursh, M. (1994). A Concentration Gradient of Retinoids in the Early *Xenopus laevis* Embryo. *Developmental Biol.* 161, 70–76. doi:10.1006/dbio.1994.1008
- Chen, Y., Pollet, N., Niehrs, C., and Pieler, T. (2001). Increased XRALDH2 Activity Has a Posteriorizing Effect on the central Nervous System of *Xenopus* Embryos. *Mech. Development* 101, 91–103. doi:10.1016/S0925-4773(00)00558-X
- Cho, K., Lee, S.-M., Heo, J., Kwon, Y. M., Chung, D., Yu, W.-J., et al. (2021). Retinaldehyde Dehydrogenase Inhibition-Related Adverse Outcome Pathway: Potential Risk of Retinoic Acid Synthesis Inhibition during Embryogenesis. *Toxins* 13, 739. doi:10.3390/toxins13110739
- Cho, K. W. Y., Blumberg, B., Steinbeisser, H., and De Robertis, E. M. (1991). Molecular Nature of Spemann's Organizer: the Role of the *Xenopus* Homeobox Gene Goosecoid. *Cell* 67, 1111–1120. doi:10.1016/0092-8674(91)90288-a
- Creech Kraft, J., Schuh, T., Juchau, M. R., and Kimelman, D. (1994). Temporal Distribution, Localization and Metabolism of All-Trans-Retinal, Dihydroretinol and All-Trans-Retinal during *Xenopus* Development. *Biochem. J.* 301 (Pt 1), 111–119. doi:10.1042/bj3010111
- Dale, L., and Slack, J. M. (1987). Fate Map for the 32-cell Stage of *Xenopus laevis*. *Development* 99, 527–551. doi:10.1042/dev.99.4.527
- Davidson, L. A., Keller, R., and DeSimone, D. W. (2004). Assembly and Remodeling of the Fibrillar Fibronectin Extracellular Matrix during Gastrulation and Neurulation in *Xenopus laevis*. *Dev. Dyn.* 231, 888–895. doi:10.1002/dvdy.20217
- De Robertis, E. M., Fainsod, A., Gont, L. K., and Steinbeisser, H. (1994). The Evolution of Vertebrate Gastrulation. *Dev. Suppl.* 1994, 117–124. doi:10.1242/dev.1994.supplement.117
- Draut, H., Liebenstein, T., and Begemann, G. (2019). New Insights into the Control of Cell Fate Choices and Differentiation by Retinoic Acid in Cranial, Axial and Caudal Structures. *Biomolecules* 9, 860. doi:10.3390/biom9120860
- Durston, A. J., Timmermans, J. P. M., Hage, W. J., Hendriks, H. F. J., de Vries, N. J., Heideveld, M., et al. (1989). Retinoic Acid Causes an Anteroposterior Transformation in the Developing central Nervous System. *Nature* 340, 140–144. doi:10.1038/340140a0
- Epstein, M., Pillemer, G., Yelin, R., Yisraeli, J. K., and Fainsod, A. (1997). Patterning of the Embryo along the Anterior-Posterior axis: the Role of the Caudal Genes. *Development* 124, 3805–3814. doi:10.1242/dev.124.19.3805
- Fagotto, F. (2020). Tissue Segregation in the Early Vertebrate Embryo. *Semin. Cell Developmental Biol.* 107, 130–146. doi:10.1016/j.semcdb.2020.05.020
- Fagotto, F., Winklbauer, R., and Rohani, N. (2014). Ephrin-Eph Signaling in Embryonic Tissue Separation. *Cell Adhes. Migration* 8, 308–326. doi:10.4161/19336918.2014.970028
- Forecki, J., Van Antwerp, D. J., Lujan, S. M., and Merzdorf, C. S. (2018). Roles for *Xenopus* Aquaporin-3b (aqp3L) During Gastrulation: Fibrillar Fibronectin and Tissue Boundary Establishment in the Dorsal Margin. *Dev. Biol.* 433, 3–16. doi:10.1016/j.ydbio.2017.11.001
- Ghyselinck, N. B., and Duester, G. (2019). Retinoic Acid Signaling Pathways. *Development* 146. doi:10.1242/dev.167502
- Gorny, A.-K., and Steinbeisser, H. (2012). Brachet's Cleft: a Model for the Analysis of Tissue Separation in *Xenopus*. *Wires Dev. Biol.* 1, 294–300. doi:10.1002/wdev.24
- Gur, M., Bendelac-Kapon, L., Shabtai, Y., Pillemer, G., and Fainsod, A. (2022). Reduced Retinoic Acid Signaling during Gastrulation Induces Developmental Microcephaly. *Front. Cell Dev. Biol.* 10, 844619. doi:10.3389/fcell.2022.844619
- Halilagic, A., Zile, M. H., and Studer, M. (2003). A Novel Role for Retinoids in Patterning the Avian Forebrain during Presomite Stages. *Development* 130, 2039–2050. doi:10.1042/dev.00423
- Harada, Y., Yokota, C., Habas, R., Slusarski, D. C., and He, X. (2007). Retinoic Acid-Inducible G Protein-Coupled Receptors Bind to Frizzled Receptors and May Activate Non-canonical Wnt Signaling. *Biochem. Biophysical Res. Commun.* 358, 968–975. doi:10.1016/j.bbrc.2007.04.208
- Hogan, B. L. M., Thaller, C., and Eichele, G. (1992). Evidence that Hensen's Node Is a Site of Retinoic Acid Synthesis. *Nature* 359, 237–241. doi:10.1038/359237a0
- Holleman, T., Chen, Y., Grunz, H., and Pieler, T. (1998). Regionalized Metabolic Activity Establishes Boundaries of Retinoic Acid Signalling. *EMBO J.* 17, 7361–7372. doi:10.1093/emboj/17.24.7361
- Huang, Y., and Winklbauer, R. (2018). Cell Migration in the *Xenopus* Gastrula. *Wires Dev. Biol.* 7, e325. doi:10.1002/wdev.325
- Jacobson, M., and Hirose, G. (1981). Clonal Organization of the central Nervous System of the Frog. II. Clones Stemming from Individual Blastomeres of the 32- and 64-cell Stages. *J. Neurosci.* 1, 271–284. doi:10.1523/jneurosci.01-03-00271.1981
- Janesick, A., Tang, W., Shioda, T., and Blumberg, B. (2018). RAR γ Is Required for Mesodermal Gene Expression Prior to Gastrulation. *Development* 145, dev147769. doi:10.1242/dev.147769
- Kaneda, T., and Motoki, J.-y. D. (2012). Gastrulation and Pre-gastrulation Morphogenesis, Inductions, and Gene Expression: Similarities and Dissimilarities between Urodelean and Anuran Embryos. *Developmental Biol.* 369, 1–18. doi:10.1016/j.ydbio.2012.05.019
- Kedishvili, N. Y. (2016). Retinoic Acid Synthesis and Degradation. *Subcell Biochem.* 81, 127–161. doi:10.1007/978-94-024-0945-1_5
- Keller, R., Davidson, L. A., and Shook, D. R. (2003). How We Are Shaped: the Biomechanics of Gastrulation. *Differentiation* 71, 171–205. doi:10.1046/j.1432-0436.2003.710301.x
- Keller, R., and Jansa, S. (1992). *Xenopus* Gastrulation without a Blastocoel Roof. *Dev. Dyn.* 195, 162–176. doi:10.1002/aja.1001950303
- Keller, R., and Shook, D. (2008). Dynamic Determinations: Patterning the Cell Behaviours that Close the Amphibian Blastopore. *Phil. Trans. R. Soc. B* 363, 1317–1332. doi:10.1098/rstb.2007.2250
- Keller, R., and Sutherland, A. (2020). Convergent Extension in the Amphibian, *Xenopus laevis*. *Curr. Top. Dev. Biol.* 136, 271–317. doi:10.1016/bs.ctdb.2019.11.013
- Klein, S. L. (1987). The First Cleavage Furrow Demarcates the Dorsal-Ventral axis in *Xenopus* Embryos. *Developmental Biol.* 120, 299–304. doi:10.1016/0012-1606(87)90127-8
- Köster, I., Jungwirth, M. S., and Steinbeisser, H. (2010). xGit2 and xRhoGAP 11A Regulate Convergent Extension and Tissue Separation in *Xenopus* Gastrulation. *Developmental Biol.* 344, 26–35. doi:10.1016/j.ydbio.2010.03.025
- Kot-Leibovich, H., and Fainsod, A. (2009). Ethanol Induces Embryonic Malformations by Competing for Retinaldehyde Dehydrogenase Activity during Vertebrate Gastrulation. *Dis. Model. Mech.* 2, 295–305. doi:10.1242/dmm.001420
- Kraft, B., Berger, C. D., Wallkamm, V., Steinbeisser, H., and Wedlich, D. (2012). Wnt-11 and Fz7 Reduce Cell Adhesion in Convergent Extension by Sequestration of PAPC and C-Cadherin. *J. Cell Biol.* 198, 695–709. doi:10.1083/jcb.2011110076
- Kraft, J. C., Schuh, T., Juchau, M., and Kimelman, D. (1994). The Retinoid X Receptor Ligand, 9-Cis-Retinoic Acid, Is a Potential Regulator of Early *Xenopus* Development. *Proc. Natl. Acad. Sci. U.S.A.* 91, 3067–3071. doi:10.1073/pnas.91.8.3067
- le Maire, A., and Bourguet, W. (2014). Retinoic Acid Receptors: Structural Basis for Coregulator Interaction and Exchange. *Subcell Biochem.* 70, 37–54. doi:10.1007/978-94-017-9050-5_3
- Lee, H., Lee, S. J., Kim, G.-H., Yeo, I., and Han, J.-K. (2016). PLD1 Regulates *Xenopus* Convergent Extension Movements by Mediating Frizzled7 Endocytosis for Wnt/PCP Signal Activation. *Developmental Biol.* 411, 38–49. doi:10.1016/j.ydbio.2016.01.013
- Leibovich, A., Edri, T., Klein, S. L., Moody, S. A., and Fainsod, A. (2020). Natural Size Variation Among Embryos Leads to the Corresponding Scaling in Gene Expression. *Developmental Biol.* 462, 165–179. doi:10.1016/j.ydbio.2020.03.014
- Liang, D., Zhang, M., Bao, J., Zhang, L., Xu, X., Gao, X., et al. (2008). Expressions of Raldh3 and Raldh4 during Zebrafish Early Development. *Gene Expr. Patterns* 8, 248–253. doi:10.1016/j.gep.2007.12.007
- Lloret-Vilaspa, F., Jansen, H. J., Deroos, K., Chandraratna, R. A. S., Zile, M. H., Stern, C. D., et al. (2010). Retinoid Signalling Is Required for Information Transfer from Mesoderm to Neuroectoderm during Gastrulation. *Int. J. Dev. Biol.* 54, 599–608. doi:10.1387/ijdb.082705fl

- Lupo, G., Liu, Y., Qiu, R., Chandraratna, R. A. S., Barsacchi, G., He, R.-Q., et al. (2005). Dorsal-ventral Patterning of the *Xenopus* Eye: a Collaboration of Retinoid, Hedgehog and FGF Receptor Signaling. *Development* 132, 1737–1748. doi:10.1242/dev.01726
- Luu, O., Damm, E. W., Parent, S. E., Barua, D., Smith, T. H. L., Wen, J. W. H., et al. (2015). PAPC Mediates Self/non-Self-Distinction during Snail1-dependent Tissue Separation. *J. Cell Biol.* 208, 839–856. doi:10.1083/jcb.201409026
- Medina, A., Swain, R. K., Kuerner, K.-M., and Steinbeisser, H. (2004). *Xenopus* Paraxial Protocadherin Has Signaling Functions and Is Involved in Tissue Separation. *EMBO J.* 23, 3249–3258. doi:10.1038/sj.emboj.7600329
- Metzler, M. A., and Sandell, L. L. (2016). Enzymatic Metabolism of Vitamin A in Developing Vertebrate Embryos. *Nutrients* 8, E812. pii. doi:10.3390/nu8120812
- Moody, S. A. (1987). Fates of the Blastomeres of the 32-Cell-Stage *Xenopus* Embryo. *Dev. Biol.* 122, 300–319. doi:10.1016/0012-1606(87)90296-X
- Moody, S. A. (2018). Lineage Tracing and Fate Mapping in *xenopus* Embryos. *Cold Spring Harb. Protoc.* 2018, 1. doi:10.1101/pdb.prot097253
- Morgan, C. A., Parajuli, B., Buchman, C. D., Dria, K., and Hurley, T. D. (2015). N,N-diethylaminobenzaldehyde (DEAB) as a Substrate and Mechanism-Based Inhibitor for Human ALDH Isoenzymes. *Chem. Biol. Interact.* 234, 18–28. doi:10.1016/j.cbi.2014.12.008
- Nakamura, O., Takasaki, H., and Nagata, A. (1978). Further Studies of the Prospective Fates of Blastomeres at the 32-cell Stage of *Xenopus laevis* Embryos. *Med. Biol.* 56, 355–360.
- Neijts, R., and Deschamps, J. (2017). At the Base of Colinear Hox Gene Expression: Cis-Features and Trans-factors Orchestrating the Initial Phase of Hox Cluster Activation. *Dev. Biol.* 428, 293–299. doi:10.1016/j.ydbio.2017.02.009
- Ng, L. F., Kaur, P., Bunnag, N., Suresh, J., Sung, I. C. H., Tan, Q. H., et al. (2019). WNT Signaling in Disease. *Cells* 8, 826. doi:10.3390/cells8080826
- Niederreither, K., McCaffery, P., Dräger, U. C., Chambon, P., and Dollé, P. (1997). Restricted Expression and Retinoic Acid-Induced Downregulation of the Retinaldehyde Dehydrogenase Type 2 (RALDH-2) Gene during Mouse Development. *Mech. Dev.* 62, 67–78. doi:10.1016/S0925-4773(96)00653-3
- Niederreither, K., Subbarayan, V., Dollé, P., and Chambon, P. (1999). Embryonic Retinoic Acid Synthesis Is Essential for Early Mouse post-implantation Development. *Nat. Genet.* 21, 444–448. doi:10.1038/7788
- Nieuwkoop, P. D., and Faber, J. (1967). *Normal Table of Xenopus laevis (Daudin): A Systematical and Chronological Survey of the Development from the Fertilized Egg till the End of Metamorphosis*. Amsterdam: North-Holland Publishing Company.
- Nolte, C., De Kumar, B., and Krumlauf, R. (2019). Hox Genes: Downstream “Effectors” of Retinoic Acid Signaling in Vertebrate Embryogenesis. *Genesis* 57, e23306. doi:10.1002/dvg.23306
- Ohkawara, B., and Niehrs, C. (2011). An ATF2-Based Luciferase Reporter to Monitor Non-canonical Wnt Signaling in *Xenopus* Embryos. *Dev. Dyn.* 240, 188–194. doi:10.1002/dvdy.22500
- Penzel, R., Oschwald, R., Chen, Y., Tacke, L., and Grunz, H. (1997). Characterization and Early Embryonic Expression of a Neural Specific Transcription Factor xSOX3 in *Xenopus laevis*. *Int. J. Dev. Biol.* 41, 667–677.
- Ribes, V., Fraulob, V., Petkovich, M., and Dollé, P. (2007). The Oxidizing Enzyme CYP26a1 Tightly Regulates the Availability of Retinoic Acid in the Gastrulating Mouse Embryo to Ensure Proper Head Development and Vasculogenesis. *Dev. Dyn.* 236, 644–653. doi:10.1002/dvdy.21057
- Rossant, J., Zirngibl, R., Cado, D., Shago, M., and Giguère, V. (1991). Expression of a Retinoic Acid Response Element-hsplaZ Transgene Defines Specific Domains of Transcriptional Activity during Mouse Embryogenesis. *Genes Dev.* 5, 1333–1344. doi:10.1101/gad.5.8.1333
- Sandell, L. L., Sanderson, B. W., Moiseyev, G., Johnson, T., Mushegian, A., Young, K., et al. (2007). RDH10 Is Essential for Synthesis of Embryonic Retinoic Acid and Is Required for Limb, Craniofacial, and Organ Development. *Genes Dev.* 21, 1113–1124. doi:10.1101/gad.1533407
- Sarmah, S., Srivastava, R., McClintick, J. N., Janga, S. C., Edenberg, H. J., and Marrs, J. A. (2020). Embryonic Ethanol Exposure Alters Expression of Sox2 and Other Early Transcripts in Zebrafish, Producing Gastrulation Defects. *Sci. Rep.* 10, 3951. doi:10.1038/s41598-020-59043-x
- Shabtai, Y., Bendelac, L., Jubran, H., Hirschberg, J., and Fainsod, A. (2018). Acetaldehyde Inhibits Retinoic Acid Biosynthesis to Mediate Alcohol Teratogenicity. *Sci. Rep.* 8, 347. doi:10.1038/s41598-017-18719-7
- Shabtai, Y., and Fainsod, A. (2018). Competition between Ethanol Clearance and Retinoic Acid Biosynthesis in the Induction of Fetal Alcohol Syndrome. *Biochem. Cell Biol.* 96, 148–160. doi:10.1139/bcb-2017-0132
- Shabtai, Y., Jubran, H., Nassar, T., Hirschberg, J., and Fainsod, A. (2016). Kinetic Characterization and Regulation of the Human Retinaldehyde Dehydrogenase 2 Enzyme during Production of Retinoic Acid. *Biochem. J.* 473, 1423–1431. doi:10.1042/BCJ20160101
- Shih, J., and Keller, R. (1992). The Epithelium of the Dorsal Marginal Zone of *Xenopus* Has Organizer Properties. *Development* 116, 887–899. doi:10.1242/dev.116.4.887
- Shook, D. R., and Keller, R. (2008). Epithelial Type, Ingression, Blastopore Architecture and the Evolution of Chordate Mesoderm Morphogenesis. *J. Exp. Zool. B Mol. Dev. Evol.* 310, 85–110. doi:10.1002/jez.b.21198
- Shukrun, N., Shabtai, Y., Pillemer, G., and Fainsod, A. (2019). Retinoic Acid Signaling Reduction Recapitulates the Effects of Alcohol on Embryo Size. *Genesis* 57, e23284. doi:10.1002/dvg.23284
- Sidik, A., Dixon, G., Buckley, D. M., Kirby, H. G., Sun, S., and Eberhart, J. K. (2021). Exposure to Ethanol Leads to Midfacial Hypoplasia in a Zebrafish Model of FASD via Indirect Interactions with the Shh Pathway. *BMC Biol.* 19, 134. doi:10.1186/s12915-021-01062-9
- Sive, H. L., Draper, B. W., Harland, R. M., and Weintraub, H. (1990). Identification of a Retinoic Acid-Sensitive Period during Primary axis Formation in *Xenopus laevis*. *Genes Dev.* 4, 932–942. doi:10.1101/gad.4.6.932
- Sokol, S. Y. (2015). Spatial and Temporal Aspects of Wnt Signaling and Planar Cell Polarity during Vertebrate Embryonic Development. *Semin. Cell Dev. Biol.* 42, 78–85. doi:10.1016/j.semcdb.2015.05.002
- Summerbell, D., and Maden, M. (1990). Retinoic Acid, a Developmental Signalling Molecule. *Trends Neurosci.* 13, 142–147. doi:10.1016/0166-2236(90)90006-v
- Thatcher, J. E., and Isoherranen, N. (2009). The Role of CYP26 Enzymes in Retinoic Acid Clearance. *Expert Opin. Drug Metab. Toxicol.* 5, 875–886. doi:10.1517/17425250903032681
- Wacker, S., Grimm, K., Joos, T., and Winklbauer, R. (2000). Development and Control of Tissue Separation at Gastrulation in *Xenopus*. *Dev. Biol.* 224, 428–439. doi:10.1006/dbio.2000.9794
- Wallingford, J. B. (2012). Planar Cell Polarity and the Developmental Control of Cell Behavior in Vertebrate Embryos. *Annu. Rev. Cell Dev. Biol.* 28, 627–653. doi:10.1146/annurev-cellbio-092910-154208
- Wilson, P. A., Oster, G., and Keller, R. (1989). Cell Rearrangement and Segmentation in *Xenopus*: Direct Observation of Cultured Explants. *Development* 105, 155–166. doi:10.1242/dev.105.1.155
- Winklbauer, R., Medina, A., Swain, R. K., and Steinbeisser, H. (2001). Frizzled-7 Signalling Controls Tissue Separation during *Xenopus* Gastrulation. *Nature* 413, 856–860. doi:10.1038/35101621
- Winklbauer, R. (2020). Mesoderm and Endoderm Internalization in the *Xenopus* Gastrula. *Curr. Top. Dev. Biol.* 136, 243–270. doi:10.1016/bs.ctdb.2019.09.002
- Winklbauer, R., and Schürfeld, M. (1999). Vegetal Rotation, a New Gastrulation Movement Involved in the Internalization of the Mesoderm and Endoderm in *Xenopus*. *Development* 126, 3703–3713. doi:10.1242/dev.126.16.3703
- Yan, B., Neilson, K. M., and Moody, S. A. (2009). foxD5 Plays a Critical Upstream Role in Regulating Neural Ectodermal Fate and the Onset of Neural Differentiation. *Dev. Biol.* 329, 80–95. doi:10.1016/j.ydbio.2009.02.019
- Yanagi, T., Ito, K., Nishihara, A., Minamino, R., Mori, S., Sumida, M., et al. (2015). The Spemann Organizer Meets the Anterior-Most Neuroectoderm at the Equator of Early Gastrulae in Amphibian Species. *Dev. Growth Differ.* 57, 218–231. doi:10.1111/dgd.12200
- Yelin, R., Kot, H., Yelin, D., and Fainsod, A. (2007). Early Molecular Effects of Ethanol during Vertebrate Embryogenesis. *Differentiation* 75, 393–403. doi:10.1111/j.1432-0436.2006.00147.x
- Yelin, R., Schyr, R. B.-H., Kot, H., Zins, S., Frumkin, A., Pillemer, G., et al. (2005). Ethanol Exposure Affects Gene Expression in the Embryonic Organizer and Reduces Retinoic Acid Levels. *Dev. Biol.* 279, 193–204. doi:10.1016/j.ydbio.2004.12.014

- Zhang, T., Guo, X., and Chen, Y. (2013). Retinoic Acid-Activated NdrG1a Represses Wnt/ β -Catenin Signaling to Allow *Xenopus* Pancreas, Oesophagus, Stomach, and Duodenum Specification. *PLoS ONE* 8, e65058. doi:10.1371/journal.pone.0065058
- Zhao, X., and Duester, G. (2009). Effect of Retinoic Acid Signaling on Wnt/ β -Catenin and FGF Signaling during Body axis Extension. *Gene Expr. Patterns* 9, 430–435. doi:10.1016/j.gep.2009.06.003
- Zile, M. H. (2010). Vitamin A-Not for Your Eyes Only: Requirement for Heart Formation Begins Early in Embryogenesis. *Nutrients* 2, 532–550. doi:10.3390/nu2050532

Conflict of Interest: The authors declare that the research was conducted in the absence of any commercial or financial relationships that could be construed as a potential conflict of interest.

Publisher's Note: All claims expressed in this article are solely those of the authors and do not necessarily represent those of their affiliated organizations, or those of the publisher, the editors and the reviewers. Any product that may be evaluated in this article, or claim that may be made by its manufacturer, is not guaranteed or endorsed by the publisher.

Copyright © 2022 Gur, Edri, Moody and Fainsod. This is an open-access article distributed under the terms of the Creative Commons Attribution License (CC BY). The use, distribution or reproduction in other forums is permitted, provided the original author(s) and the copyright owner(s) are credited and that the original publication in this journal is cited, in accordance with accepted academic practice. No use, distribution or reproduction is permitted which does not comply with these terms.



Maternal Factors and Nodal Autoregulation Orchestrate *Nodal* Gene Expression for Embryonic Mesendoderm Induction in the Zebrafish

Cencan Xing^{1,2}, Weimin Shen¹, Bo Gong¹, Yaqi Li¹, Lu Yan¹ and Anming Meng^{1,3*}

¹Laboratory of Molecular Developmental Biology, State Key Laboratory of Membrane Biology, Tsinghua-Peking Center for Life Sciences, School of Life Sciences, Tsinghua University, Beijing, China, ²Daxing Research Institute, University of Science and Technology, Beijing, China, ³Guangzhou National Laboratory, Guangzhou, China

OPEN ACCESS

Edited by:

Silvia L. López,
CONICET Instituto de Biología Celular
y Neurociencias (IBCN), Argentina

Reviewed by:

Kyo Yamasu,
Saitama University, Japan
Scott T. Dougan,
University of Georgia, United States
Clémence Carron,
Sorbonne Université, France

*Correspondence:

Anming Meng
mengam@mail.tsinghua.edu.cn

Specialty section:

This article was submitted to
Morphogenesis and Patterning,
a section of the journal
Frontiers in Cell and Developmental
Biology

Received: 02 March 2022

Accepted: 05 May 2022

Published: 26 May 2022

Citation:

Xing C, Shen W, Gong B, Li Y, Yan L
and Meng A (2022) Maternal Factors
and Nodal Autoregulation Orchestrate
Nodal Gene Expression for Embryonic
Mesendoderm Induction in
the Zebrafish.
Front. Cell Dev. Biol. 10:887987.
doi: 10.3389/fcell.2022.887987

Nodal proteins provide crucial signals for mesoderm and endoderm induction. In zebrafish embryos, the *nodal* genes *ndr1/squint* and *ndr2/cyclops* are implicated in mesendoderm induction. It remains elusive how *ndr1* and *ndr2* expression is regulated spatiotemporally. Here we investigated regulation of *ndr1* and *ndr2* expression using *Mhwa* mutants that lack the maternal dorsal determinant Hwa with deficiency in β -catenin signaling, *Meomesa* mutants that lack maternal Eomesodermin A (*Eomesa*), *Meomesa*;*Mhwa* double mutants, and the Nodal signaling inhibitor SB431542. We show that *ndr1* and *ndr2* expression is completely abolished in *Meomesa*;*Mhwa* mutant embryos, indicating an essential role of maternal *eomesa* and *hwa*. Hwa-activated β -catenin signaling plays a major role in activation of *ndr1* expression in the dorsal blastodermal margin, while *eomesa* is mostly responsible for *ndr1* expression in the lateroventral margin and Nodal signaling contributes to ventral expansion of the *ndr1* expression domain. However, *ndr2* expression mainly depends on maternal *eomesa* with minor or negligible contribution of maternal *hwa* and Nodal autoregulation. These mechanisms may help understand regulation of Nodal expression in other species.

Keywords: Nodal, Eomes, Hwa, maternal factor, mesoderm induction, zebrafish

INTRODUCTION

The *Nodal* gene was first identified in mouse and its encoded protein belongs to a member of transforming growth factor β (TGF β) family (Zhou et al., 1993). Disruption of the mouse *Nodal* gene results in failure of primitive streak formation and mesoderm induction during embryonic development (Zhou et al., 1993; Conlon et al., 1994). There are three *nodal* genes in the zebrafish genome, *ndr1/squint* (*sqt*) (Erter et al., 1998; Rebagliati et al., 1998), *ndr2/cyclops* (*cyc*) (Rebagliati et al., 1998), and *ndr3/southpaw* (*spaw*) (Long et al., 2003). Simultaneous deficiency of zebrafish zygotic *ndr1* and *ndr2*, which is caused by gene mutations, leads to loss of most, if not all, endodermal and mesodermal tissues (Feldman et al., 1998), indicating that these two Nodal proteins produced zygotically are mesendoderm inducers during zebrafish embryogenesis. Interestingly, *ndr1* is also maternally expressed with maternal transcripts localized in the presumptive dorsal blastomeres during cleavage period (Gore and Sampath, 2002; Gore et al., 2005); it is believed

that maternal *ndr1* transcripts act as scaffold noncoding RNAs to spatially regulate β -catenin signaling (Lim et al., 2012). Maternal *ndr1* has been shown to cooperate with extraembryonic (yolk syncytial layer) *ndr1* and extraembryonic *ndr2* to specify endoderm and anterior mesoderm fates (Hong et al., 2011), but it remains elusive if this function of maternal *ndr1* is executed through classical Nodal signaling. The zebrafish *ndr3* gene is not expressed until the completion of gastrulation, and it is required for left-right asymmetrical development after the completion of gastrulation (Long et al., 2003; Hashimoto et al., 2004; Zhang et al., 2012; Zhang et al., 2016). The importance of Nodal signaling in mesendoderm induction has also been revealed in frog embryos (Jones et al., 1995; Joseph and Melton, 1997; Osada and Wright, 1999; Agius et al., 2000; Takahashi et al., 2000; Luxardi et al., 2010). It is now widely accepted that zygotically expressed Nodal proteins are essential for mesendoderm induction and patterning in vertebrate embryos (Schier and Shen, 2000; De Robertis and Kuroda, 2004; Tian and Meng, 2006; Zinski et al., 2018).

In frog and fish embryos, mesendoderm induction occurs during middle to late blastulation. As essential mesendoderm inducers, the expression of zygotic *nodal* genes is activated by maternal factors soon after midblastula transition (MBT), which happens in zebrafish embryos around 3 h postfertilization (hpf) (1 k-cell stage) (Kimmel et al., 1995). In frog blastulas, the maternal T-box transcription factor VegT activates the expression of *Xenopus* Nodal-related (*Xnr*) genes in the vegetal blastomeres and maternally regulated nuclear β -catenin in dorsal blastomeres acts in synergy with VegT to enhance *Xnr* genes expression so that a Nodal gradient is formed along the dorsal-ventral axis to induce and pattern the mesendoderm (Zhang et al., 1998; Kofron et al., 1999; Agius et al., 2000; Takahashi et al., 2000; Rex et al., 2002; Xanthos et al., 2002). In the zebrafish, *ndr1* and *ndr2* genes are initially activated in the dorsal blastodermal margin at about 3.3 h hpf and 3.7 hpf respectively, and their expression domains then extend throughout the blastodermal margin to induce the mesendodermal fate (Feldman et al., 1998; Rebagliati et al., 1998). β -catenin signaling plays a role in activating *ndr1* and *ndr2* expression in the dorsal blastodermal margin (Kelly et al., 2000; Dougan et al., 2003; Bellipanni et al., 2006). It has been recently disclosed that β -catenin signaling is activated by maternal *huluwa* (*hwa*), which encodes a transmembrane protein, in zebrafish and *Xenopus* blastulas (Yan et al., 2018). Maternal *hwa* transcripts in both species are located in the vegetal pole of the mature oocyte. Upon fertilization in *Xenopus*, maternal *hwa* transcripts shift to one side with cortical rotation and are apparently enriched in the dorsal blastomere at 2-cell stage; after fertilization in zebrafish, *hwa* transcripts in the vegetal pole transport to the cytoplasm in the animal pole and become ubiquitously distributed in blastulas, but Hwa protein is located in a few blastomeres in the prospective dorsal side at 2.75 hpf (Yan et al., 2018). Zebrafish *Mhwa* mutants are severely ventralized (Yan et al., 2018), which are similar to the most severe phenotype (Class I) in β -catenin2 deficient *ichabod* mutants (Kelly et al., 2000). The zebrafish T-box transcription factor Eomesodermin (Eomesa) is maternally expressed with a vegetal-to-animal gradient distribution of transcripts during cleavage period and around MBT stages (Bruce et al., 2003). We

previously demonstrate that zygotic expression of zebrafish *ndr1* and *ndr2* also requires Eomesa, in particular in ventral and lateral blastodermal margins, which is then assumed to be a zebrafish functional counterpart of frog VegT (Xu P. et al., 2014). It remains genetically unverified whether VegT/Eomesa and Hwa/ β -catenin signaling are essential maternal factors for zygotic *nodal* genes expression in vertebrate embryos, and if they are, it needs to be investigated whether they differentially contribute to initiation, range and level of zygotic *nodal* genes expression.

Nodal proteins bind to specific receptors on the cytoplasm membrane, which recruit and phosphorylate the intracellular effectors Smad2 and Smad3 (Tian and Meng, 2006; Shen, 2007). The activated Smad2/3 (p-Smad2/3) bind to Smad4 and the formed complexes translocate into the nucleus to activate, with help of FoxH1 or/and other transcription factors, target genes expression. Studies in model animals have disclosed that *nodal* genes themselves contain Nodal-responsive elements (Adachi et al., 1999; Norris and Robertson, 1999; Osada et al., 2000; Fan et al., 2007; Liu et al., 2011), implying that Nodal signaling reinforces itself *via* positive feedback regulation. On the other hand, as diffusible proteins (Jones et al., 1996; Chen and Schier, 2002; Schier, 2009; Muller et al., 2012; Muller et al., 2013), Nodal proteins produced in one area are able to transduce the signal to neighboring areas that previously lack *nodal* transcripts to initiate *nodal* gene expression for self-propagation or relay (Meno et al., 1999; Hyde and Old, 2000; Brennan et al., 2001; Chen and Schier, 2001; Dougan et al., 2003; Williams et al., 2004; Muller et al., 2012; Xu P.-F. et al., 2014). However, it is unclear how much autoregulation of Nodal signaling adds to Nodal activity during vertebrate mesendoderm induction.

In this study, we systematically investigated spatiotemporal regulation of zygotic *ndr1* and *ndr2* expression during mesendoderm induction. We show that maternal Eomesa, maternal Hwa-activated β -catenin signaling, and Nodal positive self-regulation, are required, but to different degrees, for correct spatiotemporal expression of *ndr1* and *ndr2*.

MATERIALS AND METHODS

Zebrafish Strains and Embryo Incubation

The zebrafish Tuebingen strain was used as wildtype fish and for generating mutants. The *eomesa*^{tsu007} mutant line that carries a 353-bp deletion was generated by the CRISPR-Cas9 system with a gRNA (5'-ggcggaaagtgggtgacctgcgg-3') targeting the second exon of *eomesa* (Figure 1A). For genotyping the *eomesa*^{tsu007} mutant allele, the upper primer (5'-CTCAGCTCGATGCCCATTC-3') and the lower primer (5'-ATACAGTCTTTGTCTCGAGATG-3') were used for PCR. Like the previously reported *eomesa*^{fh105} mutant line (Du et al., 2012), zygotic *eomesa*^{tsu007} (*Zeomesa*^{tsu007}) homozygous embryos were able to grow up to adulthood with loss of the dorsal fin (Figure 1A). The *hwa*^{tsu01sm} mutant line was used and its genotyping was described before (Yan et al., 2018). The *eomesa*^{tsu007/+}; *hwa*^{tsu01sm/+} double heterozygotes were obtained by crossing *eomesa*^{tsu007/+} female to *hwa*^{tsu01sm/+} male. Then, *Zeomesa*^{tsu007/tsu007}; *Zhwa*^{tsu01sm/tsu01sm} double homozygous fish (i.e., *Zeomesa*;

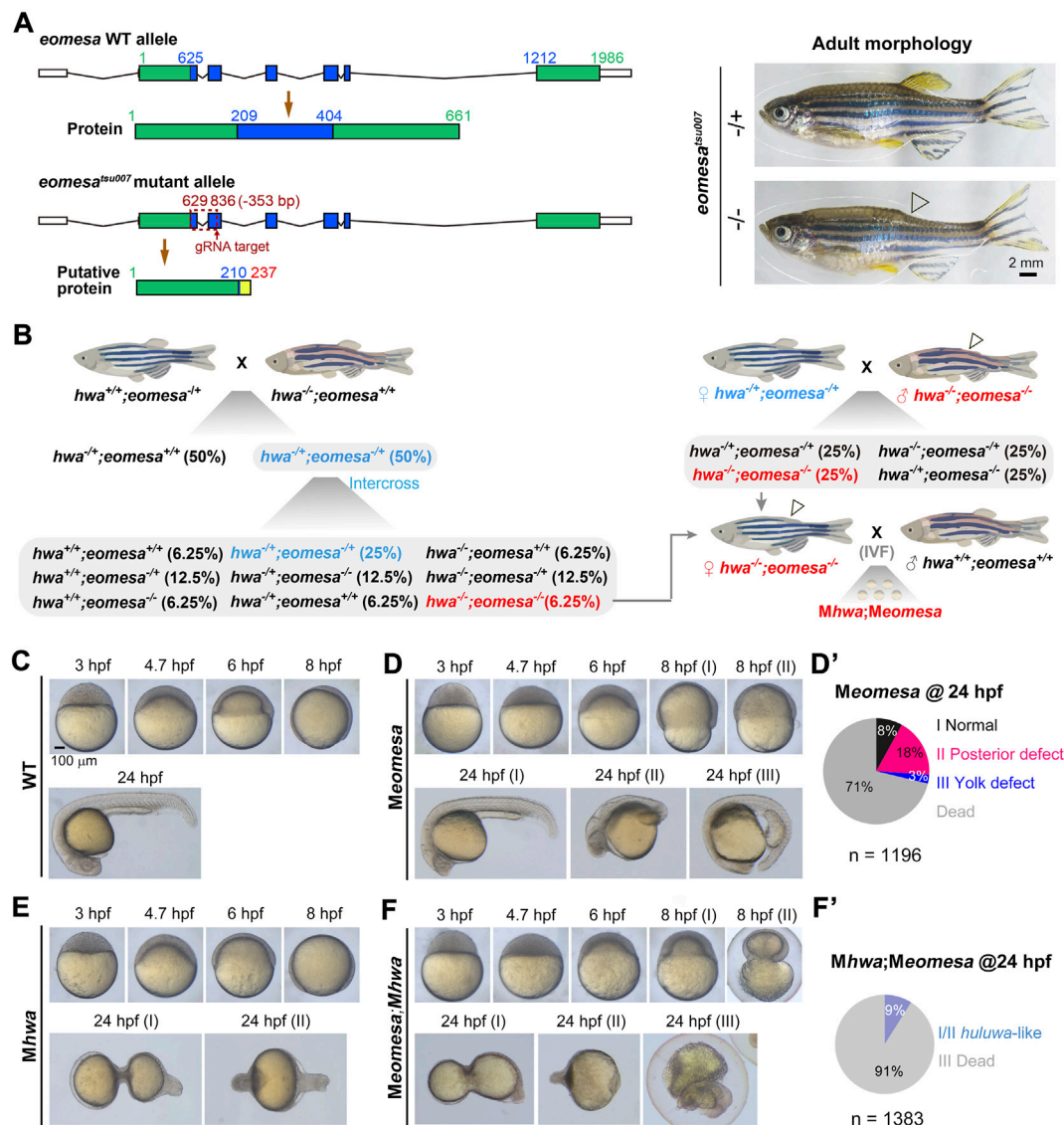


FIGURE 1 | Phenotypes of different mutants at various stages. **(A)** Generation of *eomesa*^{tsu007} mutant allele. Left: genomic structures and putative coding products of *eomesa* WT allele and *tsu007* allele. The exons were colored and positions of nucleotides and amino acids were indicated. The mutant allele carries a 353-bp deletion. Right: morphology of *eomesa*^{+/tsu007} (heterozygote) and *eomesa*^{tsu007/tsu007} (zygotic mutant) adults. Note that the posterior dorsal fin (indicated by an hollow arrowhead) is absent in mutant adult. **(B)** Scheme of generation of *Mhwa*; *Meomesa* double mutants. Zygotic genotypes were indicated. *Zhwa*^{-/-}; *Zeomesa*^{-/-} homozygous female adults could not ovulate naturally, and eggs squeezed from these fish were used for *in vitro* fertilization (IVF) using sperms squeezed from wildtype males (*Zhwa*^{+/+}; *Zeomesa*^{+/+}). **(C)** Wildtype (WT) embryos at indicated stages. **(D,D')** *Meomesa* mutants. Mutant embryos exhibited variable phenotypes at 8 hpf and 24 hpf, and the ratios of 24-hpf mutants categorized into different classes (I-III), which were derived from several homozygous females, were shown in **(D')**. **(E)** *Mhwa* mutants at indicated stages. **(F,F')** *Meomesa*; *Mhwa* double mutants. The ratios of embryos with different phenotypes at 24 hpf were shown in **(F')**. Embryos were laterally positioned when the dorsal or tail was recognizable. The scale bar in **(C)** was also applied to **(D-F)**.

Zhwa double homozygotes) were obtained by intercrossing the double heterozygotes (Figure 1B). Like *Zeomesa* mutant female that were unable to naturally ovulate (Du et al., 2012; Xu P. et al., 2014), *Zeomesa*; *Zhwa* double homozygous female were unable to naturally ovulate and *in vitro* fertilization using their squeezed eggs and wildtype male-derived sperms were performed to obtain maternal double mutant (*Meomesa*; *Mhwa*) embryos (Figure 1B).

Embryos were maintained in Holtfreter's water at 28.5°C. Developmental stages of WT embryos were determined as

described before (Kimmel et al., 1995) while those of mutants were indirectly judged by developmental time matching to WT embryos in the same conditions. Embryo treatment with SB431542 (SB) were performed as described before (Sun et al., 2006). Briefly, One-cell stage embryos of different mutant or WT lines were incubated in Holtfreter's water with addition of freshly made SB to a final concentration of 50 μM in a dish and then harvested for observation or assays at desired stages. All experiments were approved by Tsinghua University Animal Care and Use Committee.

Constructs and Microinjection

The plasmids *pCS2-eomesa-Myc* (Bruce et al., 2003) and *pCS2-hwa-HA* (Yan et al., 2018) were used to *in vitro* synthesize capped mRNAs using mMESSAGE mMACHINE Kit (Ambion). To knock down zebrafish β -catenin2, β -cat2-MO and its control morpholino (cMO) were used as described before (Zhang et al., 2012). mRNA or MO was injected into embryos at the one-cell stage.

Quantitative RT-PCR

Embryos or eggs (15 per sample) were harvested at desired stages, and used to extract total RNA by RNeasy Mini Kit (Qiagen) as previously described (Jia et al., 2009). cDNA was synthesized using the M-MLV reverse transcriptase (Promega) and qRT-PCR was performed with TransStart Top Green qPCR SuperMix (TransGen Biotech) as described (Sun et al., 2018). Expression levels were normalized to the reference gene *ef1a2* unless otherwise stated. The Student's *t*-test (two-tailed, unequal variance) was used to determine *p*-values. Primers and sequences for qRT-PCR analysis were as follows: *ndr1*-F (5'-TTGGATATGCTCCTTGACCC-3'), *ndr1*-R (5'-ACAGATAAGGCAAACACGCAAA-3'); *ndr2*-F (5'-GAAATATCATCACCCAGTCGT-3'), *ndr2*-R (5'-CTCCACCTGCATGTCCTCGT-3'); *tbxta*-F (5'-TTGGAACAACCTTGAGGGTGA-3'), *tbxta*-R (5'-CGGTCACCTTTTCAAAGCGTAT-3'); *sox32*-F (5'-TCTGCCACGGTCTGCTTAC-3'), *sox32*-R (5'-CAGAGAAGGTCCACCCAAAC-3'); *gata2a*-F (5'-CTCCTCAGCGGATCCGCTCCAGC-3'), *gata2a*-R (5'-GGTCGTGGTTGTCTGCGAGTTCGC-3'); *gsc*-F (5'-GAGACGACACCGAACCATT-3'), *gsc*-R (5'-CCTCTGACGACGACCTTTTC-3').

Statistics

The graphs and *t*-test were finished with GraphPad Prism 7. Error bars represent mean \pm SD. *p* values are two-sided. Significance levels were indicated by nonsignificant (ns); *, *p* < 0.05; **, *p* < 0.01; ***, *p* < 0.001.

RESULTS

Loss of Mesendodermal Fates and Nodal Genes Expression in *Meomesa*;*Mhwa* Double Mutants

The *eomesa*^{*tsu007*} mutant allele harbors a 353-bp deletion between the first and the second exon, resulting in a premature stop codon upstream of the T-box coding region (Figure 1A). Maternal *eomesa* mutants (*Meomesa*^{*tsu007*}) showed delayed epibolic process; the majority of *Meomesa*^{*tsu007*} mutants died before 24 hpf and survivors at 24 hpf had a normal head with thin posterior trunk (posterior defect) or had thin anterior trunk with a bulged yolk extension (yolk defect) (Figures 1C–D'). These defects are similar to those observed in *Meomesa*^{*fh105*} mutants (Du et al., 2012).

Using *eomesa*^{*tsu007*} and *hwa*^{*tsu01sm*} lines (Yan et al., 2018), we managed to obtain *eomesa*;*hwa* double homozygotes (*Zeomesa*; *Zhwa*) female fish, which were fertile and used to produce *Meomesa*;*Mhwa* embryos by *in vitro* fertilization using sperms squeezed from WT males. Generally, the *Meomesa*;*Mhwa* double mutants exhibited more severe phenotype than either of single

mutants (Figures 1D–F). An average of 91% maternal double mutant embryos were arrested and deformed during gastrulation and the remaining embryos at 24 hpf had a degenerating tail-like structure with missing of other tissues such as head and anterior trunk (Figures 1F, F'), indicating cooperative roles of maternal *eomesa* and *hwa* in embryonic survival.

Then, we examined expression patterns of the endodermal marker *sox32*, the mesodermal marker *tbxta* (previously named *ntl*) and the epidermal marker *gata2a* in the single and double mutants at 4.7 hpf (30% epiboly stage) and 6 hpf (shield stage) by whole mount *in situ* hybridization (WISH) (Figure 2A). Compared to WT embryos, *sox32* expression in either of single mutants was weaker with some missing domains in the blastodermal margin, whereas it was completely abolished in *Meomesa*;*Mhwa* double mutants. *Meomesa* mutants showed missing of *tbxta* expression in some portions of the margin, which is consistent with the pattern observed in *Meomesa*^{*fh105*} embryos (Xu P. et al., 2014), and *Mhwa* mutants appeared to express *tbxta* in the whole margin; in contrast, 73% of *Meomesa*;*Mhwa* double mutants lacked *tbxta* expression and the remaining proportion had a few small *tbxta*-expressing patches that might be caused by evoked genetic compensation through unknown mechanisms. The expression domain of *gata2a* was dorsally expanded in either of single mutants but further expanded throughout the blastoderm in the double mutants. qRT-PCR analysis using specific primers revealed a drastic decrease of *sox32* and *tbxta* expression levels with a concomitant increase of *gata2a* levels in the double mutants (Figure 2B). These results indicate that maternal *eomesa* and *hwa* are two essential genes for mesendoderm induction and the whole blastoderm with their simultaneous loss may acquire the *epidermis* fate.

Given that Nodal signaling is critical for mesendoderm induction, we wondered how *ndr1* and *ndr2* expression were altered in *Meomesa*;*Mhwa* double mutants. WISH results showed that either *ndr1* or *ndr2* expression was undetectable in the double mutants at 4.3 hpf and 4.7 hpf while detected in either of the single mutants (Figure 2C). qRT-PCR analyses using embryo pools disclosed that, compared to those in WT embryos, *ndr1* and *ndr2* levels were decreased significantly in *Meomesa* mutant embryos and further dropped in *Meomesa*;*Mhwa* double mutants whereas their expression levels were not changed significantly in *Mhwa* embryos (Figure 2D). These results indicate that *ndr1* and *ndr2* expression is initiated in the absence of either maternal *eomesa* or *hwa* but fail to initiate in the absence of both maternal factors.

eomesa or *hwa* Overexpression Distinctly Activates *ndr1* and *ndr2* Expression in *Meomesa*;*Mhwa* Double Mutants

Next, we tested the capability of exogenous *eomesa* and *hwa* to induce *ndr1* and *ndr2* in the absence of both endogenous *Eomesa* and *Hwa*. We injected *myc-eomesa*, *hwa* or both mRNAs into *Meomesa*;*Mhwa* double mutant embryos at the one-cell stage. Morphological observation at 6 hpf indicated that *eomesa* but not *hwa* overexpression could largely rescue the *Meomesa*;*Mhwa* phenotype of slow epiboly, and co-overexpression of *eomesa* and *hwa* could restore the embryonic shield (Figure 3A). The injected embryos were then examined for *ndr1* and *ndr2* expression at 4.3 hpf

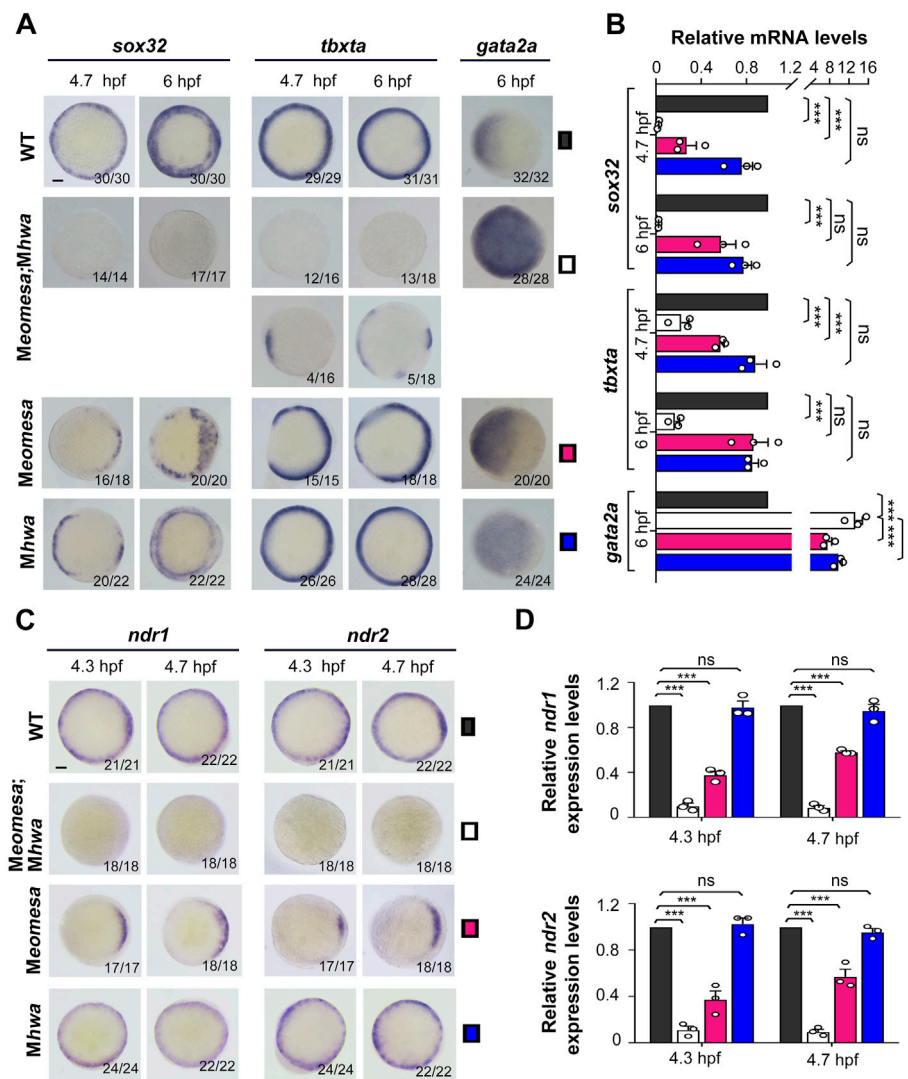


FIGURE 2 | Expression patterns of mesendodermal markers and *nodal* genes in WT and mutant embryos. The expression of the endodermal marker *sox32*, the mesodermal marker *tbxta* and the epidermal marker *gata2a* as well as *ndr1* and *ndr2* was examined by WISH (A,C) or qRT-PCR (B,D) at indicated stages. Embryos in (A,C) were shown in animal-pole view with dorsal to the right if the dorsal was recognizable. The ratio of embryos with the representative pattern was indicated at the right bottom. Note that the majority of *Meomesa;Mhwa* embryos completely lacked *tbxta* expression while the other had some *tbxta* expression. Scale bars: 100 μ m. For RT-PCR analysis, 15 embryos were pooled for each assay, and the expression level was normalized to that of *ef14g2a* in WT embryos at the same stage. Error bars indicated S.D. based on three biological replicates (indicated by small circles). Color keys for embryo types were shown in (A,C). Statistically significant levels: ns, nonsignificant; **, $p < 0.01$; ***, $p < 0.001$.

and 4.7 hpf by WISH. Results disclosed that *myc-eomesa* overexpression induced *ndr1* and *ndr2* expression in the whole blastodermal margin, *hwa* overexpression activated their expression only in one side of the blastoderm (presumably dorsal side), and co-overexpression induced their expression at higher levels (Figure 3B). The induction of *ndr1* and *ndr2* by *hwa* mRNA was abolished when β -catenin was knocked down with an antisense morpholino, which corroborates that *hwa* mainly exerts its effect through activation of β -catenin signaling (Yan et al., 2018). Besides, *hwa* showed a stronger induction activity for *ndr1* than for *ndr2* while *eomesa* had a stronger induction activity for *ndr2* than for *ndr1*. These observations were confirmed by qRT-PCR data (Figure 3C). These results imply that

either *Eomesa* or *Hwa* is sufficient to activate *nodal* genes expression, however, the former may be a more general activator while the latter may act as a regional activator.

We then investigated mesendoderm induction capacity of *eomesa* and *hwa* in maternal double mutants. We found that overexpression of *eomesa* or *hwa* alone or together in *Meomesa;Mhwa* embryos could induce expression of *sox32*, *gsc* and *tbxta* but reduce *gata2* expression as examined by WISH and qRT-PCR (Figures 3D,E). Notably, overexpression effect of *hwa* was eliminated (on *sox32*, *gsc* and *tbxta*) or reduced (on *tbxta* and *gata2a*) when β -catenin2 was knocked down at the same time, which confirmed dependence of *hwa* function on β -catenin2 (Yan et al., 2018). Besides, compared to

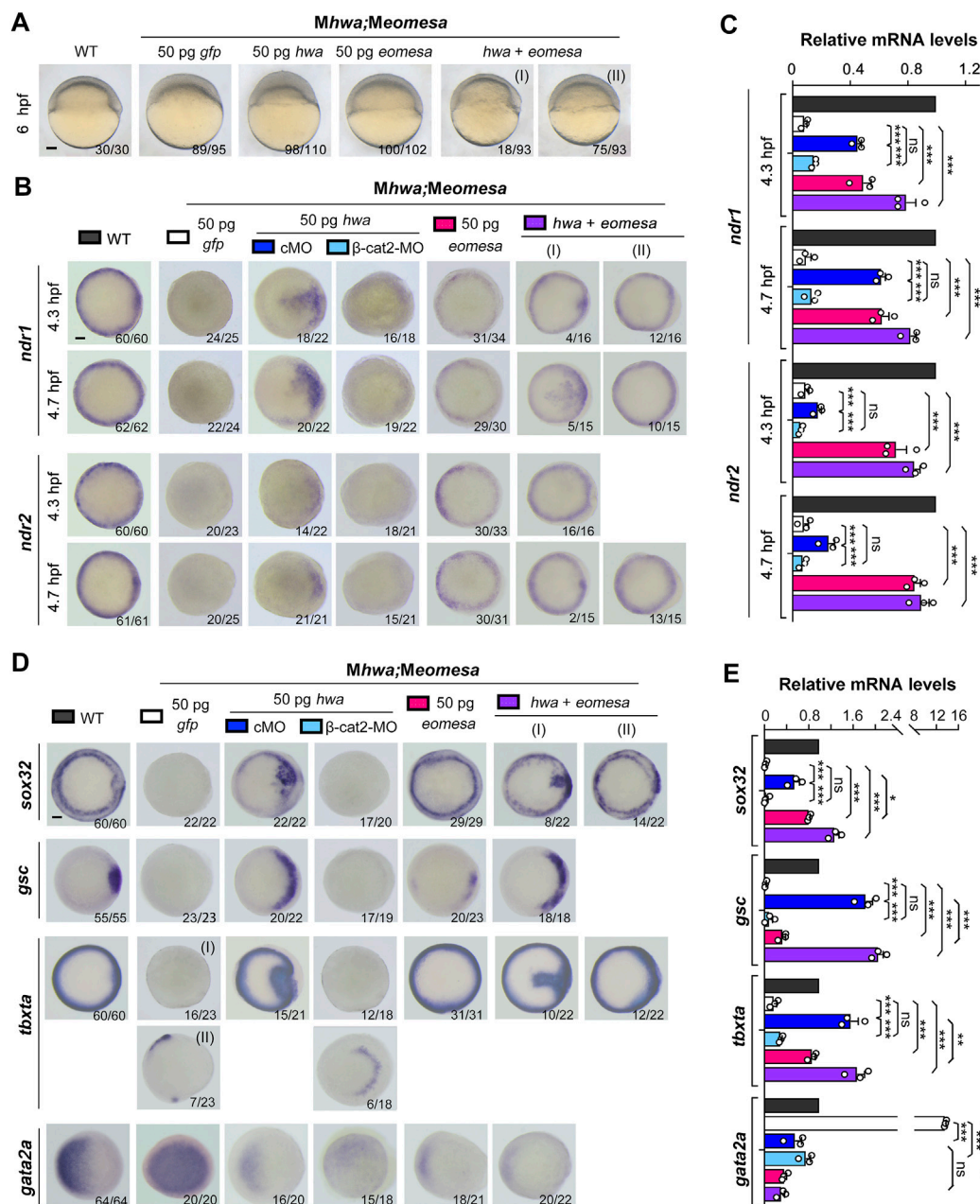


FIGURE 3 | Induction of *nodal* genes and mesendodermal markers in *Meomesa;Mhwa* mutants by ectopic *hwa* or/and *eomesa*. One-cell stage mutant embryos were injected with corresponding mRNA or/and MO and observed for morphology at 6 hpf (A) or harvested at indicated stages for detection of selected genes by WISH (B,D) or by RT-PCR analysis (C,E). Embryos were positioned laterally (A) or in animal-pole view (B,D) with dorsal to the right if the dorsal side was perceptible. The ratio of embryos with the representative pattern was indicated in the right bottom. Scale bars: 100 μ m. Injection doses of mRNA or MO: *hwa* and *myc-eomesa*, 50 pg/embryo; *cMO* (as control MO) and β -cat2-MO, 20 ng/embryo. qRT-PCR analysis was performed using 15 embryos per sample, and the expression level was normalized to that of *elf4g2a* in WT embryos at the same stage. Error bars indicated S.D. based on three biological replicates (indicated by small circles). Color keys for embryo types and treatments were shown in (A,B,D). Statistically significant level: ns, nonsignificant; *, $p < 0.05$; **, $p < 0.01$; ***, $p < 0.001$.

hwa, ectopic *eomesa* exhibited a stronger inductive effect on *sox32* and *tbxta* but weaker effect on the dorsal mesodermal marker *gsc*, supporting the idea that *eomesa* plays a more general role in mesendoderm induction.

We extended our observation to morphological changes in WT, *Mhwa*, *Meomesa*, or *Meomesa;Mhwa* embryos at 24 hpf after

overexpression of *eomesa*, *hwa* or together. Generally, *hwa* overexpression in WT embryos led to strong embryonic dorsalization with missing posterior structures as reported before (Yan et al., 2018), whereas *eomesa* overexpression caused relatively weak dorsalization with thinner posterior structures (Figure 4A). Notably, 90.6% ($n = 96$) of *Mhwa* mutants, which lack the head and

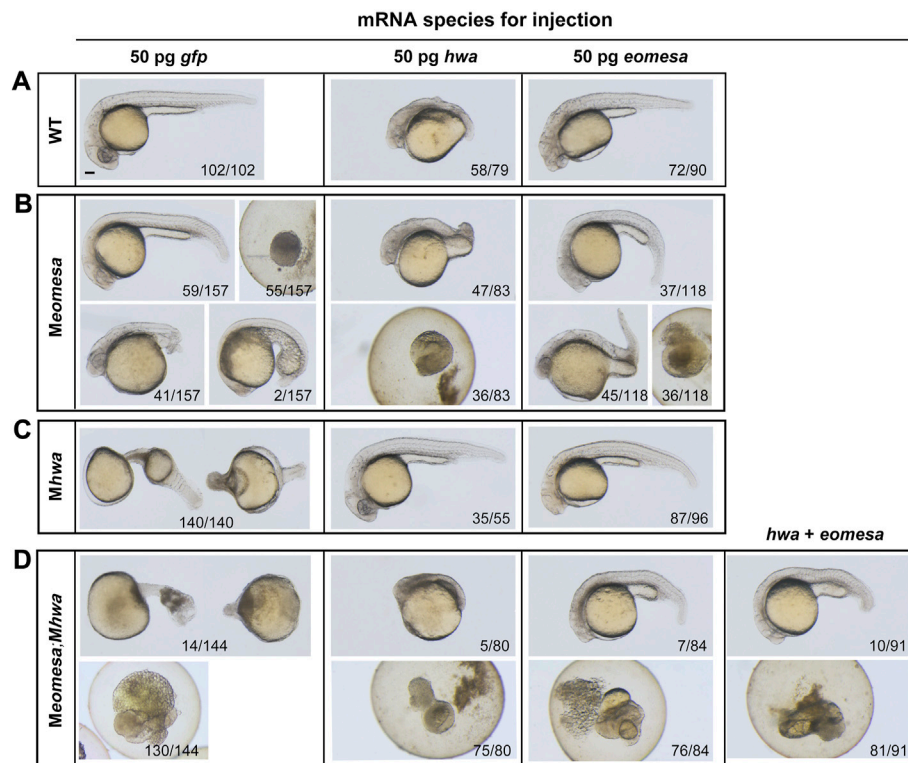


FIGURE 4 | Overexpression effect of *eomesa* and *hwa* in WT and different types of mutant embryos on morphological changes at 24 hpf. **(A–D)** Morphology of WT or mutants at 24 hpf under different mRNAs injection. One-cell stage WT or mutant embryos were injected with corresponding mRNA and observed for morphology at 24 hpf. Embryos were positioned laterally with the head to the left. The ratio of embryos with the representative pattern was indicated at bottom. Injection doses: *hwa* and *myc-eomesa*, 50 pg/embryo. Scale bars: 100 μ m.

anterior trunk structures (Yan et al., 2018), were able to form the head and the whole trunk following *eomesa* overexpression (**Figure 4C**), while *hwa* overexpression in *Meomesa* mutants still caused strong dorsalized phenotype (**Figure 4B**). As described above, most of *Meomesa*; *Mhwa* double mutants died before 24 hpf and the survivors all had a degenerating tail-like structure without a head; however, overexpression of *eomesa* or *hwa* alone or together appeared unable to evidently reduce the mortality (**Figure 4D**). Nevertheless, *eomesa* overexpression alone or co-overexpression with *hwa* allowed 8–11% of embryos to form the head and the trunk, whereas *hwa* overexpression alone allowed only 6.3% of embryos to form an abnormal head and anterior trunk with missing of posterior trunk structures (**Figure 4D**). Although the above overexpression effects should be investigated further by titrating dosages of ectopic mRNA species, our observations support an idea that the role of *eomesa* in development of ventrolateral mesendoderm-derived tissues may not be replaced by *hwa*.

Inhibition of Nodal Signaling Impairs Mesendoderm Induction in Mutant Embryos

Previous studies have demonstrated that the TGF β signaling inhibitor SB431542 (SB) or SB505124 can efficiently block Nodal signaling, resulting in loss of mesendodermal tissues in

zebrafish embryos (Sun et al., 2006; Hagos and Dougan, 2007). We set out to look into effect of Nodal signaling inhibition on mesendodermal induction in *Meomesa*, *Mhwa* or *Meomesa*; *Mhwa* mutant embryos. One-cell stage embryos of different mutant or WT lines were incubated in the presence of 50 μ M SB until harvested for observation or assays. As shown before (Sun et al., 2006), SB treatment caused loss of the embryonic shield at the shield stage (6 hpf) and most mesendodermal tissues in WT embryos at 24 hpf (**Figure 5A**). SB-treated *Mhwa* or *Meomesa* mutant embryos at 24 hpf also showed more severe defects compared to the untreated control mutants (**Figure 5A**). The complete loss of the Nodal target genes *lefty1* and *lefty2* in SB-treated WT embryos confirmed the effectiveness of SB treatment (**Figure 5B**). Then, we examined expression of *sox32* and *tbxta* at 4.7 hpf and 6 hpf by WISH and qRT-PCR analysis (**Figures 5C,D**). WISH results showed that *sox32* and *tbxta* expression became very weak at 4.7 hpf and largely recovered at 6 hpf in SB-treated WT and *Mhwa* embryos; in contrast, their expression appeared undetectable at both stages in SB-treated *Meomesa* embryos (**Figure 5C**). qRT-PCR results also confirmed that SB treatment significantly inhibited *sox32* and *tbxta* expression in WT and *Mhwa* embryos but caused loss of *sox32* and *tbxta* expression in *Meomesa* embryos (**Figure 5D**). Taken together, these results suggest that Nodal signaling may contribute to

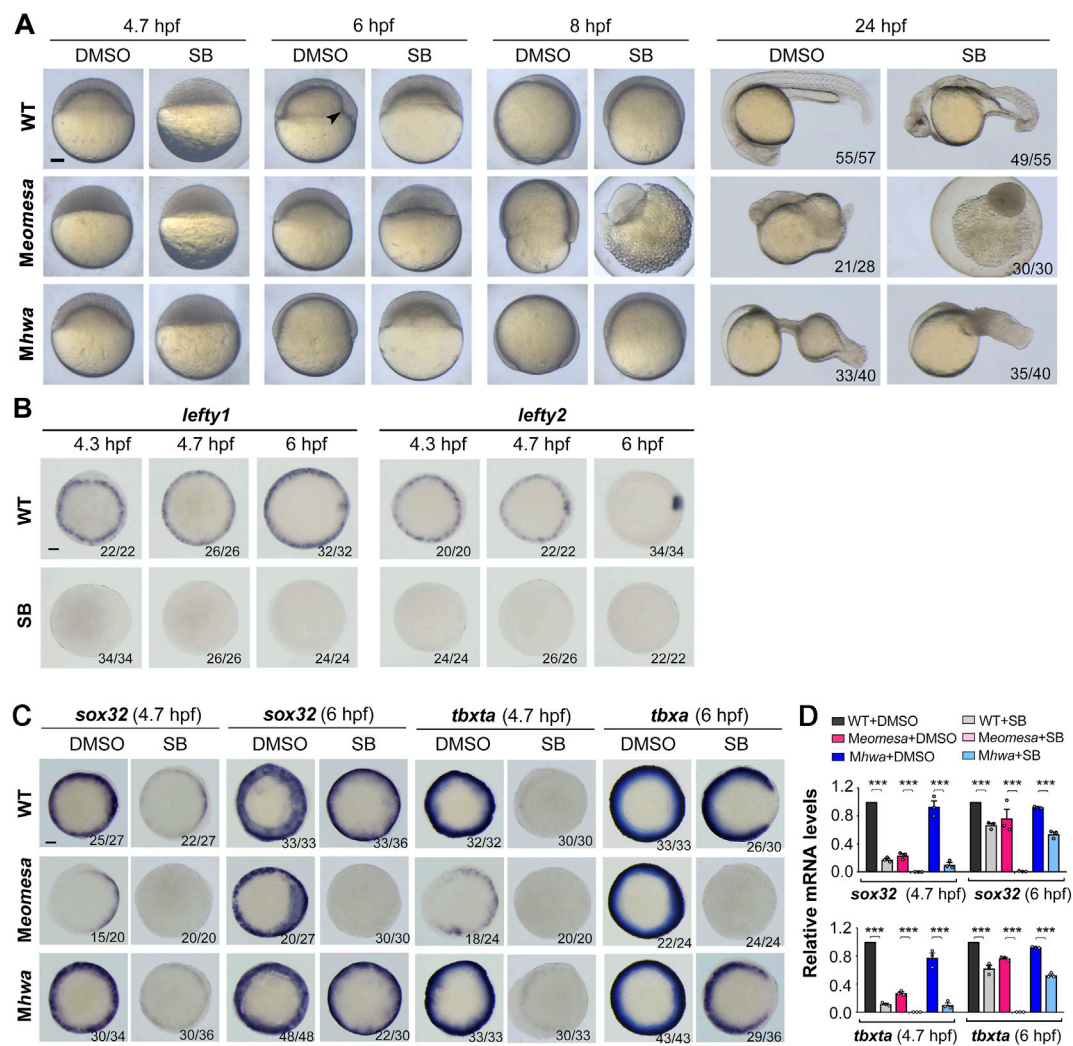


FIGURE 5 | Responses of *Meomesa* and *Mhwa* mutants to Nodal signaling inhibition. One-cell stage embryos (10 min postfertilization) were incubated in Holtfreter's water with 1% DMSO (control) or 50 μ M SB431542 (SB, the Nodal signaling inhibitor), and harvested at 24 hpf for morphological observation (**A**) or for detection of marker gene expression by WISH (**B,C**) or qRT-PCR analysis (**D**) at indicated stages. Note that inhibition of Nodal signaling aggravated mesendodermal defects in both *Meomesa* and *Mhwa* mutants (**A**). Embryos were positioned laterally (**A**) or in animal-pole view with dorsal to the right (**B,C**) if the dorsal or tail was perceptible. The embryonic shield in WT embryo at the shield stage was indicated by an arrowhead. Scale bars, 100 μ m. The ratio of embryos with the representative pattern was indicated in the right bottom (**B,C**). qRT-PCR analysis was performed using 15 embryos per sample, and the expression level was normalized to that of *efl4g2a* in WT embryos at the same stage. Error bars indicated S.D. based on three biological replicates (indicated by small circles). Statistically significant level: ***, $p < 0.001$.

mesendoderm induction at variable levels in different genetic backgrounds.

Maternal *eomesa*, Maternal *hwa* and Nodal Autoregulation Contribute to *ndr1* Expression

Based on the above data, we hypothesize that the mesendodermal fate in the zebrafish embryo is induced via Ndr1 and Ndr2 by three factors, i.e., maternal *eomesa*, maternal *hwa*-activated β -catenin signaling and Nodal autoregulation. We assume that zygotic *ndr1* and *ndr2* expression in *Meomesa*

mutants depends on maternal *hwa* and Nodal autoregulation while their expression in *Mhwa* mutants relies on maternal *eomesa* and Nodal autoregulation. To assess contributions of individual factors, we examined *ndr1* and *ndr2* expression patterns by WISH as well as their total levels by qRT-PCR analysis in WT, *Meomesa* and *Mhwa* embryos from 3.7 hpf to 6 hpf without or with SB treatment (Figures 6, 7).

We first investigated *ndr1* expression in detail. In SB-treated WT embryos, the expression pattern of *ndr1* was unaltered as indicated by WISH (Figure 6A), but its expression level decreased from 3.7 hpf to 6 hpf as examined by qRT-PCR (Figure 6B), which suggest a role of

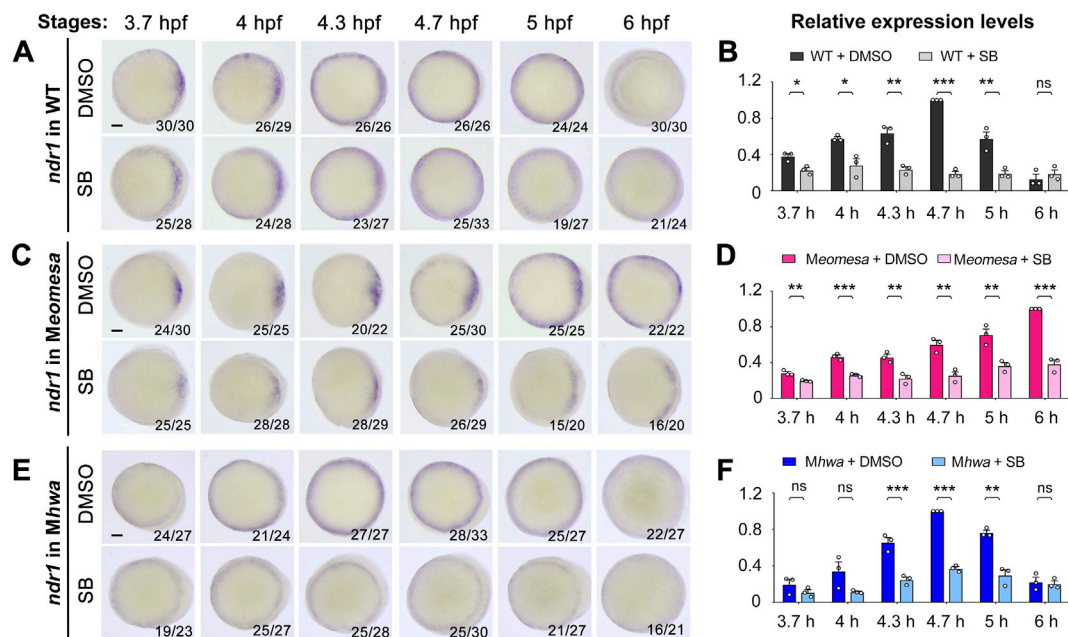


FIGURE 6 | Effect of Nodal signaling inhibition on *ndr1* expression in WT and mutant embryos. WT, *Meomesa* or *Mhwa* embryos at the one-cell stage were incubated in Holfreter's water with 1% DMSO (control) or 50 μ M SB431542 (SB) and harvested at indicated stages for detection of *ndr1* expression by WISH (A,C,E) or qRT-PCR analysis (B,D,F). Embryos (A,C,E) were positioned in animal-pole view with dorsal to the right if the dorsal side was distinguishable. The ratio of embryos with the representative pattern was indicated in the right bottom. Scale bars, 100 μ m. qRT-PCR analysis was performed using 15 embryos per sample. The expression level at 3.7, 4, 4.3, 5 and 6 hpf in WT or *Mhwa* embryos was normalized to that at 4.7 hpf in WT embryo, while the expression level at different stages in WT or *Meomesa* embryos was normalized to that at 6 hpf in WT embryos. Error bars indicated S.D. based on three biological replicates (indicated by small circles). Statistically significant levels: ns, nonsignificant; *, $p < 0.05$; **, $p < 0.01$; ***, $p < 0.001$.

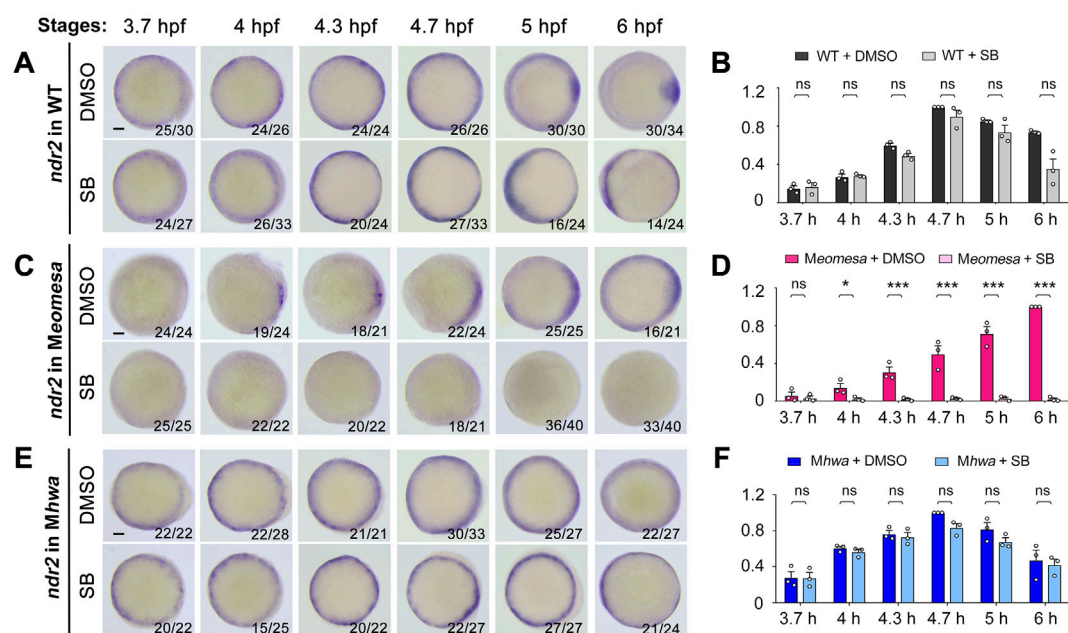


FIGURE 7 | Effect of Nodal signaling inhibition on *ndr2* expression in WT and mutant embryos. Embryo treatment and data presentation were similar to those described in Figure 6 legend.

Nodal autoregulation in maintaining *ndr1* expression. Interestingly, the degree of *ndr1* reduction due to SB treatment gradually increased from 3.7 hpf to 4.7 hpf, implying that Nodal autoregulation contributes to *ndr1* expression more and more during that period.

In *Meomesa* mutants without SB treatment, *ndr1* expression was activated in the dorsal margin with a smaller area than in WT embryos at 3.7 hpf, then propagated ventrally with a slower rate than in WT embryos, and occurred in the whole blastodermal margin at 5 hpf (Figure 6C, upper panel), which were consistent with previous observation (Xu P. et al., 2014). In SB-treated *Meomesa* mutants, in contrast, *ndr1* was still activated in the dorsal margin at a reduced level at 3.7 hpf, its expression domain expanded ventrally but never occupied the whole margin (Figure 6C, lower panel). qRT-PCR results showed that SB-treatment caused a significant reduction (by 31%–62%) of the *ndr1* expression level from 3.7 hpf to 6 hpf (Figure 6D). Thus, in the absence of maternal *eomesa*, maternal *hwa* alone can activate *ndr1* expression in the dorsal margin; and the ventral expansion of *ndr1* expression domain as well as increments of *ndr1* expression heavily depend on positive feedback of Nodal signaling.

In *Mhwa* mutants without SB treatment, *ndr1* expression was not prominent in the dorsal margin but similar to WT in the other marginal areas at 3.7 hpf, and its expression pattern later on was comparable to WT embryos (Figure 6E, upper panel; and also see Figure 2C). In SB-treated *Mhwa* mutants, *ndr1* expression pattern was not obviously altered at all examined stages as detected by WISH (Figure 6E, lower panel); however, qRT-PCR results showed a significant reduction of *ndr1* expression level at 4.3 hpf, 4.7 hpf and 5 hpf while changes at other stages were not significant (Figure 6F). Apparently, maternal *Eomesa* alone is capable of activating *ndr1* expression in the whole blastoderm margin but its enhancement during late blastulation requires the contribution of Nodal autoregulation.

Taken together, these results suggest that maternal *eomesa* can activate *ndr1* expression in the whole blastodermal margin, maternal *hwa* activates *ndr1* only in the dorsal margin, and Nodal autoregulation contributes to enhancement of *ndr1* expression.

ndr2* Expression Mostly Relies on Maternal *eomesa

We similarly investigated implication of maternal *eomesa*, maternal *hwa* and Nodal autoregulation in *ndr2* expression. In SB-treated WT embryos, the *ndr2* expression pattern was not obviously altered from 3.7 hpf to 4.7 hpf (Figure 7A). However, unlike in untreated WT embryos, *ndr2* expression in SB-treated WT embryos at 5 hpf and 6 hpf was not prominently enriched in the dorsal margin, instead it appeared enhanced in the ventrolateral margin, for which we did not find an explanation at the moment. The total expression level of *ndr2* in SB-treated embryos, as revealed by qRT-PCR analysis, was not significantly decreased at all examined stages (Figure 7B). It appears that Nodal autoregulation is less important for *ndr2* expression than for *ndr1* expression in WT embryos.

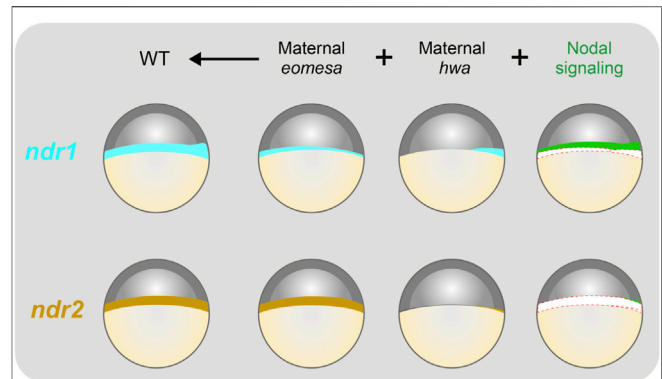


FIGURE 8 | Illustration of contributions of maternal *eomesa*, *hwa*/β-catenin signaling and Nodal signaling to *ndr1* and *ndr2* expression. The expression pattern of *ndr1* and *ndr2* in the late blastula (in lateral view with dorsal to the right and animal pole to the top) is depicted. The overall expression level of *ndr1* or *ndr2* is the sum of contributions from maternal *eomesa* (as seen in *Mhwa* without Nodal signaling), maternal *hwa*/β-catenin signaling (as seen in *Meomesa* without Nodal signaling) and Nodal signaling (autoregulation). In wildtype (WT) embryos, all of the three forces make a significant contribution to *ndr1* expression; however, maternal *eomesa* makes a predominant contribution to *ndr2* expression while maternal *hwa*/β-catenin signaling may contribute a little to *ndr2* expression by activating *ndr1* in the dorsal blastodermal margin and thereof Nodal signaling. In the last column, *ndr1* and *ndr2* levels contributed by *eomesa* and *hwa* were shown as empty to highlight the contribution of Nodal signaling.

In *Meomesa* mutants without SB treatment (Figure 7C, upper panel), *ndr2* expression occurred in the dorsal margin from 4 hpf to 5 hpf and extended to the whole margin at 6 hpf as reported before (Xu P. et al., 2014). In SB-treated *Meomesa* mutants, however, *ndr2* expression was hardly detectable by WISH (Figure 7C, lower panel). qRT-PCR results showed that, compared to untreated *Meomesa* mutants, the *ndr2* expression level in SB-treated *Meomesa* mutants was almost abolished (Figure 7D). This observation implies that, in the absence of maternal *eomesa*, maternal *hwa* might initiate *ndr1* expression in the dorsal margin at low levels and existing *Ndr1* thereof promotes *ndr2* expression through Nodal signaling feedback.

As previously shown in Figure 2D, overall level of *ndr2* expression in *Mhwa* was comparable to that in WT embryos. Surprisingly, we observed that the expression pattern and overall level of *ndr2* in *Mhwa* embryos was unchanged by SB treatment (Figures 7E,F). Taken together, these data strongly suggest that maternal *eomesa* plays a major role in activation and maintenance of *ndr2* expression in WT background.

DISCUSSION

In this study, we delineated the roles of maternal *eomesa*, maternal *Hwa*-activated β-catenin signaling and Nodal autoregulation in spatiotemporal regulation of *ndr1* and *ndr2* expression during early development of zebrafish embryos. As illustrated in Figure 8, maternal *hwa* contributes to *ndr1* expression in the dorsal blastodermal margin, maternal *eomesa* promotes *ndr1* expression throughout the blastodermal margin,

and positive feedback of Nodal signaling enhances *ndr1* expression (**Figure 8**, upper panel). By contrast, *ndr2* expression mostly relies on maternal *eomesa* with minor contribution of maternal *hwa* and Nodal autoregulation during initial activation (**Figure 8**, lower panel). However, when maternal *Eomesa* is absent as the case in *Meomesa*, Nodal signaling feedback, which is most likely derived from existing *Ndr1*, contributes more to *ndr2* expression. Given that *hwa* is maternally expressed only (Yan et al., 2018) and *MZeomesa* and *Meomesa* mutants show the same *ndr1* and *ndr2* expression patterns before the shield stage (Xu P. et al., 2014), it is unlikely that zygotically expressed *eomesa* and *hwa* transcripts participate in activation of zygotic *ndr1* and *ndr2* expression.

The mouse genome contains a single *Nodal* gene. Its expression may start in the inner cell mass of blastocysts, well before the onset of gastrulation (Granier et al., 2011; Papanayotou et al., 2014), and will be gradually restricted to the posteroproximal region of the primitive streak at the onset of gastrulation (Shen, 2007). Based on transgenic reporter assay, early expression of *Nodal* in mouse blastocysts has been suggested to require the pluripotency factor Oct4, Activin/Nodal signaling and β -catenin signaling (Granier et al., 2011; Papanayotou et al., 2014). A previous study demonstrated that the mouse *Nodal* locus contains an upstream *Eomes* binding site and overexpression of zebrafish *eomesa* promotes the expression of endogenous *Nodal* gene with mesendoderm induction in murine embryonic stem cells (Xu P. et al., 2014). Given that *Eomes* protein is expressed in mouse oocytes and early embryos (McConnell et al., 2005), maternal *Eomes* likely participates in early *Nodal* gene activation in the mouse blastocyst, which needs to be explored in the future.

We observed that the expression of either *ndr1* or *ndr2* in *Meomesa*;*Mhwa* double mutant embryos is completely abolished (**Figures 2C,D**), suggesting that maternal *eomesa* and maternal *hwa* are two essential factors for *nodal* genes expression. Consequently, none of the double mutants showed the expression of the endodermal marker *sox32* (**Figures 2A,B**), implying that endoderm induction totally depends on Nodal signaling. However, 25–28% of the double mutants retained *tbxta* expression episodically in the blastodermal margin of the double mutants (**Figure 2A**). It is likely that the mesodermal fate, or *tbxta* expression only, might be induced by other factors or compensatory signaling pathway(s) in the complete absence of Nodal signaling. Our observations are consistent with the fact that *ndr1*;*ndr2* double mutants completely lack endodermal tissues but still have some posterior mesodermal tissues (Feldman et al., 1998).

A puzzling observation is that inhibition of Nodal signaling has a little effect on *ndr2* expression in WT or *Mhwa* embryos (**Figures 7A,B,E,F**), which suggests a minor or negligible role of Nodal autoregulation in *ndr2* expression. However, in *Meomesa* mutant embryos, Nodal autoregulation makes an obvious contribution to *ndr2* expression (**Figures 7C,D**). A possible explanation is that association of *Eomesa* with the general transcription machinery at the *ndr2* locus may mask the

Nodal responsive element(s), and these elements can be bound by the Nodal effectors Smad2/3 only when *Eomesa* is unavailable. The abandonment of Nodal autoregulation for *ndr2* expression might facilitate spatial control of *ndr2* expression domain and function.

Initiation of zygotic *ndr1* and *ndr2* expression occurs after MBT (Rebagliati et al., 1998). However, *Eomesa* protein exists in the cytoplasm of oocytes and fertilized eggs (Bruce et al., 2003) and *hwa* is also maternally expressed (Yan et al., 2018). An interesting question is why maternal *Eomesa* and/or maternal *Hwa* are unable to activate *ndr1* and *ndr2* expression well before MBT. The timing of the zygotic genome activation (ZGA) is proposed to be controlled by the nucleocytoplasmic ratio or the maternal-clock (Tadros and Lipshitz, 2009; Schulz and Harrison, 2019). It remains elusive which ZGA mechanism is adopted by *Eomesa*/*Hwa*-activated *ndr1* and *ndr2* expression.

DATA AVAILABILITY STATEMENT

The original contributions presented in the study are included in the article, further inquiries can be directed to the corresponding author.

ETHICS STATEMENT

The animal study was reviewed and approved by the Tsinghua University Animal Care and Use Committee.

AUTHOR CONTRIBUTIONS

Conceptualization: AM; Methodology: CX, BG; Validation: CX; Formal analysis: CX, AM; Investigation: CX, YL; Resources: CX, WS, LY, and AM; Data curation: CX; Writing—original draft: CX; Writing—review and editing: AM; Visualization: CX; Supervision: AM; Project administration: AM; Funding acquisition: AM.

FUNDING

This work was financially supported by the National Key Research and Development Program of China (#2019YFA0801400 and #2018YFC1003304) and the National Natural Science Foundation of China (31988101 to AM).

ACKNOWLEDGMENTS

We thank Alex Schier for discussions and suggestions. We are also grateful to the members of Meng laboratory for help and discussion and the staff at the Cell Facility in Tsinghua Center of Biomedical Analysis for technical assistance.

REFERENCES

- Adachi, H., Saijoh, Y., Mochida, K., Ohishi, S., Hashiguchi, H., Hirao, A., et al. (1999). Determination of Left/right Asymmetric Expression of Nodal by a Left Side-specific Enhancer with Sequence Similarity to a Lefty-2 Enhancer. *Genes Dev.* 13 (12), 1589–1600. doi:10.1101/gad.13.12.1589
- Agius, E., Oelgeschlager, M., Wessely, O., Kemp, C., and De Robertis, E. M. (2000). Endodermal Nodal-Related Signals and Mesoderm Induction in *Xenopus*. *Development* 127 (6), 1173–1183. doi:10.1242/dev.127.6.1173
- Bellipanni, G., Varga, M., Maegawa, S., Imai, Y., Kelly, C., Myers, A. P., et al. (2006). Essential and Opposing Roles of Zebrafish β -catenins in the Formation of Dorsal Axial Structures and Neurectoderm. *Development* 133 (7), 1299–1309. doi:10.1242/dev.02295
- Brennan, J., Lu, C. C., Norris, D. P., Rodriguez, T. A., Beddington, R. S. P., and Robertson, E. J. (2001). Nodal Signalling in the Epiblast Patterns the Early Mouse Embryo. *Nature* 411 (6840), 965–969. doi:10.1038/35082103
- Bruce, A. E. E., Howley, C., Zhou, Y., Vickers, S. L., Silver, L. M., King, M. L., et al. (2003). The Maternally Expressed Zebrafish T-Box Gene *omesodermin* Regulates Organizer Formation. *Development* 130 (22), 5503–5517. doi:10.1242/dev.00763
- Chen, Y., and Schier, A. F. (2001). The Zebrafish Nodal Signal Squint Functions as a Morphogen. *Nature* 411 (6837), 607–610. doi:10.1038/35079121
- Chen, Y., and Schier, A. F. (2002). Lefty Proteins are Long-Range Inhibitors of Squint-Mediated Nodal Signaling. *Curr. Biol.* 12 (24), 2124–2128. doi:10.1016/s0960-9822(02)01362-3
- Conlon, F. L., Lyons, K. M., Takaes, N., Barth, K. S., Kispert, A., Herrmann, B., et al. (1994). A Primary Requirement for Nodal in the Formation and Maintenance of the Primitive Streak in the Mouse. *Development* 120 (7), 1919–1928. doi:10.1242/dev.120.7.1919
- De Robertis, E. M., and Kuroda, H. (2004). Dorsal-ventral Patterning and Neural Induction in *Xenopus* Embryos. *Annu. Rev. Cell Dev. Biol.* 20, 285–308. doi:10.1146/annurev.cellbio.20.011403.154124
- Dougan, S. T., Warg, R. M., Kane, D. A., Schier, A. F., and Talbot, W. S. (2003). The Role of the Zebrafish Nodal-Related Genes Squint and Cyclopsin Patterning of Mesendoderm. *Development* 130 (9), 1837–1851. doi:10.1242/dev.00400
- Du, S., Draper, B. W., Mione, M., Moens, C. B., and Bruce, A. (2012). Differential Regulation of Epiboly Initiation and Progression by Zebrafish *Eomesodermin*. *A. Dev. Biol.* 362 (1), 11–23. doi:10.1016/j.ydbio.2011.10.036
- Erter, C. E., Solnica-Krezel, L., and Wright, C. V. E. (1998). Zebrafish Nodal-Related 2 Encodes an Early Mesendodermal Inducer Signaling from the Extraembryonic Yolk Syncytial Layer. *Dev. Biol.* 204 (2), 361–372. doi:10.1006/dbio.1998.9097
- Fan, X., Hagos, E. G., Xu, B., Sias, C., Kawakami, K., Burdine, R. D., et al. (2007). Nodal Signals Mediate Interactions between the Extra-embryonic and Embryonic Tissues in Zebrafish. *Dev. Biol.* 310 (2), 363–378. doi:10.1016/j.ydbio.2007.08.008
- Feldman, B., Gates, M. A., Egan, E. S., Dougan, S. T., Rennebeck, G., Sirotkin, H. I., et al. (1998). Zebrafish Organizer Development and Germ-Layer Formation Require Nodal-Related Signals. *Nature* 395 (6698), 181–185. doi:10.1038/26013
- Gore, A. V., and Sampath, K. (2002). Localization of Transcripts of the Zebrafish Morphogen Squint is Dependent on Egg Activation and the Microtubule Cytoskeleton. *Mech. Dev.* 112 (1–2), 153–156. doi:10.1016/s0925-4773(01)00622-0
- Gore, A. V., Maegawa, S., Cheong, A., Gilligan, P. C., Weinberg, E. S., and Sampath, K. (2005). The Zebrafish Dorsal axis is Apparent at the Four-Cell Stage. *Nature* 438 (7070), 1030–1035. doi:10.1038/nature04184
- Granier, C., Gurichenkov, V., Perea-Gomez, A., Camus, A., Ott, S., Papanayotou, C., et al. (2011). Nodal Cis-Regulatory Elements Reveal Epiblast and Primitive Endoderm Heterogeneity in the Peri-Implantation Mouse Embryo. *Dev. Biol.* 349 (2), 350–362. doi:10.1016/j.ydbio.2010.10.036
- Hagos, E. G., and Dougan, S. T. (2007). Time-dependent Patterning of the Mesoderm and Endoderm by Nodal Signals in Zebrafish. *BMC Dev. Biol.* 7, 22. doi:10.1186/1471-213x-7-22
- Hashimoto, H., Rebagliati, M., Ahmad, N., Muraoka, O., Kurokawa, T., Hibi, M., et al. (2004). The Cerberus/Dan-Family Protein Charon is a Negative Regulator of Nodal Signaling during Left-Right Patterning in Zebrafish. *Development* 131 (8), 1741–1753. doi:10.1242/dev.01070
- Hong, S.-K., Jang, M. K., Brown, J. L., McBride, A. A., and Feldman, B. (2011). Embryonic Mesoderm and Endoderm Induction Requires the Actions of Non-embryonic Nodal-Related Ligands and Mxtx2. *Development* 138 (4), 787–795. doi:10.1242/dev.058974
- Hyde, C. E., and Old, R. W. (2000). Regulation of the Early Expression of the *Xenopus* Nodal-Related 1 Gene, *Xnr1*. *Development* 127 (6), 1221–1229. doi:10.1242/dev.127.6.1221
- Jia, S., Wu, D., Xing, C., and Meng, A. (2009). Smad2/3 Activities are Required for Induction and Patterning of the Neuroectoderm in Zebrafish. *Dev. Biol.* 333 (2), 273–284. doi:10.1016/j.ydbio.2009.06.037
- Jones, C. M., Kuehn, M. R., Hogan, B. L., Smith, J. C., and Wright, C. V. (1995). Nodal-related Signals Induce Axial Mesoderm and Dorsalize Mesoderm during Gastrulation. *Development* 121 (11), 3651–3662. doi:10.1242/dev.121.11.3651
- Jones, C. M., Armes, N., and Smith, J. C. (1996). Signalling by TGF- β Family Members: Short-Range Effects of *Xnr-2* and BMP-4 Contrast with the Long-Range Effects of Activin. *Curr. Biol.* 6 (11), 1468–1475. doi:10.1016/s0960-9822(96)00751-8
- Joseph, E. M., and Melton, D. A. (1997). *Xnr4*: A *Xenopus* Nodal-Related Gene Expressed in the Spemann Organizer. *Dev. Biol.* 184 (2), 367–372. doi:10.1006/dbio.1997.8510
- Kelly, C., Chin, A. J., Leatherman, J. L., Kozlowski, D. J., and Weinberg, E. S. (2000). Maternally Controlled (Beta)-catenin-mediated Signaling is Required for Organizer Formation in the Zebrafish. *Development* 127 (18), 3899–3911. doi:10.1242/dev.127.18.3899
- Kimmel, C. B., Ballard, W. W., Kimmel, S. R., Ullmann, B., and Schilling, T. F. (1995). Stages of Embryonic Development of the Zebrafish. *Dev. Dyn.* 203 (3), 253–310. doi:10.1002/aja.1002030302
- Kofron, M., Demel, T., Xanthos, J., Lohr, J., Sun, B., Sive, H., et al. (1999). Mesoderm Induction in *Xenopus* is a Zygotic Event Regulated by Maternal VegT via TGF β Growth Factors. *Development* 126 (24), 5759–5770. doi:10.1242/dev.126.24.5759
- Lim, S., Kumari, P., Gilligan, P., Quach, H. N. B., Mathavan, S., and Sampath, K. (2012). Dorsal Activity of Maternal Squint is Mediated by a Non-coding Function of the RNA. *Development* 139 (16), 2903–2915. doi:10.1242/dev.077081
- Liu, Z., Lin, X., Cai, Z., Zhang, Z., Han, C., Jia, S., et al. (2011). Global Identification of SMAD2 Target Genes Reveals a Role for Multiple Co-regulatory Factors in Zebrafish Early Gastrulas. *J. Biol. Chem.* 286 (32), 28520–28532. doi:10.1074/jbc.m111.236307
- Long, S., Ahmad, N., and Rebagliati, M. (2003). The Zebrafish Nodal-Related Gene *Southpaw* is Required for Visceral and Diencephalic Left-Right Asymmetry. *Development* 130 (11), 2303–2316. doi:10.1242/dev.00436
- Luxardi, G., Marchal, L., Thomé, V., and Kodjabachian, L. (2010). Distinct *Xenopus* Nodal Ligands Sequentially Induce Mesendoderm and Control Gastrulation Movements in Parallel to the Wnt/PCP Pathway. *Development* 137 (3), 417–426. doi:10.1242/dev.039735
- McConnell, J., Petrie, L., Stennard, F., Ryan, K., and Nichols, J. (2005). *Eomesodermin* is Expressed in Mouse Oocytes and Pre-implantation Embryos. *Mol. Reprod. Dev.* 71 (4), 399–404. doi:10.1002/mrd.20318
- Meno, C., Gritsman, K., Ohishi, S., Ohfuji, Y., Heckscher, E., Mochida, K., et al. (1999). Mouse Lefty2 and Zebrafish Antivin are Feedback Inhibitors of Nodal Signaling during Vertebrate Gastrulation. *Mol. Cell* 4 (3), 287–298. doi:10.1016/s1097-2765(00)80331-7
- Müller, P., Rogers, K. W., Jordan, B. M., Lee, J. S., Robson, D., Ramanathan, S., et al. (2012). Differential Diffusivity of Nodal and Lefty Underlies a Reaction-Diffusion Patterning System. *Science* 336 (6082), 721–724. doi:10.1126/science.1221920
- Müller, P., Rogers, K. W., Yu, S. R., Brand, M., and Schier, A. F. (2013). Morphogen Transport. *Development* 140 (8), 1621–1638. doi:10.1242/dev.083519
- Norris, D. P., and Robertson, E. J. (1999). Asymmetric and Node-specific Nodal Expression Patterns are Controlled by Two Distinct Cis-Acting Regulatory Elements. *Genes Dev.* 13 (12), 1575–1588. doi:10.1101/gad.13.12.1575
- Osada, S. I., and Wright, C. V. (1999). *Xenopus* Nodal-Related Signaling is Essential for Mesodermal Patterning during Early Embryogenesis. *Development* 126 (14), 3229–3240. doi:10.1242/dev.126.14.3229

- Osada, S. I., Saijoh, Y., Frisch, A., Yeo, C. Y., Adachi, H., Watanabe, M., et al. (2000). Activin/nodal Responsiveness and Asymmetric Expression of a Xenopus Nodal-Related Gene Converge on a FAST-Regulated Module in Intron 1. *Development* 127 (11), 2503–2514. doi:10.1242/dev.127.11.2503
- Papanayotou, C., Benhaddou, A., Camus, A., Perea-Gomez, A., Jouneau, A., Mezger, V., et al. (2014). A Novel Nodal Enhancer Dependent on Pluripotency Factors and Smad2/3 Signaling Conditions a Regulatory Switch during Epiblast Maturation. *PLoS Biol.* 12 (6), e1001890. doi:10.1371/journal.pbio.1001890
- Rebagliati, M. R., Toyama, R., Fricke, C., Haffter, P., and Dawid, I. B. (1998). Zebrafish Nodal-Related Genes are Implicated in Axial Patterning and Establishing Left-Right Asymmetry. *Dev. Biol.* 199 (2), 261–272. doi:10.1006/dbio.1998.8935
- Rex, M., Hilton, E., and Old, R. (2002). Multiple Interactions between Maternally-Activated Signalling Pathways Control Xenopus Nodal-Related Genes. *Int. J. Dev. Biol.* 46 (2), 217–226.
- Schier, A. F., and Shen, M. M. (2000). Nodal Signalling in Vertebrate Development. *Nature* 403 (6768), 385–389. doi:10.1038/35000126
- Schier, A. F. (2009). Nodal Morphogens. *Cold Spring Harb. Perspect. Biol.* 1 (5), a003459. doi:10.1101/cshperspect.a003459
- Schulz, K. N., and Harrison, M. M. (2019). Mechanisms Regulating Zygotic Genome Activation. *Nat. Rev. Genet.* 20 (4), 221–234. doi:10.1038/s41576-018-0087-x
- Shen, M. M. (2007). Nodal Signaling: Developmental Roles and Regulation. *Development* 134 (6), 1023–1034. doi:10.1242/dev.000166
- Sun, Z., Jin, P., Tian, T., Gu, Y., Chen, Y.-G., and Meng, A. (2006). Activation and Roles of ALK4/ALK7-Mediated Maternal TGF β Signals in Zebrafish Embryo. *Biochem. Biophys. Res. Commun.* 345 (2), 694–703. doi:10.1016/j.bbrc.2006.04.148
- Sun, J., Yan, L., Shen, W., and Meng, A. (2018). Maternal Ybx1 Safeguards Zebrafish Oocyte Maturation and Maternal-To-Zygotic Transition by Repressing Global Translation. *Development* 145 (19), dev166587. doi:10.1242/dev.166587
- Tadros, W., and Lipshitz, H. D. (2009). The Maternal-To-Zygotic Transition: A Play in Two Acts. *Development* 136 (18), 3033–3042. doi:10.1242/dev.033183
- Takahashi, S., Yokota, C., Takano, K., Tanegashima, K., Onuma, Y., Goto, J., et al. (2000). Two Novel Nodal-Related Genes Initiate Early Inductive Events in Xenopus Nieuwkoop Center. *Development* 127 (24), 5319–5329. doi:10.1242/dev.127.24.5319
- Tian, T., and Meng, A. M. (2006). Nodal Signals Pattern Vertebrate Embryos. *Cell. Mol. Life Sci.* 63 (6), 672–685. doi:10.1007/s00018-005-5503-7
- Williams, P. H., Hagemann, A., González-Gaitán, M., and Smith, J. C. (2004). Visualizing Long-Range Movement of the Morphogen Xnr2 in the Xenopus Embryo. *Curr. Biol.* 14 (21), 1916–1923. doi:10.1016/j.cub.2004.10.020
- Xanthos, J. B., Kofron, M., Tao, Q., Schaible, K., Wylie, C., and Heasman, J. (2002). The Roles of Three Signaling Pathways in the Formation and Function of the Spemann Organizer. *Development* 129 (17), 4027–4043. doi:10.1242/dev.129.17.4027
- Xu, P.-F., Houssin, N., Ferri-Lagneau, K. F., Thisse, B., and Thisse, C. (2014a). Construction of a Vertebrate Embryo from Two Opposing Morphogen Gradients. *Science* 344 (6179), 87–89. doi:10.1126/science.1248252
- Xu, P., Zhu, G., Wang, Y., Sun, J., Liu, X., Chen, Y.-G., et al. (2014b). Maternal Eomesodermin Regulates Zygotic Nodal Gene Expression for Mesendoderm Induction in Zebrafish Embryos. *J. Mol. Cell Biol.* 6 (4), 272–285. doi:10.1093/jmcb/mju028
- Yan, L., Chen, J., Zhu, X., Sun, J., Wu, X., Shen, W., et al. (2018). Maternal Huluwa Dictates the Embryonic Body axis through β -catenin in Vertebrates. *Science* 362 (6417), eaat1045. doi:10.1126/science.aat1045
- Zhang, J., Houston, D. W., King, M. L., Payne, C., Wylie, C., and Heasman, J. (1998). The Role of Maternal VegT in Establishing the Primary Germ Layers in Xenopus Embryos. *Cell* 94 (4), 515–524. doi:10.1016/s0092-8674(00)81592-5
- Zhang, M., Zhang, J., Lin, S.-C., and Meng, A. (2012). β -Catenin 1 and β -Catenin 2 Play Similar and Distinct Roles in Left-Right Asymmetric Development of Zebrafish Embryos. *Development* 139 (11), 2009–2019. doi:10.1242/dev.074435
- Zhang, J., Jiang, Z., Liu, X., and Meng, A. (2016). Eph/ephrin Signaling Maintains the Boundary of Dorsal Forerunner Cell Cluster during Morphogenesis of the Zebrafish Embryonic Left-Right Organizer. *Development* 143 (14), 2603–2615. doi:10.1242/dev.132969
- Zhou, X., Sasaki, H., Lowe, L., Hogan, B. L. M., and Kuehn, M. R. (1993). Nodal is a Novel TGF- β -like Gene Expressed in the Mouse Node during Gastrulation. *Nature* 361 (6412), 543–547. doi:10.1038/361543a0
- Zinski, J., Tajer, B., and Mullins, M. C. (2018). TGF- β Family Signaling in Early Vertebrate Development. *Cold Spring Harb. Perspect. Biol.* 10 (6), a033274. doi:10.1101/cshperspect.a033274

Conflict of Interest: The authors declare that the research was conducted in the absence of any commercial or financial relationships that could be construed as a potential conflict of interest.

Publisher's Note: All claims expressed in this article are solely those of the authors and do not necessarily represent those of their affiliated organizations, or those of the publisher, the editors and the reviewers. Any product that may be evaluated in this article, or claim that may be made by its manufacturer, is not guaranteed or endorsed by the publisher.

Copyright © 2022 Xing, Shen, Gong, Li, Yan and Meng. This is an open-access article distributed under the terms of the Creative Commons Attribution License (CC BY). The use, distribution or reproduction in other forums is permitted, provided the original author(s) and the copyright owner(s) are credited and that the original publication in this journal is cited, in accordance with accepted academic practice. No use, distribution or reproduction is permitted which does not comply with these terms.



OPEN ACCESS

EDITED BY

Maria Cecilia Cirio,
Molecular Biology and Neurosciences
(IFIBYNE), Argentina

REVIEWED BY

Sally Ann Moody,
George Washington University,
United States
Gopal Kushawah,
Stowers Institute for Medical Research,
United States

*CORRESPONDENCE

Liangbiao Chen,
lbchen@shou.edu.cn

SPECIALTY SECTION

This article was submitted to
Morphogenesis and Patterning,
a section of the journal
Frontiers in Cell and Developmental
Biology

RECEIVED 16 March 2022

ACCEPTED 13 July 2022

PUBLISHED 08 August 2022

CITATION

Hu R, Xu Y, Han B, Chen Y, Li W, Guan G,
Hu P, Zhou Y, Xu Q and Chen L (2022),
MiR-202-3p determines embryo
viability during mid-blastula transition.
Front. Cell Dev. Biol. 10:897826.
doi: 10.3389/fcell.2022.897826

COPYRIGHT

© 2022 Hu, Xu, Han, Chen, Li, Guan, Hu,
Zhou, Xu and Chen. This is an open-
access article distributed under the
terms of the [Creative Commons
Attribution License \(CC BY\)](https://creativecommons.org/licenses/by/4.0/). The use,
distribution or reproduction in other
forums is permitted, provided the
original author(s) and the copyright
owner(s) are credited and that the
original publication in this journal is
cited, in accordance with accepted
academic practice. No use, distribution
or reproduction is permitted which does
not comply with these terms.

MiR-202-3p determines embryo viability during mid-blastula transition

Ruiqin Hu^{1,2}, Yanna Xu^{1,2}, Bingshe Han^{1,2}, Yi Chen^{1,2},
Wenhao Li^{1,2}, Guijun Guan^{1,2}, Peng Hu^{1,2}, Yan Zhou^{1,2},
Qianghua Xu^{1,2,3} and Liangbiao Chen^{1,2*}

¹International Joint Research Centre for Marine Biosciences (Ministry of Science and Technology), College of Fisheries and Life Science, Shanghai Ocean University, Shanghai, China, ²Key Laboratory of Exploration and Utilization of Aquatic Genetic Resources (Ministry of Education) and International Research Centre for Marine Biosciences, College of Fisheries and Life Science, Shanghai Ocean University, Shanghai, China, ³Key Laboratory of Sustainable Exploitation of Oceanic Fisheries Resources, College of Marine Science, Shanghai Ocean University, Shanghai, China

Developmental growth is an intricate process involving the coordinated regulation of the expression of various genes, and microRNAs (miRNAs) play crucial roles in diverse processes throughout animal development. The mid-blastula transition (MBT) is a developmental milestone when maternal RNAs are cleared and the zygotic genome programmed asynchronous cell division begins to drive embryogenesis. While mechanisms underlying MBT have been intensively revealed, factors regulating cell proliferation at the transition remain largely unknown. We report here a microRNA, miR-202-3p to be a key factor that determines embryonic fate during MBT in zebrafish. A miR-202-3p antagomir specifically terminated embryo development at the mid-blastula stage. *In vivo* deletion of the miR-202 locus recapitulated the fatal phenotypes, which were rescued only by miR-202-3p or its precursor. Transcriptome comparison revealed >250 RNAs including both maternal and zygotic origins were dysregulated at MBT in the miR-202^{-/-} embryos, corresponding with arrays of homeostatic disorders leading to massive apoptosis. A trio of genes: *nfkbiaa*, *perp* and *mgll*, known to be intimately involved with cell proliferation and survival, were identified as direct targets of miR-202-3p. Importantly, over- or under-expression of any of the trio led to developmental delay or termination at the blastula or gastrula stages. Furthermore, *nfkbiaa* and *perp* were shown to inter-regulate each other. Thus, miR-202-3p mediates a regulatory network whose components interact closely during MBT to determine embryonic viability and development.

KEYWORDS

miR-202-3p, mid-blastula transition, NF-κB, apoptosis, zebrafish

Introduction

The Maternal-to-Zygotic Transition (MZT) is a period in which control of embryo development transitions from reliance on maternally supplied factors to newly synthesized zygotic gene products (Schier 2007). During MZT, two interacting processes are undertaken: the maternal RNAs are cleared and the zygotic genome is activated (ZGA) (Newport et al., 1982; Tadros et al., 2009). MZT occurs in all animals but at different timing depending on the animal species. In zebrafish, mid-blastula transition (MBT) phase occurs at the 10th cell cycle, which corresponds to the timing of the MZT at approximately 3.5 h post fertilization (hpf) (Kimmel et al., 1995). It also marks the commencement of asynchronous cell division, apoptosis, appearance of cell cycle checkpoints and cell motility, in contrast with the synchronous cleavage divisions in the earlier cell cycles when development is controlled by maternally stored factors (Langley et al., 2014). Especially, the S-phase lengthens, gap phases appear, and cell cycles become sensitive to DNA damage (Jukam et al., 2017). These changes are prerequisite for acquiring different cell fates and specific morphological forms during development (Siefert et al., 2015).

The factors regulating maternal RNA clearance and ZGA have been intensively investigated (Lee et al., 2014; Zhang et al., 2017). A few conserved zygotic microRNAs, such as miR-430 in zebrafish (Giraldez et al., 2006), miR-427 in frog (Lund et al., 2009), and miR-290 in mouse (Tang et al., 2007), play a role in maternal RNA degradation via post-transcriptional regulation in vertebrates (Svoboda et al., 2010; Yartseva et al., 2015). The dramatic changes that occur at the onset of MBT in aquatic animal species are precisely timed in the embryo. Cellular and molecular mechanisms such as nucleus-cytoplasm ratio (Schulz et al., 2019), chromatin architecture remodelling (Hug et al., 2017), DNA methylation patterns (Liu et al., 2018), concentrations of nuclear histones (Joseph et al., 2017; Pálffy et al., 2017) and cytoplasmic polyadenylation-mediated translational control of maternal mRNAs (Winata et al., 2018; Schulz et al., 2019) have been shown to underlie ZGA. Transcription factors such as *Zelda*, *nanog*, *pou5f3* and *soxB1* are identified to implicate in ZGA (Liang et al., 2008; Lee et al., 2014; Veil et al., 2019). Although much has been learned regarding MZT, it has been estimated that both miR-430s and *Ythdf2* pathways still account for only a portion of total maternal mRNA clearance (Giraldez et al., 2006; Zhao et al., 2017).

MicroRNAs are a class of small non-coding RNAs approximately 22 nucleotides that performs significant role in controlling the messenger RNA (mRNA) stability and translation at cellular levels. MiRNAs play essential roles in a wide variety of biological processes, including cellular differentiation, growth, development and metabolism pathways (Bhattacharya et al., 2017). Dicer is required for mature miRNA biogenesis and loss of Dicer would inhibit production of all Dicer-dependent miRNAs. The MZdicer (maternal and zygotic dicer mutant)

larvae showed retarded growth and died 2 weeks after fertilization, suggesting that miRNA functions are essential for post-embryonic development (Giraldez et al., 2005). The zebrafish miR-430 family is the most abundant miRNA family during early embryogenesis and is the first expressed during MZT (2.75 hpf). Surprisingly, miR-430 duplex rescued most of the MZdicer embryos as observed during the first 24 h that gastrulation defect (Giraldez et al., 2005). Therefore, miR-430 is an essential miRNA during zebrafish development with striking impacts on morphogenesis (Giraldez et al., 2006). Many other microRNAs like miR-30a are also important for zebrafish embryonic development (O'Brien et al., 2014). In mice, disruption of the miR-137 primary transcript results in early embryonic lethality (Crowley et al., 2015). miR-15 and miR-16 are involved in *Xenopus laevis* embryonic development through the regulation of the Wnt and Nodal signaling pathways (Shi et al., 2009). In *C. elegans*, *lin 4* and *let 7* were identified as controllers of the timing of larval development: mutations of these genes resulted in the reiteration of larval cell fates and retarded the final differentiation of subsets of specialized cells (Lee et al., 1993; Reinhart et al., 2000).

The miR-202 locus produces two types of mature microRNAs, miR-202-3p and miR-202-5p, are specific and highly conserved in vertebrates (Dai et al., 2009). MiR-202 functions to maintain spermatogonial stem cells in mouse (Chen et al., 2017; Chen et al., 2021). miR-202-3p controls the proliferation, apoptosis, and synthesis function of human sertoli cells (Yang et al., 2019). The reduction of miR-202-5p expression in medaka (*Oryzias latipes*) resulted in impairments of the early steps of oogenesis/folliculogenesis, leading to dramatically reduced female fecundity (Gay et al., 2018). However, maternal loss of miR-202-5p impaired PGC migration in zebrafish (Jin et al., 2020). Acting as a tumor suppressor, dysregulation of miR-202-3p is found to be associated with numerous cancerous transformations (Zhang et al., 2020; Wang et al., 2021).

In the study of the functions of the miR-202 locus in zebrafish development, we occasionally found that injection of a miR-202-3p antagomir into the fertilized eggs specifically terminates cell proliferation and embryogenesis at approximately 4 hpf, with no embryo progression to the epibolic stages. The blastomere cells stop proliferation but enter apoptosis instead. We then deleted the miR-202 locus from the zebrafish genome and carried out in-depth studies on the developmental consequences of this mutation and the underlying mechanisms of the cellular effects resulting from loss of miR-202-3p. We report here that miR-202-3p is a factor involved in ZGA regulation, in which it forms an inter-regulated network with its target genes in the NFκB and P53 related signaling pathways required for preventing cells entering apoptosis. The miR-202-3p-mediated regulatory network thus links ZGA with cell proliferation and survival during mid-blastula transition.

Material and methods

Fish

Zebrafish (*D. rerio*, AB strain) were maintained at 28.5°C under standard conditions. Embryos were raised and maintained at 28.5°C and staged according to standard morphological criteria (Kimmel et al., 1995). All handling of fishes was carried out in accordance with the guidelines on the care and use of animals for scientific purposes set up by the Institutional Animal Care and Use Committee (IACUC) of the Shanghai Ocean University (SHOU), Shanghai, China. This research was approved by the IACUC of SHOU.

RNA extraction and real time qRT-PCR

Embryos were collected at timed developmental stages. Total RNA was extracted from whole embryos using TRIzol Reagent according to the manufacturer's protocol (Invitrogen). For quantification of miRNAs, miRNA-specific stem-loop RT primers were designed with the software primer 5.0. The isolated RNA was reverse transcribed into cDNA by miRNA-specific stem-loop RT primers and PrimeScript® RT reagent Kit (Takara). qRT-PCR was performed using the miRNA-specific stem-loop RT primers and SYBR Green Master Mix following the manufacturer's protocol (Takara). For quantification of pri-miR-202 and protein coding transcripts, total RNA from the embryos were reverse transcribed using random primers supplied in the PrimeScript® RT kit following the same protocol as above (Takara). All samples were performed in triplicates, and expression level of target genes was calculated with the $2^{-\Delta\Delta CT}$. U6 was used as the internal control. The primers used are listed in [Supplementary Table S5](#).

Microinjection of antagomirs of miR-202

Antagomirs to miR-202-3p, miR-202-5p and the scrambled antagomir (as negative control) were designed and synthesized by GenePharma (China). The sequences are provided in [Supplementary Table S5](#). Fertilized eggs from wild type zebrafish at the one-cell stage were injected with 1 nl of each antagomir (8 μ M) by using a microinjector (Eppendorf). The injected embryos were maintained at 28.5°C for development.

In vivo miR-202 deletion by CRISPR-Cas9 system

Deletion of the miR-202 locus from the zebrafish genome was carried out using the CRISPR-Cas9 system. CRISPR-Cas9 target

sites were designed using an online tool ZiFiT Targeter software (<http://zifit.partners.org/ZiFiT>). Two gRNAs were chosen to delete the miR-202 locus; the primers are listed in [Supplementary Table S5](#). Capped Cas9 mRNA was synthesized *in vitro* by mMESSAGE mMACHINE T7 ULTRA kit (Ambion), and purified using RNeasy Mini Kit (Qiagen). gRNAs were synthesized using MAXIscript T7 kit (Ambion) following the manufacturer's protocol and purified. Approximately 400 pg mRNA encoding Cas9 and 100 pg gRNA were injected into each embryo. The embryos were raised and maintained at 28.5°C.

Screening for F0 miR-202 mutant zebrafish

To screen F0 miR-202 mutant zebrafish, genomic DNA was isolated from embryos produced by crossing microinjected F0 zebrafish with wild type partners. The target region was amplified by PCR using the specific primer pairs that were designed to distinguish wild type and mutated alleles ([Supplementary Figure S1](#), [Supplementary Table S5](#)). The F0 parents who produced the miR-202 mutant embryos were identified. Mutation status of their miR-202 locus was further verified through PCR amplification and sequencing.

Genotype identification of F2 embryos

The embryonic fatality of the homozygous miR-202 mutant rendered unavailable sexually mature miR-202^{-/-} individuals for reproduction. Therefore, investigation of miR-202^{-/-} phenotypes and underlying mechanisms relied on precise genotyping of embryos produced from heterozygous miR-202 parents. Genomic DNA was isolated from a single embryo using the alkaline lysis method: a timed embryo produced by heterozygous parents was submersed in 20 μ l of 50 mM NaOH and heated to 95 °C for 10min. The tube was then vortexed and heated again, and 2 μ l of Tris-HCl (1 M, pH = 8.0) was added to neutralize the solution. The tube was centrifuged and the supernatant was collect for PCR amplification with the proper primer ([Supplementary Figure S1A](#)). In the cases when embryos were taken prior to 10 hpf, the nested PCR was used for genotyping ([Supplementary Figure S1B](#)). The primers are listed in [Supplementary Table S5](#).

miR-202^{-/-} embryo rescue using synthetic agomirs

Agomirs for miR-202-3p, miR-202-5p and pre-miR-202 were chemically synthesized (Sangon Biotech) based on their native sequences ([Supplementary Table S5](#)). Series of

dilutions of each agomirs or mixture or precursor (10 μ M, 20 and 30 μ M) were microinjected into the one-cell fertilized eggs obtained from the miR-202 heterozygous parents with 1 nL using a microinjector (Eppendorf). Developmental status of the injected embryos were observed real-time under a stereomicroscope (Zeiss). Embryos that survived to 12 hpf were picked out, counted, and genotyped.

RNA-seq and analysis

Genomic DNA and total RNA were concurrently isolated from single embryo collected from mating of miR-202^{+/-} parents at 3.5 hpf. After genotyping of the embryos with DNA, the total RNAs from same-genotype embryos, namely miR-202 homozygous, or heterozygous, or wild type embryos were pooled to gain a sufficient amount of total RNA for each genotype for sequencing. RNA-seq was performed by NovoGenes (Tianjin, China). RNA-seq reads were trimmed using Trimmomatic (Bolger et al., 2014) (Ver. 0.33 AVGQUAL:20 TRAILING:20 MINLEN:50). The clean Illumina paired-end reads of each sample were mapped to the annotated zebrafish genome (GRCz10) using HISAT2 aligner (Kim et al., 2015) (Ver. 2.0.4). Cufflinks was used to count the reads for each gene and transformed to FPKM. Differentially expressed genes (DEGs) between the genotypes were determined using the edgeR (Robinson et al., 2010) package developed in R. Compare homo_3.5 h with hete_3.5 h and wt_3.5 h, respectively, for log2 fold change >1 or < -1 and *p*-value <0.05 was defined as differentially expressed genes (DEGs). DEGs related with the maternally inherited mRNAs were identified by adopting the following criteria: 1) if FPKM (wt_0 h \geq homo_3.5 h \geq max (hete_3.5h, wt_3.5 h), the gene was taken to indicate insufficient degradation (ID); 2) if FPKM (homo_3.5 h > max (hete_3.5h, wt_3.5h, wt_0 h), the gene was associated with over-expression (OE); and 3) if FPKM (min (hete_3.5h, wt_3.5 h) \geq homo_3.5 h \geq wt_0 h), the gene was regarded as insufficient expression (IE). Almost no genes were over degraded in miR-202^{-/-} embryos and were thus not considered for GO and KEGG enrichment.

Proteomic analyses of the miR-202 mutant and wild type embryos

The wild type and abnormally developing embryos of miR-202^{+/-} pairs were collected at 4hpf, and the embryos were removed from the egg shell. Three groups of normal WT (A_4hpf) and three groups of abnormal embryo (D_4hpf) samples (each having about 50 embryos) were used to extract protein for proteomic analysis. Proteomic analysis was performed using LC-MS/MS on a QExactive mass

spectrometer with an Easy-nLC system (Thermo Fisher Scientific). The LC-MS/MS data were analyzed using Proteome Discovery (Version 2.2, Thermo Fisher Scientific) with the zebrafish Uniprot database (uniprot-danio + rerio_170221.fasta). To quantify protein, the abundance value was normalized with the median value of the whole protein set and only unique peptides were used. Differential protein screening was performed at criteria of 1.2 and 0.833 fold change (FC).

Whole mount *in situ* hybridization

A digoxigenin (DIG) labelled RNA probe of miR-202-3p (accession number: MIMAT0001864) and a scrambled RNA probe (NC) were synthesized by Exiqon (Denmark). Whole mount *in situ* hybridization (WISH) was performed as previously described (Thisse et al., 2008). Shell-removed embryos were fixed in 4% PFA (paraformaldehyde) at 4°C overnight, dehydrated in methanol and rehydrated by a series of methanol/PBST gradients, and then treated with proteinase K and re-fixed in 4% PFA. Embryos were pre-hybridized with hybridization mixture (HM) at 58°C for 2–4 h and hybridized with DIG-labelled miR-202-3p anti-sense probe or scrambled probe (NC) at 58°C overnight. After hybridization, embryos were washed in a series of saline sodium citrate (SSC) gradients. Subsequently, the embryos were blocked in MAB buffer with 1% blocking solution (Roche) for 3 h at room temperature and incubated in alkaline phosphatase conjugated anti-DIG antibody (1:5,000 diluted in blocking solution, Roche) at 4°C overnight. The embryos were washed four times in PBST for 15 min, and the signal was developed using NBT/BCIP Staining solution. The images were documented with a stereomicroscope (Zeiss) equipped with a digital camera.

In situ hybridization of tissue sections

In situ hybridization on paraffin sections was performed as described previously (Jørgensen et al., 2010). Briefly, ovary tissue or embryos were dissected in 1 \times PBS and fixed in 4% PFA overnight at 4°C. Fixed tissues were embedded in paraffin and sectioned using a paraffin slicer microtome (Leica) at 10- μ m thickness and transferred to special coating glass slides (Leica). Slides were hybridized overnight with 1 μ g/ml digoxigenin-labeled probe at 65°C in HM solution. After washing in SSC buffer, slides were incubated with alkaline phosphatase-coupled anti-digoxigenin antibodies overnight at room temperature. Slides were then dehydrated through ethanol series and xylene (Sigma-Aldrich) then mounted using Entellan (Electron Microscopy Sciences). Images were acquired using a confocal microscope (Zeiss).

Protein translation efficiency assay

F1 heterozygous zebrafish adults were crossed in the appropriate breeding tanks. EGFP mRNA was transcribed *in vitro* as above. The fertilized eggs (one-cell stage) were collected immediately and injected with EGFP mRNA (100 pg) and then cultured at 28.5°C for 3 hours. Embryos were screened by fluorescence analysis with a stereomicroscope (Zeiss). Embryos with bright and weak green fluorescence intensities were selected for genotyping verification.

Cellular ROS detection

F1 heterozygous zebrafish adults were crossed in the appropriate breeding tanks. Fertilized eggs were collected and stored at 28.5°C to allow the embryos to develop for 3 hours. Embryos were then washed with E3 medium (Cold Spring Harbor Protocols 2011, [pdb. rec66449](#), [doi: 10.1101/pdb.rec066449](#) (2011)) and then immediately incubated with a general Oxidative Stress Indicator (CM-H2DCFDA) (Invitrogen) at a final concentration of 3 µM. Embryos were incubated in the dark for 15 min at 28.5°C. At the end of the incubation, the ROS-detection solution was immediately removed and embryos were washed three times with E3. Fluorescence intensity of the embryos was analyzed by stereomicroscope (Zeiss). Embryos with bright and weak green fluorescence were selected for genotyping verification.

SYTOX staining

SYTOX nuclear green stain is impermeable to living cells, but stains nuclei in a syncytium (or otherwise following membrane degradation) ([Goonesinghe et al., 2012](#)). To visualise migration of YSL nuclei relative to the blastoderm margin during epiboly, embryos from heterozygous parents were injected with 1 nl of 0.5 mM Sytox Green fluorescent nucleic acid dye (Invitrogen, United States) into the yolk cell at 3 hpf and then visualised at 4 hpf and 6 hpf under a fluorescence stereomicroscope (Zeiss). Embryos were kept in E3 medium for genotyping verification. Images were captured and processed using a Zeiss AxioCam MR and AxioVision 4.5 software.

Cell adhesion detection

F2 embryos from heterozygous parents were used for immunofluorescence staining. Embryos were fixed overnight in 4% PFA at 4°C, and then were peeled off the egg shells. Embryos were permeabilized in 0.5% Triton-X-100 for 30 min at room temperature. After 1 h blocking in 1% BSA/PBS at room

temperature, embryos were incubated overnight at 4°C with primary antibody anti-ZO-1 at 1:200 (Thermal Fisher Scientific). After three washes, embryos were incubated with secondary antibody at 1:3,000 (Thermal Fisher Scientific) for 2 h at room temperature. TSA-F green fluorescent dye staining (1:100) was used to amplify signals by incubation at room temperature for 30 min in the dark, and then washed with PBS for at least 1 h. DAPI (500 ng/ml) was added to counterstain the nuclei followed by washing with PBS for three times. Photographs were taken using confocal microscopy (Zeiss). Following photography, the embryos were then genotyped individually.

Apoptosis detection

F2 embryos from heterozygous miR-202 parents were used for TUNEL staining. Embryos were fixed in 4% PFA at 4°C overnight, then removed egg shell from embryos. TUNEL staining was performed using a commercially available kit (Thermo Fisher Scientific) by following the manufacturer's instructions. The embryos were stained with FITC-dUTP Labeling Mix and DAPI (500 ng/ml), then were analyzed under a laser confocal microscope (Zeiss). After being photographed, each embryo was genotyped.

Phenotype rescue using shRNAs of miR-202-3p target genes

To validate the function of the miR-202-3p target genes in the embryonic lethal phenotype of miR-202-3p deficiency, shRNAs against the Seven genes (*nfkbiaa*, *perp*, *mgll*, *atp1b1a*, *nfil3-5*, *pleca*, *nfe2l2b*) which were predicted to be miR-202-3p targets and upregulated in the miR-202^{-/-} embryos were designed through the BLOCK-iT™ RNAi Designer (Thermo Fisher Scientific), chemically synthesized (Sangon Biotech) and cloned to pLKO.1 plasmid (Addgene). shRNA plasmid was microinjected into WT embryos together with the miR-202-3p antagomir, in a final concentration of 200 ng/µL and 8 nM, respectively. Then injected embryos were raised and maintained at 28.5 °C and observed for developmental status; rescue rate was calculated for every 2 h. The shRNAs are listed in [Supplementary Table S5](#).

Knockdown and overexpression of miR-202-3p target genes in developing embryos

We manipulated the mRNA contents of miR-202-3p target genes, *nfkbiaa*, *perp* and *mgll* in developing embryos for validating the function of these genes in embryonic development. To down-regulate a gene, a single type or a mix

of the plasmid constructs containing specific shRNA was microinjected into the wild type embryos, in a final concentration of 200 ng/ μ l, and 100 ng/ μ l for each one in the mixture. To increase the mRNA content of a specific gene in developing embryos, mRNA was microinjected into wild type embryos with final concentration of 400 ng/ μ l for a single gene or 200 ng/ μ l for each one in the mixture. Each embryo was injected in 1 nl volume. Embryos after injection were cultured at 28.5°C and observed for developmental status every hour. The shRNA sequences and primers for cDNA amplification are listed in [Supplementary Table S5](#).

Embryo viability statistics

The developmental stages of embryos were examined using a stereomicroscope (Zeiss) by observing the morphological appearance. An embryo was considered to be dead if lysed cells were visible under the microscope. An embryo was considered to be abnormal if development was slower than in the wild type, and developmental termination was registered for an embryo if no morphological progression was observed within a period of 1 hour. Rescue rate is calculated through a two step procedure: 1) counting all live embryos at 12 hpf and genotyping each embryo; 2) calculating the ratio of the living miR-202^{-/-} embryos to the total number of embryos examined. The ratio is regarded as the rescue rate of a reagent because through large scale phenotype and genotype analyses, we had established that no miR-202^{-/-} embryos would survive beyond 12 hpf without rescue.

Target gene validation through dual luciferase assay

Dual luciferase assay was carried out to validate the authenticity of the predicted target genes of miR-202-3p. Native and mutated 3'UTRs of the candidate genes were amplified from zebrafish embryonic cDNA and cloned into the pmirGLO Dual-Luciferase miRNA Target Expression Vector (Promega) and sequenced. HEK293T cells were plated in a 96-well plate and incubated at 37°C for 24 h miR-202-3p agomir (or scrambled agomir) and pmirGLO-3'UTR (or mutated 3' UTR) construct were co-transfected into the HEK293T by using Attractance Transfection Reagent (QIAGEN). The transfected Cells were continuously incubated at 37 °C for 24 h, and luciferase activity was measured using the Dual-Luciferase Reporter Assay System (Promega) following the manufacturer's protocol in a luminometer. Data were first normalized to residual luminescence then to an agomir negative control. The 3'UTRs or mutation sites and primers are shown in [Supplementary Figure S3](#) and [Supplementary Table S5](#).

Imaging

Embryos were treated with 0.02% tricaine (3-amino benzoic acid ethyl ester), mounted in 3% methyl-cellulose, and visualized under a Stereoscopic Microscope (Zeiss).

Statistical analysis

Statistical analysis was conducted using the Student's t-test (two-tailed). All values are shown as mean \pm s.d. $p < 0.05$ were considered statistically significant. One asterisk, two asterisks and three asterisks indicate $p < 0.05$, $p < 0.01$ and $p < 0.001$, respectively.

Results

Inhibition of miR-202-3p but not miR-202-5p terminates embryonic development at mid-blastula stage

To test whether miR-202-3p and miR-202-5p play a role in early embryonic development, we microinjected the antagomirs of miR-202-3p and miR-202-5p respectively into fertilized embryos. Injected embryos developed normally at the initial stages, similar with the control group (injected with a scrambled antagomir) and the wild type embryos. However, starting from 4 hpf, embryos injected with the miR-202-3p antagomir demonstrated developmental stoppage and the blastomere disassociated from 6 hpf to 12hpf ([Figure 1A](#)). Once the threshold amount of miR-202-3p antagomir (8 μ M) was reached, developmental failure occurred in over 90% of the embryos during the blastula stage. In sharp contrast, no developmental abnormality was observed in the embryos injected with the miR-202-5p antagomir or the control antagomir at the same amounts ([Figure 1B](#)). The time course statistics for blastomere cytolysis in injected embryos are shown in [Figure 1C](#), which is based on more than two thousand injected embryos for each antagomir. qRT-PCR was performed to evaluate the efficiency of miRNA knockdown with their respective antagomirs; both miR-202-3p and miR-202-5p antagomirs functioned effectively ([Figure 1D](#)). These results suggested that miR-202-3p might be essential for embryonic development at the mid-blastula stage.

Deletion of miR-202 in zebrafish using CRISPR-Cas9

To ensure that the blastula lethality phenotype that occurred in the miR-202-3p antagomir injected embryos is an authentic function of this miRNA, we targeted the miR-202 locus for

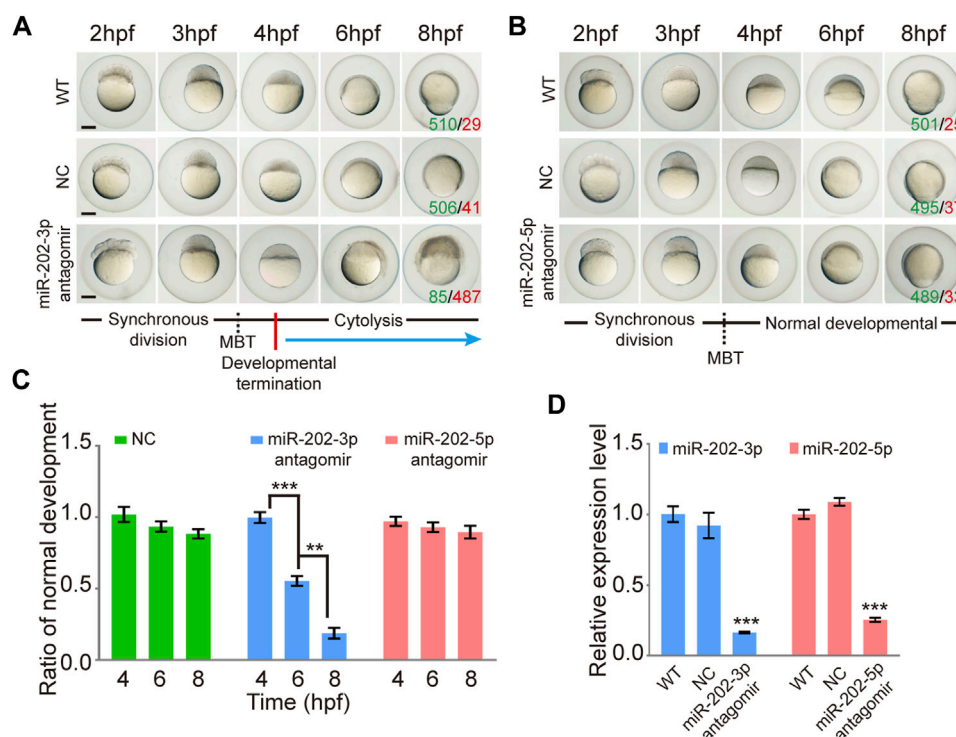


FIGURE 1

Inhibition of miR-202-3p by an antagomir results in termination of embryonic development at MBT in zebrafish. (A) Time-matched bright field images of embryos showing developmental termination at 4 hpf and, finally, cytolysis after miR-202-3p antagomir (8 μ M) injection in the fertilized embryos compared with embryos of wild type and NC embryos injected with scrambled miR-202-3p antagomir (8 μ M). The green number indicates the number of embryos with normal development and in red the number indicates the abnormal development. WT embryos at 8 hpf were used as phenotypic control. (B) Time-matched bright field images of embryos showing completely normal development of zebrafish embryos injected with miR-202-5p antagomir (8 μ M); patterns are similar with what is found for wild type (WT) and NC (scrambled antagomir) injection embryos over the same developmental time course. The green number indicates the number of embryos with normal development and in red the number indicates the abnormal development. WT embryos at 8 hpf were used as phenotypic control. (C) The statistics of embryo viability at 4 hpf, 6 hpf and 8 hpf following injection with miR-202-3p antagomir, miR-202-5p antagomir or NC (scrambled antagomir). (D) qRT-PCR analyses showing embryonic content of miR-202-3p and miR-202-5p after treatment with respective antagomirs. The scale bar is 100 μ m. Error bars, mean \pm s.d., n = 3 (biological replicates).

deletion using the CRISPR-Cas9 technology in zebrafish. Two founders (a male and a female) of zebrafish with deletions of 833 bp or 837 bp fragment were generated (Figure 2A). Heterozygous F1 lines were generated by mating the two founders to wild type female or male fish. The miR-202^{+/-} fishes developed normally like the wild type fish. However, the genotype of F2 embryos were inherited at the expected Mendelian ratio at 4 hpf, while no zygous miR-202 deletion zebrafish can survive to adulthood, indicating that miR-202 is crucial for zebrafish development (Figure 2B). *In situ* hybridization of ovary sections prepared from the wild type and miR-202^{+/-} fishes showed that in both fishes, miR-202-3p was expressed in the developed oocytes with similar intensities but absent from the underdeveloped oocytes (Figure 2C), further suggesting maternal carryover of miR-202-3p at the initial developmental stages. By cross-mating between the miR-202^{+/-} F1 fishes, developmentally timed F2 embryos were collected at

4 hpf. Whole mount *in situ* hybridization on these embryos demonstrated differential staining intensities for miR-202-3p, corresponding to the wild type, miR-202^{+/-} and miR-202^{-/-} genotypes, respectively (Figure 2D). qRT-PCR analyses on genotyped embryos clearly indicated reduced miR-202-3p expression in the miR-202^{+/-} embryos and only residual levels of miR-202-3p in the miR-202^{-/-} embryos at 4 hpf, which was carried over from the oocyte. However, it could not detect the miR-202-3p in the miR-202^{-/-} embryos at 6 hpf (Figure 2E).

Deletion of the miR-202 locus recapitulated the fatal phenotype of miR-202-3p inhibition

The miR-202^{+/-} F1 females were paired with F1 miR-202^{+/-} males to examine the viability of embryos. While the majority of

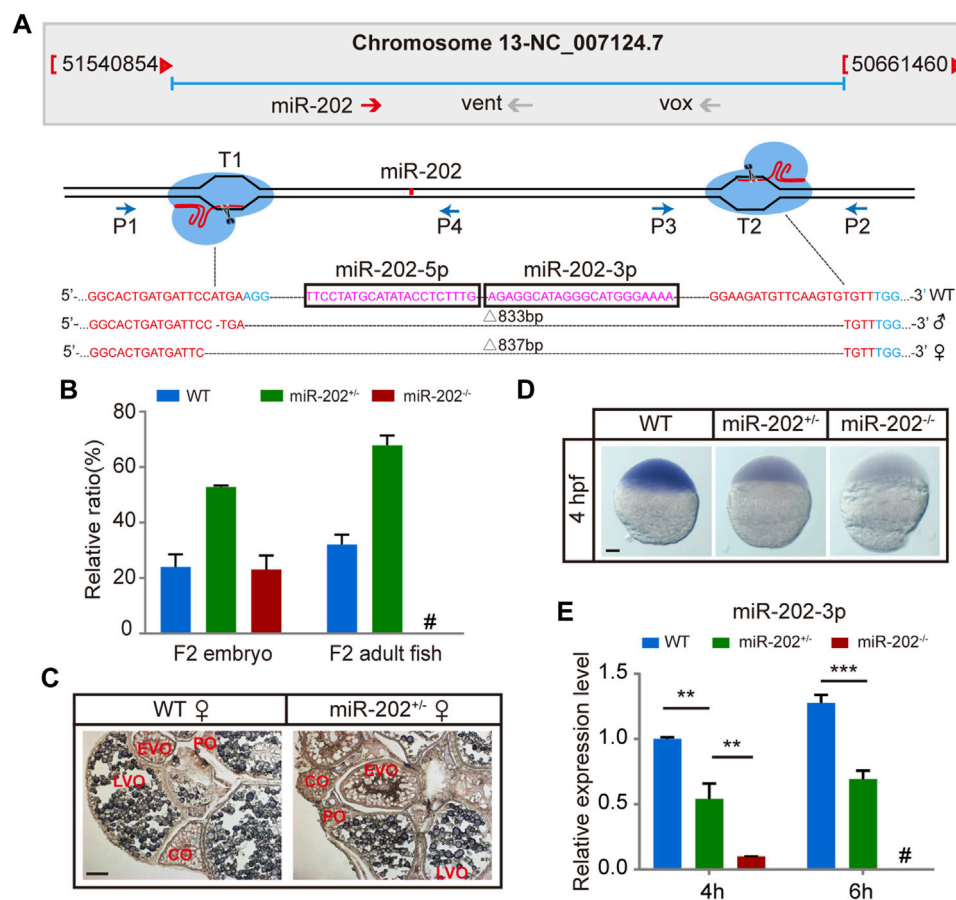


FIGURE 2

Deletion of miR-202 from the zebrafish genome using CRISPR-Cas9 system. (A) Schematic illustration of CRISPR/Cas9 system used to produce the knock-out lines of miR-202. The miR-202 sequences are in magenta, miR-202-3p and miR-202-5p are marked with a rectangular frame; the sgRNA target sites are in red; the PAM motif (NGG) is shown in blue. The location and direction of primers (P1-P4) used for PCR screening are also shown with arrow. (B) Genotyping of miR-202 mutant F2 embryos at 4hpf and F2 adults (3 month). (C) *In situ* hybridization of ovaries from miR-202 wild type (WT) and heterozygotes (miR-202^{+/+}) to examine expression of miR-202-3p. The developmental stages of ovarian oocytes include the primary oocytes: perinuclear oocytes (PO) and cortical alveolar oocytes (CO); the mature oocytes: early vitellogenin oocytes (EVO) and late vitellogenin oocytes (LVO). The scale bar is 10 μ m. (D) Whole mount *in situ* hybridization showing expression of miR-202-3p in wild type (WT), heterozygous (miR-202^{+/+}) and homozygous (miR-202^{-/-}) embryos at 4 hpf. The scale bar is 100 μ m. (E) qRT-PCR analysis of miR-202-3p expression in wild type, heterozygous and homozygous embryos at 4 hpf and 6 hpf. Error bars, mean \pm s.d., n = 3 (biological replicates).

F2 embryos developed normally, about 1/4 stopped development and become visibly abnormal starting from 4 hpf, followed by cytolysis within next few hours (Figure 3A). This fatal phenotype highly resembled that of the embryos in which miR-202-3p is knocked down in the timing of occurrence and severity of the phenotype. In the more than 2000 F2 embryos genotyped, more than 90% of miR-202^{-/-} embryos demonstrated developmental termination and cytolysis within 4–6 hpf, and no miR-202^{-/-} embryos survived beyond 12 hpf (Figure 3B). No developmental abnormality occurred in the miR-202^{+/+} embryos at this stage.

To verify whether the fatal miR-202^{-/-} phenotype was a bona fide outcome from miR-202 deletion, we performed rescue attempts by injecting agomir of miR-202-3p, miR-202-5p, pre-miR-202, a combination of miR-202-3p and

miR-202-5p, and a scrambled miR-202-3p (i.e., NC) to the F2 embryos. By extensive genotyping of viable embryos at 4, 6, 8, 10, and 12 hpf for each rescue agent, we found $80 \pm 12\%$, $75 \pm 12\%$ and $77 \pm 16\%$ of miR-202^{-/-} embryos demonstrated delayed development not the cytolysis at the 12 hpf time point for miR-202-3p, pre-miR-202, the combination of miR-202-3p and miR-202-5p, respectively, while none of the miR-202^{-/-} embryos were rescued by miR-202-5p and the scrambled miRNA (Figures 3C,D). Thus the fatal phenotype of miR-202^{-/-} at the blastula stage could be rescued if miR-202-3p is present in the rescue agents. Rescuing efficiencies of miR-202-3p and pre-miR-202 both peaked at 20 μ M, with under- and over-doses resulting in two to three folds lower rescue rates (Figure 3E). Interestingly, both overdosed and inadequate

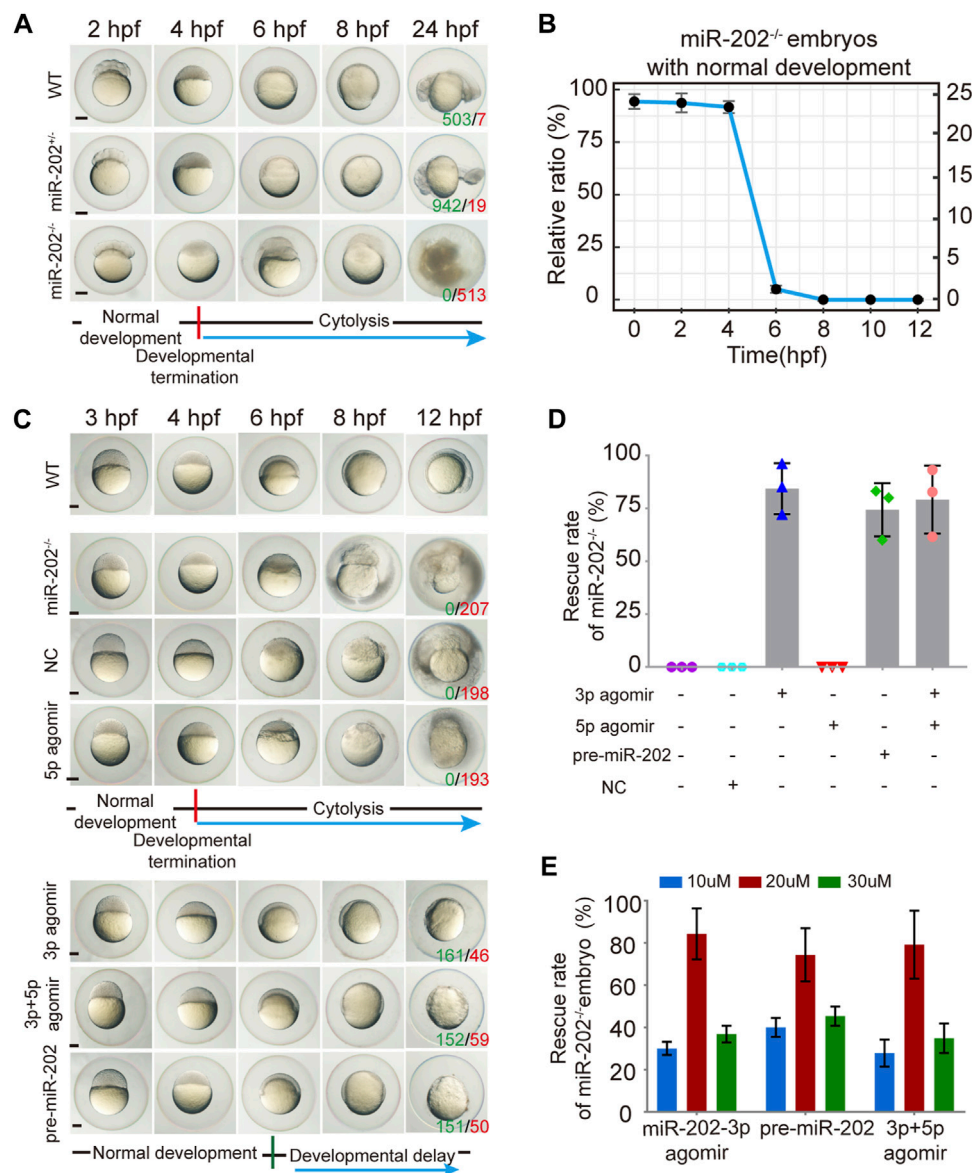


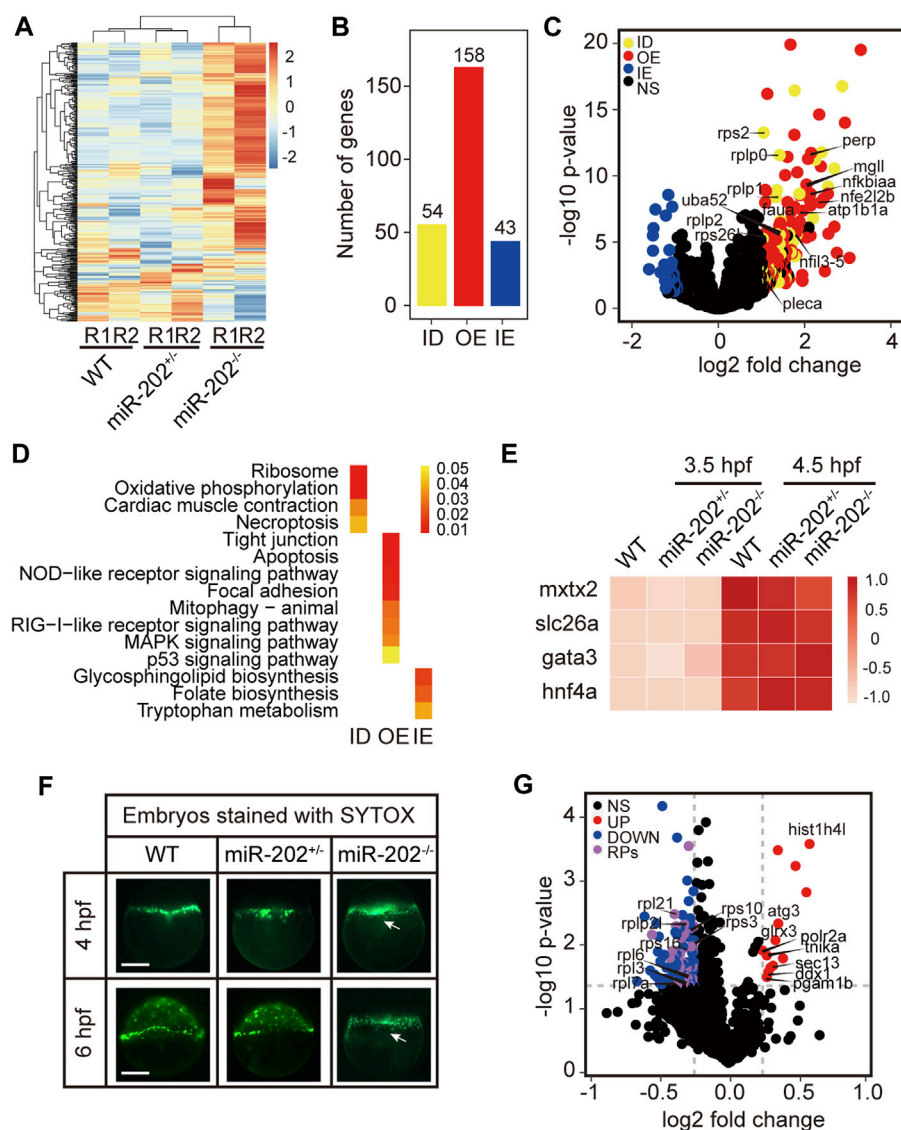
FIGURE 3

Deletion of the miR-202 locus recapitulated the phenotype of miR-202-3p knockdown. (A) Time-matched bright field images showing developmental termination of homozygous (miR-202^{-/-}) embryos at 4 hpf in contrast with normal development of heterozygous (miR-202^{+/-}) and wild type (WT) embryos. The green number indicates the number of embryo with normal development and in red the number indicates the abnormal development. WT embryos at 24 hpf were used as phenotypic control. (B) The survival rate curve for miR-202^{-/-} embryos from 0 to 12 hpf. (C) Time-matched bright field images of miR-202^{-/-} embryos when rescued by various reagents. The green number indicates the number of embryo that has been rescued and in red the number indicates the unsalvaged. 3p agomir embryos at 12 hpf were used as the control of successful rescue phenotype. (D) Rescue rates of miR-202^{-/-} homozygotes by miR-202-3p agomir, miR-202-5p agomir, pre-miR-202 and a combination of miR-202-3p and miR-202-5p agomirs measured at 12 hpf. (E) The rescue rates of miR-202^{-/-} embryos obtained with three different concentrations (10 μ M, 20 and 30 μ M) of rescue reagents measured at 12 hpf, indicating an optimal rescuing concentration for each reagent. The scale bar is 200 μ m. Error bars, mean \pm s.d., n = 3 (biological replicates).

amounts of miR-202-3p resulted in severely delayed embryo development and embryos underwent cytolysis at the blastula stage. These results indicate that miR-202-3p is required for embryonic viability and its expression be precisely regulated during MBT.

Loss of miR-202 altered embryonic mRNA repertoire during MBT

To elucidate mechanisms of miR-202-3p function in early development, we conducted transcriptome comparisons among

**FIGURE 4**

Transcriptomic and proteomic analysis for miR-202 mutant embryos. **(A)** Heat map showing distinctive gene expression patterns of miR-202^{-/-}, miR-202^{+/-} and WT embryos at 3.5 hpf. R1 and R2 indicate sampling replicates. **(B)** The number of differentially expressed genes in three subgroups: ID, insufficient degradation; OE, over-expression; IE, insufficient expression. **(C)** Volcano plot of differentially expressed genes between homozygous and heterozygous miR-202 embryos. **(D)** KEGGs enriched in the three subgroups of differentially expressed genes. **(E)** Expression of genes related to the initiation and subcapsulation of Yolk Syncytial Layer (YSL) at 3.5 and 4.5 hpf in wild type and miR-202^{+/-} and miR-202^{-/-} indicating normal expression. **(F)** Verification that the loss of the miR-202 locus cannot affect the formation of YSL at 4 hpf, but miR-202^{-/-} embryos cannot successfully achieve epibolic movement compared with wild type and miR-202^{+/-} embryos. The white arrow represents YSL. The scale bar is 200 μm. **(G)** Distribution of differentially expressed proteins in miR-202^{-/-} embryos. NS, no significant difference; UP, up-regulated; DOWN, down-regulated; RPs, ribosome-associated proteins.

the WT, miR-202^{+/-}, and miR-202^{-/-} embryos collected at 3.5 hpf. RNA and DNA from single embryos were isolated concurrently and genotyping was carried out using the DNA. RNA from embryos of same genotype was pooled for RNA-seq. As expected, gene expression profiles from the miR-202^{-/-} embryos showed greater divergence from the heterozygous and wild type embryos while the latter two are more similar

(Figure 4A). The expression levels of the DEGs were then compared with wild type embryos at the one-cell/fertilized egg stage to determine how the DEGs were related with the maternally inherited mRNAs. This comparison allowed us to divide the DEGs into three subgroups: insufficient degradation (ID) of maternal RNA, overexpression (OE) of zygotic genes, and insufficient expression (IE) of zygotic genes in the miR-

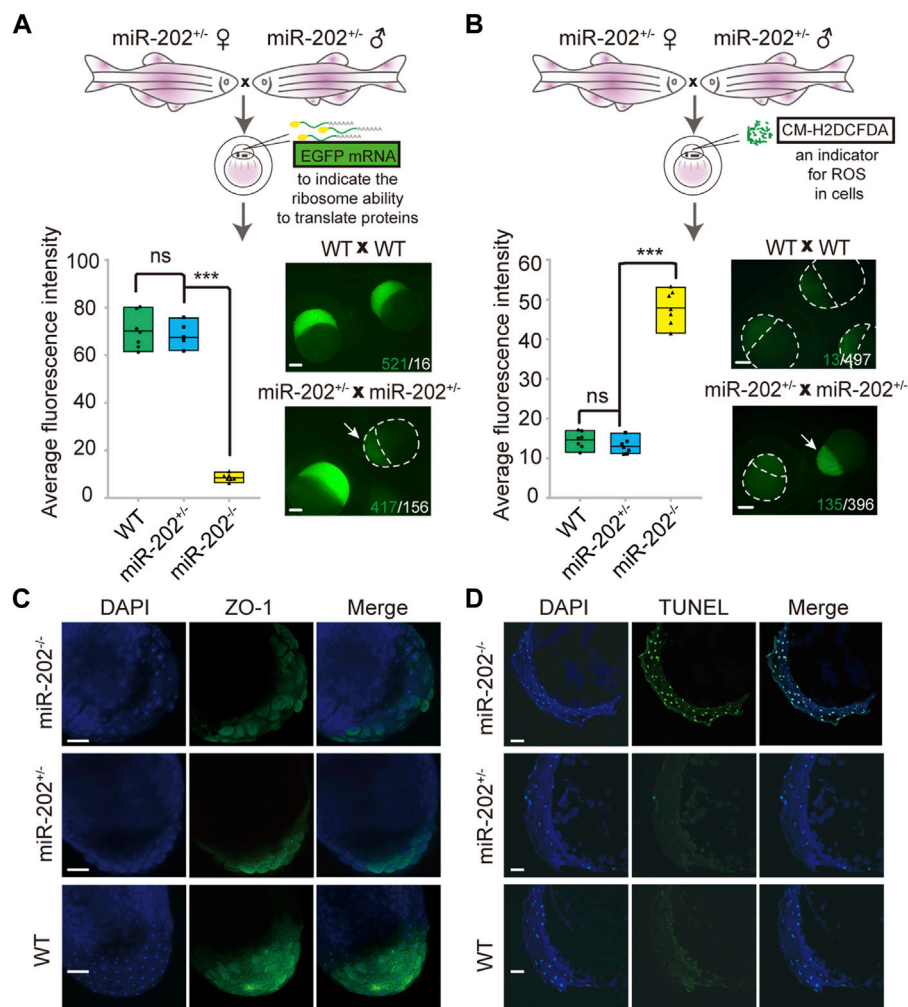


FIGURE 5

Homeostatic disorders in miR-202^{-/-} embryos. **(A)** Illustrations showing assessment of translation efficiency using polyadenylated EGFP mRNA. Embryos derived from miR-202 heterozygous parents were used for assessment. Drastically reduced fluorescence intensity (bottom left panel) and images (bottom right panel) were obtained from the miR-202^{-/-} embryos at 3.5 hpf. The embryo pointed to by white arrows was a miR-202^{-/-} embryo, as verified through genotyping. The scale bar is 200 μ m. The green number indicates the number of embryos successfully expressing EGFP, and in white the number indicates the number of embryos that unexpressed or low expressed EGFP. **(B)** Illustrations showing assessment of reactive oxygen species using CM-H2DCFDA. Embryos derived from miR-202 heterozygous parents were used for assessment. Elevated fluorescence intensity (bottom left panel) and images (bottom right panel) were obtained in the miR-202^{-/-} embryos at 3.5 hpf. The embryo indicated by the white arrow was a miR-202^{-/-} embryo, as verified through genotyping. The green number indicates the number of embryos that produce high level of ROS, and in white the number indicates the number of embryos with low ROS levels. The scale bar is 200 μ m. **(C)** Immunohistochemical detection of zonula occludens-1 (ZO-1) in wild type and miR-202 mutant embryos at 3.5 hpf. The scale bar is 100 μ m. **(D)** TUNEL staining for apoptotic signals in the wild type and miR-202 mutant embryos at 3.5 hpf. The scale bar is 100 μ m. Error bars, mean \pm s.d., $n = 3$ (biological replicates).

202^{-/-} embryos (Figure 4B, Supplementary Table S1). There are 54 genes including 7 ribosomal proteins that were insufficiently degraded, 158 genes, such as *nfkb1a*, *perp*, *mgll* involved in cell proliferation, apoptosis and cell-cell adhesion are over-expressed, and 43 genes insufficiently expressed (Figure 4C). We further analyzed the three subgroups of DEGs for KEGG enrichment; 15 pathways including ribosome, oxidative phosphorylation, apoptosis, cell junction, inflammatory and metabolic related pathways were identified (Figure 4D,

Supplementary Table S2). A larger portion of DEGs (63%) belong to the over-expressed subgroup, suggesting a suppressive role of miR-202 during zygotic genome activation. Due to failure in the initiation of epibolic movement in miR-202^{-/-} embryos, we are curious whether loss of miR-202 would affect the formation the Yolk Syncytial Layer (YSL), the structure critical for initiating epibolic cell movement and reorganization. We found transcription of the YSL marker genes (Xu et al., 2012) was

normal in miR-202^{-/-} embryos (Figure 4E). Staining of the F2 embryos using SYTOX also showed proper formation of YSL in all embryos including the miR-202 mutants at 4 hpf. However, with development progressed, YSL in the wild type embryos was shown to have a complete epibolic movement of cells towards the vegetal pole, but epibolic movement failed in the miR-202^{-/-} embryos, which clearly pinpointed the timing of developmental termination was prior to epiboly in the mutant (Figure 4F).

To evaluate the proteomic consequences of miR-202 deletion, we analyzed the proteome of miR-202^{-/-} embryos and compared it to the wild type at 4 hpf. We observed a total of 115 differentially expressed proteins, of which 100 were down-regulated and 15 were up-regulated in miR-202^{-/-} embryos (Supplementary Table S3). A most peculiar feature of the miR-202 null embryonic proteome is the reduction of 34 ribosomal proteins (Figure 4G, Supplementary Table S3).

Homeostatic disorders and embryonic apoptosis in miR-202 deletion embryo

The identification of multiple dysregulated KEGG pathways from the transcriptome comparisons prompted us to evaluate the cellular consequences that the loss of miR-202 might produce. Due to the striking presence of dysregulated ribosomal proteins in the transcripts and proteome, we first verified whether protein synthesis was impaired. Exogenous introduction of polyadenylated EGFP mRNAs to the embryos produced by miR-202^{+/-} parents showed almost complete abolishment of protein synthesis in the miR-202 null embryos (Figure 5A). The level of reactive oxygen species (ROS) was also measured to evaluate whether oxidative stress is an outcome of the dysregulated pathways. We microinjected CM-H2DCFDA, an indicator of cellular ROS level into the embryos from the miR-202^{+/-} parents. About 4-fold higher ROS intensities were detected in the miR-202 null embryos (Figure 5B). In addition, cell-cell adhesion was also affected as demonstrated by the significantly reduced presence of zonula occludens-1 (ZO-1), the marker for tight junction (Figure 5C).

Overexpression of the apoptotic pathway in the miR-202^{-/-} embryos hinted that apoptosis could be the ultimate fate of the miR-202^{-/-} embryos. We performed TUNEL staining on sections of the F2 embryos followed with genotyping of the embryos. Apoptotic signals were widely detected from the blastomere cells in the miR-202^{-/-} embryos as compared to no detected signals in the miR-202^{+/-} and wild type embryos (Figure 5D). More than 90% of the cells in the blastomere at 3.5 hpf were visibly undergoing apoptosis in the miR-202^{-/-} embryos. Taken together, results strongly indicated that miR-202, through its precisely controlled product miR-202-3p, is essential to maintain cellular homeostasis during MBT.

Screening for the target genes of miR-202-3p

Using miRNAmap2 (Hsu et al., 2008) and TargetScanFish (Ulitsky et al., 2012), we identified 24 possible target genes of miR-202-3p from the DEGs (Supplementary Table S4). We then selected seven upregulated genes (*nfkbiaa*, *mgll*, *nfil3-5*, *atp1b1a*, *pleca*, *nfe2l2b* and *perp*) for further analysis based on their potential involvement in cell proliferation and apoptosis, cell adhesion, and metabolism (Table 1). Since all these genes are up-regulated when miR-202-3p is deleted or knocked down, we first tested whether minimizing the elevation of these transcripts could alleviate the fatal phenotype when a miR-202-3p antagomir was present. We thus co-injected miR-202-3p antagomir with a designed shRNA targeting one of the seven genes (Figure 6A). We verified that the gene-specific shRNAs functioned properly to suppress the up-regulation of the intended genes before and after 4 hpf (Supplementary Figure S2). We counted the number of normally developing embryos for each of the shRNAs at 6 hpf—the timepoint when the miR-202-3p antagomir would have led to cytolysis if no shRNA had been injected. We found that down-regulated expression of three genes: *nfkbiaa*, *perp* and *mgll* was able to rescue about 80, 50 and 45% of the miR-202-3p knockdown embryos from developmental failures at MBT, respectively (Figure 6B).

To verify that these three genes are direct targets of miR-202-3p, native and mutated forms of the 3'UTRs of these genes were cloned to a luciferase report vector (Supplementary Figure S3). Both native and mutated vector were co-transfected with miR-202-3p agomir and scrambled agomir into HEK293T cells to measure luciferase activities. Results validated that *nfkbiaa*, *perp* and *mgll* are direct targets of miR-202-3p (Figure 6C).

nfkbiaa, *perp* and *mgll* are essential for early embryo development

We further investigated the inter-relationship among the trio of miR-202-3p target genes. We first examined the expression patterns of the trio in wild type embryos and in miR-202^{-/-} embryos by qRT-PCR. Data showed that all three genes were transcribed around 4 hpf during ZGA (Figures 7A–C) and were overexpressed when miR-202 is deleted (Figure 7D), coinciding the timing of the fatal phenotype of the miR-202^{-/-} mutant. To explore the relative roles of the trio in generating the phenotype, we cloned the transcripts of these genes, *in vitro* transcribed them, and microinjected them into fertilized eggs of wild type fish. Examining at 12 hpf, approximately 80%, 50%, 45% and 20% of injected embryos exhibited developmental delay or embryonic mortality when mixture of the three target gene mRNAs, *nfkbiaa* mRNA, *perp* mRNA and *mgll* mRNA were introduced, respectively (Figure 7E). These results further validated involvement of all three genes in producing the phenotype, but *nfkbiaa* and *perp* played bigger roles in the process

TABLE 1 Screened target genes.

Gene	Description	Gene ID	GO: Biological process
<i>Nfkb1a</i>	nuclear factor of kappa light polypeptide gene enhancer in B-cells inhibitor, alpha a	ENSDARG00000005481	Apoptosis; regulation cell differentiation.
<i>mgll</i>	monoglyceride lipase	ENSDARG00000036820	indirect involved in apoptosis lipid metabolic process regulation of signal transduction
<i>nfil3-5</i>	nuclear factor, interleukin 3 regulated, member 5	ENSDARG00000094965	Apoptosis; regulation of transcription.
<i>atp1b1a</i>	ATPase Na ⁺ /K ⁺ transporting subunit beta 1a	ENSDARG00000013144	establishment or maintenance of transmembrane electrochemical gradient positive regulation of ATPase activity ion transport
<i>pleca</i>	plectin a	ENSDARG00000062590	skeletal muscle tissue development locomotory behavior cytoskeleton organization
<i>nfe2l2b</i>	nuclear factor, erythroid 2-like 2b	ENSDARG00000089697	positive regulation of transcription, DNA-templated negative regulation of transcription in response to oxidative stress
<i>perp</i>	p53 apoptosis effector related to pmp22	ENSDARG00000063572	regulation of apoptotic process

than *mgll*. Interestingly, similar ratios of developmental delay and embryonic mortality were observed when the trio were suppressed by their respective shRNAs or a mixture of the three shRNAs in wild type embryos (Figure 7F). The similar fatal phenotypes produced by over- and down-regulation of the trio indicated transcription of the trio, especially those of *nfkb1a* and *perp*, need to be tightly controlled for proper embryogenesis to proceed. These findings suggested the need of tight control of miR-202-3p level during MBT.

nfkb1a, *perp* and *mgll* regulate early development via an inter-regulated network

As the similar phenotypes resulted from over- or down-regulation of the individual genes hinted potential existence of inter-regulation among the trio. The notion was proved true as we found that when *nfkb1a* was over-expressed or down-regulated, transcription of *perp* responded in the same direction during the developmental period from 2-6 hpf (Figure 8A). Similarly, over-expression or down-regulation of *perp* elicited the same responses from *nfkb1a* (Figure 8B). Therefore, *nfkb1a* and *perp* are inter-regulated. An inter-regulation relationship between genes was also true between *nfkb1a* and *mgll*, but in a slightly different manner, in which over- and under-expression of *nfkb1a* resulted in down-regulation of *mgll* (Supplementary Figure S4). Our results showed that *nfkb1a*, *perp* and *mgll* form an interconnected regulatory network and the two major factors, *nfkb1a* and *perp* are positively regulating on each other.

Taking all results together, we concluded that miR-202-3p suppressed over-expression of *nfkb1a*, *perp* and *mgll* during MZT. These three target genes formed interconnected regulatory networks with each other. Reciprocally, *nfkb1a* and *perp* regulate expression of the miR-202 locus, these inter-regulation loops acted concertedly to maintain miR-202-3p at a relatively constant level (Figure 9). This tightly regulated miR-202-3p-mediated network is essential to maintain embryonic viability during MBT.

Discussion

In this study, we accumulated solid evidence indicating that miR-202-3p plays essential roles to maintain embryonic viability during the mid-blastula transition in zebrafish. Unlike the miR-430s and miR-30 which function during MZT with tens of thousands of sequencing reads, miR-202 functions singularly with only single digits of sequencing reads (Supplementary Figure S5A) (Wei et al., 2012). miR-202 is located adjacent to *vent* and *vox* in the long arm of chromosomal 13. *Vox* and *vent* are known centralizing factors activated prior to or around the period of zygotic genome activation (Imai et al., 2001; Gilardelli et al., 2004; Pshennikova et al., 2017). Analysis of the abundance of the miR-202 products (miR-202-3p and miR-202-5p) in early development (from unfertilized cell to 10 hpf) indicated that the expression level of miR-202-5p was significantly higher than that of miR-202-3p (Supplementary Figure 5B). Although miR-202-3p normally is present only in a low concentration, the knock down or deletion of miR-202-3p resulted in the drastic fatal phenotypes at MBT. Especially convinced by the fatal phenotypes of the miR-202 null embryos are rescued only by miR-202-3p or its precursor and not by

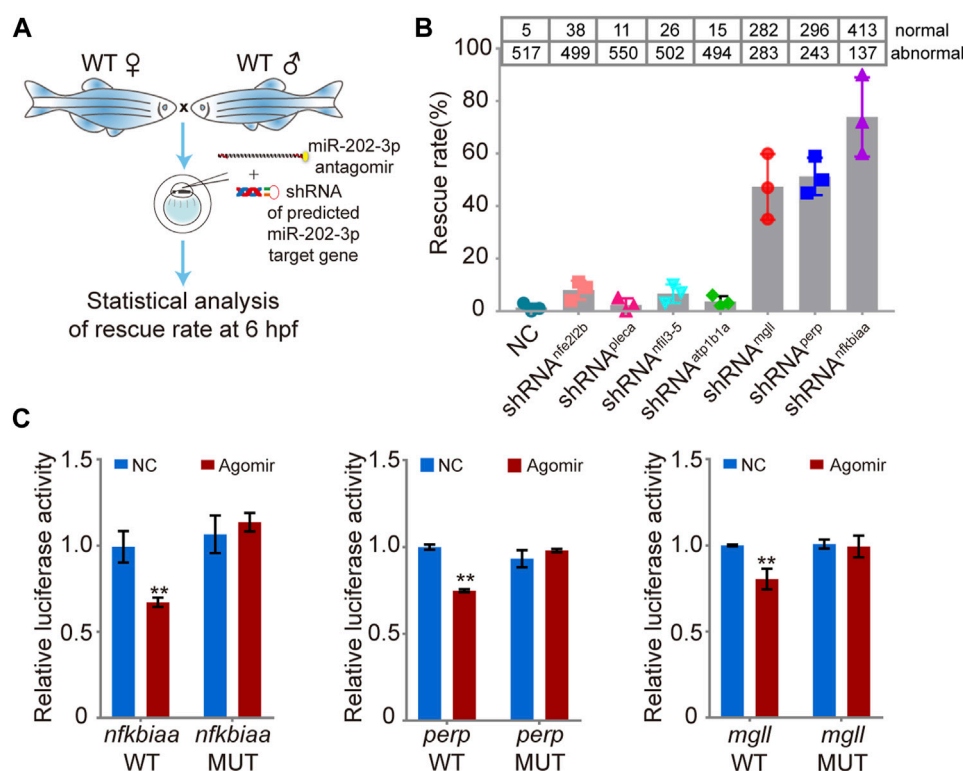


FIGURE 6

Validation of the function of the miR-202-3p target genes in embryogenesis. (A) Schematic illustration of rescue using shRNAs specific to the miR-202-3p target genes. Briefly, survival rates at 6 hpf were measured for wild type embryos co-injected with miR-202-3p antagonist (8 μ M) and the specific shRNA (200 ng/ μ l) to one of the target genes at the 1-cell stage. (B) Rescue rates at 6 hpf for various shRNAs tested. More than 500 embryos were detected for each shRNA. (C) Validation of the existence of miR-202-3p binding sites in the 3'UTRs of *nfkb1aa*, *perp* and *mgll* genes by dual luciferase assays in HEK29T cells. Luciferase activities from constructs containing the 3'UTRs of wild type (WT) or mutated miR-202-3p binding site (MUT) for each gene were measured comparatively. NC, scrambled miR-202-3p; Agomir, synthetic miR-202-3p. Error bars, mean \pm s.d., $n = 3$ (biological replicates).

miR-202-5p. These findings indicate that miR-202-3p is low in expression but essential for embryonic survival during MBT. It is so far the only miRNA found functioning in the initial stages of embryogenesis with a life/death effect.

miR-202-3p plays an essential role in MZT adds to the list of known players of this important developmental transition, such as miR-430s, *Ythdf2*, *nanog*, *pou5f3* and others (Lee et al., 2013; Pálffy et al., 2020). Unlike mutations of the other known factors that usually impair cell differentiation or lineage commitment during embryogenesis, loss of miR-202-3p resulted in catastrophic breakdown of cellular homeostasis, which eventually leads to massive apoptosis and cytolysis of the blastomere. We found distinctive pathways among the three subgroups of dysregulated genes of miR-202 null embryos. Specifically, genes showing insufficient degradation included genes belonging to the categories "Ribosome" and "oxidative phosphorylation." Over-expressed genes included those belonging to the categories "Tight junction", "Apoptosis" and a few pathways related with inflammation. While a few pathways

of biosynthesis and metabolism were represented by the insufficiently expressed genes. Correspondingly, we were able to verify such homeostatic dysfunctions as slowed protein synthesis, elevated oxidative stress, loss of tight junctions and apoptosis in the miR-202^{-/-} embryos. Remarkably, the presence of 7 less degraded ribosomal protein mRNAs did not translate into higher levels of these ribosomal proteins; instead many of the ribosomal proteins were significantly reduced and the rate of protein synthesis was impaired. How the hindered clearance of the ribosomal protein mRNAs influenced ribosome biogenesis needs to be further explored. Successful rescue of the fatal phenotypes by miR-202-3p suggested that much of the basis of these phenotypes might be attributable to the dysregulation of the miR-202-3p target genes in the miR-202 null embryos.

By a target screen followed with *in vivo* verification, *nfkb1aa*, *perp* and *mgll* were identified as direct targets of miR-202-3p. *nfkb1aa* is the fish homolog of mammalian *NFkBIA*, and its protein product is I κ Ba. It has been reported that NF κ B activation of target gene expression could be one of the first

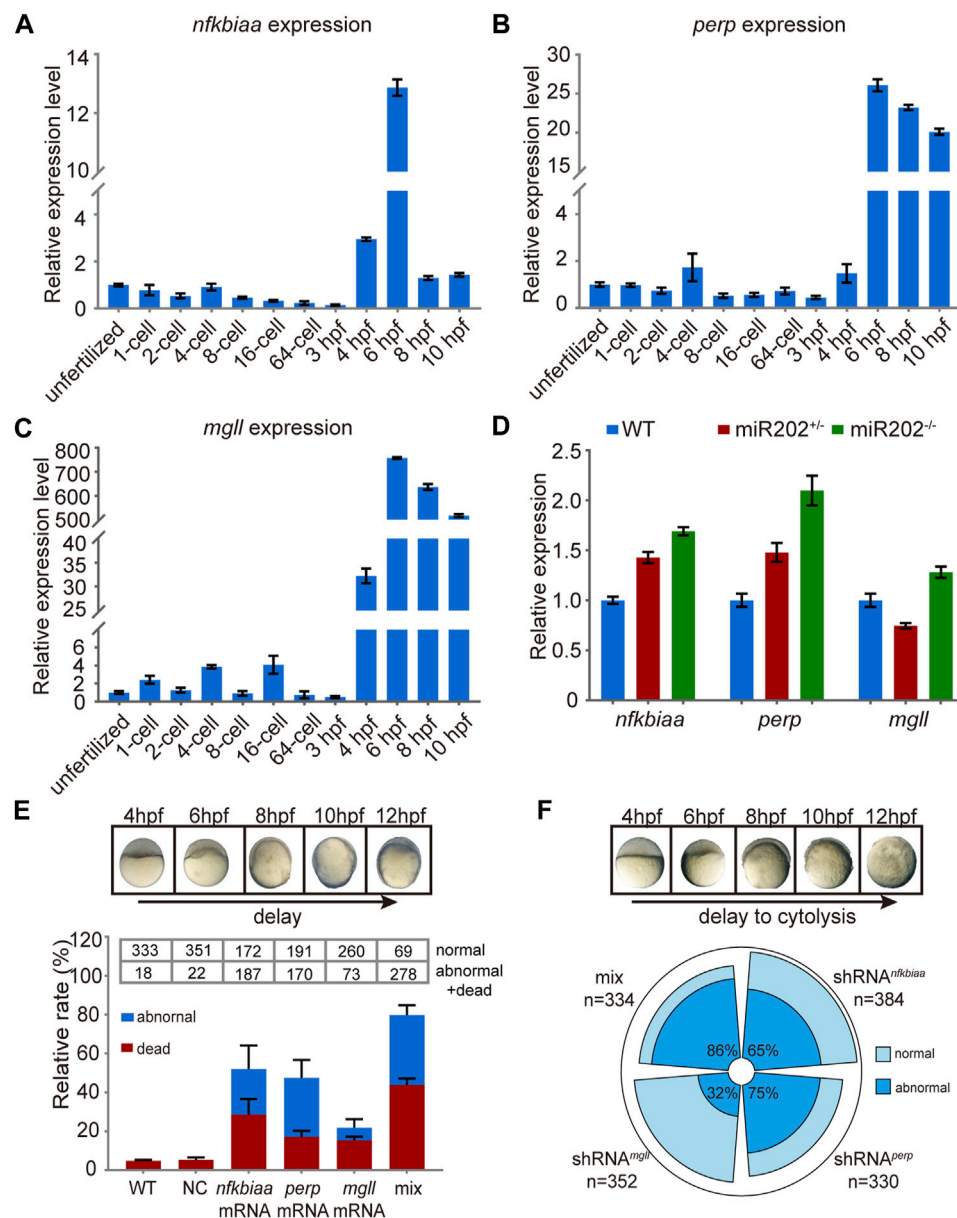


FIGURE 7

In vivo validation of the involvement of *nfkb1aa*, *perp* and *mgl1* in zebrafish early development. (A–C) qRT-PCR analysis of *nfkb1aa* (A), *perp* (B) and *mgl1* (C) expression during the course of early embryonic development from unfertilized embryo to 10 hpf. (D) Quantitative analysis of homozygous, heterozygous and wild-type embryos revealed that the expression level of *nfkb1aa*, *perp* and *mgl1* was overexpressed in miR-202 homozygous mutant. (E) Time-matched bright field images of slow-developing embryos (top) and the rate of mortality and developmental abnormality (bottom) when extra mRNA of *nfkb1aa*, *perp* and *mgl1* were introduced to wild type embryos (bottom). The “mix” indicates mixture of equal amounts of mRNAs of the three genes. The statistical assays were performed using data obtained at 12 hpf. (F) Time-matched bright field images of embryo showing developmental delay and cytolysis (top) and the rate of developmental abnormality (bottom) when shRNA of *nfkb1aa*, *perp* and *mgl1* were introduced to wild type embryos. The “mix” indicates mixture of equal amount of shRNAs of the three genes. Error bars, mean \pm s.d., $n = 3$ (biological replicates).

events in a cascade leading to major embryo genome activation (EGA) (Halstead et al., 2020). In *Xenopus*, NF- κ B activation is observed during oocyte maturation (Dominguez et al., 1993) and in late blastulae and gastrulae (Richardson et al., 1994). In mouse

embryos, activation of NF- κ B is required for the development of mouse embryos beyond the 2-cell stage (Nishikimi et al., 1999). In human, epididymal embryonic development harbors NF κ B signaling pathway as a morphogenetic player

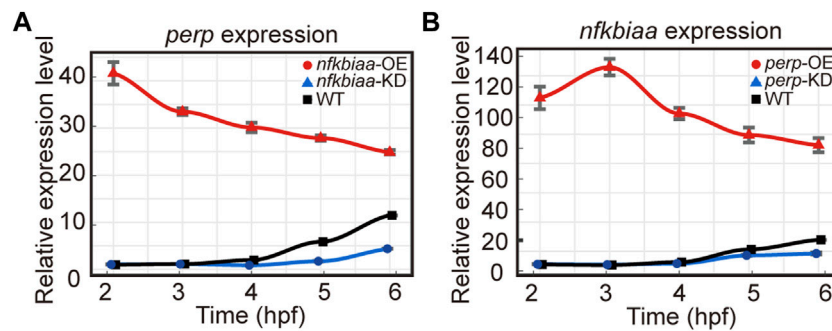


FIGURE 8

nfkb1a and *perp* are inter-regulated in early embryonic development. (A) The mRNA expression level of *perp* response to overexpression (by mRNA microinjection) and downregulation (by shRNA microinjection) of *nfkb1a* in zebrafish embryos observed from 2 hpf to 6 hpf. (B) The mRNA expression level of *nfkb1a* response to overexpression (by mRNA microinjection) and downregulation (by shRNA microinjection) of *perp* in zebrafish embryos observed from 2 hpf to 6 hpf. Error bars, mean \pm s.d., $n = 3$ (biological replicates).

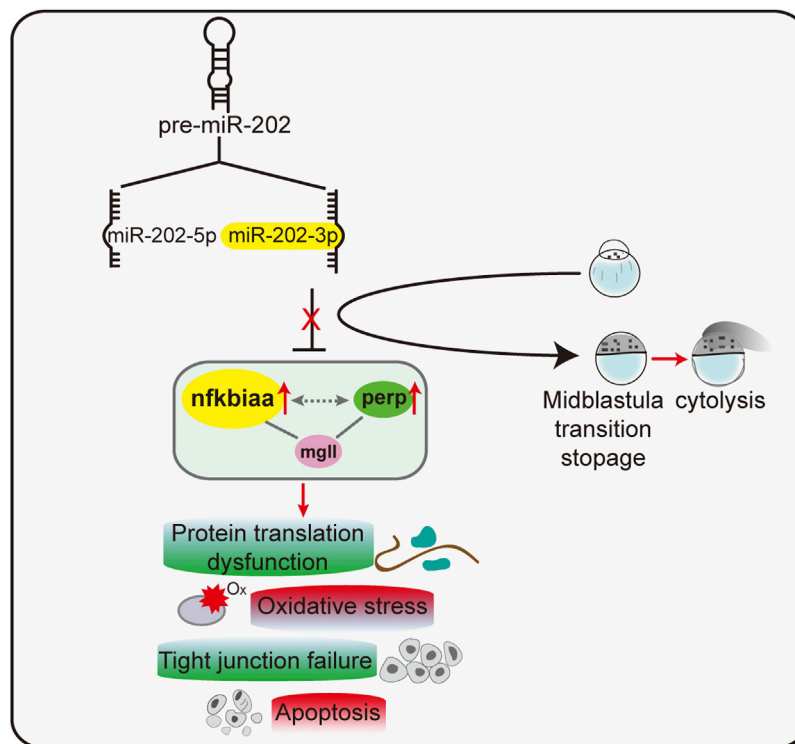


FIGURE 9

A proposed model of a miR-202-3p mediated regulatory network that determines embryonic viability during MBT in zebrafish.

(Ferreira et al., 2022). Both in the mouse and human, NF- κ B as a critical regulator of fertility is associated with oxidative damage via activation of NF- κ B (Tatone et al., 2008). Another miR-202-3p target gene identified was *perp*. *perp* contains multiple binding motifs for the tumorous suppressor

protein P53 in the promoter region, and transcription of *perp* is directly activated by P53 (Attardi et al., 2000). *perp* is a mediator of p53-dependent apoptosis in diverse cell types (Qian et al., 2020; Yuan et al., 2020). Nowak et al. (Nowak et al., 2005) reported that one- to two-cell stage zebrafish

embryos injected with *in vitro* synthesized *perp* mRNA displayed a severely malformed body shape at 24 hpf due to enhanced cell death during gastrulation and segmentation stages. The third direct target of miR-202-3p is *mgll*. Some studies show that MGLL is a key enzyme in the lipid metabolism network by supplying free fatty acids for β -oxidation and for providing components to build cell structures and effector molecules which are involved in cell proliferation, invasion, apoptosis resistance and stemness (Nomura et al., 2011; Das et al., 2013; Sun et al., 2013; Zhang et al., 2016). Overexpression of MGLL suppressed cell migration and induced cell death that was coupled with caspase activation (Yang et al., 2018; Liu et al., 2020). In this study, we showed deletion of miR-202 (and thus miR-202-3p) resulted in an elevated *nfkb1aa*, *perp* and *mgll* mRNA in the blastula. The detrimental effect of over-expressed the trio genes were rescued to a substantial degree by its inhibitory shRNA, indicated that a certain level of target gene is essential for cell viability during MBT in zebrafish.

Multiple studies in cancerous cells have shown that *nfkb1aa* and *perp* are inter-regulated. It has been reported that *perp* expression stabilizes active *p53* via modulation of *p53*-MDM2 interaction, thus forming a positive feedback between *perp* and *p53* activity (Davies et al., 2011). On the other hand, *Ikb1a* is an interacting partner of *P53* and formation of the *p53*/*Ikb1a* complex generally has an inhibitory effect on *p53* activity (Carrà et al., 2016). Thus, *nfkb1aa* and *perp* are interconnected through pathways involving *p53*. In this study, we found that knockdown of either one led to reduced expression of the other, and over-expression of either one caused elevated transcription in the other, suggesting a positive inter-regulation between the two. Whether the inter-regulation between *nfkb1aa* and *perp* could be mediated by the *P53* signaling pathway in zebrafish embryos warrants further investigation.

Many universal key post-transcriptional mechanisms are known to contribute to maternal mRNA clearance. MicroRNA-dependent mechanisms, which often promote deadenylation is common, with the miR-430 destabilizing hundreds of mRNAs in zebrafish (Bazzini et al., 2012), miR-427 acting in *Xenopus* (Lund et al., 2009), and miR-309 functioning in *Drosophila* (Bushati et al., 2008). In addition, Ythdf2 N6-methylation (m6A) also drives mRNA deadenylation of maternally provided mRNAs, whose decay is essential for zebrafish embryogenesis (Kontur et al., 2020), mouse embryonic stem cells development (Geula et al., 2015) and murine oogenesis (Ivanova et al., 2017). The targets of miR-430 and Ythdf2 exhibit notable overlap, and their common target decay earliest, followed by the specific targets of Ythdf2, and then the specific targets of miR-430 (Zhao et al., 2017). These factors suggest the importance of timely, robust removal of maternal transcripts by overlapping yet temporally distinct mechanisms for proper development (Stoeckius et al., 2014). MicroRNA-30a regulates zebrafish myogenesis through targeting the transcription factor Six1

(O'Brien et al., 2014). In our study, miR-202-3p targets the *nfkb1aa*, *perp* and *mgll* to regulate zebrafish embryonic development. Therefore, whether miR-202-3p or miR-30a has the function of deadenylation is still unknown and the specific mechanism needs to be further explored.

To summarize, we showed that miR-202-3p is essential to maintain cellular viability during MZT through modulating maternal mRNA degradation and zygotic transcription. We identified a trio of genes, *nfkb1aa*, *perp* and *mgll* that are direct targets of miR-202-3p and are inter-regulated by each other. Dysregulation of the regulatory network is directly linked to slower development progression and apoptosis through influencing the rate of protein synthesis, ROS clearance, cell adhesions and apoptosis during MBT.

Data availability statement

The datasets presented in this study can be found in online repositories. The names of the repository/repositories and accession number(s) can be found below: NCBI, accession no. PRJNA529372.

Ethics statement

The animal study was reviewed and approved by the Animal Welfare Committee of Shanghai Ocean University. Written informed consent was obtained from the owners for the participation of their animals in this study.

Author contributions

RH and YX designed, performed, and analyzed the experiments. YC designed and done the proteomics and transcriptomics, and WL analyzed the data. BH helped to direct YX and YC in the research. Other authors participated in gene knock out, genotyping, colony maintenance, quantitative PCR, and immunoblotting. LC conceived, designed, supervised the study, and with RH wrote the manuscript.

Funding

This work was supported by grants from the National Key Research and Development Program of China (2018YFD0900601); and the Natural Science Foundation of China (32130109), and the Major Science Innovation Grant (2017-01-07-00-10-E00060) from the Shanghai Education Committee to LC. Funding for open access charge: National Key Research and Development Program of China; Natural Science Foundation of China.

Conflict of interest

The authors declare that the research was conducted in the absence of any commercial or financial relationships that could be construed as a potential conflict of interest.

Publisher's note

All claims expressed in this article are solely those of the authors and do not necessarily represent those of their affiliated

organizations, or those of the publisher, the editors and the reviewers. Any product that may be evaluated in this article, or claim that may be made by its manufacturer, is not guaranteed or endorsed by the publisher.

Supplementary material

The Supplementary Material for this article can be found online at: <https://www.frontiersin.org/articles/10.3389/fcell.2022.897826/full#supplementary-material>

References

- Attardi, L. D., Reczek, E. E., Cosmas, C., Demicco, E. G., McCurrach, M. E., Lowe, S. W., et al. (2000). PERP, an apoptosis-associated target of p53, is a novel member of the PMP-22/gas3 family. *Genes Dev.* 14 (6), 704–718. doi:10.1101/gad.14.6.704
- Bazzini, A. A., Lee, M. T., and Giraldez, A. J. (2012). Ribosome profiling shows that miR-430 reduces translation before causing mRNA decay in zebrafish. *Science* 336 (6078), 233–237. doi:10.1126/science.1215704
- Bhattacharya, M., Sharma, A. R., Sharma, G., Patra, B. C., Nam, J. S., Chakraborty, C., et al. (2017). The crucial role and regulations of miRNAs in zebrafish development. *Protoplasma* 254 (1), 17–31. doi:10.1007/s00709-015-0931-1
- Bolger, A. M., Lohse, M., and Usadel, B. (2014). Trimmomatic: A flexible trimmer for Illumina sequence data. *Bioinformatics* 30 (15), 2114–2120. doi:10.1093/bioinformatics/btu170
- Bushati, N., Stark, A., Brennecke, J., and Cohen, S. M. (2008). Temporal reciprocity of miRNAs and their targets during the maternal-to-zygotic transition in *Drosophila*. *Curr. Biol.* 18 (7), 501–506. doi:10.1016/j.cub.2008.02.081
- Carrà, G., Crivellaro, S., Taulli, R., Guerrasio, A., Saglio, G., Morotti, A., et al. (2016). Mechanisms of p53 functional de-regulation: Role of the i³b-a/p53 complex. *Int. J. Mol. Sci.* 17 (12), E1997. doi:10.3390/ijms17121997
- Chen, J., Cai, T., Zheng, C., Lin, X., Wang, G., Liao, S., et al. (2017). MicroRNA-202 maintains spermatogonial stem cells by inhibiting cell cycle regulators and RNA binding proteins. *Nucleic Acids Res.* 45 (7), 4142–4157. doi:10.1093/nar/gkw1287
- Chen, J., Gao, C., Lin, X., Ning, Y., He, W., Zheng, C., et al. (2021). The microRNA miR-202 prevents precocious spermatogonial differentiation and meiotic initiation during mouse spermatogenesis. *Development* 148 (24), dev199799. doi:10.1242/dev.199799
- Crowley, J. J., Collins, A. L., Lee, R. J., Nonneman, R. J., Farrell, M. S., Ancalade, N., et al. (2015). Disruption of the microRNA 137 primary transcript results in early embryonic lethality in mice. *Biol. Psychiatry* 77 (2), e5–7. doi:10.1016/j.biopsych.2014.05.022
- Dai, Z., Chen, Z., Ye, H., Zhou, L., Cao, L., Wang, Y., et al. (2009). Characterization of microRNAs in cephalochordates reveals a correlation between microRNA repertoire homology and morphological similarity in chordate evolution. *Evol. Dev.* 11 (1), 41–49. doi:10.1111/j.1525-142X.2008.00301.x
- Das, S. K., and Hoefler, G. (2013). The role of triglyceride lipases in cancer associated cachexia. *Trends Mol. Med.* 19 (5), 292–301. doi:10.1016/j.molmed.2013.02.006
- Davies, L., Spiller, D., White, M. R., Grierson, I., and Paraoan, L. (2011). PERP expression stabilizes active p53 via modulation of p53-MDM2 interaction in uveal melanoma cells. *Cell Death Dis.* 2 (3), e136. doi:10.1038/cddis.2011.19
- Dominguez, I., Sanz, L., Arenzana-Seisdedos, F., Diaz-Meco, M. T., Virelizier, J. L., Moscat, J., et al. (1993). Inhibition of protein kinase C zeta subspecies blocks the activation of an NF-kappa B-like activity in *Xenopus laevis* oocytes. *Mol. Cell. Biol.* 13 (2), 1290–1295. doi:10.1128/mcb.13.2.1290
- Ferreira, L. G. A., Nishino, F. A., Fernandes, S. G., Ribeiro, C. M., Hinton, B. T., Avellar, M. C. W., et al. (2022). Epididymal embryonic development harbors TLR4/NFkB signaling pathway as a morphogenetic player. *J. Reprod. Immunol.* 149, 103456. doi:10.1016/j.jri.2021.103456
- Gay, S., Bugeon, J., Bouchareb, A., Henry, L., Delahaye, C., Legeai, F., et al. (2018). MiR-2002 controls female fecundity by regulating medaka oogenesis. *PLoS Genet.* 14 (9), e1007593. doi:10.1371/journal.pgen.1007593
- Geula, S., Moshitch-Moshkovitz, S., Dominissini, D., Mansour, A. A., Kol, N., Salmon-Divon, M., et al. (2015). Stem cells. m6A mRNA methylation facilitates resolution of naive pluripotency toward differentiation. *Science* 347 (6225), 1002–1006. doi:10.1126/science.1261417
- Gilardelli, C. N., Pozzoli, O., Sordino, P., Matassi, G., and Cotelli, F. (2004). Functional and hierarchical interactions among zebrafish *vox/vent* homeobox genes. *Dev. Dyn.* 230 (3), 494–508. doi:10.1002/dvdy.20073
- Giraldez, A. J., Cinalli, R. M., Glasner, M. E., Enright, A. J., Thomson, J. M., Baskerville, S., et al. (2005). MicroRNAs regulate brain morphogenesis in zebrafish. *Science* 308 (5723), 833–838. doi:10.1126/science.1109020
- Giraldez, A. J., Mishima, Y., Rihel, J., Grocock, R. J., Van Dongen, S., Inoue, K., et al. (2006). Zebrafish MiR-430 promotes deadenylation and clearance of maternal mRNAs. *Science* 312 (5770), 75–79. doi:10.1126/science.1122689
- Goonasinghe, A., Luan, X. M., Hurlstone, A., and Garrod, D. (2012). Desmosomal cadherins in zebrafish epiboly and gastrulation. *BMC Dev. Biol.* 12, 1. doi:10.1186/1471-213x-12-1
- Halstead, M. M., Ma, X., Zhou, C., Schultz, R. M., and Ross, P. J. (2020). Chromatin remodeling in bovine embryos indicates species-specific regulation of genome activation. *Nat. Commun.* 11 (1), 4654. doi:10.1038/s41467-020-18508-3
- Hsu, S. D., Chu, C. H., Tsou, A. P., Chen, S. J., Chen, H. C., Hsu, P. W., et al. (2008). miRNome 2.0: genomic maps of microRNAs in metazoan genomes. *Nucleic Acids Res.* 36, D165–D169. doi:10.1093/nar/gkm1012
- Hug, C. B., Grimaldi, A. G., Kruse, K., and Vaquerizas, J. M. (2017). Chromatin architecture emerges during zygotic genome activation independent of transcription. *Cell* 169 (2), 216–228. e219. doi:10.1016/j.cell.2017.03.024
- Imai, Y., Gates, M. A., Melby, A. E., Kimelman, D., Schier, A. F., Talbot, W. S., et al. (2001). The homeobox genes *vox* and *vent* are redundant repressors of dorsal fates in zebrafish. *Development* 128 (12), 2407–2420. doi:10.1242/dev.128.12.2407
- Ivanova, I., Much, C., Di Giacomo, M., Azzi, C., Morgan, M., Moreira, P. N., et al. (2017). The RNA m(6)A reader YTHDF2 is essential for the post-transcriptional regulation of the maternal transcriptome and oocyte competence. *Mol. Cell* 67 (6), 1059–1067. e1054. doi:10.1016/j.molcel.2017.08.003
- Jin, Y., Liu, W., Xiang, Y., Zhang, W., Zhang, H., Jia, K., et al. (2020). Maternal miR-202-5p is required for zebrafish primordial germ cell migration by protecting small GTPase Cdc42. *J. Mol. Cell Biol.* 12 (7), 530–542. doi:10.1093/jmcb/mjz103
- Jørgensen, S., Baker, A., Møller, S., and Nielsen, B. S. (2010). Robust one-day *in situ* hybridization protocol for detection of microRNAs in paraffin samples using LNA probes. *Methods* 52 (4), 375–381. doi:10.1016/j.jmeth.2010.07.002
- Joseph, S. R., Pálfi, M., Hilbert, L., Kumar, M., Karschau, J., Ziburdaev, V., et al. (2017). Competition between histone and transcription factor binding regulates the onset of transcription in zebrafish embryos. *Elife* 6, e23326. doi:10.7554/eLife.23326
- Jukam, D., Shariati, S. A. M., and Skotheim, J. M. (2017). Zygotic genome activation in vertebrates. *Dev. Cell* 42 (4), 316–332. doi:10.1016/j.devcel.2017.07.026
- Kim, D., Langmead, B., and Salzberg, S. L. (2015). Hisat: A fast spliced aligner with low memory requirements. *Nat. Methods* 12 (4), 357–360. doi:10.1038/nmeth.3317
- Kimmel, C. B., Ballard, W. W., Kimmel, S. R., Ullmann, B., and Schilling, T. F. (1995). Stages of embryonic development of the zebrafish. *Dev. Dyn.* 203 (3), 253–310. doi:10.1002/aja.1002030302

- Kontur, C., Jeong, M., Cifuentes, D., and Giraldez, A. J. (2020). Ythdf m(6)A readers function redundantly during zebrafish development. *Cell Rep.* 33 (13), 108598. doi:10.1016/j.celrep.2020.108598
- Langley, A. R., Smith, J. C., Stemple, D. L., and Harvey, S. A. (2014). New insights into the maternal to zygotic transition. *Development* 141 (20), 3834–3841. doi:10.1242/dev.102368
- Lee, M. T., Bonneau, A. R., and Giraldez, A. J. (2014). Zygotic genome activation during the maternal-to-zygotic transition. *Annu. Rev. Cell Dev. Biol.* 30, 581–613. doi:10.1146/annurev-cellbio-100913-013027
- Lee, M. T., Bonneau, A. R., Takacs, C. M., Bazzini, A. A., DiVito, K. R., Fleming, E. S., et al. (2013). Nanog, Pou5f1 and SoxB1 activate zygotic gene expression during the maternal-to-zygotic transition. *Nature* 503 (7476), 360–364. doi:10.1038/nature12632
- Lee, R. C., Feinbaum, R. L., and Ambros, V. (1993). The *C. elegans* heterochronic gene lin-4 encodes small RNAs with antisense complementarity to lin-14. *Cell* 75 (5), 843–854. doi:10.1016/0092-8674(93)90529-y
- Liang, H. L., Nien, C. Y., Liu, H. Y., Metzstein, M. M., Kirov, N., Rushlow, C., et al. (2008). The zinc-finger protein Zelda is a key activator of the early zygotic genome in *Drosophila*. *Nature* 456 (7220), 400–403. doi:10.1038/nature07388
- Liu, G., Wang, W., Hu, S., Wang, X., and Zhang, Y. (2018). Inherited DNA methylation primes the establishment of accessible chromatin during genome activation. *Genome Res.* 28 (7), 998–1007. doi:10.1101/gr.228833.117
- Liu, R., Wang, X., Curtiss, C., Sheikh, M. S., and Huang, Y. (2020). Monoglyceride lipase mediates tumor-suppressive effects by promoting degradation of X-linked inhibitor of apoptosis protein. *Cell Death Differ.* 27 (10), 2888–2903. doi:10.1038/s41418-020-0549-5
- Lund, E., Liu, M., Hartley, R. S., Sheets, M. D., and Dahlberg, J. E. (2009). Deadenylation of maternal mRNAs mediated by miR-427 in *Xenopus laevis* embryos. *Rna* 15 (12), 2351–2363. doi:10.1261/rna.1882009
- Newport, J., and Kirschner, M. (1982). A major developmental transition in early *Xenopus* embryos: I. Characterization and timing of cellular changes at the midblastula stage. *Cell* 30 (3), 675–686. doi:10.1016/0092-8674(82)90272-0
- Nishikimi, A., Mukai, J., and Yamada, M. (1999). Nuclear translocation of nuclear factor kappa B in early 1-cell mouse embryos. *Biol. Reprod.* 60 (6), 1536–1541. doi:10.1095/biolreprod60.6.1536
- Nomura, D. K., Lombardi, D. P., Chang, J. W., Niessen, S., Ward, A. M., Long, J. Z., et al. (2011). Monoacylglycerol lipase exerts dual control over endocannabinoid and fatty acid pathways to support prostate cancer. *Chem. Biol.* 18 (7), 846–856. doi:10.1016/j.chembiol.2011.05.009
- Nowak, M., Köster, C., and Hammerschmidt, M. (2005). Perp is required for tissue-specific cell survival during zebrafish development. *Cell Death Differ.* 12 (1), 52–64. doi:10.1038/sj.cdd.4401519
- O'Brien, J. H., Hernandez-Lagunas, L., Artinger, K. B., and Ford, H. L. (2014). MicroRNA-30a regulates zebrafish myogenesis through targeting the transcription factor Six1. *J. Cell Sci.* 127 (10), 2291–2301. doi:10.1242/jcs.143677
- Pálfi, M., Joseph, S. R., and Vastenhouw, N. L. (2017). The timing of zygotic genome activation. *Curr. Opin. Genet. Dev.* 43, 53–60. doi:10.1016/j.cde.2016.12.001
- Pálfi, M., Schulze, G., Valen, E., and Vastenhouw, N. L. (2020). Chromatin accessibility established by Pou5f3, Sox19b and Nanog primes genes for activity during zebrafish genome activation. *PLoS Genet.* 16 (1), e1008546. doi:10.1371/journal.pgen.1008546
- Pshennikova, E. S., Tereshina, M. B., and Voronina, A. S. (2017). Expression of vox and vent mRNAs and encoded proteins in zebrafish embryos. *Stem Cell Investig.* 4, 60. doi:10.21037/sci.2017.06.05
- Qian, Y. C., Xie, Y. X., Wang, C. S., Shi, Z. M., Jiang, C. F., Tang, Y. Y., et al. (2020). Mkn2 deficiency induces teratozoospermia and male infertility through p53/PERP-mediated apoptosis in testis. *Asian J. Androl.* 22 (4), 414–421. doi:10.4103/aja.aja_76_19
- Reinhart, B. J., Slack, F. J., Basson, M., Pasquinelli, A. E., Bettinger, J. C., Rougvie, A. E., et al. (2000). The 21-nucleotide let-7 RNA regulates developmental timing in *Caenorhabditis elegans*. *Nature* 403 (6772), 901–906. doi:10.1038/35002607
- Richardson, J. C., Garcia Estrabot, A. M., and Woodland, H. R. (1994). XrelA, a *Xenopus* maternal and zygotic homologue of the p65 subunit of NF-kappa B. Characterisation of transcriptional properties in the developing embryo and identification of a negative interference mutant. *Mech. Dev.* 45 (2), 173–189. doi:10.1016/0925-4773(94)90031-0
- Robinson, M. D., McCarthy, D. J., and Smyth, G. K. (2010). edgeR: a Bioconductor package for differential expression analysis of digital gene expression data. *Bioinformatics* 26 (1), 139–140. doi:10.1093/bioinformatics/btp616
- Schier, A. F. (2007). The maternal-zygotic transition: Death and birth of RNAs. *Science* 316 (5823), 406–407. doi:10.1126/science.1140693
- Schulz, K. N., and Harrison, M. M. (2019). Mechanisms regulating zygotic genome activation. *Nat. Rev. Genet.* 20 (4), 221–234. doi:10.1038/s41576-018-0087-x
- Shi, Y., and Jin, Y. (2009). MicroRNA in cell differentiation and development. *Sci. China. C Life Sci.* 52 (3), 205–211. doi:10.1007/s11427-009-0040-5
- Siefert, J. C., Clowdus, E. A., and Sansam, C. L. (2015). Cell cycle control in the early embryonic development of aquatic animal species. *Comp. Biochem. Physiol. C. Toxicol. Pharmacol.* 178, 8–15. doi:10.1016/j.cbpc.2015.10.003
- Stoeckius, M., Grün, D., Kirchner, M., Ayoub, S., Torti, F., Piano, F., et al. (2014). Global characterization of the oocyte-to-embryo transition in *Caenorhabditis elegans* uncovers a novel mRNA clearance mechanism. *Embo J.* 33 (16), 1751–1766. doi:10.15252/embj.201488769
- Sun, H., Jiang, L., Luo, X., Jin, W., He, Q., An, J., et al. (2013). Potential tumor-suppressive role of monoglyceride lipase in human colorectal cancer. *Oncogene* 32 (2), 234–241. doi:10.1038/onc.2012.34
- Svoboda, P., and Flemr, M. (2010). The role of miRNAs and endogenous siRNAs in maternal-to-zygotic reprogramming and the establishment of pluripotency. *EMBO Rep.* 11 (8), 590–597. doi:10.1038/embor.2010.102
- Tadros, W., and Lipshitz, H. D. (2009). The maternal-to-zygotic transition: A play in two acts. *Development* 136 (18), 3033–3042. doi:10.1242/dev.033183
- Tang, F., Kaneda, M., O'Carroll, D., Hajkova, P., Barton, S. C., Sun, Y. A., et al. (2007). Maternal microRNAs are essential for mouse zygotic development. *Genes Dev.* 21 (6), 644–648. doi:10.1101/gad.418707
- Tatone, C., Amicarelli, F., Carbone, M. C., Monteleone, P., Caserta, D., Marci, R., et al. (2008). Cellular and molecular aspects of ovarian follicle ageing. *Hum. Reprod. Update* 14 (2), 131–142. doi:10.1093/humupd/dmm048
- Thisse, C., and Thisse, B. (2008). High-resolution *in situ* hybridization to whole-mount zebrafish embryos. *Nat. Protoc.* 3 (1), 59–69. doi:10.1038/nprot.2007.514
- Ulitsky, I., Shkumatava, A., Jan, C. H., Subtelny, A. O., Koppstein, D., Bell, G. W., et al. (2012). Extensive alternative polyadenylation during zebrafish development. *Genome Res.* 22 (10), 2054–2066. doi:10.1101/gr.139733.112
- Veil, M., Yampolsky, L. Y., Gruning, B., and Onichtchouk, D. (2019). Pou5f3, SoxB1, and Nanog remodel chromatin on high nucleosome affinity regions at zygotic genome activation. *Genome Res.* 29 (3), 383–395. doi:10.1101/gr.240572.118
- Wang, S. J., Li, X. D., Wu, L. P., Guo, P., Feng, L. X., Li, B., et al. (2021). MicroRNA-202 suppresses glycolysis of pancreatic cancer by targeting hexokinase 2. *J. Cancer* 12 (4), 1144–1153. doi:10.7150/jca.43379
- Wei, C., Salichos, L., Wittgrove, C. M., Rokas, A., and Patton, J. G. (2012). Transcriptome-wide analysis of small RNA expression in early zebrafish development. *Rna* 18 (5), 915–929. doi:10.1261/rna.029090.111
- Winata, C. L., Łapiński, M., Pryszcz, L., Vaz, C., Bin Ismail, M. H., Nama, S., et al. (2018). Cytoplasmic polyadenylation-mediated translational control of maternal mRNAs directs maternal-to-zygotic transition. *Development* 145 (1), dev159566. doi:10.1242/dev.159566
- Xu, C., Fan, Z. P., Müller, P., Fogley, R., DiBiase, A., Trompouki, E., et al. (2012). Nanog-like regulates endoderm formation through the Mxt2-Nodal pathway. *Dev. Cell* 22 (3), 625–638. doi:10.1016/j.devcel.2012.01.003
- Yang, C., Yao, C., Tian, R., Zhu, Z., Zhao, L., Li, P., et al. (2019). miR-202-3p regulates sertoli cell proliferation, synthesis function, and apoptosis by targeting LRP6 and cyclin D1 of wnt/ β -catenin signaling. *Mol. Ther. Nucleic Acids* 14, 1–19. doi:10.1016/j.omtn.2018.10.012
- Yang, X., Zhang, D., Liu, S., Li, X., Hu, W., Han, C., et al. (2018). KLF4 suppresses the migration of hepatocellular carcinoma by transcriptionally upregulating monoglyceride lipase. *Am. J. Cancer Res.* 8 (6), 1019–1029.
- Yartseva, V., and Giraldez, A. J. (2015). The maternal-to-zygotic transition during vertebrate development: A model for reprogramming. *Curr. Top. Dev. Biol.* 113, 191–232. doi:10.1016/bs.ctdb.2015.07.020
- Yuan, F., Pan, X., Zeng, T., Zhang, Y. H., Chen, L., Gan, Z., et al. (2020). Identifying cell-type specific genes and expression rules based on single-cell transcriptomic atlas data. *Front. Bioeng. Biotechnol.* 8, 350. doi:10.3389/fbioe.2020.00350
- Zhang, J., Liu, Z., Lian, Z., Liao, R., Chen, Y., Qin, Y., et al. (2016). Monoacylglycerol lipase: A novel potential therapeutic target and prognostic indicator for hepatocellular carcinoma. *Sci. Rep.* 6, 35784. doi:10.1038/srep35784
- Zhang, M., Skirkanich, J., Lampson, M. A., and Klein, P. S. (2017). Cell cycle remodeling and zygotic gene activation at the midblastula transition. *Adv. Exp. Med. Biol.* 953, 441–487. doi:10.1007/978-3-319-46095-6_9
- Zhang, Y., Pan, Q., and Shao, Z. (2020). Tumor-suppressive role of microRNA-202-3p in hepatocellular carcinoma through the kdm3a/HOXA1/MEIS3 pathway. *Front. Cell Dev. Biol.* 8, 556004. doi:10.3389/fcell.2020.556004
- Zhao, B. S., Wang, X., Beadell, A. V., Lu, Z., Shi, H., Kuuspalu, A., et al. (2017). m(6)A-dependent maternal mRNA clearance facilitates zebrafish maternal-to-zygotic transition. *Nature* 542 (7642), 475–478. doi:10.1038/nature21355



OPEN ACCESS

EDITED BY

Silvia L. López,
CONICET Instituto de Biología Celular y
Neurociencias, Argentina

REVIEWED BY

Hiroshi Hamada,
RIKEN Center for Biosystems Dynamics
Research, Japan
Simone Probst,
University of Freiburg, Germany

*CORRESPONDENCE

Andrew C. Nelson,
A.Nelson.1@warwick.ac.uk

†PRESENT ADDRESS

Stephen J. Cutty,
Institute of Clinical Sciences, Imperial
College London, Hammersmith
Hospital Campus, London,
United Kingdom

SPECIALTY SECTION

This article was submitted to
Morphogenesis and Patterning,
a section of the journal
Frontiers in Cell and Developmental
Biology

RECEIVED 30 June 2022

ACCEPTED 28 July 2022

PUBLISHED 25 August 2022

CITATION

Talbot CD, Walsh MD, Cutty SJ,
Elsayed R, Vlachaki E, Bruce AEE,
Wardle FC and Nelson AC (2022),
Eomes function is conserved between
zebrafish and mouse and controls left-
right organiser progenitor gene
expression via interlocking
feedforward loops.
Front. Cell Dev. Biol. 10:982477.
doi: 10.3389/fcell.2022.982477

COPYRIGHT

© 2022 Talbot, Walsh, Cutty, Elsayed,
Vlachaki, Bruce, Wardle and Nelson.
This is an open-access article
distributed under the terms of the
[Creative Commons Attribution License
\(CC BY\)](https://creativecommons.org/licenses/by/4.0/). The use, distribution or
reproduction in other forums is
permitted, provided the original
author(s) and the copyright owner(s) are
credited and that the original
publication in this journal is cited, in
accordance with accepted academic
practice. No use, distribution or
reproduction is permitted which does
not comply with these terms.

Eomes function is conserved between zebrafish and mouse and controls left-right organiser progenitor gene expression via interlocking feedforward loops

Conor D. Talbot¹, Mark D. Walsh¹, Stephen J. Cutty^{2†},
Randa Elsayed³, Eirini Vlachaki¹, Ashley E. E. Bruce⁴,
Fiona C. Wardle² and Andrew C. Nelson^{1*}

¹School of Life Sciences, Gibbet Hill Campus, University of Warwick, Coventry, United Kingdom,

²Randall Centre for Cell and Molecular Biophysics, New Hunt's House, Guy's Campus, King's College London, London, United Kingdom, ³Warwick Medical School, Gibbet Hill Campus, University of Warwick, Coventry, United Kingdom, ⁴Department of Cell and Systems Biology, University of Toronto, Toronto, ON, Canada

The T-box family transcription factor Eomesodermin (Eomes) is present in all vertebrates, with many key roles in the developing mammalian embryo and immune system. Homozygous Eomes mutant mouse embryos exhibit early lethality due to defects in both the embryonic mesendoderm and the extraembryonic trophoblast cell lineage. In contrast, zebrafish lacking the predominant Eomes homologue A (Eomesa) do not suffer complete lethality and can be maintained. This suggests fundamental differences in either the molecular function of Eomes orthologues or the molecular configuration of processes in which they participate. To explore these hypotheses we initially analysed the expression of distinct Eomes isoforms in various mouse cell types. Next we compared the functional capabilities of these murine isoforms to zebrafish Eomesa. These experiments provided no evidence for functional divergence. Next we examined the functions of zebrafish Eomesa and other T-box family members expressed in early development, as well as its paralogue Eomesb. Though Eomes is a member of the Tbr1 subfamily we found evidence for functional redundancy with the Tbx6 subfamily member Tbx16, known to be absent from eutherians. However, Tbx16 does not appear to synergise with Eomesa cofactors Mixl1 and Gata5. Finally, we analysed the ability of Eomesa and other T-box factors to induce zebrafish left-right organiser progenitors (known as dorsal forerunner cells) known to be positively regulated by *vgl14l*, a gene we had previously shown to be repressed by Eomesa. Here we demonstrate that Eomesa indirectly upregulates *vgl14l* expression via interlocking feedforward loops, suggesting a role in establishment of left-right asymmetry. Conversely, other T-box factors could not similarly induce left-right organiser progenitors. Overall these findings demonstrate conservation of Eomes molecular function and participation in similar processes, but differential requirements across evolution due to additional co-expressed T-box factors in teleosts, albeit with markedly different

molecular capabilities. Our analyses also provide insights into the role of *Eomesa* in left-right organiser formation in zebrafish.

KEYWORDS

Eomes, T-box, *vgll4l*, left-right organiser, zebrafish

Introduction

T-box transcription factors (TFs) are an ancient family of transcriptional regulators with diverse roles in development and disease (Papaioannou, 2014). *Eomesodermin* (*Eomes*) belongs to the *Tbr1* subfamily of T-box TFs, consisting of similarly sized N- and C-terminal domains (NTD and CTD) flanking a central DNA binding domain known as the T-box. Amongst the species where *Eomes* is best studied are mouse and zebrafish (Probst and Arnold, 2017). Mice have a single copy of *Eomes*, whereas zebrafish owing to the whole genome duplication in the teleost lineage have two paralogous genes, *eomesa* and *eomesb* (Glasauer and Neuhauss, 2014). During mouse embryogenesis *Eomes* plays essential roles in trophoblast (Russ et al., 2000; Strumpf et al., 2005), in the primitive streak for epithelial-to-mesenchymal transition, mesoderm migration and specification of definitive endoderm and cardiac mesoderm during gastrulation (Arnold et al., 2008a; Costello et al., 2011). Additionally *Eomes* acts in the visceral endoderm to control anterior-posterior axis identity (Nowotschin et al., 2013) and later has key functions in cortical neuron progenitors (Arnold et al., 2008b). It is also expressed in progenitors of the left-right organiser known in mammals as the node, and is required for correct formation of the node suggesting a potential role in establishing left-right asymmetry (Arnold et al., 2008a; Costello et al., 2011). In zebrafish *Eomesa* also plays multiple roles in mesendoderm formation. It acts in conjunction with *Hwa* to control expression of Nodal pathway ligands *ndr1/2*, leading to mesendoderm induction (Xing et al., 2022). *Eomesa* can also induce ectopic endoderm if overexpressed with essential interacting factors (Bjornson et al., 2005), and is sufficient to induce dorsal mesoderm markers and represses ectoderm gene expression in early development (Bruce et al., 2003; Nelson et al., 2014). Furthermore, *Eomesa* is sufficient to induce progenitors of the left-right organiser, known as dorsal forerunner cells (DFCs) in zebrafish (Bjornson et al., 2005). However, we previously found that *Eomesa* represses expression of the transcriptional cofactor *vgll4l* (Nelson et al., 2014), a key positive regulator of DFC proliferation, survival and function (Fillatre et al., 2019). Here we further investigate these paradoxical findings.

Mouse *Eomes* and zebrafish *eomesa* display similar expression domains during early development (Russ et al., 2000; Mione et al., 2001; Pearce et al., 2003; Takizawa et al., 2007; Du et al., 2012; Takizawa et al., 2014). However, surprisingly endoderm, cardiac mesoderm and axial patterning proceed normally in *eomesa* loss-of-function mutants (Du et al., 2012). This observation cannot be explained simply by rescue by

eomesb, which is not co-expressed with *eomesa* in early development, nor is it induced in *eomesa* mutant embryos (Vesterlund et al., 2011; Nelson et al., 2014). The extent to which *Eomes* functional activities are conserved between zebrafish and mouse remains unknown.

One possibility is that these distinct loss-of-function phenotypes could potentially be due to functional diversification during evolution. The process of alternative splicing (AS) allows a single gene to give rise to multiple isoforms with different functional characteristics. The prevalence of AS has expanded across evolutionary time, allowing increased proteome diversity out of proportion with gene number (Keren et al., 2010). For example, only ~25% of nematode genes have alternative isoforms compared to >90% in human (Wang et al., 2008; Ramani et al., 2011). AS leading to functional diversification may account for altered functions of *Eomes* between species. However, it is also possible that differential requirement for *Eomes* is due to functional redundancy owing to altered complements of T-box factors in different vertebrate evolutionary lineages. The most ancient T-box factor *Brachyury* (otherwise known as *Tbxt*) is present in several non-metazoan lineages, however, the T-box family is considerably expanded in Metazoa, reflecting its developmental importance (Sebe-Pedros et al., 2013). Additionally, the complement of T-box factors has varied across vertebrate evolution, with gain or loss of individual factors in certain lineages. For example, the *Tbx6* subfamily member *tbx16* is present in fish, frogs, birds, marsupials and monotremes but lost in placental mammals (Ahn et al., 2012). The T-box domain itself directly binds DNA in a sequence-specific manner. Genome-wide profiling of multiple T-box factors including *Eomes*, *Tbx16*, *Tbx6* and *Brachyury* in zebrafish, mice, *Xenopus* and human has revealed they bind most frequently to variants of an eight to nine base pair core consensus of (T)TVRCACHT, interchangeably allowing occupancy of different T-box factors at the same genomic sites e.g. (Morley et al., 2009; Teo et al., 2011; Nelson et al., 2012; Gentsch et al., 2013; Lolas et al., 2014; Nelson et al., 2014; Faial et al., 2015; Tsankov et al., 2015; Windner et al., 2015; Gentsch et al., 2017; Nelson et al., 2017). T-box factors therefore often exhibit redundancy through regulation of the same target genes through the same *cis*-regulatory modules.

We therefore sought to answer three key questions: 1. Are zebrafish and mouse *Eomes* genes functionally equivalent? 2. What is the basis for the observed differences in severity of loss-of-function phenotypes between mouse and zebrafish? and; 3. How can *Eomesa* promote DFC gene expression while repressing the key DFC regulator *vgll4l*?

Our analyses suggest that the molecular function of *Eomes* is highly conserved throughout vertebrate evolution. Our data also reveal that while alternative splicing of mouse *Eomes* transcript occurs at exon 6, functionally the encoded proteins were virtually indistinguishable. We found that *Eomesa* and *Tbx16* share overlapping functions and capabilities in the presumptive endoderm, suggesting that phenotypic rescue by *Tbx16* may explain *eomesa* mutant viability. Finally, we found that *Eomesa* acts within interlocking feedforward loops to both repress *vgl4l* and activate it indirectly via the essential SOX family transcription factor Sox32. Our results therefore advance our understanding of T-box factor functional conservation during early vertebrate embryogenesis, and regulatory networks controlling left-right organiser progenitor gene expression.

Materials and methods

Zebrafish strains

AB and mutant zebrafish were reared as described (Westerfield, 2000). For *eomesa* mutant experiments eggs from homozygous *eomesa*^{fh105/fh105} females were *in vitro* fertilized with *eomesa*^{+/fh105} sperm yielding a mixture of *Meomesa* and *MZeomesa* mutant embryos. Since previous studies have revealed no differences in endodermal or mesodermal expression between *Meomesa* and *MZeomesa* mutant embryos we did not distinguish between them in this study (Du et al., 2012; Xu et al., 2014). All zebrafish studies complied fully with the United Kingdom Animals (Scientific Procedures) Act 1986 as implemented by King's College London, The University of Warwick, or were in accordance with the policies of the University of Toronto Animal Care Committee.

Cloning for *in vitro* production of mRNAs and mammalian expression vectors

Full length *tbx16* and *eomesb* open reading frames were cloned with C-terminal myc tags into XhoI and XbaI sites in pCS2+ by PCR from zebrafish cDNA using the following primers: *tbx16-myc* CAT ACTCGAGATGCAGGCTATCAGAGACCT and CGCGTCTAG ACTACAGATCCTCTTCTGAGATGAGTTTTTGTTCCTCCAGC ACGAGTATGAGAAAA; *eomesb-myc* ATATCTCGAGATGCC CGGAGAAGGATCCAG and GCGCTCTAGACTACAGATCCT CTTCTGAGATGAGTTTTTGTTCGCTGCTGGTGTAGAAGG CGTA. Full length *gata5* cDNA with a C-terminal HA tag was similarly cloned into pCS2+ EcoRI and XhoI sites using primers CGCCGAATTCATGTATTCGAGCCTGGCTTT and AATGCT CGAGTCAAGCGTAATCTGGAACATCGTATGGGTACGCTT GAGACAGAGCACACC. *Eomes* cloning into pCS2+ was performed between EcoRI and XhoI sites. pCS2+*eomesa*N320K was produced by PCR mutagenesis of the wild type construct

using AAAGTGAAGCTAACCAACAAGAAAGGAGCAAAT AACAACAAT and TCCGAAAGATATTTCTTGTCT followed by recircularization. *Eomesa* ΔCTD was similarly produced using the following primers TAAGAACTGCTTTTCAAGATCCTTTAT CAATCC and CGAATCATAATTGTCCCTGAA. The ΔNTD mutation was produced by removing the EcoRI/BstEII fragment from pCS2+*eomesa* and replacing with the EcoRI/BstEII fragment produced by PCR from pCS2+*eomesa* with primer pair GCCCTC GAATTCACAGTTAAGAATGGCGCGGGCGC and CCCGCA GGTCACCCACTTTCCGCCCTGAAATCTCCA.

mRNA, morpholinos and microinjections

All capped mRNA were synthesized from plasmids encoding proteins of interest in pCS2+ NotI linearization followed by SP6 transcription as described (Bruce et al., 2003), with the exception *tbxta* which was produced from pSP64T as described (Marcellini et al., 2003). mRNA quantities for T-box factors were scaled in order to inject equimolar amounts of each mRNA per embryo. One-cell stage embryos were injected with the following quantities: *eomesa* – 400pg; *EomesΔVR* – 410 pg; *EomesFL* – 420 pg; *eomesaΔNTD* – 308 pg; *eomesaΔCTD* – 285 pg; *eomesa*N320K – 400 pg; *eomesb-myc* – 286 pg, *tbx16-myc* – 217 pg; *tbxta* – 223 pg; *gata5-HA* – 140 pg; *mixl1* – 200 pg. For *Tbx16* knockdown one-cell stage embryos were injected with, 0.5 pmol of a previously characterized *tbx16* morpholino (GeneTools) (Bisgrove et al., 2005).

In vitro protein production

Unlabelled *in vitro* translated protein was produced using rabbit reticulocyte lysates according to manufacturer's protocol (Promega).

Northern blot

Total RNA was extracted from specified cell types using Rneasy Mini Kits (QIAGEN), and polyA selected using Oligotex mRNA Mini Kits (QIAGEN). 500ng polyA + RNA per lane was size fractionated on a 1.5% agarose/MOPS gel, transferred onto Hybond N membranes (GE Healthcare), and probed with ³²P-random-primed 1 kb XmaI-EcoRV cDNA fragment corresponding to the exon 1–4T-box region.

Western blot

Cell lysates were prepared using radioimmunoprecipitation assay (RIPA) buffer, subjected to SDS-polyacrylamide gel

electrophoresis and transferred onto polyvinylidene difluoride membranes. Membranes were blocked with 5% milk powder in Tris-buffered saline with Tween 20, incubated in primary antibodies overnight including rabbit anti-Eomes CTD (Abcam, ab23345, 1:2,000), rabbit anti-Eomes NTD (Santa Cruz, sc-98555, 1:1,000) and rat anti-Eomes (eBioscience, 14-4,876, 1:1,000). Secondary antibodies were donkey anti-rabbit horseradish peroxidase (GE Healthcare NA934, 1:2,000) and goat anti-rat horseradish peroxidase (GE Healthcare NA935, 1:2,000). Blots were developed by chemiluminescence using Amersham ECL Prime Detection Reagent (GE Healthcare).

Embryonic stem cell differentiation

Wild type (+), *Eomes*^{null/null} (null), feeder-depleted ESCs were cultured in DMEM (ThermoFisher) with 15% FCS, 1% non-essential amino acids, 0.1 mM β -mercaptoethanol and 1,000 U/ml recombinant leukaemia inhibitory factor (Millipore). For differentiation ESCs were resuspended at 1×10^4 cells/ml in DMEM (ThermoFisher) with 15% FCS, 1% non-essential amino acids, 0.1 mM β -mercaptoethanol in hanging drops (10 μ L) plated on the inside lids of bacteriological dishes. After 48 h embryoid bodies were transferred in 10 ml medium to 10 cm bacteriological dishes and RNA extracted at the appropriate timepoints.

P19Cl6 cell culture and differentiation

P19Cl6 embryonal carcinoma cells were cultured in α -MEM (ThermoFisher) supplemented with 10% FCS. To induce differentiation, cells were seeded at 3.7×10^5 cells/6 cm dish in media containing 1% DMSO (Sigma) and RNA harvested after 72 h.

Cytotoxic T-cell lymphocyte, neomycin- and hygromycin B-resistant STO fibroblasts (SNH) and HeLa cell culture

CTLL cells derived from the ATCC TIB-214 line were maintained at 10^4 – 10^5 cells per ml in complete T cell medium supplemented with IL-2. SNH fibroblasts and HeLa cells were maintained on 0.1% gelatin coated dishes in DMEM supplemented with 10% bovine calf serum (Hyclone).

Reverse transcription–polymerase chain reaction

Cytoplasmic RNA was produced as previously described (Eggermont and Proudfoot, 1993). Total RNA was produced using Rneasy Mini Kits according to manufacturers protocol (QIAGEN). RT-PCR was performed using OneStep RT-PCR Kit

(QIAGEN) using the following primers: Total *Eomes*–TGTTTTCGTGGAAGTGTTCTGGC and AGGTCTGAGTCTTGGAAGGTTTCATTC; *Eomes* exon 4–6 to distinguish FL and Δ VR isoforms ATCGTGGAAGTGACAGGACG and CGGGAAGAAGTTTTGAACGCC; Gapdh–TGCACCACCAACTGCTTAGC and GGCATGGAC TGTGGTCATGAG; *Eomes* start codon to Δ CTD 3' UTR–ATATCTCGAGATGCAGTTGGGAGAGCAGCTC and TGGGCTCGAAGATGAAACTC; *HBB* exon 2 to *Eomes* exon 6 – GCACGTGGATCCTGAGAACT and CGGGAAGAAGTTTGAACGCC. For nested PCR to test exon 5–6 splicing association with the long *Eomes* 3' UTR the initial primer pair used was ATCGTGGAAGTGACAGAGGACG and CAAGTACGGAGGCAGCTGAG.

Whole-mount embryo staining

Whole-mount *in situ* hybridization (WISH) of zebrafish embryos were performed as described (Jowett and Lettice, 1994). Anti-sense riboprobes for *noto* (Talbot et al., 1995), *chrd* (Miller-Bertoglio et al., 1997), *vgl14l* (Nelson et al., 2014), *zic3* (Grinblat and Sive, 2001), *mixl1* (Alexander et al., 1999) and *sox32* (Dickmeis et al., 2001) were produced as described. Blinding and randomisation was performed prior to categorical scoring of WISH embryos to prevent bias.

Cloning and mutagenesis to test eomes exon 6 splice sequences

Clones to test the splicing efficiency at *Eomes* exon 6 were generated by cloning PCR products using primers ACGGCAATTGGCCTCGAACATTCTTGCTTC and CCAGCCATCACTTTGTCAAAGGTGGAAGGCAAAAG into MfeI-BstXI sites of the human *HBB* gene (GenBank accession no. U01317) within a previously described TAT-inducible expression vector (Ashe et al., 1997). Mutation of splicing sequences for the Δ VR and FL *Eomes* isoforms were introduced by PCR using primers: Δ VR – CATGTA CACGGCTTCAGAAAACGACAGGTTAACGCCAAGTCCGAC GGATTCCCCTCGATCCCATCAGATTGTCCCTGG and CTA CAATATAAAGAGAGACACTTAAAAATAAAAAACAACCT CACGTTGTCCCCAAACAAGCTGCCTCCAGAAGC; FL–CA TGTACACGGCTTCAGAAAATGACAGGTTAACTCCA TCTC CCACGGATTCCCC and GGACATTATATACACCGCCTCTTA TATTTTACACCAACCCTCACGTTGTCCCCAAACAAGCTG CCTCCAGAAGC followed by recircularization of the resulting PCR products. Deletion of the VR was similarly performed using primers ATCCCATCAGATTGTCCCTGGA and CTACAATATAAAGAGAGACACTTAAAAATAAAAAACAACCTCACGTTGTCCCCAAACAAGC TGCCCTCCAGAAGC. *HBB* plasmids were co-transfected with a plasmid expressing the HIV

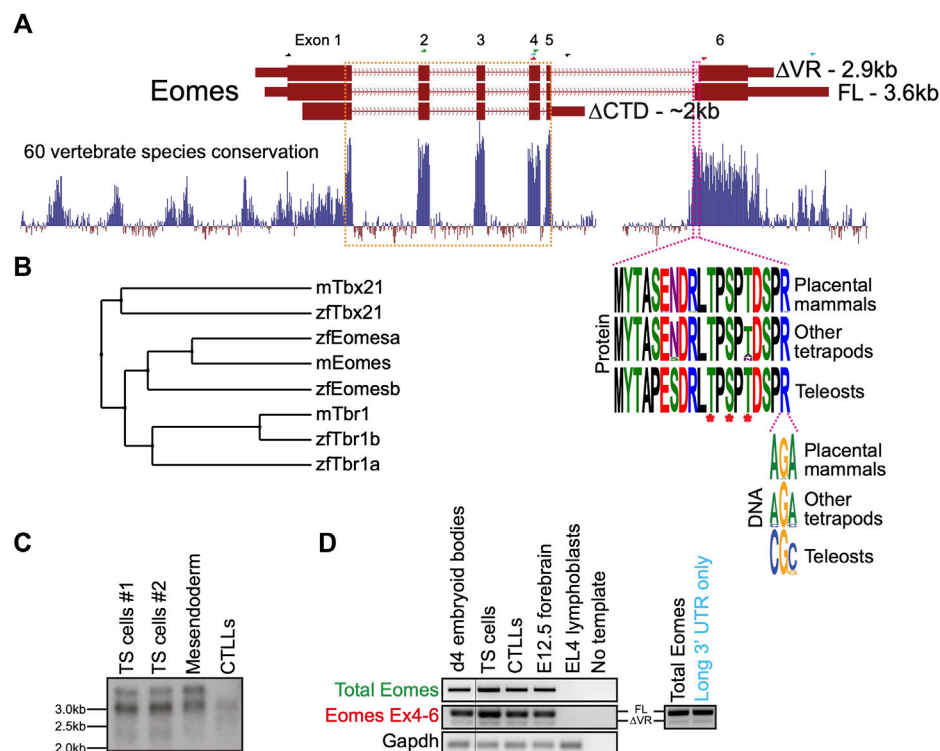


FIGURE 1

Mouse *Eomes* has multiple isoforms, including a mammalian-specific alternative splicing event. **(A)** Gene model with conservation track and sequence logos for variant region. All transcripts are Ensembl version 107 annotations - ΔVR transcript is ENSMUST00000111763; FL transcript is ENSMUST00000035020; ΔCTD transcript is ENSMUST00000150633. Annotated transcript sizes are indicated, as well as amino acid conservation of the VR between placental mammals, other tetrapods and teleosts, and the variation within the terminal VR arginine codon. The VR is defined by the amino acids present in ENSMUST00000035020 (encoded by ENSMUST00000035020) that are absent from ENSMUST00000107393 (encoded by ENSMUST00000111763). The T-box is outlined in orange and the VR in pink. Asterisks indicate known phosphorylated amino acid residues. RT-PCR primer pairs are indicated as half arrows and colour-coded as follows: black—to establish connectivity between the annotated start codon and ΔCTD isoform 3' UTR; green—to assess total *Eomes* through amplification of exon 2–4; blue—to amplify *Eomes* cDNA between exon 4 and the distal 3' UTR; red—to assess alternate splicing at exon 6. **(B)** BLOSUM62 average distance evolutionary tree of the Tbr1 subfamily showing relationships between mouse and zebrafish genes. **(C)** Northern blot showing *Eomes* transcripts in different cell types using a probe against the T-box. Data for two independent trophoblast stem (TS) cell lines are shown. Mesoderm is P19Cl6 cells after 4 days of DMSO induced differentiation. CTLLs are IL-2-dependent T-cell lymphocytes derived from ATCC TIB-214. **(D)** RT-PCR showing relative levels of FL and ΔVR isoforms (left), and nested PCR showing FL/ΔVR ratio for long 3' UTR transcripts (right). Day 4 differentiated embryoid bodies contain cells mimicking embryonic endoderm. CTLLs are IL-2-dependent T-cell lymphocytes derived from ATCC TIB-214. EL4 cells are a negative control for *Eomes* expression. *Gapdh* is a loading control. Locations of primer pairs used for RT-PCR are shown in panel A and the text colour-coded accordingly. Nested PCR to analyse exon 6 splicing in transcripts containing the long 3' UTR was performed using the blue primer pair in panel A, followed by the red primer pair.

transactivator protein TAT (Adams et al., 1988), into HeLa cells using Lipofectamine 2000 according to manufacturers protocol (ThermoFisher).

Conservation analysis

The Tbr1 subfamily Gene Tree was generated by Ensembl (Yates et al., 2016). *Eomes* conservation measurements (*phyloP*) across 60 vertebrate species were visualized in UCSC Genome Browser (<http://genome.ucsc.edu/>) (Karolchik et al., 2004; Speir et al., 2016). Sequence logos of the *Eomes* variant region in placental mammals, other tetrapods and teleosts were based on alignment of the same

60 vertebrate species and visualized using WebLogo (Crooks et al., 2004).

Full-length protein alignments were performed using Clustal Omega (Goujon et al., 2010; Sievers et al., 2011; McWilliam et al., 2013) and visualized using Jalview (Waterhouse et al., 2009). BLOSUM62 average distance gene tree was also produced using Jalview.

Single-cell ribonucleic acid sequencing analysis

Single-cell (sc) RNA sequencing count data of zebrafish embryonic cells from Wagner et al (2018) was downloaded

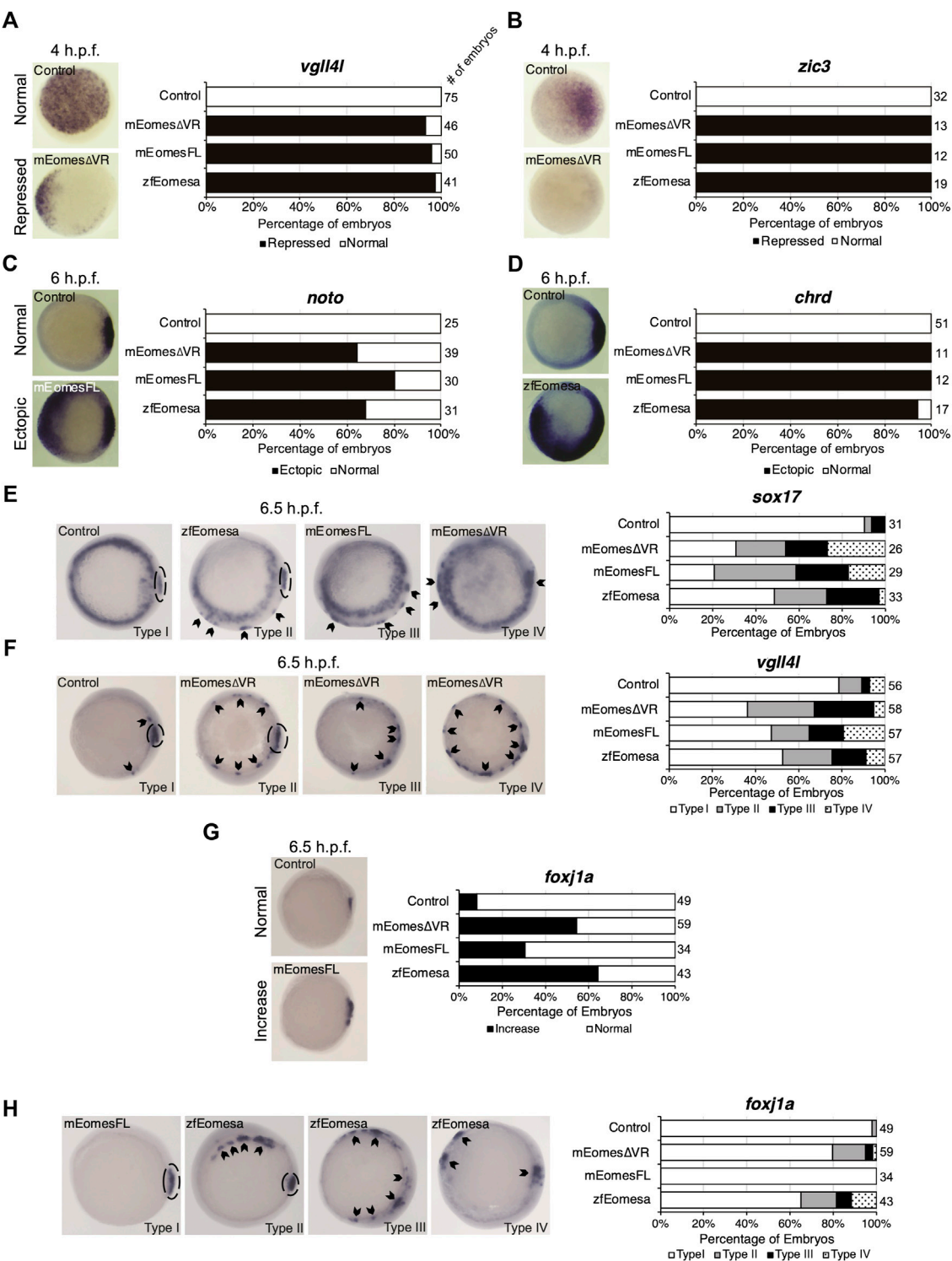


FIGURE 2 Both FL and ΔVR isoforms of mouse Eomes are functionally equivalent to zebrafish Eomesa in the early embryo. WISH analysis of ectoderm markers *vgll4l* and *zic3* in mid/late blastulas (4 h.p.f.) embryos (A,B), organiser markers *noto* and *chrd* (C,D) in early gastrulas (6 h.p.f.), or DFC markers *sox17*, *vgll4l* and *foxj1a* (E–H) in early/mid gastrulas (6.5 h.p.f.). Embryos have been injected at the 1 cell stage to overexpress either mouse EomesFL, EomesΔVR or zebrafish Eomesa. N = 2. Total numbers of embryos scored per condition are indicated. Representative images of expression patterns per gene per category are shown. (A–D) Animal views; dorsal to the right. (E–H) Vegetal views; dorsal to the right. Panel G indicates the percentage of embryos with greater intensity of dorsal *foxj1a* WISH staining, while panel H indicates percentages of (Continued)

FIGURE 2

embryos with ectopic *foxj1a* staining. Type I—wild type expression; Type II—ectopic dorsolateral expression with clear primary dorsal DFC cluster; Type III—dorsolateral expression with no defined primary cluster; Type IV—ectopic expression in the ventral margin. Dotted ovals indicate primary DFC clusters. Arrowheads indicate ectopic DFC marker expression.

from GEO (Barrett et al., 2013; Wagner et al., 2018). Raw UMI-filtered count data in CSV format from 6 h post fertilisation (h.p.f.) embryos (GSM3067190) was imported in to R v3.6.2 and analysed using Seurat v3.0.2 (Stuart et al., 2019). Cells with less than 200 features, and features detected in <3 cells were discarded. The remaining count data were then normalised via SCTransform v0.2.1 (Hafemeister and Satija, 2019) with mitochondrial genes passed as a regression variable. Genes were clustered using UMAP utilising the R package uwot v0.1.5 (Melville et al., 2020), with the following parameters: *dims* = 1:30, *n.neighbors* = 5, *min.dist* = 0.001. To assign cell identities to clusters FindAllMarkers was called in Seurat using default parameters. For consistency with the original source publication of the 6 h.p.f. scRNA-seq data we cross-referenced the marker genes for each cluster in the present study with the clusters defined by Wagner et al. (2018). Significant positive markers in each of the 14 clusters defined by our analyses in Seurat were overlapped with the top 20 markers for each identity defined by Wagner et al. (2018). Cell identities were then assigned based on maximum concordance with markers defined by Wagner et al. (2018).

Results

Eomes isoforms, conservation and expression

In mouse the three annotated *Eomes* transcripts give rise to three structurally distinct isoforms including the full length (FL) product, a splice variant having an alternative splice acceptor site within exon 6 leading to loss of a 19 amino acid variant region (Δ VR), and a transcript with an alternative mRNA 3' cleavage site leading to loss of exon 6 and its encoded CTD (Δ CTD) (Figure 1A). The highly conserved VR sequence is known to be phosphorylated at three amino acid residues in mouse spleen and kidney (Figure 1A) (Huttlin et al., 2010). The internal exon 6 splicing event emerged in the tetrapod lineage through a synonymous single nucleotide change in an arginine codon (CG>AG) introducing a splice acceptor sequence.

Because the Δ CTD transcript annotation has an incomplete 5' end, it remains unclear whether it encodes the entire NTD. However, our RT-PCR analysis using primers located in the Δ CTD 3' UTR and at the FL/ Δ VR start codon suggests that exon 1 coding information is intact (not shown). The CTD encoded by exon 6 has been shown to function in transcriptional activation

(Picozzi et al., 2009), suggesting that the Δ CTD isoform is likely to be functionally compromised in comparison to FL and Δ VR isoforms. Consistent with this, the CTD is more highly conserved than the NTD (Figure 1A). Functional differences between FL and Δ VR isoforms, however, are yet to be examined. Both *eomesa* transcripts identified in zebrafish encode the same protein (Bruce et al., 2003). Relatively little is known about the single annotated zebrafish *eomesb* transcript, which appears to be more divergent from the ancestral gene (Figure 1B).

Murine *Eomes* is expressed in numerous cell types including trophoblast stem cells (TSCs), mesendoderm, and T lymphocytes. To identify *Eomes* transcripts we initially performed Northern blot analysis (Figure 1C). Transcript sizes corresponding to all three annotated isoforms were detectable but the Δ CTD transcript was underrepresented. The FL and Δ VR annotations display different 3' UTR lengths. To test whether the two distinct upper bands detected by Northern blot correspond to alternative exon 6 splicing events or merely different UTR lengths we next performed nested PCR (Figure 1D). We found that the long 3' UTR is associated with both the FL and Δ VR coding isoforms. Strikingly, the ratio of FL/ Δ VR is similar for both total *Eomes* and the long 3' UTR transcripts. The abundance of the different coding transcripts therefore appears to be independent of UTR length. Further analysis through cloning *Eomes* intron5/exon6 to replace intron2/exon3 of the human *HBB* gene in an expression construct followed by transfection into HeLa cells revealed that the ratio of FL/ Δ VR splicing is consistent with the wild type *Eomes* gene, suggesting that the low levels of the Δ VR isoform are due to weaker splicing consensus sequences, thus favouring the FL isoform (Supplementary Figure S1). However, analysis of *Eomes* proteins by Western blot indicates that various N-terminal truncations occur which cannot be accounted for by the annotated coding transcripts (Supplementary Figure S2). We conclude that FL is clearly the most abundant of the three annotated coding isoforms. Importantly, this predominant isoform expressed by mouse cells corresponds to the single *eomesa* isoform in zebrafish.

Both mouse full length and Δ VR isoforms are functionally equivalent to zebrafish *eomesa* in early development

Zebrafish *eomesa* loss of function causes less severe phenotypes compared with the dramatic defects observed in

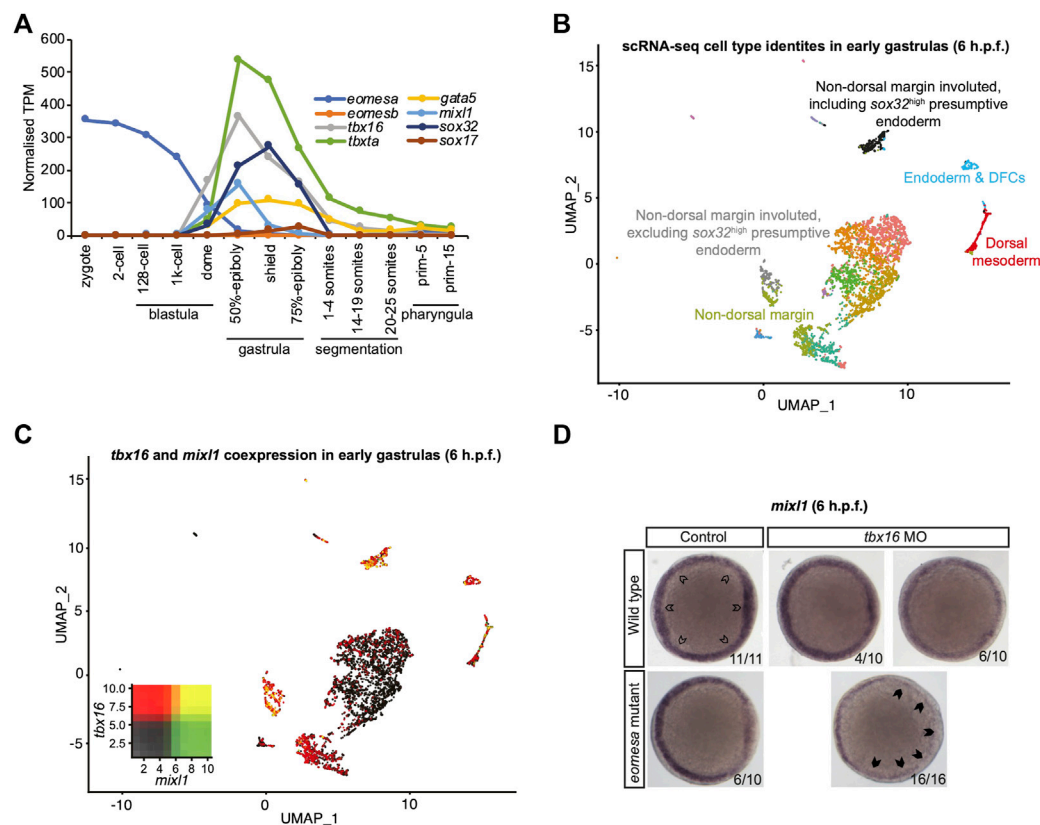


FIGURE 3

Eomes and *Tbx16* are redundantly required for *mixl1* expression in the presumptive endoderm. (A) Timing of expression of T-box factors (*eomesa*, *eomesb*, *tbx16*, *tbxta*) under study and presumptive endoderm (*mixl1*, *gata5*, *sox32*) and endoderm markers (*gata5*, *sox32*, *sox17*) indicated by bulk RNA-seq data from (White et al., 2017). Gene expression is shown as transcripts per million (TPM). Stages are as defined by (Kimmel et al., 1995). (B) UMAP clustering analysis of single-cell RNA-seq data for early gastrulas (6 h.p.f.) zebrafish embryos (Wagner et al., 2018) indicating colour-coded cell type identities. Cell types relevant to the present study are labelled. The identities of all cell types are indicated in Supplementary Figure S3. (C) UMAP clustering analysis of single-cell RNA-seq data for early gastrulas (6 h.p.f.) zebrafish embryos indicating co-expression of *tbx16* and *mixl1* (Wagner et al., 2018). Heatmap insets indicate overall expression levels per gene and co-expression. Overlapping expression is shown in yellow. (D) WISH analysis of *mixl1* in early gastrulas (5.7–6 h.p.f.) zebrafish embryos in wild type or *eomesa* mutant embryos (see Methods for information on genotype) with and without *Tbx16* morpholino knockdown. Total numbers of embryos and fractions as categorized are indicated. Animal views; dorsal to the right. Open arrowheads indicate normal *mixl1* expression at the blastoderm margin. Closed arrowheads indicate profound loss of *mixl1* expression on *tbx16* knockdown in *eomesa* mutants.

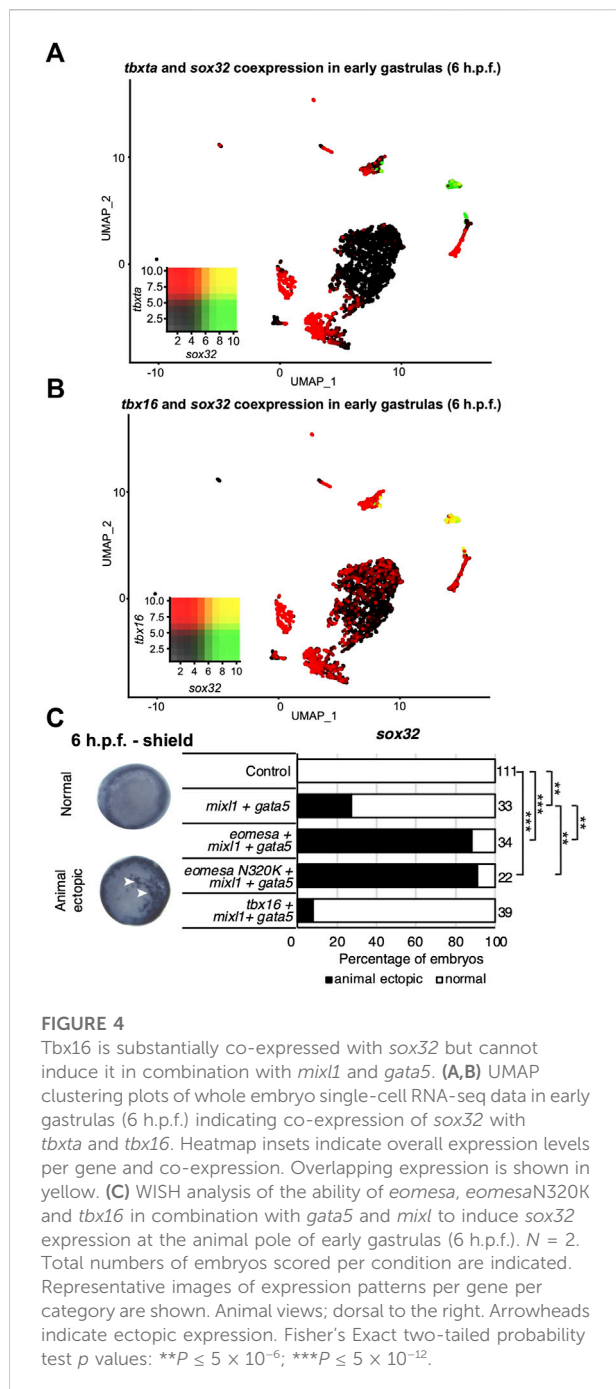
Eomes mutant mouse embryos. To further explore mouse and zebrafish *Eomes* functional capabilities we overexpressed either mouse *Eomes* FL or Δ VIR mRNAs in zebrafish embryos for comparison with those overexpressing zebrafish *eomesa*.

Zebrafish *Eomesa* represses ectoderm genes such as *vgll4l* and *zic3* during blastula stages and activates mesendoderm genes including organizer markers *noto* and *chrd* at the onset of gastrulation (Bruce et al., 2003; Nelson et al., 2014). Injecting equimolar quantities of zebrafish *eomesa* mRNA, or mouse FL or Δ VIR *Eomes* isoforms at the one-cell stage, we found that each was equally able to repress *vgll4l* and *zic3* in mid/late blastulas (4 h post-fertilisation - h.p.f.) and induce *noto* and *chrd* in early gastrulas (6 h.p.f.; Figures 2A–D).

Zebrafish *Eomesa* is suggested to induce DFCs, based on observation of ectopic *sox17* expression in cells of the outer

margin in early gastrulas (7 h.p.f.) on *eomesa* overexpression (Bjornson et al., 2005). We sought to determine whether these ectopic *sox17* + cells express a broader range of DFC markers (*sox17*, *vgll4l* and *foxj1a*), and also whether they can be similarly induced by mouse *Eomes*. Notably, though *Eomesa* represses expression of *vgll4l* during blastula stages, during gastrulation *vgll4l* is expressed in DFCs, and has recently been identified as a key regulator of DFC proliferation, survival and function (Fillatre et al., 2019). Repression of *vgll4l* at later stages in DFCs would consequently be inconsistent with promoting DFC formation.

We found that *eomesa*, and *Eomes* FL or Δ VIR isoforms were all similarly able to upregulate both *sox17* and *vgll4l* in the outer margin of gastrulas. We further note that there was a diversity of phenotypes beyond wild type expression (type I) wherein ectopic dorsolateral



expression was markedly observed in individual cells/small clusters outside the primary dorsal DFC cluster (type II), where there was dorsolateral expression with no defined primary cluster (type III), and where ectopic expression was also observed in the ventral margin (type IV) (Figures 2E,F). Conversely, for *foxj1a* we note that while *eomesa*, *Eomes* FL and Δ VVR can induce a greater intensity of dorsal staining, and expansion of the dorsal DFC cluster, ectopic expression in the ventrolateral margin is rare compared to other DFC markers (Figures 2G,H).

We conclude that both FL and Δ VVR mouse *Eomes* isoforms are functionally highly similar to zebrafish *Eomesa* in these contexts. Moreover, *Eomesa* regulation of *vgl14l* appears to be context-specific, repressing its expression during blastula stages while inducing its expression in DFCs during gastrulation. We further conclude that additional factors likely to be predominantly dorsally localised are required for robust upregulation of *foxj1a* compared to *sox17* and *vgl14l*.

Eomesa and non-mammalian T-box factor Tbx16 redundantly regulate *mixl1* expression at the initiation of zebrafish endoderm formation

Since results above strongly suggest mouse *Eomes* is functionally similar to zebrafish *Eomesa*, do *eomesa* mutants have comparatively mild defects due to functional redundancy with other T-box factors? *Eomesb* is not appreciably expressed during early zebrafish development (Figure 3A), and is not upregulated in *eomesa* mutants (Nelson et al., 2014) thus it seems unlikely that it compensates for loss of *Eomesa*. We recently identified a key role for the non-placental mammal T-box factor, Tbx16 in endoderm formation, with Brachyury homologue Tbx16 having a more minor role (Nelson et al., 2017). Both of these factors show zygotic upregulation concomitant with declining *eomesa* mRNA levels and prior to expression of key markers of presumptive endoderm (e.g., *gata5* and *mixl1*), and endoderm (e.g., *gata5*, *sox32* and *sox17*; Figure 3A), thus may compensate for the early loss of expression of such markers in MZ*eomesa* mutants (Du et al., 2012).

Moreover, single-cell RNA-seq data (Wagner et al., 2018) demonstrate that *tbx16* is robustly co-expressed with the critical endodermal regulator *mixl1* in the presumptive endoderm at early gastrulation stages (6 h.p.f.), suggesting the potential for Tbx16 to upregulate *mixl1* expression to initiate endoderm specification, as our previous published analyses suggest (Nelson et al., 2017) (Figures 3B,C). Additional specific detail on cluster identities in Figures 3B,C is provided in Supplementary Figure S3.

To test whether Tbx16 functions redundantly with *Eomesa* during endoderm formation next we performed antisense morpholino knockdown of Tbx16 in wild type and *eomesa* mutant embryos. We found that while *mixl1* expression is reduced on loss of *Eomesa* or Tbx16 alone, loss of both TFs leads to more striking loss of *mixl1* (Figure 3D). *Eomesa* and Tbx16 therefore collaboratively activate *mixl1* expression, strongly suggesting that Tbx16 relieves the requirement for *Eomesa* in zebrafish endoderm formation.

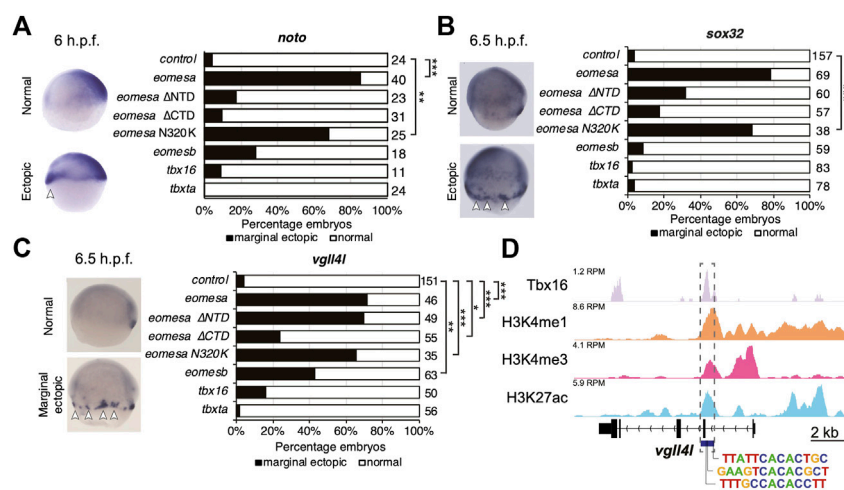


FIGURE 5

Eomesa is a more potent inducer of endoderm, organiser and dorsal forerunner cell markers than other T-box factors. (A–C) WISH analysis of dorsal mesoderm marker *noto* (A) and dorsal forerunner cell markers *sox32* (B) and *vgl141* (C) on overexpression of various wild type and mutant T-box factors. mRNAs injected at the 1 cell stage; WISH performed at stages as indicated. N = 2. Total numbers of embryos scored per condition are indicated. Representative images of expression patterns per gene per category are shown. Lateral views; dorsal to the right. Arrowheads indicate ectopic expression. Fisher's Exact two-tailed probability test *p* values: * $P \leq 5 \times 10^{-4}$; ** $P \leq 5 \times 10^{-6}$; *** $P \leq 5 \times 10^{-12}$; **** $P \leq 5 \times 10^{-30}$. (D) ChIP-seq data in mid/late gastrulas (8–8.5 h.p.f.) indicating Tbx16 binding within the *vgl141* promoter (Bogdanovic et al., 2012; Nelson et al., 2017). Scale is reads per million reads (RPM). Putative T-box binding sites identified using JASPAR are indicated (Fornes et al., 2020).

Tbx16 and *eomesa* overexpression do not equivalently induce endoderm fate in concert with *mixl1* and *gata5*

Eomesa and Mixl1 bind upstream of endoderm master regulator *sox32* to positively regulate its expression prior to endoderm specification (Nelson et al., 2014; Nelson et al., 2017). Eomesa, Mixl1 and Gata5 can physically interact and their combined overexpression has been shown to induce ectopic endoderm gene expression in late blastulas and early gastrulas (Bjornson et al., 2005). Combined expression of Tbx16 with Mixl1 and Gata5, however, is insufficient to induce *sox32* expression (Bjornson et al., 2005). This is consistent with limited co-expression between *tbxta* and *sox32* around the time of endoderm specification (Figure 4A). However, *tbx16* and *sox32* are substantially co-expressed in the endoderm at the onset of gastrulation, (Figures 3B, 4B). Tbx16 is also critical for endoderm progenitor induction (Nelson et al., 2017). We therefore extended our study to test whether Tbx16 can induce ectopic endoderm marker expression in cells at the animal pole (i.e. in cells where Tbx16, Mixl1 and Gata5 are absent in wild type embryos) through co-overexpression with Mixl1 and Gata5, as Eomesa can.

As expected, combined overexpression of *eomesa*, *mixl1* and *gata5* induces ectopic *sox32* expression at the animal pole (Figure 4C). However, *tbx16* did not synergise with *mixl1* and *gata5* to upregulate *sox32* in the animal pole. This may suggest that Tbx16 and Eomesa are not equally capable of forming a

complex with Mixl1 and Gata5 to induce endoderm and/or DFC fate, or alternatively that there are other key components of the complex which are capable of interaction with Eomesa/Mixl1/Gata5, but not Tbx16/Mixl1/Gata5. We conclude that Eomesa and Tbx16 perform similar functions in overlapping processes in the developing zebrafish embryo, but appear to do so via distinct molecular mechanisms.

T-box factors co-expressed with *eomesa* do not share its potent abilities to upregulate dorsal marker genes

Tbx16 and Eomesa lack significant sequence homology, especially outside the T-box domain (Supplementary Figure S4). However, *Xenopus* Eomes and its Tbx16 orthologue VegT have been suggested to display similar specificity in part due to a single shared asparagine residue within the T-box, rendering them functionally distinct from the Tbx16 orthologue Xbra, which has a lysine in the equivalent position (Conlon et al., 2001) (Supplementary Figure S4). We therefore sought to address the following questions: 1) Are Tbx16, Tbx16 and/or Eomesb capable of inducing Eomesa target genes in early gastrulas; 2) Is the T-box asparagine residue critical for Eomesa function; 3) Are key Eomesa functions dependent on the highly conserved CTD or relatively poorly conserved NTD.

We injected equimolar quantities of mRNA corresponding to each wild type T-box factor, or Eomesa ΔNTD, ΔCTD or N320K

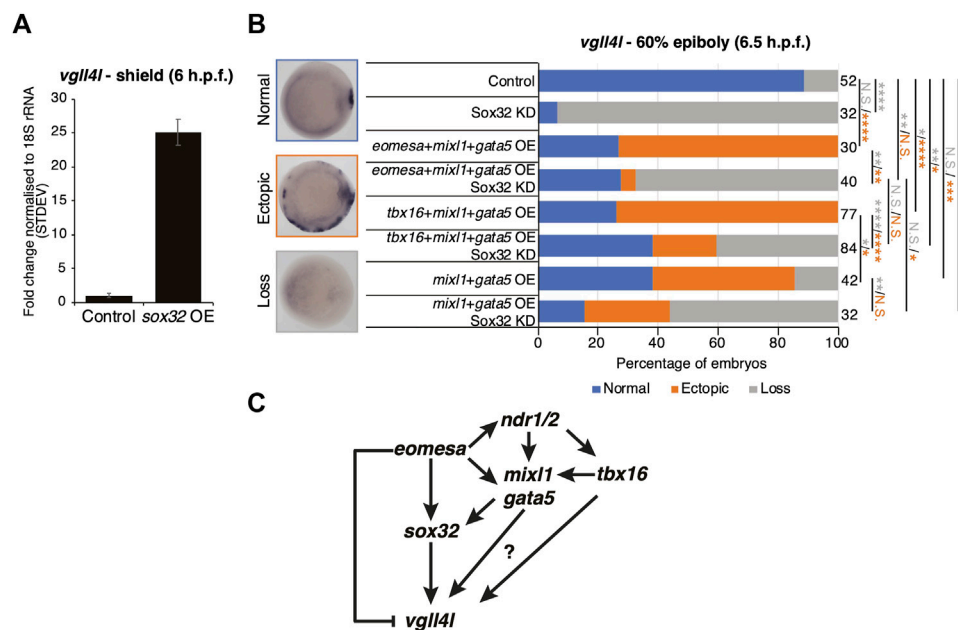


FIGURE 6

Eomesa activation of *vgl14l* is through feedforward loops via *sox32* and its upstream activators. (A) qRT-PCR analysis of *vgl14l* expression in early gastrulas (6 h.p.f.) in control embryos and those injected with *sox32* mRNA at the 1 cell stage. Expression is represented as fold change relative to control normalised to 18S rRNA. (B) WISH analysis of the ability of *vgl14l* expression in early gastrulas (6 h.p.f.) in embryos injected with mRNAs at the one-cell stage as indicated, with and without Sox32 morpholino knockdown. $N = 2$. Total numbers of embryos scored per condition are indicated. Representative images of expression patterns per gene per category are shown. Animal views; dorsal to the right. Fisher's Exact two-tailed probability test p values: $*P \leq 5 \times 10^{-2}$; $**P \leq 5 \times 10^{-4}$; $***P \leq 5 \times 10^{-8}$; $****P \leq 5 \times 10^{-12}$; N.S. = not significant. Orange asterisks indicate significant differences in fractions of embryos exhibiting ectopic expression vs. other categories. Grey asterisks indicate significant differences in fractions of embryos exhibiting loss of expression vs. other categories. (C) Model for Eomesa regulation of *vgl14l* expression in dorsal forerunner cells indicating a type 3 incoherent feedforward loop on the left as Eomesa represses *vgl14l* directly while activating via Sox32, and potential type 1 coherent feedforward loops on the right as Eomesa activates positive regulators of *sox32* and potentially also *vgl14l*.

mutants and assessed the effect on dorsal mesoderm marker *noto* and DFC/endoderm marker *sox32*, and DFC marker *vgl14l*. Deletion of the NTD or CTD ablated Eomesa ability to induce *noto* expression, while N320K mutation had no significant effect (Figure 5A). All other T-box factors failed to produce a consistent or compelling induction of ectopic *noto* (Figure 5A). Consistent with previous results, Eomesa overexpression led to ectopic *sox32* expression in the outer marginal cells indicative of increased numbers of DFC-like cells but not endoderm (Bjornson et al., 2005) (Figure 5B). NTD and especially CTD deletions markedly reduced ectopic *sox32* induction, however, N320K mutation had little effect (Figure 5B). We further note that the N320K mutation had no discernible effect on the ability of Eomesa to synergise with Mixl1 and Gata5 to induce *sox32* expression at the animal pole, suggesting that this mutation within the T-box does not interfere with the known T-box interactions with Mixl1 and Gata5 (Bjornson et al., 2005) (Figure 4C). Overexpression of *tbx16*, *tbxta* and *eomesb* did not lead to ectopic *sox32* induction highlighting functional distinctions with *eomesa* (Figure 5B). *Vgl14l* expression showed similar induction to *sox32* at the

margin by both wild type Eomesa and Δ NTD and N320K Eomesa (Figure 5C). We have previously shown by ChIP-seq that at sphere stage Eomesa binds in the first intron of *vgl14l* (Nelson et al., 2014). Analysis of Tbx16 ChIP-seq data in mid/late gastrulas (8–8.5 h.p.f.) (Nelson et al., 2017) also shows Tbx16 binding at close matches to the known T-box consensus sequence within *vgl14l* intron 1, suggesting Tbx16 does have the potential to directly participate in regulation of *vgl14l* during gastrulation (Figure 5D). However, *tbx16* overexpression suggests that it is not individually sufficient to strongly drive ectopic *vgl14l* expression (Figure 5C).

We next tested whether Tbx16 and Tbx17 can act combinatorially to induce dorsal marker gene expression. We found that on Tbx16/Tbx17 combinatorial overexpression DFC markers *vgl14l* and *sox17* were expressed over a broader region of the dorsolateral margin but showed concomitant reduction in the primary DFC cluster (Supplementary Figure S5A). Conversely, *foxi1a* expression remained localised to the dorsal margin, again suggesting that *foxi1a* expression is somewhat dependent on additional dorsally localised regulators (Supplementary Figure S5A). Furthermore, while *tbx16* and *tbxta* are coexpressed with

noto in early gastrulas (Supplementary Figures S5B,C), their combinatorial overexpression does not lead to expanded *noto* expression (Supplementary Figure S5D). We therefore conclude that combined activities of Tbx16 and Tbx1a are not sufficient to induce dorsal fates, unlike Eomesa.

Overall this suggests that Eomesb, Tbx16 and Tbx1a do not individually have similar abilities to Eomesa in inducing dorsal mesoderm and DFC gene expression, that the previously reported N/K amino acid difference between Eomesa/Tbx16 and Tbx1a does not appreciably influence specificity and function in this context, and that deletion of the relatively poorly conserved Eomesa NTD does not result in complete loss of function.

Eomesa regulates *vgll4l* expression and dorsal forerunner cell formation through interlocking feedforward loops via *sox32*

Results above suggest that Eomesa overexpression induces DFC fate based on ectopic expression of markers including *sox32* and *vgll4l* (Figures 2F, 5B,C). To resolve the conflict between the observed Eomesa-mediated repression of *vgll4l* expression at mid/late blastula stages (4 h.p.f.) but induction by early gastrulation (6 h.p.f.) we explored the role of Eomesa target Sox32 in *vgll4l* induction. We found that *sox32* overexpression through one-cell stage mRNA injection led to a dramatic upregulation of *vgll4l* expression in early gastrulas (6 h.p.f.; Figure 6A), suggesting localised Eomesa-mediated upregulation of *vgll4l* at the margin occurs through Sox32 rather than a switch in Eomesa function directly at the *vgll4l* locus. To test whether Sox32 is required for induction of *vgll4l* expression we performed knockdown using a previously validated and widely used antisense morpholino (Dickmeis et al., 2001). This knockdown clearly resulted in loss of DFC *vgll4l* expression (Figure 6B). Furthermore, *vgll4l* induction in locations outside the dorsal margin, caused by combinatorial *eomesa/mixl1/gata5* overexpression was also profoundly abrogated by Sox32 knockdown. Thus, during gastrula stages induction of *vgll4l* is via Sox32 rather than direct Eomesa activities.

Vgll4l expression was similarly upregulated outside the dorsal margin by combinatorial *mixl1/gata5* overexpression, and partially blocked by Sox32 KD (Figure 6B). However, *vgll4l* expression in *mixl1/gata5* overexpressing embryos was not as profoundly reduced on Sox32 KD as was the case for *eomesa/mixl1/gata5* overexpression. It is not completely clear whether this is because *mixl1/gata5* can activate *vgll4l* independent of Sox32 function, or due to the absence of Eomesa-mediated repression of *vgll4l*. Addition of *tbx16* to *mixl1/gata5* overexpression led to a significant increase in the fraction of embryos exhibiting ectopic *vgll4l* expression compared to *mixl1/gata5* alone (Figure 6B). We note that overexpression of *tbx16*

alone was insufficient to enhance *vgll4l* expression in a significant fraction of embryos, and showed no ability to induce *sox32* expression (Figures 5B,C). It seems likely that while *tbx16* alone does not exert a strong influence at the *vgll4l* locus, *mixl1* and *gata5* can provide a context for *tbx16* to enhance *vgll4l* expression. This likely involves Tbx16 binding to *vgll4l* intron 1 (Figure 5D) rather than occurring via *sox32*, since Tbx16 cannot induce *sox32* expression, either individually or in combination with Mixl1 and Gata5 (Figures 4C, 5B).

Overall the present results combined with previous published reports from ourselves and others suggest a model wherein Eomesa acts within interlocking incoherent type 3 and coherent type 1 feedforward loops (Mangan and Alon, 2003) to repress *vgll4l* while combining with Nodal downstream effectors Mixl1 and Gata5 to activate *sox32*, which in turn activates *vgll4l* around the time of DFC specification. In addition to this, our analyses indicate that both mouse Eomes FL and ΔVR isoforms are functionally equivalent to Eomesa, suggesting phenotypic differences between zebrafish and mouse Eomes loss-of-function mutants are not likely to be driven by functional divergence, but rather redundancy with co-expressed factors in zebrafish such as Tbx16.

Discussion

Phenotypic differences between mouse and zebrafish Eomes loss-of-function mutants are not due to molecular divergence

T-box transcription factors are an ancient family of genes with many key roles in embryogenesis and disease. Lineage-specific differences that occurred in the family during vertebrate evolution have resulted in altered gene complements and diversity of splice isoforms in distinct evolutionary lineages (DeBenedittis and Jiao, 2011; Papaioannou, 2014). While AS events in specific evolutionary lineages have led to functional diversification of certain T-box factors, we have shown that Eomes loss-of-function phenotypic differences between mouse and zebrafish are unlikely to be due to evolutionary differences in Eomes protein function, but rather a degree of compensation by Tbx16 which is present in zebrafish but not placental mammals.

Though AS is an evolutionary means of increasing functional diversity within the proteome, our data suggests that Eomes exon 6 AS is not functionally important in the context of early development. In the case of the ΔVR splicing event a synonymous mutation created an alternative splice acceptor, however, our data suggests it is hardly used leading to majority production of the FL isoform. That the ΔVR isoform arose and is maintained in the tetrapod lineage may be due to substantial functional similarity of FL and ΔVR isoforms, leading to a lack of selective pressure.

In overexpression studies the Δ VR isoform has the ability to induce trophoblast markers in embryonic stem cells (Niwa et al., 2005), and cardiac mesoderm markers in embryonal carcinoma cells (Costello et al., 2011). Moreover, both FL and Δ VR isoforms can induce organizer and DFC markers while repressing ectoderm markers on overexpression in zebrafish. These observations provide further evidence of their functional equivalence.

The present data demonstrate that the Δ VR and Δ CTD isoforms are only weakly expressed compared with FL Eomes. While we find no evidence for the functional importance of the VR it is intriguing that it is both highly conserved and known to be phosphorylated (Huttlin et al., 2010). It is possible that these isoforms potentially make substantial contributions in contexts we have not explored. The present evidence, however, suggests that in mice, as in zebrafish the FL isoform is the more important molecule.

Given the complexities of mouse Eomes mutant phenotypes it would be interesting to explore isoform-specific functions in mouse. This could be achieved through either modifying the endogenous Eomes locus in embryonic stem cells (ESCs) such that only specific isoforms could be expressed, or using isoform-specific inducible transgenes in Eomes null mutant ESCs. This could be combined with directed differentiation procedures to determine whether there are detectable isoform-specific functions in relevant cell types. Whether zebrafish Eomesa, or other T-box factors can functionally substitute for mouse Eomes could also be tested in a similar system. Alternatively, the genetically modified ESCs could be used to make mice in an attempt to study isoform and orthologue functions *in vivo*.

Functional similarities and differences of Eomesa and Tbx16

We previously demonstrated that Eomesa and Tbx16 display overlapping genomic binding profiles in early zebrafish embryos (Nelson et al., 2017). Whether they are functionally redundant, however, had not been explored. The present experiments strongly suggest that Eomesa and Tbx16 redundantly regulate the homeodomain transcription factor *mixl1*, which has key conserved functions in endoderm formation in zebrafish and mouse (Kikuchi et al., 2000; Hart et al., 2002). *Mixl1* mutants suffer profound loss of endoderm (Kikuchi et al., 2000). Reduced expression of *mixl1* in the margin of late blastulas/early gastrulas is coupled with reduced numbers of endoderm progenitors in late gastrulation in both *MZeomesa* mutants, and on *tbx16* knockdown (Du et al., 2012; Nelson et al., 2017). It therefore seems likely that the enhanced reduction of *mixl1* expression on *tbx16* knockdown in *eomesa* mutants in the present study would lead to increased loss of endoderm progenitors. Our previous RNA-seq analyses indicate that expression of *tbx16* is not significantly different in *MZeomesa* mutants (Nelson et al.,

2014). It therefore seems likely that Tbx16 partially compensates for loss of Eomesa during zebrafish endoderm formation. Our study therefore highlights a consistent requirement for T-box function in vertebrate endoderm formation. Interestingly, while multiple orthologous T-box factors have similar expression domains in early zebrafish and mouse embryogenesis, those domains are typically expanded in zebrafish (Wardle and Papaioannou, 2008). Coupled with its rapid rate of development and the greater number of T-box factors in zebrafish, there is likely to be a higher degree of T-box factor co-expression, enhancing the probability of redundancy.

While Eomesa and Tbx16 share some redundant functions we also identified key differences. It was previously shown that Eomesa can combine with Mixl1 and Gata5 to drive expression of *sox32* at the animal pole (Bjornson et al., 2005). However, Tbx16 does not appear to have the same ability as Eomesa to drive *sox32* expression either individually or in combination with Mixl1 and Gata5, even though *sox32* expressing cells appear to exhibit *tbx16* expression in single-cell RNA-seq data. This is consistent with previous observations that *Meomesa* and *MZeomesa* mutants have reduced expression of *sox32* during gastrulation without complete loss (Du et al., 2012; Xing et al., 2022). It therefore seems likely that Tbx16 is sufficient to rescue certain Eomesa functions but cannot completely compensate for its loss. It is further notable that Tbx16 does not seem individually able to induce the dorsal mesoderm marker *noto* as Eomesa can. However, given that Eomesa acts upstream of Nodal (Xu et al., 2014; Xing et al., 2022) it seems likely that major differences in outcome between *eomesa* and *tbx16* overexpression stem from enhanced Nodal signalling on *eomesa* overexpression. It will be interesting to learn more about the common and unique functional activities of Eomesa and Tbx16 that drive target gene expression.

Eomesa and Tbx16 are only distantly related within the T-box family (25.3% of Tbx16 amino acid identity), with the majority of conserved amino acids occurring within the T-box domain. Whether they are likely to act in similar protein complexes to regulate their target genes is therefore unclear. A key study in *Xenopus*, however, suggested the specificity of target gene induction is primarily mediated by the T-box itself, rather than NTDs and CTDs (Conlon et al., 2001). The same study demonstrated a single asparagine to lysine substitution in *Xenopus* Eomes and VegT T-box domains, alter their inductive properties to mimic Brachyury (Conlon et al., 2001). Importantly, both Eomesa and Tbx16 (which has been proposed as the zebrafish orthologue of *Xenopus* VegT (Griffin et al., 1998)) share the same critical asparagine. Our data suggest that the N320K mutation has little effect on induction of Eomesa target genes explored here, is unlikely to prevent T-box interaction with co-factors Mixl1 and Gata5, or substantially account for differences with Tbx16 in endoderm and DFC formation. In fact, analysis of single-cell RNA-seq data suggests that the greater importance of Eomesa and Tbx16 in endoderm formation is

more likely to be attributable to lesser *Tbx16* expression in the endoderm. It is therefore possible that *Eomesa* and *Tbx16* also have overlapping roles in endoderm formation downstream of driving *mixl1* expression in presumptive endoderm that are yet to be elucidated.

Interestingly, participation of zebrafish *Tbx16* in processes controlled by *Eomes* in mice is not limited to endoderm formation. For example, while *Eomes* acts upstream of basic helix-loop-helix transcription factor gene *Mesp1* to specify cardiac mesoderm in mice (Costello et al., 2011), *Tbx16* regulates the orthologous gene *mespaa* in zebrafish (Garnett et al., 2009). *Eomes* loss-of-function leads to aberrant mesoderm cell migration during mouse gastrulation, while *tbx16* zebrafish mutants also exhibit cell-autonomous defects in mesoderm migration (Ho and Kane, 1990; Arnold et al., 2008a). Remarkably, potentially interesting parallels continue to emerge, such as the requirements for zebrafish *Tbx16* and mouse *Eomes* in blood progenitors (Rohde et al., 2004; Harland et al., 2021). It is therefore possible that the presence of *Tbx16* in teleost fish has led to a reduced requirement for *Eomes* in multiple developmental contexts.

The present study focuses on early embryonic development, however, *Eomes* is known to have later roles in neurological development, as well as in the immune system. Importantly, *Eomes* is an key regulator of neurogenesis in the subventricular zone, and loss leads to microcephaly and severe behavioural defects (Arnold et al., 2008b). Though *eomesa* is equivalently expressed in the telencephalon of developing zebrafish larvae, whether null mutants have an equivalent phenotype is unknown (Mione et al., 2001; Du et al., 2012). If they do not, however, it is unlikely to be due to redundancy with *tbx16*, which is absent from the developing brain. Similarly, it is unclear whether *eomesa* mutants exhibit defects in the immune system, such as in T cell differentiation and NK cell development and function as in mammals (Simonetta et al., 2016; D'Cruz et al., 2009). Both *eomesa* and *eomesb* are co-expressed in lymphocytes in fish, however, suggesting they may be redundant in the immune system (Takizawa et al., 2007; Takizawa et al., 2014).

While T-box factor redundancy during development is not a novel concept e.g. (Amacher et al., 2002; Garnett et al., 2009; Jahangiri et al., 2012; Gentsch et al., 2013; Nelson et al., 2017), the molecular basis for this redundancy (or indeed T-box factor molecular interactions in general) is not well understood. In future it will be interesting to study whether redundant T-box factors recruit similar co-factors to regulate gene expression, and whether this occurs through conserved or divergent amino acid sequences and structural motifs.

On the roles of *Eomesa*, *Tbx16* and *Tbx16* in dorsal mesoderm

While *Eomesa* is capable of inducing dorsal mesoderm markers such as *noto* and *chrd* in zebrafish embryos, it is

notable that their expression is normal in the absence of *Eomesa* (Bruce et al., 2003; Du et al., 2012). However, it is also notable that *tbxta* and *tbx16* do not show altered expression in *eomesa* mutants in published WISH and RNA-seq datasets (Du et al., 2012; Nelson et al., 2014). It is therefore possible that *Tbx16* and *Tbx16* are amongst factors compensating for the loss of *Eomesa*. In support of this, *Tbx16* has been shown to directly activate *noto* expression, and *tbxta* mutants fail to maintain *noto* expression in mid/late gastrulation stages, leading to loss of notochord (Melby et al., 1997; Morley et al., 2009). Similarly, *Tbx16* is required to maintain *chrd* expression in axial structures at mid/late gastrulation stages (Miller-Bertoglio et al., 1997; Warga et al., 2013). The reduced expression of both *noto* in *tbxta* mutants and *chrd* in *tbx16* mutants follows the decline in *eomesa* mRNA expression levels, suggesting that *Tbx16* and *Tbx16* maintain the expression of dorsal mesoderm markers in the absence of *Eomesa*. Nevertheless, our results indicate that of these T-box factors, only *Eomesa* is sufficient to induce ectopic dorsal mesoderm marker expression. This suggests key differences in the molecular functions of these T-box factors. It is possible that co-factors required for dorsal mesoderm induction by *Eomesa* are localised throughout the margin while those required by *Tbx16* and *Tbx16* are restricted to the dorsal margin. Alternatively, given *Eomesa* regulates expression of Nodal pathway ligands which are required for dorsal mesoderm fates, it is possible that *Eomesa* but not *Tbx16*/*Tbx16* is capable of expanding dorsal mesoderm through upregulation of Nodal signalling (Du et al., 2012; Xu et al., 2014; Xing et al., 2022).

Eomesa, *Tbx16*, *Mixl1* and *Gata5* activities during dorsal forerunner cell formation

Loss of *Eomesa* leads to upregulation of *vgll4l* during blastula stages whereas overexpression of *eomesa* causes repression of *vgll4l* (Nelson et al., 2014). The present experiments suggests that *Eomesa* acts within feedforward loops to repress *vgll4l* expression until activators including *Sox32* accumulate to drive *vgll4l* in DFCs at the onset of gastrulation. Given that *Eomesa* is maternally contributed and not spatially restricted in early development (Du et al., 2012), while accumulation of *vgll4l* activators is principally driven by Nodal at the dorsal margin, this suggests a model wherein *Eomesa* controls the specificity and timing of *vgll4l* induction. *Eomesa* mRNA steadily declines during blastula stages as expression of *mixl1*, *gata5*, *tbx16* and *sox32* increase, and is virtually undetectable at the onset of gastrulation, (Figure 3A and Bruce et al., 2003; Figiel et al., 2021). While *Eomesa* protein does persist through gastrulation (Du et al., 2012) it seems likely that temporal and spatial changes in abundance of *vgll4l* activators and repressors acting within

these feedforward loops cooperatively regulate the specificity of *vgll4l* expression during DFC specification.

Genetic data, however, suggest that our model is likely to be incomplete. While Sox32 is required for correct DFC formation (Alexander et al., 1999; Essner et al., 2005), upstream regulators *mixl1* and *gata5* are not required for DFC formation individually or in combination. Rather *mixl1* and *gata5* seem to be strictly required upstream of *sox32* for correct endoderm formation (Reiter et al., 1999; Kikuchi et al., 2000; Reiter et al., 2001). While we cannot discount the possibility of *mixl1* and *gata5* expression in precursors of DFCs, present evidence suggests that there are either alternative upstream regulators of *sox32* in DFCs vs. endoderm, or additional redundant factors in DFCs rescuing the requirement for *mixl1* and *gata5*. However, given the apparent requirement for Nodal signalling in DFC formation (Alexander and Stainier, 1999), it seems likely that whatever the upstream regulators of *sox32* expression in DFCs they will be Nodal-dependent. Overall this highlights a lack of understanding of the gene regulatory networks that direct DFC vs. endoderm formation, which will be a key focus of our future work.

Recent evidence suggests *Vgll4l* is required for *tbx16* expression during DFC formation (Fillatre et al., 2019). That Tbx16 binds the *vgll4l* promoter during gastrulation could suggest that complex regulatory loops control DFC formation and maintenance. The ability of Eomesa to induce ectopic DFCs during early gastrulation combined with expression of mouse Eomes in progenitors of the node and requirement for correct node formation (Arnold et al., 2008a; Costello et al., 2011) suggests the potential for a conserved role in establishment of left-right asymmetry with some degree of redundancy with Tbx16 in zebrafish. However, a role for the *vgll4l* mammalian homologue *Vgll4* in left-right asymmetry has yet to be determined. Further study of the mechanistic parallels in T-box factor mediated formation of zebrafish DFCs and mouse node would be beneficial to gain a more detailed evo-devo understanding of this process.

The diversity of DFC marker gene induction observed in this study was particularly striking, and points to dorsally localised determinants of DFC identity and function that are less readily induced by Eomesa and Eomes. We found that between them Eomesa and mouse Eomes isoforms were able to induce *sox32*, *sox17*, *vgll4l* and *foxj1a*. *Sox32* is required for maintenance of DFC identity and formation of the left-right organiser (Alexander et al., 1999; Essner et al., 2005) while its downstream target *sox17* is required for correct left-right organiser function (Aamar and Dawid, 2010). *Vgll4l* is a key mediator of Hippo signalling and regulates epigenetic programming of DFC by controlling the expression of writers and readers of DNA methylation, influencing DFC proliferation, apoptosis and ciliogenesis (Fillatre et al., 2019). *Foxj1a* is the master regulator of motile cilia formation (Yu et al., 2008). That the Eomes-mediated induction of *foxj1a* was more restricted to the dorsal margin than that of other markers suggests that *Vgll4l*

and the Sox and T-box factors known to be involved in DFC formation are not sufficient to fully induce DFC identity. Other localised cues (physical, mechanical, signalling or cell intrinsic factors) are therefore likely to be involved in *foxj1a* induction.

Overall we conclude that enhanced AS in mammals has not significantly altered Eomes function in early embryogenesis. Rather we conclude that the different degrees of T-box factor co-expression and the presence/absence of additional factors including Tbx16 has modulated the severity of the Eomes null mutant phenotype in the embryo proper between mouse and zebrafish. Furthermore, we conclude that in zebrafish Eomesa participates in DFC formation through directing feedforward loops via *sox32* to control *vgll4l* expression. Our results therefore provide novel insights into evolutionary differences in vertebrate endoderm formation, and the gene regulatory networks involved in controlling the zebrafish left-right organiser formation.

Data availability statement

The datasets presented in this study can be found in online repositories. The names of the repository/repositories and accession number(s) can be found below: The single-cell RNA-seq data used in the study is from a published paper, and is available in NCBI GEO (accession GSM3067190).

Ethics statement

The animal study was reviewed and approved by Animal Welfare and Ethical Review Body, University of Warwick Animal Welfare and Ethical Review Body, King's College London University of Toronto Animal Care Committee.

Author contributions

Conceived and designed the experiments: ACN and CDT. Performed the experiments: CDT, ACN, AEEB, SJC, FCW, RE, and EV. Analysed the data: ACN, CDT, and MDW. Wrote the paper: ACN.

Funding

This research was funded in whole or in part by the BBSRC Midlands Integrative Biosciences Training Partnership (BB/M01116X/1). For the purpose of open access, the author has applied a Creative Commons Attribution (CC BY) licence to any Author Accepted Manuscript version arising from this submission. This research was also funded in part, by the Wellcome Trust through a Wellcome Seed Award in Science to ACN (210177/Z/18/Z), and a Wellcome Trust Programme

grant (102811) to Elizabeth J. Robertson. The research was also funded by Horizon 2020 MSCA-ITN project ZENCODE-ITN (GA no: 643062) to FCW. The research was also funded by a Natural Sciences and Engineering Research Council grant to Ashley Bruce (458019). CDT has a PhD studentship funded by the BBSRC Midlands Integrative Biosciences Training Partnership (BB/M01116X/1). RE was funded by the MRC Doctoral Training Partnership in Interdisciplinary Biomedical Research (MR/N014294/1).

Acknowledgments

We thank Elizabeth Bikoff and Elizabeth Robertson for reagents, valuable conversations and critical review of the manuscript. We also thank Karuna Sampath for valuable discussions and generous access to equipment, and Ita Costello, Claire Simon and Daniel Hebenstreit for valuable discussions, the Warwick zebrafish facility for zebrafish care and acknowledge the contributions of Henrietta Lacks and her family to this research. We also thank Jeffrey Amack and H. Joseph Yost for reagents.

References

- Ashe, H. L., Monks, J., Wijgerde, M., Fraser, P., and Proudfoot, N. J. (1997). Intergenic transcription and transinduction of the human beta-globin locus. *Genes Dev.* 11, 2494–2509. doi:10.1101/gad.11.19.2494
- Amar, E., and Dawid, I. B. (2010). Sox17 and chordin are required for formation of Kupffer's vesicle and left-right asymmetry determination in zebrafish. *Dev. Dyn.* 239, 2980–2988. doi:10.1002/dvdy.22431
- Adams, S. E., Johnson, I. D., Braddock, M., Kingsman, A. J., Kingsman, S. M., and Edwards, R. M. (1988). Synthesis of a gene for the HIV transactivator protein TAT by a novel single stranded approach involving *in vivo* gap repair. *Nucleic Acids Res.* 16, 4287–4298. doi:10.1093/nar/16.10.4287
- Ahn, D., You, K. H., and Kim, C. H. (2012). Evolution of the tbx6/16 subfamily genes in vertebrates: Insights from zebrafish. *Mol. Biol. Evol.* 29, 3959–3983. doi:10.1093/molbev/mss199
- Alexander, J., Rothenberg, M., Henry, G. L., and Stainier, D. Y. (1999). Casanova plays an early and essential role in endoderm formation in zebrafish. *Dev. Biol.* 215, 343–357. doi:10.1006/dbio.1999.9441
- Alexander, J., and Stainier, D. Y. (1999). A molecular pathway leading to endoderm formation in zebrafish. *Curr. Biol.* 9, 1147–1157. doi:10.1016/S0960-9822(00)80016-0
- Amacher, S. L., Draper, B. W., Summers, B. R., and Kimmel, C. B. (2002). The zebrafish T-box genes no tail and spadetail are required for development of trunk and tail mesoderm and medial floor plate. *Development* 129, 3311–3323. doi:10.1242/dev.129.14.3311
- Arnold, S. J., Hofmann, U. K., Bikoff, E. K., and Robertson, E. J. (2008a). Pivotal roles for eomesodermin during axis formation, epithelium-to-mesenchyme transition and endoderm specification in the mouse. *Development* 135, 501–511. doi:10.1242/dev.014357
- Arnold, S. J., Huang, G. J., Cheung, A. F., Era, T., Nishikawa, S., Bikoff, E. K., et al. (2008b). The T-box transcription factor Eomes/Tbr2 regulates neurogenesis in the cortical subventricular zone. *Genes Dev.* 22, 2479–2484. doi:10.1101/gad.475408
- Barrett, T., Wilhite, S. E., Ledoux, P., Evangelista, C., Kim, I. F., Tomashevsky, M., et al. (2013). NCBI GEO: Archive for functional genomics data sets—update. *Nucleic Acids Res.* 41, D991–D995. doi:10.1093/nar/gks1193
- Bisgrove, B. W., Snarr, B. S., Emrazian, A., and Yost, H. J. (2005). Polaris and Polycystin-2 in dorsal forerunner cells and Kupffer's vesicle are required for specification of the zebrafish left-right axis. *Dev. Biol.* 287, 274–288. doi:10.1016/j.ydbio.2005.08.047
- Bjornson, C. R., Griffin, K. J., Farr, G. H., 3R. D., Terashima, A., Himeda, C., Kikuchi, Y., et al. (2005). Eomesodermin is a localized maternal determinant required for endoderm induction in zebrafish. *Dev. Cell* 9, 523–533. doi:10.1016/j.devcel.2005.08.010
- Bogdanovic, O., Fernandez-Minan, A., Tena, J. J., De La Calle-Mustienes, E., Hidalgo, C., Van Kruysbergen, I., et al. (2012). Dynamics of enhancer chromatin signatures mark the transition from pluripotency to cell specification during embryogenesis. *Genome Res.* 22, 2043–2053. doi:10.1101/gr.134833.111
- Bruce, A. E., Howley, C., Zhou, Y., Vickers, S. L., Silver, L. M., King, M. L., et al. (2003). The maternally expressed zebrafish T-box gene eomesodermin regulates organizer formation. *Development* 130, 5503–5517. doi:10.1242/dev.00763
- Conlon, F. L., Fairclough, L., Price, B. M., Casey, E. S., and Smith, J. C. (2001). Determinants of T box protein specificity. *Development* 128, 3749–3758. doi:10.1242/dev.128.19.3749
- Costello, I., Pimeisl, I. M., Drager, S., Bikoff, E. K., Robertson, E. J., and Arnold, S. J. (2011). The T-box transcription factor Eomesodermin acts upstream of Mesp1 to specify cardiac mesoderm during mouse gastrulation. *Nat. Cell Biol.* 13, 1084–1091. doi:10.1038/ncb2304
- Crooks, G. E., Hon, G., Chandonia, J. M., and Brenner, S. E. (2004). WebLogo: A sequence logo generator. *Genome Res.* 14, 1188–1190. doi:10.1101/gr.849004
- D'Cruz, L. M., Rubinstein, M. P., and Goldrath, A. W. (2009). Surviving the crash: Transitioning from effector to memory CD8+ T cell. *Semin. Immunol.* 21, 92–98. doi:10.1016/j.smim.2009.02.002
- Debeneditis, P., and Jiao, K. (2011). Alternative splicing of T-box transcription factor genes. *Biochem. Biophys. Res. Commun.* 412, 513–517. doi:10.1016/j.bbrc.2011.08.010
- Dickmeis, T., Mourrain, P., Saint-Etienne, L., Fischer, N., Aanstad, P., Clark, M., et al. (2001). A crucial component of the endoderm formation pathway, CASANOVA, is encoded by a novel sox-related gene. *Genes Dev.* 15, 1487–1492. doi:10.1101/gad.196901
- Du, S., Draper, B. W., Mione, M., Moens, C. B., and Bruce, A. (2012). Differential regulation of epiboly initiation and progression by zebrafish Eomesodermin A. *Dev. Biol.* 362, 11–23. doi:10.1016/j.ydbio.2011.10.036
- Eggermont, J., and Proudfoot, N. J. (1993). Poly(A) signals and transcriptional pause sites combine to prevent interference between RNA polymerase II promoters. *EMBO J.* 12, 2539–2548. doi:10.1002/j.1460-2075.1993.tb05909.x

Conflict of interest

The authors declare that the research was conducted in the absence of any commercial or financial relationships that could be construed as a potential conflict of interest.

Publisher's note

All claims expressed in this article are solely those of the authors and do not necessarily represent those of their affiliated organizations, or those of the publisher, the editors and the reviewers. Any product that may be evaluated in this article, or claim that may be made by its manufacturer, is not guaranteed or endorsed by the publisher.

Supplementary material

The Supplementary Material for this article can be found online at: <https://www.frontiersin.org/articles/10.3389/fcell.2022.982477/full#supplementary-material>

- Essner, J. J., Amack, J. D., Nyholm, M. K., Harris, E. B., and Yost, H. J. (2005). Kupffer's vesicle is a ciliated organ of asymmetry in the zebrafish embryo that initiates left-right development of the brain, heart and gut. *Development* 132, 1247–1260. doi:10.1242/dev.01663
- Faial, T., Bernardo, A. S., Mendjan, S., Diamanti, E., Ortmann, D., Gentsch, G. E., et al. (2015). Brachyury and SMAD signalling collaboratively orchestrate distinct mesoderm and endoderm gene regulatory networks in differentiating human embryonic stem cells. *Development* 142, 2121–2135. doi:10.1242/dev.117838
- Figiel, D. M., Elsayed, R., and Nelson, A. C. (2021). Investigating the molecular guts of endoderm formation using zebrafish. *Brief. Funct. Genomics* 20, 394–406. doi:10.1093/bfgp/elab013
- Fillatre, J., Fauny, J. D., Fels, J. A., Li, C., Goll, M., Thisse, C., et al. (2019). TEADs, Yap, Taz, Vgll4s transcription factors control the establishment of Left-Right asymmetry in zebrafish. *Elife* 8, e45241. doi:10.7554/eLife.45241
- Fornes, O., Castro-Mondragon, J. A., Khan, A., Van Der Lee, R., Zhang, X., Richmond, P. A., et al. (2020). JaspAr 2020: Update of the open-access database of transcription factor binding profiles. *Nucleic Acids Res.* 48, D87–D92. doi:10.1093/nar/gkz1001
- Garnett, A. T., Han, T. M., Gilchrist, M. J., Smith, J. C., Eisen, M. B., Wardle, F. C., et al. (2009). Identification of direct T-box target genes in the developing zebrafish mesoderm. *Development* 136, 749–760. doi:10.1242/dev.024703
- Gentsch, G. E., Monteiro, R. S., and Smith, J. C. (2017). Cooperation between T-box factors regulates the continuous segregation of germ layers during vertebrate embryogenesis. *Curr. Top. Dev. Biol.* 122, 117–159. doi:10.1016/bs.ctdb.2016.07.012
- Gentsch, G. E., Owens, N. D., Martin, S. R., Piccinelli, P., Faial, T., Trotter, M. W., et al. (2013). *In vivo* T-box transcription factor profiling reveals joint regulation of embryonic neuromesodermal bipotency. *Cell Rep.* 4, 1185–1196. doi:10.1016/j.celrep.2013.08.012
- Glasauer, S. M. K., and Neuhauss, S. C. F. (2014). Whole-genome duplication in teleost fishes and its evolutionary consequences. *Mol. Genet. Genomics* 289, 1045–1060. doi:10.1007/s00438-014-0889-2
- Goujon, M., McWilliam, H., Li, W., Valentin, F., Squizzato, S., Paern, J., et al. (2010). A new bioinformatics analysis tools framework at EMBL-EBI. *Nucleic Acids Res.* 38, W695–W699. doi:10.1093/nar/gkq313
- Griffin, K. J., Amacher, S. L., Kimmel, C. B., and Kimelman, D. (1998). Molecular identification of spadetail: Regulation of zebrafish trunk and tail mesoderm formation by T-box genes. *Development* 125, 3379–3388. doi:10.1242/dev.125.17.3379
- Grimblat, Y., and Sive, H. (2001). Zic Gene expression marks anteroposterior pattern in the presumptive neuroectoderm of the zebrafish gastrula. *Dev. Dyn.* 222, 688–693. doi:10.1002/dvdy.1221
- Hafemeister, C., and Satija, R. (2019). Normalization and variance stabilization of single-cell RNA-seq data using regularized negative binomial regression. *Genome Biol.* 20, 296. doi:10.1186/s13059-019-1874-1
- Harland, L. T. G., Simon, C. S., Senft, A. D., Costello, I., Greder, L., Imaz-Rosshandler, I., et al. (2021). The T-box transcription factor Eomesodermin governs haemogenic competence of yolk sac mesodermal progenitors. *Nat. Cell Biol.* 23, 61–74. doi:10.1038/s41556-020-00611-8
- Hart, A. H., Hartley, L., Sourris, K., Stadler, E. S., Li, R., Stanley, E. G., et al. (2002). Mixl1 is required for axial mesendoderm morphogenesis and patterning in the murine embryo. *Development* 129, 3597–3608. doi:10.1242/dev.129.15.3597
- Ho, R. K., and Kane, D. A. (1990). Cell-autonomous action of zebrafish *spt-1* mutation in specific mesodermal precursors. *Nature* 348, 728–730. doi:10.1038/348728a0
- Huttlin, E. L., Jedrychowski, M. P., Elias, J. E., Goswami, T., Rad, R., Beausoleil, S. A., et al. (2010). A tissue-specific atlas of mouse protein phosphorylation and expression. *Cell* 143, 1174–1189. doi:10.1016/j.cell.2010.12.001
- Jahangiri, L., Nelson, A. C., and Wardle, F. C. (2012). A cis-regulatory module upstream of deltaC regulated by Ntla and Tbx16 drives expression in the tailbud, presomitic mesoderm and somites. *Dev. Biol.* 371, 110–120. doi:10.1016/j.ydbio.2012.07.002
- Jowett, T., and Lettice, L. (1994). Whole-mount *in situ* hybridizations on zebrafish embryos using a mixture of digoxigenin- and fluorescein-labelled probes. *Trends Genet.* 10, 73–74. doi:10.1016/0168-9525(94)90220-8
- Karolchik, D., Hinrichs, A. S., Furey, T. S., Roskin, K. M., Sugnet, C. W., Haussler, D., et al. (2004). The UCSC Table Browser data retrieval tool. *Nucleic Acids Res.* 32, D493–D496. doi:10.1093/nar/gkh103
- Keren, H., Lev-Maor, G., and Ast, G. (2010). Alternative splicing and evolution: Diversification, exon definition and function. *Nat. Rev. Genet.* 11, 345–355. doi:10.1038/nrg2776
- Kikuchi, Y., Trinh, L. A., Reiter, J. F., Alexander, J., Yelon, D., and Stainier, D. Y. (2000). The zebrafish *bonnie and clyde* gene encodes a Mix family homeodomain protein that regulates the generation of endodermal precursors. *Genes Dev.* 14, 1279–1289. doi:10.1101/gad.14.10.1279
- Kimmel, C. B., Ballard, W. W., Kimmel, S. R., Ullmann, B., and Schilling, T. F. (1995). Stages of embryonic development of the zebrafish. *Dev. Dyn.* 203, 253–310. doi:10.1002/aja.1002030302
- Lolas, M., Valenzuela, P. D., Tjian, R., and Liu, Z. (2014). Charting Brachyury-mediated developmental pathways during early mouse embryogenesis. *Proc. Natl. Acad. Sci. U. S. A.* 111, 4478–4483. doi:10.1073/pnas.1402612111
- Mangan, S., and Alon, U. (2003). Structure and function of the feed-forward loop network motif. *Proc. Natl. Acad. Sci. U. S. A.* 100, 11980–11985. doi:10.1073/pnas.2133841100
- Marcellini, S., Technau, U., Smith, J. C., and Lemaire, P. (2003). Evolution of brachyury proteins: Identification of a novel regulatory domain conserved within bilateria. *Dev. Biol.* 260, 352–361. doi:10.1016/s0012-1606(03)00244-6
- McWilliam, H., Li, W., Uludag, M., Squizzato, S., Park, Y. M., Buso, N., et al. (2013). Analysis tool web services from the EMBL-EBI. *Nucleic Acids Res.* 41, W597–W600. doi:10.1093/nar/gkt376
- Melby, A. E., Kimelman, D., and Kimmel, C. B. (1997). Spatial regulation of floating head expression in the developing notochord. *Dev. Dyn.* 209, 156–165. doi:10.1002/(SICI)1097-0177(199706)209:2<156::AID-AJA2>3.0.CO;2-H
- Melville, M., Lun, A., Djekidel, M. N., and Hao, Y. (2020). uwot: The uniform manifold approximation and projection (UMAP) method for dimensionality reduction. R package version 0.1.11. Available at: <https://cran.r-project.org/web/packages/uwot/index.html>.
- Miller-bertoglio, V. E., Fisher, S., Sanchez, A., Mullins, M. C., and Halpern, M. E. (1997). Differential regulation of chordin expression domains in mutant zebrafish. *Dev. Biol.* 192, 537–550. doi:10.1006/dbio.1997.8788
- Mione, M., Shanmugalingam, S., Kimelman, D., and Griffin, K. (2001). Overlapping expression of zebrafish T-brain-1 and eomesodermin during forebrain development. *Mech. Dev.* 100, 93–97. doi:10.1016/s0925-4773(00)00501-3
- Morley, R. H., Lachani, K., Keefe, D., Gilchrist, M. J., Flicke, P., Smith, J. C., et al. (2009). A gene regulatory network directed by zebrafish No tail accounts for its roles in mesoderm formation. *Proc. Natl. Acad. Sci. U. S. A.* 106, 3829–3834. doi:10.1073/pnas.0808382106
- Nelson, A. C., Cutty, S. J., Gasiunas, S. N., Deplae, I., Stemple, D. L., and Wardle, F. C. (2017). *In vivo* regulation of the zebrafish endoderm progenitor niche by T-box transcription factors. *Cell Rep.* 19, 2782–2795. doi:10.1016/j.celrep.2017.06.011
- Nelson, A. C., Cutty, S. J., Niini, M., Stemple, D. L., Flicke, P., Houart, C., et al. (2014). Global identification of Smad2 and Eomesodermin targets in zebrafish identifies a conserved transcriptional network in mesendoderm and a novel role for Eomesodermin in repression of ectodermal gene expression. *BMC Biol.* 12, 81. doi:10.1186/s12915-014-0081-5
- Nelson, A. C., Pillay, N., Henderson, S., Presneau, N., Tirabosco, R., Halai, D., et al. (2012). An integrated functional genomics approach identifies the regulatory network directed by brachyury (T) in chordoma. *J. Pathol.* 228, 274–285. doi:10.1002/path.4082
- Niwa, H., Toyooka, Y., Shimamoto, D., Strumpf, D., Takahashi, K., Yagi, R., et al. (2005). Interaction between Oct3/4 and Cdx2 determines trophoblast differentiation. *Cell* 123, 917–929. doi:10.1016/j.cell.2005.08.040
- Nowotzsch, S., Costello, I., Piliszek, A., Kwon, G. S., Mao, C. A., Klein, W. H., et al. (2013). The T-box transcription factor Eomesodermin is essential for AVE induction in the mouse embryo. *Genes Dev.* 27, 997–1002. doi:10.1101/gad.215152.113
- Papaioannou, V. E. (2014). The T-box gene family: Emerging roles in development, stem cells and cancer. *Development* 141, 3819–3833. doi:10.1242/dev.104471
- Pearce, E. L., Mullen, A. C., Martins, G. A., Krawczyk, C. M., Hutchins, A. S., Zedlak, V. P., et al. (2003). Control of effector CD8(+) T cell function by the transcription factor Eomesodermin. *Science* 302, 1041–1043. doi:10.1126/science.1090148
- Piccozzi, P., Wang, F., Cronk, K., and Ryan, K. (2009). Eomesodermin requires transforming growth factor-beta/activin signaling and binds Smad2 to activate mesodermal genes. *J. Biol. Chem.* 284, 2397–2408. doi:10.1074/jbc.M808704200
- Probst, S., and Arnold, S. J. (2017). Eomesodermin-at dawn of cell fate decisions during early embryogenesis. *Curr. Top. Dev. Biol.* 122, 93–115. doi:10.1016/bs.ctdb.2016.09.001
- Ramani, A. K., Calarco, J. A., Pan, Q., Mavandadi, S., Wang, Y., Nelson, A. C., et al. (2011). Genome-wide analysis of alternative splicing in *Caenorhabditis elegans*. *Genome Res.* 21, 342–348. doi:10.1101/gr.114645.110

- Reiter, J. F., Alexander, J., Rodaway, A., Yelon, D., Patient, R., Holder, N., et al. (1999). Gata5 is required for the development of the heart and endoderm in zebrafish. *Genes Dev.* 13, 2983–2995. doi:10.1101/gad.13.22.2983
- Reiter, J. F., Kikuchi, Y., and Stainier, D. Y. (2001). Multiple roles for Gata5 in zebrafish endoderm formation. *Development* 128, 125–135. doi:10.1242/dev.128.1.125
- Rohde, L. A., Oates, A. C., and Ho, R. K. (2004). A crucial interaction between embryonic red blood cell progenitors and paraxial mesoderm revealed in spadetail embryos. *Dev. Cell* 7, 251–262. doi:10.1016/j.devcel.2004.07.010
- Russ, A. P., Wattler, S., Colledge, W. H., Aparicio, S. A., Carlton, M. B., Pearce, J. J., et al. (2000). Eomesodermin is required for mouse trophoblast development and mesoderm formation. *Nature* 404, 95–99. doi:10.1038/35003601
- Sebe-pedros, A., Ariza-Cosano, A., Weirauch, M. T., Leininger, S., Yang, A., Torruella, G., et al. (2013). Early evolution of the T-box transcription factor family. *Proc. Natl. Acad. Sci. U. S. A.* 110, 16050–16055. doi:10.1073/pnas.1309748110
- Sievers, F., Wilm, A., Dineen, D., Gibson, T. J., Karplus, K., Li, W., et al. (2011). Fast, scalable generation of high-quality protein multiple sequence alignments using Clustal Omega. *Mol. Syst. Biol.* 7, 539. doi:10.1038/msb.2011.75
- Simonetta, F., Pradier, A., and Roosnek, E. (2016). T-Bet and eomesodermin in NK cell development, maturation, and function. *Front. Immunol.* 7, 241. doi:10.3389/fimmu.2016.00241
- Spir, M. L., Zweig, A. S., Rosenbloom, K. R., Raney, B. J., Paten, B., Nejad, P., et al. (2016). The UCSC genome browser database: 2016 update. *Nucleic Acids Res.* 44, D717–D725. doi:10.1093/nar/gkv1275
- Strumpf, D., Mao, C. A., Yamanaka, Y., Ralston, A., Chawengsaksophak, K., Beck, F., et al. (2005). Cdx2 is required for correct cell fate specification and differentiation of trophectoderm in the mouse blastocyst. *Development* 132, 2093–2102. doi:10.1242/dev.01801
- Stuart, T., Butler, A., Hoffman, P., Hafemeister, C., Papalexi, E., Mauck, W. M., et al. (2019). Comprehensive integration of single-cell data. *Cell* 177, 1888–1902. doi:10.1016/j.cell.2019.05.031
- Takizawa, F., Araki, K., Ito, K., Moritomo, T., and Nakanishi, T. (2007). Expression analysis of two Eomesodermin homologues in zebrafish lymphoid tissues and cells. *Mol. Immunol.* 44, 2324–2331. doi:10.1016/j.molimm.2006.11.018
- Takizawa, F., Araki, K., Ohtani, M., Toda, H., Saito, Y., Lampe, V. S., et al. (2014). Transcription analysis of two Eomesodermin genes in lymphocyte subsets of two teleost species. *Fish. Shellfish Immunol.* 36, 215–222. doi:10.1016/j.fsi.2013.11.004
- Talbot, W. S., Trevarrow, B., Halpern, M. E., Melby, A. E., Farr, G., Postlethwait, J. H., et al. (1995). A homeobox gene essential for zebrafish notochord development. *Nature* 378, 150–157. doi:10.1038/378150a0
- Teo, A. K., Arnold, S. J., Trotter, M. W., Brown, S., Ang, L. T., Chng, Z., et al. (2011). Pluripotency factors regulate definitive endoderm specification through eomesodermin. *Genes Dev.* 25, 238–250. doi:10.1101/gad.607311
- Tsankov, A. M., Gu, H., Akopian, V., Ziller, M. J., Donaghey, J., Amit, I., et al. (2015). Transcription factor binding dynamics during human ES cell differentiation. *Nature* 518, 344–349. doi:10.1038/nature14233
- Vesterlund, L., Jiao, H., Unneberg, P., Hovatta, O., and Kere, J. (2011). The zebrafish transcriptome during early development. *BMC Dev. Biol.* 11, 30. doi:10.1186/1471-213X-11-30
- Wagner, D. E., Weinreb, C., Collins, Z. M., Briggs, J. A., Megason, S. G., and Klein, A. M. (2018). Single-cell mapping of gene expression landscapes and lineage in the zebrafish embryo. *Science* 360, 981–987. doi:10.1126/science.aar4362
- Wang, E. T., Sandberg, R., Luo, S., Khrebtkova, I., Zhang, L., Mayr, C., et al. (2008). Alternative isoform regulation in human tissue transcriptomes. *Nature* 456, 470–476. doi:10.1038/nature07509
- Wardle, F. C., and Papaioannou, V. E. (2008). Teasing out T-box targets in early mesoderm. *Curr. Opin. Genet. Dev.* 18, 418–425. doi:10.1016/j.gde.2008.07.017
- Warga, R. M., Mueller, R. L., Ho, R. K., and Kane, D. A. (2013). Zebrafish Tbx16 regulates intermediate mesoderm cell fate by attenuating Fgf activity. *Dev. Biol.* 383, 75–89. doi:10.1016/j.ydbio.2013.08.018
- Waterhouse, A. M., Procter, J. B., Martin, D. M., Clamp, M., and Barton, G. J. (2009). Jalview Version 2—a multiple sequence alignment editor and analysis workbench. *Bioinformatics* 25, 1189–1191. doi:10.1093/bioinformatics/btp033
- Westerfield, M. (2000). *The zebrafish book. A guide for the laboratory use of zebrafish* (Danio rerio). 4th Ed. Eugene: University of Oregon Press.
- White, R. J., Collins, J. E., Sealy, I. M., Wali, N., Dooley, C. M., Digby, Z., et al. (2017). A high-resolution mRNA expression time course of embryonic development in zebrafish. *Elife* 6, e30860. doi:10.7554/eLife.30860
- Windner, S. E., Doris, R. A., Ferguson, C. M., Nelson, A. C., Valentin, G., Tan, H., et al. (2015). Tbx6, Mesp-b and Rippl1 regulate the onset of skeletal myogenesis in zebrafish. *Development* 142, 1159–1168. doi:10.1242/dev.113431
- Xing, C., Shen, W., Gong, B., Li, Y., Yan, L., and Meng, A. (2022). Maternal factors and nodal autoregulation orchestrate nodal gene expression for embryonic mesendoderm induction in the zebrafish. *Front. Cell Dev. Biol.* 10, 887987. doi:10.3389/fcell.2022.887987
- Xu, P., Zhu, G., Wang, Y., Sun, J., Liu, X., Chen, Y. G., et al. (2014). Maternal Eomesodermin regulates zygotic nodal gene expression for mesendoderm induction in zebrafish embryos. *J. Mol. Cell Biol.* 6, 272–285. doi:10.1093/jmcb/mju028
- Yates, A., Akanni, W., Amode, M. R., Barrell, D., Billis, K., Carvalho-Silva, D., et al. (2016). Ensembl 2016. *Nucleic Acids Res.* 44, D710–D716. doi:10.1093/nar/gkv1157
- Yu, X., Ng, C. P., Habacher, H., and Roy, S. (2008). Foxj1 transcription factors are master regulators of the motile ciliogenic program. *Nat. Genet.* 40, 1445–1453. doi:10.1038/ng.263



OPEN ACCESS

EDITED BY
Silvia Garagna,
University of Pavia, Italy

REVIEWED BY
Chiara Gamberi,
Coastal Carolina University,
United States
Oliver Wessely,
Cleveland Clinic Lerner Research
Institute, United States

*CORRESPONDENCE
Michael D. Sheets,
mdsheets@wisc.edu

†PRESENT ADDRESS
Cole R. K. Harder,
University of California Santa Cruz,
Santa Cruz, CA, United States; Samuel
Moffet, Georgetown University School
of Medicine, Washington, DC,
United States

†These authors have contributed equally
to this work

SPECIALTY SECTION
This article was submitted to
Morphogenesis and Patterning,
a section of the journal
Frontiers in Cell and Developmental
Biology

RECEIVED 29 June 2022
ACCEPTED 11 August 2022
PUBLISHED 07 September 2022

CITATION
Dowdle ME, Kanzler CR, Harder CRK,
Moffet S, Walker MN and Sheets MD
(2022), Bicaudal-C Post-transcriptional
regulator of cell fates and functions.
Front. Cell Dev. Biol. 10:981696.
doi: 10.3389/fcell.2022.981696

COPYRIGHT
© 2022 Dowdle, Kanzler, Harder,
Moffet, Walker and Sheets. This is an
open-access article distributed under
the terms of the [Creative Commons
Attribution License \(CC BY\)](#). The use,
distribution or reproduction in other
forums is permitted, provided the
original author(s) and the copyright
owner(s) are credited and that the
original publication in this journal is
cited, in accordance with accepted
academic practice. No use, distribution
or reproduction is permitted which does
not comply with these terms.

Bicaudal-C Post-transcriptional regulator of cell fates and functions

Megan E. Dowdle[†], Charlotte R. Kanzler[†], Cole R. K. Harder^{††},
Samuel Moffet^{††}, Maya N. Walker and Michael D. Sheets*

Department of Biomolecular Chemistry, School of Medicine and Public Health, University of Wisconsin, Madison, WI, United States

Bicaudal-C (Bicc1) is an evolutionarily conserved RNA binding protein that functions in a regulatory capacity in a variety of contexts. It was originally identified as a genetic locus in *Drosophila* that when disrupted resulted in radical changes in early development. In the most extreme phenotypes embryos carrying mutations developed with mirror image duplications of posterior structures and it was this striking phenotype that was responsible for the name Bicaudal. These seminal studies established Bicc1 as an important regulator of *Drosophila* development. What was not anticipated from the early work, but was revealed subsequently in many different organisms was the broad fundamental impact that Bicc1 proteins have on developmental biology; from regulating cell fates in vertebrate embryos to defects associated with several human disease states. In the following review we present a perspective of Bicc1 focusing primarily on the molecular aspects of its RNA metabolism functions in vertebrate embryos.

KEYWORDS

mRNA translation, embryonic cell fate, Bicaudal-C family RNA binding protein 1 (Bicc1), post-transcriptional control, cell fate and differentiation

Introduction

The advent of omics technologies has led to the identification of many new and novel RNA binding proteins (RBPs). Strategies such as RNA interaction capture have identified hundreds of RBPs, many of which were previously not known to associate with RNAs or be involved in RNA metabolism (Castello et al., 2016). Many RBPs are post-transcriptional regulators of gene expression that function by participating in one or more steps of mRNA metabolism; from splicing and export out of the nucleus, to subcellular localization, translation and degradation in the cytoplasm (Perez-Perri et al., 2018, 2021). Precedents from well-studied examples suggest that each protein binds to hundreds of RNAs to form a regulatory network (Hentze et al., 2018; Gebauer et al., 2021). Each individual network forms a functional unit of regulation used by cells to adapt to changing conditions or modify cellular functions as part of a developmental program.

In contrast to their identification and molecular characterization *en masse*, the contribution and relevance of individual RBPs to specific aspects of biology has

advanced much more slowly. The biological importance of individual RBPs for specific biological processes has often been revealed through either deregulation *via* increases or decreases in expression or structural changes as a result of mutation. The challenge is to define the underlying molecular mechanisms and the networks organized around a particular RBP and functionally connect these to the relevant biology.

Bicaudal-C (Bicc1) is a highly conserved RNA binding protein that functions in a regulatory capacity in many different contexts. It was originally identified as a genetic locus in *Drosophila* that when disrupted, resulted in dramatic changes in early development: embryos carrying mutations developed with mirror image duplications of the posterior structures (Bull, 1966; Mohler and Wieschaus, 1986). These initial studies established Bicaudal-C as an important regulator of *Drosophila* development. Motivated by these findings, developmental biologists identified Bicc1 orthologs and applied a number of strategies to functionally connect this protein to specific embryonic processes. What was revealed was the broad fundamental impact that Bicc1 proteins have on developmental biology and regulating cell fates in vertebrate embryos. In the following review we present a perspective of Bicc1, focusing primarily on the molecular aspects of its RNA metabolism functions in vertebrate embryos.

Bicaudal-C maternal regulatory protein discovered in *Drosophila*

One of the most critical issues in oogenesis and embryogenesis is defining how the egg and embryo establish polarity to initiate body patterning. An early study published in 1966 on this topic focused on the genetic causes of the double-abdomen or “bicaudal” phenotype in *Drosophila* embryos (Bull, 1966). Genetic analysis revealed that the bicaudal phenotype arose from maternal mutations that could be assigned to specific chromosomal regions, though not at high resolution (Bull, 1966). Subsequent studies identified the gene responsible and named it Bicaudal-C (BicC, the fly ortholog of vertebrate Bicc1) (Mohler and Wieschaus, 1986; Mahone et al., 1995). The predicted Bicaudal-C protein is composed of several putative RNA binding domains and biochemical experiments demonstrated that the protein could efficiently bind to Poly (U) *in vitro* (Mahone et al., 1995). The first evidence that Bicaudal-C functions as a translational repressor came from observations that *Drosophila* BicC loss-of-function mutants affect anterior-posterior patterning as a result of ectopic and premature translation of the posterior determinant oskar (Saffman et al., 1998). Subsequent analysis revealed that Bicaudal-C was conserved throughout the animal kingdom and the first vertebrate ortholog was identified and characterized from *Xenopus* (Wessely and De Robertis, 2000), followed shortly by a mammalian ortholog (Wessely et al., 2001).

Comparison of Bicc1 proteins from different organisms reveals several conserved features (Figure 1). The amino terminal half of the protein contains three hnRNP K homology (KH) domains (KH1, KH2 and KH3), with the KH3 domain being flanked on each side by KH-like (KHL) domains. KH domains are found in a wide variety of nucleic acid-binding proteins, especially those that function in RNA recognition (Valverde et al., 2008; Nicastro et al., 2015). Canonical KH domains contain GXXG motifs and KHL domains have the same general architecture but lack GXXG motifs. The carboxyl terminus of Bicc1 proteins contains a SAM (sterile alpha motif) domain that mediates protein-protein interactions (Rothé et al., 2018). Sequence conservation among vertebrates is very high, supporting the idea that functional analysis in model organisms can be related to potential Bicc1-related clinical conditions observed in human patients (Figure 1).

Bicaudal-C regulated biological processes

Anterior-posterior patterning

The first vertebrate Bicc1 ortholog was identified in *Xenopus* (Wessely and De Robertis, 2000). The *bicc1* mRNA is highly expressed maternally and localized to vegetal cells of developing embryos (Figure 2A). Subsequent analysis identified Bicc1 as a regulator of maternal mRNA translation and in particular translation of the *cripto1* (*tdgf1.3*) mRNA that encodes a cell fate regulatory protein (Figure 3) (Zhang et al., 2013). These connections provided the motivation for analyzing the consequences of removing Bicc1 from vertebrate embryos. To address this issue, *Xenopus* embryos depleted of maternal Bicc1 were generated using the host transfer approach (Park et al., 2016). Bicc1-depleted embryos develop with an expansion of anterior structures (enlarged heads and cement glands) and cell types at the expense of posterior cells (Figure 2B). These morphological changes are accompanied by characteristic changes in the expression of anterior/posterior-specific mRNAs (Park et al., 2016). The anteriorized phenotype due to Bicc1 depletion is the opposite of the phenotypes caused by depleting *Xenopus* embryos of maternal mRNAs encoding either the *cripto1*, *wnt11b* or *dand5* (*coco*) cell fate regulatory proteins (Tao et al., 2005; Bates et al., 2013). Since these mRNAs are known Bicc1 targets, these phenotypes suggest that a Bicc1 depletion increases the translation of these targets, a suggestion supported by data demonstrating that Bicc1 represses *cripto1*, *dand5* and *wnt11b* mRNA reporters (Zhang et al., 2013; Park et al., 2016). Thus, maternal Bicc1 in *Xenopus* embryos functions in anterior-posterior patterning by modulating the translation of mRNAs encoding cell fate determinants.

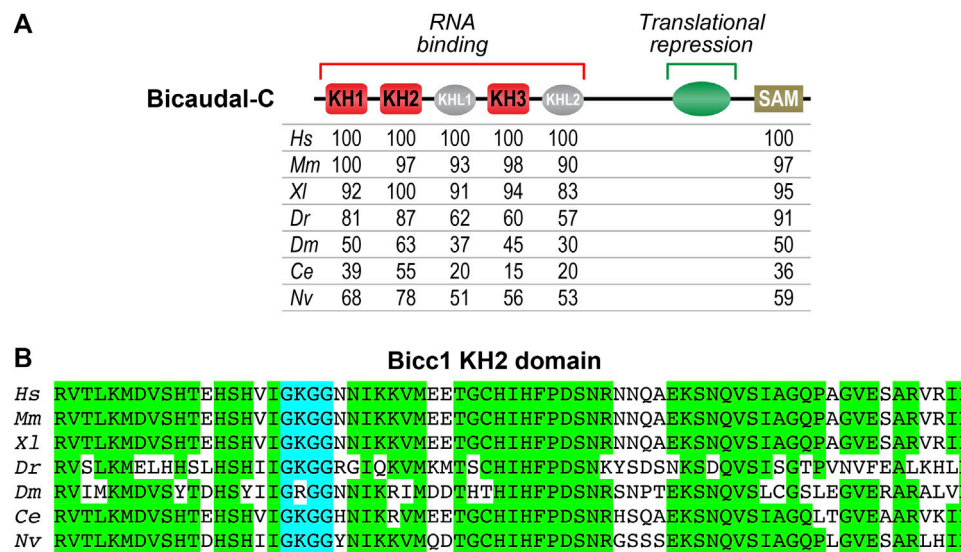


FIGURE 1 Evolutionary conservation of Bicaudal-C proteins. (A) Diagram of the Bicaudal-C protein highlighting key features. The N-terminal region contains three KH domains (KH1, KH2 and KH3) involved in RNA recognition and binding. The C-terminal region contains a SAM domain that mediates protein-protein interactions and promotes the formation of polymers. The central region of the protein (aa505–806 of *XlBicc1*) was defined through the use of the MS2 tethered function assays as being sufficient for translational repression (Zhang et al., 2013). Below the diagram are amino acid identities comparing Bicc1 proteins from different species (*Hs*—*Homo sapiens*, *Mm*—*Mus musculus*, *Xl*—*Xenopus laevis*, *Dr*—*Danio rerio*, *Dm*—*Drosophila melanogaster*, *Ce*—*Caenorhabditis elegans*, *Nv*—*Nematostella vectensis*). The numbers indicate the percent amino acid identity compared to *Hs Bicc1*. The different domains are those identified via the NCBI database. (B) Amino acid sequence comparison of the highly conserved KH2 domains from different species. This domain is a key structural feature for recognition of specific mRNAs by Bicc1 proteins and one of the most conserved features of these proteins. Amino acids that are identical are highlighted in green. The KH2 domain's GXXG motif (GGKG) is highlighted in blue.

Left-right patterning

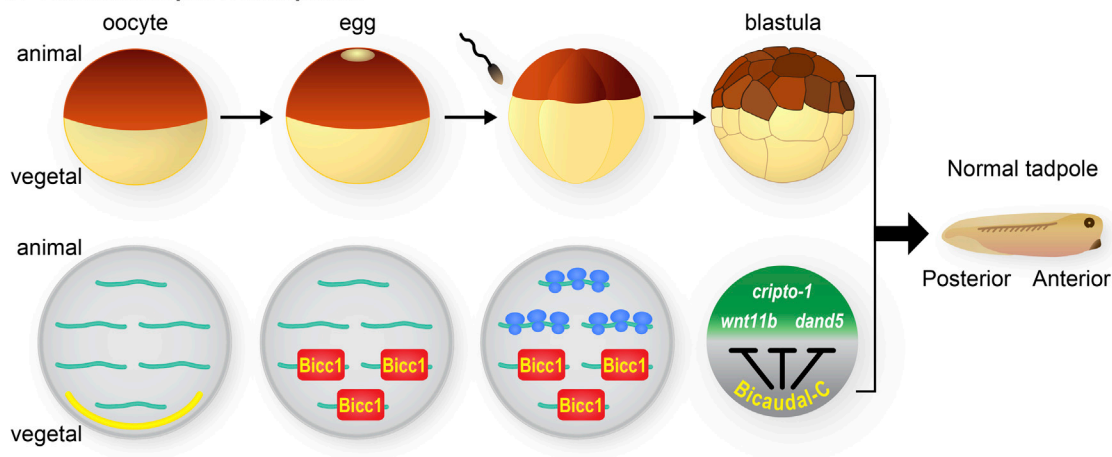
The asymmetric placement of the internal organs is critical for embryonic development of all animal species and is referred to as Left-Right (L-R) patterning (Nakamura and Hamada, 2012; Hamada, 2020). This patterning relies upon an elaborate series of well-orchestrated cellular and molecular processes. Asymmetry is initiated and driven by rotating cilia in cells of the left-right organizer (LRO) which generate an asymmetric flow. This flow is relayed to the lateral plate mesoderm (LPM) to differentially activate the Nodal signaling pathway. While the molecular cues that establish and regulate the embryonic L-R axis have been known for several years, Bicc1's role emerged relatively recently. BICC1 mutations in mouse or morpholino treatments in *Xenopus* or zebrafish embryos both revealed that disrupting Bicc1 expression leads to heterotaxy and defects in L-R patterning (Maisonneuve et al., 2009). Heterotaxy is the abnormal arrangement and structure of the abdominal organs, especially the heart. Recent evidence suggests that L-R defects due to Bicc1 are at least in part due to disrupted Bicc1 regulation of the mRNA encoding the Nodal inhibitor *dand5* (Maerker et al., 2021; Minegishi et al., 2021). The results from these studies

demonstrated the central role of Bicc1 RNA regulation in controlling L-R patterning.

Kidney function

Multiple lines of evidence have demonstrated the importance of Bicc1 for maintaining normal kidney functions. Targeted mutations of mouse *Bicc1* as well as morpholino disruption of *Xenopus* and zebrafish Bicc1 orthologs in developing embryos all result in abnormal kidneys that closely resemble defects due to polycystic kidney disease (PKD) (Cogswell et al., 2003; Tran et al., 2007, 2010; Maisonneuve et al., 2009; Bouvrette et al., 2010). In *Drosophila*, renal function is carried out by the Malpighian tubules and the nephrocytes. *Drosophila* BicC mutants develop with malformed Malpighian tubules that resemble the renal cysts found in vertebrates in which BICC1 expression is disrupted (Gamberi et al., 2017). The observed defects were attributed in part to disrupting the BicC regulation of the *myc* mRNA. While there is abundant evidence demonstrating the importance of Bicc1 in kidney functions, defining the underlying molecular mechanisms involved is an active area of investigation.

A Normal *Xenopus* Development



B Development in Absence of *Bicc1*

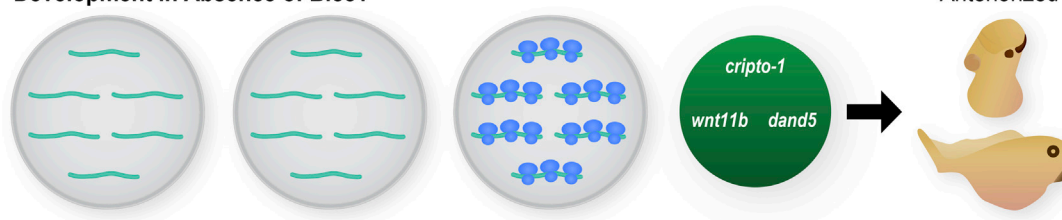
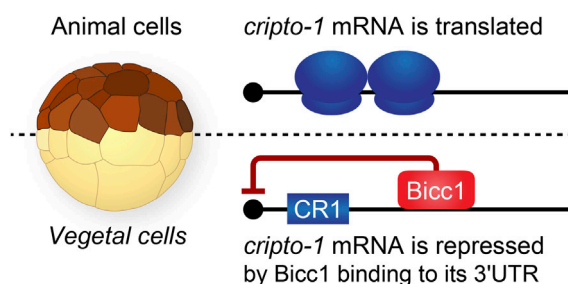


FIGURE 2

Xenopus Bicaudal-C, regulator of maternal mRNA translation and cell fates (A) The diagram at the top depicts the early stages of *Xenopus* development. Oocytes mature into eggs that are competent to be fertilized. Following fertilization the embryos undergoes a series of rapid cleavage divisions to generate blastula stage embryos. The initial stages of embryonic development occur in the absence of zygotic transcription and rely on the regulated use of maternal mRNAs and proteins. During normal development *bicc1* mRNA is localized to the vegetal cortex of fully-grown oocytes (yellow section at vegetal pole) (Wessely and De Robertis, 2000). During oocyte maturation the *bicc1* mRNA is released from the cortex and at the same time becomes translationally active to generate Bicc1 protein (Park et al., 2016). Bicc1 protein is distributed in a vegetal to animal gradient in embryos where it binds to specific mRNAs and represses their translation. Several of these target mRNAs (*cripto-1*, *wnt11b* and *dand5*) encode cell fate regulatory proteins. Bicc1 normally modulates the synthesis of these proteins and their activities contribute to the formation of a tadpole with anterior-posterior polarity. (B) Development in the absence of Bicc1. To create embryos that lack Bicc1 oocytes are injected with anti-sense oligonucleotides to specifically degrade the Bicc1 mRNA. Treated oocytes are matured and then converted to embryos using the host transfer technique (Park et al., 2016). Bicc1 target mRNAs are translated inappropriately in embryos depleted of Bicc1 and the encoded proteins accumulate to higher levels. As a consequence Bicc1 depleted embryos develop into tadpoles with an excess of anterior cell types and structures—an anteriorized phenotype (Park et al., 2016).

A *Xenopus* embryo:



B

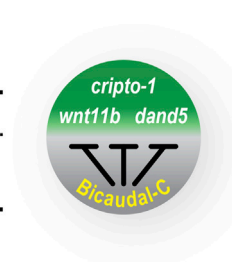


FIGURE 3

Bicaudal-C spatially regulates the accumulation of cell fate determinants in *Xenopus* embryos. (A) *Xenopus* blastula stage embryos are polarized with pigmented animal cells and non-pigmented vegetal cells. In general, mRNAs encoding cell fate determinants, such as *cripto-1* are uniformly distributed throughout the embryo. In contrast, the Bicc1 repressor protein is present in a vegetal to animal gradient in which the highest concentration of protein is present in the vegetal cells and the lowest in the animal cells (Park et al., 2016). (B) Bicc1 target mRNAs are translated into protein with different efficiencies due to their position in the Bicc1 repression gradient (Sheets et al., 2017).

Bicaudal-C target mRNAs

Xenopus *cripto1* mRNA and the spatial control of translation

The Nodal signaling pathway is critical for vertebrate development and Cripto proteins are key components of this signaling (Tao et al., 2005; Schier, 2009; Nagaoka et al., 2012; Klauzinska et al., 2014). The *Xenopus* *cripto1* mRNA is maternally expressed and its translation is both temporally and spatially regulated (Zhang et al., 2009). Specifically, the entire *cripto1* mRNA population in oocytes and eggs is translationally repressed. Then, after fertilization, the fraction of *cripto1* mRNA present in vegetal cells remains repressed while the mRNA in animal cells is actively translated (Figure 2A). Lineage-specific injection of reporter mRNAs containing the 3'UTR from the *cripto1* mRNA recapitulated the spatially regulated translation observed in embryos (Zhang et al., 2009). These results demonstrated that sequences in the 3'UTR of the *cripto1* mRNA were sufficient to direct embryonic translational repression and suggested that vegetal cells contain a repressor that functions via these 3'UTR sequences.

Multiple pieces of evidence identified Bicc1 as the vegetal cell-specific translational repressor of *cripto1* mRNA (Figures 2, 3) (Zhang et al., 2009, 2013). First, *Xenopus* *bicc1* mRNA and protein are restricted to vegetal cells of developing embryos, suggesting that the *cripto1* mRNA is not repressed in animal cells because these cells lack the Bicc1 repressor (Figures 2, 3) (Wessely and De Robertis, 2000; Park et al., 2016). This idea was tested with reporter mRNAs that were efficiently repressed in animal cells only when the animal cells ectopically expressed Bicc1 (Zhang et al., 2013). Second, the endogenous *cripto1* mRNA as well as the *cripto1* reporter mRNA were both efficiently bound by Bicc1 *in vivo* (Zhang et al., 2013). Third, a 32-nucleotide Bicc1-binding site was identified within the *cripto1* mRNA 3'UTR using biochemical approaches and reporter assays (Zhang et al., 2013, 2014; Dowdle et al., 2017). Together, these results demonstrate that *Xenopus* Bicc1 is a vegetal cell-specific repressor responsible for spatially regulating *cripto1* mRNA translation in maternal stage embryos.

Xenopus Bicc1 forms a translational repression gradient in developing embryos

The *Xenopus* maternal *bicc1* mRNA is first expressed during the early stages of oogenesis and as oogenesis proceeds the mRNA is localized to the vegetal cortex of fully-grown oocytes (Wessely and De Robertis, 2000). Then, during oocyte maturation, the *bicc1* mRNA is released from the cortex and simultaneously translationally activated to produce Bicc1 protein

(Figure 2) (Park et al., 2016). These processes create a vegetal to animal (V-A) gradient of Bicc1 protein and its repression activity that is passed on to embryonic cells after fertilization. Bicc1 repression functions are highest in vegetal cells, lowest in animal cells, and the marginal zone cells exhibit intermediate levels of activity (Park et al., 2016). There are multiple Bicc1 target mRNAs, raising the possibility that the Bicc1-repression gradient gives rise to secondary gradients of proteins encoded by Bicc1 targets. Such gradients have the potential to differ based on the affinity of individual target mRNAs for Bicc1 and the efficiency of translational repression (Sheets et al., 2017).

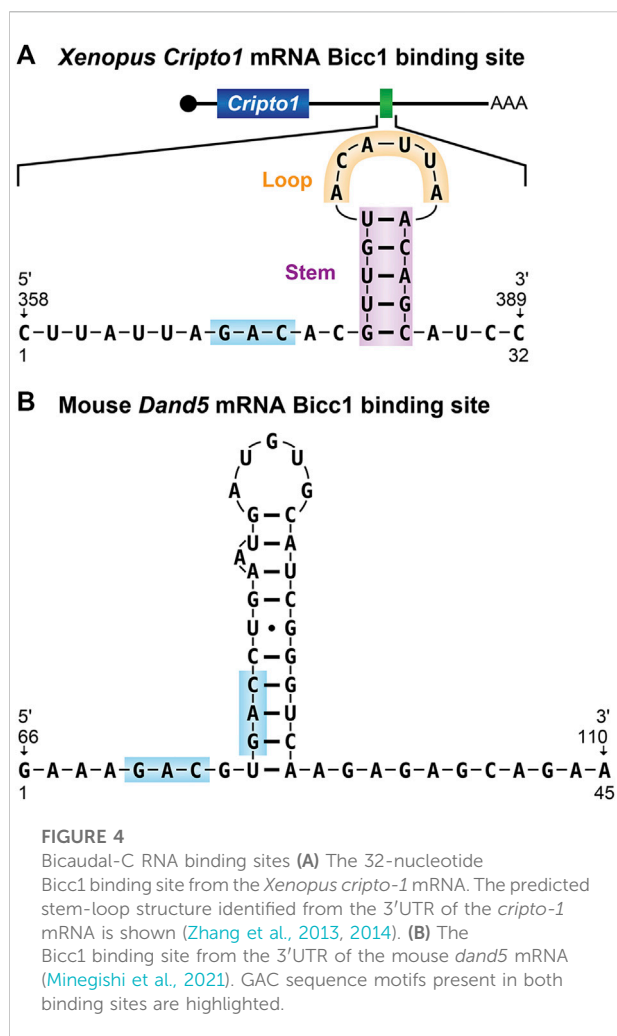
Bicc1 regulated mRNAs in mouse

The analysis of proteins whose expression increased in Bicc1^{-/-} mouse kidney tubules lead to the identification of the mRNAs encoding the adenylate cyclase-6 (Adcy6) and protein kinase inhibitor (PKIa) proteins as some of the first Bicc1 regulated mRNAs (Piazzon et al., 2012). These mRNAs were associated with Bicc1 in immunoprecipitation experiments and the translation of these mRNAs via their 3'UTRs was inhibited by Bicc1 in reporter assays. Results from co-expression network-analysis of microarray experiments, identified Bicc1 as a genetic determinant of osteoblastogenesis in part through its regulation of Pkd2 transcript levels (Lemaire et al., 2015). Additionally, comparison of mRNA changes in pancreatic cells between WT and Bicc1 knockouts indicated that Pkd2 functions downstream of Bicc1 in preventing pancreatic cyst formation (Mesner et al., 2014). Thus, Pkd2 mediates Bicc1 activity in multiple contexts. Recent studies identified mouse *dand5* as a Bicc1 regulated mRNA and a key component of the L-R patterning pathway (see below) (Minegishi et al., 2021).

The *Xenopus* Bicc1 network

mRNA binding proteins (RBPs) manifest themselves phenotypically through binding and impacting the function of specific mRNAs. Hence, the key issue for each RBP is identifying the relevant target mRNAs. The first suspected target for BicC was the *Drosophila* *oskar* mRNA (Mahone, Saffman and Lasko, 1995; Saffman et al., 1998). It was observed that in BicC^{-/-} mutant *Drosophila* embryos *oskar* mRNA was translated at higher levels than in wild-type embryos. A subsequent study in *Drosophila* identified multiple BicC target mRNAs using microarrays that included the mRNA encoding BicC itself (Chicoine et al., 2007).

In *Xenopus* embryos 63 Bicc1 target mRNAs were identified using RNA immunoprecipitation sequencing (RIP-SEQ) (Zhang et al., 2013). Many of these targets were validated using follow-up experiments, including luciferase reporter assays in which the reporters contained the 3'UTRs of potential targets. Among the



validated targets were mRNAs such as *cripto1* and *dand5* that encode known signaling proteins important for fate decisions in *Xenopus* and other vertebrate embryos (Tao et al., 2005; Bates et al., 2013). Subsequent studies in *Xenopus* also identified the *wnt11b* and *gdf3* mRNAs as additional authentic Bicc1 targets (Park et al., 2016; Maerker et al., 2021). These results defined the Bicc1 target mRNA network and provided a foundation for understanding the molecular events that underlie Bicc1 regulated biological events during vertebrate development and potentially other contexts.

Mechanisms of mRNA binding and regulation

mRNA features required for Bicaudal-C binding

The most well characterized Bicc1-RNA interface is recognition of the *Xenopus cripto1* mRNA, as described above.

A combination of EMSA (electrophoretic mobility shift assays), RNase footprinting, and reporter experiments demonstrated that Bicc1 recognizes the *cripto1* mRNA via a 32-nucleotide region located within its 3'UTR that is predicted to form a stem-loop structure (Figure 4) (Zhang et al., 2013, 2014; Dowdle et al., 2017, 2019). The double-stranded properties of the stem along with the nucleotide sequence of the loop were found to be important determinants of binding (Zhang et al., 2014). However, the stem-loop alone was not sufficient for Bicc1 binding, indicating that other important features remain to be defined (Zhang et al., 2014).

Recent work in *Xenopus*, zebrafish, and mouse identified Bicc1 as an important factor downstream of flow sensing in L-R patterning via regulation of the *dand5* and *gdf3* mRNAs. In *Xenopus* embryos Bicc1 functions in pre-flow regulation in the left-right organizer by stabilizing the *gdf3* and *dand5* mRNAs via their 3'UTRs (Maerker et al., 2021). In post-flow stages, Bicc1 functions as a potent repressor of *dand5* translation mediated by the proximal-most 139 nucleotides of the *dand5* 3'-UTR. Deleting the distal 36 nucleotides of this region renders the *dand5* mRNA insensitive to Bicc1 regulation and as such the region was referred to as the Bicc1 response element. This post-transcriptional mechanism is conserved and in mouse an analogous proximal element of the *dand5* 3'-UTR is required for Bicc1-dependent flow-mediated mRNA decay and translational inhibition (Minegishi et al., 2021). Bicc1 also represses translation of the *Xenopus gdf3* mRNA via its 3'UTR (Maerker et al., 2021). Because the *gdf3* protein also influences Nodal signaling it is clear there are multiple paths by which Bicc1 influences L-R patterning.

Studies in mouse found that the first 200 nucleotides of the *dand5* 3'UTR were both necessary and sufficient for Bicc1 regulation and binding (Minegishi et al., 2021). To define sequences with the potential for Bicc1 binding, RNA Bind-n-Seq experiments were performed using lysates generated from FLAG-tagged Bicc1-expressing 293FT cells as the source of protein. The results revealed the enrichment of primarily two sequence motifs YGAC and GACR. These motifs were present in the critical regions of both mouse and *Xenopus dand5* 3'-UTRs, adjacent to one another in a potential tandem bipartite organization. These motifs as well as their organization are conserved in 3'UTRs of *dand5* mRNAs from mammals, *Xenopus* and medaka. It was noted that while other Bicc1 regulated mRNAs, such as the Zebrafish *dand5* mRNA and *Xenopus cripto-1* mRNAs, lack such bipartite motifs, they do contain single GAC sequences in their 3'-UTRs. Thus, the generality of the bipartite GAC features for other Bicc1 target mRNAs remains to be established.

Biochemical EMSA experiments demonstrated that wild-type *dand5* RNA substrates were efficiently bound by Bicc1 and RNAs containing changes to the GAC motifs disrupted binding (Minegishi et al., 2021). Accompanying *in vivo* analysis of a *dand5* reporter mRNA containing nucleotide

changes of the GAC motif demonstrated that without the intact motif, Biccl binding in mammalian cells was inefficient. Together, these results suggest that Biccl binding to the Dand5 3'-UTR is mediated by GAC motifs in a bipartite organization (Figure 4).

Features of the biccl1 protein required for mRNA recognition

The structural features needed for efficient and specific RNA binding by Biccl have been analyzed most extensively with the *Xenopus* protein. Biochemical experiments combined with the *in vivo* results from immunoprecipitation-RT-QPCR analyses demonstrated that the *Xenopus* Biccl N-terminal region (amino acid residues 1–505) was necessary and sufficient for specific RNA binding while the C-terminal region lacked activity (Zhang et al., 2013, 2014; Dowdle et al., 2017, 2019).

The N-terminal region of Biccl contains three evolutionarily conserved KH domains (KH1, KH2 and KH3) and 2 KH-like (KHL1 and KHL2) (Figure 1). Multi-KH domain containing proteins often use only a specific subset of domains for RNA binding (Nicastrò et al., 2015; Farina et al., 2003; Chao et al., 2010). To address this issue with Biccl, variants of the *Xenopus* protein lacking one or more KH domains were examined for RNA binding both *in vivo* and *in vitro*. All three KH domains are required for specific RNA binding, suggesting a potentially complex mechanism of RNA recognition (Dowdle et al., 2019).

Canonical KH domains contain conserved GXXG motifs that provide contacts with the backbone of RNA substrates (Valverde et al., 2008; Nicastrò et al., 2015). In studies of model KH domain-containing proteins, GDDG substitutions abolish the RNA binding functions of individual domains without perturbing overall protein architecture or the function of adjacent domains (Hollingworth et al., 2012). Analyzing a collection of *Xenopus* Biccl proteins with GDDG substitutions in individual KH domains revealed that the GXXG motif of the KH2 domain (GKGG) was a major determinant of Biccl RNA binding (Dowdle et al., 2019). Consistent with its functional importance, the KH2 domain and its GKGG motif are two of the most highly conserved features of Biccl proteins (Figure 1).

Recent work analyzing mouse Biccl found a similar primary importance of the KH2 domain and its GKGG motif for recognition of the *dand5* mRNA (Minegishi et al., 2021). In addition, a requirement for the KH1 domain via its GXXG motif for *dand5* mRNA binding was also observed. This latter observation differs from what was observed with *Xenopus* Biccl and its binding to the *cripto1* mRNA where KH1 and its GXXG motif were not critical for RNA binding (Dowdle et al., 2019). These findings raise the possibility that Biccl recognizes different mRNAs and different sequences through the use of distinct combinations of KH domains.

mRNA regulation by Bicaudal-C

Identification of the BicC gene in *Drosophila* provided the amino sequence of the predicted protein and revealed the presence of putative KH domains (Saffman et al., 1998). This identification immediately suggested that the KH domains were important for the mRNA binding activities of BicC as similar domains in other proteins were known to mediate their interactions with RNA targets (Valverde et al., 2008; Nicastrò et al., 2015). In contrast, the protein sequence did not reveal any clues to suggest how BicC regulates mRNAs and addressing this issue required unbiased experimental analysis.

To begin defining *Xenopus* Biccl's mRNA regulatory functions, the protein and different subregions was analyzed using an MS2 tethering assay (Zhang et al., 2013). One of the powerful aspects of this assay is that it allows the RNA regulatory functions to be analyzed independent of Biccl's RNA binding activity. The full-length and the C-terminal region of Biccl (aa505–805) were highly effective at mRNA repression (Figure 1). In contrast, the N-terminal region and the SAM domain exhibited no detectable repression activities. Biccl repression was due to disrupting translation and not due to differences in mRNA stability or the removal of poly(A). These functions are conserved, as the C-terminal region of human Biccl also repressed efficiently (Zhang et al., 2013). Thus, the C-terminal region of *Xenopus* Biccl is sufficient for translational repression and as such represents the Biccl repression domain analogous to what has been defined for the human Pumilio protein (Figure 1) (Enwerem et al., 2021).

One of the principal mechanisms by which Biccl represses target mRNAs is through interactions with the major eukaryotic mRNA deadenylase, the Ccr4-Not deadenylase complex (CNOT complex). Studies in *Drosophila* ovarian extracts were the first to observe that BicC interacts with the Ccr4 and NOT3/5 subunits of the CNOT complex (Chicoine et al., 2007). The interaction with the NOT3/5 protein was direct as it was also detected with recombinant protein produced in *E. coli*. BicC mutant embryos exhibited a stage-dependent impact on the length of the poly(A) tails of target mRNAs. This led to a model in which BicC recruits the CNOT complex to these mRNAs and impacts their translation by poly(A) removal (Chicoine et al., 2007).

Mammalian CNOT1 was identified as an interaction partner with mouse Biccl in HEK293 cells (Leal-Esteban et al., 2018). Further connections between Biccl and the CNOT complex were investigated in the context of left/right patterning and mouse *dand5* mRNA regulation. It was observed that both the CNOT1 and CNOT3 proteins co-immunoprecipitated with mouse Biccl and these interactions depend upon the KH domains, but not the SAM domain or the presence of RNA (Minegishi et al., 2021). These results contributed to a model in

which Bicc1 in cells of the mouse node engages with the CNOT complex to regulate *dand5* mRNA.

Other evidence suggests that Bicc1 interacts with microRNAs (miRNAs) and their associated protein components to direct mRNA repression (Tran et al., 2010; Piazzon et al., 2012). In contrast to the early work done in *Drosophila*, Bicc1 did not impact the poly(A) tail of *Adcy6* target mRNA in a mouse model of polycystic kidney disease (Piazzon et al., 2012). Instead, it was hypothesized that Bicc1 was required downstream of the pri-miRNA processing enzyme Dicer to mediate an interaction between the 3'UTR of target mRNAs and the Ago2 protein, in a process that required both cognate microRNAs and the Bicc1 SAM domain (Piazzon et al., 2012). Recent studies of left-right patterning in *Xenopus* embryos implicated Bicc1 and Dicer functioning together to regulate the *dand5* mRNA (Maerker et al., 2021).

While Bicc1 has primarily been observed to impact mRNAs through mechanisms of repression, in certain contexts it may instead activate the translation of target RNAs. Specifically, in a mechanism involving miRNAs, lower levels of *Pkd2* mRNA and protein were observed in Bicc1^{-/-} mouse embryos (Tran et al., 2010). Follow-up experiments suggested that Bicc1 antagonized *miR-17*'s repressive impact on the *Pkd2* mRNA (Tran et al., 2010). Additional research will be required to elucidate the mechanistic aspects of Bicc1 mRNA activation functions.

Human BICC1 and clinical associations

Bicc1 was discovered in model organisms in the course of genetic and molecular screens designed to identify biologically important proteins. Subsequently human Bicc1 has been identified in the search for genes responsible for or associated with specific disease states.

Polycystic kidney disease

Polycystic kidney disease (PKD) is the leading cause of end-stage renal disease in children and adults. The defining characteristics of PKD are an enlargement of the kidneys accompanied by the accumulation of fluid-filled cysts that can be up to several centimeters in diameter (Bergmann et al., 2018). In model organisms mutations of mouse Bicc1 as well as morpholino disruption of *Xenopus* and zebrafish Bicc1 orthologs in developing embryos result in cystic kidneys (Cogswell et al., 2003; Tran et al., 2007, 2010; Bouvrette et al., 2010) that closely resemble the defects due to PKD. Specific BICC1 mutations have been identified in a small number of human patients with cystic kidney dysplasia (Kraus et al., 2012) as well as a cohort of fetuses affected with severe renal defects (Jordan et al., 2022).

Cholangiocarcinoma

Cholangiocarcinomas are aggressive cancers that form in the bile ducts and account for 3% of all observed gastrointestinal tumors (Schizas et al., 2020; Wang et al., 2021). Patients have a survival rate of less than 10% due to the difficulties in early detection and a lack of effective treatments. One of the most prevalent genome rearrangements that gives rise to cholangiocarcinomas is a fusion between the genes encoding FGFR2 (Fibroblast growth factor receptor 2) and BICC1 that results in the production of an FGFR2-Bicc1 fusion protein (Arai et al., 2014; Ross et al., 2014; Li et al., 2020; Scheiter et al., 2021). The kinase portion of these FGFR2-Bicc1 fusions is constitutively activated due to multimerization activities of the Bicc1 component. As part of the pathology it is the activated kinase that functions as a potent driver of cholangiocarcinoma tumors. Identifying the molecular determinants of Bicc1 multimerization is a potential strategy to develop new treatments for these cancers.

Major depressive disorder

Major Depressive Disorder (MDD) is a debilitating psychiatric condition that affects millions and significantly reduces their quality of life (Gutiérrez-Rojas et al., 2020; Cai et al., 2021; Abdoli et al., 2022; Shorey et al., 2022). BICC1 gene polymorphisms linked to MDD have been identified in several independent human Genome Wide Association Screens (Lewis et al., 2010; Bermingham et al., 2012; Ryan et al., 2016). Correlative studies of human BICC1 along with experimental investigations in rodent models have revealed potential links between the Bicc1 activity in specific neurons of the brain and severe depression. In humans, elevated levels of *bicc1* mRNA were found in postmortem brain tissues from patients that suffered from severe depression (Ota et al., 2015). In a rat model for depression the experimental reduction of *bicc1* mRNA, including the reduction through treatment with the antidepressant ketamine, significantly diminished depressive behaviors in the animals (Ota et al., 2015). These and other data provide compelling evidence that Bicc1 activity is functionally linked by poorly understood mechanisms to the pathophysiology of MDD.

Summary and conclusion

Since its discovery in *Drosophila*, Bicaudal-C has subsequently been found in a wide array of different biological contexts. However, in only a small fraction of these has it been established that Bicc1 directly impacts biology by functioning as a post-transcriptional regulator. Some of the most complete information regarding Bicc1 functions has come from the study of *Xenopus* and mouse embryos and the regulated translation of specific mRNAs. In *Xenopus* Bicc1 resides at the center of a post-transcriptional regulatory network present in early stage embryos and this network establishes the proper spatial distributions of cell fate

regulatory proteins essential for normal development. The analysis of this network has provided new insights into the regulation of cell fates in vertebrate embryos as well as providing both conceptional and technological foundations to guide the study of Bicc1 in other contexts. In particular, mutations in human BICC1 have been observed in several different disease states, but the functional consequences of these mutations in most cases have been difficult to evaluate. The ability to experimentally analyze particular aspects of Bicc1 functions in model organisms combined with the high degree of evolutionary conservation provides powerful tools to understand how defects in human BICC1 contribute to specific disease states and could lead to new diagnostics and treatments for such disorders.

Author contributions

Conceptualization: Writing—original draft: MD, CK, CH, SM, MS; Writing—review and editing: MD, CK, MW, MS; Supervision: MS; Project administration: MS; Funding acquisition: MS.

Funding

This work was supported by National Institutes of Health grant R01HD091921 to MS. MD was supported by a SciMed GRS Advanced Opportunity Fellowship through University of Wisconsin-Madison Graduate School. MD. and CK were supported by Biotechnology Training Program through the

National Institute of General Medical Sciences of the National Institutes of Health (T32GM008349 and T32GM135066).

Acknowledgments

We thank Laura Vanderploeg for preparing the figures. We thank the National *Xenopus* Resource and Xenbase for valuable information and resources. We thank Catherine Fox for her enlivening and invaluable discussions.

Conflict of interest

The authors declare that the research was conducted in the absence of any commercial or financial relationships that could be construed as a potential conflict of interest.

Publisher's note

All claims expressed in this article are solely those of the authors and do not necessarily represent those of their affiliated organizations, or those of the publisher, the editors and the reviewers. Any product that may be evaluated in this article, or claim that may be made by its manufacturer, is not guaranteed or endorsed by the publisher.

References

- Abdoli, N., Salari, N., Darvishi, N., Jafarpour, S., Solaymani, M., Mohammadi, M., et al. (2022). The global prevalence of major depressive disorder (MDD) among the elderly: A systematic review and meta-analysis. *Neurosci. Biobehav. Rev.* 132, 1067–1073. doi:10.1016/j.neubiorev.2021.10.041
- Arai, Y., Totoki, Y., Hosoda, F., Shiota, T., Hama, N., Nakamura, H., et al. (2014). Fibroblast growth factor receptor 2 tyrosine kinase fusions define a unique molecular subtype of cholangiocarcinoma. *Hepatology* 59 (4), 1427–1434. doi:10.1002/hep.26890
- Bates, T. J. D., Vonica, A., Heasman, J., Brivanlou, A. H., and Bell, E. (2013). Coco regulates dorsoventral specification of germ layers via inhibition of TGF β signalling. *Development* 140 (20), 4177–4181. doi:10.1242/dev.095521
- Bergmann, C., Guay-Woodford, L. M., Harris, P. C., Horie, S., Peters, D. J. M., and Torres, V. E. (2018). Polycystic kidney disease. *Nat. Rev. Dis. Prim.* 4 (1), 50. doi:10.1038/s41572-018-0047-y
- Bermingham, R., Carballo, A., Lisecka, D., Fagan, A., Morris, D., Fahey, C., et al. (2012). Effect of genetic variant in BICC1 on functional and structural brain changes in depression. *Neuropsychopharmacology* 37 (13), 2855–2862. doi:10.1038/npp.2012.158
- Bouvette, D. J., Sittaramane, V., Heidel, J. R., Chandrasekhar, A., and Bryda, E. C. (2010). Knockdown of bicaudal C in zebrafish (*Danio rerio*) causes cystic kidneys: a nonmammalian model of polycystic kidney disease. *Comp. Med.* 60 (2), 96–106.
- Bull, A. L. (1966). Bicaudal, a genetic factor which affects the polarity of the embryo in *Drosophila melanogaster*. *J. Exp. Zool.* 161, 221–241. doi:10.1002/jez.1401610207
- Cai, H., Xie, X. M., Zhang, Q., Cui, X., Lin, J. X., Sim, K., et al. (2021). Prevalence of suicidality in major depressive disorder: A systematic review and meta-analysis of comparative studies. *Front. Psychiatry* 12, 690130. doi:10.3389/fpsy.2021.690130
- Castello, A., Fischer, B., Frese, C. K., Horos, R., Alleaume, A. M., Foehr, S., et al. (2016). Comprehensive identification of RNA-binding domains in human cells. *Mol. Cell* 63 (4), 696–710. doi:10.1016/j.molcel.2016.06.029
- Chao, J. A., Patskovsky, Y., Patel, V., Levy, M., Almo, S. C., and SingerFischer, R. H. (2010). ZBP1 recognition of beta-actin zipcode induces RNA looping. *Gen. Develop.* 24 (2), 148–158. doi:10.1101/gad.1862910
- Chicoine, J., Benoit, P., Gamberi, C., Paliouras, M., Simonelig, M., and Lasko, P. (2007). Bicaudal-C recruits CCR4-NOT deadenylase to target mRNAs and regulates oogenesis, cytoskeletal organization, and its own expression. *Dev. Cell* 13 (5), 691–704. doi:10.1016/j.devcel.2007.10.002
- Cogswell, C., Price, S. J., Hou, X., Guay-Woodford, L. M., Flaherty, L., and Bryda, E. C. (2003). Positional cloning of jcpk/bpk locus of the mouse. *Mamm. Genome* 14 (4), 242–249. doi:10.1007/s00335-002-2241-0
- Dowdle, M. E., Imboden, S. B., Park, S., Ryder, S. P., and Sheets, M. D. (2017). Horizontal gel electrophoresis for enhanced detection of protein-RNA complexes. *J. Vis. Exp.* (125), 56031. doi:10.3791/56031
- Dowdle, M. E., Park, S., Blaser Imboden, S., Fox, C. A., Houston, D. W., and Sheets, M. D. (2019). A single KH domain in Bicaudal-C links mRNA binding and translational repression functions to maternal development. *Development* 146 (10), dev172486. doi:10.1242/dev.172486
- Enwerem, I. I. I., Elrod, N. D., Chang, C. T., Lin, A., Ji, P., Bohn, J. A., et al. (2021). Human Pumilio proteins directly bind the CCR4-NOT deadenylase complex to regulate the transcriptome. *RNA (New York, N.Y.)* 27 (4), 445–464. doi:10.1261/rna.078436.120
- Farina, K. L., Hüttelmaier, S., Musunuru, K., Darnell, R., and SingerElrod, R. H. (2003). Two ZBP1 KH domains facilitate beta-actin mRNA localization, granule

- formation, and cytoskeletal attachment. *J. Cell Biol.* 160 (1), 77–87. doi:10.1083/jcb.200206003
- Gamberi, C., Hipfner, D. R., Trudel, M., and Lubell, W. D. (2017). Bicaudal C mutation causes myc and TOR pathway up-regulation and polycystic kidney disease-like phenotypes in *Drosophila*. *PLoS Genet.* 13 (4), e1006694. doi:10.1371/journal.pgen.1006694
- Gebauer, F., Schwarzl, T., Valcarcel, J., and Hentze, M. W. (2021). RNA-binding proteins in human genetic disease. *Nat. Rev. Genet.* 22 (3), 185–198. doi:10.1038/s41576-020-00302-y
- Gutiérrez-Rojas, L., Porras-Segovia, A., Dunne, H., Andrade-Gonzalez, N., and Cervilla, J. A. (2020). Prevalence and correlates of major depressive disorder: a systematic review. *Braz. J. Psychiatry.* 42 (6), 657–672. doi:10.1590/1516-4446-2020-0650
- Hamada, H. (2020). Molecular and cellular basis of left-right asymmetry in vertebrates. *Proc. Jpn. Acad. Ser. B Phys. Biol. Sci.* 96 (7), 273–296. doi:10.2183/pjab.96.021
- Hentze, M. W., Castello, A., Schwarzl, T., and Preiss, T. (2018). A brave new world of RNA-binding proteins. *Nat. Rev. Mol. Cell Biol.* 19 (5), 327–341. doi:10.1038/nrm.2017.130
- Hollingworth, D., Candel, A. M., Nicastro, G., Martin, S. R., Briata, P., Gherzi, R., et al. (2012). KH domains with impaired nucleic acid binding as a tool for functional analysis. *Nucleic Acids Res.* 40 (14), 6873–6886. doi:10.1093/nar/gks368
- Jordan, P., Dorval, G., Arrondel, C., Moriniere, V., Tournant, C., Audrezet, M. P., et al. (2022). Targeted next-generation sequencing in a large series of fetuses with severe renal diseases. *Hum. Mutat.* 43 (3), 347–361. doi:10.1002/humu.24324
- Klauzinska, M., Castro, N. P., Rangel, M. C., Spike, B. T., Gray, P. C., Bertolette, D., et al. (2014). The multifaceted role of the embryonic gene *Cripto-1* in cancer, stem cells and epithelial-mesenchymal transition. *Semin. Cancer Biol.* 29, 51–58. doi:10.1016/j.semcancer.2014.08.003
- Kraus, M. R.-C., Clauin, S., Pfister, Y., Di Maio, M., Uliniski, T., Constam, D., et al. (2012). Two mutations in human *BICCI1* resulting in Wnt pathway hyperactivity associated with cystic renal dysplasia. *Hum. Mutat.* 33 (1), 86–90. doi:10.1002/humu.21610
- Leal-Esteban, L. C., Rothé, B., Fortier, S., Isenschmid, M., and Constam, D. B. (2018). Role of Bicaudal C1 in renal gluconeogenesis and its novel interaction with the CTLH complex. *PLoS genet.* 14 (7), e1007487. doi:10.1371/journal.pgen.1007487
- Lemaire, L. A., Goulley, J., Kim, Y. H., Carat, S., Jacquemin, P., Rougemont, J., et al. (2015). Bicaudal C1 promotes pancreatic NEUROG3+ endocrine progenitor differentiation and ductal morphogenesis. *Dev. Camb. Engl.* 142 (5), 858–870. doi:10.1242/dev.114611
- Lewis, C. M., Ng, M. Y., Butler, A. W., Cohen-Woods, S., Uher, R., Piro, K., et al. (2010). Genome-wide association study of major recurrent depression in the U.K. population. *Am. J. Psychiatry* 167 (8), 949–957. doi:10.1176/appi.ajp.2010.09091380
- Li, F., Peiris, M. N., and Donoghue, D. J. (2020). Functions of FGFR2 corrupted by translocations in intrahepatic cholangiocarcinoma. *Cytokine Growth Factor Rev.* 52, 56–67. doi:10.1016/j.cytogfr.2019.12.005
- Maerker, M., Getwan, M., Dowdle, M. E., McSheene, J. C., Gonzalez, V., Pelliccia, J. L., et al. (2021). *Bicc1* and *Dicer* regulate left-right patterning through post-transcriptional control of the Nodal inhibitor *Dand5*. *Nat. Commun.* 12 (1), 5482. doi:10.1038/s41467-021-25464-z
- Mahone, M., Saffman, E. E., and Lasko, P. F. (1995). Localized Bicaudal-C RNA encodes a protein containing a KH domain, the RNA binding motif of FMR1. *EMBO J.* 14 (9), 2043–2055. doi:10.1002/j.1460-2075.1995.tb07196.x
- Maisonneuve, C., Guilleret, I., Vick, P., Weber, T., Andre, P., Beyer, T., et al. (2009). Bicaudal C, a novel regulator of Dvl signaling abutting RNA-processing bodies, controls cilia orientation and leftward flow. *Development* 136 (17), 3019–3030. doi:10.1242/dev.038174
- Mesner, L. D., Ray, B., Hsu, Y. H., MAnichaikul, A., Lum, E., Bryda, E. C., et al. (2014). *Bicc1* is a genetic determinant of osteoblastogenesis and bone mineral density. *J. Clin. Invest.* 124 (6), 2736–2749. doi:10.1172/JCI73072
- Minegishi, K., Rothe, B., Komatsu, K. R., Ono, H., Ikawa, Y., Nishimura, H., et al. (2021). Fluid flow-induced left-right asymmetric decay of *Dand5* mRNA in the mouse embryo requires a *Bicc1*-Ccr4 RNA degradation complex. *Nat. Commun.* 12 (1), 4071. doi:10.1038/s41467-021-24295-2
- Mohler, J., and Wieschaus, E. F. (1986). Dominant maternal-effect mutations of *Drosophila melanogaster* causing the production of double-abdomen embryos. *Genetics* 112 (4), 803–822. doi:10.1093/genetics/112.4.803
- Nagaoka, T., Karasawa, H., Castro, N. P., Rangel, M. C., Salomon, D. S., and Bianco, C. (2012). An evolving web of signaling networks regulated by *Cripto-1*. *Growth Factors (Chur, Switz.)* 30 (1), 13–21. doi:10.3109/08977194.2011.641962
- Nakamura, T., and Hamada, H. (2012). Left-right patterning: Conserved and divergent mechanisms. *Development* 139 (18), 3257–3262. doi:10.1242/dev.061606
- Nicastro, G., Taylor, I. A., and Ramos, A. (2015). KH-RNA interactions: Back in the groove. *Curr. Opin. Struct. Biol.* 30, 63–70. doi:10.1016/j.sbi.2015.01.002
- Ota, K. T., Andres, W., Lewis, D. A., Stockmeier, C. A., and Duman, R. S. (2015). *BICCI1* expression is elevated in depressed subjects and contributes to depressive behavior in rodents. *Neuropsychopharmacology* 40 (3), 711–718. doi:10.1038/npp.2014.227
- Park, S., Blaser, S., Marchal, M. A., Houston, D. W., and Sheets, M. D. (2016). A gradient of maternal Bicaudal-C controls vertebrate embryogenesis via translational repression of mRNAs encoding cell fate regulators. *Dev. Camb. Engl.* 143 (5), 864–871. doi:10.1242/dev.131359
- Perez-Perri, J. I., Noerenberg, M., Kamel, W., Lenz, C. E., Mohammed, S., Hentze, M. W., et al. (2021). Global analysis of RNA-binding protein dynamics by comparative and enhanced RNA interactome capture. *Nat. Protoc.* 16 (1), 27–60. doi:10.1038/s41596-020-00404-1
- Perez-Perri, J. I., Rogell, B., Schwarzl, T., Stein, F., Zhou, Y., Rettel, M., et al. (2018). Discovery of RNA-binding proteins and characterization of their dynamic responses by enhanced RNA interactome capture. *Nat. Commun.* 9 (1), 4408. doi:10.1038/s41467-018-06557-8
- Piazzon, N., Maisonneuve, C., Guilleret, I., Rotman, S., and Constam, D. B. (2012). *Bicc1* links the regulation of cAMP signaling in polycystic kidneys to microRNA-induced gene silencing. *J. Mol. Cell Biol.* 4 (6), 398–408. doi:10.1093/jmcb/mjs027
- Ross, J. S., Wang, K., Gay, L., Al-Rohil, R., Rand, J. V., Jones, D. M., et al. (2014). New routes to targeted therapy of intrahepatic cholangiocarcinomas revealed by next-generation sequencing. *Oncologist* 19 (3), 235–242. doi:10.1634/theoncologist.2013-0352
- Rothé, B., Leettola, C. N., Leal-Esteban, L., Cascio, D., Fortier, S., Isenschmid, M., et al. (2018). Crystal structure of *Bicc1* SAM polymer and mapping of interactions between the ciliopathy-associated proteins *Bicc1*, *ANKS3*, and *ANKS6*. *Structure* 26 (2), 209–224. e6. doi:10.1016/j.str.2017.12.002
- Ryan, J., Artero, S., Carriere, I., Maller, J. J., Meslin, C., Ritchie, K., et al. (2016). GWAS-identified risk variants for major depressive disorder: Preliminary support for an association with late-life depressive symptoms and brain structural alterations. *Eur. Neuropsychopharmacol.* 26 (1), 113–125. doi:10.1016/j.euroneuro.2015.08.022
- Saffman, E. E., Styhler, S., Rother, K., Li, W., Richard, S., and Lasko, P. (1998). Premature translation of oskar in oocytes lacking the RNA-binding protein bicaudal-C. *Mol. Cell Biol.* 18 (8), 4855–4862. doi:10.1128/MCB.18.8.4855
- Scheiter, A., Keil, F., Luke, F., Grosse, J., Verloh, N., Opitz, S., et al. (2021). Identification and in-depth analysis of the novel FGFR2-NDC80 fusion in a cholangiocarcinoma patient: Implication for therapy. *Curr. Oncol.* 28 (2), 1161–1169. doi:10.3390/currenconcol28020112
- Schier, A. F. (2009). Nodal morphogens. *Cold Spring Harb. Perspect. Biol.* 1 (5), a003459. doi:10.1101/cshperspect.a003459
- Schizas, D., Mastoraki, A., Routis, E., Papapanou, M., Tsapralis, D., Vassiliu, P., et al. (2020). Combined hepatocellular-cholangiocarcinoma: An update on epidemiology, classification, diagnosis and management. *Hepatobiliary Pancreat. Dis. Int.* 19 (6), 515–523. doi:10.1016/j.hbpd.2020.07.004
- Sheets, M. D., Fox, C. A., Dowdle, M. E., Blaser, S. I., Chung, A., and Park, S. (2017). Controlling the messenger: Regulated translation of maternal mRNAs in *Xenopus laevis* development. *Adv. Exp. Med. Biol.* 953, 49–82. doi:10.1007/978-3-319-46095-6_2
- Shorey, S., Ng, E. D., and Wong, C. H. J. (2022). Global prevalence of depression and elevated depressive symptoms among adolescents: A systematic review and meta-analysis. *Br. J. Clin. Psychol.* 61 (2), 287–305. doi:10.1111/bjc.12333
- Tao, Q., Yokota, C., Puck, H., Kofron, M., Birsoy, B., Yan, D., et al. (2005). Maternal *wnt11* activates the canonical *wnt* signaling pathway required for axis formation in *Xenopus* embryos. *Cell* 120 (6), 857–871. doi:10.1016/j.cell.2005.01.013
- Tran, U., Pickney, L. M., Ozpolat, B. D., and Wessely, O. (2007). *Xenopus* Bicaudal-C is required for the differentiation of the amphibian pronephros. *Dev. Biol.* 307 (1), 152–164. doi:10.1016/j.ydbio.2007.04.030
- Tran, U., Zakin, L., Schweickert, A., Agrawal, R., Doger, R., Blum, M., et al. (2010). The RNA-binding protein bicaudal C regulates polycystin 2 in the kidney by antagonizing miR-17 activity. *Development* 137 (7), 1107–1116. doi:10.1242/dev.046045
- Valverde, R., Edwards, L., and Regan, L. (2008). Structure and function of KH domains. *FEBS J.* 275 (11), 2712–2726. doi:10.1111/j.1742-4658.2008.06411.x
- Wang, M., Chen, Z., Guo, P., Wang, Y., and Chen, G. (2021). Therapy for advanced cholangiocarcinoma: Current knowledge and future potential. *J. Cell. Mol. Med.* 25 (2), 618–628. doi:10.1111/jcmm.16151
- Wessely, O., and De Robertis, E. M. (2000). The *Xenopus* homologue of Bicaudal-C is a localized maternal mRNA that can induce endoderm formation. *Development* 127 (10), 2053–2062. doi:10.1242/dev.127.10.2053

Wessely, O., Tran, U., Zakin, L., and De Robertis, E. M. (2001). Identification and expression of the mammalian homologue of Bicaudal-C. *Mech. Dev.* 101 (1–2), 267–270. doi:10.1016/s0925-4773(00)00568-2

Zhang, Y., Cooke, A., Park, S., Dewey, C. N., Wickens, M., and Sheets, M. D. (2013). Bicaudal-C spatially controls translation of vertebrate maternal mRNAs. *RNA (New York, N.Y.)* 19 (11), 1575–1582. doi:10.1261/rna.041665.113

Zhang, Y., Forinash, K. D., McGivern, J., Fritz, B., Dorey, K., and Sheets, M. D. (2009). Spatially restricted translation of the xCR1 mRNA in *Xenopus* embryos. *Mol. Cell. Biol.* 29 (13), 3791–3802. doi:10.1128/MCB.01865-08

Zhang, Y., Park, S., Blaser, S., and Sheets, M. D. (2014). Determinants of RNA binding and translational repression by the Bicaudal-C regulatory protein. *J. Biol. Chem.* 289 (11), 7497–7504. doi:10.1074/jbc.M113.526426



OPEN ACCESS

EDITED BY

Silvia L. López,
CONICET Instituto de Biología Celular y
Neurociencias (IBCN), Argentina

REVIEWED BY

Leon Peshkin,
Harvard Medical School, United States
Nathalie Oulhen,
Brown University, United States

*CORRESPONDENCE

Radek Sindelka,
sindelka@ibt.cas.cz

[†]These authors have contributed equally
to this work

SPECIALTY SECTION

This article was submitted to
Morphogenesis and Patterning,
a section of the journal
Frontiers in Cell and Developmental
Biology

RECEIVED 30 June 2022

ACCEPTED 04 August 2022

PUBLISHED 20 September 2022

CITATION

Igorova V, Naraine R, Psenicka M,
Zelazowska M and Sindelka R (2022),
Comparison of RNA localization during
oogenesis within *Acipenser ruthenus*
and *Xenopus laevis*.
Front. Cell Dev. Biol. 10:982732.
doi: 10.3389/fcell.2022.982732

COPYRIGHT

© 2022 Igorova, Naraine, Psenicka,
Zelazowska and Sindelka. This is an
open-access article distributed under
the terms of the [Creative Commons
Attribution License \(CC BY\)](https://creativecommons.org/licenses/by/4.0/). The use,
distribution or reproduction in other
forums is permitted, provided the
original author(s) and the copyright
owner(s) are credited and that the
original publication in this journal is
cited, in accordance with accepted
academic practice. No use, distribution
or reproduction is permitted which does
not comply with these terms.

Comparison of RNA localization during oogenesis within *Acipenser ruthenus* and *Xenopus laevis*

Viktoriia Igorova^{1†}, Ravindra Naraine^{1†}, Martin Psenicka²,
Monika Zelazowska³ and Radek Sindelka^{1*}

¹Laboratory of Gene Expression, Institute of Biotechnology of the Czech Academy of Sciences, Vestec, Czechia, ²Faculty of Fisheries and Protection of Waters, South Bohemian Research Center of Aquaculture and Biodiversity of Hydrocenoses, University of South Bohemia in Ceske Budejovice, Vodnany, Czechia, ³Department of Developmental Biology and Morphology of Invertebrates, Institute of Zoology and Biomedical Research, Faculty of Biology, Jagiellonian University, Krakow, Poland

The oocyte is a unique cell, from which develops a complex organism comprising of germ layers, tissues and organs. In some vertebrate species it is known that the asymmetrical localization of biomolecules within the oocyte is what drives the spatial differentiation of the daughter cells required for embryogenesis. This asymmetry is first established to produce an animal-vegetal (A-V) axis which reflects the future specification of the ectoderm, mesoderm, and endoderm layers. Several pathways for localization of vegetal maternal transcripts have already been described using a few animal models. However, there is limited information about transcripts that are localized to the animal pole, even though there is accumulating evidence indicating its active establishment. Here, we performed comparative TOMO-Seq analysis on two holoblastic cleavage models: *Xenopus laevis* and *Acipenser ruthenus* oocytes during oogenesis. We found that there were many transcripts that have a temporal preference for the establishment of localization. In both models, we observed vegetal transcript gradients that were established during either the early or late oogenesis stages and transcripts that started their localization during the early stages but became more pronounced during the later stages. We found that some animal gradients were already established during the early stages, however the majority were formed during the later stages of oogenesis. Some of these temporally localized transcripts were conserved between the models, while others were species specific. Additionally, temporal *de novo* transcription and also degradation of transcripts within the oocyte were observed, pointing to an active remodeling of the maternal RNA pool.

KEYWORDS

oogenesis, RNA localization, *Xenopus laevis*, *Acipenser ruthenus*, TOMO-Seq

1 Introduction

The oocyte is a unique cell, whereby following its fertilization, the resulting embryo develops to produce hundreds of cell types that are later organized into many tissues and organs (reviewed by Houston, 2013). The oocyte of many species already contains all the necessary materials (e.g., the yolk and mitochondria) needed to maintain its metabolism, and also to control development during the early stages of embryogenesis. Transcripts and proteins which are accumulated during oogenesis are used by the developing embryo until zygotic genome activation (ZGA) and regulate the early stages of embryogenesis (reviewed by Gilbert, 2000; reviewed by Kim and Lee, 2014; Peshkin et al., 2015).

The process of oocyte formation starts from the primordial germ cells (PGCs) development in the gonadal ridge, arrest of meiosis at meiosis I, oocyte growth, continuation with ovulation and the resumption of meiosis, fertilization and then the beginning of the new life cycle (reviewed by Jagarlamudi and Rajkovic, 2012). In comparison to somatic cells, the oocyte is much larger, which makes studying the events of RNA localization easier (King et al., 1999). The mechanism of oogenesis varies among different species. In some organisms, like sea urchins, frogs, and fishes (eg. *Danio rerio*), the females produce hundreds to thousands of oocytes in a short period of time. In contrast, other species including humans and most mammals, produce limited number of oocytes during their lifetime (reviewed by Gilbert, 2000; reviewed by Spence et al., 2008). The number of stages that defines the oogenesis can vary between certain species. For example, based on morphological criteria and on physiological and biochemical events, 14 stages can be distinguished in fruit fly (*Drosophila melanogaster*), from the start of the formation of the egg chamber/follicle, which consists of a cyst of germ cells surrounded by somatic follicle cells, to the final matured egg (reviewed by Xu and Gridley, 2012). Five stages can be found in *D. rerio*, starting from the pre-follicle phase of primary growth followed by the cortical alveolus stage, vitellogenesis, oocyte maturation and finally the matured egg (Selman et al., 1993).

One of the most common models used for the study of oogenesis are the *Xenopus* species. *Xenopus* oogenesis is constant in the adult ovary, with continuously differentiating oogonia into oocytes. Oogenesis is not synchronized and therefore females contain oocytes of different stages. A cycle of oogenesis is considered completed when a large number of oocytes are at the stage VI (reviewed by Rasar and Hammes, 2006). *Xenopus* has continued to be an attractive model because it is easy to obtain, maintain, and produces large oocytes that can be easily manipulated and orientated due to the presence of pigmented granules at the animal pole. Currently there are nearly a thousand published studies about RNA localization using *X. laevis* oocytes (reviewed by Dettlaff and Rudneva, 1991; reviewed by Rasar and Hammes, 2006; National Library of Medicine, 2002).

Raikova (1973), Raikova (1974) pointed out that during oogenesis, the frog oocytes share strong cytological similarities with sturgeons including sterlets (*Acipenser ruthenus*), such as the

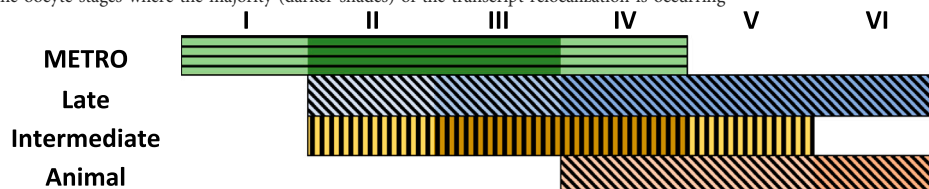
nucleolar and other nuclear structures, cytoplasmic organelles, the same structure of yolk platelets, presence of cortical granules, absence of ribosomes in previtellogenesis, extrusions of nucleolar material into the cytoplasm, and the same dense material cementing the mitochondria. The oogenesis of *X. laevis* and sturgeon comprises of six stages and can be categorized into three phases of oocyte development: pre-vitellogenesis, vitellogenesis (accumulation of yolk) and post-vitellogenesis/choriogenesis (deposition of egg envelopes) (Dumont, 1972; Dettlaff et al., 2006; Zelazowska, 2010; reviewed by Zelazowska and Fopp-Bayat, 2017; Zelazowska and Fopp-Bayat, 2019). *Xenopus* oocytes at the pre-vitellogenic phase (stage I) are transparent with a size between 50–300 µm. Vitellogenic phase takes place from stages II to V with sizes: 300–450 µm for stage II, 450–600 µm for stage III, 600–1000 µm for stage IV, and 1000–1200 µm for stage V. The visible animal - vegetal (A-V) axis is distinguishable at the stage III and is due to the pigment granules accumulated on the animal pole. Post-vitellogenic *X. laevis* eggs have sizes between 1200–1300 µm (Dumont, 1972). Although sturgeon oogenesis also passes through six developmental stages, their morphological descriptions are weak. The size of the matured sterlet egg ranges between 1900–2500 µm (Dettlaff et al., 2006), but the sizes of the developing sterlet oocytes have not yet been described. Oocyte polarization index (PI) is used in the sturgeon hatcheries to estimate the stage of sexual maturity of females. The PI is calculated by finding the ratio between the distance separating the animal pole and the germinal vesicle versus the distance between the animal to the vegetal pole (Chebanov and Galich, 2013).

During early embryonic development, sterlets, as well as *Amphibians*, represent a completely dividing (holoblastic) embryo (Dettlaff et al., 2006; reviewed by Elinson and del Pino, 2012). The development of the germ layers of many organisms is specified and predetermined by maternal RNAs and proteins that are localized unevenly along the A-V axis during oogenesis (reviewed by Marlow, 2010; reviewed by Owens et al., 2017). In *X. laevis*, the first sign of asymmetry is visible at stage I of oogenesis, whereby a spherical structure is localized in close proximity to the nucleus of the oocyte. This structure, referred to as the Balbiani body or mitochondrial cloud (MC), contains mitochondria, Golgi complex, endoplasmic reticulum, lipids and pigment granules (Heasman et al., 1984; reviewed by Kloc et al., 2004). Two localization pathways that contribute to vegetal localization have been described for the *X. laevis* oocytes: the METRO (MESsage TRANsport Organizer) and the Late pathway (Kloc and Etkin, 1995) (Table 1). Transcripts that are localized in the MC utilize the METRO pathway and migrate towards the future vegetal pole to define the A-V polarity of the oocyte from the first stages of oogenesis. By the stage II-IV, the METRO pathway localizes transcripts, including *nanos1* (previously *nos1/xcat2*), *dazl* (previously *Xdazl*), *pgat* (previously *Xpat*), *Xlsirts*, *ddx25* (previously *xcat3*), to the vegetal pole (Kloc et al., 1993; Forristall, et al., 1995; Kloc and Etkin, 1995, 1998; reviewed by King et al., 1999). Transcripts, utilizing the late pathway (eg. *gdf1* (previously *vg1*), *veg1*) are distributed throughout the cytoplasm at stage I, and do not use the

TABLE 1 Localization of maternal transcripts in the oocytes of the *Xenopus laevis*.

Pathway	RNAs	Stages and localization	References
Early pathway/METRO	<i>Xdazl</i>	I-uniform, II-IV-migration to the vegetal pole	1
	<i>dazl</i>	I-MC, III-IV-vegetal pole	2
	<i>Xcat2</i>	I-MC, but still in the cytoplasm, IV-vegetal pole	1
	<i>Xcat2</i>	I-MC, II-vegetal pole	3
	<i>Xcat2</i>	I-MC, but still in the cytoplasm, II-MC, vegetal pole	4
	<i>Xlsirt</i>	I-MC and cytoplasm, II-vegetal pole	4
	<i>Xlsirt</i>	II-MC, III-vegetal pole	5
	<i>Xlsirt</i>	II-MC, IV-vegetal pole	6
Late pathway	<i>Vg1</i>	II-III-around the nucleus, III-VI-migration to the vegetal pole	1
	<i>Vg1</i>	I-II-everywhere, III-IV-vegetal pole	3
	<i>Vg1</i>	I-cytoplasm, II-migration to the vegetal pole, III-vegetal pole with continuing streaming	4
	<i>Vg1</i>	I-everywhere, III-vegetal pole (but still migrating)	5
	<i>Vegt</i>	I-uniformly distributed, IV-vegetal pole	2; 7
Intermediate pathway	<i>fatvg</i>	I-cytoplasm, II-MC, III-V-migration to the vegetal pole	8
	<i>Hermes</i>	I-cytoplasm, early II-MC, II-III-accumulation at the vegetal cortex, IV-vegetal cortex	9
Animal pathway	<i>PABP</i>	VI	10
	β -tubulin	VI	11
	<i>An1</i>	I-III-uniform, IV-animal pole	12
	<i>An2</i>	I-III-uniform, IV-animal pole	12
	<i>An3</i>	I-III-uniform, IV-animal pole	12
	<i>An4a</i>	VI	12

Summary scheme of the oocyte stages where the majority (darker shades) of the transcript relocation is occurring



References: 1. Reviewed by King et al. (1999), 2. Houston (2013), 3. Forristall et al. (1995), 4. Kloc and Etkin (1995), 5. Kloc and Etkin (1998), 6. Kloc et al. (1993), 7. Zhang and King (1996), 8. Chan et al. (1999), 9. Zearfoss et al. (2004), 10. Schroeder and Yost (1996), 11. Yisraeli et al. (1990), 12. Reviewed by Schnapp et al. (1997).

MC. By stage III-VI these transcripts start to migrate towards the vegetal pole and anchor at a broader region of the vegetal cortex (Forristall et al., 1995; Kloc and Etkin, 1995, 1998; reviewed by King et al., 1999; Houston, 2013). An equivalent of the Balbiani body, the Balbiani cytoplasm was also described in the sturgeon species. Granular (Balbiani) ooplasm of *A. gueldenstaedtii* oocytes and *X. laevis* Balbiani bodies share similarities presented in their molecular composition and ultrastructure (Zelazowska et al., 2007). The Balbiani cytoplasm contains nuage aggregations, mitochondria and is detected around the germinal vesicle in stage I. During oocyte development, the Balbiani

cytoplasm expands toward the oocyte periphery and nuage aggregations become uniformly dispersed throughout the entire ooplasm (Zelazowska et al., 2007).

Some studies have also described an “intermediate” pathway in *X. laevis*, which is a combination or overlap of the METRO and Late pathway. Transcripts of this pathway (eg. *plin2* (previously *fatvg*), *dnd1*, *grip2*, *trim36*, *rbpms/rbpms2* (previously *hermes*)) enter the Balbiani body in stage II oocytes and distribute at the wide area of the vegetal cortex of the oocytes during stages IV-V (Chan et al., 1999; Zearfoss et al., 2004; reviewed by Houston, 2013).

Compared to the well-studied vegetal pole, very little is known about the transcripts that are localized to the animal

pole. A few studies have already demonstrated that during early oocyte development, transcripts which belong to the animal pathway are uniformly distributed. The animal localization can be first observed at stage IV in *X. laevis*. Transcripts coding *pabpc4* (previously *PABP*), *tubb* (previously β -tubulin) and *nup93* (previously *An4a*) were detected in the animal pole at VI stage only (Yisraeli et al., 1990; Schroeder and Yost, 1996; reviewed by Schnapp et al., 1997). Contrary to the few animal transcripts that have been described in the past, many recent studies have demonstrated that there are in fact hundreds of animally localized transcripts (Claußen et al., 2015; Owens et al., 2017; Sindelka et al., 2018; Naraine et al., 2022). Additionally, our recent study has shown that many of these maternal animal transcripts show a high level of conserved localization amongst diverse species (*D. rerio*, *A. ruthenus*, *X. laevis* and *Ambystoma mexicanum*) (Naraine et al., 2022). We selected the two best models (easily accessible and early oocyte coloring reflecting A-V axis) to study RNA localization during oogenesis at the complete transcriptome level. In this research, we utilized spatial RNA sequencing (TOMO-Seq) to study oocytes from early and advance vitellogenic stages in *Actinopterygii* (*A. ruthenus*) and III-V oocyte stages in *Amphibia* (*X. laevis*).

2 Materials and methods

2.1 Ethics approval

All experimental procedures involving model organisms were carried out in accordance with the Czech Law 246/1992 on animal welfare. *Acipenser ruthenus* females were kept in the Research Institute of Fish Culture and Hydrobiology in Vodňany, Czech Republic and protocols were reviewed by the Animal Research Committee of the Faculty of Fisheries and Protection of Waters, South Bohemian Research Center of Aquaculture and Biodiversity of Hydrocenoses, Research Institute of Fish Culture and Hydrobiology, Vodňany, Czech Republic. The *X. laevis* females were from the colony of the Institute of Biotechnology and protocols were approved by the animal committee of the Czech Academy of Sciences.

2.2 Sample collection

Xenopus laevis females were anesthetized with benzocaine for 1 h. Their abdomen was then opened with surgical scissors and the oocytes were placed into High Salt Solution (HSS). Oocytes were observed under the microscope, manually separated, and visually divided by size from the smallest oocytes with signs of pigmentation on the animal pole (stage III) to the late stage V (big oocytes). Collected oocytes had sizes from 560 to 1200 μ m. Four groups were created: very small oocytes (stage III, size 560–580 μ m); small oocytes (stage IV, size 720–810 μ m), medium (early stage V, size 1050 μ m) and big (late stage V, size 1140–1200 μ m).

Different stages of *A. ruthenus* oocytes were collected by biopsy of matured females (5–8 years old). The samples contained small, individual ovarian follicles in which early previtellogenic, diplotene stage oocytes (according to Zelazowska and Fopp-Bayat, 2019) grew, as well as large ovarian follicles. The nucleoplasm of all previtellogenic oocytes contained lampbrush chromosomes and multiple nucleoli. In the vicinity of the nucleus the granular ooplasm and lipid body were present. In the large follicles the vitellogenic, pigmented oocytes developed. Two groups of vitellogenic *A. ruthenus* oocytes were created: small (early vitellogenic, size 1320–1500 μ m) and big (advanced vitellogenic, size 1920–2100 μ m) (Supplementary Figure S1).

Light and electron microscopy were used to characterize the stages of interest for the *A. ruthenus* oocytes. Samples of *A. ruthenus* ovaries were fixed for 2 weeks in 2.5% glutaraldehyde (POCH) in 0.1 M phosphate buffer (pH 7.3). Then, they were rinsed and postfixed in 1% osmium tetroxide in 0.1 M phosphate buffer (pH 7.3) containing saccharose (5.6 g in 100 ml). Next, they were dehydrated in a series of ethanol and acetone and embedded in glycid ether 100 (Serva Electrophoresis). Semi-thin sections (0.7 μ m) were stained with methylene blue in 1% borax and photographed using a Leica DMR light microscope. Ultrathin sections (90 nm) were contrasted with uranyl acetate and observed in a transmission electron microscope (JEOL JEM 2100 in the Laboratory of Microscopy, Department of Cell Biology and Imaging, Institute of Zoology and Biomedical Research, Jagiellonian University) at 80 kV. The ovarian follicles were also photographed under a Nikon SMZ 1500 (Tokyo, Japan).

To detect nucleus position in the early and advanced vitellogenic eggs, sampled oocytes were fixed at least for 24 h in a freshly made medium (10 ml 99% acetic acid with 30 ml 32–35% formaldehyde with 60 ml 70–98% ethanol per 100 ml of Serra solution). The fixed oocytes were rinsed with tap water and were sectioned into two parts with a razor blade in the plane of the longitudinal axis (Rodina, 2006).

Early and advance vitellogenic stages of *A. ruthenus* and III-V oocyte stages of *X. laevis* were embedded in Tissue-Tek O.C.T. Compound, oriented using delicate forceps along the A-V axis (animal pole positioned at the top) and immediately frozen on dry ice and stored at -80°C .

2.3 Sample preparation

Samples were incubated for 10 min in the cryostat chamber (-20°C) and then cut into 30 μ m slices along the A-V axis. Number of obtained slices were counted, equally distributed in sequential order into five tubes with the same number of slices per tube. The diameter of the oocyte was calculated by multiplying the thickness of the slices by the number of slices obtained. Tubes were then labelled to correspond to the relevant segments of the oocyte (A—extremely animal, B—animal, C—central, D—vegetal, E—extremely vegetal).

Total RNA was extracted using Qiagen RNeasy Minikit according to the manufacturer's instructions. The concentration of total RNA was measured using a spectrophotometer (Nanodrop 2000; ThermoFisher Scientific), and the quality of RNA was assessed using a Fragment Analyzer (AATI, Standard Sensitivity RNA analysis kit, DNF-471). No signs of RNA degradation were observed. Absence of inhibitors and the precision of the orientation of the embedded oocyte were evaluated using RT-qPCR quantification of the RNA spike (TATAA Biocenter) and several known localized marker (animal and vegetal) transcripts respectively.

The cDNA was prepared using total RNA (*X. laevis*: 20–50 ng, *A. ruthenus*: 20–50 ng), 0.5 µl of oligo dT and random hexamers (50 µM each), 0.5 µl of dNTPs (10 mM each) and 0.5 µl of RNA spike (TATAA Universal RNA Spike, TATAA Biocenter), which were mixed with RNase free water to a final volume 6.5 µl. Samples were incubated for 5 min at 75°C, followed by 20 s at 25°C and cooling to 4°C. In the second step, 0.5 µl of SuperScript III Reverse Transcriptase (Invitrogen), 0.5 µl of recombinant ribonuclease inhibitor (RNaseOUT, Invitrogen), 0.5 µl of 0.1 M DTT (Invitrogen), and 2 µl of 5 × First strand synthesis buffer (Invitrogen) were added and incubated: 5 min at 25°C, 60 min at 50°C, 15 min at 55°C and 15 min at 75°C. Obtained cDNAs were diluted to a final volume of 100 µl and stored at –20°C.

2.4 Primer design and quantitative PCR

Primer assays of selected maternal transcripts were designed using NCBI Primer-Blast (<https://www.ncbi.nlm.nih.gov/tools/primer-blast/>) (Ye et al., 2012). Expected amplicon length was set to 97–187 bp and T_m to 60°C. Primer sequences are available in [Supplemental Material S2: Supplementary Table S1](#). The RT-qPCR reaction contained 3.5 µl of TATAA SYBR Grand Master Mix, 0.29 µl of forward and reverse primers mix (mixture 1:1, 10 µl each), 2 µl of cDNA and 1.21 µl of RNase-free water in 7 µl final volume. qPCR was performed using the CFX384 Real-Time system (BioRad) with conditions: initial denaturation at 95°C for 3 min, 45 repeats of denaturation at 95°C for 15 s, annealing at 60°C for 20 s and elongation at 72°C for 20 s. Melting curve analysis was performed after to evaluate reaction specificity and only one product was detected for all assays. Only samples with continuous gradient profiles of the marker transcripts were selected for library preparation.

2.5 Library preparation

Libraries were prepared using 100 ng (big *A. ruthenus* oocytes, *n* = 5), 25 ng (small *A. ruthenus* oocytes *n* = 5) and 50 ng (all *X. laevis* oocytes; big *n* = 2 (stage late V), medium *n* = 2 (stage early V), small *n* = 5 (stage IV), very small *n* = 3 (stage III)) of total RNA. Samples were depleted using RiboCop rRNA Depletion kit (Lexogen) and

libraries were prepared using SureSelect XT (Agilent). Optimum PCR cycles (13–17) were determined based on starting RNA amount during library preparation. Library qualities were assessed using the Fragment Analyzer (AATI, NGS High Sensitivity kit (DNF-474) and the concentrations were determined by the Qubit 4 Fluorometer (ThermoFisher Scientific). Equimolar library pools were prepared and sequenced using two 2x80 bp, NextSeq 500 runs. Obtained sequencing yield were on average 6.8 M reads in *A. ruthenus* and 5.5 M reads in *X. laevis*.

2.6 Preprocessing of RNA-Seq data

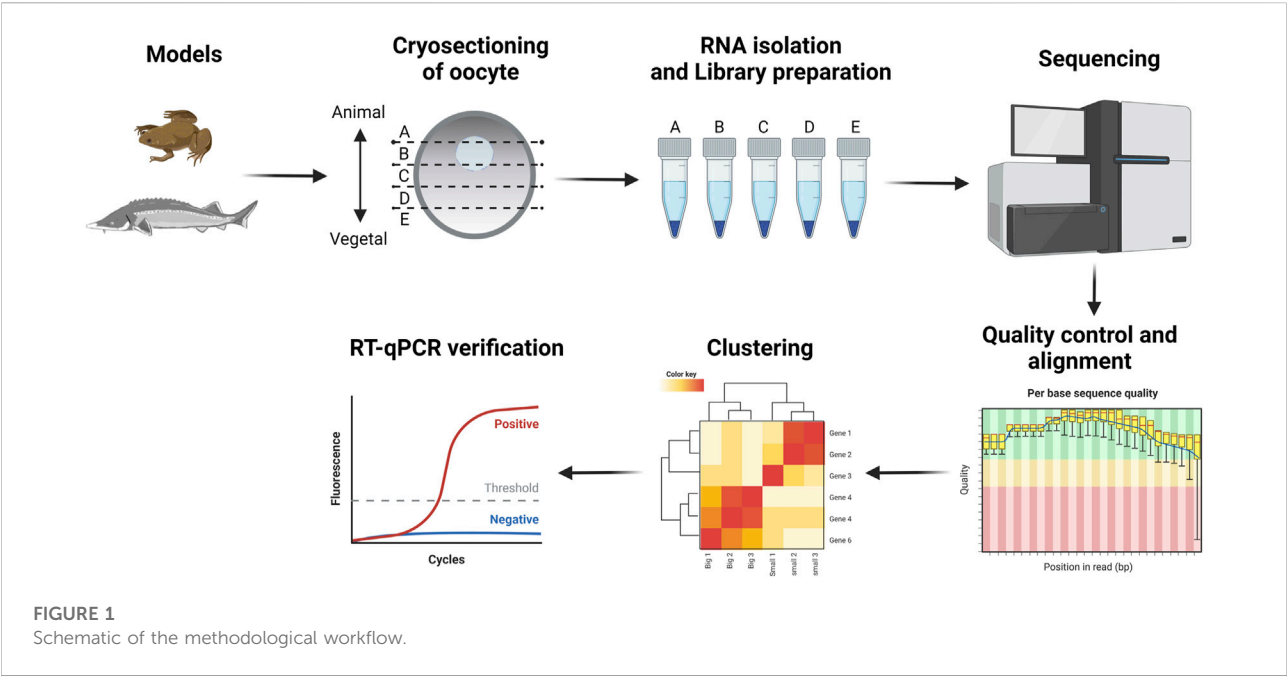
RNA-Seq reads were processed as previously described in [Naraine et al. \(2022\)](#). In brief, TrimmomaticPE (v. 0.36) ([Bolger et al., 2014](#)) was used to remove adaptor sequences and low-quality reads, while SortMeRNA (v. 2.1b) ([Kopylova et al., 2012](#)) was used to remove mtRNA reads (GenBank id: [NC_001573.1](#), [KF153104.1](#)) and any remaining rRNA reads. The *X. laevis* reads were then aligned to the *X. laevis* v9.1 genome ([Fortriede et al., 2020](#)) using STAR v2.5.2b ([Dobin et al., 2013](#)) and counted using htseq-count. The *A. ruthenus* reads were pseudoaligned using kallisto (v. 0.43.1) ([Bray et al., 2016](#)), to the initial *A. ruthenus de novo* transcriptome from [Naraine et al. \(2020\)](#). The data were deposited in the National Center for Biotechnology Information's Gene Expression Omnibus (GEO).

2.7 RNA-Seq analysis

Transcripts were initially filtered to remove those that had zero counts across all samples. The DESeq2 (v. 1.32.0) package was used to normalize the transcript counts (median-of-ratios method) and detect differentially localized transcripts (DLTs) between the sections or oocyte stages using the Likelihood Ratio Test (LRT) ([Love et al., 2014](#)). To identify transcript alterations between the sections or stages the following design models were used:

- 1) Alteration between the sections at the same stage:
 - a) design: ~replicate + position; reduced design: ~replicate.
- 2) Alteration in the profiles across the different stages:
 - a) Transcripts with altered profiles: design: ~Size + position + Size:position; reduced: ~Size + position
 - b) Transcripts with altered magnitudes: design: ~Size + position; reduced: ~Size
- 3) Alteration of the total transcript count between the different stages
 - a) design: ~Size; reduced: ~1; uses the sum of the normalized counts for each sample as input counts

Principal component analysis (PCA) was used to visually inspect the replicates and identify if there were any observable differences between the stages and the sections. DLTs were



defined as those with an adjusted p -value ($padj$) value less than 0.1 and also a total transcript count greater than 20 within the whole oocyte. The transcript counts for each section was summarized as a percentage relative to the total transcripts within the oocyte. These relative expression values were used to categorize the DLTs into localization profiles based on defined thresholds as previously defined (Sindelka et al., 2018; Naraine et al., 2022). The profiles comprised of the extreme animal, animal, central, vegetal, and extreme vegetal profiles. Categorization of any alterations in the profiles of the DLTs across the different stages was done using the degPatterns function from DEGreport (v. 1.28.0) package (Pantano, 2021). The “group difference” option was used to select for DLTs that showed at least a 1.5x or 2x fold change difference between either the stages or the sections, while the “summarize” option was used to identify those that were also reproducible across replicates. The profiles were verified manually and some clusters re-analyzed using optCluster (v. 1.3.0) with the “Diana” clustering algorithm (Sekula et al., 2017). The transcripts were annotated using the annotations derived from the previous ortholog analysis done by Naraine et al. (2022). In brief, protein sequence similarity and gene symbol matching were used to find the most probable orthologs between the two models. An orthologous unit number was used to denote orthologous genes in the absence of a common gene symbol.

Gene Ontology terms associated with the genes were derived using the gprofiler2 package (v. 0.2.1) (Raudvere et al., 2019) with the default parameters except for correction method = “bonferroni”, user threshold = “0.05”, domain scope = “annotated”, background organism = “*H. sapiens*” and significance = “FALSE”.




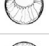


Model	Egg Group	Oocyte size (μm)	Stage*
	Big	1140-1200	late V 
	Medium	1050	early V 
	Small	720-810	IV 
	Very small	560-580	III 
	Big	1920-2100	advanced vitellogenic
	Small	1320-1500	early vitellogenic

FIGURE 2
Summary of the different oocyte sizes assessed for each of the models. Shown for the *X. laevis* model are the schematic drawings for the equivalent stages for the given oocyte as derived from *Carotenuto and Tussellino (2018). Stage classification of the *X. laevis* oocytes are from Dumont (1972).

3 Results

We studied RNA localization during oogenesis using the TOMO-Seq approach in five (A - extremely animal, B - animal, C - central, D - vegetal, E - extremely vegetal) sections along the A-V axis (Figure 1). Oocytes of *X. laevis* were divided into four categories reflecting already known stages (III stage - very small, IV stage - small, early V stage-medium and late V - big) while *A. ruthenus* oocytes

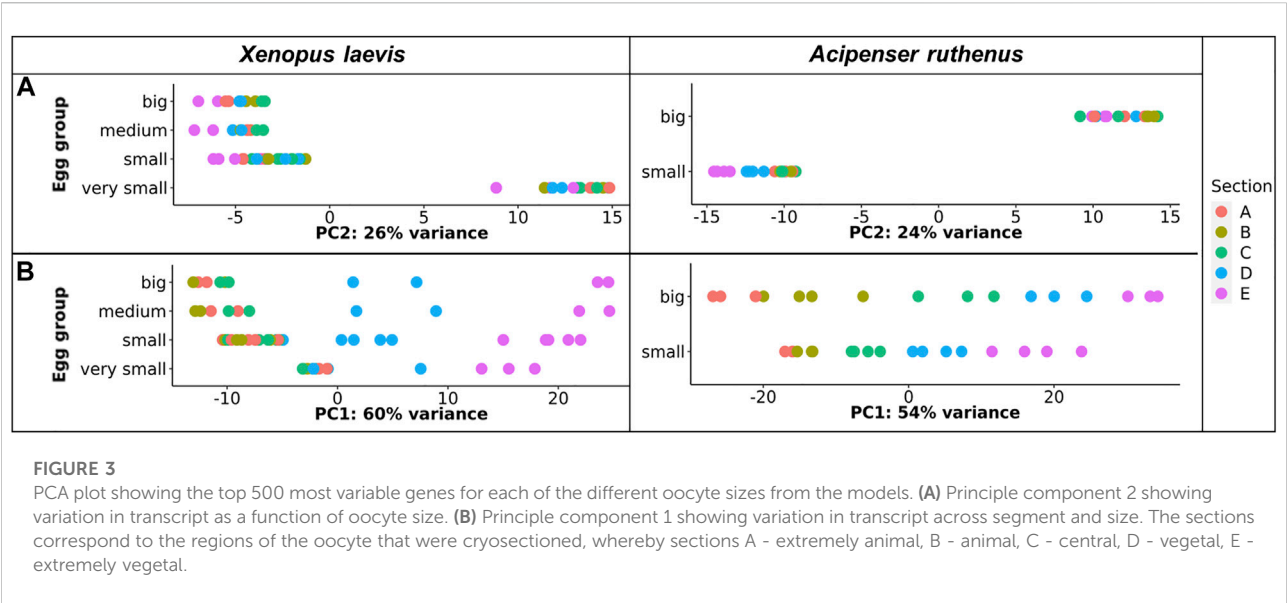


TABLE 2 Number of differentially localized transcripts that are overabundant in the five defined localized profiles.

	<i>Xenopus laevis</i>				<i>Acipenser ruthenus</i>	
	Big	Medium	Small	Very small	Big	Small
Total transcripts	16,045	16,076	15,832	15,952	22,591	21,862
DLTs	1,331	1,248	1,714	450	13,901	3,184
Annotated DLTs	1,127	1,068	1,482	359	7,550	1,847
Extreme animal	381	424	506	53	3,456	908
Animal	20	12	57	10	1,684	15
Center	0	0	1	2	5	31
Vegetal	444	502	229	98	4,280	639
Extreme vegetal	205	164	142	91	363	263
Undefined	281	146	779	196	4,113	1,328

DLTs are defined by <0.1 padj and >20 transcripts/oocyte.

were divided into two categories (early vitellogenic-small and advanced vitellogenic-big) (Figure 2). Microscopic analysis was used to characterize the differences between the early and advanced vitellogenic oocytes of the *A. ruthenus*. There was a distinct size difference between these two stages (Supplementary Figure S1). Microscopic observations showed in the early previtellogenic oocyte that the nuclear region was much larger than in the mid-previtellogenic oocyte. This large nuclear region in the early pre-vitellogenic oocyte encompassed a large area within the central region of the oocyte while in the mid-previtellogenic oocyte the nuclear region was more condensed and animally localized, with large spaces flanking both sides (Supplementary Figure S2).

In the small (early vitellogenic) oocytes the nucleus was located in the center while in the big (advanced vitellogenic) oocytes, the nucleus was in the animal hemisphere (Supplementary Figure S1). TOMO-Seq results were analyzed by in-house workflow and the PCA of the 500 most variable transcripts revealed that the greatest difference was between the very small oocytes and the larger (small, medium, big) oocytes of the *X. laevis* (Figure 3A). A similar difference was found between *A. ruthenus* small and big oocytes (Figure 3A). Analysis of the PC1 reflected variation among the individual sections and showed that the largest variations were observable relative to the size of oocyte suggesting a continuous increase of RNA asymmetry during oogenesis (Figure 3B).

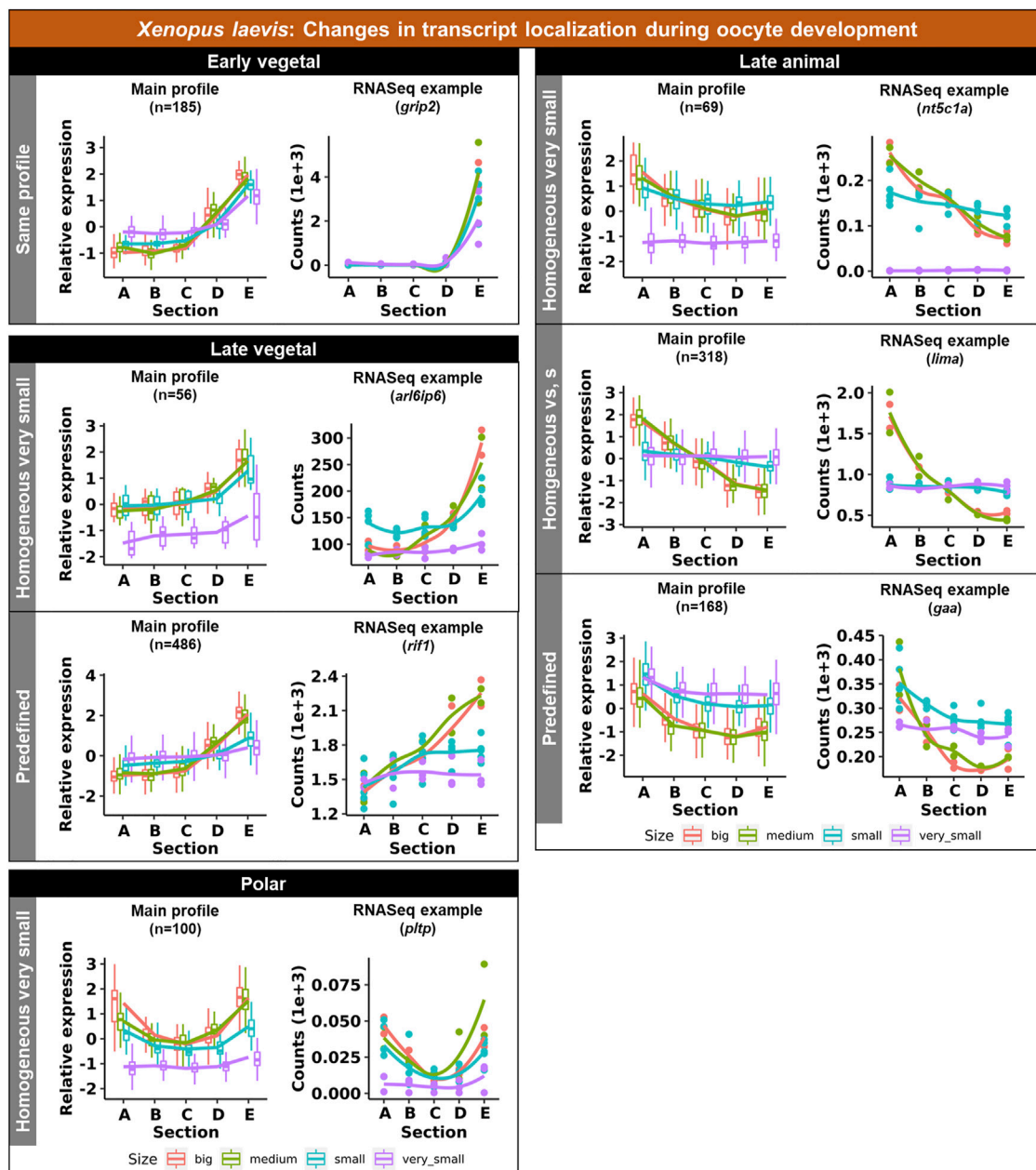


FIGURE 4

Unique groups representing the significant transcript sub-cellular alterations between the different oocyte sizes of the *Xenopus laevis*. Four groups of localization profiles were observable, early vegetal, late vegetal, late animal and polar. The following subgroups were observed: same profile - similar profile in early and late stages; predefined - profile already established in the early stages; homogeneous very small/small - profile is ubiquitous in the small/very small stage; homogeneous vs., s - profile is ubiquitous in both the small and very small stage. The sections correspond to the regions of the oocyte that were cryosectioned, whereby sections A - extremely animal, B - animal, C - central, D - vegetal, E - extremely vegetal.

More than 15000 or 21000 different transcripts (>20 counts in oocyte) were identified in *X. laevis* or *A. ruthenus* oocytes, respectively (Table 2). DLTs were identified as described in the methods, followed by categorization of the transcript profiles. On average more than 1000 DLTs were identified per oocyte stage,

with the exception of 450 DLTs in the very small *X. laevis* oocyte. The numbers of DLTs were larger in the *A. ruthenus*, suggesting a more polarized oocyte (Table 2). Relatively similar numbers of DLTs were found in the animal and vegetal localization groups (Table 2). We compared the number of identified DLTs and their

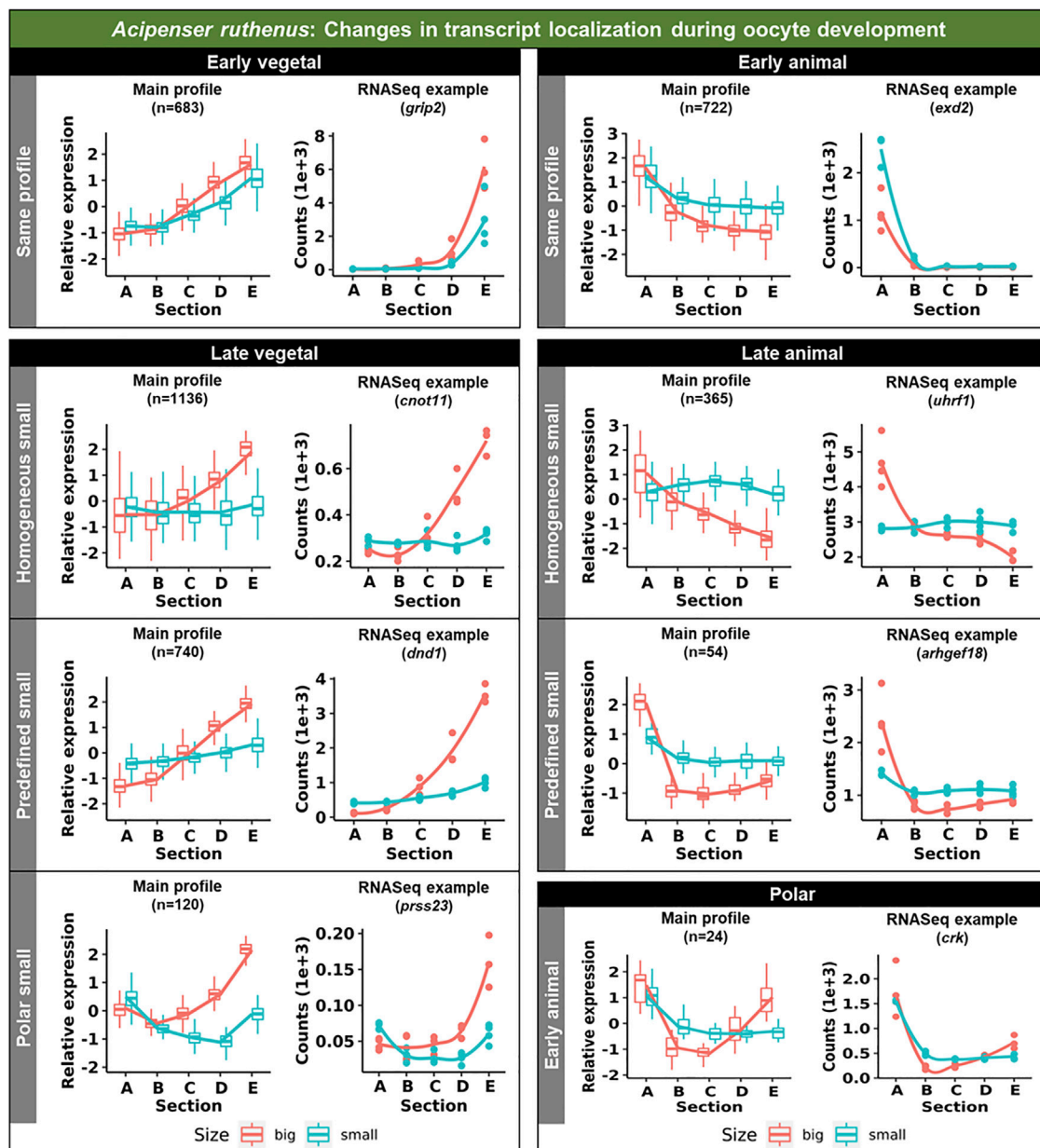


FIGURE 5

Unique groups representing the significant sub-cellular transcript alterations between the different oocyte sizes of the *Acipenser ruthenus*. Five groups of localization profiles were observable, early vegetal, late vegetal, early animal, late animal and polar. The following subgroups were observed: same profile - similar profile in early and late stages; predefined small - profile already established in the early stage; homogeneous small - profile is ubiquitous in the small stage; polar small—profile shows maximum expression in the polar regions of the oocyte; early animal—profile shows animal distribution in the early stage. The sections correspond to the regions of the oocyte that were cryosectioned, whereby sections A - extremely animal, B - animal, C - central, D - vegetal, E - extremely vegetal.

localization profiles observed in the big oocytes relative to the matured *X. laevis* and *A. ruthenus* eggs published by Naraine et al. (2022). There was a high concordance (>96%) between the identified animal (animal and extreme animal) and ~50% of vegetal transcripts with the previous results for both *X. laevis* and *A. ruthenus*.

3.1 Multiple profile changes were detected in both species

Transcript changes across the oocyte stages were assessed as either a change in the profile across the stages or a change in the magnitude of the transcript within a given segment across the stages.

The identified DLTs were then further filtered during clustering to identify those with greater than a 1.5x fold change difference between any given segment between the stages. In *X. laevis*, 1479 DLTs (Supplementary Material S2: Supplementary Table S2) were observed that had sub-sectional alterations across the stages, while in *A. ruthenus* 10225 (Supplementary Material S2: Supplementary Table S3). Given the large quantity of DLTs in *A. ruthenus*, a fold change of 2x was used instead, and resulted in the detection of 4743 DLTs instead. The cluster profiles of these filtered DLTs were then assessed to group together transcripts that had either already established their localization profile during the early stages of oogenesis or instead during the late stages.

3.1.1 Vegetally localized transcripts

Vegetal transcripts are key for early development and the functions of many of them have already been elucidated during the last decades. Several changes in the vegetal profiles can be observed in both models. The localization of the vegetal transcripts can be described as either “early vegetal” or “late vegetal”. In the early vegetal group, the profile and majority of the transcripts have already been created and localized to the vegetal region in the small stage. In this group, 185 transcripts were observed for *X. laevis* (Figure 4; Supplementary Figure S3; Supplementary Table S2), while 683 for *A. ruthenus* (Figure 5; Supplementary Table S3). The “late vegetal” was characterized by the lack or weak vegetal profile in the early stages compared to the later stages and comprised of two unique subgroups. In the first subgroup, the vegetal transcripts showed relocalization during oogenesis from ubiquitous distribution in very small/small oocytes to the vegetal region in the medium and big stages (56 *X. laevis* and 1136 *A. ruthenus*) (Figures 4, 5; Supplementary Table S2, S3). In the second subgroup, the vegetal transcripts (486 *X. laevis* and 740 *A. ruthenus*) had already formed a slight vegetal gradient (referred to as predefined) in the early stage, but it became more pronounced during the later stages of oogenesis (Figures 4, 5; Supplementary Figure S4; Supplementary Tables S2, S3). We compared these stage dependent vegetal transcripts with those previously described as early, intermediate, and late in the literature. Out of the published maternal transcripts for *X. laevis*, we observed 16 out of 20 correlated as early, 3 out of 9 for intermediate and 8 out of 19 for late (Supplementary Table S4).

3.1.2 Animally localized transcripts

Similar changes in profiles were also observed for the animally localized transcripts. An “early animal” group was detected only for the *A. ruthenus* (722 transcripts), where the profile was already markedly established in the early stage (Figure 5; Supplementary Figure S4; Supplementary Table S3). A “late animal” group was observed in both the *X. laevis* and *A. ruthenus* (Figures 4, 5; Supplementary Figure S3; Supplementary Tables S2, S3). This group contained several subgroups. In the first subgroup, the relocalization from ubiquitous to animal hemisphere during oogenesis was observed between the very

small/small and the big oocytes (387 *X. laevis* and 365 *A. ruthenus*). The other subgroup of animal transcripts showed a predefined animal profile in the small oocytes and more pronounced animal profile in the big (168 *X. laevis* and 54 *A. ruthenus*) (Figures 4, 5; Supplementary Tables S2, S3).

3.1.3 Polar localization of transcripts

An interesting group of transcripts was identified in both species and showed an increased localization towards the poles (transcript abundance in both animal and vegetal regions) during oogenesis. In *X. laevis*, 100 different transcripts were enriched at the poles in the small, medium and big oocytes (Figure 4; Supplementary Table S2). In contrast, *A. ruthenus* showed two polar transcript groups (Figure 5; Supplementary Table S3). The first group contained transcripts (120) localized to both poles (animal and vegetal) in the small oocytes and relocalization to vegetal gradient in big. The second group contained transcripts (24) localized preferentially in the animal region of the small oocytes and a polar profile in the big oocytes.

3.2 Transcript number alteration during oogenesis responsible for gradient formations

Transcript count numbers obtained by TOMO-Seq were used to estimate the level of DLTs in particular oocyte stages and to identify significantly degraded (decreased) or *de novo* synthesized (increased) transcripts (Figure 6). There were 9533 and 13024 DLTs (padj <0.1, >20 transcripts in at least one stage) that showed total transcript alterations between stages in the *X. laevis* and *A. ruthenus* respectively. Out of these DLTs, in the *X. laevis* 13% (1188) and in the *A. ruthenus* 41% (5283) showed greater than 1.5x fold alterations (Figure 6; Supplementary Tables S2, S3). These transcripts represented 7% for *X. laevis* and 22% for *A. ruthenus* of the total maternal transcripts (>20 transcripts/oocyte).

It was found that 720 *X. laevis* and 2960 *A. ruthenus* transcripts showed degradation during oogenesis (Figure 6; Supplementary Tables S2, S3). In contrast, the transcript levels of 468 *X. laevis* and 2323 *A. ruthenus* showed an increase during oogenesis (Figure 6; Supplementary Tables S2, S3). In *X. laevis*, the largest differences were observed between the very small and small oocytes and nicely correlated with the PCA results (Figures 3, 6).

Subgroups can be distinguished based on localization profile changes. The first subgroup (7 *X. laevis* and 220 *A. ruthenus*) showed animal degradation leading to vegetal gradients in big oocytes (Figure 6; Supplementary Tables S2, S3). The second subgroup showed an increase (*de novo*) of transcripts within the vegetal region in the big oocytes (37 *X. laevis* and 1591 *A. ruthenus*), resulting in a

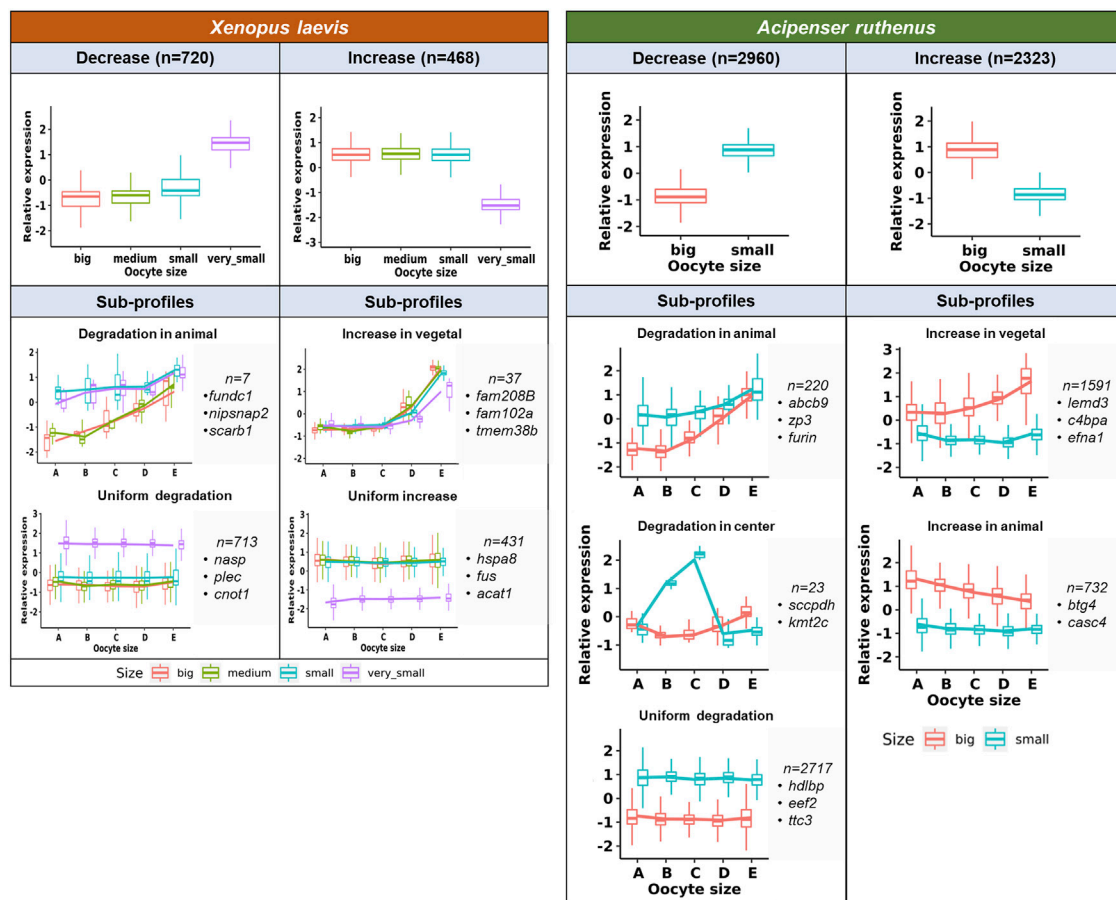


FIGURE 6

Unique profiles representing the significant total transcript count alterations between the different oocyte sizes of the *Xenopus laevis* and *Acipenser ruthenus*. The sections correspond to the regions of the oocyte that were cryosectioned, whereby sections A - extremely animal, B - animal, C - central, D - vegetal, E - extremely vegetal.

more profound vegetal profile (Figure 6; Supplementary Tables S2, S3). There were also transcripts that were uniformly degraded without gradient changes (713 *X. laevis* and 2717 *A. ruthenus*) or uniformly synthesized without gradient changes (431 *X. laevis* and 0 *A. ruthenus*) (Figure 6; Supplementary Tables S2, S3). *A. ruthenus* oocytes also showed animal localization in the big oocytes caused by *de novo* synthesis in 732 cases and another subgroup with degradation in the small oocyte center region (23) (Figure 6; Supplementary Tables S2, S3).

3.3 Interspecies similarities

We were able to identify 128 DLTs, that showed similar profiles during oogenesis between *X. laevis* and *A. ruthenus*. Twelve of them showed a stable and steep vegetal gradient already at the very small/small stages (early vegetal), which

was preserved to the big oocytes (eg. *dazl* and *grip2* transcripts) (Figure 7; Supplementary Table S5). Other groups of 80 and 36 DLTs showed conserved formation of late vegetal or animal profiles during oogenesis, respectively (Figure 7; Supplementary Tables S6, S7). Gene Ontology terms associated with these conserved DLTs, although insignificant, supported their function in gonad formation and regulation of development in the vegetal region, in contrast to the more nucleus related functions found for the transcripts conserved within the animal region (Figure 7). Levels of transcript counts among the oocyte stages were used to compare conserved degradation or *de novo* transcription during oogenesis (Figure 8; Supplementary Tables S8, S9). The transcripts of 27 genes were found to be newly produced with the majority being observed during the small (*X. laevis*) or big (*A. ruthenus*) stages (Figure 8; Supplementary Table S9). On the other hand, transcripts of 50 genes were degraded during oogenesis (Figure 8; Supplementary Table S8).

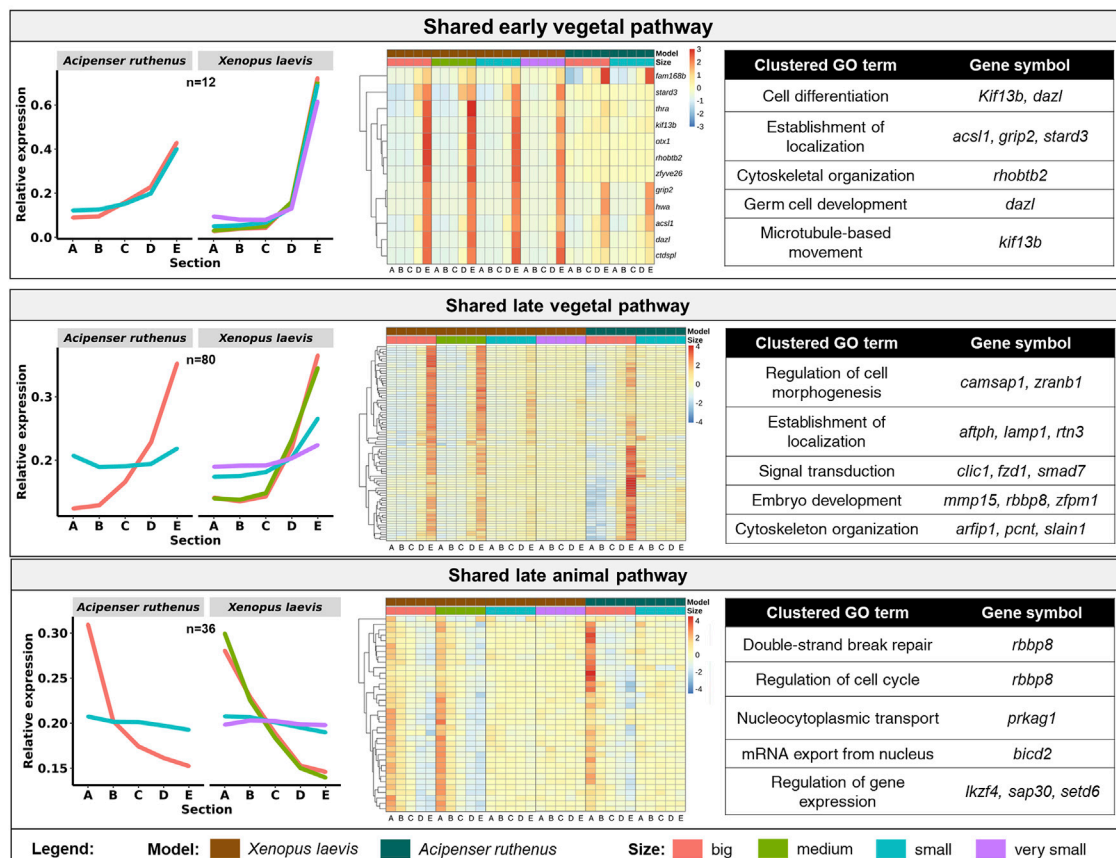


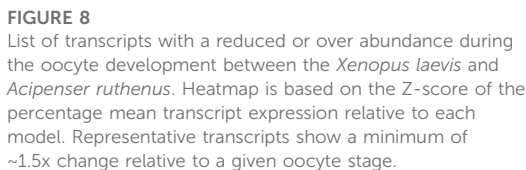
FIGURE 7

Vegetal and animal transcripts with similar temporal sub-cellular profiles in *Xenopus laevis* and *Acipenser ruthenus*. Heatmap is based on the Z-score of the transcript expression relative to the oocyte stage of the model. The Gene Ontology terms are those found associated with the given group of transcripts. Transcripts were filtered to include only those with either limited (early vegetal < ~1.5x) or enhanced (late pathways > ~1.2x) fold differences between stage sections of interest. The sections correspond to the regions of the oocyte that were cryosectioned, whereby sections A - extremely animal, B - animal, C - central, D - vegetal, E - extremely vegetal.

4 Discussion

Oocytes contain a unique set of transcripts coding genes that are important for their growth, meiotic recombination and division, metabolism of nutrients, and directing of early embryonic development (Song et al., 2006; Lyman-Gingerich and Pelegri, 2007). Here, we compared oocytes of representatives from the class *Amphibia* (*X. laevis*) and class *Actinopterygii* (*A. ruthenus*). It is known that both species show similarities during their oocyte development (Raikova, 1973; Raikova, 1974) and therefore there was an expectation that this may also be reflected in a high conservation of their maternal transcript localization. Additionally, microscopically it can be seen that the two models share similar transition of their nuclear region from a central location to a more animal localization from the transition from small (early vitellogenic) oocyte to the big (advanced vitellogenic) oocyte (Dumont, 1972).

Most of our knowledge about transcript localization have focused mainly on the vegetal localization, and primarily within the *X. laevis* model. This has led to the elucidation of three main pathways, those being the METRO, intermediate and Late pathways (Forristall et al., 1995; Kloc and Etkin, 1995). However, there is still controversy about the temporal regulation of each pathway, and it is common that pathways may actually overlap during multiple stages of the oocyte development. In addition, there is a lack of knowledge about animal localization and the mechanism driving it. *In situ* hybridization has been a prime method for studies of transcript localization during oogenesis and a few transcripts have already been analyzed (Kloc and Etkin, 1995, 1998; reviewed by King et al., 1999; Schroeder and Yost, 1996). However, large-scale analyses offer the potential to assess the full transcriptomic landscape and therefore offer a clearer picture on the complex drivers for development. Using TOMO-Seq approach, we measured the spatial transcript localization of nearly



Little is known about animal localization. In our previous study we hypothesized that animal DLTs are produced in the oocyte germinal vesicle, which is located in the animal hemisphere, and DLTs diffuse during oogenesis, without active transport, producing the observed peak in the first 1/3 of the egg from the animal pole (Sindelka et al., 2010, 2018). Previously we had identified an additional animal localization profile called extremely animal, which formed a gradient from animal to vegetal poles and we speculated that extremely animal DLTs are localized actively using an unknown mechanism. Using DESeq2 normalization (median-of-ratios method) we removed the majority of the animal transcripts (forming >90% of total maternal DLTs in mature eggs) and focused primarily on extremely localized transcripts. We found that both species utilized the animal pathway. The majority of animal localization in *X. laevis* appeared during the late stages of oogenesis, while in *A. ruthenus* we revealed two potential pathways: early and late. Animal localization during the late phases of *X. laevis* oogenesis has been already suggested by other studies (Yisraeli et al., 1990; Schroeder and Yost, 1996; reviewed by Schnapp et al., 1997). In *A. ruthenus*, the early group is localized into the animal pole already in the small oocytes and their animal gradient become steeper during oogenesis. The late group is localized ubiquitously in the small oocytes and the animal gradient is formed during oogenesis. We

identified a potentially interesting group of DLTs, which were localized to both poles of the oocytes: animal and vegetal at the same time. To reveal whether there is biological relevance of polar localization or if it is just a result of data normalization would require more thorough analysis using alternative approaches such as *in situ* hybridization and functional validation.

Changes in the transcript levels during oogenesis indicate a dramatic dependence of gene expression during oocyte maturation and tight regulation of oocyte polarity. The largest difference was observed comparing very small (*X. laevis*) and small (*A. ruthenus*) oocyte with the other stage, while only minor differences can be observed when comparing small and medium sizes of *X. laevis* oocytes. Transcripts coding hundreds (*X. laevis*) or thousands (*A. ruthenus*) of maternal genes were degraded or *de novo* synthesized during oogenesis and in many cases led to changes in localization profiles. Vegetal gradients were formed preferentially in *X. laevis* in contrast to both animal and vegetal gradients formation caused by degradation or *de novo* transcription in *A. ruthenus*. Such extensive transcriptional activity and *de novo* transcription was also described by Meneau et al. (2020) and Session et al. (2016) for the *X. laevis*, whereby they observed that between stages I-II and stages V-VI, 1557 transcripts showed an increased abundance in the oocytes, while 17 transcripts showed a decreased abundance. This correlates with what we observed whereby *de novo* and degradation of transcripts were observed from stages IV (small) to late stage V (big), relative to the stage III (very small).

The overall overlap between the two models in temporal localization profiles was relatively small. However, these few conserved DLTs are known to be important for early embryonic development. Group of vegetal DLTs, which are formed early (*dazl* and *grip2*), but also many DLTs localized late in oogenesis (*dnd1*) are known determinants of PGC formation or early development regulators. In contrast, conserved anally localized DLTs are important for cell cycle regulation and other nuclear processes.

In summary our data reflect highly dynamic changes at the transcript level during oogenesis. Precise spatial and temporal regulation of biomolecule localization are required for final oocyte quality, which is potentially crucial for normal development of the fast-dividing embryos, such as the studied examples of frogs and fishes. We found in our results examples for most of the theoretical scenarios including relocalization in space and time and spatially controlled degradation of transcripts. We believe that our data will serve as an essential initial source for target identification in oogenesis and future consequential studies will benefit from using alternative approaches to analyze gene functions during oogenesis and early embryogenesis.

Data availability statement

All raw and processed sequencing data generated in this study have been submitted to the National Center for Biotechnology Information's Gene Expression Omnibus (GEO) database, at <https://www.ncbi.nlm.nih.gov/geo/>, and can be accessed with the GEO deposition number: GSE211415 (*Xenopus laevis*) and GSE211412 (*Acipenser ruthenus*).

Ethics statement

All experimental procedures involving model organisms were carried out in accordance with the Czech Law 246/1992 on animal welfare. *Acipenser ruthenus* females were kept in the Research Institute of Fish Culture and Hydrobiology in Vodňany, Czech Republic and protocols were reviewed by the Animal Research Committee of the Faculty of Fisheries and Protection of Waters, South Bohemian Research Center of Aquaculture and Biodiversity of Hydrocenoses, Research Institute of Fish Culture and Hydrobiology, Vodňany, Czech Republic. The *X. laevis* females were from the colony of the Institute of Biotechnology and protocols were approved by the animal committee of the Czech Academy of Sciences.

Author contributions

VI, RS and RN wrote the manuscript and formulated methods. RS and VI performed library preparation. RN performed bioinformatics analysis and result interpretation. VI performed cryosection of the oocytes, RNA isolation and RT-qPCR. RS, VI, MZ, MP prepared samples and were involved in result interpretation. All authors reviewed the manuscript.

Funding

This work was supported by 86652036 from RVO; the Czech Science Foundation (grant number 19-11313S); Program for the support of promising human resources—postdoctoral students (registration number L200972002); the Ministry of Education, Youth and Sports of the Czech Republic - project CENAKVA (grant number LM2018099) and Biodiversity (grant number CZ.02.1.01/0.0/0.0/16_025/0007370); and from the European Union's Horizon 2020 Research and Innovation Programme [grant number 871108 (AQUAEXCEL3.0)]; the Polish Ministry of Science and Higher Education (MNiSW) no. N18/DBW/000016 and from the Polish Ministry of Education and Science (MEN) no. N18/DBS/000013 – Institute of Zoology and Biomedical

Research, Faculty of Biology, Jagiellonian University in Kraków, Poland (UJ).

Acknowledgments

We thank Ing. Lucie Langerova from GeneCore facility in BIOCEV for assistance during library preparation and Dr. Pavel Abaffy for help during data analysis.

Conflict of interest

The authors declare that the research was conducted in the absence of any commercial or financial relationships that could be construed as a potential conflict of interest.

References

- Bolger, A. M., Lohse, M., and Usadel, B. (2014). Trimmomatic: A flexible trimmer for illumina sequence data. *Bioinformatics* 30, 2114–2120. doi:10.1093/bioinformatics/btu170
- Bray, N. L., Pimentel, H., Melsted, P., and Pachter, L. (2016). Near-optimal probabilistic RNA-seq quantification. *Nat. Biotechnol.* 34, 525–527. doi:10.1038/nbt.3519
- Carotenuto, R., and Tussellino, M. (2018). *Xenopus laevis* oocyte as a model for the study of the cytoskeleton. *C. R. Biol.* 341 (4), 219–227. doi:10.1016/j.crv.2018.04.001
- Chan, A. P., Kloc, M., and Etkin, L. D. (1999). Fatv encodes a new localized RNA that uses a 25-nucleotide element (FVLE1) to localize to the vegetal cortex of *Xenopus* oocytes. *Development* 126 (22), 4943–4953. doi:10.1242/dev.126.22.4943
- Chebanov, M., and Galich, E. (2013). *Sturgeon hatchery manual*. Ankara: FAO FISHERIES AND AQUACULTURE TECHNICAL PAPER 558.
- Claußen, M., Lingner, T., Pommerenke, C., Opitz, L., Salinas, G., and Pieler, T. (2015). Global analysis of asymmetric RNA enrichment in oocytes reveals low conservation between closely related *Xenopus* species. *Mol. Biol. Cell* 26, 3777–3787. doi:10.1091/mbc.E15-02-0115
- Dettlaff, T. A., and Rudneva, T. B. (1991). “The South African clawed toad *Xenopus laevis*. 231–281,”. *Animal species for developmental studies*. Editors T. A. Dettlaff and S. G. Vassetszky (New York: Consultants Bureau), Vol. 2. doi:10.1007/978-1-4615-3654-3_9
- Dettlaff, T., Ginsburg, A., and Schmalgausen, O. I. (2006). *Razvitije osetrovnykh ryb (in Russian)*. Moscow: Development of sturgeon fishes, 3–223.
- Dobin, A., Davis, C. A., Schlesinger, F., Drenkow, J., Zaleski, C., Jha, S., et al. (2013). Star: Ultrafast universal RNA-seq aligner. *Bioinformatics* 29, 15–21. doi:10.1093/bioinformatics/bts635
- Dumont, J. N. (1972). Oogenesis in *Xenopus laevis* (Daudin). I. Stages of oocyte development in laboratory maintained animals. *J. Morphol.* 136 (2), 153–179. doi:10.1002/jmor.1051360203
- Elinson, R. P., and del Pino, E. M. (2012). Developmental diversity of amphibians. *Wiley Interdiscip. Rev. Dev. Biol.* 1 (3), 345–369. doi:10.1002/wdev.23
- Forristall, C., Pondel, M., Chen, L., and King, M. L. (1995). Patterns of localization and cytoskeletal association of two vegetally localized RNAs, Vg1 and Xcat-2. *Development* 121, 201–208. doi:10.1242/dev.121.1.201
- Fortriede, J. D., Pells, T. J., Chu, S., Chaturvedi, P., Wang, D. Z., Fisher, M. E., et al. (2020). Xenbase: Deep integration of GEO & SRA RNA-seq and ChIP-seq data in a model organism database. *Nucleic Acids Res.* 48, D776–D782. doi:10.1093/nar/gkz933
- Gilbert, S. F. (2000). *Oogenesis. Developmental Biology*. 6th edition. Sunderland (MA): Sinauer Associates.
- Heasman, J., Quarmby, J., and Wylie, C. C. (1984). The mitochondrial cloud of *Xenopus* oocytes: The source of germinal granule material. *Dev. Biol.* 105, 458–469. doi:10.1016/0012-1606(84)90303-8
- Houston, D. W. (2013). Regulation of cell polarity and RNA localization in vertebrate oocytes. *Int. Rev. Cell Mol. Biol.* 306, 127–185. doi:10.1016/B978-0-12-407694-5.00004-3
- Jagarlamudi, K., and Rajkovic, A. (2012). Oogenesis: Transcriptional regulators and mouse models. *Mol. Cell. Endocrinol.* 356, 31–39. doi:10.1016/j.mce.2011.07.049
- Kim, K. H., and Lee, K. A. (2014). Maternal effect genes: Findings and effects on mouse embryo development. *Clin. Exp. Reprod. Med.* 41 (2), 47–61. doi:10.5653/ce.2014.41.2.47
- King, M. L., Zhou, Y., and Bubunenko, M. (1999). Polarizing genetic information in the egg: RNA localization in the frog oocyte. *Bioessays* 21, 546–557. doi:10.1002/(SICI)1521-1878(199907)21:7<546::AID-BIES3>3.0.CO;2-Z
- Kloc, M., and Etkin, L. D. (1995). Two distinct pathways for the localization of RNAs at the vegetal cortex in *Xenopus* oocytes. *Development* 121 (2), 287–297. doi:10.1242/dev.121.2.287
- Kloc, M., and Etkin, L. D. (1998). Apparent continuity between the messenger transport organizer and late RNA localization pathways during oogenesis in *Xenopus*. *Mech. Dev.* 73, 95–106. doi:10.1016/S0925-4773(98)00041-0
- Kloc, M., Spohr, G., and Etkin, L. D. (1993). Translocation of repetitive RNA sequences with the germ plasm in *Xenopus* oocytes. *Science* 262, 1712–1714. doi:10.1126/science.7505061
- Kloc, M., Bilinsky, S., and Etkin, L. (2004). The Balbiani body and germ cell determinants: 150 Years later. *Curr. Top. Dev. Biol.* 59, 1–36. doi:10.1016/S0070-2153(04)59001-4
- Kopylova, E., Noe, L., and Touzet, H. (2012). SortMeRNA: Fast and accurate filtering of ribosomal RNAs in metatranscriptomic data. *Bioinformatics* 28, 3211–3217. doi:10.1093/bioinformatics/bts611
- Love, M. I., Huber, W., and Anders, S. (2014). Moderated Estimation of Fold Change and Dispersion for RNA-Seq Data With DESeq2. *Genome Biol.* 15 (12), 1–21.
- Lyman-Gingerich, J., and Pelegri, F. (2007). “Maternal factors in fish oogenesis and embryonic development,” in *The fish oocyte: From basic studies to biotechnological applications*. Editor P. J. Babin, et al. (Springer), 141–174. doi:10.1007/978-1-4020-6235-3_6
- Marlow, F. L. (2010). “Oocyte polarity and the embryonic axes: The Balbiani body, an ancient oocyte asymmetry,” in *Maternal control of development in vertebrates: My mother made me do it! Morgan & claypool life Sciences*. Available at: <https://www.ncbi.nlm.nih.gov/books/NBK53187/>.
- Meneau, F., Dupré, A., Jessus, C., and Daldello, E. M. (2020). Translational control of *Xenopus* oocyte meiosis: Toward the genomic era. *Cells* 9, E1502. doi:10.3390/cells9061502
- Naraine, R., Abaffy, P., Sidova, M., Tomankova, S., Pocherniaieva, K., Smolik, O., et al. (2020). NormQ: RNASeq normalization based on RT-qPCR derived size factors. *Comput. Struct. Biotechnol. J.* 18, 1173–1181. doi:10.1016/j.csbj.2020.05.010

Publisher's note

All claims expressed in this article are solely those of the authors and do not necessarily represent those of their affiliated organizations, or those of the publisher, the editors and the reviewers. Any product that may be evaluated in this article, or claim that may be made by its manufacturer, is not guaranteed or endorsed by the publisher.

Supplementary material

The Supplementary Material for this article can be found online at: <https://www.frontiersin.org/articles/10.3389/fcell.2022.982732/full#supplementary-material>

- Naraine, R., Igorova, V., Abaffy, P., Franek, R., Soukup, V., Psenicka, M., et al. (2022). Evolutionary conservation of maternal RNA localization in fishes and amphibians revealed by TOMO-Seq. *Dev. Biol.* 489, 146–160. doi:10.1016/j.ydbio.2022.06.013
- National Library of Medicine(2022)National library of medicine. Available at: <https://pubmed.ncbi.nlm.nih.gov/> (Accessed 2022).
- Owens, D. A., Butler, A. M., Aguero, T. H., Newman, K. M., Van Booven, D., and King, M. L. (2017). High-throughput analysis reveals novel maternal germline rnas crucial for primordial germ cell preservation and proper migration. *Dev. Camb.* 144 (2), 292–304. doi:10.1242/dev.139220
- Pantano, L. (2021). *DEGreport: Report of DEG analysis*. R package version 1.28.0. Available at: [lpantano.github.io/DEGreport/](https://github.com/lpantano/DEGreport/).
- Peshkin, L., Wuhr, M., Pearl, E., Haas, W., Freeman, R. M., Jr., Gerhart, J. C., et al. (2015). On the relationship of protein and mRNA dynamics in vertebrate embryonic development. *Dev. Cell* 35, 383–394. doi:10.1016/j.devcel.2015.10.010
- Raikova, E. (1973). Ultrastructure of sturgeon oocytes at the end of previtellogenesis. II. Cytoplasmic fine structure (in Russian, English summary). *Tsitologiya* 15, 1352–1361. Available at: <https://pubmed.ncbi.nlm.nih.gov/4361019/>.
- Raikova, E. (1974). Ultrastructure of the sterlet oocytes during early vitellogenesis. II. Cytoplasmic fine structure (in Russian, English summary). *Tsitologiya* 16, 1345–1351. Available at: <https://pubmed.ncbi.nlm.nih.gov/4858119/>.
- Rasar, M. A., and Hammes, S. R. (2006). “The physiology of the *Xenopus laevis* ovary.”. *Xenopus protocols*. Editor X. J. Liu (Methods Mol Biol), 322, 17–30. doi:10.1007/978-1-59745-000-3_2
- Raudvere, U., Kolberg, L., Kuzmin, I., Arak, T., Adler, P., Peterson, H., et al. (2019). G:Profiler: A web server for functional enrichment analysis and conversions of gene lists (2019 update). *Nucleic Acids Res.* 47, W191–W198. doi:10.1093/nar/gkz369
- Rodina, M. (2006). Application of image analysis for the determination of nucleus position in sturgeon oocytes. *J. Appl. Ichthyol.* 22, 373–374. doi:10.1111/j.1439-0426.2007.00988.x
- Schnapp, B. J., Arn, E. A., Deshler, J. O., and Highett, M. I. (1997). RNA localization in *Xenopus* oocytes. *Semin. Cell Dev. Biol.* 8, 529–540. doi:10.1006/scdb.1997.0178
- Schroeder, K. E., and Yost, H. J. (1996). *Xenopus* poly (A) binding protein maternal RNA is localized during oogenesis and associated with large complexes in blastula. *Dev. Genet.* 19, 268–276. doi:10.1002/(SICI)1520-6408(1996)19:3<268::AID-DVG10>3.0.CO;2-W
- Sekula, M., Datta, S., and Datta, S. (2017). optCluster: An R package for determining the optimal clustering algorithm. *Bioinformatics* 13, 101–103. doi:10.6026/97320630013101
- Selman, K., Wallace, R. A., Sarka, A., and Qi, X. (1993). Stages of oocyte development in the zebrafish, *Brachydanio rerio*. *J. Morphol.* 218, 203–224. doi:10.1002/jmor.1052180209
- Session, A. M., Uno, Y., Kwon, T., Chapman, J. A., Toyoda, A., Takahashi, S., et al. (2016). Genome evolution in the allotetraploid frog *Xenopus laevis*. *Nature* 538, 336–343. doi:10.1038/nature19840
- Sindelka, R., Sidova, M., Svec, D., and Kubista, M. (2010). Spatial expression profiles in the *Xenopus laevis* oocytes measured with qPCR tomography. *Methods* 51, 87–91. doi:10.1016/j.jymeth.2009.12.011
- Sindelka, R., Abaffy, P., Qu, Y., Tomankova, S., Sidova, M., Naraine, R., et al. (2018). Asymmetric distribution of biomolecules of maternal origin in the *Xenopus laevis* egg and their impact on the developmental plan. *Sci. Rep.* 8, 8315. doi:10.1038/s41598-018-26592-1
- Song, J. L., Wong, J. L., and Wessel, G. M. (2006). Oogenesis: Single cell development and differentiation. *Dev. Biol.* 300, 385–405. doi:10.1016/j.ydbio.2006.07.041
- Spence, R., Gelach, G., Lawrence, C., and Smith, C. (2008). The behaviour and ecology of the zebrafish, *Danio rerio*. *Biol. Rev. Camb. Philos. Soc.* 83, 13–34. doi:10.1111/j.1469-185X.2007.00030.x
- Xu, J., and Gridley, T. (2012). *Notch signaling during oogenesis in Drosophila melanogaster*. *Genetics Research International*. doi:10.1155/2012/648207
- Ye, J., Coulouris, G., Zaretskaya, I., Cutcutache, I., Rozen, S., and Madden, T. L. (2012). Primer-BLAST: A tool to design target-specific primers for polymerase chain reaction. *BMC Bioinforma.* 13, 134. doi:10.1186/1471-2105-13-134
- Yisraeli, J. K., Sokol, S., and Melton, D. A. (1990). A two-step model for the localization of maternal mRNA in *Xenopus* oocytes: Involvement of microtubules and microfilaments in the translocation and anchoring of Vg1 mRNA. *Development* 108, 289–298. doi:10.1242/dev.108.2.289
- Zearfoss, N. R., Chan, A. P., Wu, C. F., Kloc, M., and Etkin, L. D. (2004). Hermes is a localized factor regulating cleavage of vegetal blastomeres in *Xenopus laevis*. *Dev. Biol.* 267, 60–71. doi:10.1016/j.ydbio.2003.10.032
- Zelazowska, M., and Fopp-Bayat, D. (2017). Previtellogenic and vitellogenic oocytes in ovarian follicles of cultured siberian sturgeon *Acipenser baerii* (chondrostei, acipenseriformes). *J. Morphol.* 278, 50–61. doi:10.1002/jmor.20618
- Zelazowska, M., and Fopp-Bayat, D. (2019). Germline cysts and asymmetry in early previtellogenic ovarian follicles in cultured albino females of sterlet *Acipenser ruthenus* L. 1758 (Chondrostei, Acipenseriformes). *Protoplasma* 256 (5), 1229–1244. doi:10.1007/s00709-019-01376-0
- Zelazowska, M. (2010). Formation and structure of egg envelopes in Russian sturgeon, *Acipenser gueldenstaedtii* (Acipenseriformes: Acipenseridae). *J. Fish. Biol.* 76, 694–706. doi:10.1111/j.1095-8649.2009.02527.x
- Zelazowska, M., Kilarski, W., Bilinski, S. M., Podder, D. D., and Kloc, M. (2007). Balbiani cytoplasm in oocytes of a primitive fish, the sturgeon *Acipenser gueldenstaedtii*, and its potential homology to the Balbiani body (mitochondrial cloud) of *Xenopus laevis* oocytes. *Cell Tissue Res.* 329, 137–145. doi:10.1007/s00441-007-0403-9
- Zhang, J., and King, L. (1996). *Xenopus* VegT RNA is localized to the vegetal cortex during oogenesis and encodes a novel T-box transcription factor involved in mesodermal patterning. *Development* 122, 4119–4129. doi:10.1242/dev.122.12.4119



OPEN ACCESS

EDITED BY
Silvia Garagna,
University of Pavia, Italy

REVIEWED BY
Yuichiro Nakajima,
The University of Tokyo, Japan
Mike Boxem,
Utrecht University, Netherlands

*CORRESPONDENCE
Zhongying Zhao,
zyzhao@hkbu.edu.hk

[†]These authors share first authorship

SPECIALTY SECTION
This article was submitted to
Morphogenesis and Patterning,
a section of the journal
Frontiers in Cell and Developmental
Biology

RECEIVED 27 June 2022
ACCEPTED 20 September 2022
PUBLISHED 25 October 2022

CITATION
Wong M-K, Ho VWS, Huang X, Chan L-Y,
Xie D, Li R, Ren X, Guan G, Ma Y, Hu B,
Yan H and Zhao Z (2022), Initial
characterization of gap phase
introduction in every cell cycle of
C. elegans embryogenesis.
Front. Cell Dev. Biol. 10:978962.
doi: 10.3389/fcell.2022.978962

COPYRIGHT
© 2022 Wong, Ho, Huang, Chan, Xie, Li,
Ren, Guan, Ma, Hu, Yan and Zhao. This is
an open-access article distributed
under the terms of the [Creative
Commons Attribution License \(CC BY\)](#).
The use, distribution or reproduction in
other forums is permitted, provided the
original author(s) and the copyright
owner(s) are credited and that the
original publication in this journal is
cited, in accordance with accepted
academic practice. No use, distribution
or reproduction is permitted which does
not comply with these terms.

Initial characterization of gap phase introduction in every cell cycle of *C. elegans* embryogenesis

Ming-Kin Wong^{1†}, Vincy Wing Sze Ho^{1†}, Xiaotai Huang^{2,3},
Lu-Yan Chan¹, Dongying Xie¹, Runsheng Li¹, Xiaoliang Ren¹,
Guoye Guan⁴, Yiming Ma¹, Boyi Hu^{1,5}, Hong Yan³ and
Zhongying Zhao^{1,6*}

¹Department of Biology, Hong Kong Baptist University, Kowloon, Hong Kong SAR, China, ²School of Computer Science and Technology, Xidian University, Xi'an, China, ³Department of Electronic Engineering, City University of Hong Kong, Kowloon, Hong Kong SAR, China, ⁴Center for Quantitative Biology, Peking University, Beijing, China, ⁵Department of Biology, Southern University of Science and Technology, Shenzhen, China, ⁶State Key Laboratory of Environmental and Biological Analysis, Hong Kong Baptist University, Kowloon, Hong Kong SAR, China

Early embryonic cell cycles usually alternate between S and M phases without any gap phase. When the gap phases are developmentally introduced in various cell types remains poorly defined especially during embryogenesis. To establish the cell-specific introduction of gap phases in embryo, we generate multiple fluorescence ubiquitin cell cycle indicators (FUCCI) in *C. elegans*. Time-lapse 3D imaging followed by lineal expression profiling reveals sharp and differential accumulation of the FUCCI reporters, allowing the systematic demarcation of cell cycle phases throughout embryogenesis. Accumulation of the reporters reliably identifies both G1 and G2 phases only in two embryonic cells with an extended cell cycle length, suggesting that the remaining cells divide either without a G1 phase, or with a brief G1 phase that is too short to be picked up by our reporters. In summary, we provide an initial picture of gap phase introduction in a metazoan embryo. The newly developed FUCCI reporters pave the way for further characterization of developmental control of cell cycle progression.

KEYWORDS

FUCCI, cell cycle phase, embryogenesis, *C. elegans*, cell lineage

Introduction

The developmental control of cell cycle progression is essential to ensure a balance between cell proliferation or growth and cell fate differentiation. Dysregulation of the balance may lead to catastrophes such as carcinogenesis or abnormal cell death. Unlike cell division in a single-celled organism or a cultured cell, which progresses through a full cell cycle with four phases: two gap phases, G1 and G2, that interrupt the DNA synthesis (S) phase from mitosis (M) phase, early embryonic division in most metazoans consists of

M and S phases only without any gap phase (Farrell and O'Farrell, 2014). After certain rounds of synchronous divisions that are mostly driven by maternal factors, cell cycles become asynchronous, and gap phases are presumably introduced in a cell type- or developmental time-dependent manner. The transition from synchronous to asynchronous divisions coincides with zygotic genome activation when zygotic gene expression is initiated (Lee et al., 2014; Pálffy et al., 2017). However, the exact details of when the gaps are systematically introduced spatiotemporally during embryogenesis remains poorly defined.

One of the major difficulties in defining embryonic cell cycle phases is the lack of reliable reporters for a precise demarcation of cell cycle phases. The recent development of fluorescent ubiquitination-based cell cycle indicator (FUCCI) has paved the way for demarcation of cell cycle phases, especially in cultured cells (Sakaue-Sawano et al., 2008). The initial FUCCI system developed in human cell line relied on pairs of fluorescent proteins fused to the degrons derived from Cdt1 and Geminin proteins which are a DNA replication licensing factor and its inhibitor, respectively (Arias and Walter, 2007). The CDT1 level peaks in the G1 phase, and declines quickly after the initiation of the S phase due to the degradation by SCF^{Skp2} (Li et al., 2003; Nishitani et al., 2004); whereas the Geminin reaches a high level in the S and G2 phases, but falls to a low level in the late M and G1 phases due to the degradation by APC/C^{Cdh1} (McGarry and Kirschner, 1998; Arias and Walter, 2007). The reciprocal oscillations of the two factors during the cell cycle progression permit distinguishing cells in G1 phase from those in S/G2/M phase. Since their first introduction in human cell lines, FUCCI reporters have been developed in both cultured cells and intact animals (Sakaue-Sawano et al., 2013; Zielke et al., 2014; Bajar et al., 2016; Özpolat et al., 2017), greatly facilitating the study of regulation of developmental control over cell cycle progression. However, these reporters have not been generated in *C. elegans*, a well-established model organism.

Another difficulty in defining embryonic cell cycle phases lies in the systematic acquisition of the cellular accumulation patterns of fluorescence reporters with a high temporal resolution. This is because that cell divisions are rapid during early embryogenesis, which can be as fast as 8.6 min per generation (Foe and Alberts, 1983; Farrell and O'Farrell, 2014). Therefore, tracing the division of individual cells and measurement of reporter accumulation therein become a great challenge. *C. elegans* embryo is an excellent model for investigating gap phase introduction with cellular resolution. First, its embryo is transparent and develops with an invariant cell lineage within roughly 14 h at room temperature (Sulston et al., 1983), allowing live-cell imaging of the entire embryogenesis process at a high temporal resolution. Second, various automated tools have been developed to trace cell division and profile reporter accumulation with cellular resolution at 1.5-min intervals (Bao et al., 2006; Murray et al.,

2008; Zhao et al., 2010a). Third, *C. elegans* embryogenesis demonstrates frequent division asymmetry in cell cycle length between two sister cells that develop into the same or different fate(s) (Sulston et al., 1983). We have previously shown that these asymmetries are primarily controlled by the regulatory factors determining fate differentiation (Ho et al., 2015). However, the method for systematic profiling of gap phase introduction has not been established in *C. elegans* though a postembryonic fluorescence reporters for cell cycle entry has been developed, which were based on reporter's translocation rather than its accumulation or degradation to mark cell cycle commitment (vanRijnberk et al., 2017; Adikes et al., 2020). In addition, their dependence on the ratio between cytoplasmic and nuclear CDK abundance makes it not feasible for automated quantification of reporter intensity that relies on expression in nuclei, especially in late embryonic cells with minimal cytoplasm.

In this study, we determined the gap phase introduction for every cell during the embryogenesis of *C. elegans*. This was achieved by the development of multiple FUCCI reporters as a single-copy transgene in *C. elegans* (hereafter referred to as Worm-FUCCI), the degradation of which was biochemically and functionally validated. Aided by the automated tools for lineage and expression analysis (Bao et al., 2006; Murray et al., 2008), a combination of the individual FUCCI reporters with a lineaging marker allowed us to quantify the reporters' lineal accumulation level for every cell at 1.5-min intervals throughout *C. elegans* embryogenesis, leading to a first-ever global picture of gap phase introduction throughout metazoan embryogenesis. We demonstrated that most embryonic cells appear to divide either with a very brief G1 phase or skipping the G1 and G2 phases altogether except one pair of cells, which apparently divide with a full cell cycle. We also demonstrated the potential of the reporters for cell cycle analysis during postembryonic development, including the development of germline and intestine. Availability of the Worm-FUCCI will aid future study of the coordination between cell division and fate differentiation during embryonic and postembryonic development.

Materials and methods

Worm strains and maintenance

All the animals were maintained on NGM plates seeded with OP50 at room temperature. The genotypes of the strains used in this paper were listed in the [Supplementary Table S1](#). Imaging of postembryonic tissues was performed as described (Shao et al., 2013).

DNA constructs

his-72 promoter (2,349 bps from immediately upstream of its start codon), *pie-1* 3'UTR (787bp immediately after the stop codon),

the nuclear localization signal (NLS) of EGL-13 (1-25aa), the degrons of CDT-1 (1-189aa) and CYB-1 (8-80aa) were amplified from the N2 genomic DNA, respectively. mCherry fragment was amplified from pCFJ104 (Frokjaer-Jensen et al., 2014), while eGFP was amplified from pZZ31 (Zhao et al., 2010a). The fusion cassette consisting of *Phis-72::mCherry::CDT-1(1-189aa)::pie-1* 3'UTR was cloned into the *miniMos* vector pCFJ909 (Frokjaer-Jensen et al., 2014) to generate plasmid pZZ176 using Gibson Assembly according to the manufacturer's description. Plasmid pZZ180 [*Phis-72::GFP::EGL-13* (1-25aa)::*CYB-1* (8-80aa)::*pie-1* 3'UTR + *unc-119(+)*] was generated in the similar way as pZZY176. EGL-13 (1-25aa) was fused with the N-terminal of CYB-1 degron to serve as an NLS (Lyssenko et al., 2007). pZZ147 [*Phis-72::mCherry::EGL-13* (1-25aa)::*CYB-1* (8-80aa)::*pie-1* 3'UTR + *unc-119(+)*] was made by cutting the pZZ141 (Supplementary Table S1) with *ApaI* and *SpeI*, respectively, to replace the *HIS-24* coding region with the fusion between EGL-13 (1-25aa) and CYB-1 (8-80aa). The details of these constructs built in this study was listed in the Supplementary Table S2. Vector sequences and annotations can be found in the links below:

pZZ176—CDT-1D: <https://benchling.com/s/seq-iUCSfeZlgDycQ5RkrD2s/edit> pZZ147—CYB-1D: <https://benchling.com/s/seq-mN00xlJVIAwAU66QJIDA/edit> pZZ180—CYB-1DG: <https://benchling.com/s/seq-LBAUfkXMHsEbc8Z6uRE4/edit>.

5-ethynyl-2'-deoxyuridine staining

Prior to EdU staining, L4 worms were fed with *perm-1* RNAi bacteria to permeabilize the eggshell as described (Carvalho et al., 2011). To confirm the permeabilization of eggshell, part of the embryos from the RNAi animals were stained with FM[®] 4-64 dyes (Invitrogen). Embryos were retrieved from about 10 dissected worms and allowed to develop under the Boyd's buffer/methyl cellulose for 3 h (Murray et al., 2006). Click-iT[®] EdU Imaging Kit (Invitrogen) was used for EdU staining. After 3 h development, embryos were incubated with EdU for 15 min, followed by freeze-cracking, fixation and DAPI staining as described (Seydoux and Dunn, 1997). Embryos were then imaged for DAPI and mCherry accumulation of CDT-1^D and CYB-1^D, followed by EdU staining with Alexa Fluor[®] 647 using Leica SP5 Confocal microscope. Both DAPI and Alexa Fluor[®] 647 in the same embryos were imaged again, using DAPI for cell alignment to overlay the Worm-FUCCI accumulation with EdU signal in the nuclei.

RNA interference

RNAi against *cdt-2*, *fzr-1*, *cul-1*, *pat-3* or *cyd-1* was performed by microinjection as described (Ho et al., 2015). RNAi against *ddb-1* was performed by feeding on the NGM plates supplemented with 50 µg/ml Ampicillin and 1 mM IPTG. RNAi against *perm-1* was performed similar to that of *ddb-1*,

except the *perm-1* RNAi bacteria was diluted by “empty” vector (L4440) expressing bacteria in 1:6 ratio as described (Carvalho et al., 2011). The RNAi bacteria was derived from the Ahringer *C. elegans* RNAi feeding library (Kamath et al., 2001).

Fluorescence microscopy for embryo

Micrographs of embryos were acquired with a Leica SP5 confocal microscope with an objective of ×63 magnification. Early embryos were dissected from young adult worms and mounted with Boyd's buffer/methyl cellulose (Murray et al., 2006), and late embryos were picked from the NGM plate. For 3D imaging, GFP and mCherry were simultaneously illuminated with 488nm and 594 nm laser beams, respectively, and micrographs of their expression were collected with two separate hybrid detectors through a water immersion objective. Imaging setting was similar to what was used previously using a frame size of 712 × 512 pixels except the scanning speed was changed to 200 Hz (hz) (Ho et al., 2015). Laser compensation was applied during the stack acquisition to ensure the comparable brightness of the images acquired between the lower stack and upper stack. DIC images were acquired separately for a single focal plane typically in the middle of the embryo. For time lapse 3D imaging, it was performed as described (Murray et al., 2006) with the following modifications. Micrographs from 41 focal planes were collected consecutively for three embryos per imaging session from top to bottom of the embryo at an interval of about 1.5 min with a Z-axis resolution of 0.71 µm. Images were continuously collected for at least 200 time points. The entire imaging duration was divided into four blocks based on the time point, i.e., 1–60, 61–130, 131–200, and beyond 201. Z axis compensation was 0.4%–4% for 488 nm laser and 19%–95% for the 594 nm laser. The pinhole sizes for the four blocks were 2.3, 2.0, 1.6, 1.3 AU (airy unit). In general, the imaging duration for control embryos were around 6 h, whereas for the *cyd-1* RNAi embryos, the imaging duration was extended to 7 h to compensate the slower development of the embryo after RNAi. 3D projection was generated using Leica Application Suite X (LAS X).

Imaging and data analysis beyond time point when embryo starts twitching

To image a developing embryo beyond the time point when it started twitching, knockdown of *pat-3* by RNAi was performed through microinjection. For automated lineaging of all embryonic cells up to 1.5-fold stage, the same settings were used as described above except the imaging duration was extended from 6 h to 9 h. For manual curation of the cells, V5QL/R, beyond the 1.5-fold stage, the RNAi embryo arrested at two-fold stage that specifically accumulated CYB-1^{DG} was traced backward till the time point when their exact identities were established through automated lineaging at approximately 1.5-fold stage.

Automated lineaging and gene expression profiling

Strains expressing Worm-FUCCI were individually crossed either with strain RW10029 that broadly expresses a fusion between histone and GFP or RW10226 that broadly expresses a fusion between histone and mCherry, which were referred to as lineaging marker (Chen et al., 2018). FUCCI reporter contains mCherry or GFP was crossed with RW10029 and RW10226, respectively to allow automated cell tracing and lineal expression profiling. Both the lineaging marker and FUCCI reporter were rendered homozygous before automated lineaging and lineal gene expression profiling as described (Murray et al., 2008). Automated lineaging results were manually curated up to approximately 1.5-fold stage unless stated otherwise. All the expression data were normalized for the subsequent comparison.

Transgenesis

The Worm-FUCCI strains carrying a single-copy transgene were generated using *miniMos* technique (Frokjaer-Jensen et al., 2014). Only strains with bright maternal and zygotic expression of Worm-FUCCI transgene were selected for the subsequent analysis (Supplementary Table S2). Transgene insertion site was mapped using inverse PCR as described (Frokjaer-Jensen et al., 2014). To facilitate simultaneous visualization of both degron reporters in the same animal, the transgenes consisting of *Phis-72::mCherry::CDT-1(1-189aa)::pie-1* 3'UTR and *Phis-72::GFP::EGL-13(1-25aa)::CYB-1(8-80aa)::pie-1* 3'UTR were rendered doubly homozygous by crossing.

Fluorescence microscopy for postembryonic stages

Micrographs of larvae and gonads were acquired with tile scanning using the same confocal microscope as that for the embryo. Dissected gonads or intact adults were mounted with Boyd's buffer/methyl cellulose (Murray et al., 2006) for imaging. Animals were mounted on a 1% agarose pad with 0.1 M sodium azide in M9 buffer for imaging with scanning speed of 200–400 hz depending on the size of the animals. For acquisition of 3D image stacks, imaging settings were similar to those used for the embryo except using 1 μm per z-step vs. 0.71 μm per z-step for the embryo.

Time-lapse imaging of larvae

Synchronized L1 larvae were obtained through egg prep. Animal development time (in hour) was counted from the start of feeding. Five larvae were selected for imaging each

hour before and after the feeding for a continuous duration of 13 h. Micrographs were acquired only for part of the intestine using 0.3 μm per z-step and 200 hz scanning speed. Micrographs of mCherry and DIC were collected simultaneously. A representative micrograph for the cells int2 and int3 were collected for illustration.

Quantification and statistical analysis

To facilitate the comparison of accumulation intensities of the two reporters in the same cells from two different embryos throughout embryogenesis, two sets of reporter expression series (E) were acquired from an embryo expressing CDT-1^D (E_R ; red; EmbryoR) and another embryo expressing CYB-1^D (E_G ; green; EmbryoG). The expression intensity, i.e., fluorescent signal intensity, of a cell ω at time point T was expressed by $E(\omega, T)$, where $T = 1, 2, 3, \dots$ and its corresponding actual time was denoted by t ($t = T \cdot \text{Resolution}$). The confocal imaging started from a 4-cell stage embryo and ended in approximately 550-cell stage. A previously established quality control cell list, which provided a group of conserved and comparable developmental stages, was applied on both embryos (Cao et al., 2020; Guan et al., 2020). In brief, The quality control required the embryonic stage between $T_{4\text{-cell}}$ and $T_{\sim 350\text{-cell}}$ that must be imaged continuously, whereas the last co-existence time point of “ABa”, “ABp”, “EMS,” and “P2” cells were labelled as $T_{4\text{-cell}}$ and the first co-existence time points of “AB256”, “MS32”, “E16”, “C16”, “D8”, “Z2,” and “Z3” cells were labelled as $T_{\sim 350\text{-cell}}$.

There were four types of unavoidable experimental variations that needed to be normalized before the comparison of reporter expressions.

A. Due to high dynamic range of the lineaging marker expression values, the entire imaging process was separated by multiple blocks that applying different pinholes. However, the changes of pinhole would also sharply and constantly change the absolute recorded value of FUCCI reporter expressions. To maintain the continuity and comparability of both sets of the reporter expression series, linear scaling on the expression data was subsequently applied on each change of pinhole at the exact time point ($T_i = 60, 130, 200$). The proportional scaling coefficient $K_{E,i}$ was obtained by fitting the global FUCCI reporter expressions before and after the adjustment into similar and smooth values, according to $E(\omega, T)' = E(\omega, T) \cdot K_{E,i}$ ($T > T_i$); here, $K_{E,i} = \frac{\sum_{\omega \in \Omega} E(\omega, T_i)}{\sum_{\omega \in \Omega} E(\omega, T_i + 1)}$, where Ω was the cells present at both time points T_i and $T_i + 1$.

B. The expression level of both FUCCI reporters varied globally among the embryos. Therefore, the data from them were linearly scaled to a closer order of magnitude for better visualization and comparison. The proportional scaling coefficient K'_E was obtained by fitting the maximum reporter expression detected before the time point $T_{\sim 350\text{-cell}}$ in those two embryos into the same value, according to

$E_G(\omega, T)' = E_G(\omega, T) \cdot K_E'$; here, $K_E' = \frac{\sum_{\omega \in \Omega', T \leq T_{350}} E_G(\omega, T)}{\sum_{\omega \in \Omega', T \leq T_{350}} E_R(\omega, T)}$, where Ω' were the cells existing before the time point $T_{\sim 350\text{-cell}} + 1$.

C. The global variation in developmental paces between embryos, which was revealed by the slightly changeable cell cycle length (C), were frequently observed among individual embryos owing to multiple factors, such as individual fitness and the variation of room temperature. To normalize these variations, the cell cycle length of all cells that had complete lifespan and divided before $T_{\sim 350\text{-cell}}$ in both embryos were compared, and the relative growth rate K_C of Embryo G compared to Embryo R, was calculated according to a method described previously (Guan et al., 2019). Then, the cell cycle length of all cells in Embryo G was transformed into $C_G(\omega)' = C_G(\omega)/K_C$.

D. Despite the global normalization on developmental pace, the cell cycle length of each specific cell would still be different in the two embryos. Hence, for each cell with complete lifespan recorded, its time points in Embryo G to fit the ones in Embryo R were linearly transformed by setting the actual time of appearance and the end of a cell that was totally same for both embryos, namely, $t_G(\omega, 1)' = t_R(\omega, T_{\min})$, $t_G(\omega, T_{\max})' = t_R(\omega, T_{\max})$. The transformation of each time point followed the formula $t_G(\omega, T)' = [t_G(\omega, T) - t_G(\omega, T_{\min})] \cdot \frac{t_R(\omega, T_{\max}) - t_R(\omega, T_{\min})}{t_G(\omega, T_{\max}) - t_G(\omega, T_{\min})} + t_R(\omega, 1)$ ($T_{\min} \leq T \leq T_{\max}$). For the cell without complete life span, its actual time of appearance was directly translated to Embryo R, and no linear scaling was performed.

All four experimental variations were normalized, and the expression data of Embryo G were aligned onto that of Embryo R, which served as a reference regarding both reporter expression level and developmental pace. Finally, the expression values of two reporters from two different embryos were drawn on a single lineage tree or plotted individually for each cell.

Results

Generation of Worm-fluorescence ubiquitin cell cycle indicators

To map the developmental introduction of gap phases during *C. elegans* development, we built a worm version of FUCCI, which consisted of degron reporters derived from two proteins: *C. elegans* orthologues of human CDT1 and cyclin B1 (CCNB1) protein, i.e., CDT-1 and CYB-1. Initial CDT1 derived FUCCI relied on one of its two degrons, i.e., Cy motif (Sakaue-Sawano et al., 2008). Although the degron is absent in the *C. elegans* CDT-1, the other degron of CDT1, PIP box, is present. As the PIP degron is rapidly degraded by CUL4^{Ddb1} during the S phase onset in humans (Sakaue-Sawano et al., 2017), CDT1 is extremely abundant in the G1 phase but barely detectable in the S phase. This degradation pathway was also shown to be conserved in *C.*

elegans (Zhong et al., 2003; Kim and Kipreos, 2007; Özpölat et al., 2017). A recent study demonstrated the superiority of the PIP-containing degron as a G1-specific degron over the Cy motif, as it provided a sharper boundary between G1 and S phases in a human cell line (Sakaue-Sawano et al., 2017). To generate a G1- and G2-specific reporter in *C. elegans*, a sequence consisting of 1–189 CDT-1 amino acids that carried the PIP box but lacked the putative cyclin binding motif was fused with the C-terminus of mCherry (referred to as CDT-1^D hereafter) (Figures 1A,B). To achieve broad spatial and temporal expression, the fusion was flanked by a *his-72* promoter and a *pie-1* 3' untranslated region (UTR). The *his-72* promoter drives strong zygotic expression but is less capable in driving germline expression (Ooi et al., 2006). The inclusion of a *pie-1* 3' UTR has been shown to significantly boost germline expression (Merritt et al., 2008; Zhao et al., 2010a) (Figure 1B). Therefore, the reporters are expected to show strong and broad expression in both germline and Soma in the absence of robust degradation. The truncated CDT-1 sequence seems to contain a cryptic NLS that directs the reporters into nuclei (Figures 2A, 3B). The cassette was introduced into random locations of the *C. elegans* genome as a single copy using the *miniMos* technique (Frokjaer-Jensen et al., 2014). The transgenic strain with the brightest and broadest expression but without apparent developmental defect was selected for the subsequent analysis. Nuclear expression is important to the subsequent analysis of reporter expression based on automated lineaging and expression profiling technologies (Bao et al., 2006; Murray et al., 2008). Broad accumulation of the reporter was observed for nearly all cells after they completed their last round of division during embryogenesis (Supplementary Figure S1). The accumulation dynamics of the reporter were expected to mimic those of their human equivalents, i.e., accumulation of the reporter was high in the G1 but completely absent in the S phase, followed by accumulation starting from the G2 and peaking again in the G1 phase (Figures 1C,D).

To develop a second reporter in assisting the CDT-1^D in defining cell phase boundaries, we attempted to use a *C. elegans* equivalent as that in humans, i.e., Geminin. However, the Geminin orthologue (*gmn-1*) was barely identifiable by sequence alignment in *C. elegans*, although its function appeared to be conserved (Yanagi et al., 2005). We therefore used a highly conserved degron of cyclin B1 (CYB-1), whose *Drosophila* orthologue has been demonstrated to show accumulation dynamics that is comparable to those of human Geminin (Zielke et al., 2014). The N-terminal sequences of both *C. elegans* CYB-1 and its mouse orthologue, cyclin B1, contain a degron called the destruction box (D-box) (Figure 1A). The mouse cyclin B1 was demonstrated to be degraded by APC/C^{Fzr/Cdh1} in human cell line (Zur and Brandeis, 2002). The CYB-1 N-terminal sequence (8–80 amino acid) contains the first two D-boxes but lacks the putative mitotic chromosome association motif (Pfaff and King, 2013). The full N-terminal sequence also carries another two putative D-box degrons located within the

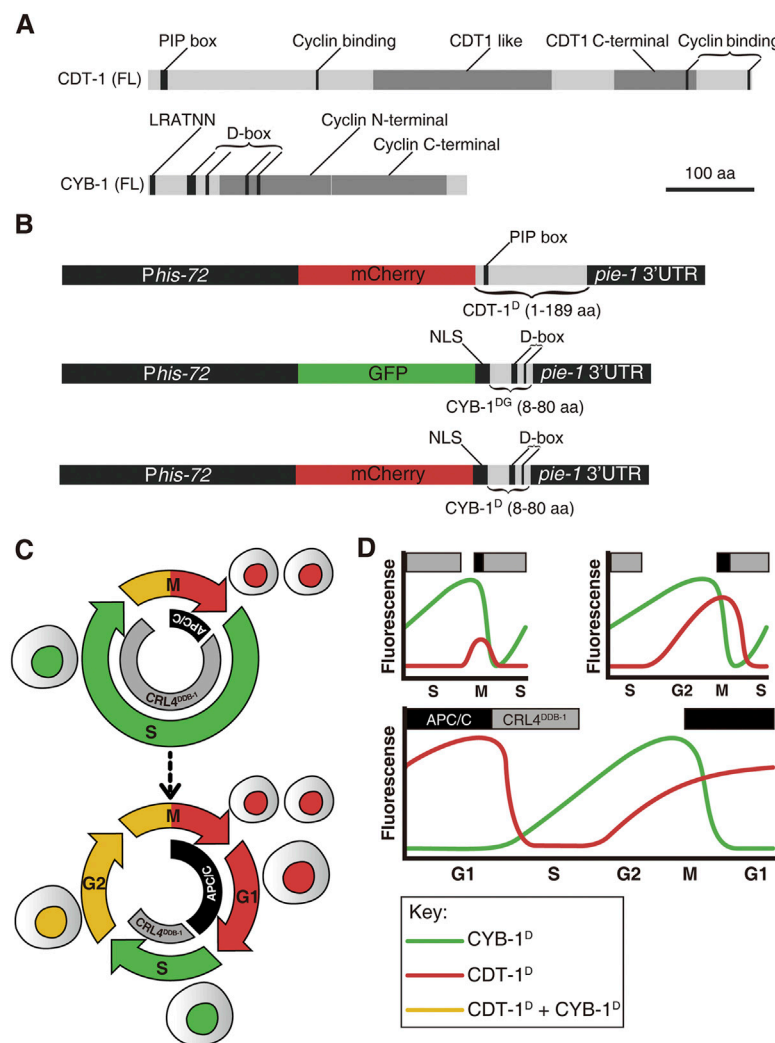


FIGURE 1

An overview of Worm-FUCCI design and expected marker expression dynamics in embryos. **(A)** Schematic representations of predicted domains in the full-length (FL) CDT-1 (top) and CYB-1 (bottom) proteins. Protein size in amino acid (aa) is shown in scale. PIP box: PCNA-interacting protein (CDT-1 degron). D-box: Destruction box (CYB-1 degron). LRATNN: amino acid sequence of a chromosome localization motif. **(B)** Worm-FUCCI construct design. To ensure broad expression both maternally and zygotically, all expression cassettes are driven by a *his-72* promoter and flanked by a *pie-1* 3' UTR. Top: the CDT-1 degron consisting of 1–189 aa of CDT-1 is fused to the C-terminus of mCherry (referred to as CDT-1^D) to label the G0/G1 and G2 phases. The PIP box with the sequence of QTAVTDF in the degron is targeted for degradation by CRL4^{DB-1} complex. Middle: the CYB-1 degrons consisting of 8–80 aa of CYB-1 is fused to the C-terminus of GFP (referred to as CYB-1^{DG}) to label the S and G2 phases. The putative D-boxes are targeted for degradation by APC/C^{FZR-1} complex. An NLS from EGL-13 (1–25 aa) is introduced between the GFP and the truncated CYB-1 to ensure nuclear localization of expression. Bottom: Same as the CYB-1 fusion with GFP except the substitution of the GFP with mCherry (referred to as CYB-1^D). All of the fusion constructs are integrated into *C. elegans* genome as a single copy transgene via *miniMos* technique. **(C)** Current view of early embryonic cell cycle (top) and full cell cycle (bottom) with the reported degradation complexes for the degrons mentioned in "B" in *C. elegans* indicated, i.e., degradation of CDT-1 (red) and CYB-1 (green) by CRL4^{DB-1} and APC/C complex at S and M/G1 phase respectively. **(D)** Predicted expression dynamics of the degron reporters mentioned in "B" during *C. elegans* embryogenesis. The degron reporters and their corresponding degradation complexes are color coded as in "C". Three different cell cycle scenarios, i.e., with no gap phase, with only G2 phase, and with both G1 and G2 phases, are shown. Note that the introduction of G2 phase results in an earlier increase in CDT-1^D accumulation before M phase, whereas the introduction of G1 phase results in accumulation of CDT-1^D but degradation of CYB-1^D or CYB-1^{DG} after M phase. The upper rectangle boxes denote the timing of the active degradation complexes (gray: CRL4^{DB-1}; black: APC/C).

cyclin N-terminal domain. We omitted the two D-box degrons within the cyclin N-terminal domain to avoid the potential functional interference of the native protein, which may lead to abnormal degradation. The truncated fragment was fused with

the C-terminus of either GFP (referred to as CYB-1^{DG}) or mCherry (referred to as CYB-1^D) (Figure 1B). The truncated CYB-1 sequence contains the first two D-boxes with the sequences of REILALKPSN and RINL, respectively. Again, the

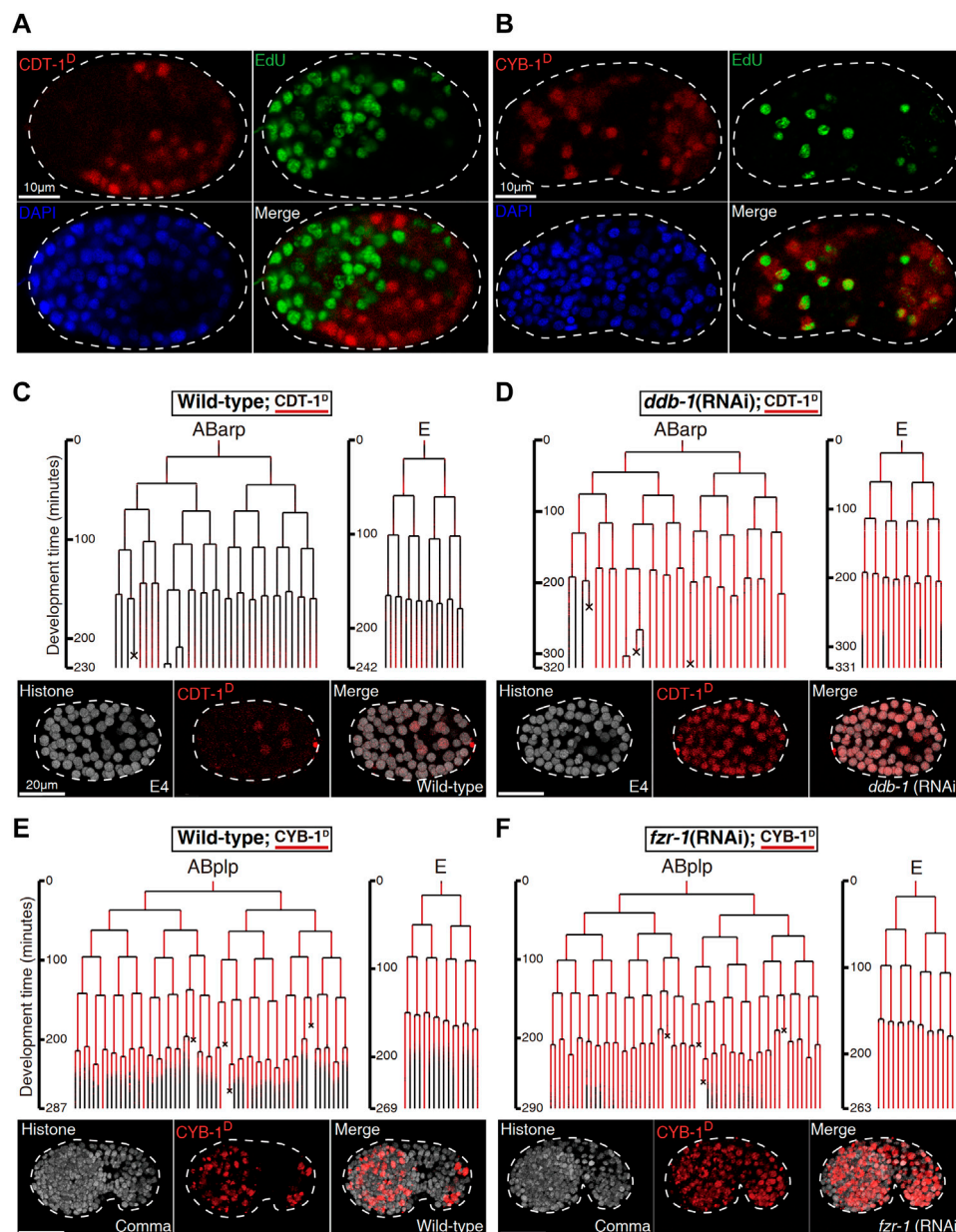


FIGURE 2

Biochemical and functional validation of Worm-FUCCI degradation (See also [Supplementary Figures S3,S4](#)). (A). EdU staining of the embryo expressing mCherry::CDT-1_{PIP-box} (referred to as CDT-1^D). Note that the localization of CDT-1^D (red) is mutually exclusive (merge) with the nuclei showing the staining of EdU (green) in a *perm-1* RNAi embryo. Nuclei stained with DAPI are shown in blue. (B). Same as (A) except the embryo is expressing mCherry::CYB-1_{D-box} (referred to as CYB-1^D). Note that the reporter-expressing cells (red) cover all the cells stained with EdU. The CYB-1-expressing cells that do not incorporated with EdU are presumably at G2/M phase. (C) Lineal expression (redness) of CDT-1^D in the sublineages, “ABarp” and “E” in a wild-type embryo. Development time starting from the birth of the ancestral cell of interest is shown on the left and cell deaths are indicated with an “x”. Epifluorescence micrographs for a representative time point at the “E4” stage [“E” divides into four daughters] are shown at the bottom. Histone, histone::GFP used for cell tracking during lineage analysis. (D) Same as (C) except the embryo is treated by RNAi against *ddb-1*. Note that expression onset of CDT-1 becomes much earlier and expression intensity becomes much higher in most cells after the RNAi. (E) Lineal expression of CYB-1^D in the sublineages of “ABplp” and “E” in a wild-type embryo. Development time and cell deaths are shown as in (C). Epifluorescence micrographs for a representative embryo at comma stage are shown at the bottom. (F). Same as (E) except that the embryo is treated by RNAi against *fzr-1*. Note that the degradation of the reporter during late embryogenesis is mostly abolished after the RNAi.

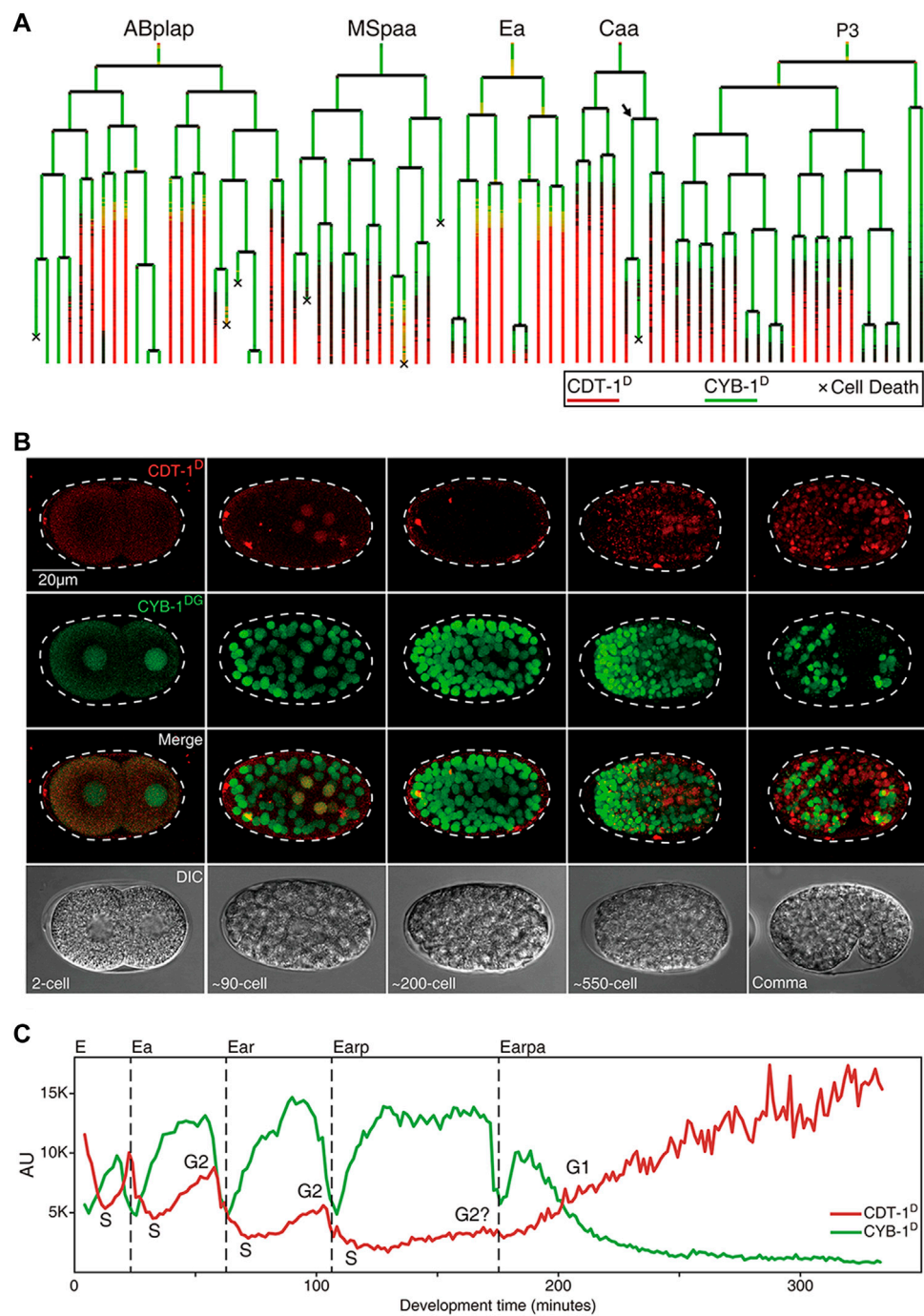


FIGURE 3
Expression dynamics of Worm-FUCCI in representative cell lineages during *C. elegans* embryogenesis (see also [Supplementary Figures S1,S2](#)). **(A)** Cell lineage trees showing the superimposed lineal accumulation of CDT-1^D (colored in red) and CYB-1^D (colored in green) in the representative sublineages of “ABplap”, “MSpaa”, “Ea”, “Caa”, and “P3”. Asynchrony of division between sister cells, “Caapa” and “Caapp”, is indicated with an arrow. Cell death is indicated with a “x”. Note the overall complementary expression patterns between the two reporters, i.e., the CYB-1^D is ubiquitously expressed during early embryogenesis, while the CDT-1^D is usually not expressed until a cell completes its last round of division. Long lasting CDT-1 expression is predictive of a cell cycle exit. **(B)** Epifluorescence micrographs of the embryos at different stages as indicated, which simultaneously express CDT-1^D and CYB-1^{DG} in the same embryo in some cells. The Nomarski micrographs of the same embryos are shown at the bottom. **(C)** Quantification of accumulation dynamics of CDT-1^D (red) and CYB-1^D (green) during the development of E lineage (only “Earpa” sublineage is shown). Normalized fluorescence intensity in the arbitrary unit (AU) is plotted on the Y axis. Development time from “E” to “Earpa” cells starting from the birth of “E” is plotted on the X axis. Cell cycle phases are indicated based on the expression dynamics of the two reporters. Division time point of each cell are indicated with a dashed line.

fusion was flanked by the same regulatory sequences as those for the cassette CDT-1^D to achieve broad expression in germline and Soma. However, the transgenic animals generated with these constructs were not expressed in the nuclei (Wang et al., 2013). An NLS sequence derived from EGL-13 (Lyssenko et al., 2007) was fused between the fluorescence protein sequence and the degron sequence, resulting in bright expression of the single-copy transgenes in the nuclei (Figures 2B, 3B). In contrast with the high abundance of CDT-1^D in the G1 phase, the accumulation of the CYB-1^D was expected to be barely detectable in the G1 phase, but to accumulate from the S phase and peak at the start of the G2 phase (Figures 1C,D). In summary, we created the transgenic strains that carry a single copy of reporters fused with degrons from CDT-1 or CYB-1, which we referred to as Worm-FUCCI. The high abundance of CDT-1^D accumulation in the absence of the CYB-1^D or CYB-1^{DG} would be indicative of the G1 or G0 phase of a cell; whereas the absence of the CDT-1^D with the initial accumulation of CYB-1^D or CYB-1^{DG} would be indicative of the S phase; and a high abundance of both degron reporters would be indicative of the G2 phase (Figures 1C,D).

Validation of degradation dynamics of the Worm-fluorescence ubiquitin cell cycle indicators

To validate whether the Worm-FUCCI was temporally degraded as expected, we first examined whether the CDT-1^D was absent but the CYB-1^D was present in the S phase of embryonic cells. To this end, we investigated the concurrence between the incorporation of 5-ethynyl-2'-deoxyuridine (EdU) and the accumulation of the CDT-1^D. EdU was expected to be incorporated into DNA only at the S phase. To permeabilize the egg shell for EdU, we partially inactivated *perm-1* by RNA interference (RNAi) as reported previously (Carvalho et al., 2011). As expected, the accumulation of CDT-1^D was mutually exclusive to the staining of EdU in nearly all embryonic cells (Figure 2A; Supplementary Figure S4A), while the accumulation of CYB-1^D was mostly overlapped with the staining of EdU (Figure 2B; Supplementary Figure S4B). Because the CYB-1^D was expected to be accumulated also in the G2 phase, those cells showing CYB-1^D accumulation but no staining of EdU were expected to be at the G2 phase.

We next functionally validated the S phase-specific degradation of CDT-1^D, which was reported to be degraded by cullin 4-based complex, i.e., cullin-RING ligase (CRL) coupled with adaptor protein DDB-1 (together referred to as CRL4^{DDB-1}), in *C. elegans* (Kim and Kipreos, 2007). We first performed RNAi against the gene encoding the adaptor of CUL-4, *ddb-1*, using a strain that simultaneously expressed the degron reporter and a lineaging marker, i.e., histone::GFP (Murray et al., 2008). We then performed automated lineaging and lineal gene expression

analysis using this strain with and without RNAi treatment as described (Zhao et al., 2010b). We did not detect any accumulation of CDT-1^D in most cells until about 550-cell stage of embryogenesis in a control embryo, which refers to a wild-type embryo without any perturbation except transgenesis-related genetic modification (Figures 2C; Supplementary Figure S1). In contrast, the RNAi led to the continuous accumulation of the degron reporter much earlier than that in the control embryo (Figure 2D), confirming that the degron had been targeted by the degradation pathway involving DDB-1 as expected. In addition to the adaptor DDB-1, CDT-2 was shown to function as a substrate recognition subunit in the CRL4 ubiquitin ligase for CDT-1^D degradation (Kim et al., 2008). RNAi against *cdt-2* led to an increased accumulation of CDT-1^D in most cells when compared with the control embryo (Supplementary Figure S3), further confirming that the CDT-1^D was degraded by the cullin-RING ubiquitin ligase, CRL4^{DDB-1}, in *C. elegans*.

The CYB-1^D was expected to accumulate in any cells with an active S and/or G2 phase and to abolish its accumulation in embryonic cells starting from M phase until the end of G0/G1 phase. The transgenic strain carrying CYB-1^D construct indeed demonstrated CYB-1^D accumulation throughout early embryonic cell cycle but degraded in most of the late embryonic cells (Figure 2E; Supplementary Figure S2). Notably, CYB-1^D also demonstrated an unexpected accumulation during and after the M phase. This could be due to the omission of other degrons within the CYB-1^D sequence, which led to a deviation from its native degradation pattern. A previous study showed that the mammalian CYB-1 orthologue, cyclin B1 was first targeted by APC/C^{Fzy/Cdc20} for degradation from prometaphase up to late M phase or anaphase (Clijsters et al., 2013). The degradation was relayed by APC/C^{Fzy/Cdh1}, which remained active till late G1 phase (Zur and Brandeis, 2002). Since the functions of both degradation complexes were known to be conserved in *C. elegans* (Fay et al., 2002; The et al., 2015; Kipreos and van denHeuvel, 2019), we reasoned that one the one hand the improper perdurance of CYB-1^D through M phase till the early stage of next cycle (Figure 2E), could be due to the failure of the Cdc20/Fzy orthologue (FZY-1) to target the truncated cyclin for degradation because of missing degrons. On the other hand, it was possible that the Cdh1/Fzy orthologue (FZR-1) may not be robust enough to completely degrade CYB-1^D before the end of the M phase. In addition, mutation in *fzy-1* led to early embryonic arrest (Tarailo et al., 2007), making it infeasible to perform lineage analysis. We therefore performed RNAi against *C. elegans fzy-1* followed by automated lineage and lineal gene expression analysis to see if CYB-1^D was indeed targeted by APC/C^{FZR-1} for degradation. Instead of the absence of accumulation in the wild-type embryo around 550-cell stage, we observed a substantial increase in the accumulation of CYB-1^D in most of the embryonic cells that completed their last round of division (Figure 2F), confirming that the *C. elegans* D-boxes within CYB-1^D was targeted by the degradation complex APC/C^{FZR-1}.

Worm-fluorescence ubiquitin cell cycle indicators detects a G1 phase present at only a few embryonic cells before they complete their last round of division

Equipped with the Worm-FUCCI reporters that showed expected accumulation dynamics, which were predictive of cell cycle phases, we set out to systematically determine the gap phase introduction during *C. elegans* development, with a focus on embryonic cell cycles. Aided by the automated lineaging and gene expression profiling technologies (Bao et al., 2006; Murray et al., 2008), we took time-lapse 3D images to trace cell lineage and acquire lineal expression up to the 1.5-fold stage of embryogenesis, upon which lineaging analysis became impractical due to twitching (Supplementary Figures S1,S2, Supplementary Movie S1). Notably, most of the embryonic cells had completed their last rounds of division by this stage with a few exceptions discussed below. To facilitate the comparison and quantification of accumulation of CDT-1^D and CYB-1^D, we superimposed the lineal accumulation patterns of the two reporters in a single lineage tree (Figure 3A) as described previously (Murray et al., 2008). To allow visualization of the two reporters in the same embryo, we crossed the transgenic CDT-1^D and CYB-1^{DG} alleles into the same animal in which both were rendered homozygous (Figure 3B).

Strikingly, the accumulation patterns of the two reporters barely overlapped but were mostly complementary both spatially and temporally in nearly all embryonic cells, i.e., CYB-1^D accumulated broadly during early embryogenesis, whereas CDT-1^D did not accumulate in most of the embryonic cells until they had completed their last round of embryonic division (Figures 3A,C). These results suggest that most embryonic cell cycles progress mostly with the S and M phases only and arrest in the G0 or G1 phase after they have completed their last rounds of division. However, it remains possible that there might be some brief G1 phases present in the embryonic cells, but may not be picked up by our reporters due to the limited temporal resolution imposed by the mCherry maturation time and the degradation efficiency of the reporters. Consequently, the CDT-1^D expression signal enables the accurate prediction of cell cycle exit, i.e., the CDT-1^D signal is not observed until a cell completes its last round of division, after which the CDT-1^D signals are seen in nearly all embryonic cells in a cell fate-independent way (Figures 3A,B; Supplementary Figure S1). As our reporters could not distinguish the G1 phase from the G0 phase, we assume that most CDT-1^D-expressing cells that have completed the last round of division in their life cycle are arrested in the G0 phase.

To functionally validate this observation, we used RNAi to inactivate *cul-1*, which encodes a key cell cycle regulator required for cell cycle exit. Its perturbation was expected to prevent the embryonic cells from entering G0 or G1 phase (Kipreos et al., 1996). As expected, only CYB-1^D accumulation was detected in

the perturbed embryos even they died (Supplementary Figure S5), indicating that cells of the RNAi embryo failed to arrest in the G0 or G1 phase. Due to the inability of our markers in distinguishing G0 from G1 phase, further resolving the arresting phase in the dead embryo requires independent markers, such as those that have been recently developed (Adikes et al., 2020).

We observed an inconsistency of Worm-FUCCI in demarcating cell cycle progression of germline progenitor P4 and its two daughter cells, “Z2.” and “Z3.” Despite embryonic arrest of the “Z2” and the “Z3,” CDT-1^D accumulation was not observed, while CYB-1^D accumulation was lost after the 350-cell stage (Figure 3A, Supplementary Figures S1,S2). This appeared to be due to the inability of the *his-72* promoter to drive the zygotic expression of Worm-FUCCI in the germline progenitors of the embryo rather than its cell cycle-specific degradation (Murray et al., 2006; Ooi et al., 2006; Zhao et al., 2010a). Therefore, a promoter that is able to simultaneously drive reporter expression in the germline progenitors is necessary to indicate cell cycle progression therein.

Division asynchronies between sister cells seem mainly due to the differential durations of the S phase during embryogenesis

Unlike synchronous cell divisions in the early embryo of many other metazoans, *C. elegans* embryonic cell division is asynchronous from the very first division and becomes more obvious during late embryogenesis (Bao et al., 2008; Budirahardja and Gonczy, 2008; Rivers et al., 2008). As only CYB-1^D accumulation was seen in the sister cells between which division asymmetry in cell cycle length was observed (Figure 3A, Supplementary Figures S1,S2), lack of accumulation of CDT-1^D indicating that no involvement of G1 phase in the asymmetry. For example, the division asymmetry between the sister cells “Caapa” and “Caapp” is around 50 min during which accumulation of CDT-1^D or degradation of CYB-1^D is expected to be observed, but we did not observe either of them. Then the asymmetry could be due to differential duration of M, S or G2 phase. However, the entire duration from chromatin condensation to mitosis (assumed to be the M phase) was only around two minutes (Supplementary Figure S6), suggesting that the differential duration of the M phase between the two sister cells was unlikely to be responsible for the observed asymmetry. Therefore, a differential duration of S or G2 phase was responsible for the observed division asymmetries in cell cycle length. However, we expected accumulation of both CDT-1^D and CYB-1^D during the G2 phase. Presence of CYB-1^D accumulation only suggests that it was the differential duration of the S phase that was responsible for most of the observed division asymmetries in cell cycle length.

G2 phase is first introduced in the intestine precursors during embryogenesis

The “E2” (two daughters of “E,” the intestine progenitor) and “E4” (four granddaughters of “E”) of the intestine primordium (“E”) were found to accumulate both CDT-1^D and CYB-1^D simultaneously at the late stage in their cell cycles, indicated that a G2 phase was introduced in these cells (Figures 3A,C). Consistent with this, a previous study with DAPI staining also demonstrated that “E2” cells acquired the G2 phase (Edgar and McGhee, 1988). However, the accumulation of CDT-1^D was become barely detectable in E8 (eight daughters of E4), which suggests that the G2 phase was lost (Figures 3A,C). It was also possible that the accumulation level of CDT-1^D in the E8 cells was too low to be detected. Alternatively, maternal contribution of either mRNAs or proteins or both could boost the abundance of CDT-1^D. Consistent with this, *ddb-1* RNAi led to robust accumulation of CDT-1^D in E8 cells when it lacks degradation (Figure 2D). It remains possible that the degradation of CDT-1^D was so robust that the accumulation window of CDT-1^D was too short to be visualized due to relatively long mCherry's maturation time, whereas the G2 duration in the E2 or E4 cells could be substantially longer than that in the E8 cells. Intriguingly, upon the E16 (daughters of E8) stage, most of the cells arrested in the G1 phase unless they underwent one more round of embryonic division, as judged by the accumulation of the two degron reporters (Figure 3A, Supplementary Figures S1,S2), which mirrors the cell cycle characteristics of most other embryonic cells.

Worm-fluorescence ubiquitin cell cycle indicators reporters reliably detect an obvious G1 and G2 phase only in the last round division of “ABplapapaa” and “ABprapapaa” during embryogenesis

As stated above, most of embryonic cells did not accumulate CDT-1^D until they had completed their last round of embryonic division. Notably, a few cells did not complete their last round of division until about one hour before hatching, meaning that they had a very long cell cycle duration (Supplementary Figure S7) (Sulston et al., 1983). We wondered whether any gap phases had been introduced in these cells. However, these cells continued to divide after the embryo had started twitching, presenting a significant challenge to the live-cell imaging required for the subsequent lineaging analysis (Supplementary Movie S1) (Murray et al., 2008). To facilitate imaging during development of these cells, we depleted the activity of *pat-3*, which encodes a β -integrin subunit required for normal muscle filament assembly and function (Gettner et al., 1995). This depletion permitted the perturbed embryo to continue

developing without twitching and rotating until its arrest at around the 2-fold stage (Supplementary Movie S2). This allowed us to trace cell division beyond the 1.5-fold stage using extended imaging time. As expected, we observed a clear two-way accumulation dynamic of CDT-1^D in one cell pair, consisting of “ABplapapaa” and “ABprapapaa,” referred to as “V5QL” and “V5QR,” respectively hereafter, which divided about one hour before hatching (Supplementary Figure S7). CDT-1^D accumulated soon after birth of the two cells, peaked and got completely degraded at around 150 and 220 min after their birth, respectively, in both cells. Importantly, the CDT-1^D accumulated again at roughly 450 min and peaked around 550 min after their birth till the end of the imaging process (Figures 4A,B). The two cells developed into symmetrical cell fates, i.e., dividing into “V5L” and “QL” cells (postembryonic blast cells for hypodermis and neuron, respectively) or “V5R” and “QR” cells, respectively, during embryogenesis. The two cells resume cell division during postembryonic development, giving rise to hypodermal or neuronal cells (Sulston et al., 1983). Notably, “V5QL” and “V5QR” were the last cells to divide during embryogenesis (Supplementary Figure S7, Supplementary Movie S1) (Sulston et al., 1983). Immediately after the disappearance of CDT-1^D, CYB-1^D started to accumulate, and peaked about 7 h after their birth in the same cells (Figures 4A,B). The presence of CDT-1^D but the absence of CYB-1^D in this long duration (roughly two hours) indicated a G1 phase, whereas the absence of CDT-1^D indicated an S phase here. The simultaneous accumulation of the two degron reporters indicated a G2 phase.

In addition to “V5QL” and “V5QR,” coelomocyte precursors, “MSapapaa” and “MSppapaa,” also completed their last round of embryonic division relatively late during embryogenesis, which has long been speculated to divide with G1 phase (Boxem and van denHeuvel, 2001; Yanowitz and Fire, 2005; Kipreos and van denHeuvel, 2019). However, only CYB-1^D but not CDT-1^D showed accumulation in these two cells before their division (Supplementary Figures S8A,B), suggesting that an elongated S phase was responsible for their relative long cell cycle duration. It is also possible that the accumulation window of CDT-1^D may be too short to be detected by our reporters. To test this, we performed RNAi against *cyd-1*, which is expected to lead to arrest of these cells at the G1 phase before their last round of cell division during embryogenesis. As expected, despite the lack of CDT-1^D accumulation in the control embryo, we detected an obvious accumulation of CDT-1^D and degradation of CYB-1^D in one of the coelomocyte precursors after the RNAi (Supplementary Figures S8C,D), which strongly argue the presence of a brief G1 phase in these cells that is beyond of reach by the reporters in the control embryo.

Most other cells arrested at the G0 or G1 phase up to the late “2-fold” stage (actually beyond the 2-fold stage in a control

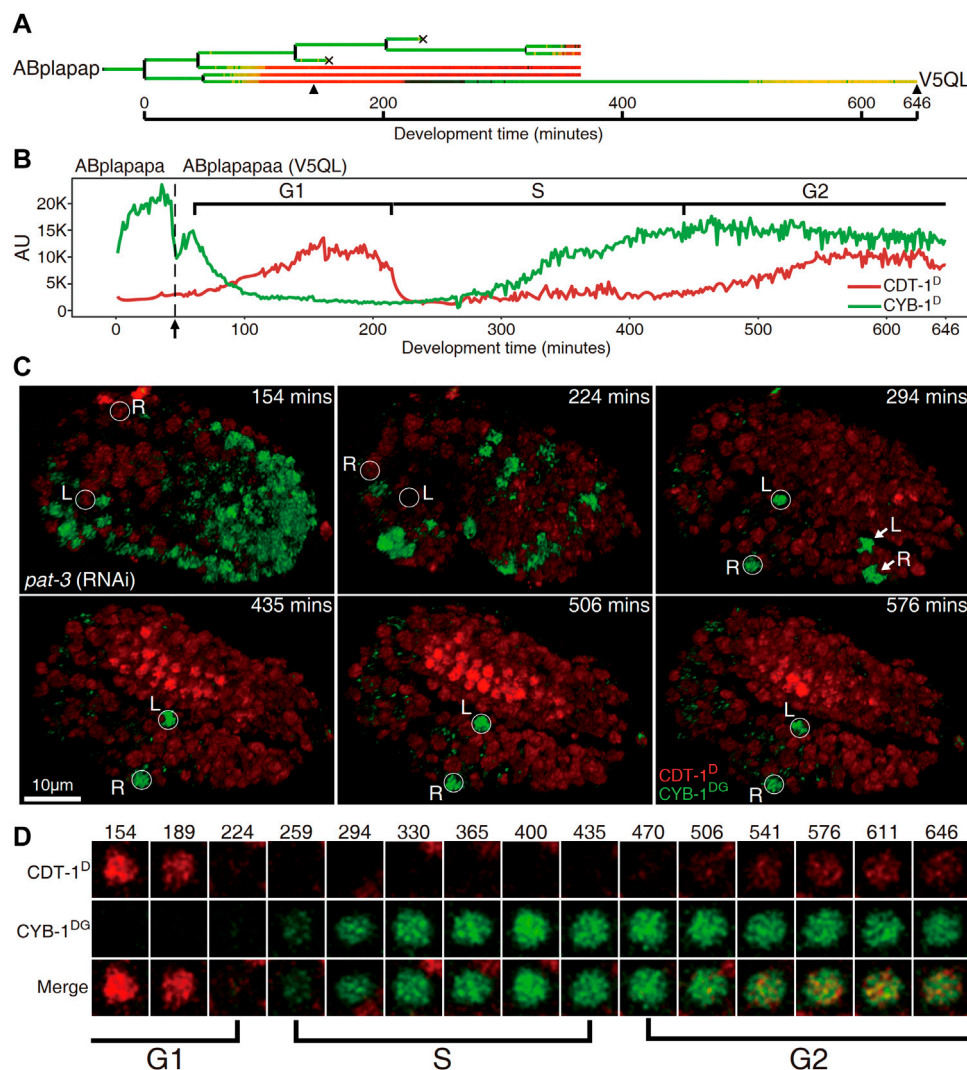
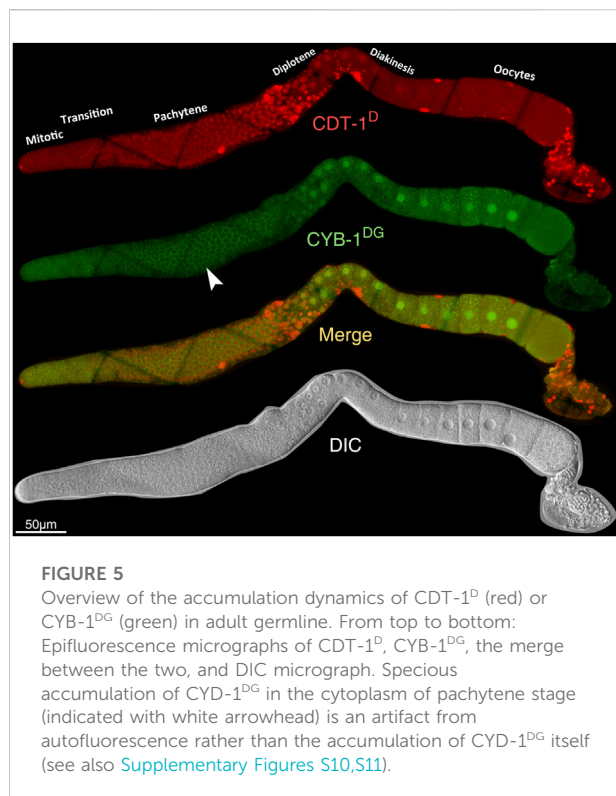


FIGURE 4

Cells “V5QL” (“ABplapapaa”) and “V5QR” (“ABprapapaa”) divide with a full cell cycle during *C. elegans* embryogenesis. **(A)** Lineal accumulation of CDT-1^D (red) and CYB-1^D (green) in the sublineage of “ABplapap,” the grandparent of V5QL in the embryos treated with RNAi against *pat-3* to inhibit twitching. All cells are curated up to 365 min after the birth of “ABplapap” or up to their apoptotic cell death except the “V5QL” cell, which is curated up to 646 min after its birth (see Materials and Methods). For simplicity, only the expression of “V5QL” is shown. **(B)** Quantification of accumulation of CDT-1^D (red) and CYB-1^D (green) in the “V5QL” cell and its parent (“ABplapap”). Fluorescence intensity in the arbitrary unit (AU) is plotted on the Y axis and development time from the birth of “ABplapap” on the X axis. Durations of cell cycle phases are indicated with scaled bar above based on the expression dynamics of the two reporters. Division time point of “ABplapap” is indicated with an arrow. **(C)** Expression dynamics of CDT-1^D and CYB-1^{DG} in a late embryo treated with RNAi against *pat-3* (see also [Supplementary Movies S1,S2](#)). Shown is the 3D projection of epifluorescence micrographs at six time points as indicated with CYB-1^{DG} (green) and CDT-1^D (red). The embryo is oriented so that both “V5QL” and “V5QR” (highlighted with white circles and indicated with L and R, respectively) are located at the posterior of the embryo. Development time is shown as in “(B)”. Note that the CYB-1^{DG} is degraded in most cells at 1.5 fold stage (224 min) but is highly accumulated only in “V5QL(R)” and “ABpl(r) apapppaa” (indicated with L and R, respectively) upon two-fold stage (294 min). The CYB-1^{DG} becomes completely degraded in the latter two cells about 140 min later. Also note that the CDT-1^D is accumulated at the bean stage (154 min) and becomes completely degraded upon 294 min in the “V5QL(R)” cells shown in “(C)” that simultaneously accumulate CDT-1^D (red) and CYB-1^{DG} (green) over development. Development time in minute is shown on the top. The first and the last time points correspond to those indicated with black triangles in “(A)”. Cell cycle phases are indicated based on reporter expression dynamics.

embryo due to embryonic arrest caused by the depletion of *pat-3*), which can be judged by the apparent accumulation of CDT-1^D. “V5QL” and “V5QR” were the only two cells still expressing CYB-1^{DG} in the late “2-fold” stage ([Figures 4C,D](#), [Supplementary](#)

[Movie S2](#)). Based on the degradation characteristics of the two degron reporters, our Worm-FUCCI demonstrated obvious G1 and G2 phases only in two embryonic cells, “ABplapapaa” and “ABprapapaa” cells, which apparently develop with a full



cycle consisting of G1, S, G2, and M phases. Ability of our degron reporters to detect G1 in V5QL/R cells but not in coelomocyte precursors indicates that G1 phase duration is not uniform and can be quite short in cells that have to wait a long time before dividing.

Accumulation dynamics of Worm-fluorescence ubiquitin cell cycle indicators during postembryonic development

The Worm-FUCCI showed accumulation dynamics not only during embryogenesis, but also during postembryonic development ([Supplementary Figures S9A–D](#)). For example, as expected, CDT-1^D but not CYB-1^{DG} was accumulated in nearly all the cells at dauer stage, indicating these cells arrested at G0 or G1 stage ([Supplementary Figure S9E](#)). Given that there is a wide spectrum of cells showing accumulation dynamics during postembryonic development, including vulva, seam cells and neurons, here we only explored on the accumulation dynamics in the germline and the intestine of larvae.

Both CDT-1^D and CYB-1^D or CYB-1^{DG} demonstrated accumulation dynamics in the germline ([Figure 5](#); [Supplementary Figures S10–12](#)). Notably, their accumulation

patterns were largely non-overlapping between each other. For example, the reporter CDT-1^D showed overall accumulation mostly at the pachytene stage; whereas the reporter CYB-1^D showed accumulation mostly at the diplotene and diakinesis stages during oogenesis ([Figure 5](#)). The specious non-nuclear accumulation of CYB-1^D in the mitotic zone and at the pachytene stage ([Figure 5](#)) apparently resulted from the autofluorescence of the tissue rather than from the CYB-1^D itself. This was because that the epifluorescence signals in these regions were comparable to those in the wild-type (N2) germline ([Supplementary Figure S11](#)). Despite the lack of CYB-1^{DG} accumulation in the mitotic zone of the germline, the reporter CYB-1^D did show additional nuclear accumulation in the mitotic zone and during oogenesis ([Supplementary Figure S10B,S12](#)). The accumulation in the mitotic zone became barely detectable upon the meiotic prophase entry that extended through late pachytene, and this accumulation drop was apparently not due to a shift to cytoplasmic enrichment ([Supplementary Figure S12](#)). Therefore, despite the consistent accumulation patterns in the Soma between CYB-1^D and CYB-1^{DG}, the two reporters did show discordant accumulation patterns in the germline, making the CYB-1-based reporters unsuitable for deducing gap phase of cell cycle progression in the tissue.

Cell cycle progression in the mitotic zone occurs rapidly, continuously, with little or no time spent on the G1 phase ([Fox et al., 2011](#)). Consistent with this, few of the cells in this region showed an accumulation of CDT-1^D only, which was indicative of G1 phase. Most cells in the mitotic zone also showed an accumulation of CYB-1^D ([Supplementary Figure S10](#)). Only a very small portion of cells in the region did not show accumulation of CDT-1^D, and most cells also show accumulation of CYB-1^D ([Supplementary Figure S10](#)). The results suggested that most of the cells were at G2 phase of cell cycle in the mitotic zone.

CDT-1^D accumulation was high in the dorsal and ventral intestine cells, including int2 (referred to as “int2D” and “int2V” hereafter, respectively) and int3 (referred to as “int3D” and “int3V” hereafter, respectively), of the synchronized L1 animals 5 h after feeding ([Supplementary Figure S13](#)). The “int2D/V” cells are known to undergo DNA endoreplication while the int3D/V cells to undergo both DNA replication and division during the late L1 stage ([Hedgecock and White, 1985](#)). The accumulation patterns of Worm-FUCCI were consistent with these observations. The presence of CDT-1^D only indicated that all of these cells arrested at the G1 phase during the first six hours of feeding of the starved L1 animals. Approximately 10 and 7 h after feeding, the int2 and int3 cells entered the S phase, as judged by the absence of CDT-1^D. CDT-1^D was observed again roughly 12 h after feeding, indicating that the cells had entered the G2 phase. For the “int2D/V” cells, which undergo endoreplication without division, we referred to the relevant cell cycle phase as the G phase rather than the G2 phase due to the endoreplication without division. For the int3D/V cells, which undergo both DNA replication and division, we referred to the

period of CDT-1^D re-accumulation before next round of division as G2 phase.

In summary, we generated Worm-FUCCI reporters whose accumulation dynamics faithfully indicates cell cycle progression in the Soma. Accumulation dynamics of the reporters during *C. elegans* embryogenesis demonstrated that only a few pairs of cells with an extended cell cycle length during the last round of division divide with a full cell cycle. The Worm-FUCCI strains constitute an invaluable resource for further study of coordination between cell cycle progression and cell fate differentiation, which has so far poorly defined in any species.

Discussion

Embryonic cell cycles are unique in that barely any gap phase is present in the early embryo of most species, including *C. elegans* (Edgar and McGhee, 1988; Farrell and O'Farrell, 2014). However, the precise knowledge on gap phase introduction throughout embryogenesis remains elusive in all the metazoans studies so far. Here we developed Worm-FUCCI as faithful cell cycle progression reporters in *C. elegans* Soma. Automated profiling of the Worm-FUCCI accumulation allowed us to produce a first ever global picture of gap phase introduction throughout metazoan embryogenesis. These reporters greatly facilitate the future study of coordination between cell cycle progression and cell fate differentiation during development.

In *Drosophila melanogaster*, the first 13 embryonic cell cycles before mid-blastula transition (MBT) are synchronous but with increasing cell cycle length, which was thought to be dominated by the DNA replication checkpoint (Blythe and Wieschaus, 2015). After MBT, cell cycle length is mainly dictated by the introduction of gap phase which coincides with zygotic genome activation. Unlike *Drosophila* embryogenesis, cell division in *C. elegans* is asynchronous during the first cell division. Division asymmetry in cell cycle length between sister cells becomes increasingly frequent over development. Our data suggest that the overall cell cycle length and the division asymmetries in cell cycle length are mainly dictated by the S phase duration in most cells, although a short G1 phase that is beyond of detection by our reporter could also contribute to the asymmetry. Consistent with this, CDK-4 and Cyclin D (CYD-1), which are required for the progression through G1 phase during larval muscle development (Korzelius et al., 2011), are dispensable for most embryonic divisions except the following cases, i.e., the final division of some intestinal cells, the division of coelomocyte mother cells and the division of V5Q cells (Kipreos et al., 1996; Bao et al., 2008; Budirahardja and Gonczy, 2008; Clijsters et al., 2013; Adikes et al., 2020). Division asymmetry of the first cell cycle in *C. elegans* involves cell cycle check point protein and asymmetric regulation of DNA replication (Brauchle et al., 2003; Benkemoun et al., 2014).

The rapid and efficient degradation of the PIP-box-containing degron, CDT-1^D, in the S phase makes this reporter an effective marker in accurately defining the boundary between the G1 and S phases. However, the Worm-FUCCI does have difficulty in defining boundary between the S and G2 phase. Despite the lack of an obvious Cy motif in CDT-1, the degradation pathway of PIP box is conserved between worm and human. However, same as the degradation of PIP-box-containing CDT1 in human, the CDT-1^D of this study accumulates slowly from the G2 phase and peaks again in the G1 phase (Figures 1C, 3C), making it difficult in defining the boundary between S and G2 than that between G1 and S. The dynamics of CYB-1^D allow it to serve as a complement to the CDT-1^D in demarcating these boundaries. This is because that CYB-1^D shows no accumulation in the G1 phase when the abundance of CDT-1^D reaches its highest level; it starts to accumulate from the S phase and peaks in the G2 phase (Figures 3C, 4B). Therefore, the high level of CDT-1^D coupled with the absence of CYB-1^D is a reliable indicator of the G1 phase, and the absence of CDT-1^D coupled with a relatively low level of CYB-1^D is indicative of the S phase. Given that histone expression can serve as a clear indicator for the M phase, simultaneous accumulation of both reporters in the same cell can reliably indicate the G2 phase (Figure 1D). Apparently, our CDT-1^D-based degradation cannot distinguish the G1 from G0 phase. Fortunately, a CDK sensor has recently been developed. The sensor consists of a fluorescently tagged CDK substrate that can steadily translocate from the nucleus to the cytoplasm in response to increasing CDK activity and consequent sensor phosphorylation, which enables distinguishing cycling cells in G1 from quiescent cells in G0 in *C. elegans* (Adikes et al., 2020).

Broad accumulation of the degron reporters was spatially and temporally achieved by *his-72* promoter and *pie-1* 3'UTR, providing an advantage in systematic delineation of cell cycle progression. Nevertheless, tissue-specific or conditionally expressed reporters may be necessary in other cases to facilitate the study of cell cycle progression and fate differentiation in specific cell types, especially during postembryonic development. Another limitation of the Worm-FUCCI reporter is the temporal sensitivity. Although the degradation of CDT-1^D is rapid, the degradation of CYB-1^D takes about 50 min to reach the basal level (Figures 3C, 4B). Also, the CDT-1^D accumulation is not fast enough to be detected due to a relatively slow maturation rate of mCherry, which may make a brief G1 phase undetectable. For example, only the two embryonic cells, "V5QL" and "V5QR," were found to divide with a full cycle, which carry an apparent G1 phase. It remains possible that a brief gap phase with a very short duration, for example, within 10–20 min, is likely to be missed by our reporters. Consistent with this, depletion of *cyd-1* that is required for cell cycle progression through G1 phase not only led to abolishment of the last round of division, but also produced a sharp increase of CDT-1^D accumulation in the precursors of coelomocyte (Supplementary Figure S8C,D), arguing the presence

of a brief G1 phase that was missed by the reporter in the wild-type embryo. A robust quantification of Worm-FUCCI accumulation may help alleviate the problem but this is further complicated by a relatively low expression level derived from single-copy transgene. Therefore, a FUCCI reporter with a faster maturation time than the mCherry is needed to provide a better temporal resolution in deducing a short G1 phase. For example, mRFP1 is approximately 15 min faster than mCherry (Balleza et al., 2018). mNeonGreen, another fast-folding fluorescence protein has a maturation time less than 10 min (Hirano et al., 2022). However, the photobleaching and quantum yield of fluorescence protein have to be taken into consideration in prioritizing a reporter. Despite the broad expression of the reporters, we observed a slightly lower expression level of CDT-1^D in some sublineages, including a few cells in the D sublineages. However, further curation of the cell lineage with an extended time point revealed a clear CDT-1^D accumulation in those D sublineage cells (Supplementary Figure S1). The lack of CDT-1^D accumulation in the Z2 and Z2 cells (Supplementary Figure S1) were probably due to maternal inhibition or transcriptional quiescence (Ghosh and Seydoux, 2008; Guven-Ozkan et al., 2008), or the inability of the *his-72* promoter in driving zygotic expression, making it unsuitable for monitoring cell cycle progression of the two germline progenitor cells.

The broad accumulation of the Worm-FUCCI offers an opportunity to study the coordination of the cell cycle and cell fate differentiation during postembryonic development, including development of seam cells and vulva. Given that some of the postembryonic intestine cells are known to undergo endoreplication, the dynamics of the reporters in these cells also lay a foundation for mechanistic research into the regulation of endoreplication. However, the CYB-1-based reporter may not be suitable for deducing cell cycle progression in the germline due to their discordant of accumulation dynamics (Supplementary Figures S10–12).

Data availability statement

The original contributions presented in the study are included in the article/Supplementary Material, further inquiries can be directed to the corresponding author.

Author contributions

Conceptualization, ZZ, M-KW; Methodology, M-KW, XH, DX, and RL; Investigation, M-KW, VH, L-YC, YM, BH, and XR;

Data Analysis, M-KW, RL, GG, and ZZ; Validation, M-KW; Resources, HY; Writing-Original Draft, M-KW, and ZZ; Writing-Review and Editing, ZZ, M-KW, VH, and HY; and Supervision, ZZ and HY.

Funding

This work is supported by the Hong Kong Research Grants Council (Project 12101522, 12101520, 12100118 and N-HKBU2018) and SKL GRF grant (2022-23) to ZZ. This work is partially supported by the Hong Kong Innovation and Technology Commission (InnoHK Project CIMDA) to HY.

Acknowledgments

We thank Dr. T Tan for logistic support and helpful discussion with the members of Z Zhao's laboratory, Dr. Marie-Ann Felix for analysis with postembryonic expression, Dr. KKY Yuen for assistance in EdU staining and reagent and Dr. YC Tse for assistance in imaging. We also thank Mr. Khandker K. ISLAM for initiation of the project.

Conflict of interest

The authors declare that the research was conducted in the absence of any commercial or financial relationships that could be construed as a potential conflict of interest.

Publisher's note

All claims expressed in this article are solely those of the authors and do not necessarily represent those of their affiliated organizations, or those of the publisher, the editors and the reviewers. Any product that may be evaluated in this article, or claim that may be made by its manufacturer, is not guaranteed or endorsed by the publisher.

Supplementary material

The Supplementary Material for this article can be found online at: <https://www.frontiersin.org/articles/10.3389/fcell.2022.978962/full#supplementary-material>

References

- Adikes, R. C., Kohrman, A. Q., Martinez, M. A. Q., Palmisano, N. J., Smith, J. J., Medwig-Kinney, T. N., et al. (2020). Visualizing the metazoan proliferation-quiescence decision *in vivo*. *Elife* 9, e63265. doi:10.7554/eLife.63265
- Arias, E. E., and Walter, J. C. (2007). Strength in numbers: Preventing rereplication via multiple mechanisms in eukaryotic cells. *Genes Dev.* 21, 497–518. doi:10.1101/gad.1508907

- Bajar, B. T., Lam, A. J., Badiee, R. K., Oh, Y. H., Chu, J., Zhou, X. X., et al. (2016). Fluorescent indicators for simultaneous reporting of all four cell cycle phases. *Nat. Methods* 13, 993–996. doi:10.1038/nmeth.4045
- Balleza, E., Kim, J. M., and Cluzel, P. (2018). Systematic characterization of maturation time of fluorescent proteins in living cells. *Nat. Methods* 15, 47–51. doi:10.1038/nmeth.4509
- Bao, Z., Murray, J. I., Boyle, T., Ooi, S. L., Sandel, M. J., and Waterston, R. H. (2006). Automated cell lineage tracing in *Caenorhabditis elegans*. *Proc. Natl. Acad. Sci. U. S. A.* 103, 2707–2712. doi:10.1073/pnas.0511111103
- Bao, Z., Zhao, Z., Boyle, T. J., Murray, J. I., and Waterston, R. H. (2008). Control of cell cycle timing during *C. elegans* embryogenesis. *Dev. Biol.* 318, 65–72. doi:10.1016/j.ydbio.2008.02.054
- Benkemoun, L., Descoteaux, C., Chartier, N. T., Pintard, L., and Labbé, J.-C. (2014). PAR-4/LKB1 regulates DNA replication during asynchronous division of the early *C. elegans* embryo. *J. Cell Biol.* 205, 447–455. doi:10.1083/jcb.201312029
- Blythe, S. A., and Wieschaus, E. F. (2015). Zygotic genome activation triggers the DNA replication checkpoint at the midblastula transition. *Cell* 160, 1169–1181. doi:10.1016/j.cell.2015.01.050
- Boxem, M., and van denHeuvel, S. (2001). lin-35 Rb and cki-1 Cip/Kip cooperate in developmental regulation of G1 progression in *C. elegans*. *Development* 128, 4349–4359. doi:10.1242/dev.128.21.4349
- Brauchle, M., Baumer, K., and Gonczy, P. (2003). Differential activation of the DNA replication checkpoint contributes to asynchrony of cell division in *C. elegans* embryos. *Curr. Biol.* 13, 819–827. doi:10.1016/s0960-9822(03)00295-1
- Budirahardja, Y., and Gonczy, P. (2008). PLK-1 asymmetry contributes to asynchronous cell division of *C. elegans* embryos. *Development* 135, 1303–1313. doi:10.1242/dev.019075
- Cao, J., Guan, G., Ho, V. W. S., Wong, M. K., Chan, L. Y., Tang, C., et al. (2020). Establishment of a morphological atlas of the *Caenorhabditis elegans* embryo using deep-learning-based 4D segmentation. *Nat. Commun.* 11, 6254. doi:10.1038/s41467-020-19863-x
- Carvalho, A., Olson, S. K., Gutierrez, E., Zhang, K., Noble, L. B., Zanin, E., et al. (2011). Acute drug treatment in the early *C. elegans* embryo. *PLoS One* 6, e24656. doi:10.1371/journal.pone.0024656
- Chen, L., Ho, V. W. S., Wong, M. K., Huang, X., Chan, L. Y., Ng, H. C. K., et al. (2018). Establishment of signaling interactions with cellular resolution for every cell cycle of embryogenesis. *Genetics* 209, 37–49. doi:10.1534/genetics.118.300820
- Clijsters, L., Ogink, J., and Wolthuis, R. (2013). The spindle checkpoint, APC/CCdc20, and APC/CCdh1 play distinct roles in connecting mitosis to S phase. *J. Cell Biol.* 201, 1013–1026. doi:10.1083/jcb.201211019
- Edgar, L. G., and McGhee, J. D. (1988). DNA synthesis and the control of embryonic gene expression in *C. elegans*. *Cell* 53, 589–599. doi:10.1016/0092-8674(88)90575-2
- Farrell, J. A., and O'Farrell, P. H. (2014). From egg to gastrula: How the cell cycle is remodeled during the *Drosophila* mid-blastula transition. *Annu. Rev. Genet.* 48, 269–294. doi:10.1146/annurev-genet-111212-133531
- Fay, D. S., Keenan, S., and Han, M. (2002). *fzr-1* and *lin-35/Rb* function redundantly to control cell proliferation in *C. elegans* as revealed by a nonbiased synthetic screen. *Genes Dev.* 16, 503–517. doi:10.1101/gad.952302
- Foe, V. E., and Alberts, B. M. (1983). Studies of nuclear and cytoplasmic behaviour during the five mitotic cycles that precede gastrulation in *drosophila* embryogenesis. *J. Cell Sci.* 61, 31–70. doi:10.1242/jcs.61.1.31
- Fox, P. M., Vought, V. E., Hanazawa, M., Lee, M. H., Maine, E. M., and Schedl, T. (2011). Cyclin E and CDK-2 regulate proliferative cell fate and cell cycle progression in the *C. elegans* germline. *Development* 138, 2223–2234. doi:10.1242/dev.059535
- Frokjaer-Jensen, C., Davis, M. W., Sarov, M., Taylor, J., Flibotte, S., LaBella, M., et al. (2014). Random and targeted transgene insertion in *Caenorhabditis elegans* using a modified Mos1 transposon. *Nat. Methods* 11, 529–534. doi:10.1038/nmeth.2889
- Gettner, S. N., Kenyon, C., and Reichardt, L. F. (1995). Characterization of beta pat-3 heterodimers, a family of essential integrin receptors in *C. elegans*. *J. Cell Biol.* 129, 1127–1141. doi:10.1083/jcb.129.4.1127
- Ghosh, D., and Seydoux, G. (2008). Inhibition of transcription by the *Caenorhabditis elegans* germline protein PIE-1: Genetic evidence for distinct mechanisms targeting initiation and elongation. *Genetics* 178, 235–243. doi:10.1534/genetics.107.083212
- Guan, G., Fang, M., Wong, M. K., Ho, V. W. S., An, X., Tang, C., et al. (2020). Multilevel regulation of muscle-specific transcription factor hlh-1 during *Caenorhabditis elegans* embryogenesis. *Dev. Genes Evol.* 230, 265–278. doi:10.1007/s00427-020-00662-9
- Guan, G., Vincy, H., Ming-Kin, W., Xiaomeng, A., Lu Yan, C., Binghui, T., et al. (2019). System-level quantification and phenotyping of early embryonic Morphogenesis of *Caenorhabditis elegans*. Beijing. bioRxiv, 776062. doi:10.1101/776062
- Güven-Ozkan, T., Nishi, Y., Robertson, S. M., and Lin, R. (2008). Global transcriptional repression in *C. elegans* germline precursors by regulated sequestration of TAF-4. *Cell* 135, 149–160. doi:10.1016/j.cell.2008.07.040
- Hedgecock, E. M., and White, J. G. (1985). Polyploid tissues in the nematode *Caenorhabditis elegans*. *Dev. Biol.* 107, 128–133. doi:10.1016/0012-1606(85)90381-1
- Hirano, M., Ando, R., Shimozono, S., Sugiyama, M., Takeda, N., Kurokawa, H., et al. (2022). A highly photostable and bright green fluorescent protein. *Nat. Biotechnol.* 40, 1132–1142. doi:10.1038/s41587-022-01278-2
- Ho, V. W. S., Wong, M. K., An, X., Guan, D., Shao, J., Ng, H. C. K., et al. (2015). Systems-level quantification of division timing reveals a common genetic architecture controlling asynchrony and fate asymmetry. *Mol. Syst. Biol.* 11, 814. doi:10.15252/msb.20145857
- Kamath, R. S., Martinez-Campos, M., Zipperlen, P., Fraser, A. G., and Ahringer, J. (2001). Effectiveness of specific RNA-mediated interference through ingested double-stranded RNA in *Caenorhabditis elegans*. *Genome Biol.* 2, RESEARCH0002. doi:10.1186/gb-2000-2-1-research0002
- Kim, Y., and Kipreos, E. T. (2007). The *Caenorhabditis elegans* replication licensing factor CDT-1 is targeted for degradation by the CUL-4/DDB-1 complex. *Mol. Cell Biol.* 27, 1394–1406. doi:10.1128/MCB.00736-06
- Kim, Y., Starostina, N. G., and Kipreos, E. T. (2008). The CRL4Cdt2 ubiquitin ligase targets the degradation of p21Cip1 to control replication licensing. *Genes Dev.* 22, 2507–2519. doi:10.1101/gad.1703708
- Kipreos, E. T., Lander, L. E., Wing, J. P., He, W. W., and Hedgecock, E. M. (1996). cul-1 is required for cell cycle exit in *C. elegans* and identifies a novel gene family. *Cell* 85, 829–839. doi:10.1016/s0092-8674(00)81267-2
- Kipreos, E. T., and van denHeuvel, S. (2019). Developmental control of the cell cycle: Insights from *Caenorhabditis elegans*. *Genetics* 211, 797–829. doi:10.1534/genetics.118.301643
- Korzelius, J., The, I., Ruijtenberg, S., Prinsen, M. B. W., Portegijs, V., Middelkoop, T. C., et al. (2011). *Caenorhabditis elegans* cyclin D/CDK4 and cyclin E/CDK2 induce distinct cell cycle Re-entry programs in differentiated muscle cells. *PLoS Genet.* 7, e1002362. doi:10.1371/journal.pgen.1002362
- Lee, M. T., Bonneau, A. R., and Giraldez, A. J. (2014). Zygotic genome activation during the maternal-to-zygotic transition. *Annu. Rev. Cell Dev. Biol.* 30, 581–613. doi:10.1146/annurev-cellbio-100913-013027
- Li, X., Zhao, Q., Liao, R., Sun, P., and Wu, X. (2003). The SCF(Skp2) ubiquitin ligase complex interacts with the human replication licensing factor Cdt1 and regulates Cdt1 degradation. *J. Biol. Chem.* 278, 30854–30858. doi:10.1074/jbc.C300251200
- Lyssenko, N. N., Hanna-Rose, W., and Schlegel, R. A. (2007). Cognate putative nuclear localization signal effects strong nuclear localization of a GFP reporter and facilitates gene expression studies in *Caenorhabditis elegans*. *Biotechniques* 43, 596–598. doi:10.2144/000112615
- McGarry, T. J., and Kirschner, M. W. (1998). Geminin, an inhibitor of DNA replication, is degraded during mitosis. *Cell* 93, 1043–1053. doi:10.1016/s0092-8674(00)81209-x
- Merritt, C., Rasoloson, D., Ko, D., and Seydoux, G. (2008). 3' UTRs are the primary regulators of gene expression in the *C. elegans* germline. *Curr. Biol.* 18, 1476–1482. doi:10.1016/j.cub.2008.08.013
- Murray, J. I., Bao, Z., Boyle, T. J., Boeck, M. E., Mericle, B. L., Nicholas, T. J., et al. (2008). Automated analysis of embryonic gene expression with cellular resolution in *C. elegans*. *Nat. Methods* 5, 703–709. doi:10.1038/nmeth.1228
- Murray, J. I., Bao, Z., Boyle, T. J., and Waterston, R. H. (2006). The lineage of fluorescently-labeled *Caenorhabditis elegans* embryos with StarryNite and AceTree. *Nat. Protoc.* 1, 1468–1476. doi:10.1038/nprot.2006.222
- Nishitani, H., Lygerou, Z., and Nishimoto, T. (2004). Proteolysis of DNA replication licensing factor Cdt1 in S-phase is performed independently of geminin through its N-terminal region. *J. Biol. Chem.* 279, 30807–30816. doi:10.1074/jbc.M312644200
- Ooi, S. L., Priess, J. R., and Henikoff, S. (2006). Histone H3.3 variant dynamics in the germline of *Caenorhabditis elegans*. *PLoS Genet.* 2, e97. doi:10.1371/journal.pgen.0020097
- Özpolat, B. D., Handberg-Thorsager, M., Vervoort, M., and Balavoine, G. (2017). Cell lineage and cell cycling analyses of the 4d micromere using live

imaging in the marine annelid *Platynereis dumerilii*. *Elife* 6, e30463. doi:10.7554/eLife.30463

Pálffy, M., Joseph, S. R., and Vastenhouw, N. L. (2017). The timing of zygotic genome activation. *Curr. Opin. Genet. Dev.* 43, 53–60. doi:10.1016/j.gde.2016.12.001

Pfaff, K. L., and King, R. W. (2013). Determinants of human cyclin B1 association with mitotic chromosomes. *PLoS One* 8, e59169. doi:10.1371/journal.pone.0059169

Rivers, D. M., Moreno, S., Abraham, M., and Ahringer, J. (2008). PAR proteins direct asymmetry of the cell cycle regulators Polo-like kinase and Cdc25. *J. Cell Biol.* 180, 877–885. doi:10.1083/jcb.200710018

Sakaue-Sawano, A., Hoshida, T., Yo, M., Takahashi, R., Ohtawa, K., Arai, T., et al. (2013). Visualizing developmentally programmed endoreplication in mammals using ubiquitin oscillators. *Development* 140, 4624–4632. doi:10.1242/dev.099226

Sakaue-Sawano, A., Kurokawa, H., Morimura, T., Hanyu, A., Hama, H., Osawa, H., et al. (2008). Visualizing spatiotemporal dynamics of multicellular cell-cycle progression. *Cell* 132, 487–498. doi:10.1016/j.cell.2007.12.033

Sakaue-Sawano, A., Yo, M., Komatsu, N., Hiratsuka, T., Kogure, T., Hoshida, T., et al. (2017). Genetically encoded tools for optical dissection of the mammalian cell cycle. *Mol. Cell* 68, 626e5–640. doi:10.1016/j.molcel.2017.10.001

Seydoux, G., and Dunn, M. A. (1997). Transcriptionally repressed germ cells lack a subpopulation of phosphorylated RNA polymerase II in early embryos of *Caenorhabditis elegans* and *Drosophila melanogaster*. *Development* 124, 2191–2201. doi:10.1242/dev.124.11.2191

Shao, J., He, K., Wang, H., Ho, W. S., Ren, X., An, X., et al. (2013). Collaborative regulation of development but independent control of metabolism by two epidermis-specific transcription factors in *Caenorhabditis elegans*. *J. Biol. Chem.* 288, 33411–33426. doi:10.1074/jbc.M113.487975

Sulston, J. E., Schierenberg, E., White, J. G., and Thomson, J. N. (1983). The embryonic cell lineage of the nematode *Caenorhabditis elegans*. *Dev. Biol.* 100, 64–119. doi:10.1016/0012-1606(83)90201-4

Tarailo, M., Kitagawa, R., and Rose, A. M. (2007). Suppressors of spindle checkpoint defect (such) mutants identify new mdf-1/MAD1 interactors in *Caenorhabditis elegans*. *Genetics* 175, 1665–1679. doi:10.1534/genetics.106.067918

The, I., Ruijtenberg, S., Bouchet, B. P., Cristobal, A., Prinsen, M. B. W., van Mourik, T., et al. (2015). Rb and FZR1/Cdh1 determine CDK4/6-cyclin D requirement in *C. elegans* and human cancer cells. *Nat. Commun.* 6, 5906. doi:10.1038/ncomms6906

vanRijnberk, L. M., van derHorst, S. E. M., van denHeuvel, S., and Ruijtenberg, S. (2017). A dual transcriptional reporter and CDK-activity sensor marks cell cycle entry and progression in *C. elegans*. *PLoS One* 12, e0171600. doi:10.1371/journal.pone.0171600

Wang, R., Kaul, Z., Ambardekar, C., Yamamoto, T. G., Kavdia, K., Kodali, K., et al. (2013). HECT-E3 ligase ETC-1 regulates securin and cyclin B1 cytoplasmic abundance to promote timely anaphase during meiosis in *C. elegans*. *Development* 140, 2149–2159. doi:10.1242/dev.090688

Yanagi, K., Mizuno, T., Tsuyama, T., Tada, S., Iida, Y., Sugimoto, A., et al. (2005). *Caenorhabditis elegans* geminin homologue participates in cell cycle regulation and germ line development. *J. Biol. Chem.* 280, 19689–19694. doi:10.1074/jbc.C500070200

Yanowitz, J., and Fire, A. (2005). Cyclin D involvement demarcates a late transition in *C. elegans* embryogenesis. *Dev. Biol.* 279, 244–251. doi:10.1016/j.ydbio.2004.12.022

Zhao, Z., Boyle, T. J., Liu, Z., Murray, J. I., Wood, W. B., and Waterston, R. H. (2010). A negative regulatory loop between microRNA and Hox gene controls posterior identities in *Caenorhabditis elegans*. *PLoS Genet.* 6, e1001089. doi:10.1371/journal.pgen.1001089

Zhao, Z., Flibotte, S., Murray, J. I., Blick, D., Boyle, T. J., Gupta, B., et al. (2010). New tools for investigating the comparative biology of *Caenorhabditis briggsae* and *C. elegans*. *Genetics* 184, 853–863. doi:10.1534/genetics.109.110270

Zhong, W., Feng, H., Santiago, F. E., and Kipreos, E. T. (2003). CUL-4 ubiquitin ligase maintains genome stability by restraining DNA-replication licensing. *Nature* 423, 885–889. doi:10.1038/nature01747

Zielke, N., Korzeliuss, J., van Straaten, M., Bender, K., Schuhknecht, G. F. P., Dutta, D., et al. (2014). Fly-FUCCI: A versatile tool for studying cell proliferation in complex tissues. *Cell Rep.* 7, 588–598. doi:10.1016/j.celrep.2014.03.020

Zur, A., and Brandeis, M. (2002). Timing of APC/C substrate degradation is determined by fzy/fzr specificity of destruction boxes. *EMBO J.* 21, 4500–4510. doi:10.1093/emboj/cdf452



OPEN ACCESS

EDITED BY

Silvia L. López,
CONICET Instituto de Biología Celular y
Neurociencias, Argentina

REVIEWED BY

Maria Ina Arnone,
Stazione Zoologica Anton Dohrn, Italy
Sergey Rozhnov,
Paleontological Institute (RAS), Russia

*CORRESPONDENCE

Jenifer C. Croce,
jenifer.croce@imev-mer.fr

†PRESENT ADDRESS

Laurent Formery,
Department of Molecular and Cell
Biology, University of California
Berkeley, Berkeley, CA, United States
Maeva Gesson,
CNRS, Institut Universitaire Européen de
La Mer, Laboratoire des Sciences de
L'Environnement Marin (LEMAR),
Plouzané, France
Ludovic Toisoul,
Department of Biology, University of
Turku, Turku, Finland

SPECIALTY SECTION

This article was submitted to
Morphogenesis and Patterning,
a section of the journal
Frontiers in Cell and Developmental
Biology

RECEIVED 10 June 2022

ACCEPTED 26 August 2022

PUBLISHED 31 October 2022

CITATION

Formery L, Wakefield A, Gesson M,
Toisoul L, Lhomond G, Gilletta L,
Lasbleiz R, Schubert M and Croce JC
(2022), Developmental atlas of the
indirect-developing sea urchin
Paracentrotus lividus: From fertilization to
juvenile stages.
Front. Cell Dev. Biol. 10:966408.
doi: 10.3389/fcell.2022.966408

COPYRIGHT

This is an open-access article distributed
under the terms of the [Creative
Commons Attribution License \(CC BY\)](#).
The use, distribution or reproduction in
other forums is permitted, provided the
original author(s) and the copyright
owner(s) are credited and that the original
publication in this journal is cited, in
accordance with accepted academic
practice. No use, distribution or
reproduction is permitted which does not
comply with these terms.

Developmental atlas of the indirect-developing sea urchin *Paracentrotus lividus*: From fertilization to juvenile stages

Laurent Formery^{1†}, Axel Wakefield¹, Maeva Gesson^{1†},
Ludovic Toisoul^{1†}, Guy Lhomond¹, Laurent Gilletta²,
Régis Lasbleiz³, Michael Schubert¹ and Jenifer C. Croce^{1*}

¹Sorbonne Université, CNRS, Institut de la Mer de Villefranche (IMEV), Laboratoire de Biologie du Développement de Villefranche-sur-Mer (LBDV), Evolution of Intercellular Signaling in Development (EvoInSiDe), Villefranche-sur-Mer, France, ²Sorbonne Université, CNRS, Institut de la Mer de Villefranche (IMEV), Laboratoire de Biologie du Développement de Villefranche-sur-Mer (LBDV), Villefranche-sur-Mer, France, ³Sorbonne Université, CNRS, Institut de la Mer de Villefranche (IMEV), Service Aquariologie du Centre de Ressources de Biologie Marine (CRBM), Villefranche-sur-Mer, France

The sea urchin *Paracentrotus lividus* has been used as a model system in biology for more than a century. Over the past decades, it has been at the center of a number of studies in cell, developmental, ecological, toxicological, evolutionary, and aquaculture research. Due to this previous work, a significant amount of information is already available on the development of this species. However, this information is fragmented and rather incomplete. Here, we propose a comprehensive developmental atlas for this sea urchin species, describing its ontogeny from fertilization to juvenile stages. Our staging scheme includes three periods divided into 33 stages, plus 15 independent stages focused on the development of the coeloms and the adult rudiment. For each stage, we provide a thorough description based on observations made on live specimens using light microscopy, and when needed on fixed specimens using confocal microscopy. Our descriptions include, for each stage, the main anatomical characteristics related, for instance, to cell division, tissue morphogenesis, and/or organogenesis. Altogether, this work is the first of its kind providing, in a single study, a comprehensive description of the development of *P. lividus* embryos, larvae, and juveniles, including details on skeletogenesis, ciliogenesis, myogenesis, coelomogenesis, and formation of the adult rudiment as well as on the process of metamorphosis in live specimens. Given the renewed interest for the use of sea urchins in ecotoxicological, developmental, and evolutionary studies as well as in using marine invertebrates as alternative model systems for biomedical investigations, this study will greatly benefit the scientific community and will serve as a reference for specialists and non-specialists interested in studying sea urchins.

KEYWORDS

echinoderm, staging scheme, larva, coelom, rudiment, metamorphosis

Introduction

The common sea urchin (or echinoid) *Paracentrotus lividus* (Figure 1A) (Lamarck, 1816) is a Mediterranean and Atlantic species (Figure 1B), which is particularly common in Western Europe and North Africa (Ouréns et al., 2011). It is usually found in shallow coastal waters and living on rocky substrates or in seagrass meadows (Boudouresque and Verlaque, 2013). Phylogenetically, *P. lividus* belongs to the phylum Echinodermata (Cannon et al., 2014; Telford et al., 2014). As such, it is characterized anatomically, in its adult form, by four echinoderm synapomorphies: a calcite endoskeleton, a mutable collagenous tissue, a water vascular system, and a pentaradial symmetry (Hyman, 1955; Nichols, 1972; Wilkie, 2002; Smith, 2008). In addition, as an echinoid, *P. lividus* is anatomically distinguishable from other echinoderms 1) by the presence of a

complex masticatory apparatus called Aristotle's lantern (Figure 1C) and 2) by a rigid endoskeleton made of tightly jointed skeletal plates forming a hard shell (or test) (Figure 1D), which protects the internal organs and bears articulated spines. In echinoids, the pentaradial symmetry of the animal is further obvious, chiefly, at the level of the endoskeleton and of the water vascular system (Figures 1E,F). The endoskeleton is characterized by ten discernable fields, i.e., five ambulacra separated by five interambulacra (Figure 1E). The water vascular system, which consists of an internal network of fluid-filled canals, has five radial canals, each one spreading along one of the five ambulacral fields and protruding outside the test through multiple podia (or tube feet) (Figure 1F) (Nichols, 1972).

As all other echinoids, *P. lividus* animals are gonochoric. This means that even though males and females are indiscernible

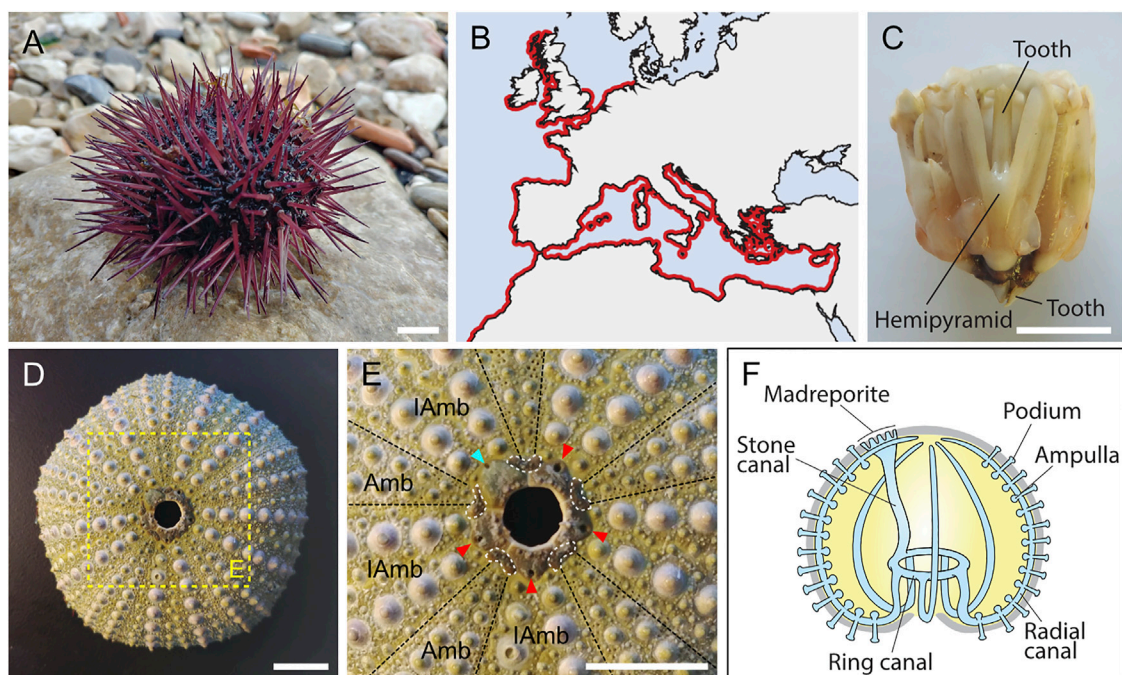


FIGURE 1

General information on *Paracentrotus lividus* adults. (A) Photograph of an adult specimen of the sea urchin species *P. lividus*. In the wild, *P. lividus* adults can be purple (as shown here), green, or brown. (B) Schematic representation of the geographical distribution of *P. lividus*, based on the Ocean Biodiversity Information System (OBIS, 2021). (C) Photograph of a dissected masticatory apparatus of a *P. lividus* adult (i.e., Aristotle's lantern). (D) Photograph of the calcitic endoskeleton of a *P. lividus* adult. No matter the outer color of the adult, its endoskeleton is always green, more or less pale. (E) Close-up of the aboral surface and the central disk of the calcitic endoskeleton of a *P. lividus* adult, corresponding to the region highlighted by the yellow box in (D). In (E), note that the endoskeleton is composed of five ambulacra separated from each other by five interambulacra. Note further that each of the five gonopores (pores through which the gametes are released) is held by a genital plate (marked by the cyan and red arrowheads). One of the five genital plates is bigger than the others, it is the madreporite (marked by the cyan arrowhead), which corresponds to a sieve plate enabling water to enter the water vascular system. In addition, each genital plate is interconnected by five ocular plates (delineated by the white dotted lines), which together form the central disk of the aboral surface. The hole, in the middle of the central disk, does not correspond to the anus of the animal. In live animals, this hole is filled by periproct plates, which are not attached to the rest of the endoskeleton and are thus rarely conserved on an endoskeleton stripped of the 'living parts'. The anus itself is almost impossible to see when the periproct system is intact. (F) Schematics of the echinoid water vascular system. The water vascular system is composed of a stone canal connected, on one side, to the madreporite, and, on the other side, to the ring canal. The ring canal is itself connected to five radial canals that are connected to ampullae and podia (or tube feet). Circulation of water through the water vascular system enables the podia to extend and retract, allowing the animal to move on the substrate. Scale bar: (A,C–E) 1 cm. Amb: ambulacra, IAmb: interambulacra.

externally, each individual produces only one of the two types of gametes, eggs or spermatozooids (Gianguzza et al., 2009). Spawning takes place in the water column during coordinated events, and fertilization is external, hence making this species easily amenable for *in vitro* fertilization in the laboratory (Tenuzzo et al., 2012; Ortiz et al., 2019). Following fertilization, like many other echinoids, *P. lividus* exhibits an indirect mode of development (Cellario and Fenaux, 1990; Gosselin and Jangoux, 1998). Thus, the animal undergoes a bi-phasic lifecycle with the initial formation, following embryogenesis, of a pelagic, planktotrophic larva called the echinopluteus (or pluteus) larva that exhibits a classical bilateral symmetry. The pentaradial adult body plan forms only later, within the larva, on the left side of the digestive tract, as a vesicle called the rudiment. Once the rudiment is fully formed, the larva has reached competency, and, upon adequate environmental cues, it will undergo a dramatic morphological reorganization, called metamorphosis. During metamorphosis, the planktonic, bilateral larva thus transforms into a benthic, pentaradial juvenile. The juvenile corresponds to a miniature version of the adult and, upon grazing on algae, it will eventually grow in size and develop reproductive organs.

Over the past century, the interest in the sea urchin species *P. lividus* has been substantial, not only because of its ecological and economic significance, but also because it is a suitable model system for biological and biomedical research (McClay, 2011; Bernardo and Carlo, 2017). Indeed, over the past years, *P. lividus* has been an important model organism in ecotoxicological and climate change surveys (Aluigi et al., 2008; Dorey et al., 2018). From a biological and biomedical point of view, *P. lividus* has further contributed to a number of important discoveries. Most importantly, it enabled the demonstration of the concepts of regulative development (Driesch, 1892), of chromosomal inheritance (Boveri, 1902), and of inductive interaction (reviewed in Hörstadius, 1973). In addition, based on the use of modern gene manipulation approaches, it provided important insights into developmental gene regulatory networks, patterning mechanisms, and morphogenesis (e.g., Saudemont et al., 2010; Lhomond et al., 2012; Gildor et al., 2016). On a different note, the gonads of *P. lividus* are further considered a delicacy and luxury seafood in many Mediterranean countries, making *P. lividus* adults a valuable resource with important commercial value (Matsiori et al., 2012; Baião et al., 2021) and a target for aquaculture-related research (Castilla-Gavilán et al., 2018).

Due to both the scientific and commercial importance of *P. lividus*, several studies have already reported the different phases of the life cycle of this sea urchin species. For instance, classical developmental descriptions of embryos and larvae have been published by Boveri (1901), von Ubisch (1913), and Hörstadius (1973). Likewise, the transition from the larval to the adult stage of *P. lividus*, i.e., from competent larva to early juvenile, has been reported by Gosselin and Jangoux (1998). A staging scheme for early juvenile stages of *P. lividus*, i.e., during the first 4 weeks of its

post-metamorphic life, has also recently been provided by Thompson et al. (2021). Similarly, the adult stage of *P. lividus* has been carefully studied over the past decades by several zoologists interested in muscular or skeletal anatomy (Stauber, 1993; Wilkie et al., 1998; Ziegler et al., 2012), pigmentation (Goodwin and Srisukh, 1950), and calcification (Ameys et al., 1999; Politi et al., 2004). Despite these previous investigations, some aspects of *P. lividus* development remain largely unknown. These include, for instance, the development of the coeloms and the rudiment within the larva as well as the development of the ciliated structures and muscles during the embryonic and larval periods.

Our goal here is to describe the aspects of *P. lividus* development that have so far been neglected and to provide a rigorous and exhaustive staging scheme for this sea urchin species from fertilization to post-metamorphic juvenile stages. For all stages, even those previously described, we provide a detailed and comprehensive morphological description, using images recorded on live specimens. In addition, we report the details of ciliogenesis and muscle development based on immunohistochemistry assays. Altogether, this study hence offers a valuable and complete reference for all aspects of *P. lividus* development, including an analysis, in live specimens, of the process of metamorphosis. Over the past decades, the scientific community has been looking for alternative model systems with experimental amenability and relatively short life-cycles. *P. lividus* is certainly a suitable candidate, with existing genomic and transcriptomic resources, working protocols for functional analyses, and sexual maturity reached in 6–8 months. The present work hence represents an additional tool for future research using *P. lividus* as a model system. It provides an updated staging scheme for *P. lividus* that the scientific community will be able to rely on for future research in this species, allowing standardized and comparable surveys to be carried out across different laboratories. Given the level of detail provided in this study, the stage descriptions for *P. lividus* development can further serve as a valuable basis for detailed comparisons with other echinoid species.

Materials and methods

Animal husbandry

Adults *Paracentrotus lividus* were collected in the bay of Villefranche-sur-Mer (France). Gamete collection was performed as previously described (Lepage and Gache, 1989). For fertilization, 10 µL of sperm was diluted in 1 ml of sea water. The sperm dilution was validated by eye, by estimating the turbidity of the sea water. The dilution was added to a beaker containing unfertilized eggs in about 150 ml of sea water and a manual stirring was applied to homogenize the distribution of sperm. After adding the sperm, the success of fertilization,

marked by the elevation of the fertilization envelope, was immediately monitored under a binocular, to make sure that the sperm concentration added was sufficient to enable fertilization but low enough to avoid triggering polyspermy. Fertilized eggs were then rinsed twice to remove the excess of sperm. After settlement of the eggs at the bottom of the beaker, about 120 ml of sea water were thus replaced each time. Embryos and larvae were then cultured, under constant mechanical stirring, at 18°C in natural seawater collected at “point B” in the bay of Villefranche-sur-Mer (43°41 N 07°19 E) at a depth of 200 m and filtered using a 0.2 µm mesh. Following fertilization, embryos were cultured at a density of 100 embryos per mL until 48 h post-fertilization (hpf). At 48 hpf, the culture concentration was adjusted to 1 larva per mL. From 48 hpf on, water exchange and feeding were performed as previously reported (Formerly et al., 2021), except that the larvae were fed, every week day, with freshly grown cultures of the microalgae *Dunaliella salina* (strain MCCV127) and *Rhodomonas salina* (strain MCCV118). After about 30 days post-fertilization (dpf), the larvae started undergoing spontaneous metamorphosis in the culture vessels. However, to document this event, synchronous metamorphosis of competent larvae was triggered by adding Dibromomethane (Sigma-Aldrich, Saint-Quentin-Fallavier, France), in the culture vessels, at a final concentration of 1.25 mg/mL. Dibromomethane is a halogenated aliphatic compound secreted by red coralline algae that has been reported as a chemical inducer of larval metamorphosis for several marine species (Agatsuma et al., 2006; Taris et al., 2010). Upon metamorphosis, the juveniles were cultured at 16°C, under constant seawater flow, with the water being pumped at a depth of 5 m, decanted, and cooled down to 16–18°C. Starting 7 days post-metamorphosis (dpm), the juveniles were fed with rehydrated *Tetraselmis suecica* algae (Inalve, Villefranche-sur-Mer, France).

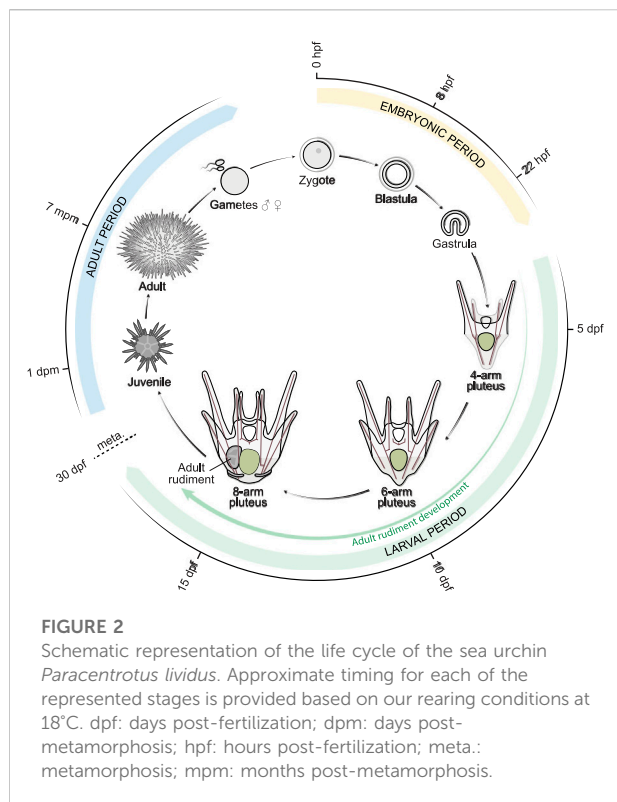
Anatomical observation (light microscopy)

P. lividus development, from fertilization to juvenile stages, was recorded on specimens mounted alive. *P. lividus* embryos, larvae, and juveniles were imaged using a Zeiss A2 (Axio Imager 2) light microscope (Zeiss, Jena, Germany), under either bright-field, differential interference contrast (DIC), or polarized light. *P. lividus* larvae were also imaged, under dark-field, using a Zeiss SteREO Discovery V20 microscope (Zeiss, Jena, Germany). Metamorphosis was imaged using a Zeiss Axio Observer Z1 microscope (Zeiss, Jena, Germany). In all cases, images were captured using the Zen software suite (Zeiss, Jena, Germany). To record embryos, larvae, and juveniles, specimens were mounted in 0.2 µm filtered seawater, between a slide and a cover slip, using clay to generate spacers and enable orientation of the specimens. Specimens were mounted alive, except, in some cases, for the larvae between the 4-arm and 8-arm *pluteus* stages. At these stages, larvae were immobilized, when

needed, before mounting and imaging, to prevent them from swimming. For this, a drop of 8% paraformaldehyde (#P6148, Sigma-Aldrich, Saint-Quentin-Fallavier, France) prepared in sea water was added to a small Petri dish containing the larvae in filtered sea water. Multiple z-stacks were taken manually when required. To record metamorphosis, a multi-well agarose gel was generated using a 3D-printed mold that was deposited within a Petri dish containing a 1% agarose gel prepared in 0.2 µm filtered seawater. The mold was designed with conical spikes to create well diameters from 1.5 mm at the bottom to 5 mm at the top. In addition, the spikes were generated with an angle lower than the numerical aperture of the objectives used on the microscope to avoid light reflection. Competent larvae were placed in the agarose wells individually, with 0.2 µm filtered seawater filling the wells. Images were acquired using a Marzhauser SCAN IM (Inverse Microscopes) 130 × 10 motorized stage (Marzhauser, Wetzlar, Germany), allowing acquisitions in multi-position. Images were further acquired in z-stacks with a 20 µm step every 1 min and for about 2 h. For all images, projections were generated, when needed, using the focus merging option of Affinity Photo (Serif, Nottingham, United Kingdom). Images were further processed using Adobe Photoshop (Adobe Inc., San Jose, United States) or Affinity Photo (Serif, Nottingham, United Kingdom), and scale bars were added using ImageJ version 1.44o (Schneider et al., 2012), which was also used to generate the movie of metamorphosis. All figures were formatted using Adobe Illustrator (Adobe Inc., San Jose, United States) or Affinity Designer (Serif, Nottingham, United Kingdom).

Immunohistochemistry (confocal microscopy) and *in situ* hybridization

Immunohistochemistry assays were performed as previously described in Formerly et al. (2021). The primary antibody used was a mouse anti-acetylated α-tubulin (#T6793, Sigma-Aldrich, Saint-Quentin-Fallavier, France) prepared at 1:200 in PBST or in PBST plus 0.005 U/µl rhodamine phalloidin (#R415, Thermo Fisher Scientific, Illkirch-Graffenstaden, France) to label F-actin particularly enriched in muscles. The secondary antibody used was an Alexa Fluor 647 goat anti-mouse IgG H&L (#ab150115, Abcam, Cambridge, United Kingdom) diluted at 1:200 in PBST. In all specimens, nuclear staining was also performed following the method of Formerly et al. (2021), except that we used either TO-PRO1 Iodide (515/531) or TO-PRO3 Iodide (642/661) (#T3602 or #T3605, Thermo Fisher Scientific, Illkirch-Graffenstaden, France), depending on the fluorochrome needed. Observation and imaging of the labeled specimens were carried out using a Leica SP8 confocal microscope (Leica, Wetzlar, Germany). For each sample, series of optical sections were taken at a z-step interval of 1–2 µm and multichannel acquisitions were obtained by sequential imaging. Confocal optical sections were compiled into maximum intensity



z-projections using ImageJ version 1.44o (Schneider et al., 2012), and scale bars were added using the same software.

In situ hybridization assays were carried out as previously described in Robert et al. (2014). The riboprobe used for the *P. lividus* myosin heavy chain (*mhc*) gene corresponded to a 2066 base pair-long partial cDNA (GenBank accession number: OM307457). The probe was used at a final concentration of 1 ng/μL, and images were acquired using a Zeiss A2 (Axio Imager 2) microscope (Zeiss, Jena, Germany) under differential interference contrast (DIC) light. Scale bars were added using ImageJ version 1.44o (Schneider et al., 2012). For immunohistochemistry, as for *in situ* hybridization, images were processed using either Adobe Photoshop (Adobe Inc., San Jose, United States) or Affinity Photo (Serif, Nottingham, United Kingdom), and figures were compiled using either Adobe Illustrator (Adobe Inc., San Jose, United States) or Affinity Designer (Serif, Nottingham, United Kingdom).

Results

Paracentrotus lividus development: Staging scheme overview and nomenclature

The development of *P. lividus*, observed under our rearing conditions from egg to post-metamorphic juveniles, occurred as

depicted in Figures 2, 3. We defined each developmental stage based on ontogenic features, which were readily detectable in whole-mount specimens using regular transmitted light microscopy and which we will describe in detail in the subsequent sections. We subdivided the development of *P. lividus* in three main periods: the embryonic period (or embryogenesis), the larval period, and the adult period (Figures 2, 3). The embryonic period covers the development of the embryo from fertilization to the *prism* stage, right before the opening of the larval mouth and the establishment of the larval body plan. The larval period subsequently covers the larval growth and formation of the adult rudiment within the larva. This period starts upon the opening of the larval mouth, at the so-called *early pluteus* stage, and ends with metamorphosis. The adult period finally covers the growth of the juvenile and the acquisition of sexual maturity. This period starts right after metamorphosis, with the formation of the benthic, pentaradial juvenile and ends with the death of the animal, which has been estimated to occur after 6–9 years for wild *P. lividus* adults (Cropp and Willis, 1975). Each of the defined developmental periods was then subdivided into several distinct developmental stages, which cover various time spans (Figure 3). The stages during the embryonic and larval periods as well as for rudiment and juvenile development were defined based on previous descriptions made for *P. lividus* and other sea urchin species (Hörstadius, 1973; Okazaki, 1975; Gosselin and Jangoux, 1998; Smith, 2008; Heyland and Hodin, 2014).

After recording the development of thousands of embryos and larvae, from more than thirty independent cultures, we found that the timing of development, during the embryonic period, was stereotypical (i.e., similar within and between cultures). By contrast, during the larval and adult periods, a certain degree of variation was observed, even within a given culture, and despite the fact that the larvae and juveniles were healthy throughout the culture period. With time, and even though the larvae were fed *ad libitum*, differences were observed between larvae, chiefly due to a heterochrony of ontogenic events, which is consistent however with previous reports (Strathmann et al., 1992; Carrier et al., 2015). For instance, we observed that the duration of the larval period varied between 4 and 7 weeks, that rudiment formation started between 7 and 14 days post-fertilization, and that spontaneous metamorphosis occurred between 1 day and 3 weeks after acquisition of competency. The most significant and recurrent heterochrony observed was between the developmental trajectories of the larva and the adult rudiment. The ontogeny of certain larval structures, such as the larval arms and the epaulettes, were often mismatched with the growth of the coeloms and the adult rudiment, and this even if development of the larval structures, on one hand, and of the coeloms and adult rudiment, on the other hand, followed their respective, stereotypical developmental paths. In Figure 3, we thus propose a separate set of staging schemes for the development of the coeloms and the adult rudiment, which corresponds to a subset of the larval period (Figure 3). This subset usually started during the 4-

Period	Stage	Abbr.	Time ¹
Cleavage	1-cell stage (zygote)	1-cell	0:00 hpf
	2-cell stage	2-cell	1:40 hpf
	4-cell stage	4-cell	2:30 hpf
	8-cell stage	8-cell	3:20 hpf
	16-cell stage	16-cell	4:10 hpf
	28-cell stage	28-cell	4:45 hpf
	32-cell stage	32-cell	5:00 hpf
	56-cell stage	56-cell	5:30 hpf
	60-cell stage	60-cell	5:50 hpf
Embryonic Blastula	very early blastula stage	vEB	6:50 hpf
	early blastula stage	EB	7:50 hpf
	mid-blastula stage	mid-B	8:50 hpf
	late blastula stage	late-B	9:50 hpf
	hatched blastula stage	HB	11:00 hpf
	swimming blastula stage	SB	12:00 hpf
	late swimming blastula stage	late-SB	13:00 hpf
Gastrulation	early mesenchyme blastula stage	eMB	14:00 hpf
	late mesenchyme blastula stage	late-MB	17:00 hpf
	blastopore formation stage	BF	18:00 hpf
	early gastrula stage	EG	20:00 hpf
	mid-gastrula stage	mid-G	22:00 hpf
	late gastrula stage	LG	24:00 hpf
	prism stage	prism	32:00 hpf
Larval	early pluteus stage	eP	40:00 hpf
	2-arm pluteus stage	2-arm	2 dpf
	4-arm pluteus stage	4-arm	3 dpf
	6-arm pluteus stage	6-arm	~ 10 dpf
	8-arm pluteus stage	8-arm	~ 15 dpf
	competent pluteus stage	Cpt	~ 30 dpf
	metamorphosis	Meta	~ 30 dpf
Adult	early juvenile stage	EJuv	0 dpm
	late juvenile stage	LJuv	~ 8 dpm
	adult stage	Adult	~ 7 mpm

Coeloms and Adult rudiment stage ²	Abbr.
hydroporic canal stage	HypC
constricted coelomic pouch stage	ConsCP
stone canal stage	StC
vestibule invagination stage	VesInv
vestibule contact stage	VesCon
vestibule flattened stage	VesFlat
vestibule waving stage	VesWav
5-fold mesoderm stage	5foldMe
5-fold ectoderm stage	5foldEc
primary podia stage	PPodia
primary podia touching stage	PTouch
primary podia twisting stage	PTwist
primary podia papilla stage	PPap
juvenile spine stage	JuvS
mature rudiment stage	MRud

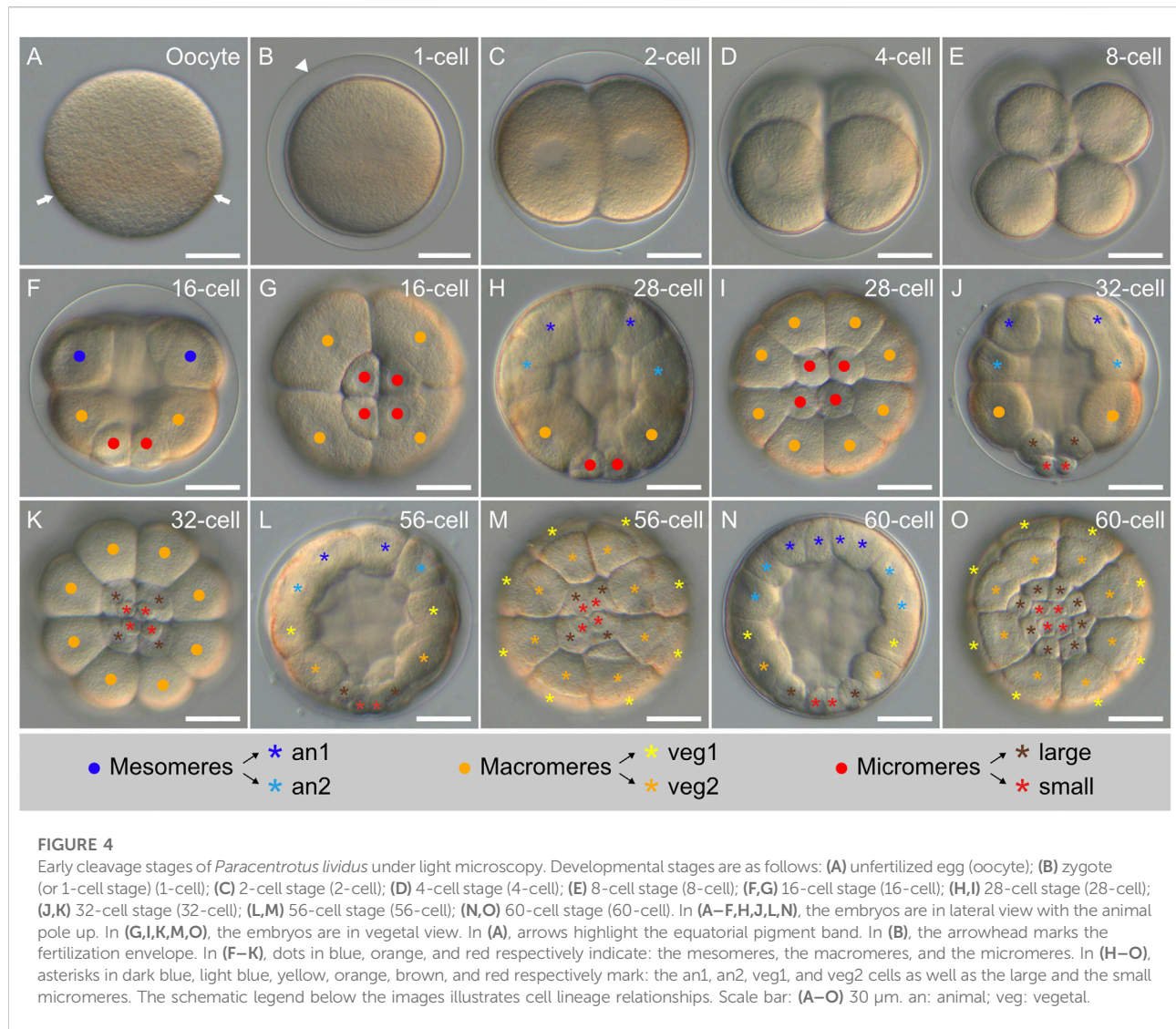
FIGURE 3

Paracentrotus lividus staging scheme. In the left panel, timing ⁽¹⁾ is provided for our rearing conditions at 18°C. Note that a certain degree of heterochrony was observed during larval and adult periods (-). As development of the coeloms and the adult rudiment proceeded in parallel to that of the larva, during the 4-, 6-, and 8-arm pluteus stages, a subsection for coeloms and adult rudiment development is provided in the right panel. ⁽²⁾ Due to the heterochrony of the developmental trajectories of the coeloms and the adult rudiment, even within a given culture, a developmental timing for these events cannot be provided. Abbr.: abbreviation; dpf: days post-fertilization; dpm: days post-metamorphosis; hpf: hours post-fertilization; mpm: months post-metamorphosis.

arm pluteus stage and always ended during the 8-arm pluteus stage. In addition, although we provide an approximate timing for the main stages of the embryonic, larval, and adult periods (Figure 3), due to the heterochronic nature of their development, we decided not to include such a timing for the stages related to the formation of the coeloms and the adult rudiment. Instead, we named these stages according to morphological traits that were easily identifiable (Figure 3).

It should be noted, furthermore, that different terms have been used in previous studies to identify the main body axes of echinoid embryos, larvae, and juveniles (e.g., Hyman, 1955;

Okazaki, 1975; Gosselin and Jangoux, 1998; Smith et al., 2008; Range et al., 2013). Here, the set of terms that will be used is illustrated in Supplementary Figure S1. For embryos, we chose to refer to the primary body axis as the animal-vegetal axis, with the vegetal pole being marked by the presence of the micromeres and then the blastopore. For larvae, we identified the axes following their ontogenetic appearance during embryonic development, meaning that we considered that the anus marks the posterior pole. We further considered that the larval arms develop on the ventral side of the larvae, corresponding to the side bearing the mouth. Consequently, the



larval apex forms on the dorsal side. For juveniles and adults, we finally referred to the side bearing the adult mouth as the oral side, with the side bearing the anus thus being the aboral side. To define the pentaradial symmetry of the adult body, already distinguishable in the rudiment, we chose to use the nomenclature proposed by Carpenter (Carpenter, 1884). In this nomenclature, the five rays correspond to the position of the ambulacra and they are respectively called ambulacrum A, B, C, D, and E, with ambulacrum A facing the madreporite, a specific skeletal piece of the central disk on the aboral surface (Figure 1E, Supplementary Figure S1). In addition, these letters are positioned counterclockwise when the juvenile is looked at from the aboral side, and clockwise when it is looked at from the oral side (Carpenter, 1884; Paul and Hotchkiss, 2020) (Supplementary Figure S1). Accordingly, the interambulacra

are named AB, BC, CD, DE, and EA, respectively, with the madreporite being located in interambulacrum CD (Supplementary Figure S1).

Embryonic development

Spawning and fertilization

Sexually mature adult males and females of *P. lividus* displayed 5 gonopores (see Figure 1E). During spawning, spermatozooids and oocytes were released through the gonopores by the males and by the females, respectively. Freshly-spawned *P. lividus* oocytes had a size of about 90 μ m (Figure 4A). They were spherical and mostly transparent, with a conspicuous band of orange-pigmented granules in a

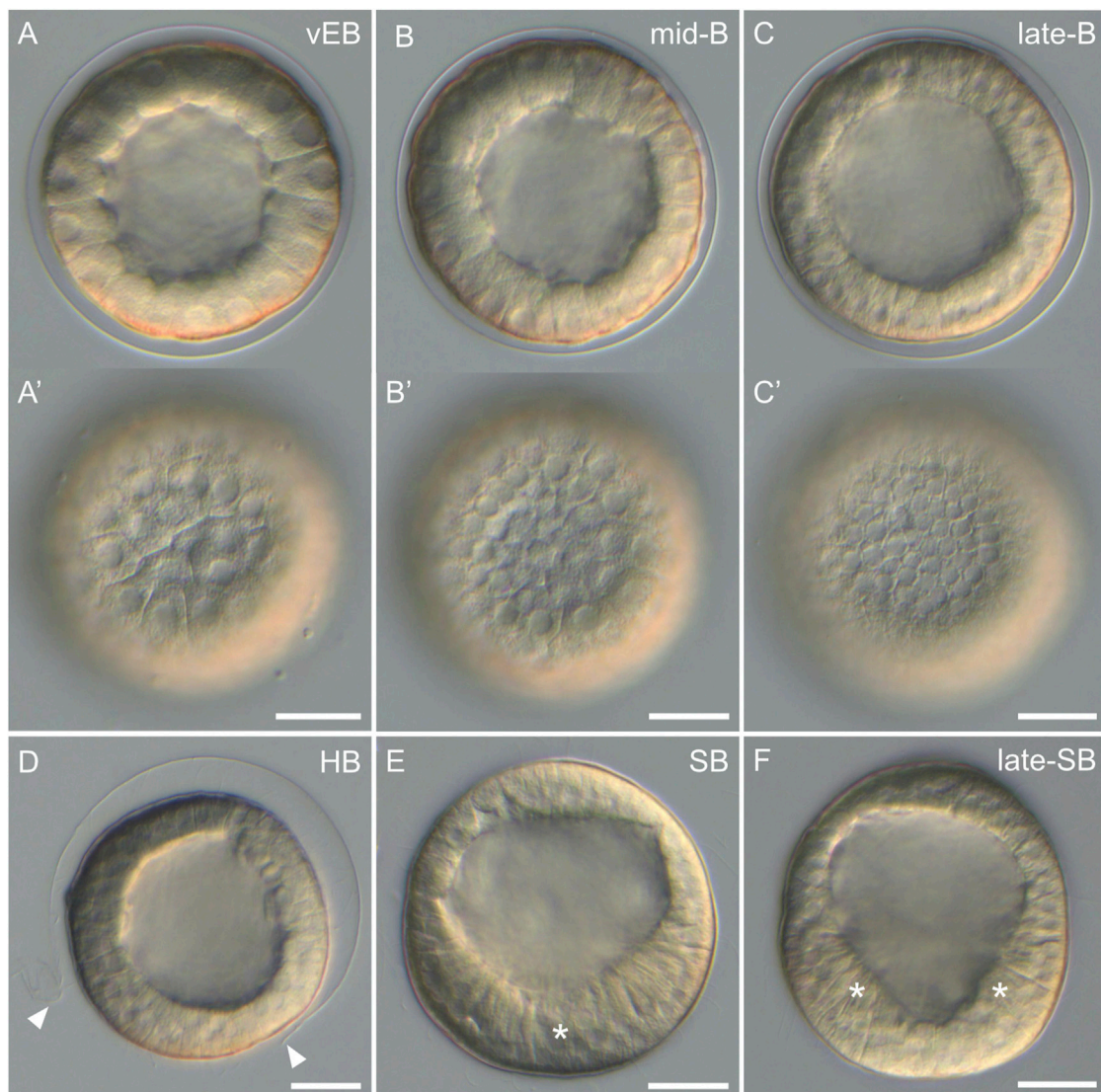


FIGURE 5

Blastula stages of *Paracentrotus lividus* under light microscopy. Developmental stages are as follows: (A,A') very early blastula stage (vEB); (B,B') mid-blastula stage (mid-B); (C,C') late blastula stage (late-B); (D) hatched blastula stage (HB); (E) swimming blastula stage (SB); (F) late swimming blastula stage (late-SB). In (A–F), the embryos are in lateral view with the animal pole up. (A',B',C') are optical surface views of, respectively, (A–C). In (D), arrowheads mark the rupture of the fertilization envelope. In (E), the asterisk indicates the thickening of the cells constituting the vegetal plate, at the vegetal pole. In (F), asterisks highlight the "V" shape of the vegetal plate. Scale bar: (A–F) 30 μ m.

subequatorial position, which remained visible during subsequent developmental stages (Figure 4). In the wild, *P. lividus* fertilization takes place externally and can thus easily be reproduced in the laboratory (Foltz et al., 2004). Entry of a spermatozoid into an oocyte triggers, in the latter, the immediate separation of the vitelline envelope from the surface of the oocyte. Accordingly, within seconds after spermatozoid addition, we observed inflation of the vitelline envelopes. This led to the appearance of a thin translucent membrane, called the fertilization envelope, which surrounded the zygote (or 1-cell stage embryo) (Figure 4B). Fertilizations were extremely

synchronous, with thousands of oocytes fertilized simultaneously.

Cleavage stages

Following fertilization, the zygotes underwent first cleavage after about 1 h and 40 min (1:40 h post-fertilization - 1:40 hpf), when reared at 18°C. This cleavage was holoblastic and meridional. It gave rise to a 2-cell stage embryo, composed of two blastomeres, separated by a plane parallel to the animal-vegetal axis (Figure 4C). The second cleavage occurred 2:30 hpf and resulted in a 4-cell stage embryo (Figure 4D). This cleavage

was also holoblastic and meridional, yet perpendicular to the first one. At the *4-cell stage*, the embryos were thus composed of four blastomeres of equal size, each containing an equal volume of both animal and vegetal cytoplasm. The third cleavage took place 3:20 hpf and resulted in an *8-cell stage* embryo (Figure 4E). This cleavage was equatorial, i.e., perpendicular to the two first ones. It separated four animal from four vegetal blastomeres, generating two territories with different cytoplasmic contents: the animal and the vegetal territories. The fourth cleavage subsequently occurred at 4:10 hpf and resulted in a *16-cell stage* embryo (Figures 4F,G). At this stage, cell division patterns became different between the animal and the vegetal hemispheres as well as unequal in the vegetal hemisphere. Thus, in the animal hemisphere, the fourth cleavage was meridional, generating a ring of eight blastomeres of equal size (referred to as the mesomeres). In the vegetal hemisphere, the fourth cleavage was equatorial and unequal, producing four large cells (referred to as the macromeres) positioned right below the mesomeres and four small cells (referred to as the micromeres) marking the vegetal pole.

Following fourth cleavage, cell divisions became furthermore asynchronous, with the mesomeres and the macromeres dividing prior to the micromeres. Fifth cleavage started in the mesomeres and macromeres at 4:45 hpf, giving rise to an initial, intermediate *28-cell stage* embryo (Figures 4H,I). The eight mesomeres divided equatorially and equally, producing two cell tiers of eight cells each: the animal tier 1 (an1), marking the animal pole, and the animal tier 2 (an2), located below an1. The macromeres divided meridionally and equally, generating a single ring of eight cells of equal volume located below an2. After 15 min, the micromeres also underwent their fifth cleavage, leading to a *32-cell stage* embryo (Figures 4J,K). The micromeres divided equatorially and unequally, producing four large micromeres (just below the macromeres) and four small micromeres (marking the vegetal pole).

Sixth cleavage took place in the mesomeres and the macromeres at 5:30 hpf and resulted in an intermediate *56-cell stage* embryo (Figures 4L,M). During this cleavage, the cells of the an1 and an2 tiers divided equally and meridionally, producing a new an1 and a new an2 tier now composed of 16 cells each. The macromeres underwent an equal but equatorial cleavage, thereby leading to the emergence of two vegetal tiers, each composed of eight cells: the vegetal tier 1 (veg1), located below an2, and the vegetal tier 2 (veg2), located below veg1. 20 min later, at 5:50 hpf, the large micromeres underwent their sixth cleavage, which was meridional and equal. This thus generated a single ring of eight micromeres of equal volume, with the small micromeres at their center not displaying any sign of cell division (Figures 4N,O). By 6:00 hpf, the embryos were thus at the *60-cell stage* and composed, from the animal to the vegetal pole, of sixteen

an1 cells, sixteen an2 cells, eight veg1 cells, eight veg2 cells, eight large micromeres, and four small micromeres (Figures 4N,O).

Blastula stages

After the *60-cell stage*, cell divisions continued, but the embryos stopped displaying any visual landmark to differentiate the animal-vegetal axis, the distinct cell tiers, or the different developmental stages. As such, the embryos were now referred to as blastulae, and we observed and imaged them every hour after the *60-cell stage*. Starting at the *very early blastula stage* (1 h after the *60-cell stage*), the embryos, still enclosed in the fertilization envelope, exhibited a characteristic spherical organization (Figure 5A). The cells formed a monolayered, hollow sphere that surrounded a central, fluid-filled cavity called the blastocoel. During the subsequent stages, i.e., the *early blastula stage* (2 h after the *60-cell stage*), the *mid-blastula stage* (3 h after the *60-cell stage*), and the *late blastula stage* (4 h after the *60-cell stage*), the embryos were still enclosed in the fertilization envelope and were morphologically very similar to each other. They exhibited a spherical shape composed of a monolayer of cells surrounding the blastocoel (Figures 5B,C). Yet, during these stages, and without affecting the overall size of the embryos, the cells continued to divide and became smaller (Figures 5A'–C'), thereby progressively thinning the wall of the blastulae (Figures 5A–C). Consequently, the blastocoel expanded and widened. In addition, starting at the *mid-blastula stage* (i.e., at about 9 hpf), the embryos began to rotate within the fertilization envelope, which indicated the presence of cilia on the cell surfaces (for details on cilia see the ciliogenesis section below).

By 11 hpf, the fertilization envelope surrounding the embryos started to rupture (Figure 5D). This indicated that the embryos reached the *hatched blastula stage*. Rupture of the fertilization envelope is ensured by a specific enzyme, called the hatching enzyme, which is synthesized by the animal cells to free the embryos from the fertilization envelope (Lepage et al., 1992). As such, by 12 hpf, all embryos were swimming freely in the cultures. This corresponded to the *swimming blastula stage* (Figure 5E). At this stage, although the embryos remained spherical, the animal-vegetal axis became once again morphologically discernable. The cells at the vegetal pole were now thicker and flatter compared to the rest of the embryo (Figure 5E). This thicker and flatter area corresponds to a specific embryonic structure called the vegetal plate (Ruffins and Ettensohn, 1996). At 13 hpf, the embryos were at the *late swimming blastula stage*. They had elongated along the animal-vegetal axis and their vegetal cells were even thicker, especially on each side of the vegetal pole, resulting in a vegetal plate with a characteristic “V” shape (Figure 5F). Of note, at this stage, the vegetal plate was composed, in a concentric manner, by the small

micromeres at the center, followed by the descendants of the large micromeres, and the descendants of the veg2 cells.

Gastrulation stages

In *P. lividus*, as in any other echinoids with micromeres (also called the euechinoids), gastrulation started by the ingression, into the blastocoel, of the descendants of the large micromeres (Figure 6A). This ingression takes place by an epithelial-to-mesenchymal transition and gives rise to the skeletogenic mesoderm (SM) cells (also referred to as the primary mesenchyme cells or PMCs) (Fink and McClay, 1985). Ingression of the SM cells began at the *early mesenchyme blastula stage* (i.e., at around 14 hpf) (Figure 6A), and proceeded until the *late mesenchyme blastula stage* (i.e., at around 17 hpf) (Figure 6B). During this period, the embryos were characterized by an increasing number of SM cells within the blastocoel (up to 32 cells), which, for the time being, remained in the vicinity of the vegetal plate (Figures 6A,B). During this period, the embryos further continued to exhibit, at the vegetal pole, a flattened vegetal plate (Figures 6A,B), which by 17 hpf was only composed of the small micromeres at the center, surrounded by the descendants of the veg2 cells (Ruffins and Ettensohn, 1996; Lyons et al., 2012). By 17 hpf, the descendants of the veg2 cells were also segregated into two different cell tiers, with two distinct cell fates: an inner cell tier surrounding the small micromeres that will develop into non-skeletogenic mesoderm (NSM) cells (also referred to as the secondary mesenchyme cells or SMCs) and an outer cell tier located at the periphery of the vegetal plate that will develop into endoderm cells (Ruffins and Ettensohn, 1996; Lhomond et al., 2012). In addition, at 17 hpf (i.e., at the *late mesenchyme blastula stage*), the embryos were also characterized by the presence, at the animal pole, of a patch of elongated cells (Figure 6B), which will be visible until the end of gastrulation (Figure 6). These cells delimited the animal (or apical) pole domain, within which the neuroectodermal territory will form (Angerer et al., 2011).

The second main morphogenetic movement observed during *P. lividus* gastrulation was subsequently the invagination of the archenteron (i.e., the primordium of the digestive tract). Invagination of the archenteron started at around 18 hpf, at the *blastopore formation stage* (Figures 6C,D). At this stage, the embryos were characterized by the inward bending of the remaining vegetal plate, which created the first opening of the future digestive tract, the blastopore, which will subsequently develop into the anus. This morphogenetic movement has been proposed to be driven by various mechanisms, such as swelling, cell shape changes, pulling, and/or apical secretion, but the exact mechanism at play still remains enigmatic (Ettensohn, 2020). Within the blastocoel, the SM cells concomitantly started migrating, extending filopodia, and attaching and detaching them from the blastocoel wall. By doing so, they progressively adopted a characteristic pattern, forming a ring around the

anlage of the archenteron (Figure 6D). At the *early gastrula stage* (20 hpf), the embryos were characterized by an archenteron that had extended within the blastocoel, reaching the approximate level of a quarter of the blastocoel (Figure 6E). This extension was likely due to the invagination of additional NSM cells within the blastocoel. Meanwhile, some SM cells migrated along the inside of the blastocoel wall, towards the animal pole, thereby constituting two lateral chains, the right and the left lateral chains (Figure 6E). In addition, and although the embryos were still relatively spherical at this stage, the ring formed by the SM cells, around the anlage of the archenteron, started to display an asymmetric shape, providing the first morphological landmark for the dorsal-ventral axis. This ring of SM cells was organized into a short ventral and a long dorsal chain, linked by a right and a left aggregate (Figure 6F), which are respectively referred to as the right and the left ventrolateral cluster (Peterson and McClay, 2003).

At the *mid-gastrula stage* (22 hpf), the embryos were characterized by an archenteron length that reached the approximate level of half of the blastocoel (Figure 6G). The archenteron was now likely composed of all of the NSM cells and most of the endoderm cells. Some of the NSM cells, at the tip of the archenteron, started to ingress within the blastocoel (Figure 6G). These cells were undergoing an epithelial-to-mesenchymal transition, extending and projecting thin filopodia to detach from the archenteron (Figure 6G inset). Within the blastocoel, the SM cells still displayed the same characteristic organization as before: an asymmetric ring around the archenteron and two lateral chains along the blastocoel wall. At this stage, the epithelium constituting the ventral side of the embryo further started to flatten, and the epithelium at the boundary between the vegetal ventral and the vegetal dorsal ectoderm started to thicken (Figure 6H), marking the future position of the two first larval arms. At the *late gastrula stage* (24 hpf), the archenteron extended all the way through the blastocoel, up to the blastocoel roof (Figure 6I). At the tip of the archenteron, more delaminating NSM cells were distinguishable (Figure 6I). Within the blastocoel, the SM cells still displayed the same organization as before, and, at the level of the ventrolateral clusters, two skeletal pieces became discernable (Figures 6I,J) (for details on skeleton development see the skeletogenesis section below). At the level of the epithelium, the same features as before were observed, including a flattened ventral ectoderm, thickened areas between the vegetal dorsal and the vegetal ventral ectoderm, and elongated cells constituting the animal pole domain (Figures 6I,J).

In sea urchins, the process of gastrulation ends with the *prism stage* (Kominami and Takata, 2004), which also marks the end of the embryonic period. In *P. lividus*, this stage was observed at around 32 hpf (Figures 6K,L). It was characterized by a notable change in the overall shape of the embryo, as seen

in other sea urchin species. The embryo was characterized by a typical triangular (“prism”) shape, with a rounded, elongated dorsal ectoderm and a flattened ventral ectoderm (Figure 6K). The flat ventral ectoderm further formed an almost perfect right angle with the flat vegetal ectoderm (Figure 6K) and contained a small depression right below the apical pole domain (Figures 6K,L). This depression, called the stomodeum, corresponds to the site where the future larval mouth will form (Bergeron et al., 2011). The dorsal ectoderm also contained red-pigmented cells (Figure 6K), which

correspond to differentiated NSM cells that are part of the immune system of the embryo and the future larva (Hibino et al., 2006). Within the blastocoel, the archenteron was also bent toward the stomodeum, and a constriction was distinguishable below its tip (Figure 6K). This constriction marked the position of the future cardiac sphincter, which will eventually separate the larval esophagus (above the constriction, close to the stomodeum) from the future larval stomach (below the constriction) (Annunziata et al., 2014).

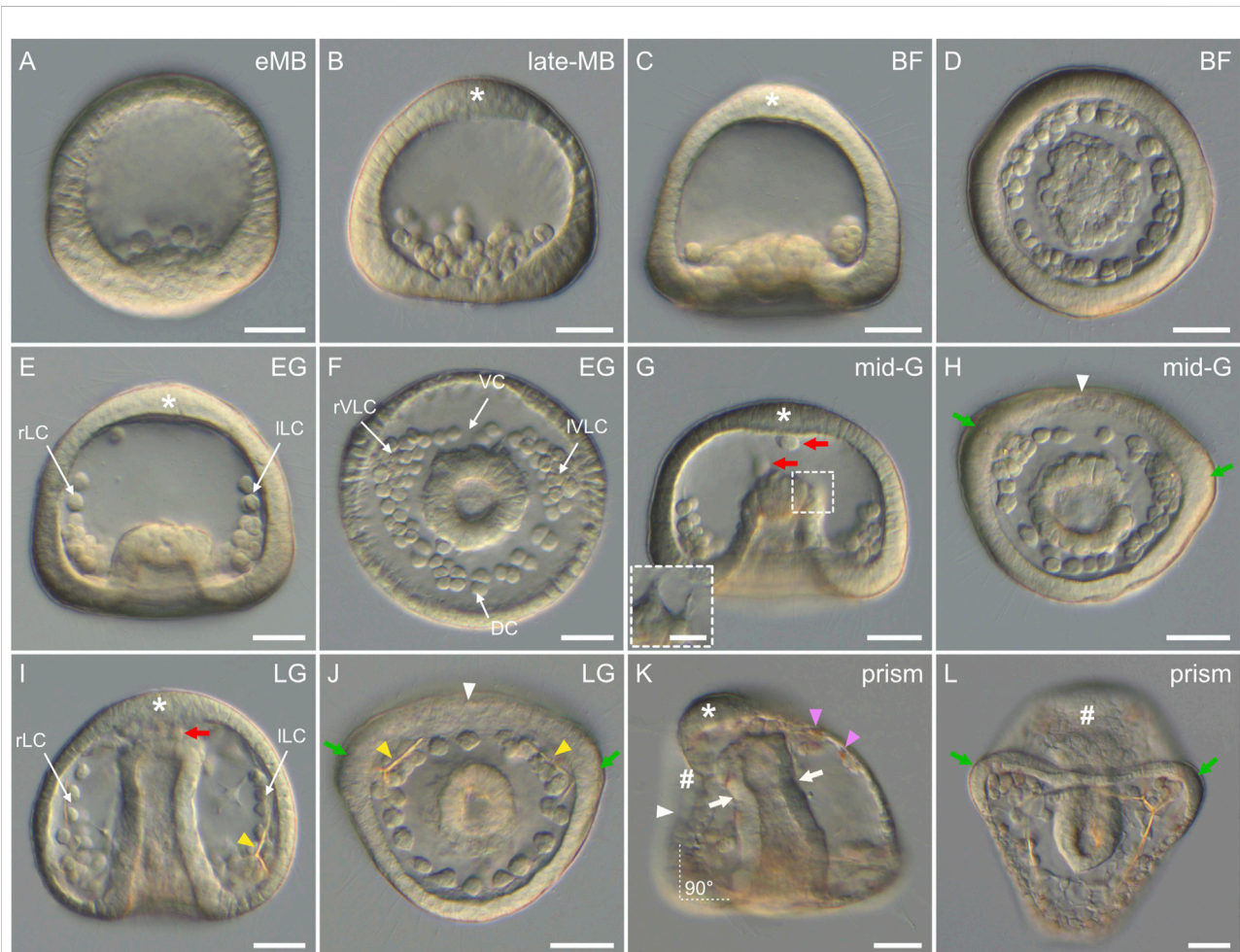
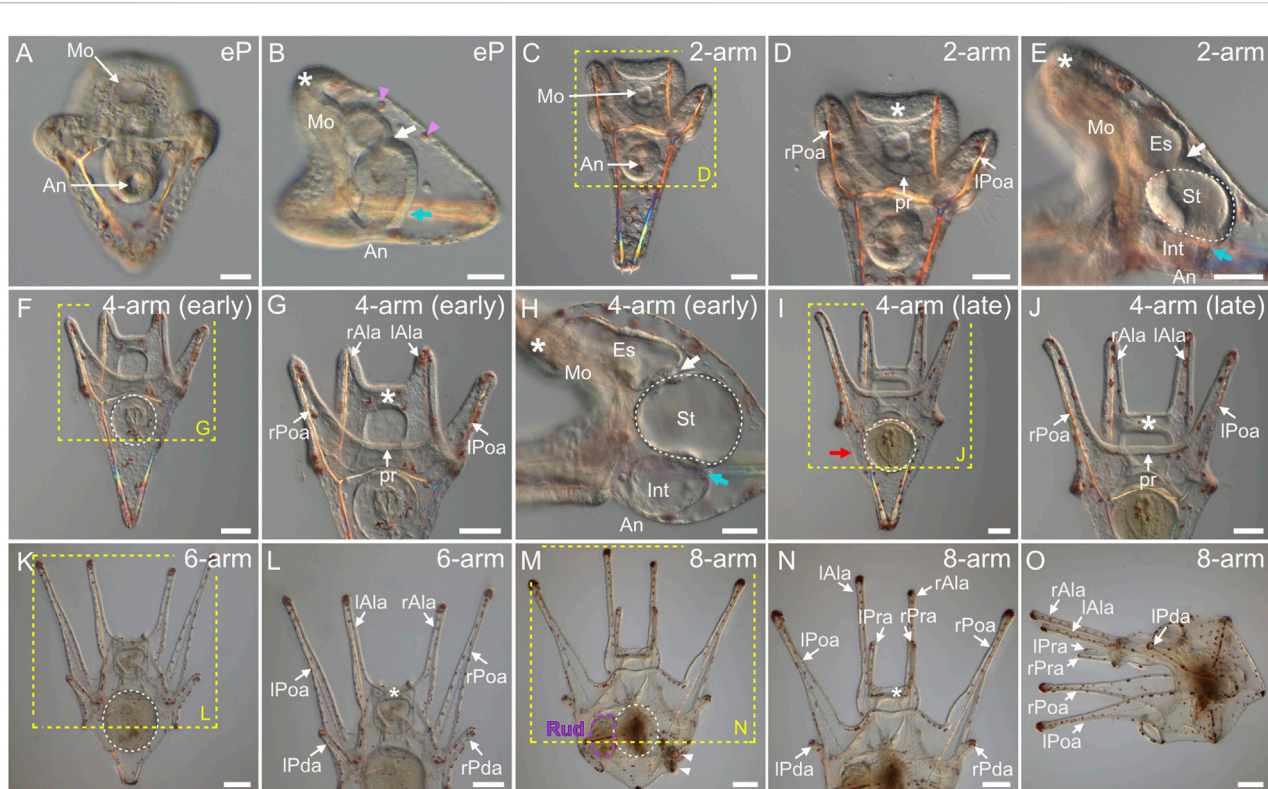


FIGURE 6

Gastrulation stages of *Paracentrotus lividus* under light microscopy. Developmental stages are as follows: (A) early mesenchyme blastula stage (eMB); (B) late mesenchyme blastula stage (late-MB); (C,D) blastopore formation stage (BF); (E,F) early gastrula stage (EG); (G,H) mid-gastrula stage (mid-G); (I,J) late gastrula stage (LG); (K,L) prism stage (prism). In (A–C,E,G,I,K), the embryos are in lateral view with the animal pole up, and in (K) the ventral side is left. In (D,F,H,J,L), the embryos are in vegetal view with the ventral side up. In (B,C,E,G,I,K), the asterisk marks the animal (or apical) pole domain. In (G,I), red arrows indicate non-skeletogenic mesoderm cells migrating within the blastocoel. ((G) inset) Close-up of the tip of the archenteron of the same embryo as in (G), but at a different focal plane to illustrate non-skeletogenic mesoderm cell ingression. In (H,J,K), the white arrowhead marks the flattening of the ventral ectoderm. In (H,J,L), green arrows highlight the thickened epithelium at the boundary between the vegetal ventral and the vegetal dorsal ectoderm. In (I,J), yellow arrowheads highlight the presence of skeletal elements. In (K), pink arrowheads indicate red-pigmented cells inserted in the aboral ectoderm, and white arrows mark the constriction of the archenteron segregating the esophagus from the stomach. The white dotted lines with the annotation “90°” further indicate the right angle between the ventral and the vegetal ectoderm. In (K,L), the sign “#” highlights the position of the stomodeum, and thus where the mouth will form. Scale bar: (A–L) 30 μ m; ((G) inset) 10 μ m. DC: dorsal chain; ILCL: left lateral chain; IVLC: left ventrolateral cluster; rLC: right lateral chain; rVLC: right ventrolateral cluster; VC: ventral chain.

**FIGURE 7**

Paracentrotus lividus larval development under light microscopy. Developmental stages are as follows: (A,B) early pluteus stage (eP); (C–E) 2-arm pluteus stage (2-arm); (F–J) 4-arm pluteus stage (4-arm); (K–O) 6-arm pluteus stage (6-arm); (M–O) 8-arm pluteus stage (8-arm). The use of (early) and (late) associated with the stage names simply highlights here more specific periods during the 4-arm pluteus stage. In (A,C,D,F,G,I–N), the larvae are in anterior view with the ventral side up. In (B,E,H,O), the larvae are in left view, with the ventral side left and the anterior side up. In (B,D,E,G,H,J,L,N), the asterisk marks the oral hood located above the mouth. In (B,E,H), the white arrow indicates the cardiac sphincter separating the esophagus and the stomach, and the cyan arrow marks the pyloric sphincter separating the stomach and the intestine. In (B), pink arrowheads highlight red-pigmented cells present within the dorsal ectoderm. In (D,G,J,L,N), the images correspond to close-ups of the regions outlined by yellow boxes in (C,F,I,K,M), respectively. In (E,F,H,I,K,M), the white dotted line outlines the stomach. In (I), the red arrow designates the larval stomach region. In (M), the purple dotted line highlights the adult rudiment, and white arrowheads mark the pedicellariae. Scale bar: (A–E,H) 30 μ m; (F,G,I,J) 50 μ m; (K–O) 100 μ m. An: anus; Es: esophagus; Int: intestine; lAla: left anterolateral arm; lPda: left posterodorsal arm; lPoa: left postoral arm; lPra: left preoral arm; Mo: mouth; pr: postoral region; rAla: right anterolateral arm; rPda: right posterodorsal arm; rPoa: right postoral arm; rPra: right preoral arm; Rud: adult rudiment; St: stomach.

Larval development

As in many other animals with indirect development, larval development in echinoids begins when the mouth opens (Parichy et al., 2009; Rahman et al., 2012; Carvalho et al., 2021). In *P. lividus*, this event took place at the so-called *early pluteus stage* (i.e., at around 40 hpf), upon the fusion of the tip of the archenteron with the ventral ectoderm, at the level of the stomodeum (Figures 7A,B). At this stage, the archenteron was characterized by a tripartite organization, constituting a functional digestive tract. This tripartite organization was noticeable thanks to the cardiac sphincter, which became clearly apparent at the *early pluteus stage*, as well as to the appearance of a second sphincter, the pyloric sphincter (Figure 7B), which will eventually separate the larval

stomach (above the pyloric sphincter) from the larval intestine (below the pyloric sphincter, close to the anus) (Annunziata et al., 2014). At the *early pluteus stage*, the larva also still exhibited red-pigmented cells scattered within the dorsal ectoderm (Figures 7A,B), and these pigmented cells will persist until metamorphosis (Figures 7N,O). Likewise, by this stage, the animal pole domain had extended further into an oral hood (Figure 7B), which protruded above the mouth, and this structure will also persist until metamorphosis (Figure 7N).

By 48 hpf (or 2 days post-fertilization, 2 dpf), the larva had elongated along the dorsal-ventral axis (i.e., from the mouth to the apex) (Figure 7C). The larva had 2 arms positioned posteriorly, on the ventral side, indicating that it reached the *2-arm pluteus stage* (Figures 7C,D). The 2 arms are

called the left and the right postoral arms (Thet et al., 2004; Smith et al., 2008), and they delimited, between them, what we named the postoral region. At this stage, the cardiac and pyloric sphincters were clearly constricted, demarcating three compartments within the digestive tract, from the mouth to the anus: the esophagus, the stomach, and the intestine (Figure 7E). At 3 dpf, the larva had grown one additional pair of arms, located anteriorly on the ventral side, at the edges of the oral hood (Figures 7F,G). The emergence of these two additional arms, called the left and the right anterolateral arms (Thet et al., 2004; Smith et al., 2008), marked the beginning of the 4-arm *pluteus* stage. At this stage, the epithelium of the digestive tract became thinner (Figure 7H), and the sphincters began to function (for details on muscle development see the myogenesis section below). Starting at the 4-arm *pluteus* stage the larvae thus began to feed, as demonstrated by the presence of algae in their stomach and intestine, while in younger larvae, algae were present exclusively in the mouth but were not swallowed (data not shown).

Between 3 and 10 dpf, no significant morphological changes were detected, and the larvae thus remained at a so-called 4-arm *pluteus* stage until 10 dpf (Figures 7I,J). However, between 3 and 10 dpf, the four arms of the larvae elongated (Figures 7G,I) and their stomach increased in size (Figures 7F,I), thereby leading to the broadening of the larval apex, at the level of the stomach, along both the anterior-posterior and the left-right axes (Figure 7I). As development proceeded, the only part of the digestive tract that continued to enlarge until metamorphosis was the stomach and its surrounding larval ectodermal region (Figures 7I–O). The development of the digestive tract will thus not be discussed any further. After the 4-arm *pluteus* stage, the larvae developed a third pair of arms called the left and the right posterodorsal arms (Thet et al., 2004; Smith et al., 2008). These arms formed in a posterior and dorsal position relative to the anterolateral arms, and their emergence marked the beginning of the 6-arm *pluteus* stage (Figures 7K,L), which began at around 10 dpf and lasted until approximately 15 dpf. Subsequently, starting at around 15 dpf, the larva developed a fourth and last pair of arms, called the left and the right preoral arms (Thet et al., 2004; Smith et al., 2008). The preoral arms developed posterior to the anterolateral arms, on the ventral side of the oral hood, and they will be maintained, along with the other three pairs of arms, until metamorphosis. The development of the preoral arms indicated that the larvae entered the 8-arm *pluteus* stage, which lasted for about 2 weeks (Figures 7M–O). Through the 6-arm and 8-arm *pluteus* stages, a structure on the left side of the stomach, called the rudiment and corresponding to the anlage of the future sea urchin adult, further considerably increased in size (Figure 7M) (for details on rudiment formation see the coelomogenesis and adult rudiment ontogeny sections below). Due to the presence of this structure and its growth through time, the stomach region of the 8-arm *pluteus* stage larva expanded and acquired a cuboidal shape (Figures 7M,O). In

addition to the rudiment, the larva further developed additional structures of the future adult on its right side, such as the pedicellariae and the genital plates (for details on the formation of other adult structures see the development of complementary adult structures section below).

Ciliogenesis in *Paracentrotus lividus* embryos and larvae

Upon hatching, sea urchin embryos and larvae swim in the water column using ciliary beating (Strathmann, 1971). To describe the ciliated structures of *P. lividus* embryos and larvae, we next performed an immunohistochemical assay using anti-acetylated α -tubulin antibodies. During embryonic development, *P. lividus* embryos first started to develop cilia at the mid-blastula stage (Figure 8A). It was only at this stage that we started detecting, on the apical surface of some embryonic cells, the presence of a unique cilium (Figure 8A). At this stage, already, these cilia were further functional and capable of metachronal beating, as demonstrated by the rotative movement at the mid-blastula stage of the embryos within their fertilization envelope (data not shown). As development proceeded, every cell of the embryo eventually formed a unique cilium (Figure 8B), and, upon hatching, these cilia allowed the embryos to swim freely in the water column. Furthermore, starting at the early mesenchyme blastula stage, the cilia located in the animal pole domain grew longer than those present on other cells of the embryo. By the late mesenchyme blastula stage, these animal pole cilia reached a size of about 100 μ m and formed a conspicuous patch of long, immotile cilia referred to as the apical tuft (Figure 8C). During gastrulation, the cells invaginating into the blastocoel and constituting the archenteron further conserved their short cilia on their apical surface. These short cilia thus lined the lumen of the archenteron (Figure 8D) and subsequently that of the functional digestive tract of the larva, until metamorphosis (Figures 8E,F,I–K).

At the 2-arm *pluteus* stage, the larvae still exhibited the long immotile cilia of the apical tuft and cilia on all other cells of the outer epithelium as well as in the lumen of the archenteron (Figure 8E). As development proceeded, the long immotile cilia of the apical tuft regressed and completely disappeared during the 4-arm *pluteus* stage (Figure 8F). In addition, the distribution of the cilia on the outer epithelium of the larva progressively changed. During the 4-arm *pluteus* stage, the epidermal cells constituting the ventral and dorsal epithelium remained squamous and shortened their cilia, while those along the lining of the anterolateral and postoral arms as well as those on the ventral edge of the oral hood (i.e., all the cells located at the interface between the ventral and the dorsal ectoderm) adopted a cuboidal shape and continued to bear medium-sized cilia (Figure 8F). Furthermore, the cuboidal cells started to organize themselves into a compact row (Figures 8G,H),

resulting in a significant local increase of ciliary density (Figures 8F,G). This row of tightly-packed ciliated cells is commonly referred to as the ciliary band (Slota et al., 2020), although some authors refer to it as the neotroch (Nielsen, 1998).

During the 6-arm and 8-arm *pluteus* stages, the ciliary band extended along the newly developing posterodorsal and preoral pairs of arms (Figures 8I–K), and additional ciliated structures, called the epaulettes, emerged from the ciliary band (Figures 8I–S). At the 6-arm *pluteus* stage, patches of ciliary band spread towards the dorsal side of the larva, on both the right and the left sides (Figure 8L). These patches spread from the hinges between the anterolateral and the posterodorsal arms as well as between the postoral arms and the postoral region (Figures 8L,M). As development proceeded, the emerging patches progressively isolated themselves from the ciliary band (Figure 8N) and elongated along the left-right axis of the larva (Figure 8O). They further migrated either anteriorly, spreading from underneath the anterolateral and the posterodorsal arms, or posteriorly, spreading from below the postoral arms and the postoral region. Thus, starting early during the 8-arm *pluteus* stage, the larva was characterized by a complex ciliary band outlining the oral region and by four large, independent patches of ciliated cells corresponding to the two anterior and the two posterior epaulettes (Figures 8I,J,O). During the 8-arm *pluteus* stage, the four epaulettes further continued to extend laterally, adopting an arc-shaped conformation (Figures 8J,K). They also thickened considerably and increased their ciliary density (Figures 8J,K,P,Q). During this process, the cilia of the epaulettes grew in length, reaching a size longer than the cilia of the ciliary band (Figure 8K). The two posterior and the two anterior epaulettes also eventually fused, respectively, at the level of the larval anus (Figures 8R,S) and on the opposite anterior side (Figure 8K). Late during the 8-arm *pluteus* stage, the epaulettes thus covered most of the circumference of the larval stomach region (Figure 8K), being interrupted only in two areas on each side of the larva. These two areas are referred to as the lateral fields (Gosselin and Jangoux, 1998), and they were outlined by two large folds of ciliary band located on each side of the larva between the postoral and the posterodorsal arms (Figures 8J,K).

Skeletogenesis in *Paracentrotus lividus* embryos and larvae

In *P. lividus*, the formation of the larval endoskeleton began at the early *gastrula* stage, with the SM cells extending filopodia towards each other (Figures 9A,B). The extension of filopodia was detectable initially in the ventrolateral clusters and in the ventral and dorsal chains (Figure 9B), before it took place also in the lateral chains. The filopodia fused the SM cells together and generated long syncytial cables, onto which a spicular matrix subsequently accumulated, allowing calcium carbonate deposition and formation of calcified skeletal elements (Figures 9C–L')

(Okazaki, 1965; Decker and Lennarz, 1988). The first of these calcified elements appeared at the *mid-gastrula* stage in the two ventrolateral clusters, in the form of a calcite crystal of rhombohedral shape (Figures 9C,D). By the *late gastrula* stage, each crystal had developed three smooth, rounded rods, forming a triradial spicule on each side of the embryo (Figures 9E,F). Each rod had elongated in the direction of the a-axis of the calcite crystal (Kitajima and Urakami, 2000) and formed an angle of 120° with the two other rods. By the *prism* stage, each rod had further elongated along the a-axes, on both the left and right sides of the embryo, generating two mirror triradial skeletal pieces (Figures 9G,H). Each of these pieces was thus constituted of three elongated skeletal rods referred to as: 1) the ventral transverse rod, which grew along the vegetal and ventral side of the embryo (Figure 9G), 2) the dorsoventral connecting rod, which elongated towards the animal pole and along the ventral side of the embryo (Figures 9G,H), and 3) the body rod, which formed along the vegetal side of the embryo towards the apex (Figures 9G,H) (MacBride, 1911; Smith et al., 2008). Of note, at this stage, we further observed that the dorsoventral connecting rods were bent towards the ventral ectoderm at the level of the stomodeum (Figure 9H). The site of this bent marked the limit between the dorsoventral connecting rods and the anlage of the anterolateral rods (Figure 9H), which will later support the anterolateral arms. We further observed, at this stage, the anlage of the postoral rods, which will support the postoral arms. The postoral rods were pointing towards the ventral side of the embryo, in extension of the body rods (Figure 9H).

During the subsequent larval period, the organization of the endoskeleton became increasingly more complex (Figures 9I–L'). At the 2-arm *pluteus* stage, no additional skeletal pieces were observed, but each of the existing rods elongated to varying degrees. For instance, the postoral rods extended to form the anlage of the postoral arms, and the body rods elongated to touch each other at their dorsal extremities, giving the larval apex its distinctive pointy shape (Figures 9I,I'). Likewise, the anterolateral rods expanded to support the oral hood (Figure 9I), however they only individualized and spread into the anterolateral arms at the 4-arm *pluteus* stage. The 4-arm *pluteus* stage was further marked by a significant extension of the postoral arms and rods (Figures 9J,J') as well as by the emergence of another branching at the junction between the dorsoventral connecting rods and the anterolateral rods. This new branching resulted in two short rods extending towards the apex on each of the lateral sides of the stomach (Figures 9J', O). These two short rods are respectively referred to as the right and the left recurrent rods (MacBride, 1911).

Thereafter, three new skeletal elements appeared, each one of them independent of the rods already in place. These new skeletal elements were the two posterodorsal spicules and the dorsal arch (MacBride, 1911; Smith et al., 2008). The posterodorsal spicules formed on each side of the larva, just above the junctions between the ventral transverse, dorsoventral connecting, postoral, and body rods (Figures 9K,K',M,N). The dorsal arch formed just above the stomach, in a dorsal-anterior position relative to the

esophagus (Figures 9K,K',O,P). Development of these new skeletal elements followed the same developmental trajectory as the previous skeletal rods. Between the 4-arm and 6-arm *pluteus* stages, they emerged as three new rhombohedral-shaped crystals, from which three smooth, rounded rods developed, one along each of the three a-axes (Figures 9M,O). At the level of the posterodorsal spicules, the rod facing out from the larva and referred to as the posterodorsal rod (Smith et al., 2008), will later support the posterodorsal arm (Figures 9K,K',M,N). This rod extended earlier than the other two rods of the posterodorsal spicules, and its extension marked the beginning of the 6-arm *pluteus* stage (Figure 9K'). At the level of the dorsal arch, the two rods facing the oral hood also extended earlier than the one facing the apex (Figures 9O,P). These two rods extended first laterally towards the anterolateral rods. Then, once they reached the edge of the esophagus, they bent along a 120° angle and extended ventrally, thereby giving rise to the anlage of the preoral rods (Figure 9K').

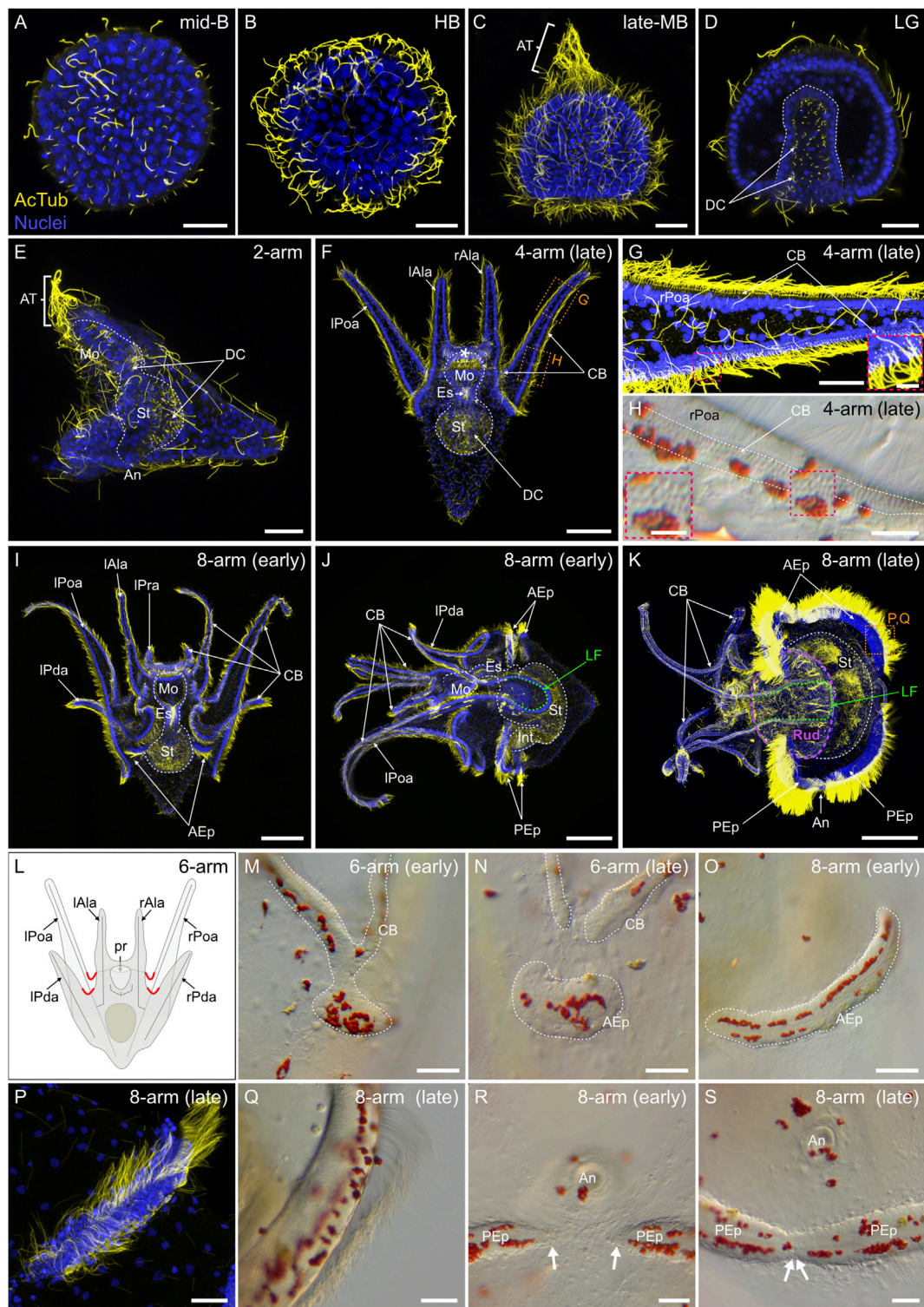
As development proceeded, the preoral rods protruded outside the ventral side of the oral hood and generated the preoral arms, hence marking the beginning of the 8-arm *pluteus* stage (Figures 9L,L'). At this stage, the posterodorsal rods were considerably extended, and additional rods were formed from the posterodorsal spicules and the dorsal arch. At the level of the posterodorsal spicules, for instance, two smooth rods were now facing the inside of the larval body and elongated both above and below the stomach, into what we referred to as the anteroventral and the anterodorsal transverse rods (Figures 9L,L',Q). Likewise, at the level of the dorsal arch, the smooth rod facing the apex extended above the stomach into a rod that we named the anteromedial rod (Figures 9L,L',Q). The 8-arm *pluteus* stage was further marked, at the tip of the apex, by the rupture of the body rods (Figure 9R), which was concomitant with a significant enlargement of the larval body at the level of the stomach region (Figure 9L). It is worth noting that we did not identify any fenestrated skeletal rods in the *P. lividus* larva. Instead, the rods of the *P. lividus* larva were full and spiny (Figure 9S), which is similar to what has been observed in some other sea urchin species (Wray, 1992). Supplementary Figure S2 provides a scheme highlighting all the different larval skeletal rods along with fixed landmarks to facilitate identification.

Myogenesis in *Paracentrotus lividus* embryos and larvae

We next investigated muscle development in *P. lividus* during the embryonic and larval periods. For this, we used two complementary approaches. First, we carried out *in situ* hybridization assays for the muscle terminal differentiation gene *myosin heavy chain* (*mhc*) (Wessel et al., 1990). Second, we took advantage of the enrichment of F-actin in muscles and performed F-actin immunohistochemistry assays using a rhodamine-

labeled phalloidin derivative. The expression of the *mhc* gene was the first to be detected in embryos, at the *prism* stage (Figures 10A,B). At this stage, *mhc* staining was detected at the tip of the gut on the oral side and, more subtly, at the level of the cardiac sphincter (Figures 10A,B). By the 2-arm *pluteus* stage, *mhc* staining was visible in the muscle fibers extending around the esophagus as well as in those surrounding the cardiac sphincter (Figures 10C,D). At this stage, we also started detecting phalloidin staining, which revealed a signal in circumferential fibers surrounding the esophagus (Figure 10E). The signal in these muscle fibers, referred to as the circumesophageal muscles (Annunziata et al., 2014), became more conspicuous right at the beginning of the 4-arm *pluteus* stage (Figure 10F), the stage at which the larvae started feeding, swallowing microalgae using the contraction and relaxation movements of the muscles surrounding the esophagus and the cardiac sphincter (Supplementary Video S1). During the 4-arm *pluteus* stage, the anatomical organization of the larval muscles did not significantly change (Figures 10F,G,K,M). However, the circumesophageal muscles accumulated more F-actin (Figures 10F,G), increased in number around the esophagus (Figure 10M), and started to be distinguishable as a series of thin stripes under a regular transmitted light microscope (Figure 10K).

By the end of the 4-arm *pluteus* stage and during the 6-arm *pluteus* stage, several additional muscles appeared. These muscles were located chiefly in the oral hood and along the circumesophageal muscles (Figures 10G,H,L–N), and they continued to develop during the 8-arm *pluteus* stage (Figures 10I,J,O–Q). In the oral hood, a first new pair of muscles emerged at the base of the left and the right anterolateral arms (Figure 10M). These muscles were identified as those called the anterior dilator muscles by Strathmann (1971) or the star-shaped muscles by Dyachuk and Odintsova (2013). By the 8-arm *pluteus* stage, these muscles were joined by two additional left and right muscles projecting into the left and the right preoral arms (Figures 10N,P,Q). We here referred to these muscles as the preoral dilator muscles, with the idea that they likely have the same function as the anterior dilator muscles. At the level of the circumesophageal muscles, between the end of the 4-arm *pluteus* stage and the 8-arm *pluteus* stage, three additional pairs of lateral muscles further formed, on both the left and the right sides of the larva (Figures 10L–O,Q). The most ventral of these muscle pairs, i.e., the posterior dilator muscles (Strathmann, 1971), extended to the rim of the mouth and connected the anterior dilator muscles (Figures 10L,N,O,Q). The intermediate pairs, which we referred to as the lateral muscles, projected to the larval epidermis (Figures 10L,N,O,Q). Last, the most dorsal pair, referred to as the ventrolateral processes (Burke and Alvarez, 1988) or the longitudinal musculature (Dyachuk and Odintsova, 2013), extended dorsally and connected the esophagus with the stomach (Figures 10M–O,Q). At the 8-arm *pluteus* stage, we were further able to identify additional muscles associated with the digestive tract.

**FIGURE 8**

Ciliogenesis in *Paracentrotus lividus* during the embryonic and larval periods. Developmental stages are as follows: (A) mid-blastula stage (mid-B); (B) hatched blastula stage (HB); (C) late mesenchyme blastula stage (late-MB); (D) late gastrula stage (LG); (E) 2-arm pluteus stage (2-arm); (F–H) 4-arm pluteus stage (4-arm); (I–K, O–S) 8-arm pluteus stage (8-arm); (L–N) 6-arm pluteus stage (6-arm). The use of (early) or (late) associated with the stage names simply highlights here more specific periods during the 4-, 6- or 8-arm pluteus stages. In (A–G, I–K, P), images are maximum intensity projections of confocal z-stacks of embryos and larvae co-labeled for acetylated α -tubulin (cilia; yellow) and DNA (nuclei; blue), and they

(Continued)

FIGURE 8 (Continued)

correspond to projections of the entire specimen, except for (D) that is a cross-section through the embryo. In (H,M–O,Q–S), images were acquired using light microscopy. (L) Schematics of a larva at the 6-arm pluteus stage illustrating in red the areas of the ciliary band that will bud to form the epaulettes. In (A–D), embryos are in lateral view with the animal pole up. In (E,J,K), larvae are in left view, with the anterior side up and the ventral side left. In (F,I), larvae are in anterior view, with the ventral side up. (G,H) Close-ups of the ciliary band of a late 4-arm pluteus stage larva, corresponding to the regions outlined by orange boxes in (F). ((G) inset, (H) inset), Close-ups of the ciliary band to highlight the distribution of cuboidal cells and their associated cilia. (M–O) Close-ups of a ciliary band bud and its related epaulette during the 6- and 8-arm pluteus stages. (P,Q) Close-ups of the anterior epaulette in a larva at a late 8-arm pluteus stage, corresponding to the region outlined by the orange box in (K). (R,S) Close-ups of the posterior epaulettes in a larva at the begin and at the end of the 8-arm pluteus stage, respectively. In (D), the white dotted line outlines the archenteron and, in (E) (F), (I–K), the digestive tract. In (F), the white asterisk marks the oral hood. In (H), white dotted lines delineate the three rows of cuboidal cells and their associated cilia. In (J,K), the green dotted line indicates the position of the lateral field. In (K), the purple dotted line outlines the adult rudiment. In (M–O), the white dotted line highlights the ciliary band and the developing epaulette. In (R), white arrows mark the posterior end of the two posterior epaulettes and in (S) the site of fusion of the two posterior epaulettes. Scale bar: (A–E,G,M–N,P–S) 30 μ m; (F) 50 μ m; ((G) inset, (H) inset) 7.5 μ m; (I) 15 μ m; (I–K) 150 μ m. AcTub: acetylated α -tubulin; AEp: anterior epaulette; An: anus; AT: apical tuft; CB: ciliary band; DC: digestive tract cilia; Es: esophagus; Int: intestine; lAla: left anterolateral arm; LF: lateral field; lPda: left posterodorsal arm; lPoa: left postoral arm; lPra: left preoral arm; Mo: mouth; PEp: posterior epaulette; pr: postoral region; rAla: right anterolateral arm; rPda: right posterodorsal arm; rPoa: right postoral arm; Rud: adult rudiment; St: stomach.

Among these muscles were those associated with the pyloric and anal sphincters (Figures 10R,T). These muscles initially formed by the end of the 4-arm pluteus stage (data not shown), but became clearly distinguishable with phalloidin staining only much later in development. In addition, while the muscles associated with the cardiac sphincter were found embedded within the circumesophageal muscles (Figure 10M), those of the pyloric and anal sphincters corresponded to individual and independent ring-shaped muscles (Figure 10R). At the 8-arm pluteus stage, we also found two other types of muscles to be associated with the digestive tract: a pair of muscles located on each side of the stomach that we named the lateral stomach muscles (Figures 10S,T) and several thin muscle fibers extending around the digestive tract that we referred to as mesenteries (Figure 10T).

Coelomogenesis in *Paracentrotus lividus* embryos and larvae and emergence of the adult rudiment

One important feature of *P. lividus* larval development was the ontogeny of the larval coeloms, from which the adult body plan subsequently arose. As in many other sea urchins, coelomogenesis in *P. lividus* took place by enterocoely, meaning that the coelomic compartments initially formed by evagination from the archenteron (Technau and Scholz, 2003). This process started at the prism stage, at the tip of the archenteron (Figure 11A). The evaginating cells thus formed a coelomic sac covering the tip of the archenteron. Then, this sac progressively extended laterally, establishing, by the early pluteus stage, a bilobed-shaped structure (Figure 11B). At the early pluteus stage, the lobes were still connected to each other by an isthmus, and one lobe was positioned to the right side, while the other one was to the left side, of the digestive tract (Figure 11B). By the 2-arm pluteus stage, the lobes were completely separated from one another (Figure 11C), leading to the emergence of two independent, epithelial coelomic pouches, one on each side of the digestive tract, and which

are commonly referred to as, respectively, the right and the left coelomic pouch (Molina et al., 2013).

At subsequent stages, we noticed a certain heterochrony between the trajectories of the coeloms and the larval development, although we always observed the same sequence of events for both the coeloms and the larval development. We thus decided, for now long, not to refer to the larval stages anymore when describing the development of the coeloms and their subsequent related structures. Instead, we decided to use a specific staging scheme that is included as a subsection in Figure 3. Following the 2-arm pluteus stage, and despite the heterochrony, we thus always observed at the level of the coeloms: 1) a progressive elongation of the right and the left coelomic pouches along the esophagus (Figure 11D) and 2) the emergence of a duct-like structure extending from the left coelomic pouch towards the anterior larval epidermis (Figure 11E). This duct-like structure is referred to as the hydroporic canal, and it opened in the larval epidermis through a hole called the hydropore (Figure 11E) (Luo and Su, 2012). The presence of this anatomical structure defined what we referred to as the hydroporic canal stage, and the emergence of the hydroporic canal and the hydropore constituted the first landmarks of the left-right asymmetry of the larva, with these two structures forming only on the left side. Moreover, they were the first indication of the formation of the adult water vascular system and the first connection of the left coelomic pouch to the external environment (Luo and Su, 2012).

As development proceeded, both the right and the left coelomic pouches elongated towards the larval apex. By the time they reached the anterior part of the stomach, they displayed several distinct constrictions (Figure 11F). The appearance of these constrictions marked the constricted coelomic pouch stage. At this stage, the pouches started to segregate into distinct compartments, and the morphological events taking place in the left coelomic pouch became more elaborate than those occurring in the right coelomic pouch. For instance, at the constricted coelomic pouch stage, while the left coelomic pouch was characterized by two constrictions, the right

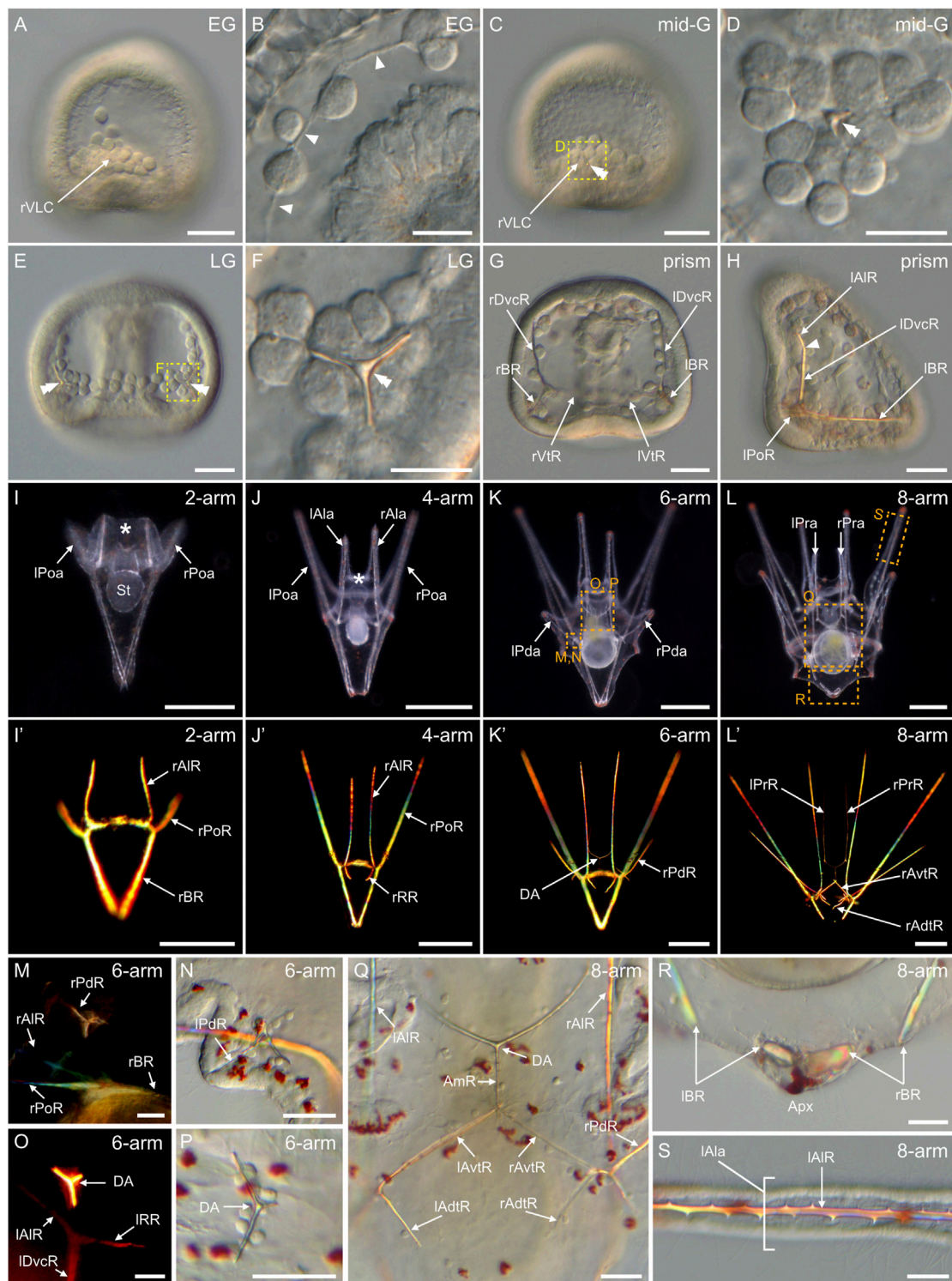


FIGURE 9

Skeletogenesis in *Paracentrotus lividus* during the embryonic and larval periods. Developmental stages are as follows: (A,B) early gastrula stage (EG); (C,D) mid-gastrula stage (mid-G); (E,F) late gastrula stage (LG); (G,H) prism stage (prism); (I,I') 2-arm pluteus stage (2-arm); (J,J') 4-arm pluteus stage (4-arm); (K,K',M–P) 6-arm pluteus stage (6-arm); (L,L',Q–S) 8-arm pluteus stage (8-arm). In (A–L,N,P–S), images were acquired using light microscopy either in bright-field for (A–H,N,P–S), or dark-field for (I–L). In (I'–L',M,O), images were obtained using polarized light to highlight the skeletal elements. In (A,C,H), embryos are in right view, with the animal pole up and, for (H), with the ventral side left. In (E,G), embryos are in (Continued)

FIGURE 9 (Continued)

ventral view, with the animal pole up. In (I–L'), larvae are in anterior view, with the ventral side up. (B) Close-up of the skeletogenic mesoderm cells and their related filopodia in a ventral chain. (D,F) Close-ups of a ventrolateral cluster to highlight the rhombohedral crystal in (D) and the triradiate spicule in (F), the two images corresponding, respectively, to the regions highlighted by yellow boxes in (C) and (E). (M–P) Close-ups of the regions outlined by orange boxes in (K) with larvae in lateral view, except for (M) where the larva is in anterior view. (M,N) Close-ups of the developing posterodorsal spicule. (O,P) Close-ups of the developing dorsal arch. (Q–S) Close-ups of the regions highlighted by orange boxes in (L) with larvae in anterior view. (Q) Close-up of the skeletal elements located in the vicinity of the larval digestive tract. (R) Close-up of the body rods in the most dorsal region of the larva. (S) Close-up of the non-fenestrated spicule of an anterolateral arm. In (B), arrowheads highlight the filopodia extended by skeletogenic mesoderm cells. In (C–F), double arrowheads mark the skeletal elements forming in the ventrolateral clusters. In (H), the arrowhead highlights the limit between the right dorsoventral connecting rod and the right anterolateral rod. In (I,J), the asterisk marks the oral hood. Scale bar: (A,C,E,G,H,M–S) 30 μ m; (B,D,F) 15 μ m; (I) 100 μ m; (J–L,J'–L') 200 μ m. AmR: anteromedial rod; Apx: apex; DA: dorsal arch; lAdtR: left anterodorsal transverse rod; lAla: left anterolateral arm; lAIR: left anterolateral rod; lAvtR: left anteroventral transverse rod; lBR: left body rod; lDvcR: left dorsoventral connecting rod; lPoa: left postoral arm; lPoR: left postoral rod; lPda: left posterodorsal arm; lPdR: left posterodorsal rod; lPra: left preoral arm; lPrR: left preoral rod; lRR: left recurrent rod; lVtR: left ventral transverse rod; rAdtR: right anterodorsal transverse rod; rAla: right anterolateral arm; rAIR: right anterolateral rod; rAvtR: right anteroventral transverse rod; rBR: right body rod; rDvcR: right dorsoventral connecting rod; rPoa: right postoral arm; rPoR: right postoral rod; rPda: right posterodorsal arm; rPdR: right posterodorsal rod; rPra: right preoral arm; rPrR: right preoral rod; rRR: right recurrent rod; rVLC: right ventrolateral cluster; rVtR: right ventral transverse rod; St: stomach.

coelomic pouch only had one (Figure 11F). At the subsequent stage, which we named the *stone canal stage*, each pouch had further considerably extended towards the mouth and the middle part of the stomach, and each pouch was now separated into several, clearly distinguishable coelomic compartments, on each side of the larval digestive tract (Figures 11G,H). On the left side, for instance, the coelomic pouch had given rise to three compartments, referred to, from the mouth to the stomach, as the left axocoel, the left hydrocoel, and the left somatocoel (Peterson et al., 2000; Smith et al., 2008). On the right side, the coelomic pouch had formed two compartments, called, from the mouth to the stomach, the right axohydrocoel and the right somatocoel (Peterson et al., 2000). On the left side, the left axocoel was further still connected, anteriorly, to the external environment, through the hydroporic canal and the hydropore, and it was connected, posteriorly, to the left hydrocoel by a thin, tubular structure referred to as the stone canal (Figures 11G,H) (Smith et al., 2008). On the right side, by contrast, the right axohydrocoel and somatocoel were not connected to the external environment, but they were still attached to one another by a thin isthmus (Figure 11G), which however disappeared soon thereafter (Figures 11J,K).

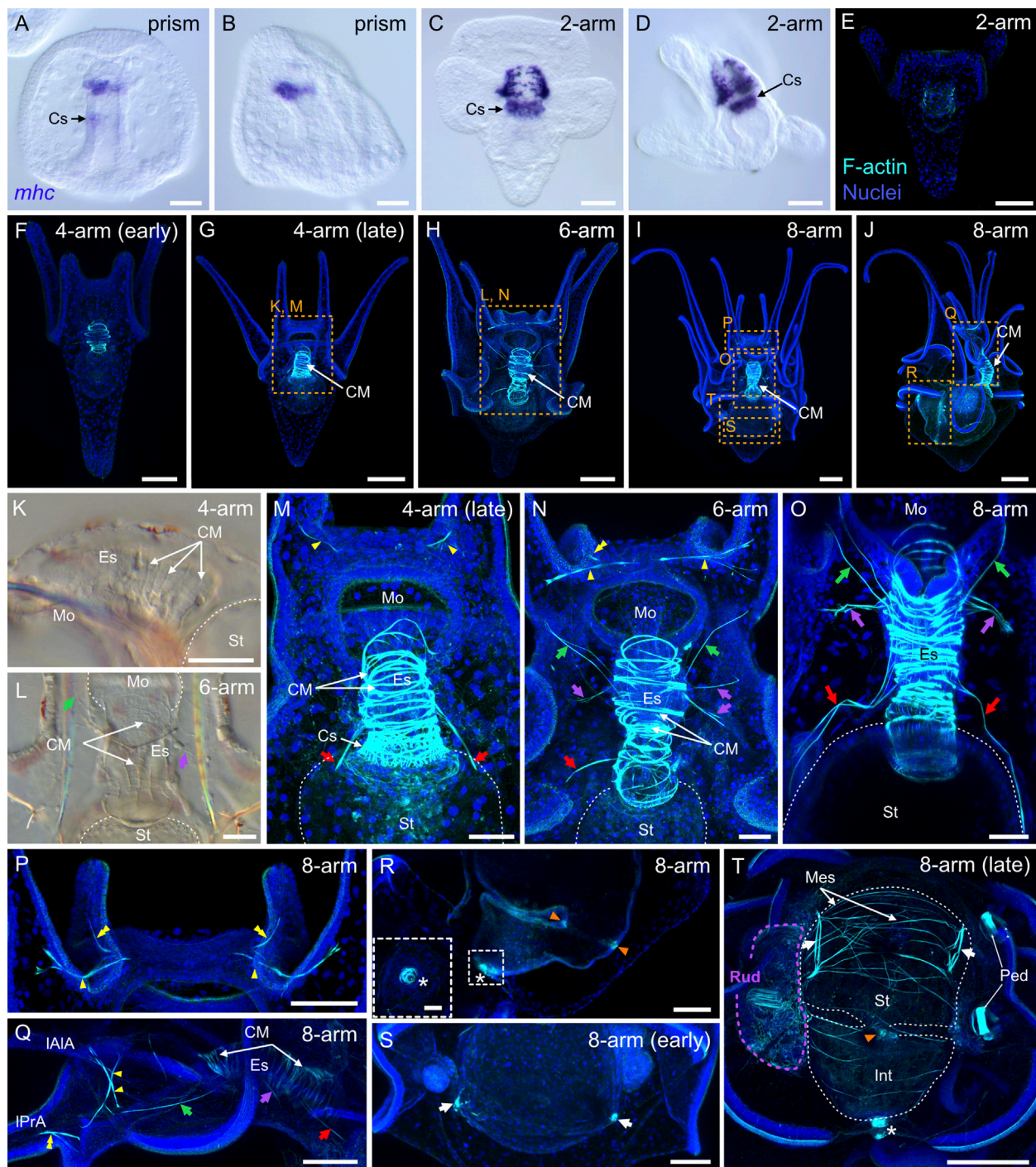
During subsequent development, the left and the right coelomic compartments continued to extend along the anterior-posterior axis of the larva (Figures 11I–K). On the left side, at the level of the larval ectoderm, we further started to observe a thickening and invagination of a portion of the epidermis located at the base of the left postoral and the left posterodorsal arms (Figure 11I). This invagination is referred to as the vestibule (Smith et al., 2008; Heyland and Hodin, 2014), and it will greatly contribute to the development of the adult rudiment (for details on adult rudiment development see the adult rudiment ontogeny section below). The appearance of this invagination marked the *vestibule invagination stage* (Figure 11I), and its subsequent contact with the left hydrocoel defined the *vestibule contact stage* (Figure 11J). At

the *vestibule contact stage*, several additional observations were made. For instance, through an immunohistochemistry assay carried out using the anti-acetylated α -tubulin antibodies, we revealed that the lumen of the hydropore, of the hydroporic canal, of the left axocoel, of the stone canal, and of the left hydrocoel (which are all components of the adult water vascular system) was packed with cilia, while the lumen of the left somatocoel, of the right axohydrocoel, and of the right somatocoel was deprived of cilia (Figures 11K–M). We further noted that the hydropore migrated from its initial left-sided position next to the esophagus (Figure 11H) towards a more medial position above the cardiac sphincter (Figure 11L). Finally, we also found that the left axocoel was significantly inflated, forming a large, coelomocyte-filled bag between the left hydrocoel and the hydropore (Figures 11K–N).

Adult rudiment ontogeny

In echinoids, although the left axocoel, the left somatocoel, the hydropore, the hydroporic canal, and the stone canal contribute to the development of adult tissues, formation of the adult rudiment, *per se*, on the left side of the larval stomach, chiefly involves the left hydrocoel and the larval vestibule (Smith et al., 2008; Heyland and Hodin, 2014). This section thus focuses on the complex morphogenetic changes occurring at the level of the left hydrocoel and the larval vestibule during adult rudiment ontogeny, even though mention of associated structures on the left side will be made when appropriate. By contrast, the ontogeny of the right coelomic compartments will not be treated here, as these coeloms do not significantly contribute to the development of adult structures (Ziegler et al., 2009; Ezhova et al., 2014).

At the *vestibule contact stage*, as mentioned above, the vestibule, composed of the thickened larval epidermis, of ectodermal origin, and the left hydrocoel, of mesodermal

**FIGURE 10**

Myogenesis in *Paracentrotus lividus* during the embryonic and larval periods. Developmental stages are as follows: (A,B) prism stage (prism); (C–E) 2-arm pluteus stage (2-arm); (F,G,K,M) 4-arm pluteus stage (4-arm); (H,L,N) 6-arm pluteus stage (6-arm); (I,J,O–T) 8-arm pluteus stage (8-arm). The use of (early) or (late) associated with the stage names simply highlights here more specific periods during the 4- or 8-arm pluteus stages. In (A–D), images were acquired using bright-field, differential interference contrast light, and they correspond to embryos and larvae labeled for the muscle terminal differentiation gene *myosin heavy chain* (*mhc*). In (E–J,M–T), images are maximum intensity projections of confocal z-stacks of larvae co-labeled for F-actin (muscles; cyan) and DNA (nuclei; blue), and they correspond to projections of the entire specimen. In (K,L), images were acquired using bright-field light microscopy. In (A), the embryo is in ventral view, with the animal pole up. In (B,D,J,K,Q,R), embryos and larvae are in left view, with either the animal pole up and the ventral side left in (B) or with the anterior pole up and the ventral side left in (D,K,Q,R) or with the anterior pole right and the ventral side up in (J). In (C,E–I,L–P,S,T), larvae are in anterior view, with the ventral side up. (K–T) Close-ups of the regions outlined by orange boxes in (G–J). (K–O,Q) Close-ups of the esophageal region. (P) Close-up of the oral hood. (R) Close-up of the intestinal region. (Continued)

FIGURE 10 (Continued)

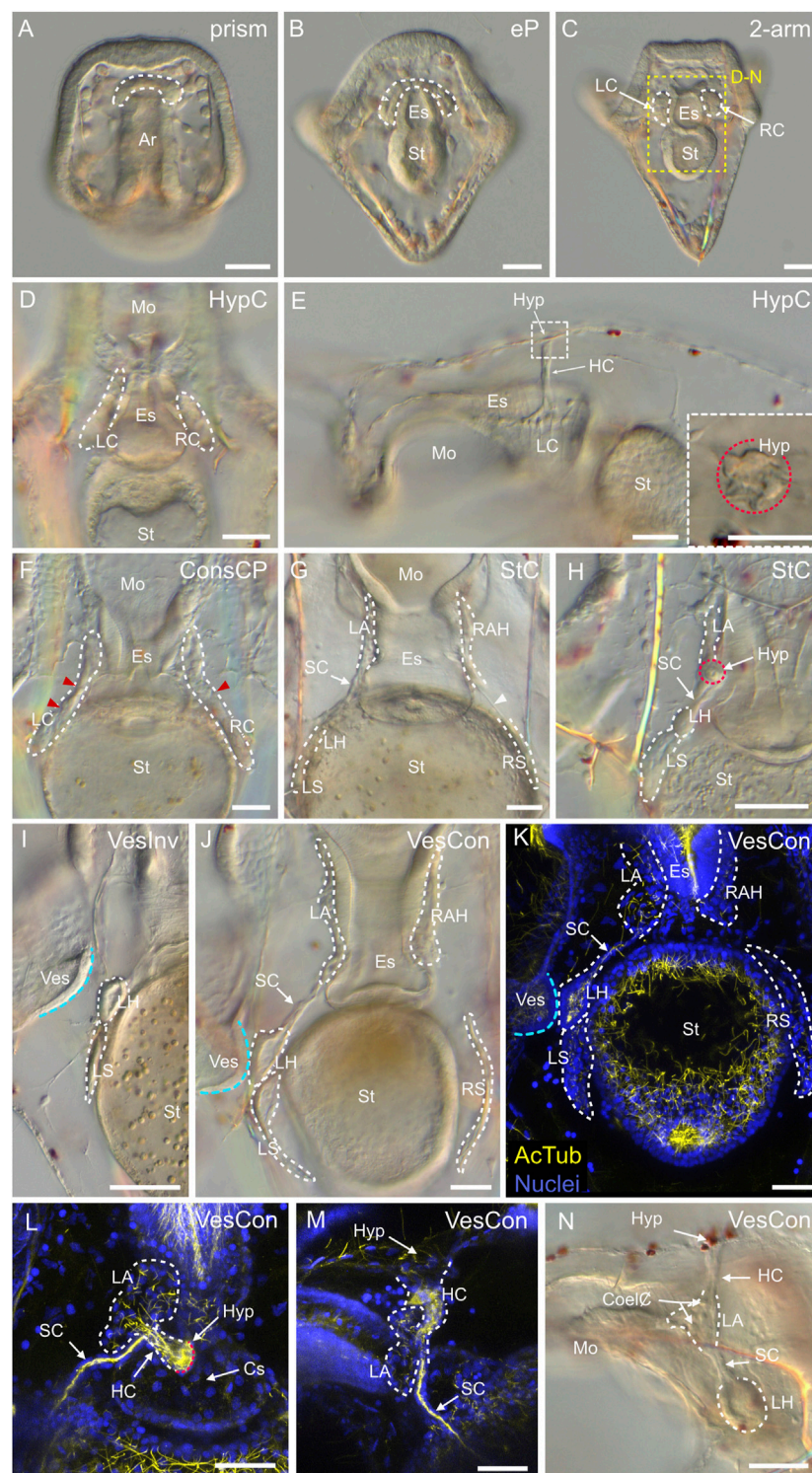
((R) inset) Close-up of the anal sphincter. (S,T) Close-ups of the stomach region. In (K–O,T), the white dotted line outlines the larval digestive tract. In (L,N,O,Q), green arrows highlight the posterior dilator muscles, and purple arrows mark the lateral muscles. In (M–O,Q), red arrows indicate the ventrolateral processes (or longitudinal musculature). In (M,N,P,Q), yellow arrowheads mark the anterior dilator muscles (or star-shaped muscles). In (N,P,Q), yellow double arrowheads highlight the preoral dilator muscles. In (R,T), orange arrowheads mark the pyloric sphincter, and the white asterisk marks the anal sphincter. In (S,T), white arrows indicate the lateral stomach muscles. In (T), the purple dotted line delineates the adult rudiment. In (H,J,M,N,P,Q,S,T), the F-actin staining detected along the ciliary band and the epaulettes corresponds to a counterstain of the apex of the cuboidal cells and thus not to muscle cells. Scale bar: (A–D,M–O) 30 μ m; (E,F,K,L,P–T) 50 μ m; (G–J) 100 μ m; ((R) inset) 10 μ m. CM: circumesophageal muscle; Cs: cardiac sphincter; Es: esophagus; Int: intestine; lAlA: left anterolateral arm; lPrA: left preoral arm; Mes: mesentery; Mo: mouth; Ped: pedicellariae; Rud: adult rudiment; St: stomach.

origin, were thus in contact. A larval anterior view revealed the C-shape of the vestibule (Figures 12A,B), while a larval left view disclosed the invagination of the vestibule (Figures 12A,C), on top of the left hydrocoel, which, at this stage, was a simple vesicle (Figures 12A,D). At the following stage, named the *vestibule flattened stage*, the epidermis of the vestibule flattened on the left hydrocoel (Figure 12E^A). The portion of the vestibule spread over the left hydrocoel corresponded to the vestibular floor, while the remaining vestibule epidermis, still in continuity with the larval epidermis, constituted the vestibular walls (Figure 12E^A). Thereafter, the larval epidermis started to close above the vestibular cavity, and the apical surface of the vestibular floor, in contact with the left hydrocoel, started to show folds (Figure 12F^A). This marked the *vestibule waving stage*. Closure of the larval epidermis induced the emergence of a hole on the larval epidermis, delineated by the vestibular lip (Figure 12F^B). Furthermore, at the level of the left hydrocoel, a critical morphogenetic reorganization took place at this stage. The left hydrocoel began folding at the *vestibule waving stage*, thereby taking a flower-like shape composed of five lobes and connected, at its center, to the left axocoel by the stone canal (Figure 12F^B). This reorganization marked the first stage in the acquisition of the adult pentaradial symmetry and highlighted the central role of the left hydrocoel (and hence of the mesodermal coelomic tissue) in the switch of animal body plan symmetry in *P. lividus*. The five lobes prefigured already the five ambulacra of the adult, and their respective position relative to that of the stone canal indicated that their identity was already defined, with the stone canal facing ambulacrum A and being located between ambulacra C and D (Supplementary Figure S1). Of note, we here used a regular clockwise Carpenter's nomenclature to identify the five lobes, taking into consideration that we observed the rudiment from the left side of the larva, which corresponds to the future oral side of the adult.

The next developmental stage, called the *5-fold mesoderm stage*, was characterized by the protrusion of the five lobes of the left hydrocoel into the vestibular floor (Figure 12G^A), which otherwise did not show any sign of folding or of pentaradial symmetry on its basal side (Figure 12G^A). This stage was observed during (Figure 12G^S) or after (Figure 12G^A) closure of the vestibular lip. Closure of the vestibular lip was often completed by this stage, although, in some larvae, a small bridge between the

larval ectoderm and the vestibular roof remained until later stages. Nevertheless, by the *5-fold mesoderm stage*, the vestibule was always composed of a roof, a floor, and walls, all of which were surrounding a cavity (Figure 12G^A). In addition, by this stage, the left hydrocoel had always undergone additional morphological changes. For instance, a lumen expanded within each of the five lobes (Figure 12G^B). These five lumens represented the anlage of the five radial canals of the adult water vascular system. Moreover, at the center of the left hydrocoel, the anlage of the future ring canal, which will later connect the five radial canals, was discernable (Figure 12G^B). However, at the *5-fold-mesoderm stage*, the ring canal was still C-shaped (Figure 12G^B) and thus not yet closed. Furthermore, at the *5-fold-mesoderm stage*, each of the lumen of the five lobes of the left hydrocoel was a direct prolongation of the lumen of the stone canal, which was still connected to the left axocoel, and therefore to the external environment through the hydroporic canal and the hydropore (Figure 12G^B). At this stage, the adult rudiment was thus already susceptible of experiencing a seawater flow.

Subsequently, the *5-fold ectoderm stage* was characterized by the complete folding of the vestibular floor onto the underlying left hydrocoel (Figure 12H^A). At this stage, both the apical and basal surfaces of the vestibular floor were folded (Figure 12H^A), and the vestibular floor thus exhibited, such as the left hydrocoel, a pentaradial symmetry (Figure 12H^B). At this stage, within the hydrocoel, the extremities of the C-shaped ring canal also fused into a proper ring, and, within the lobes, the radial canals became more conspicuous (Figure 12H^B). Thereafter, the five lobes and their associated inner radial canals extended even further, pushing the vestibular floor into the vestibular cavity (Figure 12I^A). As the lobes elongated, they became recognizable as the primary podia, another component of the water vascular system (MacBride, 1918). Accordingly, this stage was named the *primary podia stage*. The primary podia were composed of two tissue layers: on the outside, the vestibular floor, of ectodermal origin, and on the inside, the left hydrocoel, of mesodermal origin and delineating the radial canals (Figures 12I^A–I^D). By the *primary podia stage*, the left somatocoel also extended anteriorly along the stomach and underneath the left hydrocoel and adopted a pentaradial symmetry. At this stage, the left somatocoel was discernable as five buds alternating with the five primary podia (Figure 12I^A).

**FIGURE 11**

Coelomogenesis in *Paracentrotus lividus* during the embryonic and larval periods. Developmental stages are as follows: (A) prism stage (prism); (B) early-pluteus stage (eP); (C) 2-arm pluteus stage (2-arm); (D,E) hydroporic canal stage (HypC); (F) constricted coelomic pouch stage (ConsCP); (G,H) stone canal stage (StC); (I) vestibule invaginated stage (VesInv); (J–N) vestibule contact stage (VesCon). In (A–J,N), images were acquired using bright-field light microscopy. In (K–M), images are maximum intensity projections of confocal z-stacks of larvae co-labeled for acetylated α -tubulin (cilia; yellow) and DNA (nuclei; blue), and they correspond to projections of the entire specimen. In (A), the embryo is in ventral view, with the animal pole up. In (B–D,F–L), larvae are in anterior view, with the ventral side up. In ((E) inset, (M,N)), larvae are in left view, with the ventral side to the (Continued)

FIGURE 11 (Continued)

left. (D–N) Close-ups of the region outlined by the yellow box in (C). (D,F,G,J,K) Close-ups of the larval digestive tract to show the right and the left coelomic pouches. (E,H,I,L–N) Close-ups of the left coelomic pouch region. In (A–D,F–N), white dotted lines outline the right and the left coelomic pouches as well as their derivatives. In ((E), inset (H,L)), the red dotted line delineates the hydropore. ((E) inset) Close-up of the hydropore in anterior view. In (F), red arrowheads highlight constrictions within the coelomic pouches. In (G), the white arrowhead marks the isthmus between the right axohydrocoel and the right somatocoel. In (I–K), the cyan dotted line highlights the vestibule. Scale bar: (A–N) 30 μ m; ((E) inset) 7.5 μ m. AcTub: acetylated α -tubulin; Ar: archenteron; Coel: coelomocyte; Cs: cardiac sphincter; Es: esophagus; HC: hydroporic canal; Hyp: hydropore; LA: left axocoel; LC: left coelomic pouch; LH: left hydrocoel; LS: left somatocoel; Mo: mouth; RAH: right axohydrocoel; RC: right coelomic pouch; RS: right somatocoel; SC: stone canal; St: stomach; Ves: vestibule.

As developmental proceeded, the primary podia continued to extend into the vestibular cavity. As they became longer, they progressively bent inward into the cavity, ultimately touching each other at their tips (Figure 12J^P). This marked the *primary podia touching stage*. Optical sections through the podia and the rudiment at this stage revealed the radial canals at the center of the podia (Figures 12J^P,J^{D+}) as well as the ring canal, which was now fully formed and functional and started to contain coelomocytes (Figure 12J^{D+}). Subsequently, the continuous growth of the podia forced them to bend even further and to twist within the vestibular cavity (Figure 12K^D). This marked the *primary podia twisting stage*. At this stage, the epidermis at the tip of the primary podia started to thicken and to adopt an arrow-like shape (Figure 12K^P). An additional characteristic of this stage was the emergence of five groups of four spine sacs, in alternation with the five primary podia (Figure 12K^P), hence resulting in a total of twenty spine sacs within the rudiment.

At the following developmental stage, called the *primary podia papilla stage*, the most easily recognizable morphological change was the appearance, at the tip of the primary podia, of a fully formed papilla (Figures 12L^P,M). At this stage, the primary podia were thus composed of a stem and a papilla (Figure 12M), the latter being a flat, discoid structure used in the adult for adhesive attachment as well as for mechano-, chemo-, and photo-reception (Ullrich-Lüter et al., 2011). By this stage, each spine sac also elongated, giving rise to the anlage of the so-called definitive (or adult) spines (Figure 12M), as they will be maintained through metamorphosis and in adult life (Hyman, 1955; Emlet, 2010). In addition, at the level of the water vascular system, a growing number of coelomocytes became visible at the *primary podia papilla stage*, both in the ring canal and in the radial canals (Figure 12N^{D+}). A water flow was now clearly visible, with external water being pumped into the water vascular system by the left axocoel (Supplementary Video S2). Coelomocytes were thus carried back and forth by the water flow (Supplementary Video S3), and the podia were mobile within the vestibular cavity as they were injected with water (Supplementary Video S4).

The next stage was characterized by the emergence of a new set of spines called the juvenile spines (Figures 12O,P), which correspond to spines that will be maintained through metamorphosis, but will not persist in adult life (Emlet, 2010).

The appearance of these new spines marked the *juvenile spine stage*. The juvenile spines formed as a pair at the base of each of the five primary podia, with one juvenile spine on each side of the primary podium stems (Figures 12O,P). This resulted in a total of ten juvenile spines within the rudiment. At the *juvenile spine stage*, the podia also continued to expand, leading to the shrinking of their stem, which developed an accordion-like aspect (Figure 12P). The definitive spines also extended (Figure 12P), and the rudiment significantly increased its overall size (Figure 12O). The last stage of rudiment development corresponded to the *mature rudiment stage*. At this stage, the rudiment had a diameter of about 350 μ m. It was bigger in size than the larval stomach and occupied almost the complete left side of the larva (Figure 12Q^A). At this stage, the juvenile spines elongated and reached about half the size of the definitive spines (Figures 12R,S). Of note, although the previous steps of rudiment development were largely heterochronous with respect to the development of the larva, the *mature rudiment stage* was exclusively observed once the larvae were fully developed, i.e., by the end of the *8-arm pluteus stage*.

Skeletogenesis and myogenesis in the adult rudiment

During rudiment development, several rudiment-specific skeletal structures and muscles were also formed. Skeletogenesis in the rudiment usually started at the *primary podia twisting stage* with the emergence of spicules associated with the definitive spines (Figure 13A). As in the larva, most skeletal elements formed in the rudiment from an initial crystal that subsequently developed smooth rods along each of its a-axes. This was the case, for instance, for the definitive spines (Figure 13A), but not every rudiment skeletal piece emerged from a new, independent crystal. Some branched out indeed directly from neighboring larval rods. In the case of the definitive spines, the spicules that emerged from the crystals were moreover peculiar, in that they displayed a unique hexaradiate structure (i.e., a structure with six apices instead of three, as seen for all other larval or rudiment spicules) (Figures 13B,C). Development of the hexaradiate spicules was characterized by the emergence, from the initial crystal, of six smooth skeletal rods that grew

laterally, in the same plane, for a short distance (Figure 13C). A new branch then extended perpendicular to the first ones from the center of the hexaradiate spicule (Figure 13D). From the top of this perpendicular branch, three processes grew outward, generating a three-rayed star, from which an additional hexagon formed, parallel to the initial hexaradiate spicule, but smaller in diameter (Figures 13D,E). From this second hexagon, six branches extended longitudinally inside the spine sacs and towards the vestibular cavity (Figure 13E). These branches constituted the endoskeleton of the elongating definitive spines. They were periodically joined by regularly spaced stereomic bridges, thereby creating a long, fenestrated skeletal element (Figure 13E).

The next skeletal elements to develop were those associated with the primary podia, referred to as the primary podia skeletal disks (Figures 13F,G) (Formerly et al., 2021). The primary podia skeletal disks first emerged between the *primary podia twisting* and the *primary podia papilla* stages. They initially appeared as a single, triradiate spicule located at the base of the papilla. Then, two of the three apices of the spicule grew laterally, creating an arch (Figure 13F). The two growing apices eventually fused and gave rise to a disk (Figure 13G), before, due to subsequent branching events, the architecture of the disk became even more sophisticated (Figure 13H). Between the *primary podia twisting* and the *primary podia papilla* stages, additional triradiate spicules further started to form at the periphery of the rudiment, which constituted the first components of the future adult test (Figure 13I). These spicules subsequently underwent extensive branching and resulted, at the *mature rudiment* stage, in the establishment of very distinctive endoskeletal plates (Figure 13J). The names of these distinct endoskeletal plates depends on their position within the rudiment (Gordon, 1926). For instance, the plates forming at the base of the primary podia stem and the juvenile spines are referred to as the ocular plates, while these developing at the level of the definitive spines are the interambulacral plates.

At the *primary podia papilla* stage, the skeletal elements holding the juvenile spines also started to appear. Initially, the spicules at the origin of these elements arose as triradiate crystals (Figures 13K,L), even though most of them subsequently developed into tetraradiate spines (Figure 13N). The transition of an initial triradiate crystal to an elongated tetraradiate spine was a multi-step process. First, each of the three apices of the initial triradiate crystal grew laterally for a short distance. Then, halfway along each of the three smooth rods, a new branch emerged, which grew perpendicular to the initial plane of the triradiate spicule, i.e., towards the vestibular cavity (Figure 13M). Of these perpendicular branches, two usually continued to extend upwards, while the third one divided into two distinct branches before resuming its upwards growth (Figure 13M). As a result, most juvenile spines were composed of four longitudinal processes, which, like in definitive spines, were connected by regularly spaced stereomic bridges (Figure 13N). The last

skeletogenic event that we observed in the rudiment was the development of skeletal structures associated with the future masticatory apparatus. This event took place at the *juvenile spine* stage, in the five buds formed by the left somatocoel and located between the primary podia (Figure 13O). These buds correspond to the dental sacs (MacBride, 1903) and, at the center of each one of them, we identified a calcite crystal corresponding to the primordium of the future adult teeth (Figure 13O).

In addition to the skeletal structures, we also characterized the muscles that developed within the adult rudiment, carrying out an immunohistochemistry assay for F-actin. Myogenesis started in the rudiment at the *primary podia* stage with an accumulation of F-actin at the center of each emerging primary podium, revealing the presence of growing muscle fibers (Figure 13P). By the *primary podia papilla* stage, we were able to confirm the presence of these muscle fibers within each of the five primary podia as long muscle strands outlining the water vascular system (Figure 13Q). At the *juvenile spine* and *mature rudiment* stages, additional muscle fibers were found in other compartments of the water vascular system as well as at the level of the definitive spines (Figures 13R,S). At the center of the rudiment, our F-actin staining highlighted muscle fibers associated with the ring canal as well as with the radial canals, which extended from the ring canal to the stem of the primary podia (Figures 13R,S). In addition, at the base of each definitive spine, several muscle fibers were detected that were arranged in a circular manner (Figures 13R,S) and constituted the so-called ring muscles (Formerly et al., 2021).

Development of complementary adult structures: The pedicellariae and the genital plates

Apart from the rudiment, developing on the left side of the larval digestive tract, some additional adult structures further developed in the larva that persisted after metamorphosis. These structures included the pedicellariae and the genital plates as well as additional juvenile spines associated with the genital plates. The pedicellariae and three of the five genital plates developed on the right side of the larva (and thus on the opposite side of the rudiment), while the two other genital plates developed, respectively, at the level of the dorsal arch and near the apex (Figure 14A). All these structures usually developed once the larva had reached the *8-arm pluteus* stage and after coelomogenesis started, but their ontogeny was not linked to that of the larva, the coeloms, or the rudiment. As such, their development was thus not included in the general staging scheme or in the coeloms and rudiment development subsection in Figure 3.

The pedicellariae are a special type of appendages found in asteroids and echinoids, which are used to protect the animal (Hyman, 1955; Peters and Campbell, 1987). In *P. lividus*, we

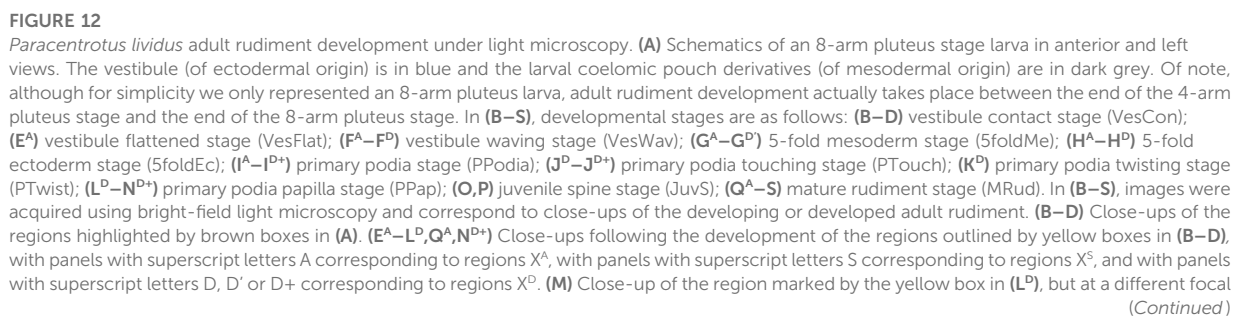


FIGURE 12 (Continued)

plane. (P) Close-up of the region highlighted by the yellow box in (O). (S) Close-up of the region outlined by the yellow box in (R). In (E^A–L^D, Q^A, N^{P+}), superscript letters refer to the position of the larva in order to observe the developing rudiment as presented, hence A (E^A, F^A, G^A, H^A, I^A, Q^A) refers to larva in anterior view (such as is (B)), S (F^S, G^S) refers to larva in left view, with a focal plane set at the surface of the vestibular floor (such as is (C)), and D (F^D, G^D, G^D, H^D, I^D, J^D, J^{D+}, K^D, L^D, N^{P+}) refers to larva in left view, but with a focal plane positioned at a deeper level than the vestibular floor (such as is (D)). (G^P) is the same as (G^D) but zoomed out and ((G^P) inset) is a close-up of the stone canal. (I^{P+}) and (J^{P+}) correspond to views even deeper than (I^D) and (J^D), and (N^{P+}) is at the same depth as (J^{P+}). In (O, R), the larva is in a tilted view and in (Q^A) a zoom of the larval apex is presented, with the larva in anterior view. In (B, C), the cyan dotted line outlines the vestibule. In (B, D), the white dotted line delineates the left hydrocoel. In (F^D, G^D, G^D, H^D, I^D–J^{D+}, N^{P+}), the letters @–@ identify the developing primary podia according to Carpenter's nomenclature (1884). In ((G^D, G^D, G^D) inset), blue dotted lines outline the position of the developing water vascular system. In (G^D), green dotted lines highlight the left axocoel, and in ((G^D) inset) red dotted lines mark the stone canal. In (H^A), red arrowheads mark the folded vestibule epidermis. In (H^D), blue dotted lines mark the ring canal and radial canals of the water vascular system. In (I^A), the yellow arrow marks one left somatocoel bud. In (K^D, L^D, M, P, S), green asterisks indicate the definitive spines, and red asterisks mark a primary podia papilla. In (M), the white dotted line delineates a primary podia papilla. In (P, S), magenta asterisks and white dotted lines mark the juvenile spines. In (Q^A), the magenta dotted line outlines the developed adult rudiment, and the white dotted line delineates the larval stomach. Scale bar: (B–E^A, K^D–M, O–S) 50 µm; (F^A–J^{D+}, N^{P+}) 30 µm; ((G^D) inset) 20 µm. Coel: coelomocyte; Epi: larval epidermis; HC: hydroporic canal; Hyp: hydropore; JS: juvenile spine; LA: left axocoel; LH: left hydrocoel; LS: left somatocoel; Mo: mouth; Pap: papilla; PP: primary podium; RaC: radial canal; RiC: ring canal; Rud: adult rudiment; SC: stone canal; St: stomach; Ves: vestibule; VesC: vestibular cavity; VesF: vestibular floor; VesL: vestibular lip; VesP: vestibular pore; VesR: vestibular roof; VesW: vestibular wall.

observed the development of one to four pedicellariae per larva, although, in some rare cases, no pedicellariae were formed. The development of the pedicellariae started by a condensation of mesenchymal cells below the larval epidermis, at the level of the branching points between the right posterodorsal and the right dorsoventral connecting rods and/or between the right postoral and the right dorsoventral connecting rods (Figure 14B). Soon thereafter, the condensed cells formed a well-differentiated bud protruding outside the larval epidermis (Figure 14C), with skeletal elements starting to develop inside the bud shortly after it was formed (Figure 14D). Subsequently, the bud segregated into three lobes (Figure 14E), which progressively differentiated into three calcified jaws, with an indented extremity and an inner skeleton characterized by a complex fenestrated architecture (Figures 14F,G). The jaws rapidly showed motility, being capable of opening and closing (Figures 14F,G; Supplementary Video S5). They were thus already functional in the larva. A labeling for F-actin moreover revealed that the pedicellariae had their own muscular system (Figures 14H–J). The first muscle fibers appeared in the buds of the pedicellariae when the three lobes started to individualize (Figures 14H,I). Then, once the lobes were fully developed, the pedicellariae were characterized by two sets of three muscles, connecting the jaws and allowing them to open and close (Figure 14J). These muscles are called the large adductor muscles, located near the indented extremities, and the thin abductor muscles, located closer to the stem (Peters and Campbell, 1987).

The genital plates are specific endoskeletal plates that, in the adult, form the most aboral part of the test and bear the gonopores, hence their name (see Figure 1E) (Hyman, 1955). According to Carpenter's nomenclature, the genital plates are identified as AB, BC, CD, DE, and EA due to their interambulacral position in the adult (Supplementary Figure S1) (Carpenter, 1884). In the larva, the genital plates AB, CD, and DE were the first to develop, and they all formed from the branching of a larval rod (Figures 14K–M). The genital plates AB

and DE developed from an outgrowth, respectively, of the right postoral and the right posterodorsal rods. They were hence often found at the base of a pedicellaria (Figures 14K,L). The genital plate CD developed at the branching point of the dorsal arch (Figure 14M). It was thus located next to the hydropore, where it will differentiate into the madreporite of the adult. The next genital plate to develop was the genital plate BC, which, unlike its counterparts, did not form from a larval skeletal rod but from a *de novo* triradiate spicule positioned in the right lateral field near the genital plate DE (Figures 14K,L). Finally, the last genital plate to form was the genital plate EA (Figure 14N), which emerged near the larval apex at the *mature rudiment stage*. Since it formed significantly later than the other genital plates, the genital plate EA was always the smallest. By the time of metamorphosis, all genital plates, including the genital plate EA, were further supporting one or two juvenile spines (Figures 14K–M). Therefore, by the time of metamorphosis, a total of fifteen to nineteen juvenile spines were discernable on the larva: ten associated with the rudiment and five to nine associated with the genital plates.

Competent pluteus stage and metamorphosis

Once the larvae were at the 8-arm *pluteus stage*, the pedicellariae and the genital plates were formed, and the rudiment was at the *mature rudiment stage*, the larvae were at the so-called *competent pluteus stage* (Figures 15A,B). In echinoids, competency means that the larva is morphologically ready to undergo metamorphosis, although it relies on the detection of appropriate environmental cues to trigger this process (Strathmann, 1978; Burke, 1980). Under our culture conditions, the *competent pluteus stage* was reached at around 30 dpf, as assessed both morphologically and by the observation of spontaneous metamorphosis in our culture

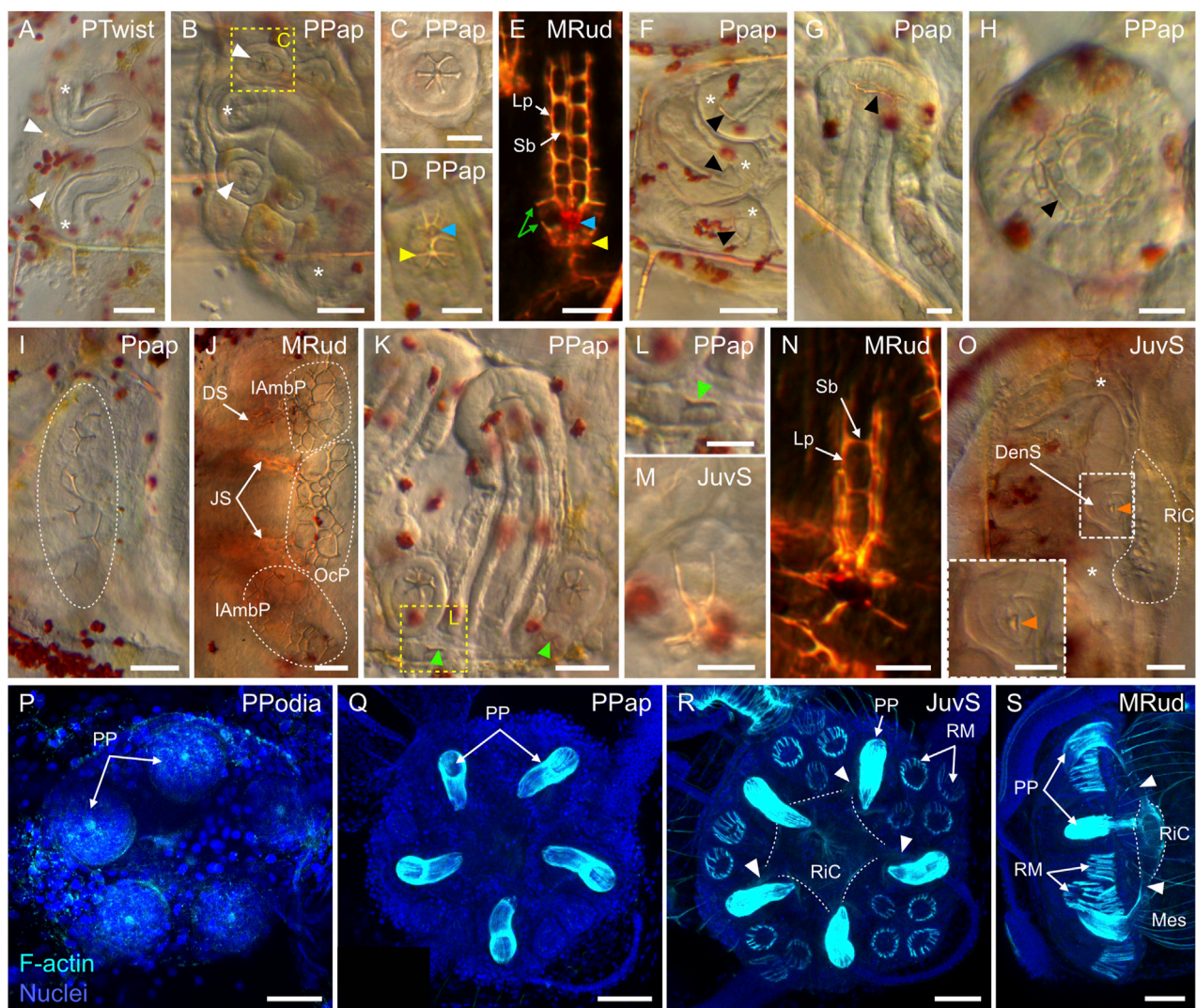


FIGURE 13

Skeletogenesis and myogenesis in the *Paracentrotus lividus* adult rudiment. Developmental stages are as follows: (A) primary podia twisting stage (PTwist); (B–D,F–I,K,L,Q) primary podia papilla stage (PPap); (E,J,N,S) mature rudiment stage (MRud); (M,O,R) juvenile spine stage (JuvS); (P) primary podia stage (PPodia). In (A–D,F–M,O), images were acquired using bright-field light microscopy. In (E,N), images were obtained using polarized light. In (P–S), images are maximum intensity projections of confocal z-stacks of larvae co-labeled for F-actin (muscles; cyan) and DNA (nuclei; blue), and they correspond to projections of the entire rudiment. (A–E) Close-ups of the skeletal element associated with the definitive spines in top, oral view in (A–D) and in lateral view in (E). (C) Close-up of the region outlined by the yellow box in (B). (F–H) Close-ups of primary podia, in lateral view in (F,G) and in papilla view in (H). (I,J) Close-up of the anlage of the future adult skeletal shell at the surface of the developing adult rudiment, which is in side view. (K–N) Close-up of the skeletal element associated with the juvenile spines in top, oral view in (K–M) and in lateral view in (N). (L) Close-up of the region highlighted by the yellow box in (K). (O) Close-up of the ring canal and of a dental sac in an adult rudiment in side view. ((O) inset) Close-up of the dental sac. (P–S) Close-ups of the developing adult rudiment in oral, deep view in (P–R) and in side view in (S). In (A,B), white arrowheads highlight the developing skeletal spicules of definitive spines. In (A,B,F,O), white asterisks mark the primary podia. In (D,E), the yellow arrowhead indicates the hexaradiate spicule of a definitive spine, and the blue arrowhead marks the hexagonal ring. In (E), green arrows highlight additional skeletal branches emerging from either the hexaradiate spicule or the hexagonal ring. In (F–H), black arrowheads highlight developing primary podia skeletal disks. In (I,J), white dotted lines delineate the anlage of the future adult skeletal shell in (I), and the developing ocular and interambulacral plates in (J). In (K,L), green arrowheads mark the developing triradiate spicules of juvenile spines. In ((O), (O) inset), orange arrowheads highlight a primordium of a developing tooth located within a dental sac. In (O,R,S), white dotted lines outline the ring canal. In (R,S), white arrowheads mark the muscles associated with the radial canals. Scale bar: (A,B,F) 50 μ m; (C,D,L,M) 12.5 μ m; (E,K,N,P–S) 25 μ m; (G,H) 20 μ m; (I,J,O) 15 μ m; ((O) inset) 7.5 μ m. DenS: dental sac; DS: definitive spine; IAmbP: interambulacral plate; JS: juvenile spine; Lp: longitudinal processes; Mes: mesentery; OcP: ocular plate; PP: primary podium; RiC: ring canal; RM: ring muscle; Sb: stereomic bridge.

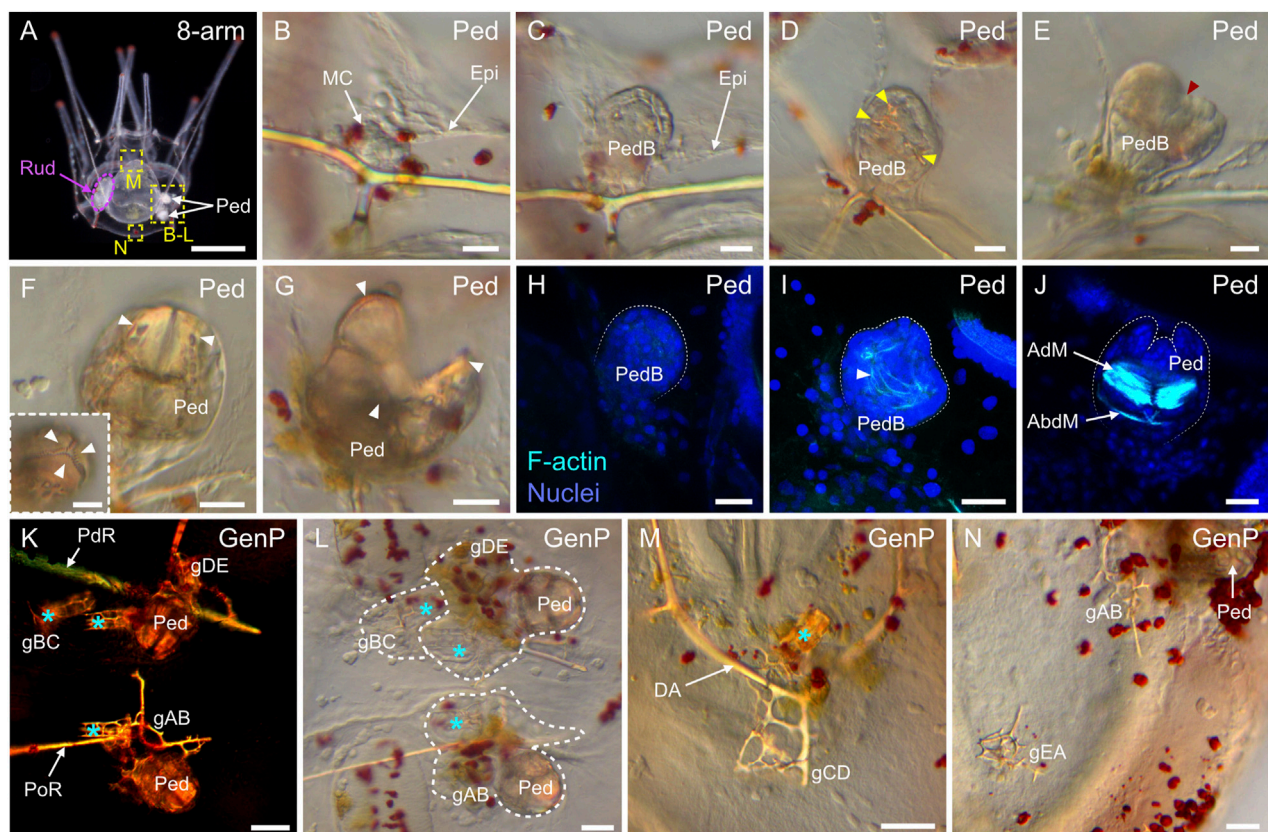


FIGURE 14

Development of the pedicellariae and the genital plates in *Paracentrotus lividus* larvae. In (A–N), images are from larvae at the 8-arm pluteus stage (8-arm). In (A), the image was acquired using dark-field light microscopy. In (B–G, L–N), images were obtained using bright-field light microscopy. In (H–J), images are maximum intensity projections of confocal z-stacks of larvae co-labeled for F-actin (muscles; cyan) and DNA (nuclei; blue), and they correspond to projections of the entire pedicellaria. In (K), the image was taken using polarized light to highlight the skeletal elements. In (A), the larva is in anterior view, with the ventral side up and the left side to the left. (B–N) Close-ups of the regions outlined by yellow boxes in (A). (B–J) Close-ups of pedicellariae (Ped). (K–N) Close-ups of genital plates (GenP). In (A), the purple dotted line delineates the adult rudiment on the left side of the larva. In (D), yellow arrowheads indicate the skeletal elements developing inside the pedicellaria bud. In (E), the red arrowhead shows the individualization of the three lobes within the bud. In ((F), (F) inset, (G)), white arrowheads mark the three jaws of the pedicellaria, which can be either closed like in (F) and ((F) inset) or open like in (G). In (H–J), white dotted lines outline the pedicellaria bud in (H–I) or the pedicellaria jaws in (J). In (I), the white arrowhead points to the first muscle fibers appearing within a pedicellaria bud. In (K–M), cyan asterisks indicate the position of juvenile spines associated with the genital plates. In (L), white dotted lines delineate the genital plates and their associated juvenile spines developing in the vicinity of pedicellariae. Scale bar: (A) 200 μ m; ((B–G), (F) inset) 15 μ m; (H–J, K–M) 30 μ m; (N) 50 μ m. AdM: adductor muscle; AbdM: abductor muscle; DA: dorsal arch; Epi: larval epidermis; gAB: genital plate AB; gBC: genital plate BC; gCD: genital plate CD; gDE: genital plate DE; gEA: genital plate EA; GenP: genital plate; MC: mesenchyme cell; PdR: posterodorsal rod; Ped: pedicellaria; PedB: pedicellaria bud; PoR: postoral rod; Rud: adult rudiment.

vessels. However, all larvae of a given culture vessel never underwent metamorphosis simultaneously. This was primarily due to the heterochrony of rudiment, pedicellaria, and genital plate development, but potentially also because some larvae detected the required environmental cues earlier than others. Thus, the duration of the *competent pluteus stage* was variable within a given culture, with the initiation of metamorphosis by some larvae happening up to a couple of weeks after the first larvae of that culture underwent metamorphosis.

Larvae at the *competent pluteus stage* were characterized by subtle morphological features. First, the rudiment was at the

mature rudiment stage and occupied all of the larval body on the left side of the stomach (Figures 15A,B). Second, a hole was present in the left larval epidermis, in front of the rudiment (Figure 15B). This hole, identified as the vestibular pore (Smith et al., 2008), arose either from the bridge between the larval epidermis and the vestibular roof or resulted from a *de novo* fusion of these two tissues (data not shown). In addition, at the *competent pluteus stage*, the larvae displayed some behavioral changes. First, ciliary beating of the epaulettes (Figure 15C) was reduced periodically, and the larvae thus sank to the bottom of the culture vessel (data not shown). Second, while at the bottom

of the culture vessel, one or more primary podia extended through the vestibular pore and probed the substrate, presumably in search of an adequate environment for settlement (Figure 15D). This behavior was observed during the *competent pluteus stage* but also upon initiation of the process of metamorphosis, which was always marked by the shrinking of the ectoderm at the level of the larval arms (Figure 15D).

The process of metamorphosis, leading to the transformation of the larvae into benthic juveniles, took between 1 and 2 h under our culture conditions (Figures 15D–J; Supplementary Video S6). Its onset was always characterized by a specific sequence of fast and irreversible morphological events. First, the larva stopped swimming and the epidermis of the larval arms shrank, leaving behind the skeletal rods (Figure 15D; Supplementary Video S6). Then, the vestibular pore opened up, thereby creating a bulge on the edge of the vestibular pore (constituted of the vestibular lip and part of the vestibular walls) and pushing upwards the epidermis of the larval body towards the ventral and right sides of the larva (Figure 15E; Supplementary Video S6). Concomitantly, the podia and spines of the rudiment, inside the vestibular cavity, started to move very actively and to spread laterally, leading to an additional enlargement of the vestibular pore, to the protrusion of the podia and spines outside of the vestibular cavity, and to the continued condensation of the larval body epidermis on the ventral and right sides of the larva (Figure 15F; Supplementary Video S6). The accumulation of the larval epidermal tissue resulted in the formation of noticeable folds on the ventral and right sides of the larva (Figures 15F,I inset). In addition, at the level of the vestibular pore, the bulge eventually everted, spreading away from the podia and the spines, towards the ventral and right sides of the larva (Figure 15F). Thereafter, a large number of cells started to delaminate from the ventral and right regions of the larval epidermis (Figures 15G–I; Supplementary Video S6). While the cells delaminated, the folds of the larval epidermis gradually disappeared, the bulge resorbed, and the epidermis stretched out (Figures 15G–I). Once cell delamination stopped, the pentaradial juvenile appeared and started to crawl on the substrate (Figure 15J). It was covered by an epidermis punctuated with red-pigmented cells and still featured, on the surface facing away from the substrate, remnants of the larval arm rods (Figure 15J). It is worth noting that metamorphosis led to a radical modification of the animal body axes: the left side of the larva became the oral side of the juvenile (facing toward the substrate) and the right side of the larva became the aboral side of the juvenile (facing away from the substrate) (Supplementary Figure S1).

Juvenile stages

Following metamorphosis, the animal entered the adult period, i.e., living in a different environment (from pelagic to

benthic), with a different lifestyle (from swimming and particle feeding to crawling and grazing), and exhibiting a completely different body organization (from bilateral to pentaradial symmetry). Because of the heterochrony observed during the *competent pluteus stage*, with respect to the timing of metamorphosis, a certain level of anatomical heterogeneity was observed among post-metamorphic juveniles. This was particularly obvious when comparing, for instance, the size of the skeletal plates or the length of the spines between different juveniles, as these structures continued to develop in the rudiment and the larva upon acquisition of competency and before metamorphosis. Despite these differences, the overall anatomy of the juveniles was very similar, and 1 day post-metamorphosis (dpm) all juveniles resembled miniature versions of *P. lividus* adults with spherical bodies bearing different appendages, including podia, spines, and pedicellariae (Figure 16A).

A major difference to the adult was that the post-metamorphic juvenile, at 1 dpm, lacked a fully formed mouth and anus and thus a functional digestive system. The juvenile hence exclusively relied on internal sources of energy, and this endotrophic state was the main characteristic of the *early juvenile stage*. At 1 dpm, the juvenile was further characterized by the lack of a complete skeletal test. The test was only composed of the endoskeletal plates inherited from the rudiment and the larva, which were not yet large enough to fuse and cover the entire animal (Figures 16B,C). For instance, on the aboral side, the five genital plates were present (Figure 16B), but they were still independent from one another as well as from the ocular and the interambulacral plates. Nonetheless, 1 dpm, the genital plates (AB, BC, CD, DE, and EA) were already exhibiting a characteristic circular arrangement corresponding to Carpenter's nomenclature (Figure 16B). In addition, the genital plates AB, CD, and DE, which developed from the larval rods, were still generally marked by the presence of remnants of their respective rods (Figure 16B). On the oral side, the buccal plates and the newly developing ambulacral plates were also still, 1 dpm, simple triradial spicules with only a few branches (Figure 16C). In the center of the oral side, 25 small ossicles were further distinguishable, which were arranged in a circular manner (Figure 16C). These small ossicles corresponded to the primordia of the skeletal pieces of the future masticatory apparatus of the adult, i.e., Aristotle's lantern. The five most conspicuous of these ossicles corresponded to the tooth primordia (Figure 16C inset). These were flanked on both sides by a pair of developing hemipyramids and a pair of developing epiphyses (Figure 16C inset), two elements that will later form the skeletal structure supporting the teeth (Vellutini and Migotto, 2010; Ziegler et al., 2012).

Concerning the appendages, the 1 dpm juvenile inherited from the larva: the pedicellariae, the primary podia and their related water vascular system, and the definitive and juvenile spines. On the aboral surface of the juvenile, the pedicellariae

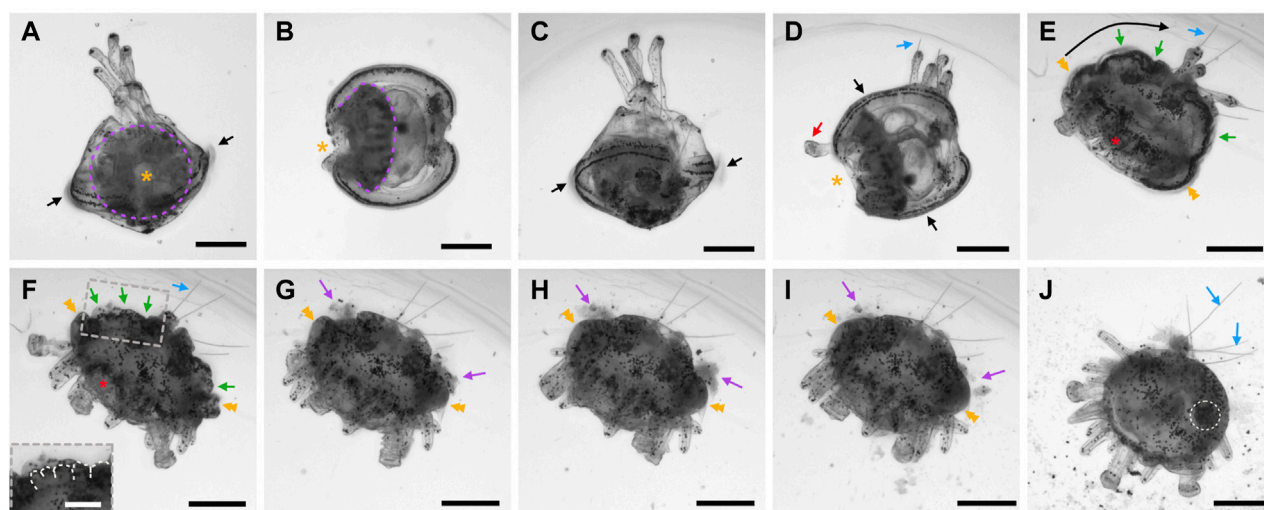


FIGURE 15

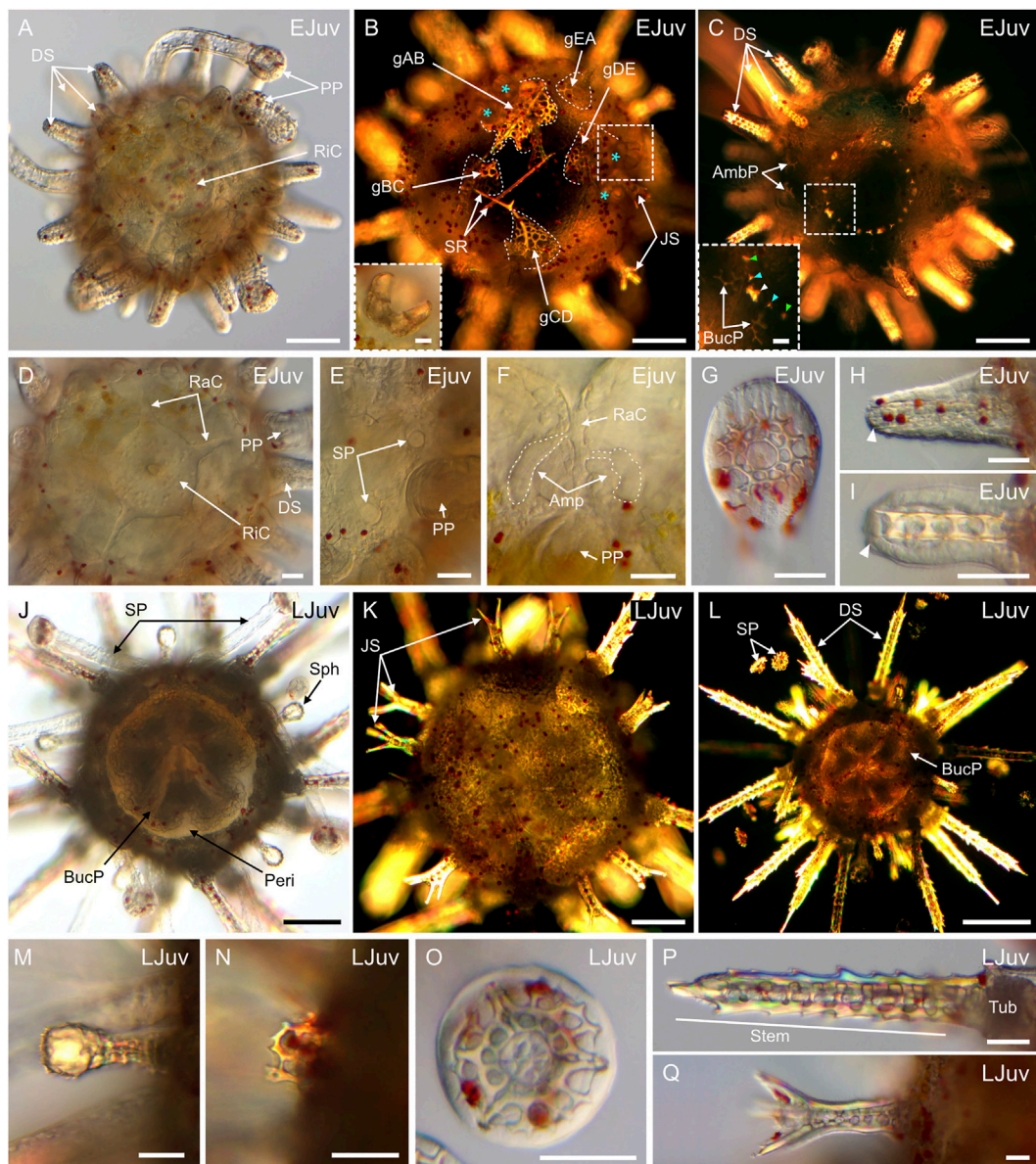
The competent pluteus stage and metamorphosis in *Paracentrotus lividus*. In (A–J), images were extracted from a movie recorded using bright-field light microscopy. In (A), the larva is in left view, with the ventral side up. In (B), the larva is in dorsal view, with the rudiment on the left. In (C), the larva is in right view, with the ventral side up. In (D), the larva is in dorsal, tilted view, with the rudiment on the left. In (E–J), the developing juvenile is in side view, with the oral surface towards the bottom left corner. ((F inset) Close-up of the folds at the level of the larval body epidermis. In (A,B), purple dotted lines outline the adult rudiment. In (A,B,D), the orange asterisk highlights the vestibular pore. In (A,C,D), black arrows point to the larval epaulettes. In (D), the red arrow marks a protruding primary podium. In (D–F,J), blue arrows highlight the larval arms and rods. In (E), the long black arrow illustrates the movement of the larval body epidermis from the vestibular pore towards the larval arms and pedicellariae. In (E,F), green arrows highlight folds of the larval body epidermis. In (E–I), orange double arrowheads mark the bulge forming around the juvenile appendages by contraction and eversion of the vestibular lips and walls. In ((F inset), white dotted lines outline folds of the larval body epidermis. In (G–I), purple arrows point to delaminating cells. In (J), the white dotted line encircles a pedicellaria. Scale bar: (A–H) 200 μ m; ((F inset) 100 μ m.

remained attached to the genital plates and were functional (Figure 16B). The water vascular system was still composed of a functional ring canal and five radial canals, enabling the extension and retraction of the five primary podia (Figures 16A,D). At 1 dpm, the juveniles were also characterized by a set of ten growing secondary podia, located, in pairs, underneath the primary podia (Figure 16E), and a set of ten ampullae, emerging, in pairs, on each side of the proximal extremity of the radial canals (Figure 16F). At this stage, the primary podia further exhibited a complete skeletal disk formed, as indicated above, from a single spicule (Figure 16G). The definitive and juvenile spines, inherited from both the rudiment and the larva, were also still present in 1 dpm juveniles, although they usually featured rounded tips (Figures 16A–C,H,I), indicating that they were not yet fully developed.

Following metamorphosis, the development of the animal did not stop. The juveniles entered a new phase of gradual reorganization of both their inner and outer anatomy. This reorganization included, for instance, the reshaping of the digestive tract with the opening of the adult mouth and anus, the formation of Aristotle's lantern, the growth of the endoskeleton, the maturation of the appendages already present, as well as the formation of new ones. At 8 dpm, the juveniles (Figure 16J) were hence bigger in size and more opaque to light

than at 1 dpm (Figure 16A). More importantly, the juveniles were now grazing on the substrate, and were thus exotrophic. The initiation of grazing was the main landmark for the beginning of the *late juvenile stage*, which lasted for several months, until the reproductive organs were fully developed, and the animals started to produce gametes, marking the beginning of the *adult stage*. At 8 dpm, the juveniles had further a complete test. All of the initial skeletal plates (the genital, ocular, interambulacral, and ambulacral plates) were expanded and fused to one another. This generated a rigid shell protecting the inner organs, with the suture between the plates no longer being clearly observable (Figures 16J–L). On the oral side, the ambulacral and interambulacral plates were excluded from a zone free of endoskeleton, called the peristome (Formery et al., 2021), but in which the buccal plates developed (Figure 16J). At 8 dpm, the buccal plates were fully formed, and they created a protective skeletal structure below Aristotle's lantern (Figures 16J,L). Yet, they remained independent of the other plates of the test to ensure the motility of the masticatory apparatus (Supplementary Video S7), which was now composed of five functional, pointed teeth protruding from the center of the oral surface (Figures 16J,L; Supplementary Video S7).

On the aboral surface of the 8 dpm juveniles, the pedicellariae inherited from the larva were still present, although they will eventually be replaced by stalked, adult pedicellariae (Gosselin

**FIGURE 16**

Anatomy of early and late juveniles of *Paracentrotus lividus*. Developmental stages are as follows: (A–I) early juvenile stage, 1 day post-metamorphosis (EJuv); (J–Q) late juvenile stage, 8 days post-metamorphosis (LJuv). In (A, D–J, M–Q), images were acquired using bright-field light microscopy. In (B, C, K, L), images were obtained using polarized light microscopy. In (A–D, J–L), images correspond to specimens in oral view in (A, C, D, J, L) and in aboral view in (B, K). ((B) inset) Close-up of an opened pedicellaria. ((C) inset) Close-up of the skeletal elements constituting the primordia of the adult masticatory apparatus. (D) Close-up of the ring and radial canals. (E) Close-up of a pair of growing secondary podia located underneath a primary podium. (F) Close-up of the ampullae formed at the proximal tip of a radial canal. (G) Close-up of the skeletal disk within the papilla of a primary podium. (H) Close-up of a developing definitive spine. (I) Close-up of a developing juvenile spine. (M) Close-up of a sphaeridium. (N) Close-up of a degenerated primary podium. (O) Close-up of the skeletal disk within the papilla of a secondary podium. (P) Close-up of a fully formed definitive spine. (Q) Close-up of a fully formed juvenile spine. In (B), cyan asterisks mark the pedicellariae present on the aboral surface of the juvenile, and white dotted lines delineate the genital plates. In ((C) inset), the white arrowhead indicates a tooth primordium, cyan arrowheads highlight primordia of the hemipyramids, and green arrowheads mark primordia of the epiphyses. In (F), white dotted lines outline two ampullae formed at the proximal tip of a radial canal. In (H, I), white arrowheads indicate the apex of a growing definitive spine in (H) and of a growing juvenile spine in (I). Scale bar: (A–C, J–L) 100 μm; ((B) inset, (C) inset, (D–I, M–Q)) 30 μm. Amp: ampulla; AmbP: ambulacral plate; BucP: buccal plate; DS: definitive spine; gAB: genital plate AB; gBC: genital plate BC; gCD: genital plate CD; gDE: genital plate DE; gEA: genital plate EA; JS: juvenile spine; Peri: peristome; PP: primary podium; RaC: radial canal; RiC: ring canal; SP: secondary podium; Sph: sphaeridium; SR: skeletal rod; Tub: tubercle.

and Jangoux, 1998). At 8 dpm, the juveniles were also characterized by new, round-tipped appendages on their lateral sides (Figures 16J,M). These were the so-called sphaeridia, which are believed to correspond to sensory organs involved in regulating the balance of the animal (Märkel et al., 1992). Regarding the podia, the primary podia were significantly reduced in size and exhibited less activity, corresponding only to protruding remnants at the level of the ocular plates (Figure 16N). In contrast, the ten initial secondary podia had considerably grown in size (Figures 16J,L) and were now the principal locomotor apparatus of the animal, along with other, additional secondary podia that formed following a stereotypical pattern of appearance referred to as the “baaba pattern” (Mooi et al., 2005; Morris, 2009). At their tip, all secondary podia had further a skeletal disk (Figure 16L), which, as opposed to the single spicule found in the skeletal disks of the primary podia (Figure 16G), were composed of three spicules that were fused together (Figure 16O). Finally, at 8 dpm, the definitive and juvenile spines inherited from the rudiment and the larva also reached their maximum length (Figures 16P,Q). The mature definitive spines had a single, pointed end resulting from the fusion of the six longitudinal processes constituting their stem, and they were motile by means of an articulated basal tubercle (Figure 16P). In contrast, the mature juvenile spines were multi-pointed, due to the outgrowth of their three or four longitudinal processes, and they were immotile (Figure 16Q).

Discussion

The sea urchin *P. lividus* is one of the historical echinoid model species and, as such, has already been at the center of a large number of studies (e.g., Boveri, 1901; Hörstadius, 1939). Despite this fact, a rigorous developmental staging scheme from fertilization to juvenile stages, with details on coeloms and rudiment development, was still missing for this species. To fill this gap, we here propose an up-to-date staging scheme for the development of *P. lividus* from fertilization through metamorphosis to juvenile stages. Following the developmental trajectory of this animal in live specimens enabled us to recognize a total of 33 easily distinguishable stages divided into three main periods: embryonic, larval, and adult (Figure 3). In addition, we described 15 additional stages that specifically apply to the development of the coeloms and the rudiment and that take place independently during the larval period (see subsection in Figure 3). We further provide, for each of these 48 stages, key anatomical features that will enable both specialists and non-specialists to easily distinguish the different developmental stages using a simple compound microscope (Supplementary Figure S3). Taken together, this proposed developmental atlas compiles the fragmentary knowledge and existing descriptions of *P. lividus* development and adds new data

on ciliogenesis, myogenesis, and development of the coeloms and the rudiment as well as on the process of metamorphosis. As such, it provides a wealth of high-resolution images and morphological descriptions to define the development of this species and to facilitate comparisons with other echinoids and beyond.

The study of echinoid development has led through the years to major breakthroughs in our understanding of cell biology, embryology, and gene regulation. However, unlike classical model systems, like the arthropod *Drosophila melanogaster* or the nematode *Caenorhabditis elegans*, studies on echinoid development have been carried out on different species, chiefly based on geographical availability (McClay, 2011; Ettensohn, 2017). This use of different echinoid species has been beneficial to provide a more accurate view of the conservation and divergence of genetic and developmental mechanisms within echinoids. Thus, although most species used in research laboratories are regular, indirect-developing echinoids, a number of species-specific traits have been identified, some of which proved challenging for establishing inter-species comparisons. In the following sections, we assess how our developmental staging scheme for *P. lividus* compares to that of other echinoid species and how it might be used to inform inter-species comparisons.

Embryonic period

During the embryonic period, we retrieved the main developmental stages and features that were previously reported for *P. lividus* (e.g., Boveri, 1901; Hörstadius, 1973; von Ubisch, 1913), although for some stages or features we provided a more rigorous nomenclature and/or description.

A first example of a key feature that we retrieved, is the presence, in the egg, of a specific band of orange-pigmented granules, which had previously been described by several zoologists (e.g., Boveri, 1901; Sardet and Chang, 1985). This pigment band was located in the eggs in a subequatorial position and persisted throughout the cleavage period. This pigment band is a specificity of *P. lividus* and provides a considerable advantage for micromanipulation experiments, as it reveals the position of the first embryonic axis, the animal-vegetal axis, which is perpendicular to the band (Hörstadius, 1973; Croce et al., 2011).

Subsequently, during cleavage, blastula, and gastrula stages, we also found the same sequence of cell divisions and morphogenetic movements that had previously been described for *P. lividus* (e.g., Hörstadius, 1973; Robert et al., 2014). One important feature during these stages is the development of different types of cilia to enable propelling and directionality of the embryos and to ensure feeding and population dispersal (Metaxas, 2001; Chan et al., 2015). Using immunohistochemistry assays, we corroborated that cilia emerged in *P. lividus* embryos prior to hatching, when the embryo is composed of several

hundred cells arranged as a spherical monolayer (Prulière et al., 2011). Yet, more specifically, we demonstrated that ciliogenesis started at the *mid-blastula stage*, as further corroborated by the rotating movement of the embryos within the fertilization envelope. Similarly, the apical tuft had previously been reported to emerge when the embryos began gastrulating (Prulière et al., 2011). Here, we sustained this finding, but established, more precisely, that the first long cilia, on the apical pole domain, appeared at the *mesenchyme blastula stage*.

Comparisons of the *P. lividus* data with those from other echinoid species, including some belonging to other echinoid groups (Supplementary Figure S4), revealed subtle differences during cleavage, blastula, and gastrula stages. For instance, although most echinoid species have a *16-cell stage* (e.g., this study, Hart, 1996; Vellutini and Migotto, 2010; Bennett et al., 2012; Dautov et al., 2020), the 28- and 56-*cell stages* we described for *P. lividus* have so far only been reported in a couple of camarodont and clypeasteroid species (Okazaki, 1975; Morrill and Marcus, 2005; Vellutini and Migotto, 2010; Nesbit and Hamdoun, 2020). In most other echinoids, the micromeres do not seem to divide later than the other embryonic cells, meaning that the *32-cell stage* directly follows the *16-cell stage* and directly precedes the *60-cell stage*, without intermediate 28- or 56-*cell stages*. Similarly, in at least one cidaroid (*Prionocidaris baculosa*), one diadematoid (*Centrostephanus rodgersii*), and one clypeasteroid (*Dendraster excentricus*), a *64-cell stage* was reported instead of a *60-cell stage* (Huggett et al., 2005; Olivares-Bañuelos et al., 2012; Yamazaki et al., 2012). In addition, ciliogenesis does not seem to take place at the same stage in all echinoids. For instance, in the camarodont *Lytechinus variegatus*, initiation of rotation within the fertilization envelope was reported as early as at the *early blastula stage*, and the first trace of an apical tuft was observed at hatching (Conway et al., 1984). Moreover, although gastrulation occurs in *P. lividus* as described in most other euechinoid species, it substantially differs from that reported in cidaroids, in which mesenchyme cells do not ingress prior to gut invagination (Schroeder, 1981; Bennett et al., 2012; Yamazaki et al., 2012). Other modifications to gastrulation compared to *P. lividus* have also been observed, for instance, in the camarodont *Colobocentrotus mertensii*, in which skeletogenesis is initiated prior to gut formation (Thet et al., 2004).

Despite these differences, one can reasonably consider that the embryonic period is very similar in most echinoid groups. As a matter of fact, the cleavage phase always includes holoblastic, meridional, and equatorial cleavages, which equivalently lead to the formation of a hollow sphere composed of a monolayer of cells surrounding an inner fluid-filled cavity. Following the cleavage period, the blastulae are also always ciliated prior to hatching, and hatching takes place prior to gastrulation. Likewise, the first elements of the larval skeleton always arise post-hatching, as two triradiate spicules within two bilateral cell

clusters positioned in the vicinity of the vegetal pole. In all groups, gut formation also occurs by tissue invagination, and the gut elongates from the vegetal pole to the animal pole. Furthermore, in all echinoids studied so far, the embryonic period ends, at the *prism stage*, with the emergence of a triangular-shaped embryo lacking an opened mouth.

Larval development

Regarding the larval period, we also identified the same main stages that had previously been reported for *P. lividus*, and which were named based on the development of the larval arms and the behavior of the larva (e.g., Gosselin and Jangoux, 1998; Paredes et al., 2015; von Ubisch, 1913). In *P. lividus*, the beginning of the larval period was marked by the opening of the mouth at the *early pluteus stage*, followed by the acquisition of the capacity to feed at the beginning of the *4-arm pluteus stage*. The larval period further featured the appearance and growth of 4 pairs of arms at the 2-, 4-, 6-, and 8-*arm pluteus stages*. Between the end of the *4-arm* and *8-arm pluteus stages*, the larval period was also characterized by the development of adult structures, and the larval period ended with competency, i.e., when the larval and adult structures were fully developed.

Although, in most echinoid species, the larval period is characterized by a similar set of features, including the opening of the mouth, feeding, the growth of arms, and the development of adult structures, there are marked differences between different echinoid groups. For instance, while in most indirect developing camarodonts and clypeasteroids the larva has eight arms by the end of the larval period, in diadematoids the fully developed larva only has two arms, in cidaroids eight arms and several vibratile lobes, and in spatangoids twelve arms and an apical process (e.g., Mortensen, 1921; 1931; Wray, 1992). Similarly, while in most echinoid species the opening of the mouth takes place at the onset of the larval period, in the cidaroid *Cidaris blakei*, the mouth only opens at the *2-arm pluteus stage* (Bennett et al., 2012). Moreover, in some species, such as the spatangoid *Echinocardium cordatum*, adult structures, like the hydropore, the vestibule, and the pedicellariae, do not form until the larva is fully developed (Nunes and Jangoux, 2007).

Another striking trait of larval development in *P. lividus* was the formation of the posterodorsal spicules, the dorsal arch, the pedicellariae, and the genial plates. In *P. lividus*, all these structures emerged from aggregates of mesenchyme cells of unknown origin. In the camarodonts *Pseudocentrotus depressus* and *Hemicentrotus pulcherrimus*, these structures have been suggested to derive from non-skeletogenic mesoderm cells delaminating, at the *late gastrula stage*, from the tip of the archenteron (Yajima, 2007). Whether this is also the case in *P. lividus* remains however to be demonstrated.

One additional major event taking place during the larval period in *P. lividus* was the establishment of the ciliary band and

the epaulettes. We found that, in the *P. lividus* larva, the ciliated cells, within these structures, are organized into several rows and that a total of two pairs of epaulettes formed, two anteriorly and two posteriorly. The total number of epaulettes, their site of origin, their position, and their nomenclature actually vary between echinoid species (e.g., Wray, 1992). In the camarodonts *Echinus esculentus*, *Mesocentrotus nudus*, *Strongylocentrotus purpuratus*, and *H. pulcherrimus*, for instance, a total of six epaulettes form (organized in three pairs), referred to as either anterior and posterior or upper and lower epaulettes (MacBride, 1903; Mogami et al., 1991; Smith et al., 2008; Dautov et al., 2020). In *S. purpuratus* and *H. pulcherrimus*, the third pair of epaulettes arises as two buds from the ciliary band located, on each side of the larva, at the base of the posterodorsal and the postoral arm (i.e., from the lateral fields). These two buds subsequently migrate to a more dorsal (or lower) position than the two other pairs and eventually encircle the dorsal (or lower) end of the larva (Mogami et al., 1991; Smith et al., 2008). In *P. lividus*, we never observed a third pair of epaulettes, and the ciliary band always remained intact at the extremity of the lateral fields.

One last important characteristic of the larval period in *P. lividus* was the development of the larval musculature, for which we determined the ontogeny and organization. We showed that the *myosin heavy chain (mhc)* gene, an evolutionary conserved marker for the terminal differentiation of muscles (Wessel et al., 1990), was first expressed in *P. lividus* at the *prism stage* and that a more conspicuous musculature, surrounding the esophagus and allowing the larvae to feed, became detectable as early as at the beginning of the *4-arm pluteus stage*. In the camarodont species *S. purpuratus* and *H. pulcherrimus*, similar circumesophageal muscles, encircling the esophagus, have been described, and it has been suggested that these muscles form from muscle progenitor cells delaminating from the left and the right coelomic pouches (Ishimoda-Takagi et al., 1984; Burke and Alvarez, 1988). In *P. lividus*, we did not observe such a delamination, but the overall ontogeny of the circumesophageal muscles suggests that a similar process might exist in this species as well. Contrasting with studies in other echinoids (e.g., Strathmann, 1971; Burke and Alvarez, 1988; Dyachuk and Odintsova, 2013; MacNeil et al., 2017), we did not find, in *P. lividus*, the basal ring muscles reported in the camarodont *L. variegatus* and the cidaroid *Eucidaris tribuloides* (MacNeil et al., 2017). However, our work revealed, in *P. lividus* larvae, two additional muscular structures: the preoral dilator muscles, extending in the preoral arms, and the mesenteries, surrounding the larval digestive tract. The preoral dilator muscles, like the anterior dilator muscles, are positioned in the arms borne by the oral hood. We thus propose that, similar to the anterior dilator muscles (Strathmann, 1971), the preoral dilator muscles are involved in widening the mouth aperture and bending the arms to optimize food catching. The mesenteries appeared shortly before the larva reached

competency and were chiefly surrounding the larval stomach. Although the roles of the mesenteries remain unknown, they are likely to persist in the juvenile (Formery et al., 2021), which also inherits the larval stomach (Fenaux et al., 1994).

Coeloms and adult rudiment development

Despite the wealth of developmental and anatomical studies on *P. lividus*, and the importance of the coeloms and the rudiment for the formation of the adult in indirect-developing echinoids, detailed staging schemes covering the development of the coeloms and the rudiment in echinoids have so far only been compiled for two camarodont species, *H. pulcherrimus* and *S. purpuratus* (Chino et al., 1994; Smith et al., 2008; Heyland and Hodin, 2014). In these two camarodonts, as in *P. lividus*, development of the coeloms and the rudiment takes place in the feeding larva, in trajectories that are independent of that of the rest of the larva. The staging scheme we propose here for *P. lividus* is largely similar to that of the other two camarodonts, following the logic of the developing anatomical landmarks. For instance, in *S. purpuratus*, as in *P. lividus*, the development of the coeloms starts with the projection of the hydroporic canal and the formation of the hydropore, and hence by an equivalent *hydroporic canal stage* (Smith et al., 2008). Thereafter, the vestibule invaginates and contacts the left hydrocoel, the pentaradial symmetry of the adult emerges at the level of the hydrocoel, and the primary podia appear (Chino et al., 1994; Smith et al., 2008; Heyland and Hodin, 2014). In all three camarodont species, the development of the rudiment also then ends at a *mature rudiment stage* with a fully developed rudiment characterized by five primary podia, a number of juvenile and definitive spines, pedicellariae, and genital plates (Chino et al., 1994; Smith et al., 2008; Heyland and Hodin, 2014). Despite these similarities, we defined two additional stages in *P. lividus* corresponding to the twisting of the primary podia and the emergence of the juvenile spines. These events are also likely to occur in the two other camarodont species, *S. purpuratus* and *H. pulcherrimus*, but in these species they have not yet been recognized as individual stages. We were further able to observe the circularization of the left hydrocoel leading to the establishment of the ring canal at the *5-fold mesoderm stage*, an event that has so far only been documented by von Ubsch (1913).

Apart from these species, relatively little is known about the development of the coeloms and the rudiment in other echinoids. It has been shown, for instance, that in the cidaroids *Eucidaris thouarsi* (Emlet, 1988) and *C. blakei* (Bennett et al., 2012), the clypeasteroid *Clypeaster subdepressus* (Vellutini and Migotto, 2010), and the spatangoid *E. cordatum* (Gordon, 1926; Nunes and Jangoux, 2007) a rudiment also forms after the larva starts feeding, on the left side of the digestive tract, at the level of the

stomach. These echinoids also feature a *mature rudiment stage* characterized by a fully developed adult rudiment with 5 primary podia and several spines. The type of spines formed at the level of the rudiment, their number as well as the timing of their formation, however, vary between species (e.g., [Emlet, 1988](#); [Huggett et al., 2005](#); [Nunes and Jangoux, 2007](#); [Vellutini and Migotto, 2010](#); [Bennett et al., 2012](#); [Rahman et al., 2012](#); [Rahman et al., 2015](#)). Other differences observed between echinoid species concern the morphological changes leading to the emergence of the rudiment. In the camarodont Temnopleurid species, *Temnopleurus toreumaticus* and *Temnopleurus reevesii*, for instance, the rudiment does not form by invagination of the larval epidermis as in *P. lividus*, *S. purpuratus*, and *H. pulcherrimus*. In these Temnopleurid species, instead, an inner cell mass forms during the larval stages, and the adult rudiment subsequently develops from this inner cell mass ([Kitazawa et al., 2014](#)). Similarly, in cidaroids, development of the rudiment does not involve the emergence of a vestibule and the establishment of a vestibular cavity. Instead, in this echinoid group, the rudiment develops directly by embedding and folding of the larval epidermis onto the left hydrocoel ([Emlet, 1988](#); [Bennett et al., 2012](#)). Given that the cidaroids are the earliest-branching group of echinoids ([Supplementary Figure S3](#)) ([Thompson et al., 2017](#); [Mongiardino Koch et al., 2018](#); [Lin et al., 2020](#); [Horton et al., 2022](#)), studying development of the coeloms and the rudiment in this group hence has the potential to provide important insights into the evolution of this process in echinoids.

Competency and metamorphosis

In *P. lividus*, the end of the larval period was marked by the *competent pluteus stage* and by metamorphosis, i.e., the transformation of the larva into a benthic juvenile. In previous reports, competency of the larva to undergo metamorphosis has been defined either by the appearance of novel larval behaviors ([Strathmann, 1978](#)), by using metamorphosis-inducing pharmacological agents (e.g., [Nunes and Jangoux, 2007](#)), or by the protrusion of primary podia through the vestibular pore ([Smith et al., 2008](#)). In our hands, metamorphosis was inducible using dibromomethane treatments ([Agatsuma et al., 2006](#); [Taris et al., 2010](#)) even in premature larvae, leading to non-viable juveniles. We thus propose to refer to the *competent pluteus stage* as: 1) the stage at which the larva has completed its development and the rudiment has reached the *mature rudiment stage*, and 2) the stage at which the larva starts exhibiting new behaviors, such as reduced swimming and probing the environment with primary podia protruding through the vestibular pore. This definition is coherent with what has been reported both in other camarodont species and in other echinoids, including the cidaroids, diadematoids, clypeasteroids, and spatangoids (e.g., [Emlet, 1988](#); [Nunes and Jangoux, 2007](#); [Vellutini and Migotto, 2010](#); [Rahman et al., 2015](#); [Nesbit and Hamdoun, 2020](#)).

In *P. lividus*, the process of metamorphosis has previously been described using scanning electron microscopy ([Gosselin and Jangoux, 1998](#)). Here, we used live recordings of metamorphosis to obtain a better resolution of the sequence of events defining this process. We thus identified two main steps of metamorphosis: 1) the opening of the vestibular pore, concomitant with the retraction of the epidermis of the larval arms along the skeletal rods and the folding of the epidermis of the larval body, and 2) the delamination of cells on the ventral side of the larva, concomitant with the smoothening of the epidermis. These two steps led to the emergence of the benthic, pentaradial juvenile, an observation that is once again consistent with previous descriptions of metamorphosis in other echinoids (e.g., [Emlet, 1988](#); [Nunes and Jangoux, 2007](#); [Vellutini and Migotto, 2010](#); [Rahman et al., 2015](#); [Nesbit and Hamdoun, 2020](#)). However, differences exist between echinoid species. For instance, due to the lack of vestibule formation, cidaroids also lack a vestibular pore ([Emlet, 1988](#); [Bennett et al., 2012](#)). Also, in the camarodont species *C. mertensii*, resorption at the level of the larval arms concerns both the larval arm epithelium and the endoskeleton ([Thet et al., 2004](#)), while in *P. lividus* as well as in other camarodont, diadematoid, and clypeasteroid species it only affects the larval arm epithelium ([Huggett et al., 2005](#); [Vellutini and Migotto, 2010](#)).

[Gosselin and Jangoux \(1998\)](#) reported that, during metamorphosis, parts of the larval epidermis, such as the epidermis associated with the genital plates and their appendages, merged with the everted vestibular lip and walls. As we could not confirm this observation, additional experiments, involving, for instance, cell tracking analyses, will be required to assess the fate of the larval epidermis during and after metamorphosis in *P. lividus*. More generally, it will be important to determine, which portions of larval tissues, including at the level of the digestive tract and the apex, are inherited by the juvenile upon metamorphosis. Likewise, future research should determine the origin of the cells that delaminate at the time of metamorphosis. Furthermore, previous studies investigating the role of programmed cell death in echinoid larva undergoing metamorphosis have concluded that apoptosis was chiefly limited to the larval arms during resorption of the epidermis ([Roccheri et al., 2002](#); [Sato et al., 2006](#)). However, given the importance of programmed cell death for tissue remodeling during metamorphosis in a number of different animals, including frogs, insects, phoronids, mollusks, and hemichordates ([Gifondorwa and Leise, 2006](#); [Heyland and Moroz, 2006](#); [Temereva and Tsitrin, 2014](#); [Bump et al., 2022](#)), additional analyses of this process in echinoids, such as in *P. lividus*, might be warranted. They should reveal novel information on the involvement of programmed cell death in the transition from larval to adult life ([Heyland and Moroz, 2006](#); [Fuchs and](#)

Steller, 2011) and should thus contribute to a more general understanding of the evolution of animal metamorphosis (Heyland and Hodin, 2014; Holstein and Laudet, 2014).

Adult period

Following metamorphosis, the *P. lividus* juvenile had a spherical body with different appendages. Although its development was initially endotrophic, it soon started grazing on algae (i.e., about 8 days post-metamorphosis), thereby growing in size and eventually developing reproductive capabilities. Three major phases characterize the adult life of an echinoid, and this despite the echinoid group (Gosselin and Jangoux, 1998; Nunes and Jangoux, 2007; Vellutini and Migotto, 2010; Rahman et al., 2015; Nesbit and Hamdoun, 2020). The first phase is the endotrophic phase, which immediately follows metamorphosis (i.e., the *early juvenile stage*). The mouth and anus of the juvenile are still closed and the digestive tract is not yet functional. The second phase starts when the juvenile becomes exotrophic (i.e., the *late juvenile stage*). The digestive tract is now functional and the animal grazes on algae, although it is not yet sexually mature. The third phase begins when the animal becomes sexually mature (i.e., the *adult stage*). It thus possesses gonads and produces gametes.

In *P. lividus*, previous work has already reported on the anatomy of the *early* and *late juvenile stages*, using essentially immunohistochemistry and scanning electron microscopy (Gosselin and Jangoux, 1998; Formerly et al., 2021; Thompson et al., 2021). Here, we corroborated the previously described structural features defining these two developmental stages. Our work thus lends further support to the observation that newly-metamorphosed juveniles of echinoids are characterized by a highly conserved morphology, in the form of a spherical body with different types of appendages, and this even in species with radically divergent adult anatomies, such as in irregular echinoids (e.g., Gordon, 1929; Okazaki and Dan, 1954; Emlet, 1988). However, from one species to another, these appendages differ in number and type. There might be different numbers and types of spines, for instance, as well as more or fewer podia, pedicellariae, and sphaeridia (Gosselin and Jangoux, 1998; Emlet, 1999; Nunes and Jangoux, 2007). As an example, following metamorphosis, a *P. lividus* juvenile always has five primary podia, twenty definitive spines, fifteen to nineteen juvenile spines, and zero to four pedicellariae. In contrast, at the same stage, the clypeasteroid *C. subdepressus* has no pedicellariae (Vellutini and Migotto, 2010) and the cidaroid *C. blakei* has one to three pedicellariae along with five to twenty-three spines of the same type (Bennett et al., 2012).

Conclusion

Taken together, this study represents a comprehensive description of *P. lividus* development, providing a complete compendium of its embryonic, larval, and adult periods. This dataset thus represents a useful framework for future research on this species as well as for future comparisons with other animals, echinoids, echinoderms, and beyond. Our results will also be useful for developing reliable rearing conditions for echinoid aquaculture, as they provide easily recognizable characteristics to identify specific developmental stages during different periods of the life cycle. With the advancement of genome editing techniques in marine organisms and the relatively short generation time of *P. lividus*, this work also creates a solid basis for the creation of stable transgenic lines in this echinoid species, opening the door for genetic approaches in this animal model system.

Data availability statement

The original contributions presented in the study are included in the article/Supplementary Material, further inquiries can be directed to the corresponding author.

Author contributions

LF, MS, and JC designed the study and wrote and edited the manuscript. LT, MG, GL, RL, and LG provided editorial input. LF, AW, LT, MG, and JC performed experiments and acquired images. LF, AW, LT, RL, LG, and JC designed husbandry procedures for *P. lividus* and maintained the cultures. LF, LT, MG, and JC provided illustrations. MS and JC provided funding. All authors have read and approved the final version of the manuscript.

Funding

This work was supported by the Centre National de la Recherche Scientifique (CNRS) to all authors, by the French Ministry of Research and Technology (2173/2015) and the Japan Society for the Promotion of Science (PE18758) to LF, by the ANR grant MusMod4EDC (ANR-21-CE34-0006-02) to MS, and by the André Picard Network (ANR-11-IDEX-0004-02) and a CNRS Institute of Biological Sciences grant (DBM254552) to JC.

Acknowledgments

The authors would like to thank the Mediterranean Culture Collection of Villefranche (MCCV) and the Plateforme

d'Imagerie par Microscopie (PIM), two services of the Institut de la Mer de Villefranche (IMEV), supported by the grant EMBRC-France (ANR-10-INBS-02) from the Agence Nationale pour la Recherche. From these services, the authors are particularly thankful to Sophie Marro and Sébastien Schaub for their technical support.

Conflict of Interest

The authors declare that the research was conducted in the absence of any commercial or financial relationships that could be construed as a potential conflict of interest.

References

- Agatsuma, Y., Seki, T., Kurata, K., and Taniguchi, K. (2006). Instantaneous effect of dibromomethane on metamorphosis of larvae of the sea urchins *Strongylocentrotus nudus* and *Strongylocentrotus intermedius*. *Aquaculture* 251, 549–557. doi:10.1016/j.aquaculture.2005.05.043
- Aluigi, M. G., Angelini, C., Corte, G., and Falugi, C. (2008). The sea urchin, *Paracentrotus lividus*, embryo as a “bioethical” model for neurodevelopmental toxicity testing. *Cell Biol. Toxicol.* 24, 587–601. doi:10.1007/s10565-008-9061-2
- Ameys, L., Hermann, R., Killian, C., Wilt, F., and Dubois, P. (1999). Ultrastructural localization of proteins involved in sea urchin biomineralization. *J. Histochem. Cytochem.* 47, 1189–1200. doi:10.1177/002215549904700911
- Angerer, L. M., Yaguchi, S., Angerer, R. C., and Burke, R. D. (2011). The evolution of nervous system patterning: Insights from sea urchin development. *Development* 138, 3613–3623. doi:10.1242/dev.058172
- Annunziata, R., Perillo, M., Andrikou, C., Cole, A. G., Martinez, P., and Arnone, M. I. (2014). Pattern and process during sea urchin gut morphogenesis: The regulatory landscape. *Genesis* 52, 251–268. doi:10.1002/dvg.22738
- Baiao, L. F., Moura, A. P., Rocha, C., Valente, L. M. P., and Cunha, L. M. (2021). Dimensions for the valorisation of sea urchin (*Paracentrotus lividus*) gonads production through the eyes of experienced chefs. *Int. J. Gastron. Food Sci.* 26, 100438. doi:10.1016/j.ijgfs.2021.100438
- Bennett, K. C., Young, C. M., and Emlet, R. B. (2012). Larval development and metamorphosis of the deep-sea cidaroid urchin *Cidaris blakei*. *Biol. Bull.* 222, 105–117. doi:10.1086/BBLv222n2p105
- Bergeron, K.-F., Xu, X., and Brandhorst, B. P. (2011). Oral–aboral patterning and gastrulation of sea urchin embryos depend on sulfated glycosaminoglycans. *Mech. Dev.* 128, 71–89. doi:10.1016/j.mod.2010.11.001
- Bernardo, M. D., and Carlo, M. D. (2017). “The sea urchin embryo: A model for studying molecular mechanisms involved in human diseases and for testing bioactive compounds” in *Sea Urchin - from environment to aquaculture and biomedicine*. 119–144. doi:10.5772/intechopen.70301
- Boudouresque, C. F., and Verlaque, M. (2013). “*Paracentrotus lividus*,” in *Developments in aquaculture and fisheries science*. Editor J. M. Lawrence (Amsterdam: Elsevier), 297–327. doi:10.1016/B978-0-12-396491-5.00021-6
- Boveri, T. (1901). Die Polarität von Ovocyte, Ei Und Larve des *Strongylocentrotus lividus*. *Jahrb. Abt. Anat. Ontol.* 14, 630–653.
- Boveri, T. (1902). Über mehrpolige Mitosen als Mittel zur Analyse des Zellkerns. *Verhandl. Phys.-Med. Ges. Würzburg* 35, 67–90.
- Bump, P., Khariton, M., Stubbart, C., Moyon, N. E., Yan, J., Wang, B., et al. (2022). Comparisons of cell proliferation and cell death across life histories in the hemichordate *Schizocardium californicum*. *bioRxiv* 0216, 480686. doi:10.1101/2022.02.16.480686
- Burke, R. D., and Alvarez, C. M. (1988). Development of the esophageal muscles in embryos of the sea urchin *Strongylocentrotus purpuratus*. *Cell Tissue Res.* 252, 411–417. doi:10.1007/BF00214384
- Burke, R. D. (1980). Podial sensory receptors and the induction of metamorphosis in echinoids. *J. Exp. Mar. Biol. Ecol.* 47, 223–234. doi:10.1016/0022-0981(80)90040-4
- Cannon, J. T., Kocot, K. M., Waits, D. S., Weese, D. A., Swalla, B. J., Santos, S. R., et al. (2014). Phylogenomic resolution of the hemichordate and echinoderm clade. *Curr. Biol.* 24, 2827–2832. doi:10.1016/j.cub.2014.10.016
- Carpenter, P. H. (1884). Report upon the Crinoidea collected during the voyage of H.M.S. Challenger during the years 1873–76. Part I: General morphology, with descriptions of the stalked crinoids. *Rep. Sci. Results Explor. Voyage H.M.S. Chall. Zool.* 11, 1–442.
- Carrier, T. J., King, B. L., and Coffman, J. A. (2015). Gene expression changes associated with the developmental plasticity of sea urchin larvae in response to food availability. *Biol. Bull.* 228, 171–180. doi:10.1086/BBLv228n3p171
- Carvalho, J. E., Lahaye, F., Yong, L. W., Croce, J. C., Escrivá, H., Yu, J.-K., et al. (2021). An updated staging system for cephalochordate development: One table suits them all. *Front. Cell Dev. Biol.* 9, 668006. doi:10.3389/fcell.2021.668006
- Castilla-Gavilán, M., Buzin, F., Cognie, B., Dumay, J., Turpin, V., and Decottignies, P. (2018). Optimising microalgae diets in sea urchin *Paracentrotus lividus* larviculture to promote aquaculture diversification. *Aquaculture* 490, 251–259. doi:10.1016/j.aquaculture.2018.02.003
- Cellario, C., and Fenaux, L. (1990). *Paracentrotus lividus* (Lamarck) in culture (larval and benthic phases): Parameters of growth observed during two years following metamorphosis. *Aquaculture* 84, 173–188. doi:10.1016/0044-8486(90)90347-P
- Chan, K. Y. K., García, E., and Dupont, S. (2015). Acidification reduced growth rate but not swimming speed of larval sea urchins. *Sci. Rep.* 5, 9764. doi:10.1038/srep09764
- Chino, Y., Saito, M., Yamasu, K., Suyemitsu, T., and Ishihara, K. (1994). Formation of the adult rudiment of sea urchins is influenced by thyroid hormones. *Dev. Biol.* 161, 1–11. doi:10.1006/dbio.1994.1001
- Conway, C. M., Igelsrud, D., and Conway, A. F. (1984). “Ch. 4. Sea urchin development,” in *Proceedings of the third workshop/conference of the association for biology laboratory education (ABLE)* (Dubuque, Iowa: Kendall/Hunt Publishing company), 53–89.
- Crapp, G. B., and Willis, M. E. (1975). Age determination in the sea urchin *Paracentrotus lividus* (Lamarck), with notes on the reproductive cycle. *J. Exp. Mar. Biol. Ecol.* 20, 157–178. doi:10.1016/0022-0981(75)90021-0
- Croce, J., Range, R., Wu, S.-Y., Miranda, E., Lhomond, G., Peng, J. C., et al. (2011). Wnt6 activates endoderm in the sea urchin gene regulatory network. *Development* 138, 3297–3306. doi:10.1242/dev.058792
- Dautov, S., Dautova, T., and Kashenko, S. (2020). Towards a scientific-based farming of sea urchins: First steps in the cultivation of *Diadema setosum*, *Diadema savignyi* and *Mesocentrotus nudus*. *APN Sci. Bull.* 10, 109–118. doi:10.30852/sb.2020.1284
- Decker, G. L., and Lennarz, W. J. (1988). Skeletogenesis in the sea urchin embryo. *Development* 103, 231–247. doi:10.1242/dev.103.2.231

Publisher's note

All claims expressed in this article are solely those of the authors and do not necessarily represent those of their affiliated organizations, or those of the publisher, the editors and the reviewers. Any product that may be evaluated in this article, or claim that may be made by its manufacturer, is not guaranteed or endorsed by the publisher.

Supplementary material

The Supplementary Material for this article can be found online at: <https://www.frontiersin.org/articles/10.3389/fcell.2022.966408/full#supplementary-material>

- Dorey, N., Martin, S., Oberhänsli, F., Teyssié, J.-L., Jeffree, R., and Lacoue-Labarthe, T. (2018). Ocean acidification modulates the incorporation of radio-labeled heavy metals in the larvae of the Mediterranean sea urchin *Paracentrotus lividus*. *J. Environ. Radioact.* 191, 20–30. doi:10.1016/j.jenvrad.2018.04.017
- Driesch, H. (1892). "The potency of the first two cleavage cells in echinoderm development: Experimental production of partial and double formations," in *Foundation of experimental embryology*. Editors W. H. Willier and J. M. Oppenheimer (New York: Hafner), 584.
- Dyachuk, V., and Odintsova, N. (2013). Larval myogenesis in Echinodermata: Conserved features and morphological diversity between class-specific larval forms of Echinoidea, Asteroidea, and Holothuroidea. *Evol. Dev.* 15, 5–17. doi:10.1111/ede.12010
- Emlet, R. B. (1988). Larval form and metamorphosis of a "primitive" sea urchin, *Eucidaris thouarsi* (Echinodermata: Echinoidea: Cidaroida), with implications for developmental and phylogenetic studies. *Biol. Bull.* 174, 4–19. doi:10.2307/1541754
- Emlet, R. B. (2010). Morphological evolution of newly metamorphosed sea urchins - A phylogenetic and functional analysis. *Integr. Comp. Biol.* 50, 571–588. doi:10.1093/icb/icc073
- Emlet, R. B. (1999). What is a juvenile sea urchin? A comparative and phylogenetic survey of post-metamorphic juveniles. *Zygote* 8, S44–S45. doi:10.1017/S0967199400130217
- Ettensohn, C. A. (2017). "Sea urchins as a model system for studying embryonic development," in *Reference module in biomedical sciences*. Elsevier. doi:10.1016/B978-0-12-801238-3.99509-6
- Ettensohn, C. A. (2020). The gene regulatory control of sea urchin gastrulation. *Mech. Dev.* 162, 103599. doi:10.1016/j.mod.2020.103599
- Ezhova, O. V., Lavrova, E. A., and Malakhov, V. V. (2014). The morphology of the axial complex and associated structures in Asterozoa (Asteroidea, Echinoidea, Ophiuroidea). *Russ. J. Mar. Biol.* 40, 153–164. doi:10.1134/S1063074014030043
- Fenaux, L., Strathmann, M. F., and Strathmann, R. A. (1994). Five tests of food-limited growth of larvae in coastal waters by comparisons of rates of development and form of echinoplutei. *Limnol. Oceanogr.* 39, 84–98. doi:10.4319/lo.1994.39.1.0084
- Fink, R. D., and McClay, D. R. (1985). Three cell recognition changes accompany the ingress of sea urchin primary mesenchyme cells. *Dev. Biol.* 107, 66–74. doi:10.1016/0012-1606(85)90376-8
- Foltz, K. R., Adams, N. L., and Runft, L. L. (2004). Echinoderm eggs and embryos: Procurement and culture. *Methods Cell Biol.* 74, 39–74. doi:10.1016/S0091-679X(04)74003-0
- Formery, L., Orange, F., Formery, A., Yaguchi, S., Lowe, C. J., Schubert, M., et al. (2021). Neural anatomy of echinoid early juveniles and comparison of nervous system organization in echinoderms. *J. Comp. Neurol.* 529, 1135–1156. doi:10.1002/cne.25012
- Fuchs, Y., and Steller, H. (2011). Programmed cell death in animal development and disease. *Cell* 147, 742–758. doi:10.1016/j.cell.2011.10.033
- Gianguzza, P., Badalamenti, F., Gianguzza, F., Bonaviri, C., and Riggio, S. (2009). The operational sex ratio of the sea urchin *Paracentrotus lividus* populations: The case of the Mediterranean marine protected area of Ustica Island (Tyrrhenian Sea, Italy). *Mar. Ecol. Prog. Ser.* 30, 125–132. doi:10.1111/j.1439-0485.2008.00267.x
- Gifondorwa, D. J., and Leise, E. M. (2006). Programmed cell death in the apical ganglion during larval metamorphosis of the marine mollusc *Ilyanassa obsoleta*. *Biol. Bull.* 210, 109–120. doi:10.2307/4134600
- Gildor, T., Malik, A., Sher, N., Avraham, L., and Ben-Tabou de-Leon, S. (2016). Quantitative developmental transcriptomes of the Mediterranean sea urchin *Paracentrotus lividus*. *Mar. Genomics* 25, 89–94. doi:10.1016/j.margen.2015.11.013
- Goodwin, T. W., and Srisukh, S. (1950). A study of the pigments of the sea-urchins, *Echinus esculentus* L. and *Paracentrotus lividus* Lamarck. *Biochem. J.* 47, 69–76. doi:10.1042/bj0470069
- Gordon, I. (1929). Skeletal development in *Arbacia*, *Echinarachnius* and *Leptasterias*. *Philos. Trans. R. Soc. Lond., B, Contain. Pap. a Biol. Character* 217, 289–334. doi:10.1098/rstb.1929.0005
- Gordon, I. (1926). VII. The development of the calcareous test of *Echinus miliaris*. *Phil. Trans. R. Soc. Lond. B* 214, 259–312. doi:10.1098/rstb.1926.0007
- Gosselin, P., and Jangoux, M. (1998). From competent larva to exotrophic juvenile: A morphofunctional study of the perimetamorphic period of *Paracentrotus lividus* (Echinodermata, Echinoidea). *Zoomorphology* 118, 31–43. doi:10.1007/s004350050054
- Hart, M. W. (1996). Evolutionary loss of larval feeding: Development, form and function in a facultatively feeding larva. *Evolution* 50, 174–187. doi:10.1111/j.1558-5646.1996.tb04484.x
- Heyland, A., and Hodin, J. (2014). A detailed staging scheme for late larval development in *Strongylocentrotus purpuratus* focused on readily-visible juvenile structures within the rudiment. *BMC Dev. Biol.* 14, 22. doi:10.1186/1471-213X-14-22
- Heyland, A., and Moroz, L. L. (2006). Signaling mechanisms underlying metamorphic transitions in animals. *Integr. Comp. Biol.* 46, 743–759. doi:10.1093/icb/icl023
- Hibino, T., Loza-Coll, M., Messier, C., Majeske, A. J., Cohen, A. H., Terwilliger, D. P., et al. (2006). The immune gene repertoire encoded in the purple sea urchin genome. *Dev. Biol.* 300, 349–365. doi:10.1016/j.ydbio.2006.08.065
- Holstein, T. W., and Laudet, V. (2014). Life-history evolution: At the origins of metamorphosis. *Curr. Biol.* 24, R159–R161. doi:10.1016/j.cub.2014.01.003
- Hörstadius, S. (1973). *Experimental biology of echinoderms*. Oxford: Clarendon Press.
- Hörstadius, S. (1939). The mechanics of sea urchin development: Studies by operative methods. *Biol. Rev.* 14, 132–179. doi:10.1111/j.1469-185x.1939.tb00929.x
- Horton, T., Kroh, A., Ahong, S., Bailly, N., Bieler, R., Boyko, C. B., et al. (2022). World register of marine species (WoRMS). Available at: <https://www.marinespecies.org> (Accessed 04 2022, 20).
- Huggett, M. J., King, C. K., Williamson, J. E., and Steinberg, P. D. (2005). Larval development and metamorphosis of the Australian diademid sea urchin *Centrostephanus rodgersii*. *Invertebr. Reprod. Dev.* 47, 197–204. doi:10.1080/07924259.2005.9652160
- Hyman, L. H. (1955). *The invertebrates: Echinodermata*. New York: McGraw-Hill.
- Ishimoda-Takagi, T., Chino, I., and Sato, H. (1984). Evidence for the involvement of muscle tropomyosin in the contractile elements of the coelom-esophagus complex in sea urchin embryos. *Dev. Biol.* 105, 365–376. doi:10.1016/0012-1606(84)90293-8
- Kitajima, T., and Urakami, H. (2000). Differential distribution of spicule matrix proteins in the sea urchin embryo skeleton. *Dev. Growth Differ.* 42, 295–306. doi:10.1046/j.1440-169x.2000.00513.x
- Kitazawa, C., Sakaguchi, C., Nishimura, H., Kobayashi, C., Baba, T., and Yamanaka, A. (2014). Development of the sea urchins *Temnopleurus toreumaticus* Leske, 1778 and *Temnopleurus reevesii* Gray, 1855 (Camarodonta: Temnopleuridae). *Zool. Stud.* 53, 3. doi:10.1186/1810-522X-53-3
- Kominami, T., and Takata, H. (2004). Gastrulation in the sea urchin embryo: A model system for analyzing the morphogenesis of a monolayered epithelium. *Dev. Growth Differ.* 46, 309–326. doi:10.1111/j.1440-169x.2004.00755.x
- Lamarck, J.-B. (1816). "Echinides" in *Histoire naturelle des animaux sans vertèbres*. Paris: Verdière, 1–59.
- Lepage, T., and Gache, C. (1989). Purification and characterization of the sea urchin embryo hatching enzyme. *J. Biol. Chem.* 264, 4787–4793. doi:10.1016/s0021-9258(18)83659-6
- Lepage, T., Sardet, C., and Gache, C. (1992). Spatial expression of the hatching enzyme gene in the sea urchin embryo. *Dev. Biol.* 150, 23–32. doi:10.1016/0012-1606(92)90004-z
- Lhomond, G., McClay, D. R., Gache, C., and Croce, J. C. (2012). Frizzled1/2/7 signaling directs β -catenin nuclearisation and initiates endoderm specification in macromeres during sea urchin embryogenesis. *Development* 139, 816–825. doi:10.1242/dev.072215
- Lin, J.-P., Tsai, M.-H., Kroh, A., Trautman, A., Machado, D. J., Chang, L.-Y., et al. (2020). The first complete mitochondrial genome of the sand dollar *Sinaechinocyamus mai* (Echinoidea: Clypeasteroidea). *Genomics* 112, 1686–1693. doi:10.1016/j.ygeno.2019.10.007
- Luo, Y.-J., and Su, Y.-H. (2012). Opposing Nodal and BMP signals regulate left-right asymmetry in the sea urchin larva. *PLoS Biol.* 10, e1001402. doi:10.1371/journal.pbio.1001402
- Lyons, D., Kaltenbach, S., and McClay, D. R. (2012). Morphogenesis in sea urchin embryos: Linking cellular events to gene regulatory network states. *Wiley Interdiscip. Rev. Dev. Biol.* 1, 231–252. doi:10.1002/wdev.18
- MacBride, E. W. (1911). Studies in heredity. I. - The effects of crossing the sea-urchins *Echinus esculentus* and *Echinocardium cordatum*. *Philos. Trans. R. Soc. Lond., B, Contain. Pap. a Biol. Character* 84, 394–403. doi:10.1098/rspb.1911.0085
- MacBride, E. W. (1918). The artificial production of echinoderm larvae with two water-vascular systems, and also of larvae devoid of a water-vascular system. *Philos. Trans. R. Soc. Lond., B, Contain. Pap. a Biol. Character* 90, 323–348. doi:10.1098/rspb.1918.0019
- MacBride, E. W. (1903). VI. The development of *Echinus esculentus*, together with some points in the development of *E. miliaris* and *E. acutus*. *Philos. Trans. R.*

- Soc. Lond., B, Contain. Pap. a Biol. Character 195, 285–327. doi:10.1098/rstb.1903.0006
- MacNeil, K. E. A., Scaros, A. T., Croll, R. P., and Bishop, C. D. (2017). Differences in larval arm movements correlate with the complexity of musculature in two phylogenetically distant echinoids, *Eucidaris tribuloides* (Cidaroida) and *Lytechinus variegatus* (Euechinoidea). *Biol. Bull.* 233, 111–122. doi:10.1086/694892
- Märkel, K., Mackenstedt, U., and Röser, U. (1992). The sphaeridia of sea urchins: Ultrastructure and supposed function (Echinodermata, Echinoidea). *Zoomorphology* 112, 1–10. doi:10.1007/BF01632989
- Matsiori, S., Aggelopoulos, S., Tsoutsou, A., Neofitou, C., Soutsas, K., and Vafidis, D. (2012). Economic value of conservation. The case of the edible sea urchin *Paracentrotus lividus*. *J. Environ. Prot. Ecol.* 13, 269–274.
- McClay, D. R. (2011). Evolutionary crossroads in developmental biology: Sea urchins. *Development* 138, 2639–2648. doi:10.1242/dev.048967
- Metaxas, A. (2001). Behaviour in flow: Perspectives on the distribution and dispersion of meroplanktonic larvae in the water column. *Can. J. Fish. Aquat. Sci.* 58, 86–98. doi:10.1139/f00-159
- Mogami, Y., Fujima, K., and Baba, S. A. (1991). Five different states of ciliary activity in the epaulette of echinoplutei. *J. Exp. Biol.* 155, 65–75. doi:10.1242/jeb.155.1.65
- Molina, M. D., de Crozé, N., Haillot, E., and Lepage, T. (2013). Nodal: Master and commander of the dorsal–ventral and left–right axes in the sea urchin embryo. *Curr. Opin. Genet. Dev.* 23, 445–453. doi:10.1016/j.gde.2013.04.010
- Mongiardino Koch, N., Coppard, S. E., Lessios, H. A., Briggs, D. E. G., Mooi, R., and Rouse, G. W. (2018). A phylogenomic resolution of the sea urchin tree of life. *BMC Evol. Biol.* 18, 189. doi:10.1186/s12862-018-1300-4
- Mooi, R., David, B., and Wray, G. A. (2005). Arrays in rays: Terminal addition in echinoderms and its correlation with gene expression. *Evol. Dev.* 7, 542–555. doi:10.1111/j.1525-142X.2005.05058.x
- Morrill, J., and Marcus, L. (2005). *An atlas of the development of the sea urchin Lytechinus variegatus*. Sarasota, Florida: New College of Florida. Available at: https://ftp.echinobase.org/pub/WikiDownloads/Atlas_of_Lytechinus_variegatus_development.pdf.
- Morris, V. B. (2009). On the sites of secondary podia formation in a juvenile echinoid: Growth of the body types in echinoderms. *Dev. Genes Evol.* 219, 597–608. doi:10.1007/s00427-010-0321-9
- Mortensen, T. (1931). *Contributions to the study of the development and larval forms of echinoderms, I-II*. København: A.F. Holst & Son.
- Mortensen, T. (1921). *Studies of the development and larval forms of echinoderms*. Copenhagen: G. E. C. Gad. doi:10.5962/bhl.title.11376
- Nesbit, K. T., and Hamdoun, A. (2020). Embryo, larval, and juvenile staging of *Lytechinus pictus* from fertilization through sexual maturation. *Dev. Dyn.* 249, 1334–1346. doi:10.1002/dvdy.223
- Nichols, D. (1972). The water-vascular system in living and fossil echinoderms. *Palaeontology* 15, 519–538.
- Nielsen, C. (1998). Origin and evolution of animal life cycles. *Biol. Rev.* 73, 125–155. doi:10.1111/j.1469-185X.1997.tb00027.x
- Nunes, C. D. A. P., and Jangoux, M. (2007). Larval growth and perimetamorphosis in the echinoid *Echinocardium cordatum* (Echinodermata): The spatangoid way to become a sea urchin. *Zoomorphology* 126, 103–119. doi:10.1007/s00435-007-0032-6
- OBIS (Ocean Biodiversity Information System) (2021). Intergovernmental oceanographic commission of UNESCO. Available at: <https://www.sciencebase.gov/catalog/item/579b64c6e4b0589fa1c98118> (Accessed February 15, 2022).
- Okazaki, K. (1975). “Normal development to metamorphosis,” in *The sea urchin embryo: Biochemistry and morphogenesis*. Editor G. Czihak (Berlin, Heidelberg: Springer Berlin Heidelberg), 177–232. doi:10.1007/978-3-642-65964-5_9
- Okazaki, K. (1965). Skeleton formation of sea urchin larvae: V. Continuous observation of the process of matrix formation. *Exp. Cell Res.* 40, 585–596. doi:10.1016/0014-4827(65)90236-3
- Okazaki, K., and Dan, K. (1954). The metamorphosis of partial larvae of *Peronella japonica* Mortensen, a sand dollar. *Biol. Bull.* 106, 83–99. doi:10.2307/1538781
- Olivares-Bañuelos, T., Figueroa-Flores, S., and Carpizo-Ituarte, E. (2012). Gonad index and larval development of the sand dollar *Dendraster excentricus* (Echinodermata; Echinoidea) in Baja California, Mexico. *Cienc. Mar.* 38, 411–425. doi:10.7773/cm.v38i2.1922
- Ortiz, A., Kardash, E., and Peyri  ras, N. (2019). 3D + time imaging of normal and twin sea urchin embryos for the reconstruction of their cell lineage. *Methods Cell Biol.* 151, 399–418. doi:10.1016/bs.mcb.2019.01.008
- Our  ns, R., Fern  ndez, L., and Freire, J. (2011). Geographic, population, and seasonal patterns in the reproductive parameters of the sea urchin *Paracentrotus lividus*. *Mar. Biol.* 158, 793–804. doi:10.1007/s00227-010-1607-1
- Paredes, E., Bellas, J., and Costas, D. (2015). Sea urchin (*Paracentrotus lividus*) larval rearing - Culture from cryopreserved embryos. *Aquaculture* 437, 366–369. doi:10.1016/j.aquaculture.2014.12.022
- Parichy, D. M., Elizondo, M. R., Mills, M. G., Gordon, T. N., and Engeszer, R. E. (2009). Normal table of postembryonic zebrafish development: Staging by externally visible anatomy of the living fish. *Dev. Dyn.* 238, 2975–3015. doi:10.1002/dvdy.22113
- Paul, C. R. C., and Hotchkiss, F. H. C. (2020). Origin and significance of Lov  n’s Law in echinoderms. *J. Paleontol.* 94, 1089–1102. doi:10.1017/jpa.2020.31
- Peters, B. H., and Campbell, A. C. (1987). Morphology of the nervous and muscular systems in the heads of pedicellariae from the sea urchin *Echinus esculentus* L. *J. Morphol.* 193, 35–51. doi:10.1002/jmor.1051930105
- Peterson, K. J., Arenas-Mena, C., and Davidson, E. H. (2000). The A/P axis in echinoderm ontogeny and evolution: Evidence from fossils and molecules. *Evol. Dev.* 2, 93–101. doi:10.1046/j.1525-142x.2000.00042.x
- Peterson, R. E., and McClay, D. R. (2003). Primary mesenchyme cell patterning during the early stages following ingress. *Dev. Biol.* 254, 68–78. doi:10.1016/S0012-1606(02)00025-8
- Politi, Y., Arad, T., Klein, E., Weiner, S., and Addadi, L. (2004). Sea urchin spine calcite forms via a transient amorphous calcium carbonate phase. *Science* 306, 1161–1164. doi:10.1126/science.1102289
- Pr  li  re, G., Cosson, J., Chevalier, S., Sardet, C., and Chenevert, J. (2011). Atypical protein kinase C controls sea urchin ciliogenesis. *Mol. Biol. Cell* 22, 2042–2053. doi:10.1091/mbc.e10-10-0844
- Rahman, M. A., Yusoff, F. Md., Arshad, A., Shamsudin, M. N., and Amin, S. M. N. (2012). Embryonic, larval, and early juvenile development of the tropical sea urchin, *Salmacis sphaeroides* (Echinodermata: Echinoidea). *Sci. World J.* 938482. doi:10.1100/2012/938482
- Rahman, M., Yusoff, F., and Arshad, A. (2015). Embryonic, larval and juvenile development of tropical sea urchin, *Diadema setosum*. *Iran. J. Fish. Sci.* 2, 409–424.
- Range, R. C., Angerer, R. C., and Angerer, L. M. (2013). Integration of canonical and noncanonical Wnt signaling pathways patterns the neuroectoderm along the anterior–posterior axis of sea urchin embryos. *PLoS Biol.* 11, e1001467. doi:10.1371/journal.pbio.1001467
- Robert, N., Lhomond, G., Schubert, M., and Croce, J. C. (2014). A comprehensive survey of wnt and frizzled expression in the sea urchin *Paracentrotus lividus*. *Genesis* 52, 235–250. doi:10.1002/dvg.22754
- Roccheri, M. C., Tipa, C., Bonaventura, R., and Matrangola, V. (2002). Physiological and induced apoptosis in sea urchin larvae undergoing metamorphosis. *Int. J. Dev. Biol.* 46, 801–806. doi:10.1387/ijdb.12382946
- Ruffins, S. W., and Ettensohn, C. A. (1996). A fate map of the vegetal plate of the sea urchin (*Lytechinus variegatus*) mesenchyme blastula. *Development* 122, 253–263. doi:10.1242/dev.122.1.253
- Sardet, C., and Chang, P. (1985). A marker of animal-vegetal polarity in the egg of the sea urchin *Paracentrotus lividus*. *Exp. Cell Res.* 160, 73–82. doi:10.1016/0014-4827(85)90237-X
- Sato, Y., Kaneko, H., Negishi, S., and Yazaki, I. (2006). Larval arm resorption proceeds concomitantly with programmed cell death during metamorphosis of the sea urchin *Hemicentrotus pulcherrimus*. *Cell Tissue Res.* 326, 851–860. doi:10.1007/s00441-006-0212-6
- Saudemont, A., Haillot, E., Mekpoh, F., Bessodes, N., Quirin, M., Lapraz, F., et al. (2010). Ancestral regulatory circuits governing ectoderm patterning downstream of Nodal and BMP2/4 revealed by gene regulatory network analysis in an echinoderm. *PLoS Genet.* 6, e1001259. doi:10.1371/journal.pgen.1001259
- Schneider, C. A., Rasband, W. S., and Eliceiri, K. W. (2012). NIH image to ImageJ: 25 years of image analysis. *Nat. Methods* 9, 671–675. doi:10.1038/nmeth.2089
- Schroeder, T. E. (1981). Development of a “primitive” sea urchin (*Eucidaris tribuloides*): Irregularities in the hyaline layer, micromeres and primary mesenchyme. *Biol. Bull.* 161, 141–151. doi:10.2307/1541114
- Slota, L. A., Miranda, E., Peskin, B., and McClay, D. R. (2020). Developmental origin of peripheral ciliary band neurons in the sea urchin embryo. *Dev. Biol.* 459, 72–78. doi:10.1016/j.ydbio.2019.12.011
- Smith, A. B. (2008). Deuterostomes in a twist: The origins of a radical new body plan. *Evol. Dev.* 10, 493–503. doi:10.1111/j.1525-142X.2008.00260.x
- Smith, M. M., Cruz Smith, L., Cameron, R. A., and Urry, L. A. (2008). The larval stages of the sea urchin, *Strongylocentrotus purpuratus*. *J. Morphol.* 269, 713–733. doi:10.1002/jmor.10618

- Stauber, M. (1993). The lantern of Aristotle: Organization of its coelom and origin of its muscles (Echinodermata, Echinoidea). *Zoomorphology* 113, 137–151. doi:10.1007/BF00403091
- Strathmann, R. R. (1978). “Larval settlement in echinoderms,” in *Settlement and metamorphosis of marine invertebrate larvae*. Editors F. S. Chia and M. E. Rice (New York: Elsevier), 235–247.
- Strathmann, R. R. (1971). The feeding behavior of planktotrophic echinoderm larvae: Mechanisms, regulation, and rates of suspensionfeeding. *J. Exp. Mar. Biol. Ecol.* 6, 109–160. doi:10.1016/0022-0981(71)90054-2
- Strathmann, R. R., Fenaux, L., and Strathmann, M. F. (1992). Heterochronic developmental plasticity in larval sea urchins and its implications for evolution of nonfeeding larvae. *Evolution* 46, 972–986. doi:10.1111/j.1558-5646.1992.tb00613.x
- Taris, N., Comtet, T., Stolba, R., Lasbleiz, R., Pechenik, J. A., and Viard, F. (2010). Experimental induction of larval metamorphosis by a naturally-produced halogenated compound (dibromomethane) in the invasive mollusc *Crepidula fornicata* (L.). *J. Exp. Mar. Biol. Ecol.* 393, 71–77. doi:10.1016/j.jembe.2010.07.001
- Technau, U., and Scholz, C. B. (2003). Origin and evolution of endoderm and mesoderm. *Int. J. Dev. Biol.* 47, 531–539. doi:10.1387/ijdb.14756329
- Telford, M. J., Lowe, C. J., Cameron, C. B., Ortega-Martinez, O., Aronowicz, J., Oliveri, P., et al. (2014). Phylogenomic analysis of echinoderm class relationships supports Asterozoa. *Proc. Biol. Sci.* 281, 20140479. doi:10.1098/rspb.2014.0479
- Temereva, E. N., and Tsitrin, E. B. (2014). Organization and metamorphic remodeling of the nervous system in juveniles of *Phoronopsis harmeri* (Phoronida): Insights into evolution of the bilaterian nervous system. *Front. Zool.* 11, 35. doi:10.1186/1742-9994-11-35
- Tenuzzo, B. A., Zaccarelli, N., and Dini, L. (2012). The reproductive cycle of the commercial sea urchin *Paracentrotus lividus* (Lamarck, 1816) (Echinodermata: Echinoidea) in the Ionian Sea. *Ital. J. Zool. (Modena)*. 79, 200–211. doi:10.1080/11250003.2011.626803
- Thet, M. M., Noguchi, M., and Yazaki, I. (2004). Larval and juvenile development of the echinometrid sea urchin *Colobocentrotus mertensii*: Emergence of the peculiar form of spines. *Zool. Sci.* 21, 265–274. doi:10.2108/zsj.21.265
- Thompson, J. R., Erkenbrack, E. M., Hinman, V. F., McCauley, B. S., Petsios, E., and Bottjer, D. J. (2017). Paleogenomics of echinoids reveals an ancient origin for the double-negative specification of micromeres in sea urchins. *Proc. Natl. Acad. Sci. U. S. A.* 114, 5870–5877. doi:10.1073/pnas.1610603114
- Thompson, J. R., Paganos, P., Benvenuto, G., Arnone, M. I., and Oliveri, P. (2021). Post-metamorphic skeletal growth in the sea urchin *Paracentrotus lividus* and implications for body plan evolution. *EvoDevo* 12, 3. doi:10.1186/s13227-021-00174-1
- Ullrich-Lüter, E. M., Dupont, S., Arboleda, E., Hausen, H., and Arnone, M. I. (2011). Unique system of photoreceptors in sea urchin tube feet. *Proc. Natl. Acad. Sci. U. S. A.* 108, 8367–8372. doi:10.1073/pnas.1018495108
- Vellutini, B. C., and Migotto, A. E. (2010). Embryonic, larval, and juvenile development of the sea biscuit *Clypeaster subdepressus* (Echinodermata: Clypeasteroidea). *PLoS One* 5, e9654. doi:10.1371/journal.pone.0009654
- von Ubisch, L. (1913). Die Entwicklung von *Strongylocentrotus lividus*. *Z. für Wiss. Zool.* 106, 409–488.
- Wessel, G. M., Zhang, W., and Klein, W. H. (1990). Myosin heavy chain accumulates in dissimilar cell types of the macromere lineage in the sea urchin embryo. *Dev. Biol.* 140, 447–454. doi:10.1016/0012-1606(90)90093-X
- Wilkie, I. C., Candia Carnevali, M. D., and Andrietti, F. (1998). Mechanical properties of sea-urchin lantern muscles: A comparative investigation of intact muscle groups in *Paracentrotus lividus* (lam.) and *Stylocidaris affinis* (phil.) (Echinodermata, Echinoidea). *J. Comp. Physiology B Biochem. Syst. Environ. Physiology* 168, 204–212. doi:10.1007/s003600050138
- Wilkie, I. C. (2002). Is muscle involved in the mechanical adaptability of echinoderm mutable collagenous tissue? *J. Exp. Biol.* 205, 159–165. doi:10.1242/jeb.205.2.159
- Wray, G. A. (1992). The evolution of larval morphology during the post-paleozoic radiation of echinoids. *Paleobiology* 18, 258–287. doi:10.1017/s0094837300010848
- Yajima, M. (2007). A switch in the cellular basis of skeletogenesis in late-stage sea urchin larvae. *Dev. Biol.* 307, 272–281. doi:10.1016/j.ydbio.2007.04.050
- Yamazaki, A., Kidachi, Y., and Minokawa, T. (2012). “Micromere” formation and expression of endomesoderm regulatory genes during embryogenesis of the primitive echinoid *Prionocidaris baculosa*. *Dev. Growth Differ.* 54, 566–578. doi:10.1111/j.1440-169X.2012.01360.x
- Ziegler, A., Faber, C., and Bartolomeaus, T. (2009). Comparative morphology of the axial complex and interdependence of internal organ systems in sea urchins (Echinodermata: Echinoidea). *Front. Zool.* 6, 10. doi:10.1186/1742-9994-6-10
- Ziegler, A., Schröder, L., Ogurreck, M., Faber, C., and Stach, T. (2012). Evolution of a novel muscle design in sea urchins (Echinodermata: Echinoidea). *PLoS ONE* 7, e37520. doi:10.1371/journal.pone.0037520



OPEN ACCESS

EDITED BY

Maria Cecilia Cirio,
CONICET Institute of Physiology,
Molecular Biology, and Neurosciences
(IFIBYNE), Argentina

REVIEWED BY

Adam Pare,
University of Arkansas, United States
David McClay,
Duke University, United States

*CORRESPONDENCE

Emmanuel Farge,
efarge@curie.fr

[†]These authors have contributed equally
to this work

SPECIALTY SECTION

This article was submitted to
Morphogenesis and Patterning,
a section of the journal
Frontiers in Cell and
Developmental Biology

RECEIVED 12 July 2022

ACCEPTED 01 November 2022

PUBLISHED 01 December 2022

CITATION

Nguyen NM, Merle T,
Broders-Bondon F, Brunet A-C,
Battistella A, Land EBL, Sarron F, Jha A,
Gennisson J-L, Röttinger E,
Fernández-Sánchez ME and Farge E
(2022), Mechano-biochemical marine
stimulation of inversion, gastrulation,
and endomesoderm specification in
multicellular Eukaryota.
Front. Cell Dev. Biol. 10:992371.
doi: 10.3389/fcell.2022.992371

COPYRIGHT

© 2022 Nguyen, Merle, Broders-
Bondon, Brunet, Battistella, Land,
Sarron, Jha, Gennisson, Röttinger,
Fernández-Sánchez and Farge. This is
an open-access article distributed
under the terms of the [Creative
Commons Attribution License \(CC BY\)](#).
The use, distribution or reproduction in
other forums is permitted, provided the
original author(s) and the copyright
owner(s) are credited and that the
original publication in this journal is
cited, in accordance with accepted
academic practice. No use, distribution
or reproduction is permitted which does
not comply with these terms.

Mechano-biochemical marine stimulation of inversion, gastrulation, and endomesoderm specification in multicellular Eukaryota

Ngoc Minh Nguyen ^{1†}, Tatiana Merle ^{1†},
Florence Broders-Bondon ¹, Anne-Christine Brunet ¹,
Aude Battistella ², Emelie Britt Linnea Land ¹,
Florian Sarron ³, Aditya Jha ⁴, Jean-Luc Gennisson ⁵,
Eric Röttinger ^{6,7}, María Elena Fernández-Sánchez ¹ and
Emmanuel Farge ^{1*}

¹Mechanics and Genetics of Embryonic Development Group, Institut Curie, Centre OCAV PSL Research University, CNRS, UMR168, Inserm, Sorbonne University, Paris, France, ²Biochemistry, Molecular Biology, and Cells Platform, Institut Curie, CNRS, UMR 168, Inserm, Sorbonne University, Paris, France, ³Sorbonne Université, CNRS, UMR 7095, Institut d'Astrophysique de Paris, Paris, France, ⁴Laboratoire Physique et Mécanique des Milieux Hétérogènes (PMMH), CNRS, ESPCI ParisTech, Université Pierre et Marie Curie, Université Paris Diderot, Paris, France, ⁵Université Paris-Saclay, CEA, CNRS, Inserm, BioMaps, Service Hospitalier Frédéric Joliot, Orsay, France, ⁶Université Côte d'Azur, CNRS, INSERM, Institute for Research on Cancer and Aging (IRCAN), Nice, France, ⁷Université Côte d'Azur, Institut Fédératif de Recherche Ressources Marines (IFR MARRES), Nice, France

The evolutionary emergence of the primitive gut in Metazoa is one of the decisive events that conditioned the major evolutionary transition, leading to the origin of animal development. It is thought to have been induced by the specification of the endomesoderm (EM) into the multicellular tissue and its invagination (i.e., gastrulation). However, the biochemical signals underlying the evolutionary emergence of EM specification and gastrulation remain unknown. Herein, we find that hydrodynamic mechanical strains, reminiscent of soft marine flow, trigger active tissue invagination/gastrulation or curvature reversal *via* a Myo-II-dependent mechanotransductive process in both the metazoan *Nematostella vectensis* (cnidaria) and the multicellular choanoflagellate *Choanoeca flexa*. In the latter, our data suggest that the curvature reversal is associated with a sensory-behavioral feeding response. Additionally, like in bilaterian animals, gastrulation in the cnidarian *Nematostella vectensis* is shown to participate in the biochemical specification of the EM through mechanical activation of the β -catenin pathway *via* the phosphorylation of Y654- β -catenin. Choanoflagellates are considered the closest living relative to metazoans, and the common ancestor of choanoflagellates and metazoans dates back at least 700 million years. Therefore, the present findings using these evolutionarily distant species suggest that the primitive emergence of the gut in Metazoa may have been initiated in response to marine mechanical stress already in multicellular pre-Metazoa. Then, the evolutionary transition may have been achieved by specifying the EM *via* a mechanosensitive Y654- β -catenin dependent mechanism, which

appeared during early Metazoa evolution and is specifically conserved in all animals.

KEYWORDS

hydrodynamic mechanical strains, cnidaria *Nematostella vectensis*, choanoflagellate *Choanoeca flexa*, mechanotransduction, evolutionary emergence of first Metazoa organisms, myosin-dependent mechanosensitivity, beta-catenin-dependent mechanosensitivity, primitive motor-sensorial behavioral mechanosensing

Introduction

Metazoa are composed of complex body plans, each defining its distinct functional organs (De Robertis, 2008). The emergence of the first Metazoa organism probably resulted from the evolutionary development of multicellularity, reproduction by egg–sperm fusion, and the formation of the first organ: the primitive gut (Haeckel, 1874; Brunet and King, 2017). The primitive gut was probably formed from primitive multicellular blastulae hollow spheres *via* gastrulation. In today's early embryos, this process consists of an active morphogenetic movement initiated by the inversion of the geometric curvature of the two-dimensional multicellular leaflet-like tissue (invagination) pre-specified as the endomesoderm (EM) (Arendt, 2004). It remains unclear whether the biochemical signals involved in EM specification and gastrulation are conserved in current early Metazoa embryos. However, the reversal of the curvature in these multicellular leaflets (responsible for the initiation of gastrulation) is regulated by several distinct signaling pathways (EphA4, Fog, and Stb) that depend on the species involved (Sweeton et al., 1991; Kumburegama et al., 2011; Evren et al., 2014). Similarly, the biochemical specification of the EM is regulated by multiple diverse signaling pathways, including Nodal, Dorsal, or Wnts, and is also species-dependent (Roth, 2004; Kusserow et al., 2005; Hagos and Dougan, 2007). Thus, the existence of a common evolutionary origin in the emergence of the primitive digestive organ in Metazoa remains uncertain.

Molecular activation of the Myo-II motor by internal mechanical strains has been shown to trigger invaginations of the mesoderm and endoderm during gastrulation in bilaterian *Drosophila* embryos (Mitrossilis et al., 2017; Bailles et al., 2019). Additionally, mechanical strains were involved in the expression of endodermal and mesodermal genes in early *Drosophila* and zebrafish bilaterian embryos (Desprat et al., 2008; Brunet et al., 2013). Specifically, the mechanical stimulation of Twist and *brachyury* endomesodermal determinants expression was β -catenin (β -cat) dependent and stimulated and induced as a result of the mechanical induction of Y654- β cat phosphorylation in response to the early internal morphogenetic movements of embryogenesis, gastrulation, and epiboly, respectively (Desprat et al., 2008; Brunet et al., 2013). Furthermore, the expression of *brachyury* in the blastopore of the cnidarian sea anemone *Nematostella vectensis* (*N. vectensis*) can be repressed by blocking gastrulation and can be partially re-established in response to

uniaxial global deformation applied to early *N. vectensis* blastulae in a β -cat dependent way. Thus, the blastopore specification, which determines the ectoderm of the pharynx and has been proposed to separate the ectoderm from other tissue types (Servetnick et al., 2017; Steinmetz et al., 2017), was suggested to be mechanically induced by the gastrulation morphogenetic movement (Pukhlyakova et al., 2018).

The cnidarian *N. vectensis* and the bilaterians *Drosophila* and zebrafish diverged from the common ancestor of bilaterians and cnidarians at least 600 million years ago (Park et al., 2012; dos Reis et al., 2015). Thus, alternatively to biochemical signals, mechanical signals could be plausible initiators of the intracellular biochemical reactions that, in turn, resulted in the evolutionary emergence of EM specification and gastrulation in early Metazoa. Such mechanical signals could, in this case, have been conserved during evolution and in current species of cnidarians and bilaterians.

Here this hypothesis was evaluated in the marine mechanical, environmental context in which pre-metazoan multicellular colonies evolved, using both evolutionarily pivotal multicellular and colonial species: the metazoan cnidarian *N. vectensis* and the choanoflagellate *Choanoeca flexa* (*C. flexa*). The common ancestor of these species with bilateria dates back 600–700 million years and more than 700 million years ago, respectively (Park et al., 2012; dos Reis et al., 2015). Soft waves were used to mimic the hydrodynamic mechanical stresses developed at the marine coastlines and applied to both species to test the sharing of mechanotransductive activation of i) the myosin-dependent morphogenetic movement of inversion of the geometric curvature of multicellular leaflets that initiates metazoan gastrulation and ii) Y654- β cat phosphorylation involved in EM specification in these evolutionarily distant species of Bilateria. The sharing of mechanical stimulation of EM morphogenesis and specification could allow the dating of the evolutionary emergence of these mechanical/molecular processes, possibly conserved relative to the last common ancestor of these two species with Bilateria.

Materials and methods

Nematostella vectensis

N. vectensis culture and spawning

N. vectensis sea anemones (WT, males and females, more than 1-year-old, accession number ABAV01000000) are kept in

artificial seawater (ASW) at 18°C in the dark and fed every day with fresh *Artemia* nauplii. Females and males are kept separately in different glass bowls (ϕ15x6 cm), half-filled with ASW made by dissolving 10 g of Instant Ocean salt (Aquarium Systems) in 1 L of deionized water (1/3x SW). Approximately 30–40 individuals are cultivated in each bowl. Animals are moved to clean bowls with fresh 1/3x SW every 2 weeks. No further care is required during the weekend.

Adult animals were prepared for spawning every 3 weeks. Animals are fed with defrosted oysters 24–48 h before spawning day. The night before spawning, the animals/culture medium temperature was slightly increased (~25°C) and exposed to light for 9 h. After this spawning stimulation, animals are moved to new bowls with fresh, cool (18°C) 1/3x SW awaiting the release of gametes. Sperms and eggs are collected separately. Oocytes are fertilized *in vitro* to synchronize development by dropping sperms into the egg beaker, which is then gently shaken for 15 min at room temperature. The fertilized eggs are kept in the dark at 18°C. In this condition, most embryos reach the blastula stage 18 h after fertilization. For each individual experiment, all embryos (controls and perturbed embryos) are taken from the same lay synchronized by common fertilization in the same solution before being separated, treated, and fixed in parallel at the same time. Thus, they are analyzed at the same stage.

Hydrodynamic stimulation experiment

A liquid silicone-based elastomer (Sylgard 184, Dow Corning) and a curing agent were mixed at a 10:1 ratio and then poured into ϕ 10 mm Falcon Petri dishes (4 g of mixture/dish). The dishes were left on a 37°C heater for 3 h. When the mixture was almost dried out but remained sticky, sand with an average grain size of 1 mm was added and spread out to fully cover the dish floor. Sanded dishes were rinsed thoroughly with MilliQ water and then 1/3x filtered sea water (FSW) before the experiment. These dishes can be reused.

The sand was glued to reflect the granularity of the seashore ground that kept sand on the ground under flow, whereas in the Petri dishes, the sand would have been removed by the flow leading to flat ground. The flow near the ground is probably slightly different at the 0.5–1 mm (size of sand grains) distance over the surface in the loose configuration compared to fixed sand but should remain on the same order of magnitude at the larger distance of 1.5–4 mm scale of the gel in which embryos are embedded. Indeed, because of the existence of a fixed sand surface below the loose one on the seashore, the flow velocities with sand glued should remain on the same order of magnitude compared to the seashore configuration. The granularity of the ground of a sea-shore natural environment should result in friction between the granular surface and the jelly because even the loose sand surface is necessarily a fixed granular sand surface inducing such friction.

At 16 h, embryos were transferred to sanded petri dish filled with 22 ml of 1/3x FSW. The dish was then put on shaker's plateaus (Major Science MS-NOR-30), which rotated at 85 rounds per minute and reversed the direction of rotation every 2.5 s for 2 h, from 16 to 18 h. All experiments were performed at 18°C unless otherwise stated.

Jellied embryos were then de-jellied using an L-cysteine solution (0.4 g/10 ml of 1/3x FSW, pH adjusted to 7.4–7.6).

Stochastic stimulations were performed by applying the following stochastic rpm, duration (min), and period sequence:

Stochasticity was computer-generated randomly within the limit conditions of the instrumentation.

RPM	Duration (min)	Period (s)
58	5	5
81	27	2
76	16	9
98	22	6
76	29	5
55	28	2

Morphologic measurements

The length L to width W ratio (ratio elliptic ratio) of hydrodynamically deformed embryos, and the invagination depth d divided by diameter D of the embryos were measured with ImageJ. The surface of apexes in the most curvature-inverted domain of the embryo, divided by their surface outside of the most curvature-inverted domain, was measured on nearly 20 cells each, on control and hydrodynamically stimulated embryos.

Oxygenation measurement

Dissolved oxygen was measured with a Hanna kit (Hanna instruments) using the HI764080 probe. The probe is calibrated at two points: i) 100% oxygen-saturated calibration when the probe is placed in the air near and above a water surface and ii) zero oxygen calibration when the probe's membrane is dipped in Hanna HI7040 Zero oxygen solution. Once calibrated, the relative oxygen solubility is measured by directly submersing the probe tip into the solution. Relative oxygen solubility was measured just before and after 2 h of hydrodynamic stimulation in two duplicated independent experiments ($N = 2$).

Global compression experiment

Embryos were compressed between a coverslip and agar between 16 and 18 h (Brunet et al., 2013; Pukhlyakova et al., 2018).

Rapid camera deformation imaging

The videos were recorded using a uEye camera equipped with a Navitar 4X Zoom lens, providing a depth of field on the order of 100 μm . The movies were shot at 10 frames per second with a resolution of 1 μm per pixel. A Petri dish containing embryos was put on an LED light source attached to the shaker's plateaus, and the whole system was placed under the camera. After 1 h of stimulation, the top-down 30 s videos were captured every 5 min in order not to overheat samples. The images extracted from the videos showed how embryos deformed in response to the stimulation. This deformation is measured by their length-to-width ratio.

Inhibitors

ML7 inhibitor (Sigma I2764) stock solution was prepared with 50% (v/v) ethanol at a concentration of 22 mM. ML7 treatment was carried out at 14 h and with a final concentration of 10 μM until the end of the experiment.

A commercial in-solution blebbistatin inhibitor was purchased from Sigma-Aldrich (2203389). Blebbistatin treatment was carried out at 14 h and at a final concentration of 50 μM until the end of the experiment.

The S381-0393 small molecule (<https://www.chemdiv.com/search-element.php?q=S381-0393>) has been selected *in silico* by ChemDiv upon request from *in silico*-designed inhibitors of βcat signaling targeting all of the βcat reactive and protein interacting site (<https://www.chemdiv.com/catalog/focused-and-targeted-libraries/inhibitors-of-beta-catenin-signaling/?sphrase-id=40485>). The S381-0393 was selected by ChemDiv as a specific inhibitor of Y654- βcat phosphorylation by mimicking best the α -helix subdomain of E-cadherin that includes I657, A656, and D665 and interacts with Y654 βcat to dock Y654- βcat and thus prevent its phosphorylation. It was validated experimentally by its effect on the inhibition of Y654- βcat phosphorylation in 21 h *N. vectensis* embryos in immunofluorescence at a final concentration of 100 μM (see Results section).

This compound was dissolved in DMSO because of good solubility. Only for experiments followed by an *in situ* hybridization labeling, because DMSO perturbed *fz10* expression, the compound was suspended at the same concentration in ASW (100 μM) instead.

Note that DMSO delayed embryonic development of 1 h, such that, in the presence of DMSO, embryos were fixed at the 19 h stage, equivalent to the 18 h untreated embryo stage.

Rhodamine phalloidin staining

Embryos were fixed in fresh 4% paraformaldehyde (PFA) supplemented with 0.2% glutaraldehyde in 1/3x FSW for 30 min at room temperature. Fixed embryos were thoroughly rinsed in PBS-Tween 1% (PTw) and then incubated in fetal bovine serum (FBS) at 10% (v/v). Finally, embryos were incubated in 300x diluted rhodamine phalloidin (Life Technologies, R415). Images were taken in black and white and colored in green for better visualization.

β -Catenin and p-Y654 β -catenin staining Immunohistochemistry

On the first day, fixed embryos were rinsed in PTw followed by FBS 10% (v/v) for 30 min. Then, embryos were incubated overnight at 4°C in the primary human antibody (anti- β -catenin produced in rabbit (Sigma, C2206) validated in *N. vectensis* in reference (Leclerc et al., 2016) or human anti-p-Y654- β -catenin produced in mouse (CliniSciences, NB-22-0209-S and 1:250, Santa Cruz Biotechnology (1B11) Ref 57533)) for one night at 4°C.

The following day, embryos were thoroughly rinsed in PTw and again in FBS 10% for 30 min. After that, embryos were incubated in a secondary Alexa Fluor 488 conjugated antibody. Rhodamine phalloidin was also added in this step to the secondary antibody.

Western blot

Nematostella embryos (~40–50 embryos per condition) were harvested at 18 h or 21 h of development and resuspended in 75 μL of ice-cold AT protein extraction buffer (20 mM HEPES pH 7.9, 1 mM EDTA, 1 mM EGTA, 20% glycerol, 1% Triton X-100, 20 mM NaF, 1 mM $\text{Na}_4\text{P}_2\text{O}_7 \cdot 10\text{H}_2\text{O}$, 1 mM dithiothreitol, 1% phosphatase inhibitor cocktail, and 1% protease inhibitors). Embryos were pulverized in the AT buffer with a plastic pestle and sonicated twice for 10 s at setting 5 on a 550 sonic dismembrator. Afterward, NaCl was added to each lysate to get a final concentration of 150 mM NaCl. Samples were centrifuged at 16,000 g for 20 min at 4°C, and the supernatant was transferred to a fresh 1.5 ml microcentrifuge tube. 50 μL of ice-cold AT buffer was added to the remaining lysate pellet and resuspended by drawing it through a 27.5-gauge needle. Protein concentrations of the pellets were determined by Bradford. An equivalent quantity of protein (50 mg) was resolved by SDS-PAGE, transferred to a nitrocellulose membrane (Invitrogen), incubated o/n with TBS-Tween 5% milk supplemented with 1% bovine serum albumin blocking buffer, and hybridized with the appropriate antibodies for 4 h. The detection of proteins was realized using enhanced chemiluminescence (Amersham, ECL Prime Western Blotting Detection Reagent). The following antibodies were used: anti-p-Y654- β -catenin produced in mice [Santa Cruz Biotechnology (1B11) Ref 57533 1:1,000], anti-GAPDH produced in rabbit (Sigma Ref G9545 1:1,000) (HRP) conjugated secondary antibodies (Jackson ImmunoResearch, 1:1,000) in the same blot, with phosphoY654- βcat ~70KD (<https://www.clinisciences.com/autres-produits-186/anti-phospho-ctnnb1-tyr654-antibody-921000209.html>) and GAPDH 37 KDa.

In situ hybridization of *fz10* gene

Fixation

We followed the fixation protocol described in Genikhovich&Technau DOI: 10.1101/pdb.prot5282. Briefly, embryos were rinsed in PTw, then rapidly pre-fixed in PFA

4% + glutaraldehyde 0.8% for 90 s, and finally fixed in PFA 4% for 2 h. Fixed embryos are then rinsed 3x in PTw, 2x in sterile water, 1x in pure methanol. All steps were done on ice. Embryos were stored at -20°C in pure methanol for at least one night.

Preparation of mRNA probe

pCS2 DNA recombinant plasmids were used as templates to amplify the cDNA inserts by PCR. The PCR products were used as templates to synthesize anti-sense RNA probes containing digoxigenin-11-UTP (Roche Biochemicals).

In vitro transcription was carried out using the T7 Ambion message machine kit (Ambion, United States) to synthesize anti-sense probes for *fz10*, *bmp-1 like*. After DNase RNase-free treatment, RNA was dissolved in RNase-free water.

Procedure

We followed the *in situ* hybridization protocol optimized by E. Röttinger's team (Rottinger et al., 2012). All duplicated experiments were realized and revealed with controls and perturbed conditions at the same time with the same mother solutions and timing conditions.

mRNA microinjection

Preparation of mRNA

The non-phosphorylatable dominant negative of Y654- β cat RNA, Y654F- β cat, was produced by mutating the nucleotide sequence of Y tyrosine "tac" in the F Phenylalanine sequence "ttc" on the Y641 of *N. vectensis* (http://nvertx.ircan.org/ER/ER_plotter/home) that, following a sequence alignment, was determined to correspond to the Y654 residue in mice (Roper et al., 2018). The sequence was cloned in pCS2+, and mRNA was produced with mMESSAGE mMACHINE® Kit, High Yield Capped RNA Transcription Kit, SP6, Catalog Numbers AM1340.

Stb-MO and *stb* were designed (Kumburegama et al., 2011), with the following standard sequence as a Control-MO sequence: CCTCTTACCTCAGTTACAATTTATA.

Microinjection experiment

Embryos are maintained at 1/3x FSW at 16°C after being fertilized and dejellied to slow down their development. The injection must be done within the first 4 h after fertilization, before the first cleavage. For the injection experiment, embryos were deposited on a Falcon Petri dish (351007) along some parallel scratches, which served as landmarks with manipulation under a microscope. These dishes are recommended for good adhesion of embryos on the floor. We used home-made micro-needles fabricated by a capillary pulling machine. The FemtoJet microinjector enables one to adjust a constant, permanent pressure and injection pressure. In practice, these parameters are tuned so that the liquid volume at the needle end, when injected, makes a spot of diameter roughly 20% of the embryo diameter. Phymep micromanipulator SM3.25 was used.

Injected embryos are kept at 20°C . In this condition, embryos normally reach the blastula stage at 20 h. Before any further experiments, we select only successfully injected embryos by removing all broken or without detectable fluorescent marker embryos.

Hydrodynamic stimulation was thus applied between 18 and 20 h embryos for *stb-MO* experiments.

Imaging and analysis

Spinning and microscope

Fluorescent imaging and morphological observation were performed with a Yokogawa spinning dish confocal (CSU-X1) coupled to Olympus inverted microscope (IX70). The actin, nucleus, or β -cat of *N. vectensis* embryos in this study was an image extracted from a stack or MAX intensity projection of a whole stack obtained with ImageJ software.

Cell size analysis was performed on the max projection image of each stack. A $50 \times 50 \mu\text{m}^2$ zone was chosen inside the invaginating domain to measure apex constriction in the gastrulating EM and outside, far from the invaginating area (when applicable, given the embryo orientation images) to avoid apex deformation by gastrulation. The average cell size was then determined by dividing the area by the number of cells within the zone.

The quantitative analysis of nuclear β -cat intensity was done in the invagination area (if applicable) or on domains of maximal nuclear β -cat intensity for non-invaginating embryos. The nuclear β -cat signal of each cell was normalized to the intensity of an equivalent area but outside of the nucleus in the cytoplasm of the same cell. For each embryo, this measurement was applied to about 10 cells randomly in the concerned domain.

Y654- β -cat phosphorylation quantitative analysis at the tissue scale was performed by ImageJ. Image stacks of the embryo were taken every two microns on half of the embryo. The total intensity/pixel of the embryo was measured and normalized to the average intensity of the external background after the summing of all stacks.

The intensity gradient was systematically measured based on the plan in the blastopore (invagination area) of maximal intensity, normalized to the intensity of the rest of the embryo. At 18 h of development, non-gastrulated embryos were systematically orientated along the direction of the maximum gradient for the measurement.

Y654- β -cat phosphorylation quantitative analysis at the cell scale was performed by an algorithm using the Phalloidin junctional signal to discriminate between two different cells (see Code in [Supplementary Material](#)) after imaging stacks of images separated by 1 micron of each embryo along its three principal axes (Merle, 2018).

To precisely analyze large numbers of embryos at the cell scale, we created an algorithm using Python programming. 3D images (stack) were projected to get 2D images (sum of 5 pixels

around the z maximum). We first applied an Otsu filter to discriminate the background signal from the embryo signal. Then, based on the actin signal, we realized skeletonization using the DisPerSE software (Sousbie, 2011). The skeleton was dilated up to 5 pixels to correspond to the width of the cell junctions. A watershed-based segmentation allowed us to create a cell catalog, reporting for each cell its apical area and its apical perimeter. Moreover, for each channel (actin and pY654- β cat signals), the catalog contains the mean intensities of the junctional and cytosolic cell signals, respectively. All these measures were normalized to the background mean intensity.

Hybridization images were taken with a CoolSNAP (HQ2) camera mounted on an upright widefield Leica microscope.

Choanoeca flexa

Culture

The *C. flexa* strain containing the *Pseudomonas oceanii* bacteria only (that lacks genes in the retinal photosensitive pathway biosynthesis) was obtained from Thibaut Brunet (UC-Berkeley) and cultured in 10 ml sea water medium in a sea salt 16.45 g/L culture flask, in the presence of rifampicin 20 μ g/ml antibiotic to which *Pseudomonas oceanii* is resistant, selecting this bacteria only into the culture (Brunet et al., 2019), with the difference that the antibiotic was directly diluted into the sea water medium without DMSO. Culture let to around 70 microns multicellular half-spheres. Adding a rice grain into the culture following reference (King et al., 2009) led, in addition, to numerous 500 to 1,000 microns multicellular sheets mixing half-spheres and almost complete spheres.

Hydrodynamic stimulation

Rice cultured *C. flexa* were hydrodynamically stimulated after 4–5 days of culture, for 2 min directly in three flasks, by the Major Science MS-NOR-30 shaker used for *Nematostella* hydrodynamic stimulation, with a speed of 105 rpm and a positive-to-negative cycling period of 2.5 s, leading to a flow on the order of 20 cm/s, after removing the rice grain.

ML7 treatment

10 ml of the sea water cultured *C. flexa* was implemented with 1–22.5 μ L of a 22 mM concentration of ML7 suspended in 50% water and 50% ethanol for 30 min before hydrodynamic stimulation. Note that ML7 treatment did not perturb unstimulated *C. flexa* structures but systematically weakened hydrodynamically stimulated *C. flexa* structures, leading to smaller pieces of multicellular tissues after hydrodynamic stimulation.

Morphological observation

The *C. flexa* morphological phenotypes were observed in transmission with a DMIRB inverted microscope Leica recorded

with a C4742-95 Hamamatsu camera. Phenotype counting was initiated 20 min after the end of the stimulation.

Fluorescent labeling and imaging

C. flexa were fixed following reference procedures described by Brunet et al. (2019) on FluoroDishes and mini glass slides pre-treated with a handheld Corona surface treater (Electro-Technic Products BD-20AC) and coated with poly-D-lysine (Sigma Aldrich P6407-5 MG). Immunofluorescence staining was performed using rabbit anti-myosin (1:10, M7648 Sigma Aldrich) primary antibody following reference²¹ and rhodamine phalloidin (1:100, Thermo Fisher Scientific). Secondary antibodies were used: anti-rabbit Alexa 488 (1:300, Invitrogen) and anti-mouse Alexa 647 (1:300, Invitrogen). Sections were cover-slipped with Prolong Gold Antifade (Thermo Fisher Scientific). Images were taken with a Nikon A1R 25HD confocal microscope at the Nikon Imaging Centre located at the Curie Institute. Images were processed using Fiji/ImageJ software.

Note that inverted and ML7-treated structures revealed much more fragility than non-inverted structures with regard to fixation, showing partly and rod-like fully inverted small patches of tissues for hydrodynamically stimulated conditions only and no multicellular structure at all in ML7-treated conditions.

Feeding efficiency essays on 200-micron fluorescent beads were performed following reference procedures as described by Brunet et al. (2019).

Statistical tests

Statistical tests were the Fisher's exact test (for the number of positive and negative embryos) and the non-parametric Mann-Whitney *U* test (for quantitative analysis associated with each embryo). In the specific case in which a bimodal distribution with an important difference between the two populations appears in the un-jelled stimulated condition, the five elements of the upper population were compared with five elements representative of the mean value of the downer population. The sample size was empirically increased until an initial tendency in a first experiment could be confirmed by a *p*-value <0.05 in a replicate. All experiments were replicated independently at least *N* = 2 times (biological replicates).

Results

Hydrodynamic mechanical stimulation triggers gastrulation in the cnidaria *Nematostella*

In *N. vectensis*, EM development is initiated by its biochemical specification at the future oral pole of the embryo (Rottinger et al., 2012) that conditions its subsequent

invagination (gastrulation) (Magie et al., 2007). As shown in Figure 1A, the *N. vectensis* embryo (of diameter D), still isotropic 18 h after fertilization (h), presents an invagination after 21 h of development at 18°C (of depth d). This invagination coincides with an apex contraction seen on actin-labeled gastrulating embryos (orange arrow), known to be a driving force of invagination initiation (Magie et al., 2007).

A Petri dish containing the embryos was shaken with a rotation amplitude of 2 cm radius, a speed of 85 rounds per minute, and a rotation orientation inversion every 2.5 s to test the effect of marine hydrodynamic mechanical stimulation in *N. vectensis* gastrulation. This corresponds to a flow with a velocity of ~ 10 cm/s, consistent with marine streams, with a periodicity of ~ 2 s, also consistent with the soft-ending wavelets on the sea shoreline environment (Figure 1B, Supplementary Info 1) (Prants et al., 2018). Embryos were first stimulated inside their deformable protective jelly, ~ 1 cm in diameter (Rottinger et al., 2012). Sand (~ 1 mm grains, Supplementary Figure 1A) has been glued on the Petri dish to approach non-smooth ground surface natural conditions, which should enhance the friction at the jelly surface on the ground (see section materials and methods). By taking advantage of the transparency of the jelly, embryos were observed by fast imaging and found to be deformed by the substrate rotation to adopt an ellipsoidal shape characterized by its elliptic ratio (Figure 1B, see section materials and methods). The mean elliptic deformation L/W (L is the major axis and W the minor axis) was nearly 5% under static conditions and increased to 30% under hydrodynamic flow (Figure 1C, Supplementary Figure 1B). Deformation was mostly elastic as embryos mostly returned to their original shapes after stimulation.

Blastulae were hydrodynamically stimulated for 2 h between 16 and 18 h, in a stage normally known to be largely non-gastrulating. Embryos were then dejellied and fixed, and actin filament was labeled with phalloidin at 18 h (3 h before the onset of gastrulation of un-perturbed embryos, Figure 1A). We observed that gastrulation was initiated at 18 h in 78% of the hydrodynamically stimulated embryos (Figures 1D,E), compared to the 33% of invagination observed in the static controls (Figures 1A,i, E-control). This represents 67% of the pool of non-invaginated embryos in static conditions. The hydrodynamically induced gastrulating embryos show an invagination with a normalized depth d/D greater than 18% (Figure 1E), a value from which apex contraction is observed in the invaginating tissue (Figure 1D, orange arrow, Supplementary Figure 1C, and Supplementary Info 2A).

In $\sim 60\%$ of cases, gastrulating embryos showed anomalous shapes: $\sim 30\%$ of embryos exhibited large invaginations enlarging their lateral size (first row of Figure 1D,i), and $\sim 30\%$ of embryos showed tubular-like and multiple invaginations (last photo, second row of Figure 1D,ii,iii). Although most of the stimulated invaginations look anomalous (wider, tube-like, and multi-invagination sites), all embryos for which we let

enough time to reach planula larva stage maturity were as viable as control embryos (data not shown). Oscillating soft waves on the shore cannot be perfectly tuned on a given period. Therefore, we introduced stochasticity in the stimulation of 68–99 rpm and 2–9 s, with stochastic durations from 5 to 29 min for 2 h (see section materials and methods). Stochastic stimulation led to the hydrodynamic mechanical induction of gastrulation at least as efficiently as the mono-period and rpm stimulation, indicating that gastrulation is robustly stimulated by stochastic hydrodynamic stimulation closer to the more natural marine environment (Supplementary Figure 1D). Dejellied embryos also showed a significant invagination response after hydrodynamic stimulation, although less sensitive (Supplementary Figure 1E,ii-and Supplementary Info 2B). Hence, hydrodynamic force stimulation directly applied to embryos initiates gastrulation as well.

Alternative to mechanical deformation, wavelet movements might also increase water oxygenation, thereby leading to a global acceleration of the overall embryonic development in *N. vectensis*. However, no significant increase in oxygenation after the 2 h of hydrodynamic stimulation was observed. Indeed, relative oxygen solubility in sea water of $79\% \pm 1\%$ was found before and after 2 h of hydrodynamic stimulation ($N = 2$, duplicated experiment; see section materials and methods), excluding any involvement of oxygenation in the hydrodynamic stimulation for 2 h of 18 h *N. vectensis* embryo gastrulation. Moreover, the expression level of the developmentally expressed zygotic patterning gene *bmp1-like*, known to be strongly upregulated between 18 and 21 h of development (Supplementary Figures 2A,B and Supplementary Info 2C) and NvERTx.4.130707 expression profile on NvERTx database (Amiel et al., 2017), was not upregulated in stimulation compared to control embryos (Supplementary Figures 2A,B). In addition, the size of the embryonic cell apex should decrease with the developmental stage due to asynchronous divisions between 18 and 21 h (Fritzenwanker et al., 2007). We indeed observed an apex size reduction of $\sim 15 \mu\text{m}^2$ in 21 h invaginating controls compared to 18 h in non-invaginating controls (Supplementary Figures 2C,D). In contrast, no significant decrease was observed between 18 h non-invaginating controls and 18 h invaginating stimulated embryos, confirming that stimulated invaginating embryos are 18 h embryos. These observations confirm the absence of acceleration of embryonic development under hydrodynamic stimulation. Furthermore, direct mechanical stimulation of embryos squeezed by $\sim 20\%$ between agar and a coverslip for 16–18 h led to triggering invagination similar to hydrodynamically treated embryos, further confirming mechanical strain as inductive of the invagination trigger (Supplementary Figures 2E–G).

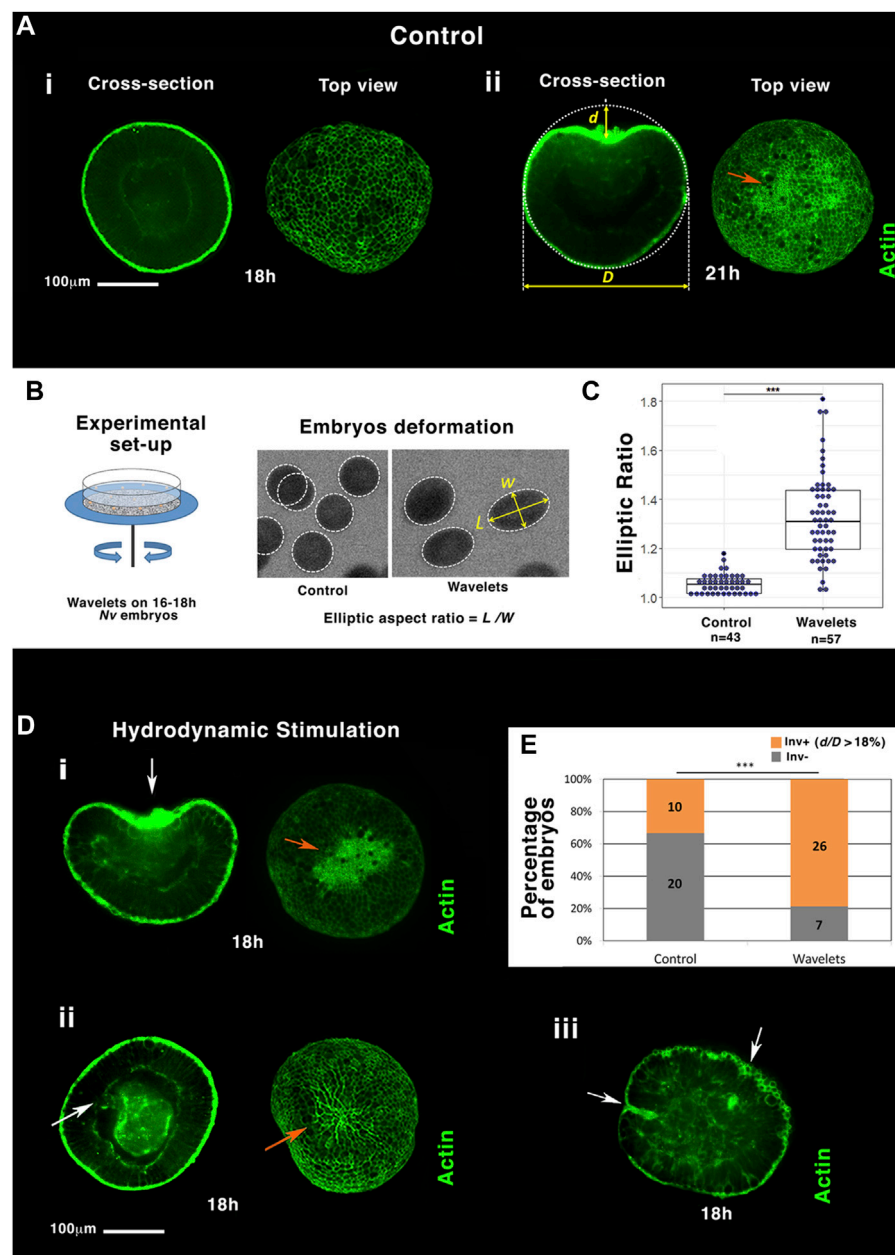


FIGURE 1

Hydrodynamic stimulation of *Nematostella* embryo gastrulation by the marine flow. **(A)** The most representative gastrulation state population of embryos at (i) 18 h and (ii) 21 h. **(B)** Setup: mimicking sea ocean stream by shaking a Petri dish with sand on its ground. Hydrodynamic deformation of jelled embryos with sand. **(C)** Quantification of the elliptic deformation of embryos. $n_{\text{Control}} = 43$ and $n_{\text{Wavelet}} = 57$, $p = 3.10^{-15}$. Mann–Whitney statistical test. **(D)** i,ii, iii: embryos representative of the majority of individuals submitted to the flow (see text). White arrows: invaginations. Orange arrows: apex constriction. Scale bar is 100 μm . **(E)** Quantitative characterization of the percentage of gastrulating embryos (in orange), submitted to the flow compared to control (in grey), based on significant normalized invagination depth d/D measurement higher to 18% (see text), $n_{\text{Control}} = 30$ and $n_{\text{Wavelet}} = 33$, $p = 7.10^{-4}$. Fisher statistical test. $N = 2$ biological replicates (embryo number inside columns).

A quantified flow-meter hydrodynamic oscillating laminar flow of ~ 10 cm/s using the same but standing still Petri dish (Supplementary Figure 3A) further confirmed the hydrodynamic stimulation of invaginations (Supplementary Figures 3B,C).

These data show that hydrodynamic mechanical strain characteristic of the sea shoreline soft waves can trigger the apical contraction-dependent multicellular sheet curvature inversion, initiating embryonic gastrulation in the *N. vectensis*

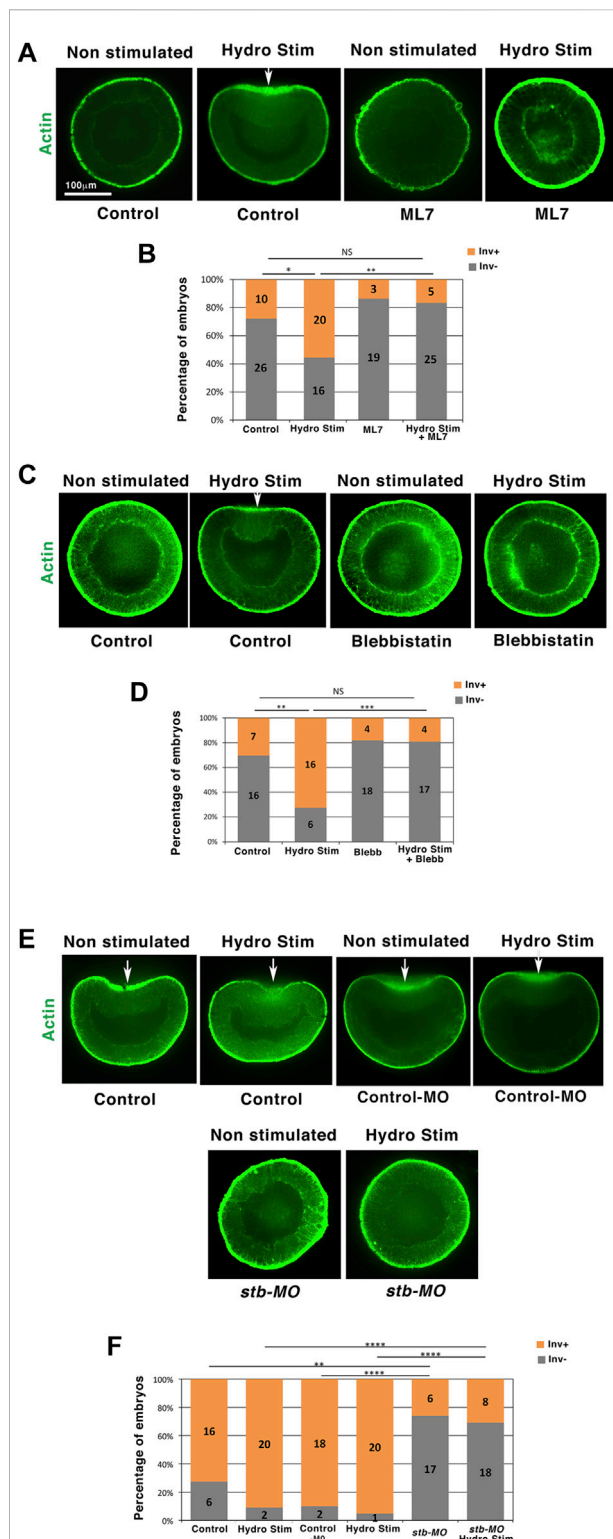


FIGURE 2
Hydrodynamic stimulation of *Nematostella* invaginations is Myo-II and *stb* dependent. (A) 18 h hydrodynamically stimulated *N. vectensis* embryos in the presence of the ML7 MLCK of Myo-II inhibitor. Control: ethanol, vehicle of ML7 (see methods). ML7-treated embryos show a slightly higher thickness than (Continued)

cnidaria representative blastula embryos (see [Supplementary Info 2D](#)).

Hydrodynamical stimulation of *Nematostella* embryo gastrulation is Myo-II-dependent

The apical contraction was observed in the invaginating tissue of all *N. vectensis* embryos initiating gastrulation with an inward curvature of more than 18% invagination depth (Figures 1A,D). Given the Myo-II dependence of apical constriction leading to gastrulation in many species (Young et al., 1991; Nance et al., 2003; Weiser et al., 2009), we tested in physiological conditions (jellied embryos) whether the Myo-II activity is required for mechanical, hydrodynamic stimulation of gastrulation. We used the ML7-specific inhibitor of Myo-II light chain kinase (Isemura et al., 1991) and the blebbistatin-specific Myo-II ATPase activity inhibitor (Kovacs et al., 2004) to block the Myo-II motor activity in *N. vectensis* embryos that remained in their natural jelly (Supplementary Info 3A). Following both treatments, we observed the inhibition of hydrodynamically induced apical constriction and gastrulation. At 18 h, the percentage of invaginating embryos subjected to flow was reduced by a factor of ~3 to ~4, which was similar to the non-stimulated control percentage (Figures 2A–D, Supplementary Info 3B).

To test whether the response of myosin II in *N. vectensis* is post-transcriptional like in *Drosophila* embryos (Pouille et al., 2009; Mitrossilis et al., 2017; Bailles et al., 2019), *N. vectensis* embryos were treated with actinomycin 2 h before hydrodynamic stimulation and during the 2 h of stimulation. Embryos did not survive drug treatment and disintegrated during treatment. Alternatively, Myo-II and phospho-Myo-II antibodies could also have been used to test for the activation of Myo-II via its phosphorylation and for the potential overexpression of Myo-II in response to the hydrodynamic treatment in *N. vectensis*. However, we did not find in the literature, or our experiments, any Myo-II and phospho-specific Myo-II antibodies that worked well in *N. vectensis*.

We observed hydrodynamically induced invaginations in multiple sites in a subset of embryos (~25%, Figure 1D,iii). In addition, these invaginations remain grouped and polarized in one hemisphere of the embryo. This observation suggests the existence of a Myo-II mechanotransductive response that is genetically dependent on embryonic animal-vegetal pre-patterning. Interestingly, the expression of *strabismus* (*stb*), a gene upstream of Myo-II and mechanosensitively activable in vertebrates (Ossipova et al., 2015), is expressed at the animal pole (future oral pole) of *N. vectensis* embryos (Kumburegama et al., 2011). Required for gastrulation, it was proposed to be genetically upstream of Myo-II activation in *N. vectensis* (Kumburegama et al., 2011). We found that after injection of

FIGURE 2 (Continued)

controls. **(B)** Quantitative analysis. $n_{\text{HydroStim}} = 36$ and $n_{\text{HydroStim+ML7}} = 30$, $p = 1.9 \cdot 10^{-3}$, $n_{\text{HydroStim+ML7}} = 30$ and $n_{\text{Control}} = 36$, $p > 0.05$. Statistical test: Fisher. **(C)** 18 h equivalent hydrodynamically stimulated *N. vectensis* embryos in the presence of the blebbistatin Myo-II inhibitor. Control: DMSO, vehicle of blebbistatin. **(D)** Quantitative analysis. $n_{\text{HydroStim}} = 22$ and $n_{\text{HydroStim+Blebb}} = 21$, $p = 6.7 \cdot 10^{-4}$, $n_{\text{HydroStim+Blebb}} = 21$ and $n_{\text{Control}} = 23$, $p > 0.05$. Statistical test: Fisher. **(E)** Hydrodynamically stimulated *Nematostella* 21 h embryos injected with the *stb-MO*. Control: water injected. Control-MO: injected with the MO control sequence (see section materials and methods). **(F)** Quantitative analysis. $n_{\text{HydroStim}} = 22$ and $n_{\text{HydroStimStb-MO}} = 26$, $p = 2.7 \cdot 10^{-5}$. $N = 2$ biological replicates. Fisher statistic test. White arrows: invaginations. The scale bar is 100 μm .

stb morpholinos (*stb-MO*), embryos failed to initiate gastrulation at 21 h, as well as following hydrodynamic stimulation, in line with the Myo-II-dependent hydrodynamic mechanotransductive stimulation of gastrulation (Figures 2E,F and Supplementary Info 4A,B). By labeling *Stb* in WT embryos, we found it to be expressed at one pole of the 18 h non-gastrulating embryos (Kumburegama et al., 2011), similar to the expression in the invaginating domain of hydrodynamically stimulated gastrulating 18 h embryos (Supplementary Figures 3D,E). This result confirms that *Stb* expression, which precedes hydrodynamic stimulation, is indeed required for mechanotransductive stimulation of Myo-II-dependent gastrulation in *Nv*. Interestingly, although *Stb* expression remained polarized after hydrodynamic stimulation, it was increased by a factor of nearly 2, suggesting *Stb*-dependent gastrulation response to hydrodynamic stimulation as re-enforced, or putatively triggered, by mechanically induced increased levels of *Stb* (Supplementary Figures 3D,E). In embryos, in which Myo-II is activated ectopically, gastrulation is inhibited due to the homogenous forces of gastrulation equilibrating and vanishing themselves all around the embryo (Morize et al., 1998). Consistently, we find the inhibition of hydrodynamic stimulation of 18 h embryo gastrulation after ectopic expression of *Stb* all around the embryo (Supplementary Figures 3D–G), further confirming that *Stb* is required for mechanical stimulation of Myo-II in *N. vectensis*. Interestingly, 30 min of hydrodynamic stimulation is not sufficient to trigger the inversion of curvature that initiates gastrulation, indicating that *Stb*-dependent mechanotransductive activation of Myo-II by hydrodynamic strains applied during 16–18 h is required for the mechanical initiation of gastrulation in 18 h embryos (Supplementary Figures 3H,I). These results suggest that Myo-II is mechanotransductively activated by hydrodynamic strains in an *Stb*-dependent process, thereby mechanically triggering the apical constriction that leads to curvature reversal and gastrulation initiation in 18 h *N. vectensis* embryos.

Together, these results indicate that the mechanical stimulation of Myo-II motor activity is involved in the

process of hydrodynamic activation of apical contraction-dependent multicellular sheet curvature inversion that drives gastrulation by means of the flow (Supplementary Info 4C).

Hydrodynamically induced gastrulation triggers *fz10* EM specification gene expression in *Nematostella* embryos

In today's bilaterian embryos, early EM specification precedes, conditions, and regulates the first morphogenetic movements of embryogenesis (Tada et al., 2002; Roth, 2004; Solnica-Krezel and Sepich, 2012). In addition, the first morphogenetic movements of embryogenesis (invagination and convergent-extension in *Drosophila* and epiboly in zebrafish) subsequently participate in turn to the stimulation or induction of endomesodermal gene expression via the mechanotransductive activation of the β -cat pathway (Farge, 2003; Brunet et al., 2013). This activation is mediated by the mechanical activation and phosphorylation of the β -cat site Y654 (pY654- β cat). Thus, we tested in *N. vectensis* whether this property was already present in the common ancestor of bilateria and cnidaria.

We first confirmed by *in situ* hybridization labeling that the spatiotemporal expression of the endomesodermal β -cat target gene *fz10* (Rottinger et al., 2012; Warner et al., 2018) happens at EM invagination in *N. vectensis* at 21 h gastrulation stage (Figures 3A,B and NvERTx.4.56484 expression dynamics on NvERTx database). Embryo top views show purple *fz10* labeling inside embryos into the gastrulating tissues only. To test whether *fz10* is induced at 21 h (early gastrulation stage), coincidentally or stimulated by gastrulation morphogenetic movements downstream of mechanical stimuli, we first triggered gastrulation at 18 h by hydrodynamically stimulating gastrulation from 16 to 18 h (Figure 1D). We found that hydrodynamically stimulated embryos show *fz10* expression at the gastrulation site at 18 h (Figures 3C,E). Consistently, the percentage of *fz10* positive individuals of both the control and hydrodynamic stimulated embryos is similar to that of gastrulating positive individuals (Figures 1E, 3E). In contrast, hydrodynamically stimulated embryos in which gastrulation was blocked by the Myo-II light chain kinase inhibitor ML7 were defective in *fz10* expression (Figures 3D,F). However, mechanical deformation application by direct uniaxial deformation on ML7 treated embryos (of necessarily higher intensity than hydrodynamic shear stress stimulation; see Supplementary Info 5) induces a rescue of *fz10* expression, showing that ML7 *per se* cannot inhibit *fz10* expression in the presence of a mechanical strain (Supplementary Figures 4A,B). In addition, a dose-response experiment using ML7 at lower (not affecting gastrulation) and higher (affecting gastrulation) concentrations revealed that *fz10* expression is inhibited only when gastrulation is blocked (Supplementary Figure 4C). This close correlation

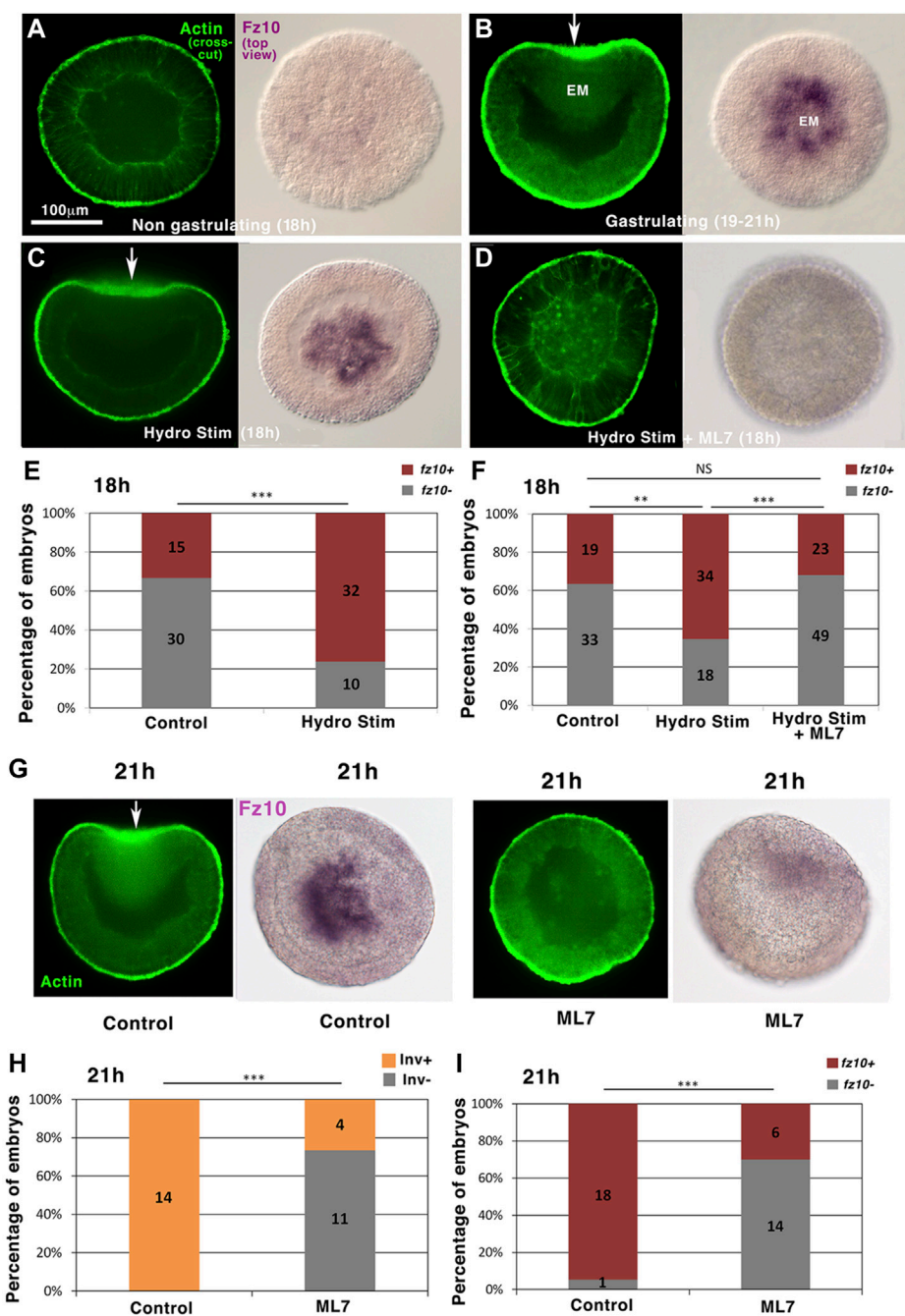


FIGURE 3
 Hydrodynamically induced and endogenous gastrulation of *Nematostella* embryos stimulates the endomesodermal *fz10* gene expression downstream of a Myo-II-dependent process. **(A)** *fz10* expression in 18 h non-invaginating embryos **(B)** and in the invaginating endomesoderm of 21 h embryos. **(C)** *fz10* expression in the invaginating tissue of 18 h hydrodynamically stimulated embryos **(D)** and in hydrodynamically stimulated non-gastrulating embryos treated with ML7. **(E,F)** Quantitative analysis. $n_{\text{Control}} = 45$ and $n_{\text{HydroStim}} = 42$, $p = 9.10^{-5}$, and $n_{\text{Control}} = 52$ and $n_{\text{HydroStim}} = 52$, $p = 5.7.10^{-3}$, $n_{\text{HydroStim}} = 52$ and $n_{\text{HydroStim+ML7}} = 72$, $p = 2.7.10^{-4}$. Control of **(F)** ethanol, vehicle of ML7. Fisher statistic test. **(G)** *fz10* expression in non-gastrulating embryos ML7-treated 21 h embryos **(H,I)** and quantitative analysis. $n_{\text{Control}} = 14$ and $n_{\text{ML7}} = 15$, $p = 5.10^{-5}$, $n_{\text{Control}} = 19$ and $n_{\text{ML7}} = 20$, $p = 3.9.10^{-5}$. Control: ethanol, vehicle of ML7. Statistical test: Fisher. N = 2 biological replicates. The scale bar is 100 µm.

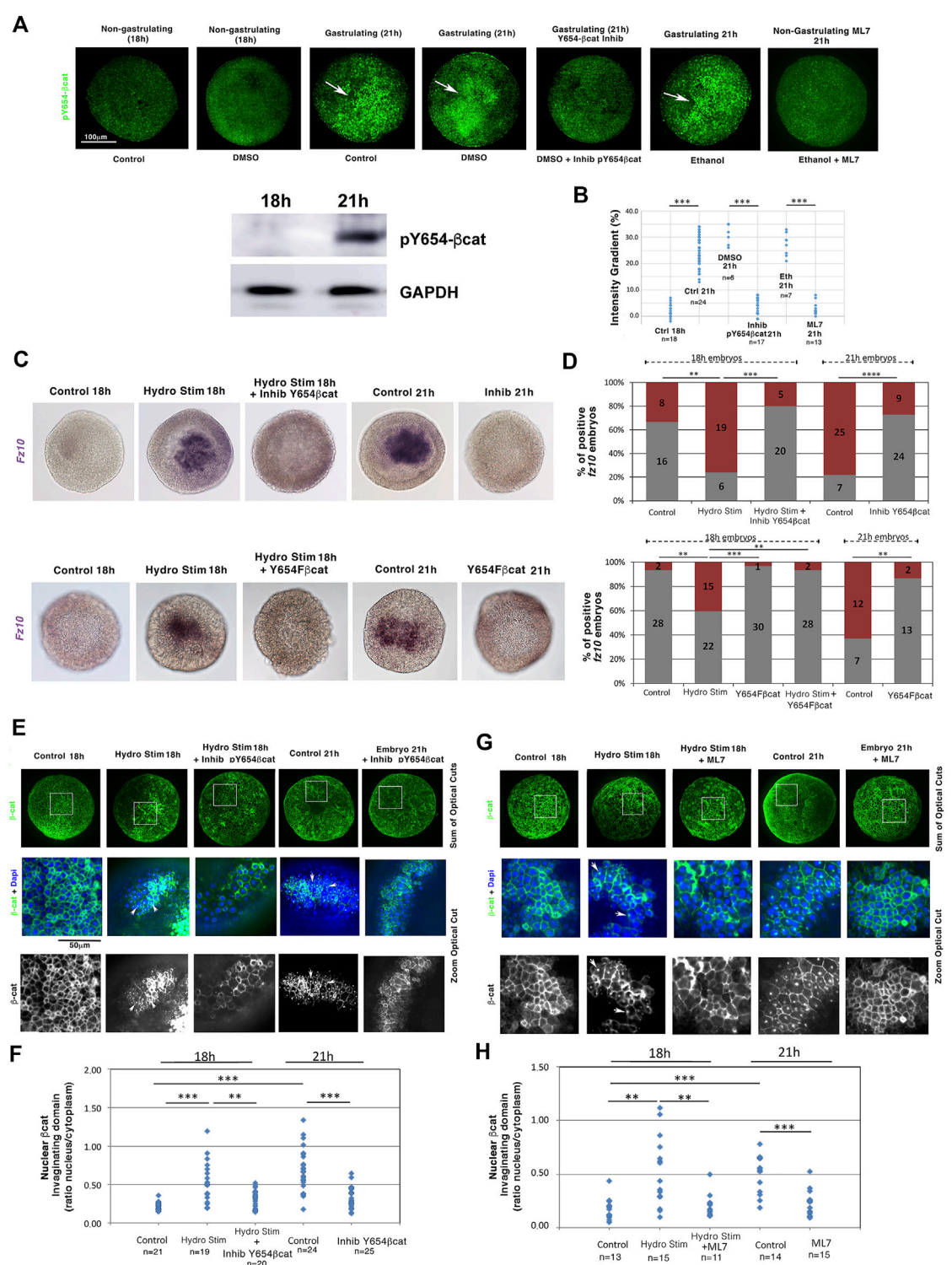


FIGURE 4
 Mechanical induction of the endomesodermal *fz10* gene expression is initiated by the mechanical activation of Y654-β-cat phosphorylation. **(A)** Y654-β-cat phosphorylation in blastulae (18 h), gastrulae (21 h), and 21 h gastrulae embryos treated with either InhibY654-βcat, the inhibitor of Y654 phosphorylation, or ML7, the inhibitor of gastrulation. Western blot: Anti-pY654 β-cat protein detection by western blotting of *N. vectensis* embryos at 18 h and 21 h of development. GAPDH was used as the loading reference. **(B)** Quantification of the gradient ratio (in percentage) of Y654-β-cat phosphorylation in invaginating compared to non-invaginating domains and from domains of maximal intensity compared to the other domains in non-gastrulating embryos of **(A)**. $n_{DMSO21h} = 6$ and $n_{InhibY654\beta cat21h} = 17$, $p = 2.3 \cdot 10^{-4}$, $n_{Eth21h} = 7$ and $n_{ML721h} = 13$, $p = 2 \cdot 10^{-4}$.
 (Continued)

FIGURE 4 (Continued)

Mann–Whitney statistical test. (C) Expression of *fz10* in hydrodynamically stimulated 18 h embryos and in 21 h gastrulae embryos: (up) treated with InhibY654- β cat—control is DMSO, (down) and injected with the *N. vectensis* Y654F- β cat RNA dominant negative—control is H₂O injected. (D) Quantification of (C) (up) $n_{\text{Control}} = 24$ and $n_{\text{HydroStim}} = 25$, $p = 4.10^{-3}$, and $n_{\text{HydroStim}} = 25$ and $n_{\text{HydroStimInhibY654Fcat}} = 25$, $p = 1.7.10^{-4}$ (down), $n_{\text{Control}} = 30$ and $n_{\text{HydroStim}} = 37$, $p = 1.7.10^{-3}$, and $n_{\text{HydroStim}} = 37$ and $n_{\text{HydroStimY654Fcat}} = 31$ $1.7.10^{-3}$ —Y654F- β cat 18h is not shown in (C). (E) Nuclear β -cat translocation state in the non-invaginating blastulae 18 h tissue, in the 21 h invaginating tissue of the gastrulating embryos, and in the hydrodynamically stimulated 18 and 21 h invaginating tissues of gastrulating embryos treated with the Y654- β -cat phosphorylation inhibitor. Control and hydrodynamically stimulated: DMSO, vehicle of Inhib-Y654- β -cat. Full embryos: sum of the optical cross-section on the half sphere. Zoom: a given optical crosscut corresponding to the white square location shown on full embryos. In invaginating embryos, observation is made in invagination lateral domains when signal intensity is lost in its middle. (F) Quantification of (E) $n_{\text{Control18h}} = 21$, $n_{\text{HydroStim18h}} = 19$, $p = 6.10^{-6}$, and $n_{\text{Control21h}} = 24$, $p = 8.6.10^{-8}$. $n_{\text{HydroStim18h}} = 19$ and $n_{\text{HydroStimInhibY654Fcat18h}} = 20$, $p = 1.6.10^{-3}$, $n_{\text{Control21h}} = 24$ and $n_{\text{InhibY654Fcat21h}} = 25$, $p = 7.10^{-6}$. (G) Nuclear β cat translocation states in both non-gastrulating ML7-treated 18 h hydrodynamically stimulated and 21 h embryos. Control and hydrodynamically stimulated: ethanol, vehicle of ML7. (H) Quantification of (G). $n_{\text{Control18h}} = 13$, $n_{\text{HydroStim18h}} = 15$, $p = 1.7.10^{-3}$, and $n_{\text{Control21h}} = 14$, $p = 10^{-4}$, $n_{\text{HydroStim18h}} = 15$ and $n_{\text{HydroStimML718h}} = 11$, $p = 6.9.10^{-3}$, $n_{\text{Control21h}} = 14$ and $n_{\text{InhibML721h}} = 15$, $p = 2.10^{-4}$. Statistical tests. Fisher for embryo number counting and Mann–Whitney for quantitative data by embryos. N = 2 biological replicates. The scale bar is 100 μ m.

between the gastrulation rate and *fz10* expression further confirms that ML7 *per se* does not prevent *fz10* expression, but the inhibition of Myo-II-dependent gastrulation mechanical strains prevents *fz10* expression. Interestingly, the lack of *fz10* expression was also observed in hydrodynamically stimulated embryos in which gastrulation was genetically blocked by *stb*-MO injection (Supplementary Figures 5A,B and Supplementary Info 6). These results show that hydrodynamic forces *per se* (i.e., without gastrulation induced) could not stimulate *fz10* expression. Rather, these results indicate that *fz10* expression in the invaginating *N. vectensis* tissue is triggered downstream of mechanical stimuli by the Myo-II-dependent mechanical strains generated during gastrulation.

This is further supported by the fact that non-stimulated 21 h embryos that were previously treated with ML7 and that do not gastrulate did not show *fz10* expression as it should be in the case of non-treated gastrulating embryos (Figures 3G,H and Figures 3G,I). This observation, in turn, indicates that endogenous (non-mechanically induced) gastrulation in *N. vectensis* stimulates *fz10* expression in the EM, downstream of mechanical stimuli (Farge, 2003; Brunet et al., 2013).

These results indicate that the expression of the EM β cat-downstream target gene *fz10* is mechanically induced in response to hydrodynamically stimulated gastrulation initiation several hours earlier than the normal transduction (16–18 h) and in response to endogenous gastrulation initiation at 21 h in *N. vectensis* embryos.

Hydrodynamically induced gastrulation triggers *fz10* EM specification gene expression in a Y654- β cat phosphorylation-dependent process in *Nematostella* embryos

We then checked the behavior of the mechanosensitive β -cat that targets *fz10*. Y654- β cat phosphorylation (pY654- β cat) leads to the release of β -cat from the junctions to the cytoplasm and

nucleus, which triggers EM gene expression in bilaterian embryos during gastrulation and epiboly (Farge, 2003; Brunet et al., 2013), as well as in human embryonic stem cells (Muncie et al., 2020). Y654- β cat is highly conserved in all Metazoa, including *N. vectensis* (Roper et al., 2018). Its phosphorylation was monitored in *N. vectensis* using antibodies against the phosphorylated form of Y654 in β cat using immunohistochemistry, as assessed in western blotting on *N. vectensis* (Figure 4A, Supplementary Info 7, Supplementary Figure 6A; see section methods). At 21 h, *N. vectensis* embryos exhibited a pY654- β cat signal in the invaginating EM (white arrows, not observed in 18 h non-gastrulating embryos). However, in ML7 treated 21 h embryos (i.e., 21 h non-gastrulating embryos), this signal was missing (Figures 4A,B, Supplementary Figures 6B,C, Supplementary Infos 8, 9). Before 18 h, hydrodynamically stimulated gastrulating embryos also showed pY654- β cat in the invagination (Supplementary Figure 6D, Supplementary Info 10). The oral-aboral signal gradient of pY654- β cat levels is in the order of 20% (Figures 4A,B), in line with the EM-ectoderm gradient of Y654- β cat level, mechanically phosphorylated in the invaginating and stretched EM of gastrulating *Drosophila* and epiboly zebrafish embryos, respectively (Brunet et al., 2013).

This indicates that the phosphorylation of the Y654- β cat site is mechanically induced by the driving forces of gastrulation.

Blocking phosphorylation of the β cat residue Y654 using the specific inhibitor S381-0393 (Y654- β cat Inhib) from 16 to 18 h and from 18 to 21 h, respectively (Figures 4A,B; see section materials and methods for validation of the inhibitor), led to defects in *fz10* expression in the invagination of both 18 h embryos in which gastrulation initiation was hydrodynamically stimulated and 21 h endogenously early-gastrulating embryos (Figures 4C,D, Supplementary Info 11A). This result was confirmed by injecting mRNA encoding a dominant negative version of *N. vectensis* β cat (Y645F) in which the tyrosine (Y) in residue 645 has been replaced by a phenylalanine (F) to prevent phosphorylation and thus activation (Figures 4C,D, Supplementary Figure 6A,

Supplementary Info 11B). This shows that the mechanical activation of the EM gene *fz10* in the invagination by either hydrodynamically induced or endogenous morphogenetic movement of gastrulation initiation requires the phosphorylation of Y654- β cat, the latter of which is mechanically induced by gastrulation movements.

Consistently, β -cat translocation to the nucleus, unobservable in the 18 h non-gastrulating embryos, was detected in the invaginating domains of embryos that were hydrodynamically stimulated between 16 and 18 h and in early gastrulating embryos at 21 h (Figures 4E–H, Supplementary Info 11C). Moreover, blocking Y654- β cat phosphorylation with Y654- β cat Inhib (Figures 4A,B, Supplementary Figure 6B) prevented nuclear β -cat nuclear translocation in 18 h embryos in which gastrulation initiation was hydrodynamically stimulated from 16 to 18 h, as well as in early gastrulating embryos at 21 h (Figures 4E,F). In addition, in embryos that were hydrodynamically stimulated between 16 and 18 h and in non-stimulated 21 h embryos, both treated with the ML7 inhibitor of Myo-II light chain (i.e., non-gastrulating embryos), β -cat nuclear translocation was defective (Figures 4G,H).

These results indicate that in the cnidaria *N. vectensis*, the nuclear translocation of β -cat in the invagination and the expression of its EM target gene *fz10* depend on the mechanical stimulation of Y654- β cat phosphorylation triggered by the initiation of the morphogenetic movement of gastrulation that can be hydrodynamically induced several hours earlier than the normal transduction (18 h), and in response to endogenous gastrulation initiation, at 21 h.

Hydrodynamic stimulation triggers curvature inversion in the choanoflagellate *C. flexa* multicellular sheet in a Myo-II-dependent process

To test whether hydrodynamically induced and Myo-II-dependent multicellular sheet curvature inversion could be found in an organism more evolutionary distant to bilateria than a cnidarian, whose common ancestor with bilateria is older than that of cnidaria and bilateria, we submitted the multicellular choanoflagellate *C. flexa*, a sister group to all Metazoa (Ruiz-Trillo and de Mendoza, 2020) to wavelet stimulation.

C. flexa is an open curved multicellular sheet whose cohesion is ensured by collar microvilli interactions, those of flagella inward of the curved surface (flagella-in). Its curvature can inverse through apex contraction in response to light-to-dark transition through a Myo-II-dependent multicellular sheet contraction process, characterized by flagellates facing outward instead of inwards (see section materials and methods) (Brunet et al., 2019). Strikingly, under conditions in which retinal-dependent light sensitivity was removed in the absence of

retinal-producing bacteria [see section materials and methods (Brunet et al., 2019)] and under light at a constant intensity, hydrodynamic wavelet stimulation of *C. flexa* colonies at 105 rpm and a rotation orientation inversion every 2.5 s triggered an inversion of *C. flexa* colony sheets curvature with outward flagellates (flagella-out) (Figures 5A,B,E, Supplementary Info 12).

Hydrodynamically induced inversion also triggered a transition to a swimming state, possibly due to the freed flagellates because of curvature inversion, similar to light-induced inversion of *C. flexa* (Brunet et al., 2019) (Supplementary Movies S1, S2, S3). Inhibition of Myo-II activity by ML7 treatment led to the inhibition of hydrodynamically induced inversion. Thus, Myo-II is necessary for the light modulation-independent hydrodynamically induced inversion of the multicellular form of *C. flexa* (Figures 5C–E and Supplementary Movies S4, S5). Interestingly, hydrodynamically stimulated inversion was accompanied by an intracellular increase of Myo-II expression of a factor of 4, 30 min after stimulation, possibly involved in the Myo-II-dependent mechanical induction of inversion (Figures 5F–H, Supplementary Info 13A).

We then investigated the efficiency of *C. flexa* feeding in response to inversion using fluorescent beads of 200 nm in diameter (i.e., the size of their bacteria prey) (Brunet et al., 2019). Quantification of the data revealed an increase in the feeding efficiency by a factor of nearly 2 in closed inverted (flagella-out) *C. flexa*, compared to agitated non-inverted (flagella-in) (Figures 5I–K and Supplementary Info 13B). These results suggest that mechanotransductively induced inversion/tissue closing increases feeding efficiency, promoted by the trapping of suspended nutrients (Supplementary Info 13C,D).

Our data indicate that marine hydrodynamic mechanical stimulation triggers the curvature inversion morphogenetic movement of the choanoflagellate *C. flexa* multicellular sheet in a Myo-II-dependent process, leading to an inversion that favors the closure of the *C. flexa* and consequently their feeding capacity.

Due to the lack of β -cat in the choanoflagellate genome repertoire (Fernandez-Sanchez et al., 2015), which we confirmed in *C. flexa* associated with the lack of *fz10* (see Supplementary Info 14), no mechanical induction of β -cat activation and *fz10* expression by inversion could be tested in *C. flexa*.

Discussion

In addition to multicellularity and reproduction by the egg–sperm fusion, the evolutionary emergence of the first Metazoa organisms is considered to have been conditioned by the formation of a first organ: the primitive gut (Haeckel, 1874; Brunet and King, 2017; Cavalier-Smith, 2017; Newman, 2020; Ruiz-Trillo and de Mendoza, 2020). This primitive gut is thought to consist of biochemically specified EM, fated to invaginate by the inversion of the geometric curvature of

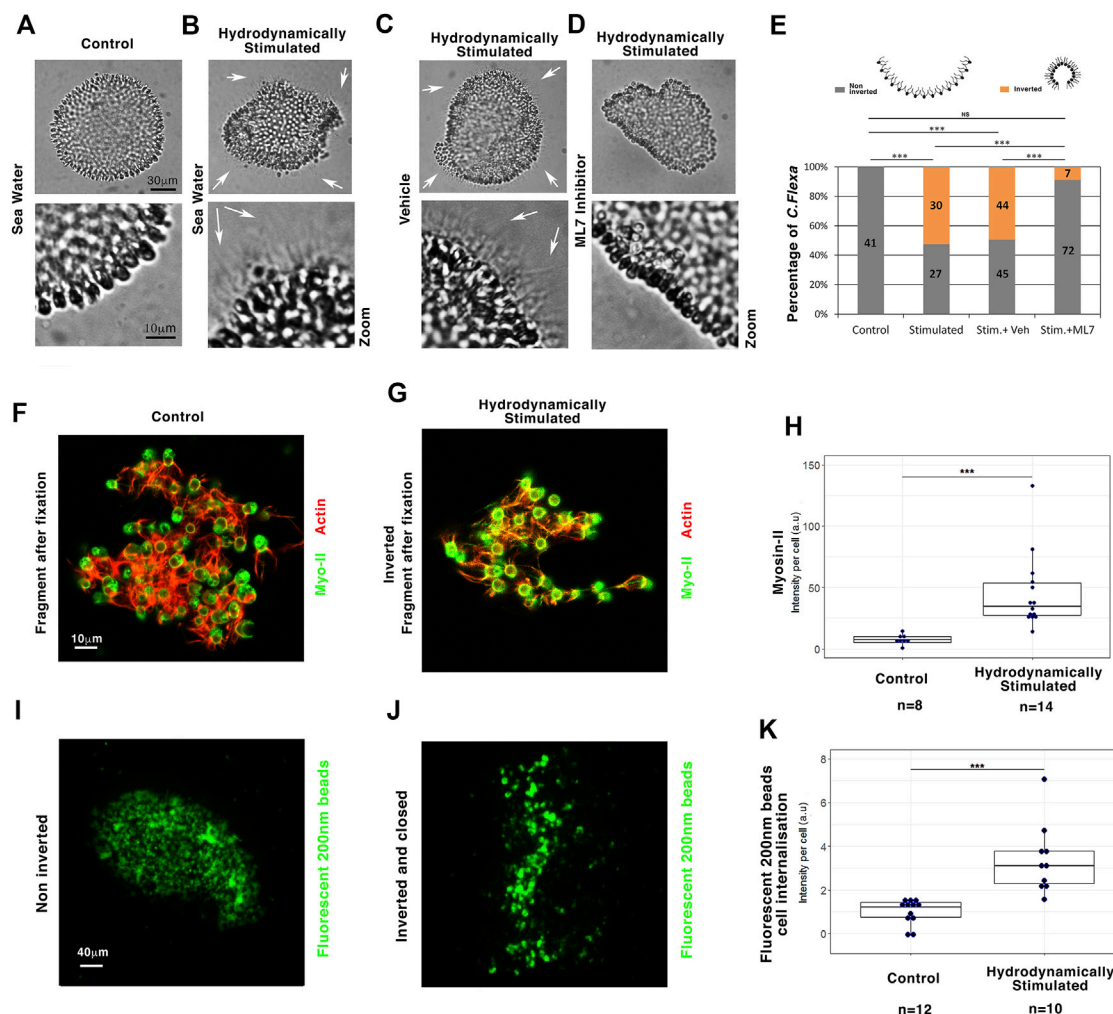


FIGURE 5

Myo-II-dependent hydrodynamic stimulation of multicellular sheet curvature inversion is conserved in *C. flexa* choanoflagellates. (A) Multicellular *C. flexa* choanoflagellate before hydrodynamic stimulation (no flagellate outside) (B) and after hydrodynamic stimulation (white arrows: flagellate outside). (C) Inversion status of hydrodynamically stimulated *C. flexa* treated with the ethanol vehicle of ML7 alone (white arrows: flagellate outside) (D) and with the Myo-II inhibitor ML7 (no flagellate outside). Zooms: with enhanced contrast to check for flagellate presence. (E) Quantitative analysis. $n_{\text{Control}} = 41$ and $n_{\text{Stimulated}} = 57$, $p = 10^{-9}$, $n_{\text{Stim+veh}} = 99$ and $n_{\text{Stim+ML7}} = 79$, $p = 4.8 \cdot 10^{-9}$. Scheme from Brunet et al. (2019). (F) Myo-II and actin in *C. flexa* before hydrodynamic stimulation (G) and after hydrodynamic stimulation. (H) Quantitative analyses of Myo-II expression per cell 20–30 min after hydrodynamic stimulation initiation. Immunofluorescence representative of $n = 8$ controls and $n = 14$ inverted structures of the hydrodynamically stimulated *C. flexa*. $n_{\text{Control}} = 8$ and $n_{\text{Stim}} = 14$, $p = 1.25 \cdot 10^{-5}$. (I) 200 nm fluorescent beads internalization in cells in non-inverted (J) and inverted *C. flexa* after hydrodynamic stimulation. (K) Quantitative analyses of particle internalization per cell 60 min after hydrodynamic stimulation initiation. Immunofluorescence representative of $n = 12$ non-inverted and $n = 10$ fully inverted structures of the hydrodynamically stimulated *C. flexa*. $n_{\text{Control}} = 12$ and $n_{\text{Stim}} = 10$, $p = 9.9 \cdot 10^{-5}$. $N = 2$ biological replicates. Statistical tests are Fisher for histograms and Mann–Whitney for quantitative analysis.

the multicellular tissue (gastrulation) from primitive multicellular hollow spheres (blastulae) (Arendt, 2004).

Due to the absence of conserved biochemical signals upstream of both EM biochemical specification (Roth, 2004; Kusserow et al., 2005; Hagos and Dougan, 2007) and biomechanical initiation of

gastrulation (Sweeton et al., 1991; Kumburegama et al., 2011; Evren et al., 2014) in present-day Metazoa embryos, the existence of a common evolutionary origin responsible for the development of the primitive digestive organ in Metazoa remains unknown.

Interestingly, mechanical signals have been found to play an increasingly important role in early embryonic development

(Brouzes and Farge, 2004; Wozniak and Chen, 2009). Indeed, the activation of Myo-II by internal mechanical strains has been shown to cause invaginations of the mesoderm and endoderm during gastrulation in *Drosophila* embryos (Mitrossilis et al., 2017; Bailles et al., 2019). In addition, mechanical stresses caused by early internal morphogenetic movements during embryogenesis were found to stimulate or induce endodermal and mesodermal gene expression in bilaterian *Drosophila* and zebrafish early embryos via the mechanical activation of the β -cat pathway by Y654- β cat phosphorylation (Desprat et al., 2008; Brunet et al., 2013). Therefore, we tested the plausibility of mechanical cues as tangible candidates involved in intracellular biochemical reactions, which led to the evolutionary emergence of EM specification and invagination. This theory was tested on two evolutionarily distant organisms spanning at least 700 million years of evolution in the marine hydrodynamic mechanical context of their common ancestors—the cnidarian metazoan *N. vectensis* and the multicellular choanoflagellate *C. flexa*—considered to be the closest living relative of the metazoans.

Myosin-dependent marine environmental mechano-biochemical stimulation that leads to contraction and inversion of pluricellular sheets is a shared property of the evolutionarily distant cnidarian and choanoflagellate species, whose common ancestor dates back at least to the last common ancestor of Metazoa

The results showed that reminiscent of bilateria (Fernandez-Gonzalez et al., 2009; Pouille et al., 2009; Mitrossilis et al., 2017; Bailles et al., 2019), the mechanical stimulation of Myo-II-dependent multicellular sheet inversion, which initiates gastrulation in closed blastulae, is shared by cnidaria embryos (*N. vectensis*) and multicellular choanoflagellates (*C. flexa*).

This indicates that Myo-II-induced mechanical contraction, leading to the inversion of the curvature of multicellular sheets in response to environmental, mechanical stresses, such as sea flow and waves on the shoreline, possibly dates back at least to the last common pre-Metazoa ancestor of the Metazoa and choanoflagellates, over 700 million years ago. Alternatively, the mechanical induction of Myo-II-dependent contraction leading to the inversion of the curvature of multicellular leaflets arose and was selected independently in these representatives of the bilaterian, cnidarian, and choanoflagellate superphyla, which have been tested, in the process of convergent-evolution. However, hydrodynamic mechanical strains do not represent the environment of gastrulating embryos of Bilateria insects, such as *Drosophila* embryos. Furthermore, environmental mechanical strains are not necessary for normal endogenous gastrulation of bilateria *Drosophila* and cnidaria *N. vectensis* embryos. This may therefore make it less

likely that the mechanical stimulation of Myo-II-dependent multicellular sheet contraction leading to inversion is the result of a convergent-evolutionary process in three evolutionarily distant species (including the choanoflagellate *C. flexa*) compared to a single evolutionary-innovation process inherited at least from the earliest pre-Metazoa (see Supplementary Info 15).

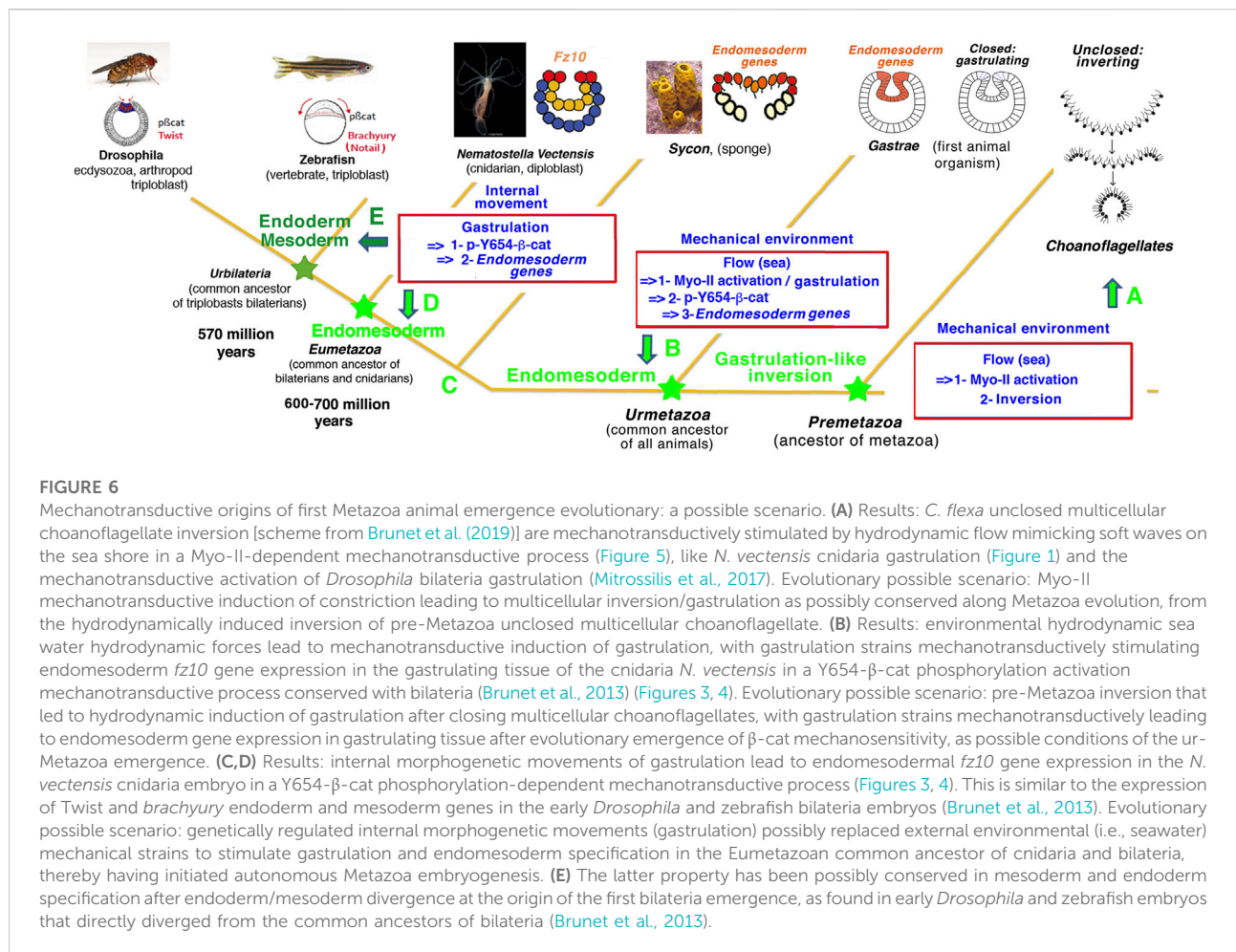
Therefore, the present work suggests that Myo-II-dependent mechanosensitive constriction by marine environmental strains in multicellular sheets may have been at the evolutionary origin of inversion in multicellular pre-Metazoa. It could have been ancestral to gastrulation by prefiguring the tissue inversion that initiated and triggered gastrulation in early Metazoa (Figures 6A,B).

In *N. vectensis*, a possibility could have been that Myo-II would already be activated in Stb-expressing domains in 16–18 h embryos independently of hydrodynamic stimulation, but not enough to cause curvature inversion leading to gastrulation initiation. In this case, hydrodynamic forces could have added to pre-existing Myo-II-dependent forces that pre-stressed the Stb-expressing domain, ultimately resulting in curvature reversal and gastrulation initiation.

Notably, if the tissue has already been pre-stressed by pre-existing Myo-II activity, then as soon as curvature reversal is initiated by incidental external forces (in non-hydrodynamically stimulated control embryos) or hydrodynamically, one should observe apical constriction initiation due to Myo-dependent internal forces that participate with external forces in curvature reversal initiation. This should start at $d/D > 0$ in Supplementary Figure 1C and include the regime $0 < d/D < 0.18$, in which constriction was systematically evaluated in the maximal inward curvature domain of the embryo. This is not the case in our study, as constriction is significantly observed in embryos only from and above the $d/D = 0.18$ state.

Moreover, if the curvature reversal leading to gastrulation initiation was purely mechanically induced by hydrodynamic forces in a pre-stressed Myo-II-activated tissue, one would expect an almost immediate hydrodynamic stimulation of curvature reversal dynamics of the order of the minute characteristic time scale, which is a known characteristic of the viscoelastic mechanical properties of embryonic tissues (Desprat et al., 2008; Doubrovinski et al., 2017). This has to be compared to the 2 h (16h–18 h) stimulation required to initiate gastrulation. Indeed, we found that 30 min of hydrodynamic stimulation is not sufficient to trigger the inversion of curvature that initiates gastrulation (Supplementary Figures 3H,I), which would be largely sufficient in the case of a purely mechanical response of the tissue pre-stressed by an already activated Myo-II that would take on the order of a few minutes only.

Therefore, Myo-II is not activated in 18 h non-gastrulating embryos. This shows that hydrodynamic mechanical stresses do not synergize with the already activated Myo-II to stimulate gastrulation at 18 h and further suggests that a gradual and probably cumulative process of mechanotransductive activation of Myo-II by hydrodynamic strains applied from



16 to 18 h is required for the mechanical initiation of gastrulation in 18 h embryos.

Along with the present 105 rpm marine-like stimulation submitted to *C. flexa* ((Nguyen et al., 2020), original BioRxiv pre-print version of the present article), 5 s short 600 rpm vortexing also led to *C. flexa* contraction (Reyes-Rivera et al., 2022). Such vortexing would correspond to a non-physiological regime of 10 waves per second. We find Myo-II mechanical induction of *C. flexa* inversion in response to a nearly six-time lower frequency, more relevant to physiological marine wave frequencies. We also find that the mechanical stimulation of Myo-II-dependent *C. flexa* inversion leads to an increase in choanoflagellate feeding efficiency (Figures 5I–K). With *C. flexa*, in the marine environment in which multicellular pre-Metazoa evolved, hydrodynamically induced inversion may have increased feeding efficiency by trapping nutrient bacteria or nutrients suspended in the water in the presence of shoreline or seabed flow.

Therefore, this process may have been selected as a favorable behavioral feeding reflex response to marine mechanical strains (Farge, 2003; Pouille et al., 2009).

The βcat-dependent property of mechano-biochemical induction of EM gene expression by tissue deformation during gastrulation dating back at least to the last common ancestor of cnidaria and bilaterians

Our observations further show the mechanical induction of the EM *fz10* gene expression through phosphorylation of Y654-βcat by the morphogenetic movement of gastrulation initiation in cnidaria *N. vectensis* embryos (Figure 6D).

In *N. vectensis* embryos, the timing and causality of this second mechanotransductive process with regard to Myo-II mechanical activation are characterized by the fact that the inhibitor of Y654-βcat phosphorylation or the dominant-negative Y654-βcat does not prevent hydrodynamic stimulation of gastrulation, indicating that Y654-βcat phosphorylation is not required for hydrodynamic stimulation of Myo-II. Indeed, gastrulation is observed on (21 h) Y654-βcat Inhib (Figure 4A) and (21 h) Y654F RNA injected (Supplementary Figure 6A), as well as Hydro Stim 18 h Inhib

pY654 β cat (Figure 4E) embryos. In contrast, Myo-II inhibitors that inhibit hydrodynamic stimulation of gastrulation also inhibit hydrodynamic stimulation of the EM *fz10* gene expression downstream of Y654- β cat phosphorylation (Figures 3C,D,F, 4C,D). Herein, mechanical stresses associated with gastrulation mechanotransductively activate *fz10* EM gene expression rather than *via* biochemical activation of Myo-II. This is indicated by the fact that *fz10* expression can be rescued by uniaxial mechanical deformation in ML7-treated embryos in which the Myo-II activity is inhibited (Supplementary Figures 4A,B).

Therefore, there are two waves of mechanotransduction: the first is the mechanical activation of Myo-II in response to environmental hydrodynamic stresses, which leads to gastrulation, and the second consists of the mechanical activation of Y654- β cat phosphorylation by the morphogenetic movement of gastrulation initiation, which participates in EM specification *via* the induction of *fz10* expression.

This mechanotransductive cascade leading to the induction of EM biomechanical morphogenesis (gastrulation) and participating in its biochemical specification (*fz10* expression) is identical to the mechanotransductive cascade observed in the morphogenesis and participation in the specification of the mesoderm of *Drosophila* embryos during gastrulation (Brunet et al., 2013). In addition, the first morphogenetic movement of zebrafish embryos is also involved in mesoderm specification *via* phosphorylation of Y654- β cat in margin cells specifically stretched by epiboly (Brunet et al., 2013).

Therefore, the mechanism of Y654- β cat phosphorylation by early morphogenetic movements initiation during embryogenesis is shared between cnidaria (*N. vectensis*) and bilaterians [zebrafish and *Drosophila* (Brunet et al., 2013)]. This strongly suggests that the mechanical induction of EM gene expression by the β cat-dependent morphogenetic movements of gastrulation dates back at least to the last common ancestor of bilateria and cnidaria, 600–700 million years ago. Additionally, an underlying alternative process of convergent-evolution that led to mechanical activation of the β -cat pathway through Y654- β cat phosphorylation in representatives of bilateria and cnidaria independently cannot be entirely excluded. However, insofar as a β -cat comprising a Y654 site capable of interacting with E-cadherin arose concomitantly with E-cadherin that has trans-cellular adhesive properties [causally to the multicellularity in the evolutionary emergence of early Metazoa (Fernandez-Sanchez et al., 2015)], multicellular tissues may not have escaped to a mechanically induced opening of Y654- β cat under stress leading to its phosphorylation from the earliest to the most recent Metazoa (see Supplementary Info 16).

Given the lack of conserved biochemical signals involved in EM specification in present-day embryonic species (Roth, 2004; Kusserow et al., 2005; Hagos and Dougan, 2007), this suggests that β cat-dependent mechanosensitive EM gene expression may have been involved in the evolutionary emergence of EM specification in early pre-Metazoa. During evolution, this mechanosensitive and β cat-dependent mechanism responding to first morphogenetic movements at the early gastrulation stage may have been

subsequently co-opted by both endoderm and mesoderm in bilateria embryos (Desprat et al., 2008; Brunet et al., 2013; Muncie et al., 2020) (Figures 6B–E, Supplementary Info 17).

Intriguingly, β cat-dependent activation of the *brachyury* EM gene has also been proposed to be activated at the time of inversion in sponge embryos (Figure 6C) (Leininger et al., 2014). Due to the absence of β -catenin–E-cadherin junctional complexes in choanoflagellates (Fairclough et al., 2013; Fernandez-Sanchez et al., 2015), this mechanism is expected to be absent in response to the reversal of curvature in *C. flexa* (Figure 6A), suggesting that the emergence of the junctional β -cat containing the major Y654 site of β -cat interaction with E-cadherins and adhesive cadherins capable of interacting with β -cat in the multicellular tissues of pre-Metazoa may have been one of the conditions required for the emergence of gastrulation-induced EM gene expression in early Metazoa (ur-Metazoa, Figure 6B). This conserved process could have subsequently been consolidated and diversified throughout evolution by the establishment of a patterned and biochemically regulated expression of EM genes (e.g., downstream of Wnts, Nodal, or Dorsal as observed today in a non-conserved species-dependent manner). Moreover, EM specification would have pre-patterned the domain of competence of mechanical or biochemical Myo-II activation (e.g., *via* Stb or Fog, as observed today in a non-conserved species-dependent manner), required to enable local invagination in a closed epithelium. In this way, the conserved mechanical cues observed here to be involved in EM specification and morphogenesis add to patterned EM specification pre-existing gene regulatory networks in early embryos of current species.

Conclusion

The observations presented in this study suggest that tissue invagination and EM specification, which jointly define primitive gut formation in early Metazoa, may have been initiated by mechanotransduction as a favorable primitive sensory and behavioral feeding response of early multicellular pre-Metazoa to the hydrodynamic mechanical stress of the marine environment (Farge, 2003; Farge, 2013). Alternative to a convergent-evolution process, the conservation of the lineage found here from bilateria to cnidaria for the mechanical activation of Myo-II and β -cat and to multicellular choanoflagellates for the mechanical activation of Myo-II lends credibility to mechanotransductive processes at the evolutionary origin of the primitive emergence of a gut in early pre-Metazoa and multicellular Metazoa.

Data availability statement

The raw data supporting the conclusion of this article will be made available by the authors, without undue reservation.

Author contributions

MN performed all hydrodynamical stimulation experiments on *N. vectensis*, including morphological phenotype analysis, *in situ* and IF labeling with and without drugs, and *stb-MO* injections, and performed uniaxial global deformations. MN and AJ realized embryo deformation measurement. TM initiated *stb-MO* injection and global uniaxial deformation in *N. vectensis* at the beginning of the present research. TM identified the β -cat phosphorylation in the invagination induced by the morphogenetic movement of gastrulation in *N. vectensis*, and set up imaging conditions of pY654- β cat and actin-labeled embryos and produced the algorithm for cell resolution image analysis with FS. EL, MN, and EF performed hydrodynamic experiments on *C. flexa*. FB-B performed *in vitro* RNA transcription to produce antisense RNA probes used for *in situ* hybridization on *N. vectensis* and carried out *C. flexa* labeling. AB optimized *C. flexa* culture conditions and produced the Y654F- β cat construction. Y654 inhibitor on pY654 and β cat IF labeling of non-hydrodynamically stimulated embryos were carried out by A-CB. A-CB set up Y654- β cat labeling conditions and quantification on *N. vectensis*. ER and MN performed part of the *N. vectensis* injections and image analysis. J-LG participated in the flow-meter experiments. MF-S realized pY654- β cat western blots. EF coordinated the work and wrote the first draft of the manuscript, that was implemented by all authors.

Funding

This work was supported by the OCAV grants n° ANR-10-IDEX-0001-02 PSL, and EF lab was supported by the FRM (grant Équipe labellisée FRM 2015 DEQ20150331702, grant Équipe labellisée FRM 2019 EQU201903007805), the Inca (PLBIO-13-172 and PLBIO-03-ICR-1), the ANR (16-CE14-002801), and the Labex Cell(n)Scale (grants ANR-11-LABX-0038, ANR-10-IDEX-0001-02). ER was supported by an ATIP-Avenir award funded by the Plan Cancer (Institut National du Cancer, C13992AS), Seventh Framework Program (CIG #631665), the Fondation ARC pour la Recherche sur le Cancer (PJA2014120186), the IDEX UCA^{jeu} (ANR-15-IDEX-01), and the LABEX SIGNALIFE (ANR-11-LABX-0028).

Acknowledgments

The authors thank Aldine Amiel, Hereroa Johnston, João Carvalho, Adrien Bouclet, and Mark Martindale for training, scientific discussions, and biological material sharing, sending, and

setup; David Quéré for scientific discussions and providing the rapid camera physical setup; Thibaut Brunet for p- β cat labeling initiation tests in *N. vectensis* and providing *C. flexa* and culture protocols and discussions; Wikramanayake's team for the kind gift of the NvStbm antibody; and Peta Bradbury for reading of the manuscript.

Conflict of interest

The authors declare that the research was conducted in the absence of any commercial or financial relationships that could be construed as a potential conflict of interest.

Publisher's note

All claims expressed in this article are solely those of the authors and do not necessarily represent those of their affiliated organizations or those of the publisher, the editors, and the reviewers. Any product that may be evaluated in this article, or claim that may be made by its manufacturer, is not guaranteed or endorsed by the publisher.

Supplementary material

The Supplementary Material for this article can be found online at: <https://www.frontiersin.org/articles/10.3389/fcell.2022.992371/full#supplementary-material>

SUPPLEMENTARY MOVIE S1

Unstimulated non-swimming spherical multicellular choanoflagellates still opened at one pole. Changes in the focal plane were induced in the movie to ensure that flagellates were not observed outside the tissue.

SUPPLEMENTARY MOVIE S2

Stimulated swimming inverted multicellular choanoflagellates with a point of attachment to the substrate maintaining it in the same optical area.

SUPPLEMENTARY MOVIE S3

Stimulated swimming inverted multicellular choanoflagellates free and, in this case, larger and laterally opened. To follow it up, the observation area has to be changed several times.

SUPPLEMENTARY MOVIE S4

Stimulated swimming inverted multicellular Choanoflagellates in the presence of the ethanol vehicle of ML7 alone.

SUPPLEMENTARY MOVIE S5

Stimulated non-swimming and non-inverted multicellular choanoflagellates in the presence of ML7. Changes in the focal plane were induced in the movie to ensure that flagellates were not observed outside the tissue.

References

- Amiel, A. R., Johnston, H., Chock, T., Dahlin, P., Iglesias, M., Layden, M., et al. (2017). A bipolar role of the transcription factor ERG for cnidarian germ layer formation and apical domain patterning. *Dev. Biol.* 430, 346–361. doi:10.1016/j.ydbio.2017.08.015
- Arendt, D. (2004). “Comparative aspects of gastrulation,” in *Gastrulation*. Editor C. D. Stern (London: University College London).
- Baillies, A., Collinet, C., Philippe, J. M., Lenne, P. F., Munro, E., and Lecuit, T. (2019). Genetic induction and mechanochemical propagation of a morphogenetic wave. *Nature* 572, 467–473. doi:10.1038/s41586-019-1492-9
- Brouzes, E., and Farge, E. (2004). Interplay of mechanical deformation and patterned gene expression in developing embryos. *Curr. Opin. Genet. Dev.* 14, 367–374. doi:10.1016/j.gde.2004.06.005
- Brunet, T., and King, N. (2017). The origin of animal multicellularity and cell differentiation. *Dev. Cell* 43, 124–140. doi:10.1016/j.devcel.2017.09.016
- Brunet, T., Bouclet, A., Ahmadi, P., Mitrossilis, D., Driquez, B., Brunet, A.-C., et al. (2013). Evolutionary conservation of early mesoderm specification by mechanotransduction in Bilateria. *Nat. Commun.* 4, 2821. doi:10.1038/ncomms3821
- Brunet, T., Larson, B. T., Linden, T. A., Vermeij, M. J. A., McDonald, K., and King, N. (2019). Light-regulated collective contractility in a multicellular choanoflagellate. *Science* 366, 326–334. doi:10.1126/science.aay2346
- Cavalier-Smith, T. (2017). Origin of animal multicellularity: precursors, causes, consequences—the choanoflagellate/sponge transition, neurogenesis and the cambrian explosion. *Philos. Trans. R. Soc. Lond. B Biol. Sci.* 372, 20150476. doi:10.1098/rstb.2015.0476
- De Robertis, E. M. (2008). Evo-devo: variations on ancestral themes. *Cell* 132, 185–195. doi:10.1016/j.cell.2008.01.003
- Desprat, N., Supatto, W., Pouille, P.-A., Beaupaire, E., and Farge, E. (2008). Tissue deformation modulates twist expression to determine anterior midgut differentiation in *Drosophila* embryos. *Dev. Cell* 15, 470–477. doi:10.1016/j.devcel.2008.07.009
- dos Reis, M., Thawornwattana, Y., Angelis, K., Telford, M. J., Donoghue, P. C., and Yang, Z. (2015). Uncertainty in the timing of origin of animals and the limits of precision in molecular timescales. *Curr. Biol.* 25, 2939–2950. doi:10.1016/j.cub.2015.09.066
- Dobrovinski, K., Swan, M., Polyakov, O., and Wieschaus, E. F. (2017). Measurement of cortical elasticity in *Drosophila melanogaster* embryos using ferrofluids. *Proc. Natl. Acad. Sci. U. S. A.* 114, 1051–1056. doi:10.1073/pnas.1616659114
- Evren, S., Wen, J. W., Luu, O., Damm, E. W., Nagel, M., and Winklbauer, R. (2014). EphA4-dependent Brachyury expression is required for dorsal mesoderm invagination in the *Xenopus* gastrula. *Development* 141, 3649–3661. doi:10.1242/dev.111880
- Fairclough, S. R., Chen, Z., Kramer, E., Zeng, Q., Young, S., Robertson, H. M., et al. (2013). Premetazoan genome evolution and the regulation of cell differentiation in the choanoflagellate *Salpingoeca rosetta*. *Genome Biol.* 14, R15. doi:10.1186/gb-2013-14-2-r15
- Farge, E. (2003). Mechanical induction of Twist in the *Drosophila* foregut/stomodaeal primordium. *Curr. Biol.* 13, 1365–1377. doi:10.1016/s0960-9822(03)00576-1
- Farge, E. (2013). Mechano-sensing in embryonic biochemical and morphologic patterning: Evolutionary perspectives in the emergence of primary organisms. *Biol. Theory* 8, 232–244. doi:10.1007/s13752-013-0119-x
- Fernandez-Gonzalez, R., Simoes Sde, M., Roper, J. C., Eaton, S., and Zallen, J. A. (2009). Myosin II dynamics are regulated by tension in intercalating cells. *Dev. Cell* 17, 736–743. doi:10.1016/j.devcel.2009.09.003
- Fernandez-Sanchez, M. E., Brunet, T., Roper, J. C., and Farge, E. (2015). Mechanotransduction's impact in animal development, evolution, and tumorigenesis. *Annu. Rev. Cell Dev. Biol.* 31, 373–397. doi:10.1146/annurev-cellbio-102314-112441
- Fritzenwanker, J. H., Genikhovich, G., Kraus, Y., and Technau, U. (2007). Early development and axis specification in the sea anemone *Nematostella vectensis*. *Dev. Biol.* 310, 264–279. doi:10.1016/j.ydbio.2007.07.029
- Haeckel, E. (1874). Die Gatræa-Theorie, die phylogenetische Klassifikation des Tierreiches und Homologie der Keimblätter. *Jena. Z. Naturwiss.* 8, 1–55.
- Hagos, E. G., and Dougan, S. T. (2007). Time-dependent patterning of the mesoderm and endoderm by Nodal signals in zebrafish. *BMC Dev. Biol.* 7, 22. doi:10.1186/1471-213X-7-22
- Isemura, M., Mita, T., Satoh, K., Narumi, K., and Motomiya, M. (1991). Myosin light chain kinase inhibitors ML-7 and ML-9 inhibit mouse lung carcinoma cell attachment to the fibronectin substratum. *Cell Biol. Int. Rep.* 15, 965–972. doi:10.1016/0309-1651(91)90146-a
- King, N., Young, S. L., Abedin, M., Carr, M., and Leadbeater, B. S. (2009). Starting and maintaining *Monosiga brevicollis* cultures. *Cold Spring Harb. Protoc.* 2009, pdb.prot5148. doi:10.1101/pdb.prot5148
- Kovacs, M., Toth, J., Hetenyi, C., Malnasi-Csizmadia, A., and Sellers, J. R. (2004). Mechanism of blebbistatin inhibition of myosin II. *J. Biol. Chem.* 279, 35557–35563. doi:10.1074/jbc.M405319200
- Kumburegama, S., Wijesena, N., Xu, R., and Wikramanayake, A. H. (2011). Strabismus-mediated primary archenteron invagination is uncoupled from Wnt/ β -catenin-dependent endoderm cell fate specification in *Nematostella vectensis* (Anthozoa, Cnidaria): Implications for the evolution of gastrulation. *Evodevo* 2, 2. doi:10.1186/2041-9139-2-2
- Kusserow, A., Pang, K., Sturm, C., Hrouda, M., Lentfer, J., Schmidt, H. A., et al. (2005). Unexpected complexity of the Wnt gene family in a sea anemone. *Nature* 433, 156–160. doi:10.1038/nature03158
- Leclerc, L., Bause, M., Sinigaglia, C., Steger, J., and Rentzsch, F. (2016). Development of the aboral domain in *Nematostella* requires β -catenin and the opposing activities of Six3/6 and Frizzled5/8. *Development* 143, 1766–1777. doi:10.1242/dev.120931
- Leininger, S., Adamski, M., Bergum, B., Guder, C., Liu, J., Laplante, M., et al. (2014). Developmental gene expression provides clues to relationships between sponge and eumetazoan body plans. *Nat. Commun.* 5, 3905. doi:10.1038/ncomms4905
- Magie, C. R., Daly, M., and Martindale, M. Q. (2007). Gastrulation in the cnidarian *Nematostella vectensis* occurs via invagination not ingression. *Dev. Biol.* 305, 483–497. doi:10.1016/j.ydbio.2007.02.044
- Merle, T. (2018). *Conservation entre Cnidaires et Bilatériens d'une voie mécanosensible induisant la formation de l'endomesoderme*. Paris: Sorbonne Université. PhD Thèse de doctorat.
- Mitrossilis, D., Roper, J. C., Le Roy, D., Driquez, B., Michel, A., Menager, C., et al. (2017). Mechanotransductive cascade of Myo-II-dependent mesoderm and endoderm invaginations in embryo gastrulation. *Nat. Commun.* 8, 13883. doi:10.1038/ncomms13883
- Morize, P., Christiansen, A. E., Costa, M., Parks, S., and Wieschaus, E. (1998). Hyperactivation of the folded gastrulation pathway induces specific cell shape changes. *Development* 125, 589–597. doi:10.1242/dev.125.4.589
- Muncie, J. M., Ayad, N. M. E., Lakins, J. N., Xue, X., Fu, J., and Weaver, V. M. (2020). Mechanical tension promotes formation of gastrulation-like nodes and patterns mesoderm specification in human embryonic stem cells. *Dev. Cell* 55, 679–694 e11. doi:10.1016/j.devcel.2020.10.015
- Nance, J., Munro, E. M., and Priess, J. R. (2003). *C. elegans* PAR-3 and PAR-6 are required for apicobasal asymmetries associated with cell adhesion and gastrulation. *Development* 130, 5339–5350. doi:10.1242/dev.00735
- Newman, S. A. (2020). Cell differentiation: What have we learned in 50 years? *J. Theor. Biol.* 485, 110031. doi:10.1016/j.jtbi.2019.110031
- Nguyen, N. M., Merle, T., Broders, F., Brunet, A. C., Batistella, A., Sarron, F., et al. (2020). Evolutionary emergence of first animal organisms triggered by environmental mechano-biochemical marine stimulation. *BiorXiv*. (Online preprint). doi:10.1101/2020.12.03.407668v1
- Ossipova, O., Kim, K., and Sokol, S. Y. (2015). Planar polarization of Vangl2 in the vertebrate neural plate is controlled by Wnt and Myosin II signaling. *Biol. Open* 4, 722–730. doi:10.1242/bio.201511676
- Park, E., Hwang, D. S., Lee, J. S., Song, J. I., Seo, T. K., and Won, Y. J. (2012). Estimation of divergence times in cnidarian evolution based on mitochondrial protein-coding genes and the fossil record. *Mol. Phylogenet. Evol.* 62, 329–345. doi:10.1016/j.ympev.2011.10.008
- Pouille, P.-A., Ahmadi, P., Brunet, A.-C., and Farge, E. (2009). Mechanical signals trigger Myosin II redistribution and mesoderm invagination in *Drosophila* embryos. *Sci. Signal.* 2, ra16. doi:10.1126/scisignal.2000098
- Prants, S. V., Uleysk, M. Y., and Budyanskiy, M. V. (2018). Lagrangian analysis of transport pathways of subtropical water to the primorye coast. *Dokl. Earth Sc.* 481, 1099–1103. doi:10.1134/s1028334x18080329
- Pukhlyakova, E., Aman, A. J., Elsayad, K., and Technau, U. (2018). β -Catenin-dependent mechanotransduction dates back to the common ancestor of Cnidaria and Bilateria. *Proc. Natl. Acad. Sci. U. S. A.* 115, 6231–6236. doi:10.1073/pnas.1713682115

- Reyes-Rivera, J., Wu, Y., Guthrie, B. G. H., Marletta, M. A., King, N., and Brunet, T. (2022). Nitric oxide signaling controls collective contractions in a colonial choanoflagellate. *Curr. Biol.* 32, 2539–2547 e5. doi:10.1016/j.cub.2022.04.017
- Roper, J. C., Mitrossilis, D., Stirnemann, G., Waharte, F., Brito, I., Fernandez-Sanchez, M. E., et al. (2018). The major beta-catenin/E-cadherin junctional binding site is a primary molecular mechano-transducer of differentiation *in vivo*. *Elife* 7, e33381. doi:10.7554/eLife.33381
- Roth, S. (2004). “Gastrulation in other insects,” in *Gastrulation. From cells to embryo*. Editor C. D. STERN (London: University College London).
- Rottinger, E., Dahlin, P., and Martindale, M. Q. (2012). A framework for the establishment of a cnidarian gene regulatory network for “endomesoderm” specification: the inputs of β -catenin/TCF signaling. *PLoS Genet.* 8, e1003164. doi:10.1371/journal.pgen.1003164
- Ruiz-Trillo, I., and de Mendoza, A. (2020). Towards understanding the origin of animal development. *Development* 147. doi:10.1242/dev.192575
- Servetnick, M. D., Steinworth, B., Babonis, L. S., Simmons, D., Salinas-Saavedra, M., and Martindale, M. Q. (2017). Cas9-mediated excision of *Nematostella* brachyury disrupts endoderm development, pharynx formation and oral-aboral patterning. *Development* 144, 2951–2960. doi:10.1242/dev.145839
- Solnica-Krezel, L., and Sepich, D. S. (2012). Gastrulation: making and shaping germ layers. *Annu. Rev. Cell Dev. Biol.* 28, 687–717. doi:10.1146/annurev-cellbio-092910-154043
- Sousbie, T. (2011). The persistent cosmic web and its filamentary structure – I. Theory and implementation. *Mon. Notices Royal Astron. Soc.* 414 (1), 350–383. doi:10.1111/j.1365-2966.2011.18394.x
- Steinmetz, P. R. H., Aman, A., Kraus, J. E. M., and Technau, U. (2017). Gut-like ectodermal tissue in a sea anemone challenges germ layer homology. *Nat. Ecol. Evol.* 1, 1535–1542. doi:10.1038/s41559-017-0285-5
- Sweeton, D., Parks, S., Costa, M., and Wieschaus, E. (1991). Gastrulation in *Drosophila*: the formation of the ventral furrow and posterior midgut invaginations. *Development* 112, 775–789. doi:10.1242/dev.112.3.775
- Tada, M., Concha, M. L., and Heisenberg, C. P. (2002). Non-canonical Wnt signalling and regulation of gastrulation movements. *Semin. Cell Dev. Biol.* 13, 251–260. doi:10.1016/s1084-9521(02)00052-6
- Warner, J. F., Guerlais, V., Amiel, A. R., Johnston, H., Nedoncelle, K., and Rottinger, E. (2018). NvERTx: a gene expression database to compare embryogenesis and regeneration in the sea anemone *Nematostella vectensis*. *Development* 145 (17), 1–10. doi:10.1242/dev.162867
- Weiser, D. C., Row, R. H., and Kimelman, D. (2009). Rho-regulated myosin phosphatase establishes the level of protrusive activity required for cell movements during zebrafish gastrulation. *Development* 136, 2375–2384. doi:10.1242/dev.034892
- Wozniak, M. A., and Chen, C. S. (2009). Mechanotransduction in development: a growing role for contractility. *Nat. Rev. Mol. Cell Biol.* 10, 34–43. doi:10.1038/nrm2592
- Young, P. E., Pesacreta, T. C., and Kiehart, D. P. (1991). Dynamic changes in the distribution of cytoplasmic myosin during *Drosophila* embryogenesis. *Development* 111, 1–14. doi:10.1242/dev.111.1.1

Frontiers in Cell and Developmental Biology

Explores the fundamental biological processes of life, covering intracellular and extracellular dynamics.

The world's most cited developmental biology journal, advancing our understanding of the fundamental processes of life. It explores a wide spectrum of cell and developmental biology, covering intracellular and extracellular dynamics.

Discover the latest Research Topics

[See more](#) →

Frontiers

Avenue du Tribunal-Fédéral 34
1005 Lausanne, Switzerland
frontiersin.org

Contact us

+41 (0)21 510 17 00
frontiersin.org/about/contact

